NASA Conference Publication 2487
Part 3

Research in Natural Laminar Flow and Laminar-Flow Control

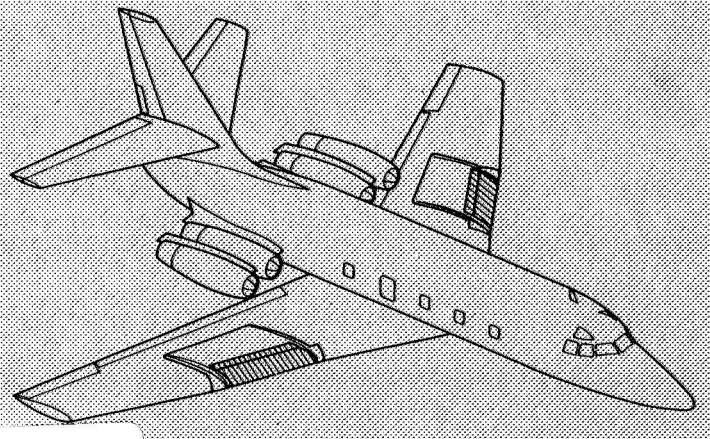

Proceedings of a symposium held at
Langley Research Center
Hampton, Virginia
March 16-19, 1987

Date for general release December 31, 1989

NASA

NASA Conference Publication 2487
Part 3

Research in Natural Laminar Flow and Laminar-Flow Control

Compiled by
Jerry N. Hefner and Frances E. Sabo
Langley Research Center
Hampton, Virginia

Proceedings of a symposium sponsored by the National Aeronautics and Space Administration and held at Langley Research Center Hampton, Virginia March 16–19, 1987

National Aeronautics and Space Administration

Scientific and Technical Information Division

1987

PREFACE

Since the mid 1970's, NASA, industry, and universities have worked together to conduct important research focused at developing laminar-flow technology that could reduce fuel consumption for general aviation, commuter, and transport aircraft by as much as 40 to 50 percent. This research, which was initiated under the NASA Aircraft Energy Efficiency Program and continued through the Research and Technology Base Program, has proved very successful with many significant and impressive results having been obtained.

This symposium was planned in view of the recent accomplishments within the areas of laminar-flow control and natural laminar flow and the potential benefits of laminar-flow technology to the civil and military aircraft communities in the United States. The symposium included technical sessions on advanced theory and design tool development, wind tunnel and flight research, transition measurement and detection techniques, low and high Reynolds number research, and subsonic and supersonic research.

CONTENTS

*Part 1 is presented under separate cover.

SESSION 3: ADVANCED STABILITY THEORY AND ITS APPLICATION
Chairman: D. M. Bushnell

Part 2*

SESSION 4: BASIC WIND TUNNEL RESEARCH/TECHNIQUES
Chairman: W. D. Harvey

*Part 2 is presented under separate cover.

Part 3

SESSION 6: ADVANCED AIRFOIL DEVELOPMENT
Chairman: J. W. Stickle

SESSION 7: FLIGHT RESEARCH EXPERIMENTS
Chairmen: T. G. Ayers and B. J. Holmes

SESSION 8: SUPERSONIC TRANSITION/LFC RESEARCH
Chairman: R. W. Barnwell

ATTENDEES

WILLIAM J. ALFORD, Jr.
DEI

TED AYERS
NASA-DFRF

JENNIFER L. BAER-RIEDHART
NASA-DFRF

WAYNE BALDWIN
AFWAL/FIMG

MARK J. BERGEE
LOCKHEED-CALIFORNIA COMPANY

SCOTT BERRY
ESC

MARK EUGENE BEYER
OMAC

S. BIRINGEN
UNIVERSITY OF COLORADO

JOHN BLASCOVICH
GRUMMAN CORPORATION

MICHAEL D. BONDY
NASA-DFRF

ALAN B. CAIN
McDONNELL DOUGLAS

GARY D. CARLSON
NASA-DFRF

FANG-JENG CHEN
HIGH TECHNOLOGY CORPORATION

RODNEY L. CLARK
AFWAL/FIMM

FAYETTE S. COLLIER
HIGH TECHNOLOGY CORPORATION

KENNETH C. CORNELIUS
LOCKHEED-GEORGIA CO.

EDWIN G. CHAPLIN
OMAC, INC.

S. DODBELE
VIGYAN

R. O. DODSON
BOEING

CO DONALDSON
TITAN ASSOCIATES

CORNELIUS DRIVER
EAGLE ENGINEERING, INC.

NABIL M. EL-HADY
ODU

DAVE ELLIS
CESSNA

JEANNE EVANS
TELEDYNE RYAN AERONAUTICAL

G. K. FAUST
GENERAL ELECTRIC

DAVID F. FISHER
NASA-AMES-DRYDEN

EDWARD A. GABRIEL
FAA

HEINZ A. GERHARDT
NORTHROP CORPORATION

DR. GERALD GREGOREK
OHIO STATE UNIVERSITY

SURESH GORADIA
VIRA

GLENN J. GRUBER
PRATT & WHITNEY

M. HUSSAINI
ICASE

DOUG HALL
NADC

PHIL HALL
ICASE

THORWALD HERBERT
VPI&SU

MICHAEL L. HINSON
GATES LEARJET CORP.

VENKIT S. IYER
VIGYAN RESEARCH ASSOC., INC.

LISA A. JENNETT
NASA-DRYDEN

JOSEPH B. JOHNSON
NASA-DRYDEN

M. JONES
PRC-KENTRON

CHANTAL JOUBERT
McDONNELL DOUGLAS CORP.

VIJAY KALBURGI
ODU

OSAMA KANDIL
ODU

ABRAHAM KAREM
LEADING SYSTEMS, INC.

K. KAUPS
DOULGAS AIRCRAFT CO.

EDWARD J. KERSCHEN
UNIVERSITY OF ARIZONA

MARK E. KIRCHNER
BOEING COMM. AIRPLANE CO.

MAX KLOTZCHE
DOUGLAS AIRCRAFT

MARTIN A KNUTSON
NASA-DRYDEN

THOMAS R. LACEY
McDONNELL AIRCRAFT CO.

ROY H. LANGE
LOCKHEED-GEORGIA CO.

SPIRO LEROUDIS
OFFICE OF NAVAL RESEARCH

JOHN O. LINDGREN
DOUGLAS AIRCRAFT CO.

GARY L. LINK
BOEING

T. M. LIU
ROHR INDUSTRIES, INC.

LAURENCE K. LOFTIN, JR.
SELF

W. K. LONDENBERG
GDS/FT. WORTH DIV.

WESLEY K. LORD
PRATT & WHITNEY

LESLIE M. MACK
JET PROPULSION LABORATORY

DR. MUJEEB MALIK
HIGH TECHNOLOGY CORPORATION

DONALD L. MALLICK
NASA-DRYDEN

SIVA M. MANGALAM
AS&M, INC.

MARK D. MAUGHMER
PENN STATE UNIVERSITY

FRED W. MAY
BOEING MILITARY AIRPLANE CO.

WILLIAM D. McCAULEY
TRW

BARNES W. McCORMICK
PENN STATE UNIVERSITY

DAVID E. MCNAY
DOUGLAS AIRCRAFT COMPANY

ROBERT R. MEYER
NASA-DRYDEN

LAWRENCE C. MONTOYA
NASA-DFRF

MARK V. MORKOVIN
ILLINOIS INSTITUTE OF TECH.

DR. THOMAS J. MUELLER
UNIVERSITY OF NOTRE DAME

PARMA MUNGUR
GENERAL ELECTRIC

JOHN W. MURDOCK
THE AEROSPACE CORPORATION

WILLIAM R. MURPHY
GULFSTREAM AEROSPACE CORP.

DEL NAGEL
BOEING

A. NAYFEH
VPI&SU

RON NEAL
BEECH AIRCRAFT

ORAN NICKS
TEXAS A&M

CLIFF OBARA
PRC-KENTRON

ARNOLD OTCHIN
TELEDYNE RYAN AERONAUTICAL

WILLIAM M. OTTO
OTTO LABORATORIES, INC.

PARESH PARIKH
VIRA, INC.

WILFRED E. PEARCE
DOUGLAS AIRCRAFT COMPANY

BRUCE PETERMAN
CESSNA

WERNER PFENNINGER
AS&M

DAVID PICKETT
BOEING MILITARY AIRPLANE CO.

DR. ARTHUR G. POWELL
DOUGLAS AIRCRAFT CO.

JOHN W. RAWLS, JR.
PRC-KENTRON

KENNETH H. ROGERS
DOUGLAS AIRCRAFT COMPANY

OLLIE J. ROSE
PRC-KENTRON

ROGER A. ROZENDAAL
BOEING COMM. AIRPLANE CO.

JIM RUNYAN
BOEING COMM. AIRPLANE CO.

DALLAS M. RYLE
LOCKHEED-GEORGIA COMPANY

F. CHRIS SAUTTER
PENN STATE UNIVERSITY

PAUL SHANG
NAVAL SHIP R&D CENTER

A. J. SMITH
SELF

GREGORY E. SMITH
DYNAMIC ENGINEERING, INC.

NORBERT F. SMITH
McDONNELL DOUGLAS

ROBERT J. STEWART
GULFSTREAM

DENNIS M. STRAUSSFOGEL
PENNSYLVANIA STATE UNIV.

G. TEMANSON
BOEING

BIANCA M. TRUJILLO
NASA-DRYDEN

CHANDRA S. VEMURU
AS&M, INC.

PAUL VIJGEN
UNIVERSITY OF KANSAS

SALLY WATSON-VIKEN
COMPLERE

GIUSEPPE VOLPE
GRUMMAN CORP. RES. CTR.

KENNETH B. WALKLEY
DYNAMIC ENGINEERING, INC.

RICHARD T. WHITCOMB
SELF

MICHAEL WUSK
ODU

LANGLEY RESEARCH CENTER ATTENDEES

RICHARD BARNWELL
HSAD

DENNIS BARTLETT
LSAD

DR. H. LEE BEACH
D/AERO

WILLIAM D. BEASLEY
TAD

IVAN E. BECKWITH
HSAD

PERCY J. BOBBITT
TAD

ALBERT L. BRASLOW
SELF

CUYLER W. BROOKS, JR.
TAD

DENNIS M. BUSHNELL
HSAD

RICHARD L. CAMPBELL
TAD

DEBRA CARRAWAY
IRD

A. M. CARY, JR.
HSAD

WILLIAM CORLETT
HSAD

THEODORE R. CREEL
HSAD

CINDY CROOM
LSAD

RAY DAGENHART
TAD

PAMELA DAVIS
SDD

RICHARD E. DAVIS
FED

DANIEL J. DICARLO
LSAD

SAM DOLLYHIGH
AVD

DOUGLAS DWOYER
HSAD

JAMES FERRIS
TAD

TOM FOUGHNER
TAD

DAVID HAHNE
LSAD

ROBERT HALL
TAD

JAMES HALLISSY
TAD

CHARLES D. HARRIS
TAK

JULIUS E. HARRIS
HSAD

ROY V. HARRIS, JR.
D/AERO

WILLIAM D. HARVEY
TAD

EARL C. HASTINGS
LSAD

JERRY N. HEFNER
AVD

TODD HODGES
MD

BRUCE HOLMES
LSAD

CHARLES JOHNSON
TAD

JOSEPH L. JOHNSON
LSAD

ROBERT A. JONES
HSAD

FRANK JORDAN
LSAD

PIERCE L. LAWING
TRAD

DAL V. MADDALON
LSAD

LUCIO MAESTRELLO
TAD

JACK MOLLOY
OFFICE OF D/AERO

GREGORY S. MANUEL
LSAD

ROBERT J. MCGHEE
TAD

JIM MEYERS
IRD

HARRY MORGAN
LSAD

C. E. K. MORRIS, JR.
AVD

SHELBY J. MORRIS
AVD

LEON MORRISETTE
HSAD

DAN MURRI
LSAD

RICHARD H. PETERSEN
DIRECTOR

PAM PHILLIPS
TAD

JAMES L. PITTMAN
HSAD

LAWRENCE E. PUTNAM
TAD

JAMES A. SCHOENSTER
AcoD

WILLIAM SEWALL
TAD

DAN SOMERS
TAD

JERRY SOUTH
OFFICE OF DIRECTOR

JOHN P. STACK
TAD

P. CALVIN STAINBACK
TAD

DAVID STEPHENS
AD

ERIC C. STEWART
LSAD

JOSEPH W. STICKLE
LSAD

H. PAUL STOUGH III
LSAD

HARRY A. VERSTYNEN, JR.
FAA

NICHOLAS G. VRETAKIS
AFSC LIAISON OFFICE

ED WAGGONER
TAD

RICHARD D. WAGNER
LSAD

BETTY S. WALKER
TAD

RALPH WATSON
HSAD

JOHN WHITCOMB
MD

RICHARD WOOD
HSAD

LONG YIP
LSAD

JAMES YOUNGBLOOD
SSD

TOM ZANG
HSAD

DESIGN OF THE LOW-SPEED NLF(1)-0414F AND THE HIGH-SPEED HSNLF(1)-0213 AIRFOILS WITH HIGH-LIFT SYSTEMS

J. K. Viken
Complere, Incorporated
Hampton, Virginia

S. A. Viken
Complere, Incorporated
Hampton, Virginia

W. Pfenninger
Analytical Services and Materials, Incorporated
Hampton, Virginia

H. L. Morgan, Jr. and R. L. Campbell
NASA Langley Research Center
Hampton, Virginia

[redacted]

OUTLINE

The Fluid Physics Branch (formerly Airfoil Aerodynamics Branch) at LaRC has been involved extensively in the design and testing of Natural Laminar-Flow (NLF) airfoils. The design of the NLF(1)-0414F was initiated in June of 1981 and completed in the summer of 1983 (ref. 1). This NLF airfoil was designed for low speed, having a low profile drag at high chord Reynolds numbers. When the wind tunnel experiment was completed in the spring of 1984 (ref. 2), a high lift system design for the NLF(1)-0414F was initiated.

The success of the low speed NLF airfoil work sparked interest in a high speed NLF airfoil applied to a single engine business jet with an unswept wing. Work began in the fall of 1984 on the two-dimensional airfoil design of HSNLF(1)-0213. The design of HSNLF(1)-0213 was conducted as a cooperative effort of several different groups at NASA LaRC with not only 2-D design but also extensive 3-D design and analysis of the wing's planform (ref. 3). Only the preliminary stages of the 2-D design will be discussed in the current paper (fig. 1). To make this single engine business jet successful, acceptable values of maximum lift had to be maintained to get the correct landing speed; therefore, work was also conducted on the 2-D flap design (ref. 4).

- Design of NLF(1)-0414F
- High lift system for NLF(1)-0414F
- Design of HSNLF(1)-0213
- High lift system for HSNLF(1)-0213

Figure 1

COMPARISON OF PRESSURE DISTRIBUTIONS OF NLF(1)-0414F AND NACA 67-314

NLF(1)-0414F was designed iteratively using analysis computer codes. After going through the design study and obtaining experimental results, it is interesting to look at the comparison and contrast of NLF(1)-0414F with a similar NACA 6-series airfoil (fig. 2). NACA 67-314 was generated, using ref. 5, for the same incompressible C_ℓ, at $\alpha = 0$, and maximum thickness as NLF(1)-0414F ($M = 0.4$ and $C_\ell = 0.461$). The favorable gradient regions are similar, although NLF(1)-0414F has slightly more acceleration on each surface. The upper surface acceleration of NLF(1)-0414F was optimized by the use of the flat spot in the pressure distribution at $x/c \approx 0.10$. The Tollmien-Schlichting (TS) disturbances are not amplified in this region, so the stabilizing effects of acceleration can be used further downstream when the TS disturbances are amplified. Concave type pressure recoveries are utilized on NLF(1)-0414F, while on the NACA 67-314, linear pressure recoveries are used. NLF(1)-0414F has a thicker, tailored leading edge than NACA 67-314. Also, a small chord trailing-edge (cruise) flap was utilized on NLF(1)-0414F and is crucial to the low drag performance.

In the summary of airfoil data (ref. 6), there is only one NACA 67-series airfoil, the NACA 67,1-215. There are no data above $R = 6 \times 10^6$, presumable because the higher Reynolds number data produced little laminar flow. There are some differences between the old NACA experiments and those conducted on NLF(1)-0414F which could make a difference on the performance of the two airfoils. The NACA tests were run with 2-foot chord models, which were at higher unit Reynolds numbers for the same chord Reynolds number as the 3-foot chord NLF(1)-0414F. Also the grit used to cause transition in the NACA tests was considerably larger and more extensive than needed to cause transition.

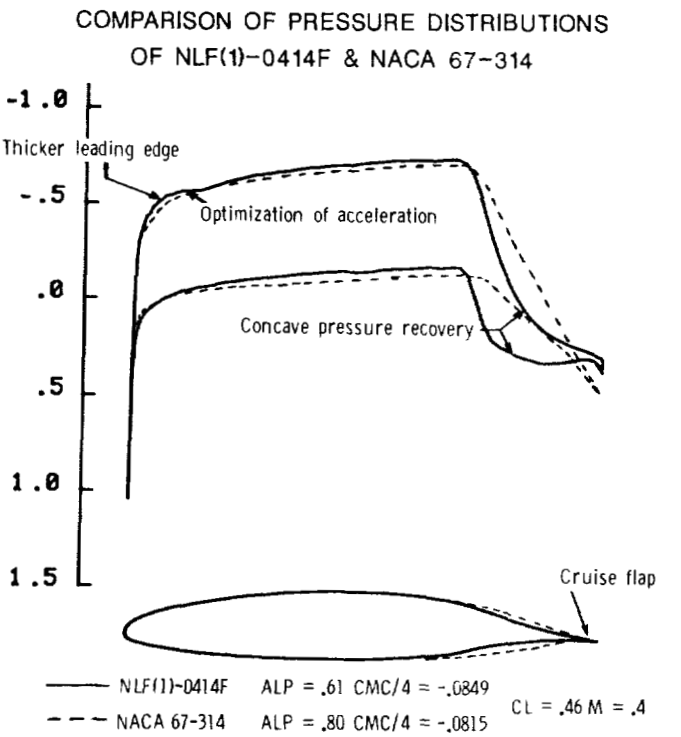
COMPARISON OF PRESSURE DISTRIBUTIONS
OF NLF(1)-0414F & NACA 67-314
-1.0
Thicker leading edge
-.5
Optimization of acceleration
.0
Concave pressure recovery
.5
1.0
1.5
Cruise flap
NLF(1)-0414F ALP = .61 CMC/4 = -.0849
NACA 67-314 ALP = .80 CMC/4 = -.0815
CL = .46 M = .4

Figure 2

NLF(1)-0414F DESIGN OBJECTIVES

The first and primary objective of the design project was to design a Natural Laminar-Flow (NLF) airfoil, for low speed applications that achieved significantly lower profile drag coefficients at cruise than existing NLF airfoils, but was still practical to use (fig. 3). This resulted in an exercise to design an airfoil with as extensive favorable gradients $(dp/dx < 0)$ as seemed practical without making the far aft pressure recoveries too severe. The airfoil was also designed for reasonably high chord Reynolds numbers, approximately 10 million.

To help lessen the severity of the far aft pressure recoveries with respect to separation, concave type pressure recoveries were utilized. A concave pressure recovery decelerates the flow when the boundary layer has the most energy, tapering the gradient of the deceleration downstream on the airfoil as the boundary loses energy. For off-design conditions, the possibility of utilizing boundary layer re-energizers or momentum redistributors was also examined as a means of alleviating the problem of turbulent separation in the pressure recovery.

To improve $C_{\ell_{max}}$ performance, a thicker leading edge was utilized than is normally considered for airfoils with such extensive laminar flow operating at such high chord Reynolds numbers. It was known that this thick leading edge would limit the low drag C_ℓ range on the bare airfoil with premature negative pressure peaks; however, the chance of a leading-edge type stall would be reduced. Also, Pfenninger's earlier work (ref. 7) showed that the use of a small chord simple trailing-edge flap could be used to regain a respectable low drag C_ℓ range. Deflection of this small chord flap, both positively and negatively, allows the conversion of lift due to angle of attack into lift due to flap deflection. By changing the lift at the design angle of attack, favorable gradients can be maintained on both surfaces simultaneously for a relatively wide range of lift coefficients.

When designing configurations for maximum cruise performance, one is inevitably led to flying as close to $(L/D)_{max}$ as possible. This means increasing the wing loading and results in the need for greater maximum lift coefficients. The NLF(1)-0414F was designed with the intent of integrating it with a slotted Fowler flap arrangement and possibly even a Krueger flap to achieve high maximim lift coefficients.

NLF (1)-0414F DESIGN OBJECTIVES

- 70% chord natural laminar flow (NLF) on both surfaces at Re_c = 10 million
- Compromise some low drag C_l range (at $\delta_f = 0°$) to improve $C_{l_{max}}$ performance by thickening the leading edge
- Increase low drag C_l range with a small chord trailing edge flap
- Implement concave pressure recovery to reduce the turbulent separation problem when transition occurs far forward on the airfoil. Also, possibly use some form of boundary layer re-energization or momentum redistribution
- Use of boundary-layer trips (tape, grit, bleed air, etc.) to eliminate laminar separation at lower Reynolds numbers, both in the rear pressure recovery and at the leading edge at high angles of attack
- Implementation of an efficient high lift system: slotted Fowler flaps and possibly a Krueger flap

Figure 3

LAMINAR BOUNDARY-LAYER STABILITY ANALYSIS

The first stage in the design was to conduct a linear stability analysis in the favorable pressure gradient region to check for the attainability of the 70% chord laminar flow. On a high Reynolds number NLF airfoil, enough acceleration is needed to attain the desired growth in TS disturbances. This acceleration essentually requires a geometry increase along the chord. Unfortunately, this increase is not the only consideration. The leading edge needs to be thick enough for acceptable C_{ℓ} max performance; however, the maximum thickness cannot be too great because of pressure recovery considerations.

A linear stability analysis was conducted on the inviscid pressure distribution (ref. 8) for the upper surface of NLF(1)-0414F at the design conditions $M = 0.4$, $C_{\ell} = 0.461$ and $R = 10 \times 10^6$ (fig. 4). The velocity profiles were calculated using the Kaups and Cebeci finite-difference code (ref. 9) and the TS amplification was calculated using the SALLY code (ref. 10). The design criterion for NLF(1)-0414F for maximum logarithmic amplification (n) was in the range of 9 to 10. The analyzed disturbance frequencies of 3000-3500 Hz were in this maximum amplified range. The locally higher growths after 70% chord are from the increased instability at the beginning of the steep pressure recovery.

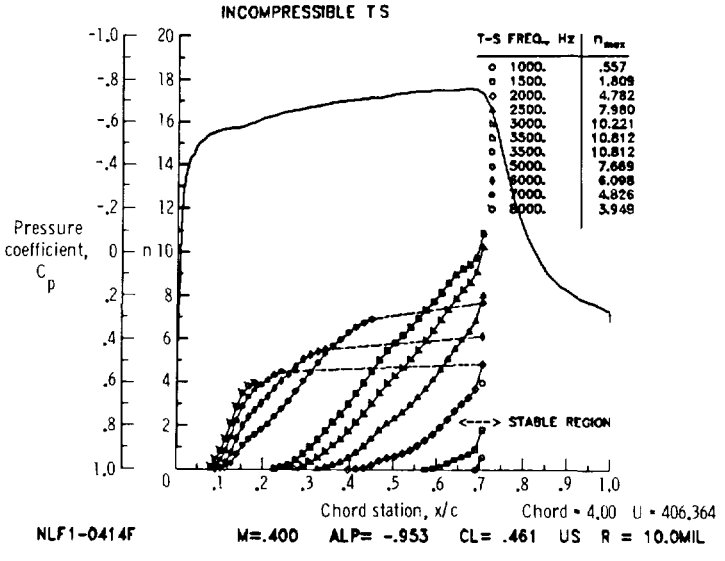

Figure 4

INCOMPRESSIBLE TS STABILITY ANALYSIS WITH UPPER SURFACE MEASURED TRANSITION LOCATIONS

Shown in figure 5 are three cases analyzed for TS amplification up to transition on the experimental data of the NLF(1)-0414F in the Langley Low-Turbulence Pressure Tunnel. These cases were for the upper surface at C_ℓ's ranging from 0.409-0.513. Correlating linear stability theory with transition data, n factors in the range of 11-12 were calculated for the three cases at $M \approx .12$ and $R = 10 \times 10^6$.

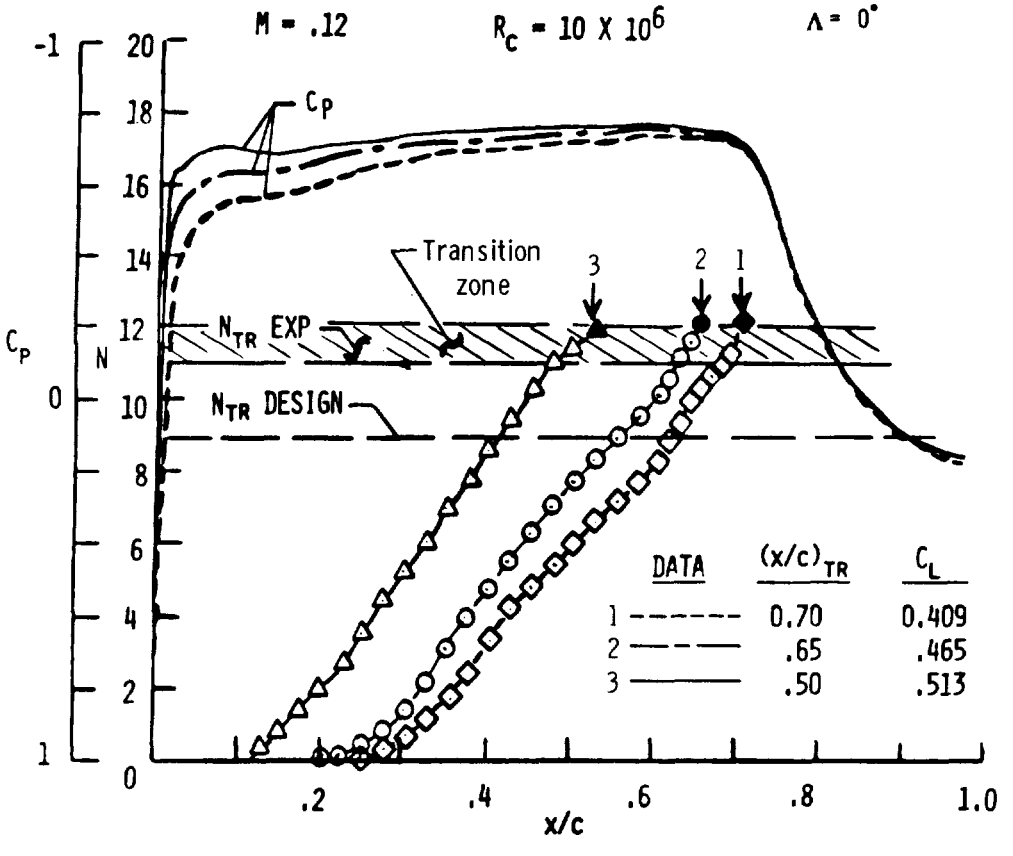

Figure 5

NLF(1)-0414F TURBULENT PRESSURE RECOVERY

The next step in the design process was to reduce the problem of turbulent separation in the pressure recovery when transition occurred near the leading edge. The energy deficient turbulent boundary layer has to have enough energy to negotiate a steep aft pressure recovery. The first route in designing the turbulent pressure recovery was to make it concave in nature, $\frac{d^2p}{dx^2} < 0$. This type of recovery decelerates the flow most at first when the boundary layer becomes more and more energy deficient. The pressure recovery was tailored using the growth in shape factor $H = \delta^*/\theta$. Schubauer and Spangenberg (ref. 11) found that for incompressible turbulent boundary layers the shape factor grows to a value of 2.0 at separation. Using the inviscid pressure distribution and the Harris finite-difference boundary layer code (ref. 12), the growth of H was tailored through the pressure recovery. To get a gradual progression of separation at off design conditions, H should grow continuously to a maximum value at the trailing edge. The H distribution in the pressure recovery for NLF(1)-0414F in figure 6 shows the shape factor growing to a maximum value of 1.9 at x/c = 0.875 with a slight decrease to 1.825 at the trailing edge. It was felt that this offered some margin for down cruise flap deflections and was left as is.

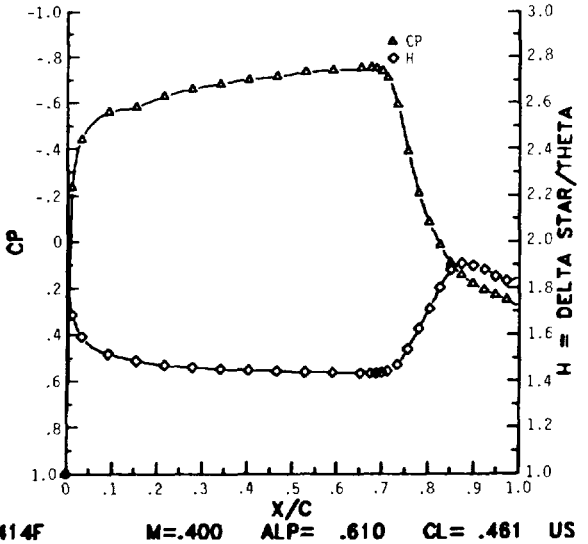

NLF1-0414F M=.400 ALP= .610 CL= .461 US R = 10.0MIL
FULLY TURBULENT

Figure 6

NACA 67-314 TURBULENT PRESSURE RECOVERY

Figure 7 shows the turbulent boundary layer analysis on the upper surface inviscid pressure distribution of the NACA 67-314 airfoil. The points shown represent the results of the boundary-layer solutions, and because of separation, the pressure distribution does not continue to the trailing edge. For the same conditions as NLF(1)-0414F ($M = 0.4$, $C_\ell = 0.461$, and $R = 10 \times 10^6$), turbulent boundary-layer separation occurred at $x/c = 0.90$ in the linear pressure recovery. The last correct solution calculated H to be at a value of 1.83.

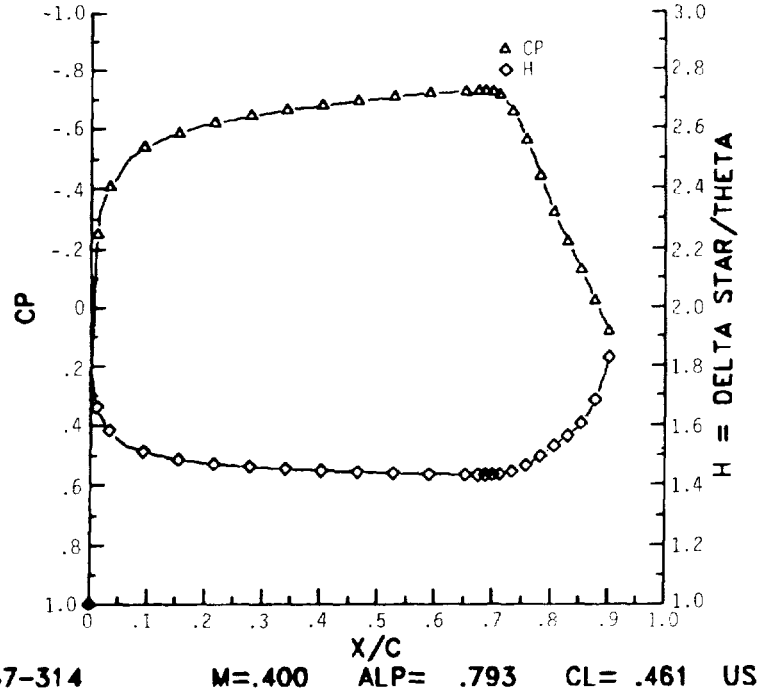

NACA 67-314 M=.400 ALP= .793 CL= .461 US R = 10.0MIL
FULLY TURBULENT

Figure 7

COMPARISON OF AIRFOIL LEADING EDGES

Extensive work was conducted in the design of the leading edge of the NLF(1)-0414F. Early in the design process a sharp leading-edge airfoil, DESB159 (fig. 8), was implemented to achieve an acceptable low drag C_ℓ range at $\delta_f = 0°$. In the low drag range, this sharp leading edge helps suppress leading-edge negative pressure peaks. However, at high angles of attack this sharp leading edge causes large negative pressure peaks as a result of the centripetal forces $C_p \approx \frac{V^2}{R}$ needed to turn the air molecules around the corner. To obtain the leading edge of NLF(1)-0414F, thickness was superimposed on the airfoil profile merging with DESB159 at $x/c = 0.15$-0.20. Then the leading edge was tailored to reduce the negative pressure peaks. The design philosophy was to turn the flow when the velocity was low, allowing a smaller radius of curvature. The radius of curvature was then increased as the velocities grew. On both the DESB159 and NACA 67-314 profiles, the smallest radius of curvature is at the leading edge, where the smallest radius of curvature on the NLF(1)-0414F profile is on the lower surface.

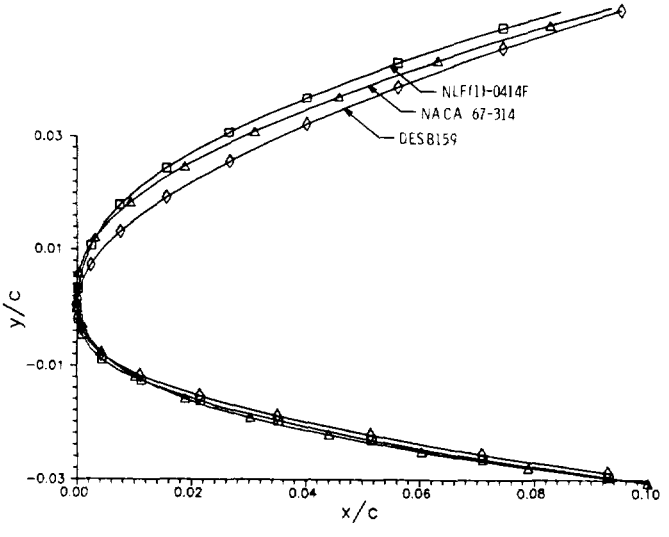

Figure 8

COMPARISON OF INVISCID $C_{p_{min}}$

Figure 9, which is a plot of the inviscid $C_{p_{min}}$ as a function of C_ℓ shows how successful this tailoring of the leading edge was. At an inviscid C_ℓ of 1.8, NLF(1)-0414F had a $C_{p_{min}}$ of -8.5 as compared with a $C_{p_{min}}$ of -11.4 on DESB159. At an inviscid C_ℓ of 2.7, NLF(1)-0414F had a $C_{p_{min}}$ of -21.2 as compared with a $C_{p_{min}}$ of -30.3 for DESB159. The free-stream Mach number was 0.10.

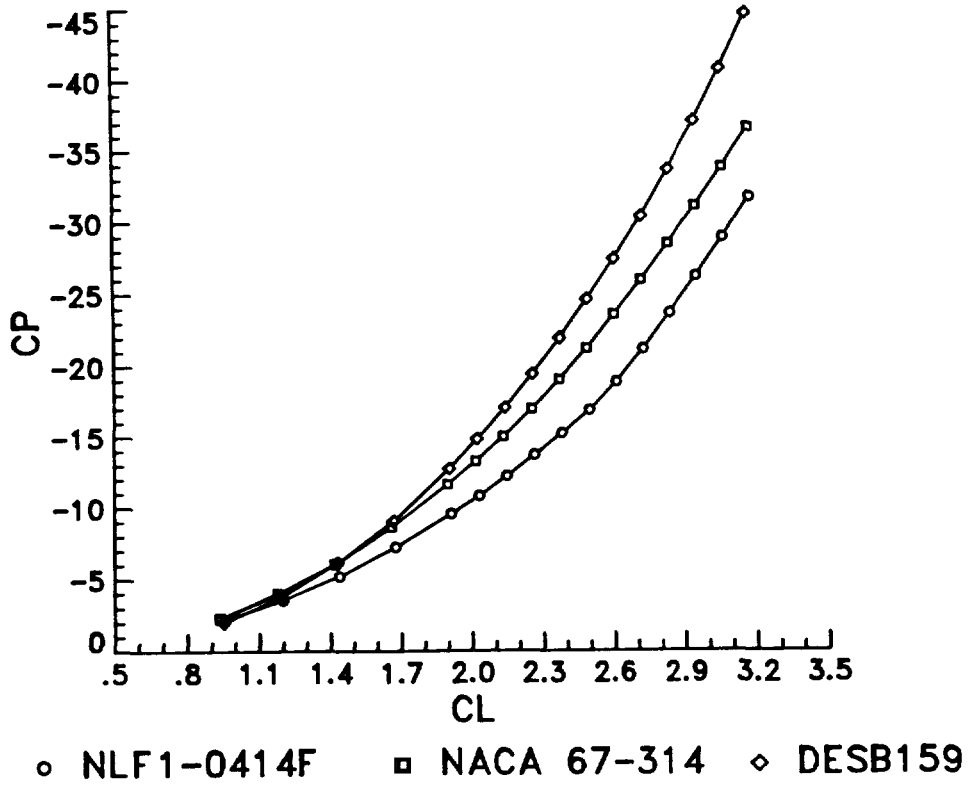

Figure 9

CRUISE FLAP DEFLECTION

Figure 10 illustrates the movement of the 12.5% chord cruise flap of NLF(1)-0414F deflection from -10° to 12.5°. The use of the cruise flap was crucial with the implementation of the thickened leading edge to achieve an acceptable C_ℓ range with low drag. The deflection of the cruise flap allows lift due to angle of attack to be converted into lift due to flap deflection by loading or unloading the aft section of the airfoil. With the use of this flap, different C_ℓ's can be achieved while still keeping the stagnation point near the leading edge and thereby keeping favorable gradients over the airfoil for a wide range of conditions.

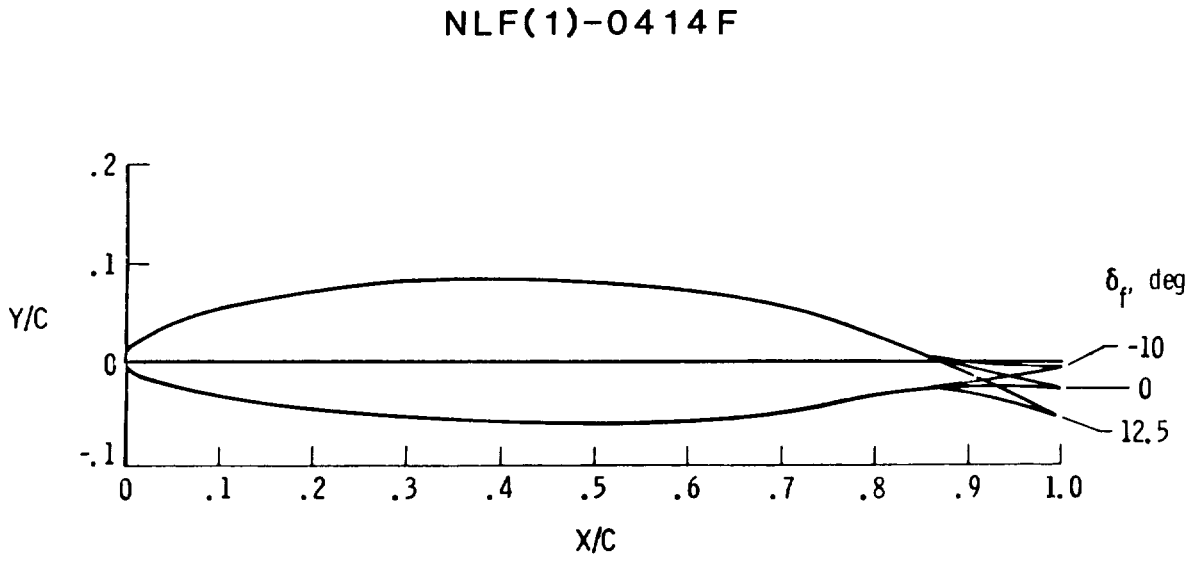

Figure 10

DRAG POLAR WITH FLAP DEFLECTION

The drag polar of NLF(1)-0414F (fig. 11), at $R = 10 \times 10^6$ for $\delta_f = -10°$ to 12.5°, reflects the success of achieving a wide low drag C_ℓ range with the use of the cruise flap. At $\delta_f = 0°$ there was a very narrow low drag C_ℓ range with the very bottom of the bucket having a $C_{d_{min}}$ of 0.0027 at $C_\ell = 0.41$. With a negative 10 degree flap deflection, the minimum drag was 0.0030 at $C_\ell = 0.01$. With a cruise flap deflection of 12.5°, the minimum profile drag was 0.0033 at a C_ℓ of 0.81 yielding a L/D of 245. The use of the cruise flap yields an overall low drag C_ℓ range of 0.80 at the high design chord Reynolds number of 10×10^6.

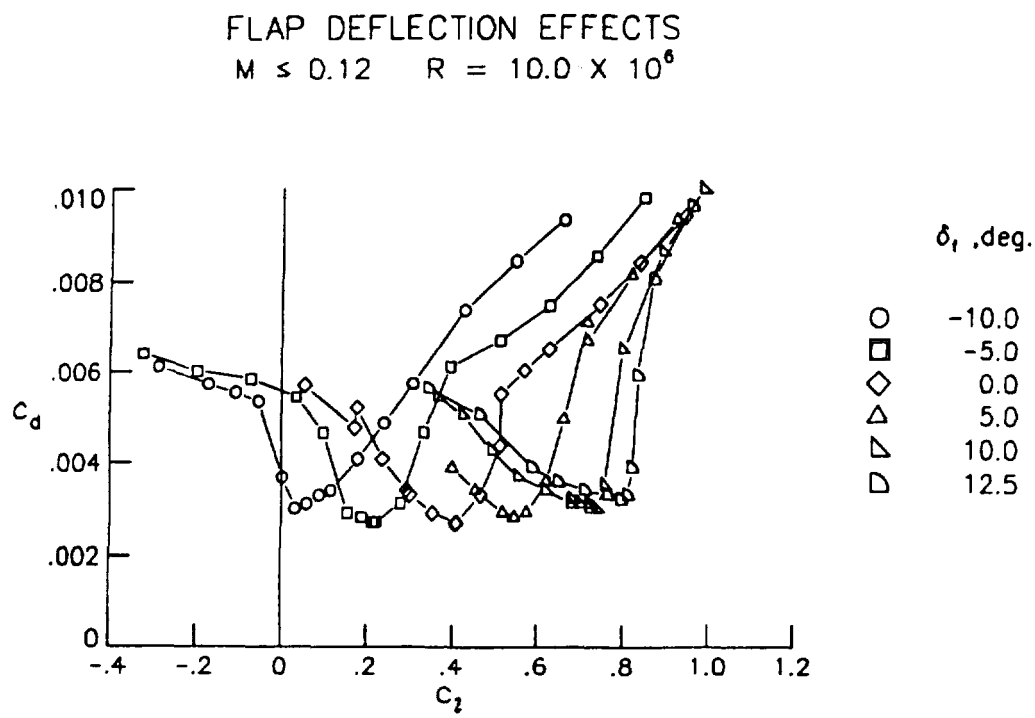

Figure 11

EXPERIMENTAL/THEORETICAL PRESSURE DATA AT DESIGN CONDITIONS

A comparison of the experimental pressure distribution of NLF(1)-0414F at $M = 0.4$, $R = 10 \times 10^6$, and $\alpha = -1°$ is compared with the theoretical pressure distribution calculated by the Korn-Garabedian potential flow analysis in figure 12. There are favorable gradients on both surfaces up to the 70% chord location. The steep concave pressure recoveries of NLF(1)-0414F are also illustrated. There is a flat spot in the upper surface pressure distribution at $x/c = 0.15$. This resulted from the addition of thickness in the leading-edge region to improve $C_{\ell_{max}}$ performance. Results from the Tollmien-Schlichting boundary-layer stability analysis showed that this flat spot in the pressure distribution yielded a smaller disturbance growth than with a continuous acceleration in this region.

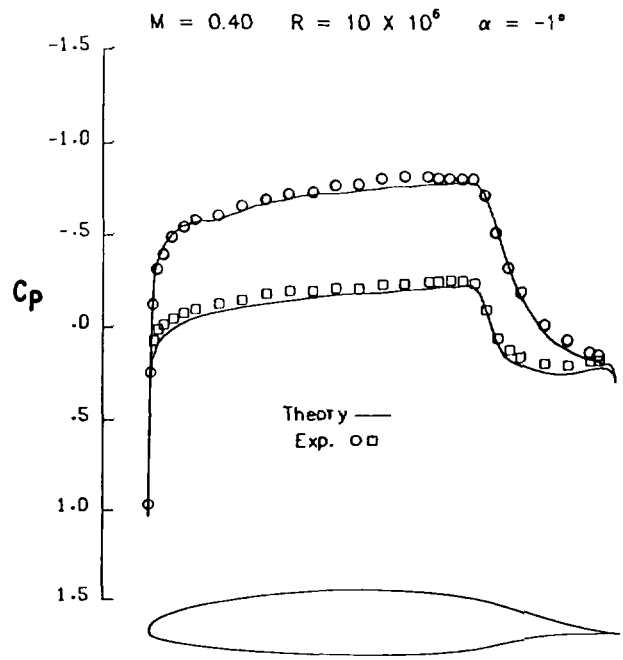

Figure 12

SECTION CHARACTERISTICS OF NLF(1)-0414F

The section characteristics of NLF(1)-0414F at a chord Reynolds number of 10 million and $\delta_f = 0°$ are shown in figure 13. The minimum profile drag coefficient was 0.0027 at $C_\ell = 0.41$. This profile drag is only 38% that of an unseparated fully turbulent airfoil. The maximum lift coefficient is 1.83 at $\alpha = 18.0°$. With transition fixed at the leading edge the lift curve essentially repeated with $C_{\ell_{max}}$ still 1.81. The pitching moment curve is unaffected with fixed transition. With the flow fully turbulent, the minimum profile drag coefficient is 0.0083, which is equal to that of normal unseparated turbulent airfoils.

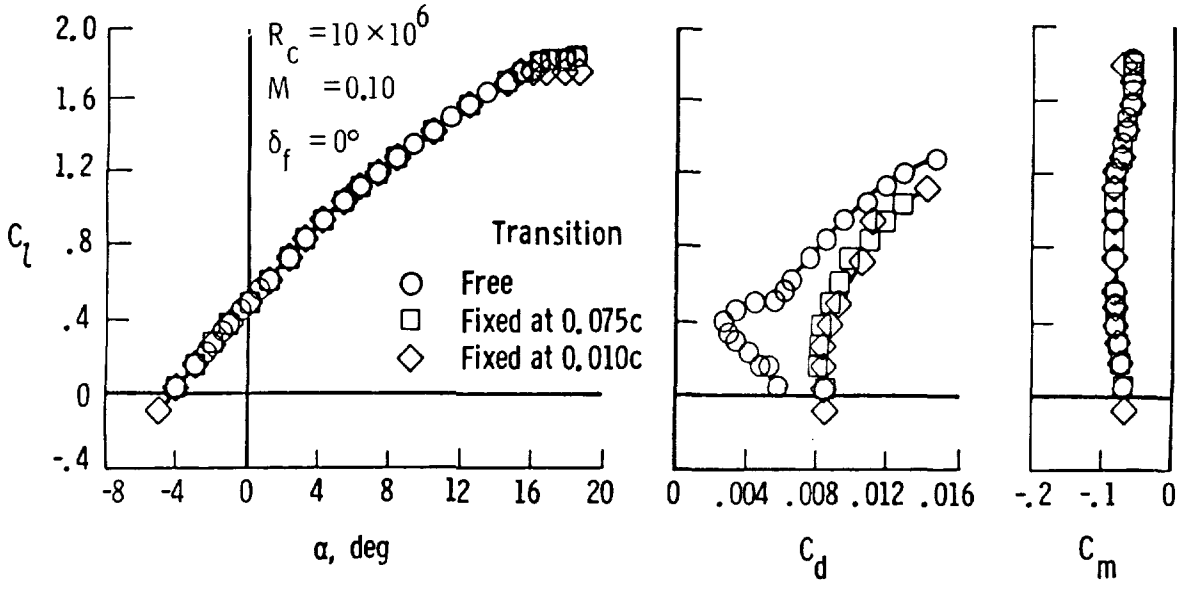

Figure 13

COMPARISON OF GA AIRFOILS

Figure 14 is a comparison of the low drag bucket of NLF(1)-0414F with other NASA and NACA general aviation (GA) airfoils at $R = 6 \times 10^6$. The low drag bucket of NLF(1)-0414F represents the envelope of low drag buckets achieved with deflection of the cruise flap from -10° to 20°. Also, the NLF(1)-0215F airfoil's low drag bucket is the envelope of performance of the deflection of a cruise flap from -10° to 10°. This figure shows the much lower profile drag coefficients possible with the NLF(1)-0414F. The large increase in profile drag of the NLF(1)-0414F outside the low drag bucket at the higher C_ℓ's is a result of the steep aft pressure recoveries.

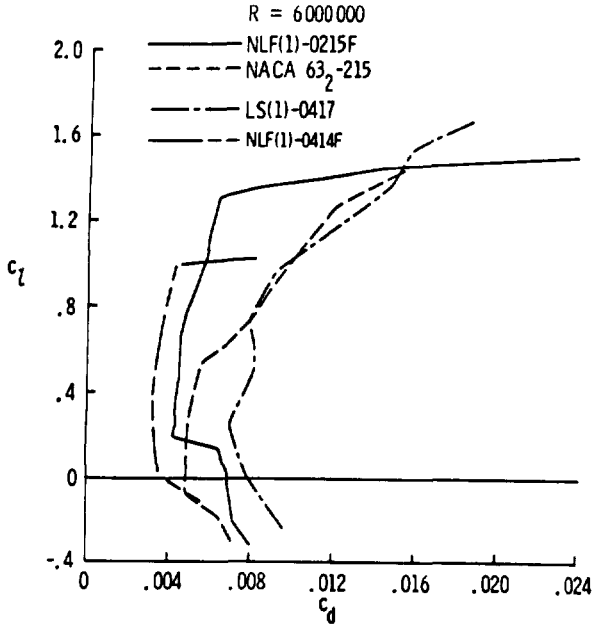

Figure 14

MULTI-ELEMENT HIGH-LIFT SYSTEM FOR NLF(1)-0414F

A multi-element high-lift flap system has been theoretically designed for the NLF(1)-0414F airfoil at a chord Reynolds number of 3 million and a free-stream Mach number of 0.15. The geometry consists of a main element, single-slotted Fowler flap or double-slotted Fowler flap (which retracts to form the single-slotted flap contour), and a Krueger flap. Both the leading- and trailing-edge high-lift systems have been integrated in a manner that still retains the action of a small chord trailing-edge cruise flap and implements as much as possible the original exterior profile contour of the NLF airfoil (fig. 15).

The main element has a chord of 0.896 with respect to the NLF airfoil chord of 1.0. The NLF contour is maintained over the entire extent of the upper surface, while on the lower surface, 70 percent of the contour is maintained before the cove region. Therefore, the 70 percent chord laminar-flow run on the upper and lower surface obtainable in the cruise condition is not disturbed.

The 28.1 percent chord single-slotted Fowler flap incorporates 10 percent of the airfoil's upper surface and 24 percent of the lower surface. The flap was designed not to exceed 30 percent of the airfoil's chord when it was retracted because the gap or step might cause transition.

The double-slotted Fowler flap was designed under the constraint that it would have the same outer contour as the single-slotted flap when retracted. The vane has a 15.81 percent chord, while the rear flap has a 16.52 percent chord (both based on the airfoil chord of 1.0).

The 17.67 percent chord Krueger flap (based on the NLF(1)-0414F chord of 1.0) was designed so that when retracted into the main element, 49.3 percent of the Krueger flap's upper surface would fare into the leading-edge lower surface of the NLF(1)-0414F. With a carefully designed sealed joint the flow should not be tripped turbulent.

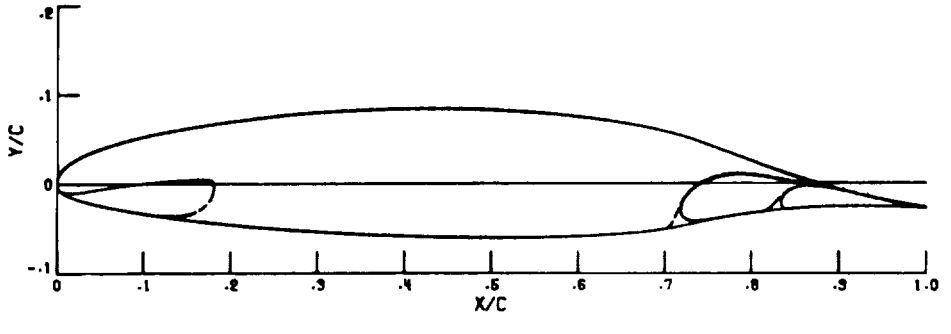

Figure 15

NLF(1)-0414F WITH SINGLE-SLOTTED
FOWLER FLAP

The high lift performance for the two element system (main element and single-slotted Fowler flap) was analyzed using the potential flow multi-element analysis (MCARF ref. 13) code at $M = 0.15$, $\alpha = 7°$, and $\delta_f = 29°$, with an inviscid $C_\ell = 3.570$ and $C_{m_{C/4}} = -0.6082$ (fig. 16). The flap has a gap/c = 0.011 and overlap/c = 0.033 (relative to the main axis system). The total pressure rises calculated on the main element and flap upper surface were 88.05 percent q_{max} and 84.90 percent q_{max}, respectively. The Harris code was used to calculate the boundary-layer development on the MCARF inviscid pressure distributions at a chord Reynolds number of 3 million, with transition set slightly ahead of the $C_{p_{min}}$. The flow was calculated to stay attached to the trailing edge on the upper surface of the main element and separate at x/c = 0.704 on the lower surface (the beginning of the cove region). On the upper surface of the flap, 36.67 percent flap chord separation was calculated with a pressure rise of 66.53 percent q_{max}.

SINGLE-SLOTTED FOWLER FLAP PRESSURE DISTRIBUTION

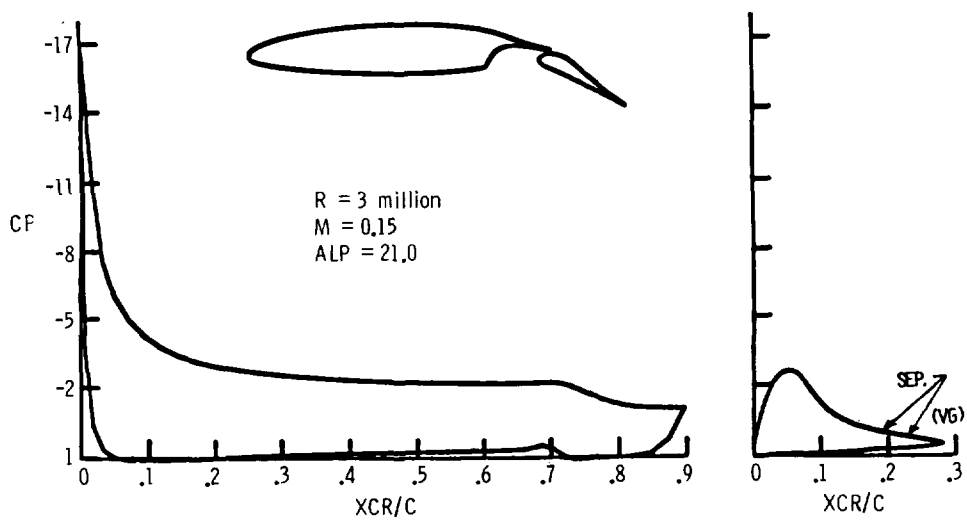

Figure 16

NLF(1)-0414F WITH KRUEGER FLAP AND DOUBLE-SLOTTED FOWLER FLAP

The high lift performance for the multi-element system [Krueger flap, main element (10° flipper flap deflection), and double-slotted Fowler flap] at $M = .15$, $\alpha = 21°$, $\delta_k = -55.4°$, $\delta_{VF} = 34.4°$, and $\delta_{RF} = 45.7°$, with an inviscid $C_\ell = 6.627$ and $C_{m_{C/4}} = -0.4055$ is shown in figure 17. The Krueger flap has a gap/c = 0.10 and overlap/c = 0.005, the vane has a gap/c = 0.018 and overlap/c = 0.033, and the rear flap has a gap/c = 0.014 and overlap/c = 0.008 (relative to the main axis system). The total pressure rises calculated on the Krueger flap, main element, vane, and rear flap upper surface were 81.67 percent q_{max}, 82.44 percent q_{max}, 84.77 percent q_{max}, and 84.90 percent q_{max}, respectively. The Harris code was used to calculate the boundary-layer development on the MCARF inviscid pressure distributions at a chord Reynolds number of 3 million, with transition set slightly ahead of the $C_{p_{min}}$. On the Krueger flap upper surface, 11.61 percent flap chord separation was calculated with a pressure rise of 63.38 percent q_{max}. For the main element upper surface, 5.91 percent main chord separation was calculated with a pressure rise of 79.35 percent q_{max}. The flow was calculated to separate at $x/c = 0.708$ on the main element lower surface. On the upper surface of the vane, 28.98 percent vane chord separation was calculated with a pressure rise of 40.10 percent q_{max}. The flow on the lower surface of the vane was calculated to separate in the cove region at $x/c = 0.944$. For the rear flap upper surface, 34.64 percent flap chord separation was calculated with a pressure rise of 63.24 percent q_{max}.

DOUBLE-SLOTTED FOWLER & KRUEGER FLAP PRESSURE DISTRIBUTION

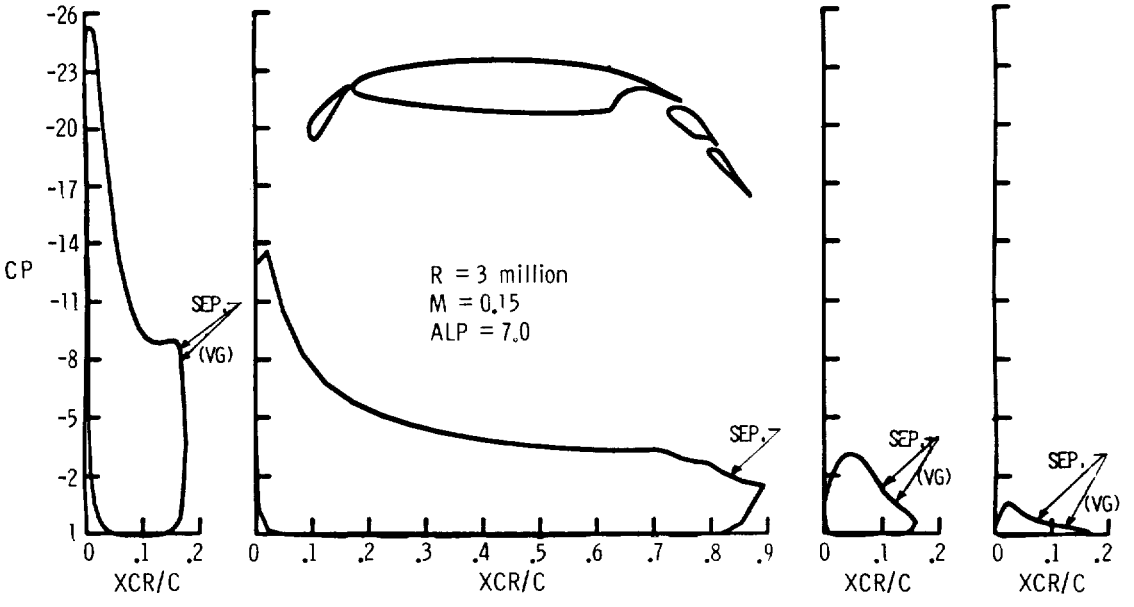

Figure 17

MAXIMUM LIFT POSSIBILITIES WITH NLF(1)-0414F MULTI-ELEMENT HIGH-LIFT SYSTEM

The NLF(1)-0414F airfoil can obtain a $C_{\ell_{max}}$ of 1.624 at a chord Reynolds number of 3 million. Estimations using inviscid pressure distributions at $R = 3 \times 10^6$ and finite-difference boundary layer calculations indicate very respectable maximum lift coefficients possible. For the cases analyzed, leading-edge negative pressure peaks were kept above C_p sonic (velocity below sonic), with overall inviscid pressure rises of 80-85% q_{max}. An analysis was also made to check for a leading-edge type stall using Horton's method (ref. 14). The results of these calculations indicated that leading-edge laminar separation bubbles would be short in nature, and the boundary layer would reattach for all cases. The multi-element high-lift system configurations designed from the NLF airfoil contour are shown in figure 18 which compare their relative performance with the baseline airfoil. The C_ℓ's are calculated from inviscid pressure distributions that were iterated with an integral boundary layer. No account has been made for separation.

The large negative C_p peaks and the corresponding steep adverse gradients caused during high angles of attack with large deflections bring about a separation problem. The flap placement, as well as the geometry, have distinct effects on the airfoil system as a whole. The effects help the turbulent boundary layer overcome a greater overall pressure rise than it would on a profile with the same outer contour without a slot. The flap must be placed such that the circulation of the main element reduces its leading-edge negative pressure peak at high angles of attack. Also, the flap's circulation should interact upon the main element to reduce the overall pressure rise by increasing the velocity field near the trailing edge. A leading-edge device will reduce the negative pressure peak on the leading-edge region of the following element, and hence the total pressure rise of that element overall.

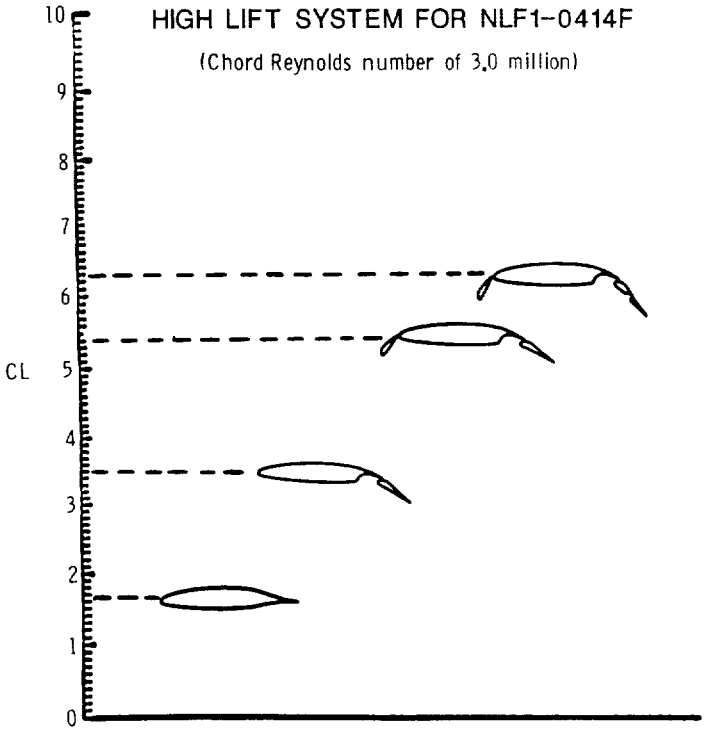
HIGH LIFT SYSTEM FOR NLF1-0414F
(Chord Reynolds number of 3.0 million)
CL
10
9
8
7
6
5
4
3
2
1
0

Figure 18

LOW-SPEED AIRFOIL SUMMARY

Figure 19 summarizes the results of the work on the 2-D profile, of the NLF(1)-0414F. Extensive work was conducted to make a high chord Reynolds number airfoil with low profile drag, while still making it practical to use. The NLF(1)-0414F at $R = 10 \times 10^6$ achieved a minimum profile drag coefficient of 0.0027 at $C_\ell = 0.41$. There was only a penalty in profile drag when transition occurred near the leading edge. The NLF(1)-0414F achieved a very respectable $C_{\ell_{max}}$ of 1.83. At worst, the NLF(1)-0414F is as good as a high Reynolds number turbulent flow airfoil except in the range of $C_\ell \approx 0.80$-1.2. The profile drags in this range are high because at these conditions the boundary layer can no longer make the turbulent pressure recovery. An experiment needs to be conducted on the high-lift system to verify the design and complete the basic work of making the NLF(1)-0414F a complete airfoil.

- Validated design theory for low-speed NLF(1)-0414F airfoil concept
- Achieved 70% chord NLF on both surfaces at design M = 0.4, $R_C = 10 \times 10^6$ in LTPT; total drag reduced 66% compared with turbulent airfoil
- Achieved wide low drag C_l range (C_l = 0 to 0.81) at high R_C with deflected 0.125C simple flap; L/D = 245 at C_l = 0.81
- Achieved $C_{l\ max}$ higher than expected; 1.83 with $\delta_f = 0°$ and 2.7 with 0.20C split flap ($\delta_f = 60°$). Achieved docile stall conditions
- Demonstrated that performance ($C_{l\ max}$ and pitch) essentially unchanged with fixed transition near leading edge with drag penalty compared to good turbulent airfoil
- Correlated linear boundary layer stability theory for design N-factor TS disturbances
- Multi-element high-lift system designed with a possibility of $C_{l\ max} > 6.0$ for the Krueger flap, main element, and double-slotted flap configuration

Figure 19

DESIGN CONSIDERATIONS FOR COMPRESSIBLE AIRFOIL DESIGN:
HSNLF(1)-0213

The HSNLF(1)-0213 was an airfoil designed for $M_\infty = 0.70$, $C_\ell = 0.25$, and $R = 11 \times 10^6$ for application to a single-engine business jet with no sweep. The design considerations for a compressible airfoil design (fig. 20) are modified somewhat from that of the incompressible case. In compressible flow the laminar boundary layer is much more stable than in the incompressible case, so not as much acceleration is needed. Also as lift increases, overall acceleration increases instead of negative pressure peaks forming at the leading edge. This gives a wider low drag C_ℓ range. However, with this added acceleration, the recovery region becomes more of a problem when transition occurs far forward. Acceleration in the favorable gradients can quickly develop into shocks at higher than design C_ℓ's and Mach numbers.

COMPRESSIBLE AIRFOIL DESIGN (NO SWEEP)

- Laminar boundary layer more stable in compressible flow than in the incompressible case - not as much accceleration needed
- Acceleration is not lost on upper surfaces as lift increases
- Turbulent pressure recovery more critical because flow accelerates to higher velocities than in incompressible case
- Watch for shock development in the acceleration

Figure 20

HSNLF(1)-0213 DESIGN PROCESS

As seen in figure 21, the camber and thickness of NLF(1)-0414F cause too much acceleration on the upper surface. The design of the high-speed airfoil had to be conducted rather hastily, so the easiest way to take out camber was to unload the airfoil by a negative deflection of the cruise flap. The resultant pressure distribution is shown in figure 22 at $M_\infty = 0.70$ with the 12.5% chord simple flap deflected -5.24°. This de-cambering was successful in reducing the upper surface velocities and the extent of the supersonic region, but there still was a steep aft pressure recovery. At a chord Reynolds number of 11 million with fully turbulent flow, analysis with the Harris program predicted separation in the aft pressure recovery for all of a series of possible recoveries. The next step in the design process was to redesign the upper surface, moving the start of the pressure recovery to $x/c = 0.55$ and flattening the pressure recovery. In the process, the overall thickness of the airfoil was reduced from 14% chord to 13% chord. The resultant airfoil is shown by the dotted line in figure 22.

EFFECT OF MACH NUMBER ON PRESSURE DISTRIBUTION OF NLF(1)-0414F

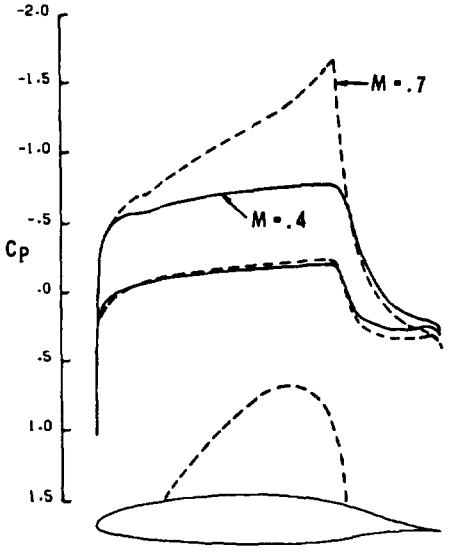

Figure 21

EFFECT OF MACH NUMBER ON PRESSURE DISTRIBUTION OF NLF(1)-0414F

Some of the problems of using a low speed airfoil at high speed Mach numbers are illustrated in figure 21. The pressure distributions of NLF(1)-0414F are shown at $M = 0.4$ and $M = 0.7$. The $M = 0.7$ case accelerates strongly to the 70% chord location and terminates in a shock with a very steep aft pressure recovery. The supersonic zone is shown by the dotted line on top of the profile geometry. Note the negligible change in lower surface pressure coefficients between the two Mach numbers.

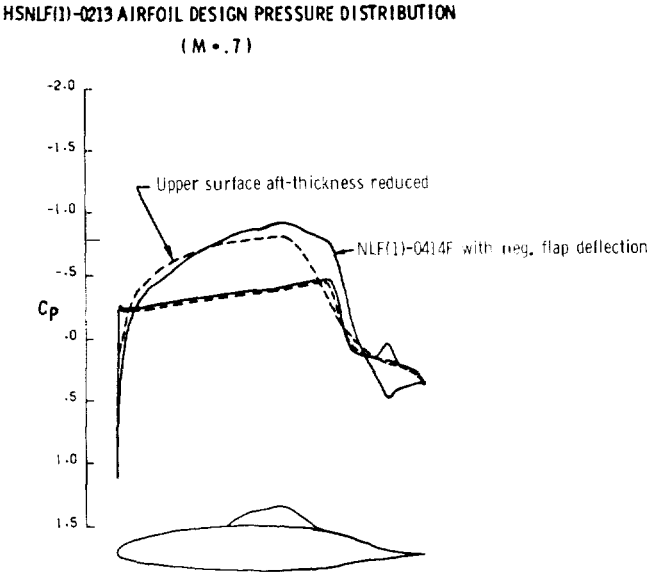

Figure 22

COMBINATION DESIGN FOR HSNLF(1)-0213

Figure 23 represents the pressure distribution at M = 0.70, C_ℓ = 0.25, and R = 11 × 10^6, for the final contour of HSNLF(1)-0213 compared to the NLF(1)-0414F airfoil with a -5.24° cruise flap deflection. The small leading-edge negative pressure peak was smoothed out from that shown in figure 22 in order to achieve the final contour of the HSNLF(1)-0213 airfoil.

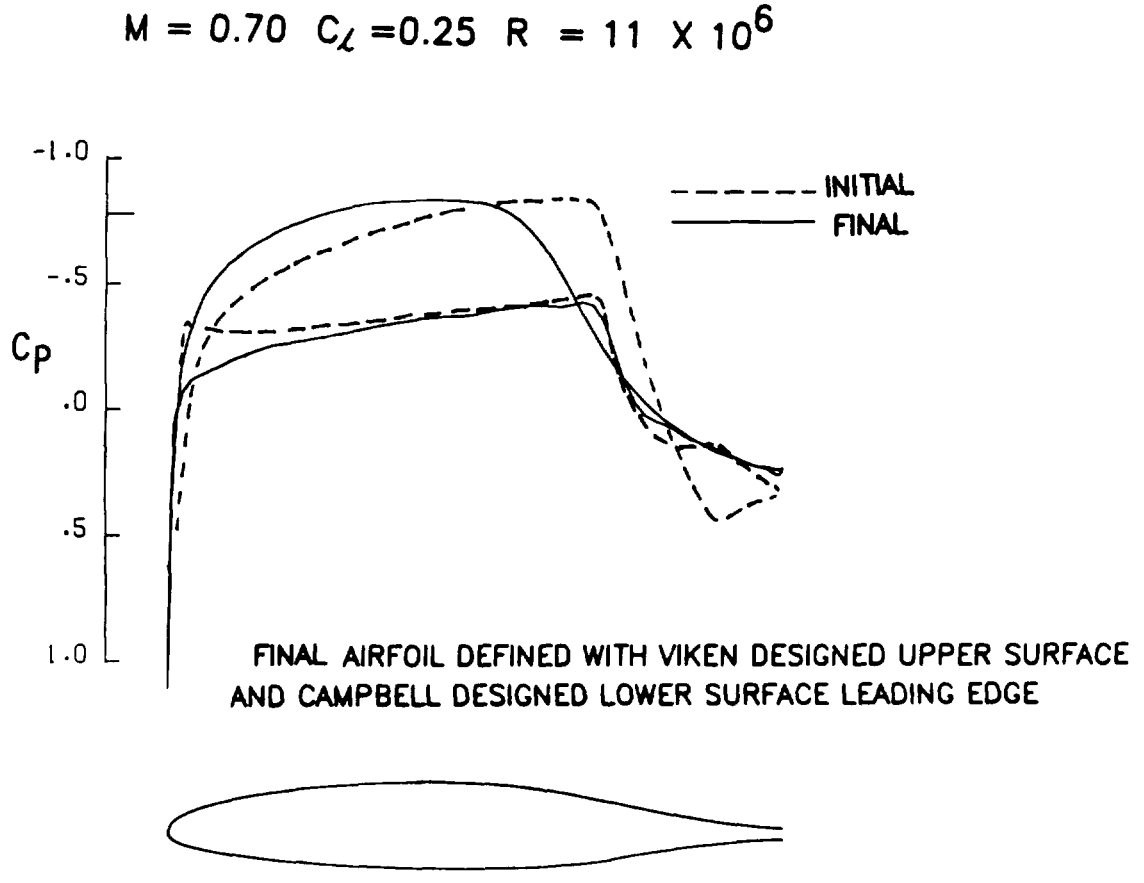

Figure 23

COMPRESSIBLE STABILITY ANALYSIS FOR HSNLF(1)-0213

The results of the compressible Tollmien-Schlichting analysis (ref. 15) for the upper surface of the HSNLF(1)-0213 at $M = 0.7$, $C_\ell = 0.26$, and $R = 10 \times 10^6$ are shown in figure 24. For the range of frequencies analyzed, the disturbances do not even start to grow until $x/c = 0.37$, and the maximum logarithmic amplification back to the laminar separation point is $n = 1.69$. This growth in TS disturbances is very small compared to the value of approximately $n = 9$ needed for transition. Therefore, TS disturbances should not cause transition in the accelerated region. This airfoil was designed for unswept applications. With sweep, care must be taken that cross-flow disturbances do not cause transition in the strong accelerated regions of the airfoil.

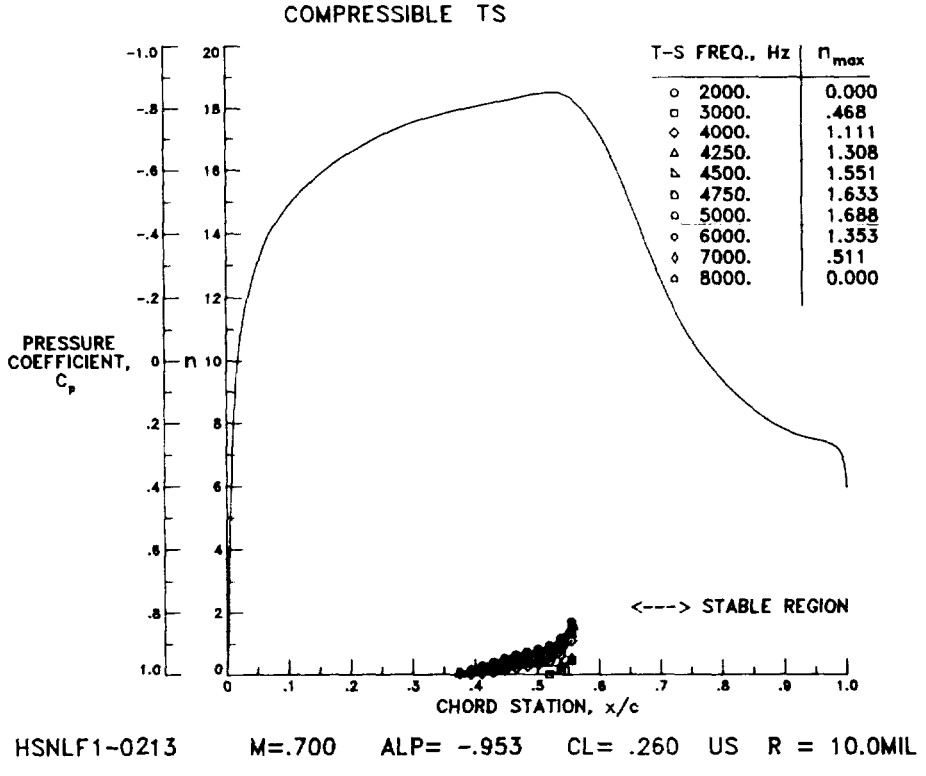

Figure 24

SINGLE-SLOTTED FLAP DESIGNS FOR HSNLF(1)-0213 AIRFOIL

The length of the structural wing box for most high speed general-aviation and transport aircraft is nominally 50 percent of the local wing chord and is positioned with 20 percent of the chord forward of the wing box available for leading-edge devices and 30 percent aft available for trailing-edge devices. For the HSNLF(1)-0213, an additional 2 percent immediately aft of the wing box was allowed for structural interface with a flap actuation system resulting in a nested trailing-edge flap chord length of 28 percent of the total wing chord. After establishing the basic chord length of the flap, the design of the flap contour became a matter of determining the upper and lower surface cutoff points on the main element and then determining the coordinates of the flap forward of the cutoff points. The cutoff point on the lower surface was set at 74 percent chord on the main element which was as far aft as possible to insure a smooth pressure recovery through the slot region between the flap and main elements. The selection of the upper surface cutoff point was not as simple. It was desirable to move the cutoff point as far as possible to increase the effective chord with the flap extended which should produce greater maximum lift. The primary disadvantage to moving the cutoff point aft is that the maximum thickness and leading-edge camber of the flap must be reduced to obtain an acceptable structural thickness in the trailing edge of the main element. The reduction in thickness and camber will most likely result in a reduction in maximum obtainable lift. During this design study upper-surface cutoff points at 88, 92, 96, and 98 percent of the main element chord were analyzed to determine the maximum obtainable lift. The flap geometries corresponding to the four cutoff points are presented in figure 25.

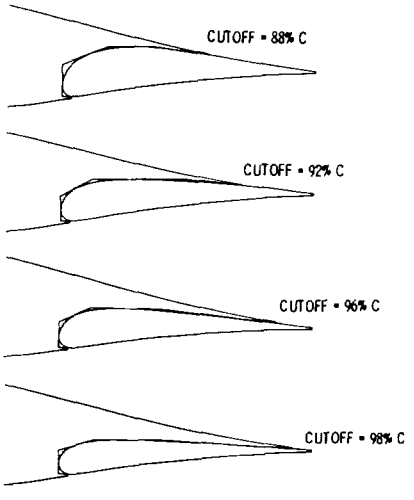

Figure 25

COMPARISON OF GEOMETRIES AND PRESSURE DISTRIBUTIONS
FOR SINGLE-SLOTTED HSNLF(1)-0213 FLAP DESIGNS

The performance of each of the four flap designs with various cutoff locations on the main element was determined using the NASA Multi-Component Airfoil Analysis (MCARF) computer program. The flap designs were analyzed for flap deflections of 35 and 40 degrees with a 2-percent gap and 0-percent overlap between the flap and main elements. The Mach number was 0.1 and the Reynolds number was 4 million. For each case, a check for flap separation was also made by performing an ordinary turbulent boundary-layer analysis of the upper-surface flap pressure distribution. As shown in figure 26, the turbulent boundary-layer analysis of the flap pressure distributions of each flap design at 35 degrees deflection indicated that approximately 31, 21, and 17 percent of the upper surface of the flap was separated for the 88-, 96-, and 98-percent designs compared to 14 percent for the 92-percent design. The comparison of the geometries also shown in this figure shows that the 92-percent design is proportionally thicker aft of the maximum thickness point compared to the others which reduced the upper surface pressure recovery resulting in less separation and higher maximum lift.

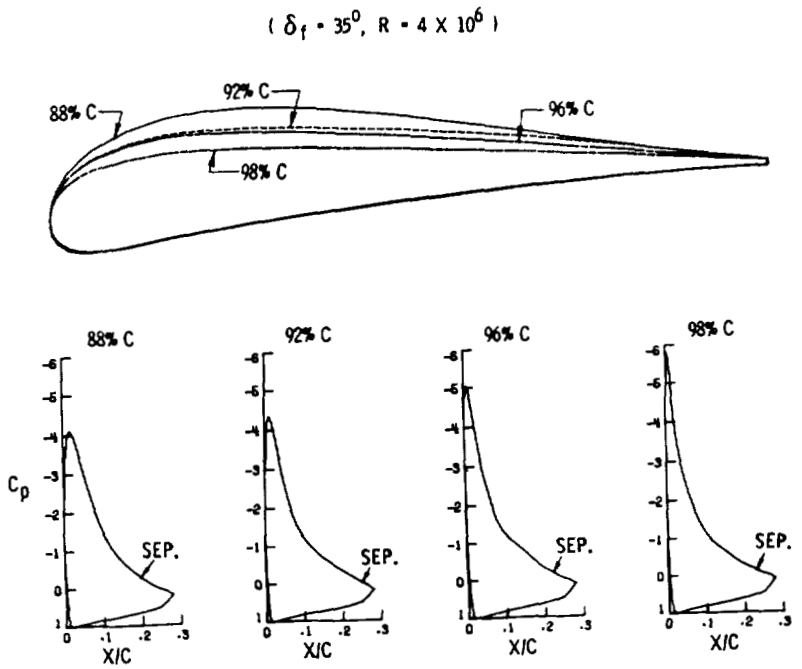

Figure 26

COMPARISON OF GEOMETRIES FOR SINGLE- AND DOUBLE-SLOTTED FLAPS FOR HSNLF(1)-0213 AIRFOIL

A double-slotted trailing-edge flap was also designed for the HSNLF(1)-0213 airfoil to provide an additional increment of lift. The vane, which is the forward flap element, had to be concealed in the cove region, and the aft-flap element had the same design constraints as that for the single-slotted flap design. The vane-flap combination was designed so that the vane remained in a fixed position relative to the aft-flap when deflected. A simple fixed external-hinge mechanism was proposed as the flap actuation device. A comparison of the finalized single- and double-slotted flap geometries is presented in figure 27. The vane element has a chord of 8 percent and the aft-flap a chord of 20.5 percent of the wing chord. The upper surface cutoff point on the main element was moved from 92 to 87 percent for the double-slotted design to allow for the passage of the vane element through the cove opening for flap deflections greater than 20 degrees. For flap deflections greater than 25 degrees, the lower surface trailing-edge deflector can be deflected upward into the cove approximately 15 degrees to improve the acceleration of the flow through the slot. The primary advantage of the double-slotted design is that the second slot allows for additional energization of the flap boundary layer which will further delay separation and increase the maximum obtainable lift.

DOUBLE- AND SINGLE-SLOTTED FLAPS FOR HSNLF(1)-0213 AIRFOIL

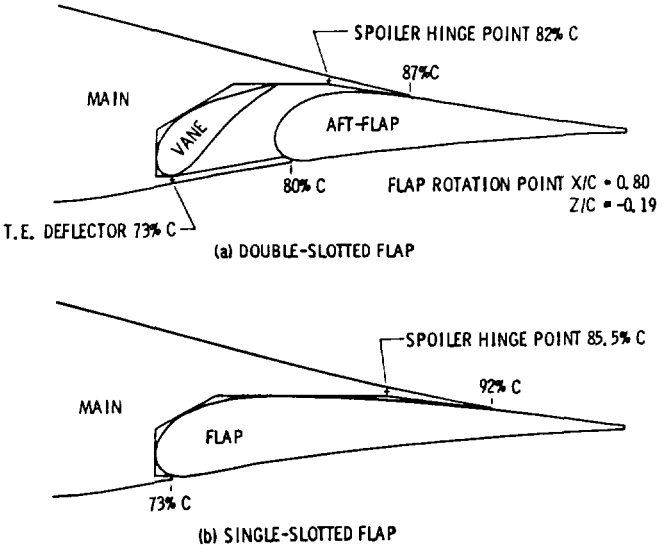

Figure 27

MAXIMUM LIFT PERFORMANCE OF HSNLF(1)-0213 WITH SINGLE- AND DOUBLE-SLOTTED FLAPS

The effect of Reynolds number on the maximum lift performance of the double-slotted flap at 55 degrees of deflection and the single-slotted flap at 40 degrees of deflection is presented in figure 28. The maximum lift values shown are based on separation of the leading-edge laminar boundary layer on the main element and do not include corrections for the effect of trailing-edge separation on the flap elements. These data show the tremendous effect of Reynolds number on the maximum lift obtainable for both types of flaps, especially at Reynolds numbers below 4 million. This trend is typical for Natural Laminar-Flow (NLF) airfoils that have small leading-edge radii which produce highly favorable pressure gradients at low angles of attack for large runs of laminar flow on both surfaces. At higher angles of attack near stall these small leading-edge radii produce rather highly unfavorable pressure gradients that are very sensitive to separation.

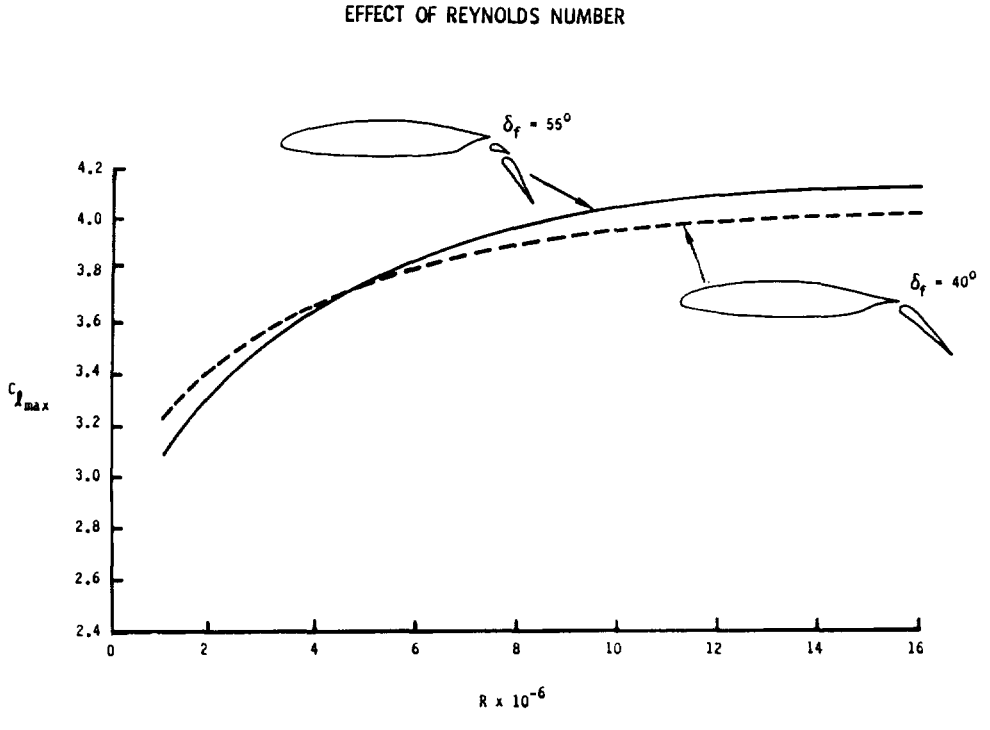

Figure 28

HSNLF(1)-0213 AIRFOIL SUMMARY

Figure 29 summarizes the work done on the 2-D airfoil design of the HSNLF(1)-0213. The airfoil was decambered by removing the aft loading; however, higher design Mach numbers are possible by increasing the aft loading and reducing the camber overall on the airfoil. This approach would also allow for flatter acceleration regions which are more stabilizing for cross-flow disturbances. Sweep could then be used to increase the design Mach number to a higher value also. There would be some degradation of high lift by decambering the airfoil overall, and this aspect would have to be considered in the final design.

SUMMARY

- Shock-free NLF airfoil designed for M = 0.70 and C_l = 0.26 for applications without sweep
- High-speed airfoil designed with favorable gradients back to 55% chord on upper surface and 65% chord on lower surface
- Linear stability analysis in the laminar boundary layer indicated that at the design point compressible Tollmien-Schlichting disturbances were not large enough to cause transition before laminar separation
- Upper surface turbulent pressure recovery optimized so that no separation occurred at design when transition occurred at the leading edge
- Single-slotted and double-slotted Fowler flap designs were optimized to get acceptable low-speed characteristics

Figure 29

REFERENCES

1. Viken, Jeffrey K.: Aerodynamic Considerations and Theoretical Results for a High Reynolds Number NLF Airfoil. Master's Thesis, George Washington University, January 1983.

2. McGhee, Robert J.; Viken, Jeffrey K.; Pfenninger, Werner; Beasley, William D.; and Harvey, William D.: Experimental Results for a Flapped NLF Airfoil with High Lift/Drag Ratio. NASA TM-85788, May 1984.

3. Waggoner, Edgar G.; Campbell, Richard L.; Phillips, Pamela S.; and Viken, Jeffrey K.: "Computational Design of Natural Laminar Flow Wings for Transonic Application", Langley Symposium on Aerodynamics, Volume I, NASA CP-2397, pp. 415-444. April 1985.

4. Morgan, Harry L.: "High Lift Flaps for Natural Laminar Flow Airfoils", Laminar Flow Aircraft Certification, NASA CP-2413, April 1985, pp. 31-66.

5. Ladson, Charles L., and Brooks, Cuyler W., Jr.: Development of a Computer Program to Obtain Ordinates for NACA 6- and 6A-Series Airfoils. NASA TM X-3069, Sept. 1974.

6. Abbott, Ira H., and von Doenhoff, Albert E.: Theory of Wing Sections: New York: Dover Publications Inc., 1959.

7. Pfenninger, W.: Investigations on Reductions of Friction on Wings, in Particular by Means of Boundary Layer Suction. NACA Technical Memorandum 1181, August 1947.

8. Bauer, F., Garabedian, P., and Korn, D.: A Theory of Supercritical Wing Sections, with Computer Programs and Examples. New York: Springer-Verlag, 1972.

9. Kaups, Kalle, and Cebeci, Tuncer: User's Guide for a Computer Program to Calculate Compressible Laminar Boundary Layers With Suction on Swept and Tapered Wings. Douglas Aircraft Co.

10. Srokowski, Andrew J.; and Orszag, Steven A.: Mass Flow Requirements for LFC Wing Design. AIAA Paper No. 77-1222.

11. Schubauer, G. B., and Spangenberg, W. G.: Forced Mixing in Boundary Layers. National Bureau of Standards Report No. 6107, August 1958.

12. Harris, Julius E., and Blanchard, Doris K.: Computer Program for Solving Laminar, Transitional, or Turbulent Compressible Boundary-Layer Equations for Two-Dimensional and Axisymmetric Flow. NASA Technical Memorandum 83207, February 1982.

13. Stevens, W. A.; Goradia, S. H.; and Braden, J. A.: Mathematical Model for Two-Dimensional Multi-Component Airfoils in Viscous Flow. NASA CR-1843, June 1971.

14. Horton, H. P.: A Semi-Empirical Theory for the Growth and Bursting of Laminar Separation Bubbles. Aeronautical Research Council Current Paper No. 1073, June 1967.

15. Malik, Mujeeb R.: COSAL--A Black Box Compressible Stability Analysis Code for Transition Prediction in Three-Dimensional Boundary Layers. NASA CR-165925, May 1982.

WIND TUNNEL RESULTS OF THE LOW-SPEED NLF(1)-0414F AIRFOIL

Daniel G. Murri, Robert J. McGhee, and Frank L. Jordan, Jr.
NASA Langley Research Center
Hampton, Virginia

Patrick J. Davis
PRC/Kentron International, Inc.
Hampton, Virginia

Jeffrey K. Viken
Mandex, Inc.
Falls Church, Virginia

INTRODUCTION

Recently, increased emphasis has been placed on the development of advanced airfoils for application to high-performance general aviation and commuter aircraft. Research conducted in this area has been directed toward developing airfoils with extensive natural laminar flow (NLF) in an attempt to obtain lower cruise drag coefficients and yet maintain acceptable maximum lift and stalling characteristics. One airfoil designed with these considerations is designated as NLF(1)-0414F.

The design, theoretical calculations, and two-dimensional airfoil test results for NLF(1)-0414F have been extensively reported in references 1-4. The results presented herein highlight some of the recent wind-tunnel tests conducted with the airfoil. The most recent wind-tunnel results have been obtained in a cooperative program with Cessna by testing a full-scale modified Cessna 210 (figure 1) in the Langley 30- by 60-Foot Wind Tunnel. This aircraft features a modified wing of increased aspect ratio and incorporates the NLF(1)-0414F airfoil. In addition to documenting the characteristics of the airfoil in this application, tests were conducted to determine the effects of premature boundary-layer transition on the overall airplane performance, stability, and control. Some supporting two-dimensional airfoil results, obtained in the Langley Low Turbulence Pressure Tunnel (LTPT), are included to describe some of the basic airfoil characteristics.

Additional results are presented concerning the effects of several wing leading-edge modifications applied to the modified Cessna 210. These tests were conducted to determine whether leading-edge modifications that previously were shown to provide excellent stall/spin resistance on more conventional, wing/airfoil configurations (references 5 through 7) could be developed for application to an NLF wing design of high aspect ratio. Results are presented which show the effects of the modifications on the wing stalling characteristics and the associated effects on cruise performance.

Figure 1

NLF(1)-0414F DESIGN CHARACTERISTICS

Some of the design characteristics of the NLF(1)-0414F airfoil are indicated in figure 2. The airfoil is designed to achieve low profile drag coefficients at a cruise condition of R = 10 x 10^6 by maintaining natural laminar flow (NLF) to about 70-percent chord on both upper and lower surfaces. Because of the favorable pressure gradients required for extensive NLF, the airfoil experiences a fairly rapid pressure recovery. At off-design conditions, flow separation in the pressure recovery region would be expected without implementation of some type of boundary-layer energizer.

To improve the stall and maximum lift characteristics, a thicker leading edge was utilized than is normally considered for airfoils with such extensive laminar flow operating at such high chord Reynolds numbers. It was known that this thick leading edge would limit the low drag C_l-range on the bare airfoil because of premature negative pressure peaks; however, the chance of a leading-edge type stall would be reduced. One possible means of regaining a wider low drag C_l-range is the use of a small chord trailing-edge flap to maintain favorable pressure gradients on both surfaces over a relatively wide range of lift coefficients.

More detailed discussions of the design objectives and the performance characteristics of the NLF(1)-0414F airfoil are found in references 1 through 4.

- **70% Natural laminar flow on both surfaces at R = 10 X 10^6**
  - **Rapid pressure recovery**
- **Thicker leading edge than normal NLF airfoils**
  - **Enhances maximum lift and stall characteristics**

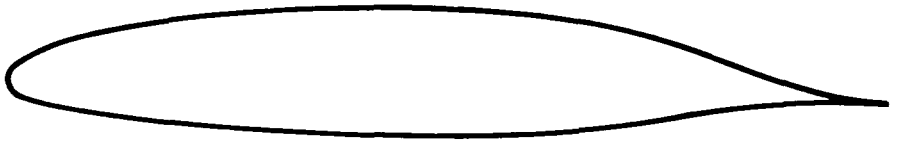

Figure 2

EFFECT OF ROUGHNESS ON SECTION CHARACTERISTICS

The effects of roughness applied near the airfoil leading edge on the two-dimensional airfoil section characteristics are shown in figure 3. These data were measured in the Langley Low Turbulence Pressure Tunnel (LTPT) at a chord Reynolds number of 6.0×10^6 which corresponds approximately to the cruise conditions of the modified Cessna 210. The data show that when transitioning from a primarily laminar to a primarily turbulent boundary layer, large increases in drag are caused by the loss of extensive laminar flow. Also, the lift and pitching moment characteristics are essentially unchanged, which is very desirable in terms of safety of flight and aircraft certification.

Another airfoil characteristic, which is independent of roughness effects, is the reduction in slope of the lift curve near 4° angle of attack. This reduction in lift-curve slope is caused by an upper-surface trailing-edge separation that occurs in the pressure recovery region. It will be shown in the next figure that the separation can be minimized by using boundary layer re-energizers (vortex generators) placed in the appropriate location.

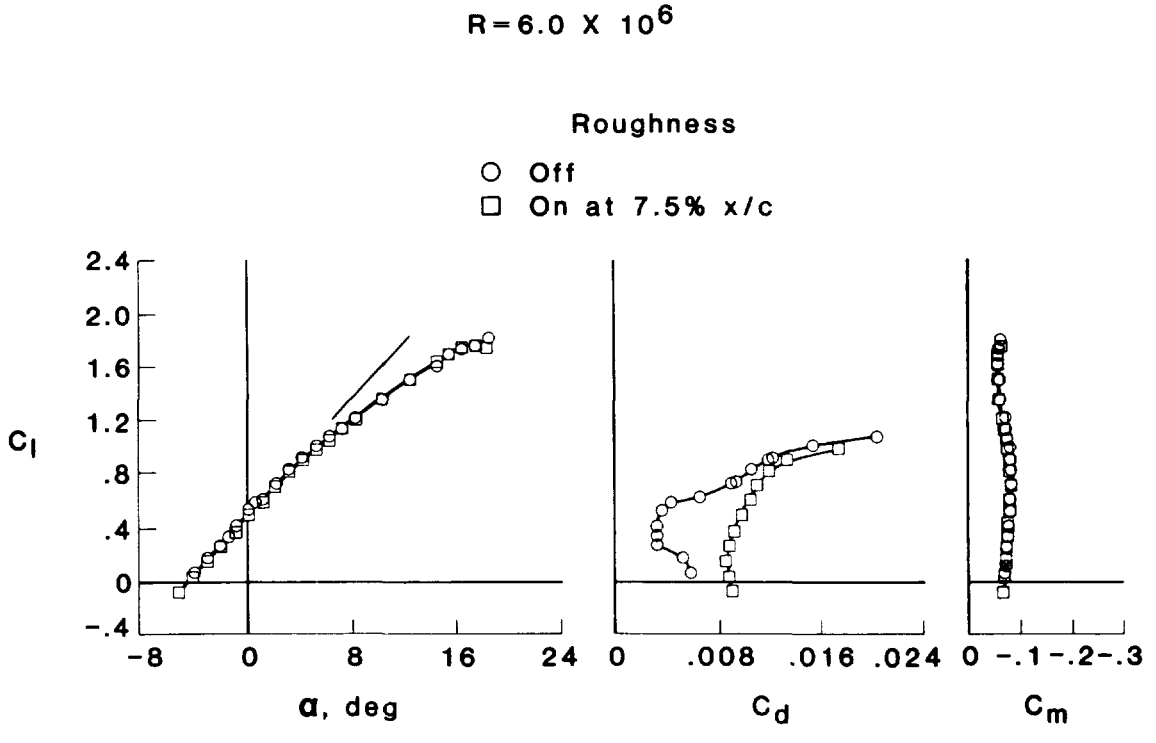

Figure 3

EFFECT OF VORTEX GENERATORS ON SECTION CHARACTERISTICS

Vortex generators are small low-aspect-ratio wings which are positioned on the airfoil surface at a high angle of incidence with respect to the local flow direction. The purpose of the vortex generator is to energize the turbulent boundary layer and thus reduce turbulent separation at off-design conditions. Figure 4 illustrates the effects of vortex generators on airfoil section characteristics for the NLF(1)-0414F airfoil at a Reynolds number of 3.0×10^6. Trailing-edge separation is indicated by the decrease in lift-curve slope for angles of attack greater than about 4 degrees for the vortex generators removed. Installation of a spanwise row of vortex generators, 0.2 inches high, spaced 1.6 inches apart, and located at 0.60 chord, results in an improvement in lift and drag performance for angles of attack greater than about 4 degrees. However, in the low lift-coefficient range a drag penalty is shown for the results with the vortex generators installed.

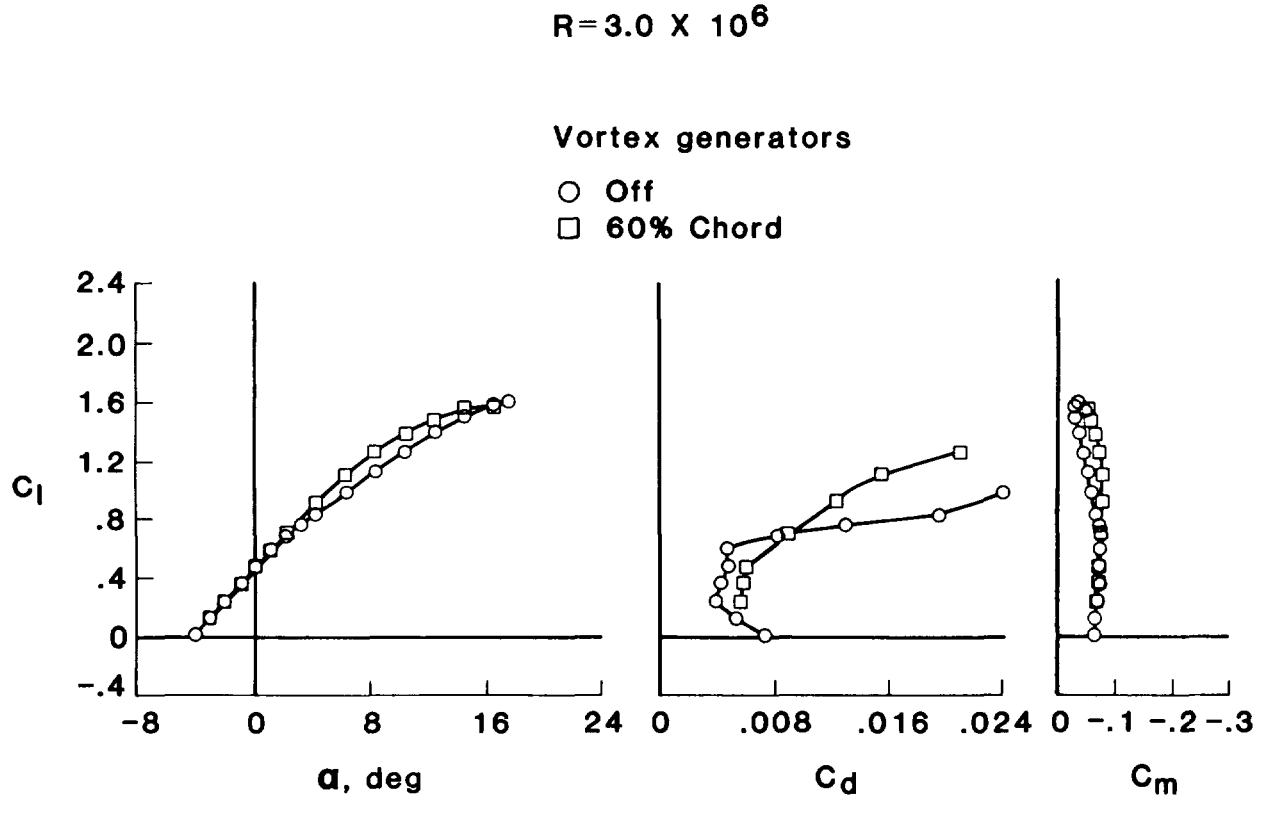

Figure 4

EFFECT OF REYNOLDS NUMBER ON SECTION CHARACTERISTICS

The effect of Reynolds number on the two-dimensional airfoil section characteristics are shown in figure 5 for Reynolds numbers of 2.0 x 10^6 and 6.0 x 10^6. A Reynolds number of 2.0 x 10^6 corresponds approximately to the high-lift (landing) condition of the modified Cessna 210 and was the Reynolds number used for the majority of the tests in the 30- by 60-Foot Wind Tunnel. As mentioned previously, a Reynolds number of 6.0 x 10^6 corresponds approximately to the cruise condition of the modified Cessna 210.

The differences in lift and drag shown in figure 5 illustrate the importance of accounting for the Reynolds number effects on airfoils such as NLF(1)-0414F. The data measured at R = 6.0 × 10^6 could be used to predict the cruise performance of the aircraft but would indicate unrealistically high levels of lift available for landing. The data measured at R = 2.0 x 10^6 (including the data from the 30- by 60-Foot Wind Tunnel) would accurately represent the landing condition but would indicate higher values of drag at cruise conditions. However, it was found that the incremental changes in total airplane drag due to roughness at R = 2.0 x 10^6 (shown in later figures) were very similar to the increments obtained in flight at higher Reynolds numbers.

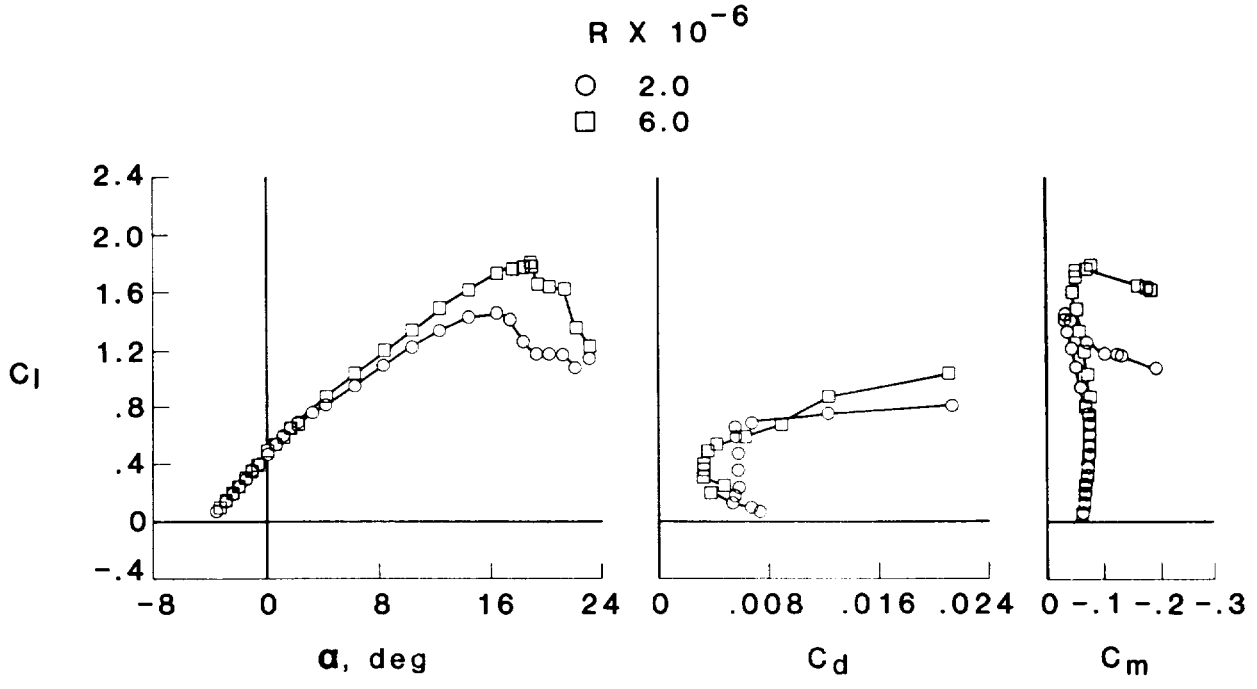

Figure 5

EFFECT OF TAPE TURBULATORS ON SECTION CHARACTERISTICS

At the lower Reynolds numbers, increases in drag can be partly due to areas of laminar separation. As the Reynolds number is decreased, the boundary layer becomes increasingly stable at the laminar separation point in the beginning of the steep pressure rises on both surfaces. When the highly stable boundary layer reaches the laminar separation point, it separates and takes a considerable distance before transitioning and reattaching back to the airfoil surface. Large drag penalties are associated with this separated region. One method of eliminating this separated region is utilizing turbulators to trip the flow before the laminar separation point is reached. Figure 6 illustrates the drag reduction realized by suppressing these laminar separation regions on the NLF(1)-0414F airfoil for a Reynolds number of 3.0×10^6. The type of turbulator used in this case was tape of 0.012 inches thick and 0.25 inches wide placed at 68-percent chord on the upper surface and 66-percent chord on the lower surface.

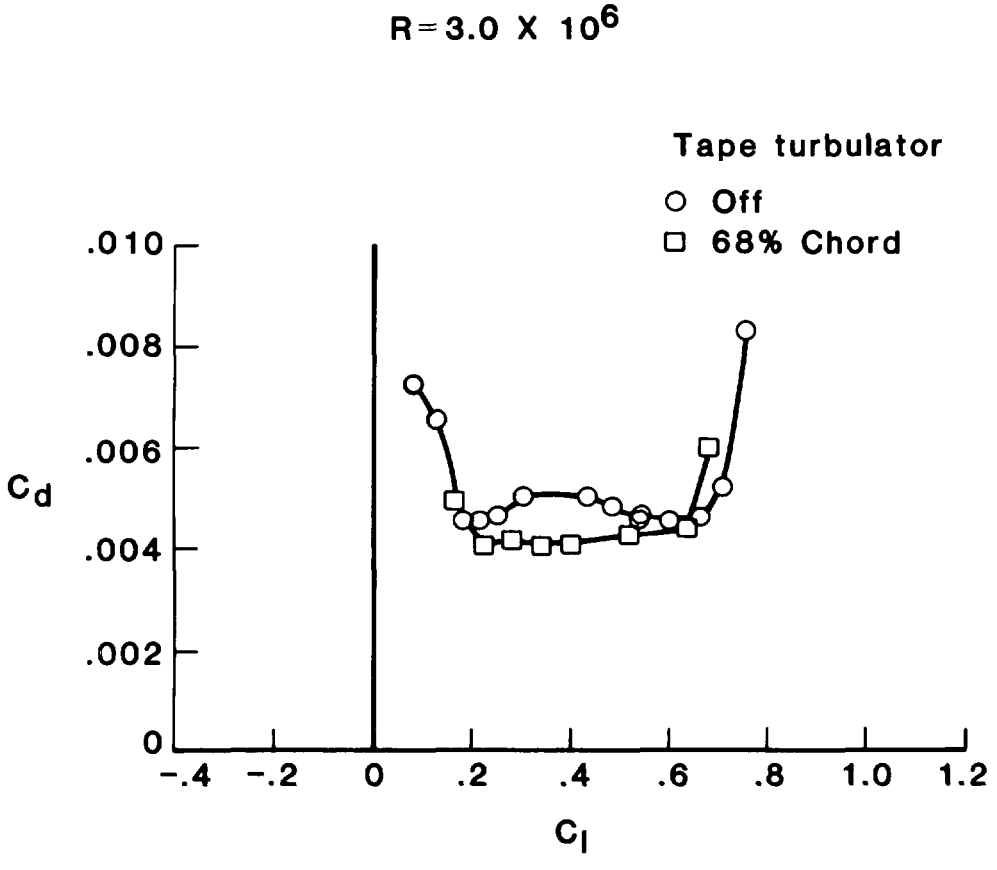

Figure 6

MODIFIED CESSNA 210 DESIGN CHARACTERISTICS

The design characteristics of the modified Cessna 210 are shown in figure 7. The modified wing is of higher aspect ratio, higher wing loading, and incorporates the NLF(1)-0414F airfoil. All of these changes are designed to improve cruise performance. A small 12.5-percent chord trailing-edge "cruise" flap is designed to vary the low-drag C_l-range with small flap deflections. This "cruise" flap could also be set to large trailing-edge-down deflections to enhance the maximum lift characteristics. Roll control is provided by a combination of ailerons and spoilers.

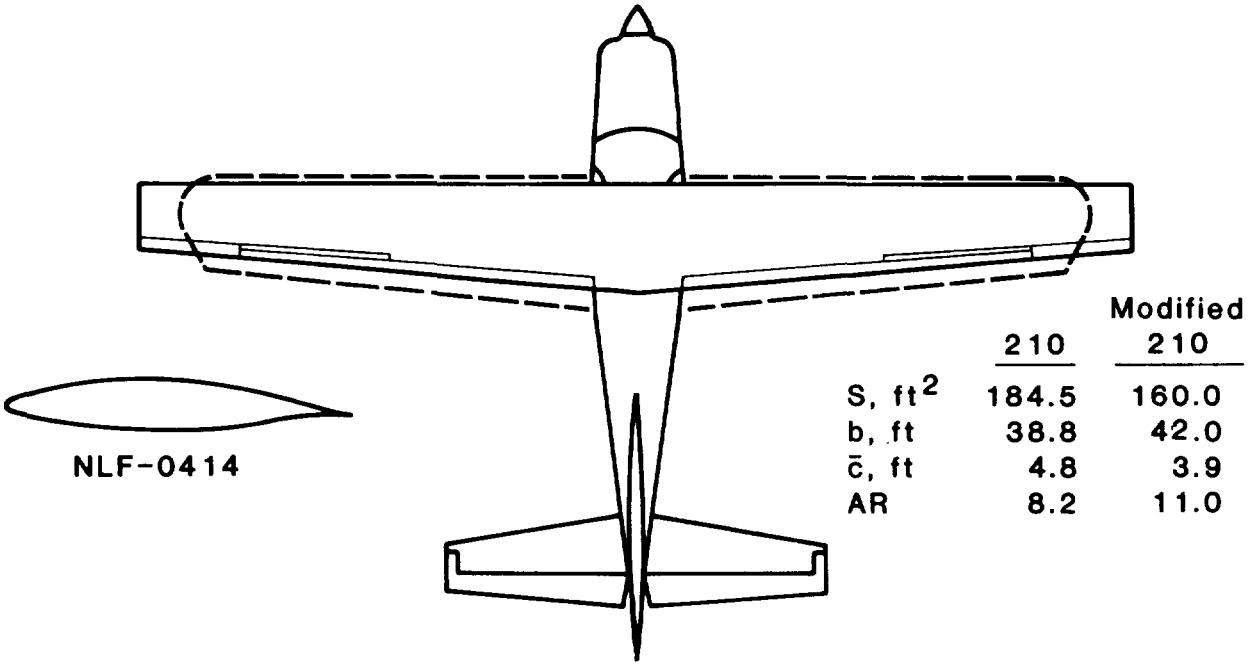

Figure 7

30- by 60-FOOT WIND-TUNNEL TESTS

The modified Cessna 210 airplane (figure 8) was mounted in the 30- by 60-Foot Wind Tunnel using the landing-gear attachment points. The tunnel conditions varied from a free-stream velocity of 40 mph to 72 mph which corresponds to Reynolds numbers based on $\bar{c}$ of 1.4×10^6 to 2.4×10^6. Overall aerodynamic forces and moments were measured over ranges of angle of attack and sideslip of -6° to 40° and -6° to 20° respectively. Additional tests were conducted to measure boundary-layer transition using both the hot-film and sublimating chemical techniques, and the wing stall pattern was documented through flow visualization studies using tufts.

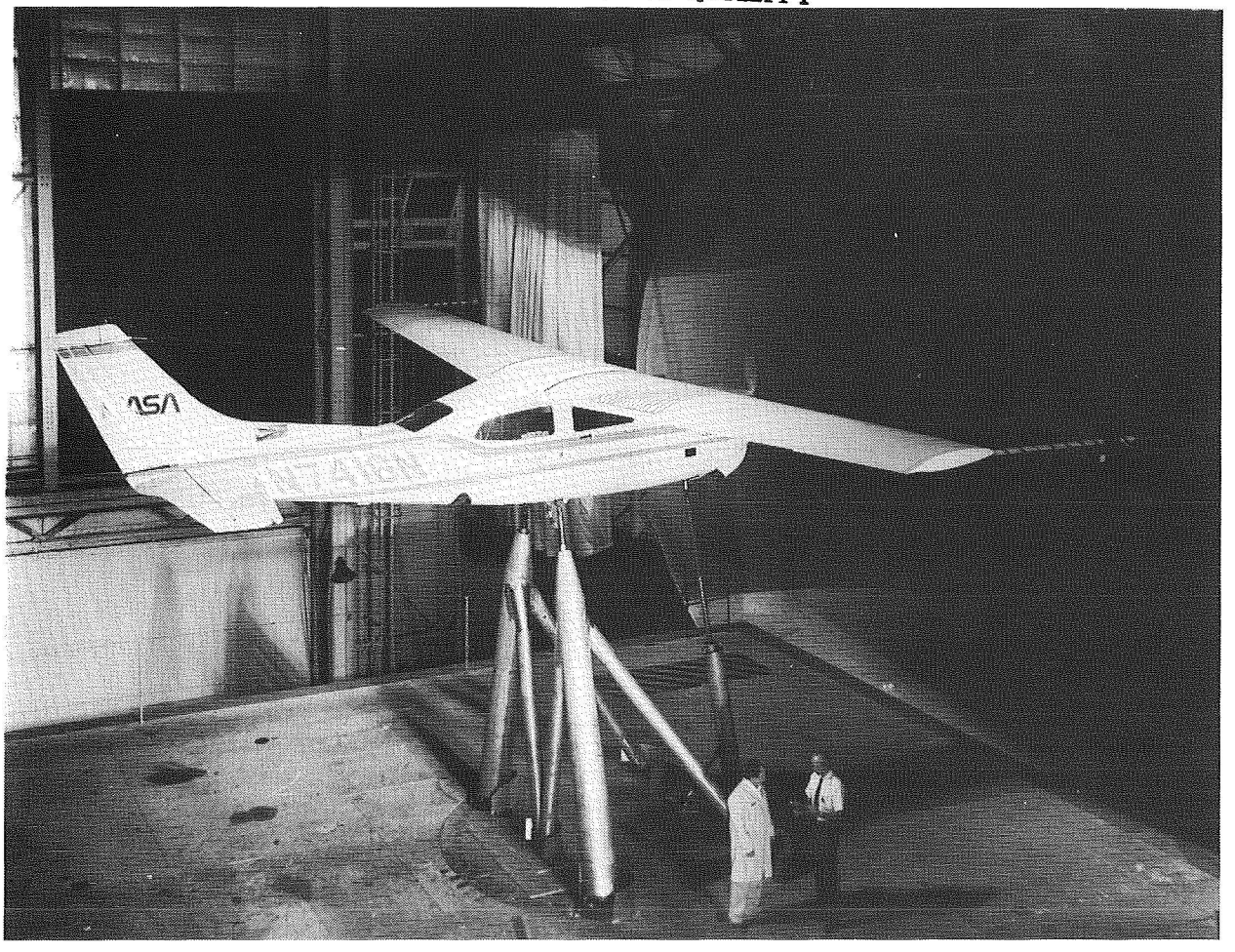

Figure 8

EFFECT OF ROUGHNESS ON AIRPLANE CHARACTERISTICS

The effects of fixing boundary-layer transition near the wing leading-edge on the lift, pitching moment, and drag characteristics are shown in figures 9 and 10. The data show that the lift and pitching moment characteristics are essentially unchanged when transition is fixed near the leading edge. Additional data (not shown) indicate that fixing transition also had essentially no effect on the lateral-directional stability and control. These characteristics are obviously very desirable from a safety and certification standpoint where premature boundary-layer transition (due to insect contamination, etc.) must be considered.

The effects of fixing transition on the drag characteristics (figure 10) illustrate the large drag reduction due to the extensive areas of laminar flow maintained on both the upper and lower wing surfaces at cruise lift coefficients (approximately C_L = .3).

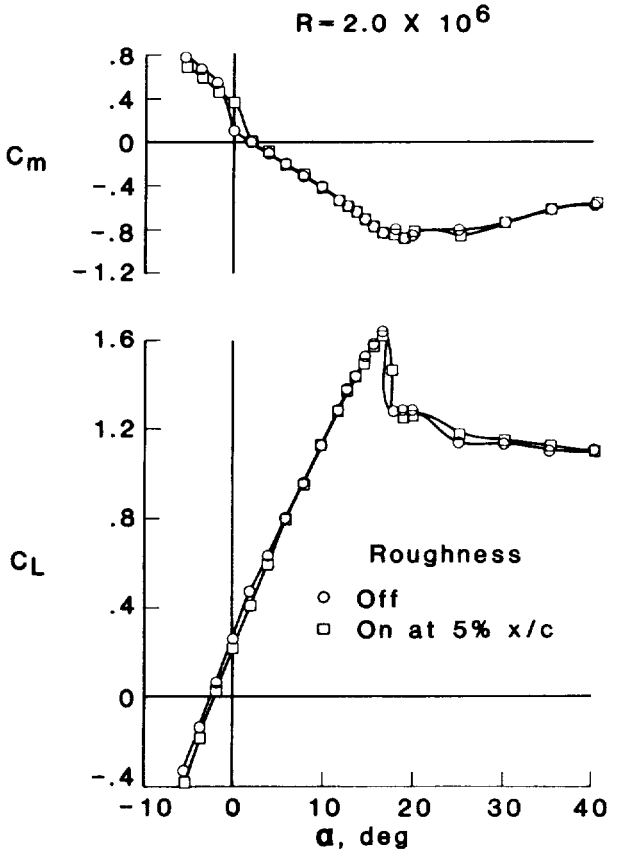

Figure 9

EFFECT OF ROUGHNESS ON AIRPLANE CHARACTERISTICS

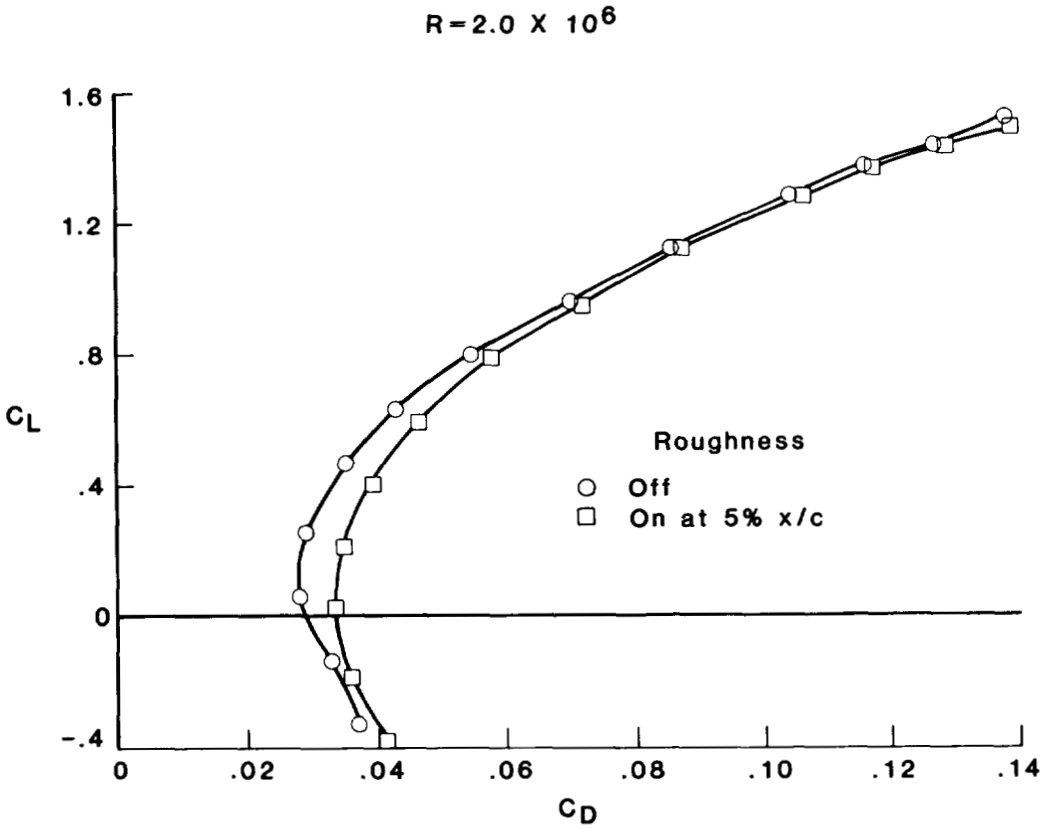

Figure 10

WIND-TUNNEL TRANSITION RESULTS

The extent of laminar flow was measured in the 30- by 60-Foot Wind Tunnel using both the hot-film and sublimating chemical techniques. An example of one of the sublimating chemical tests is shown in figure 11 for alpha = 1° and $R = 2.4 \times 10^6$. The test results showed that laminar flow was maintained to about 70-percent chord on both upper and lower surfaces at the cruise angle of attack. These results agree well with the theoretical predictions and the transition measurements made at higher Reynolds numbers in the Low Turbulence Pressure Tunnel (LTPT) with the two-dimensional airfoil model (figure 12). All of these data also agree very well with the transition measurements made by Cessna during flight tests of the modified Cessna 210 (reference 8).

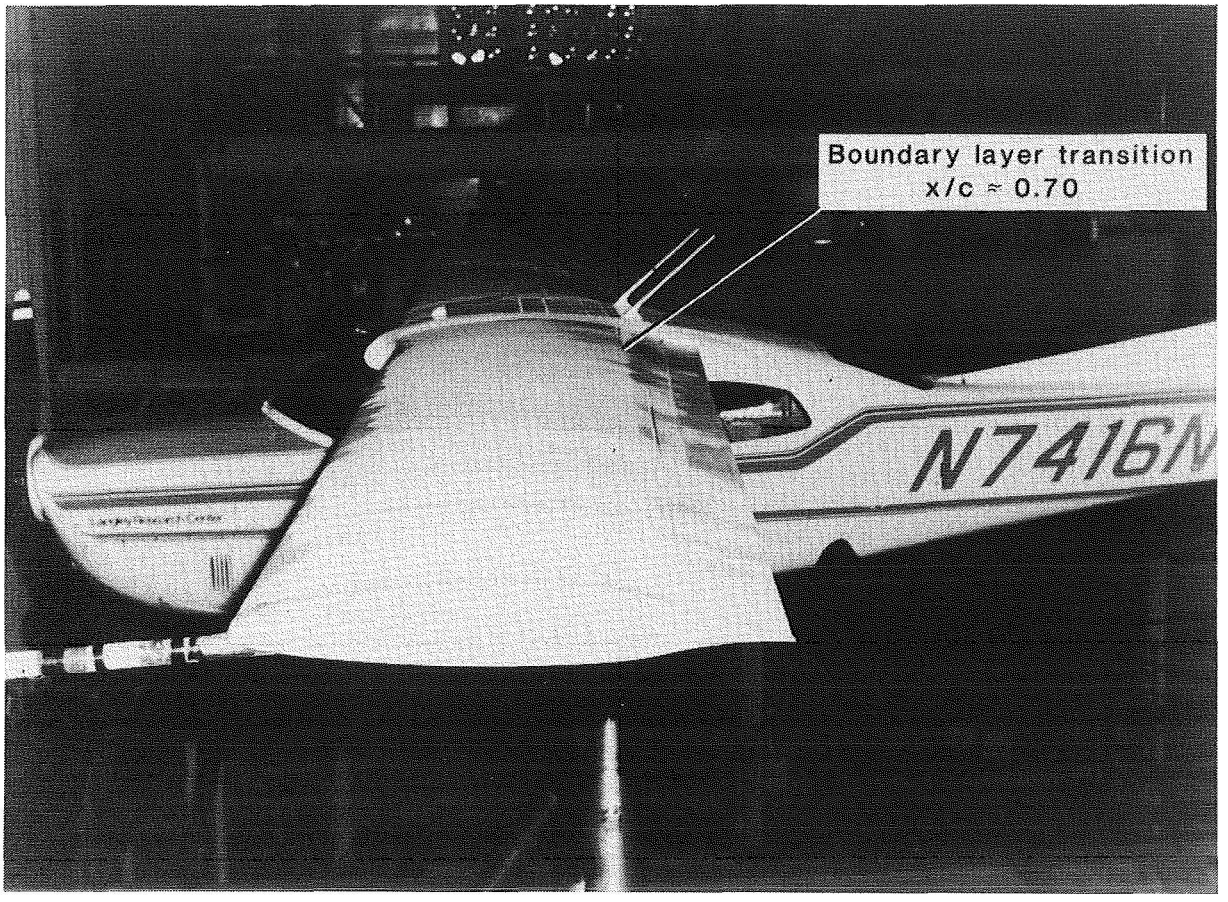

Figure 11

WIND-TUNNEL TRANSITION RESULTS

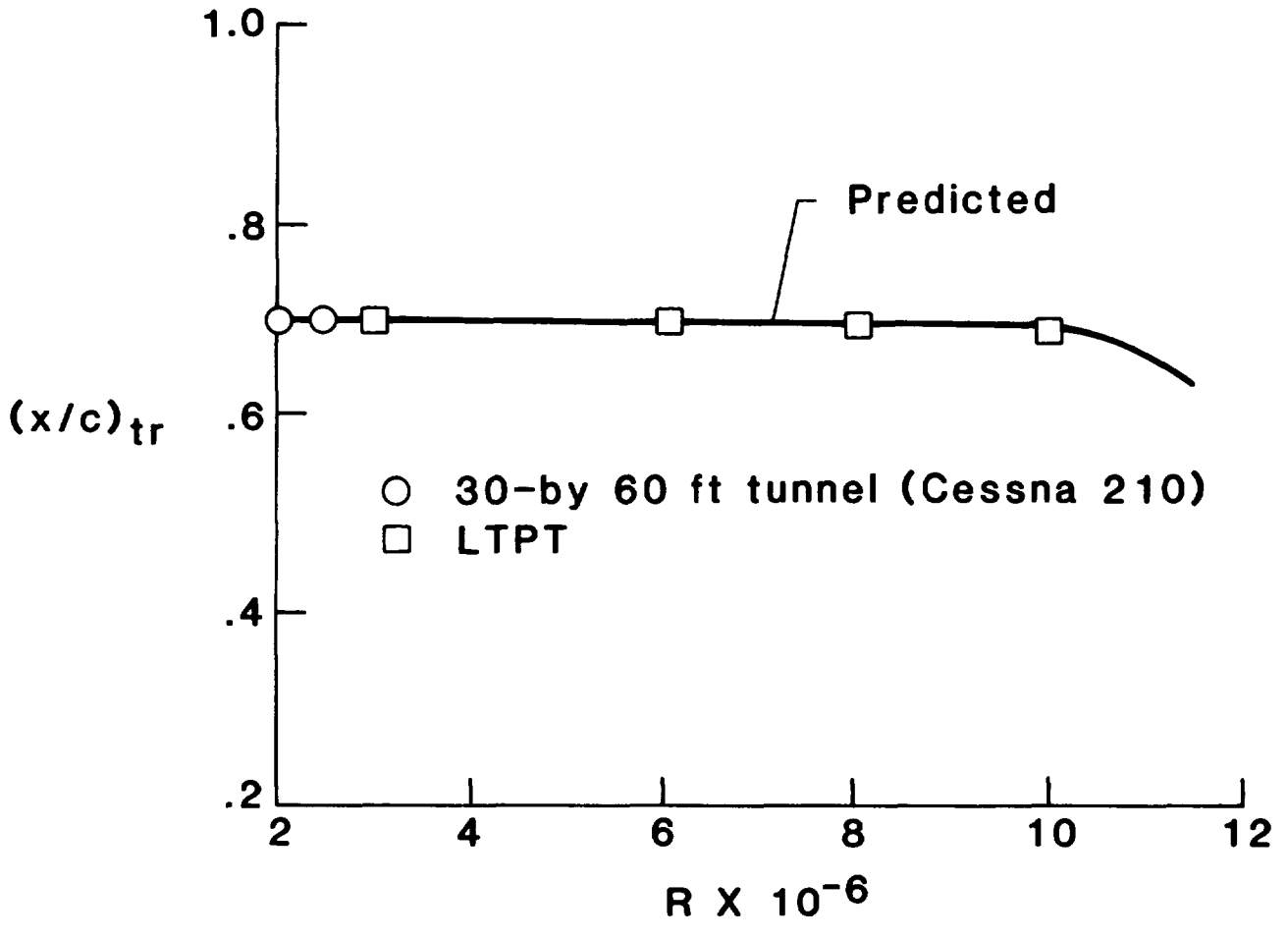

Figure 12

EFFECT OF TRANSITION ON CALCULATED CRUISE PERFORMANCE

The calculated performance increases on the modified Cessna 210 due to the large extent of laminar flow are illustrated in figure 13. These performance calculations are made for an altitude of 10,000 ft, a weight of 3,500 lbs, and 75-percent power. It is noted that these calculations are derived from the wind-tunnel data measured at $R = 2.0 \times 10^6$, where the airfoil is not performing as well (in terms of drag) as at the true cruise Reynolds number (approximately $R = 6.0 \times 10^6$). As a result, the calculated performance would be expected to be less than what could be obtained in flight; however, the calculations were found to give a reasonable estimate of the incremental effects of fixing transition.

The calculations presented in figure 13 indicate that the large extent of laminar flow would be responsible for about a 10-percent increase in speed and range for the same power setting. These incremental effects are similar to the performance measurements made by Cessna during flight tests of the modified Cessna 210 (reference 8). The calculations also show that if power were reduced to fly at the same cruise speed, then the large extent of laminar flow would be responsible for about a 29-percent increase in range.

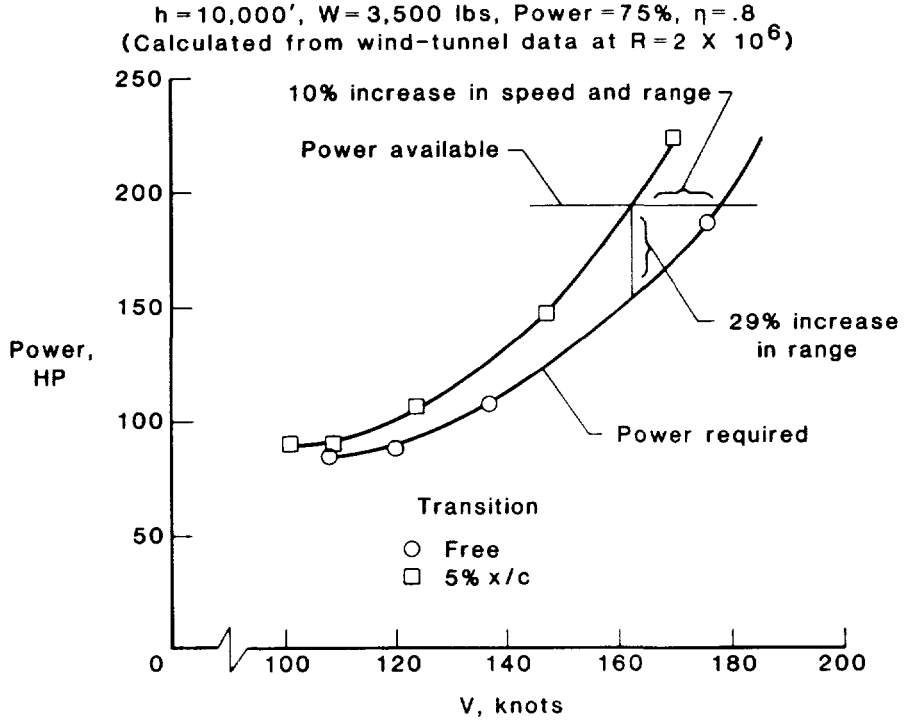

Figure 13

PRELIMINARY HIGH-LIFT RESULTS

Some preliminary high-lift results obtained with the NLF(1)-0414F airfoil are shown in figure 14. The two-dimensional airfoil data on the left show the effect of deflecting a 20-percent-chord split flap to an angle of 60°. The data on the right show the effect of deflecting the 12.5-percent-chord "cruise" flap to 40° on the modified Cessna 210. Although neither of these flap configurations was optimized to develop high lift on this airfoil, the data indicate the potential to develop effective high-lift systems. A discussion on the development of high-lift systems for this airfoil is presented in reference 4.

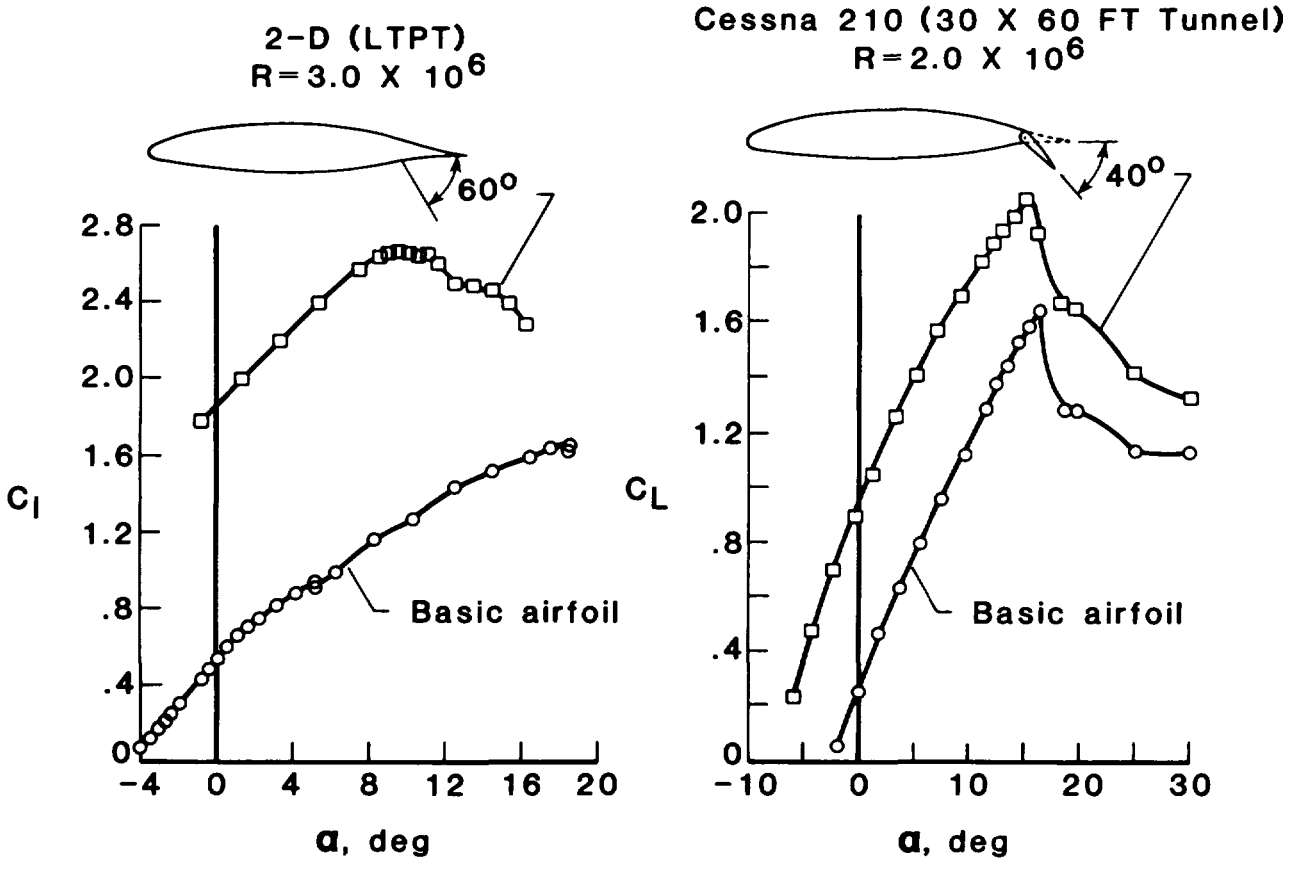

Figure 14

LEADING-EDGE DROOP DESIGN

The primary leading-edge modifications tested on the modified Cessna 210 are shown in figure 15. Research conducted on more conventional wing/airfoil configurations has shown that the application of an outboard wing leading-edge droop can significantly enhance stall/spin resistance by maintaining attached flow at the wing tips at angles of attack well above the normal wing stall (references 5 through 7). During development of an outboard droop for the modified Cessna 210, preliminary sub-scale tests showed that adding a small inboard droop segment in conjunction with the outboard droop could further enhance the stall characteristics.

In an attempt to minimize any increase in the drag characteristics of the basic wing, the droop airfoil section was derived from another NLF airfoil.

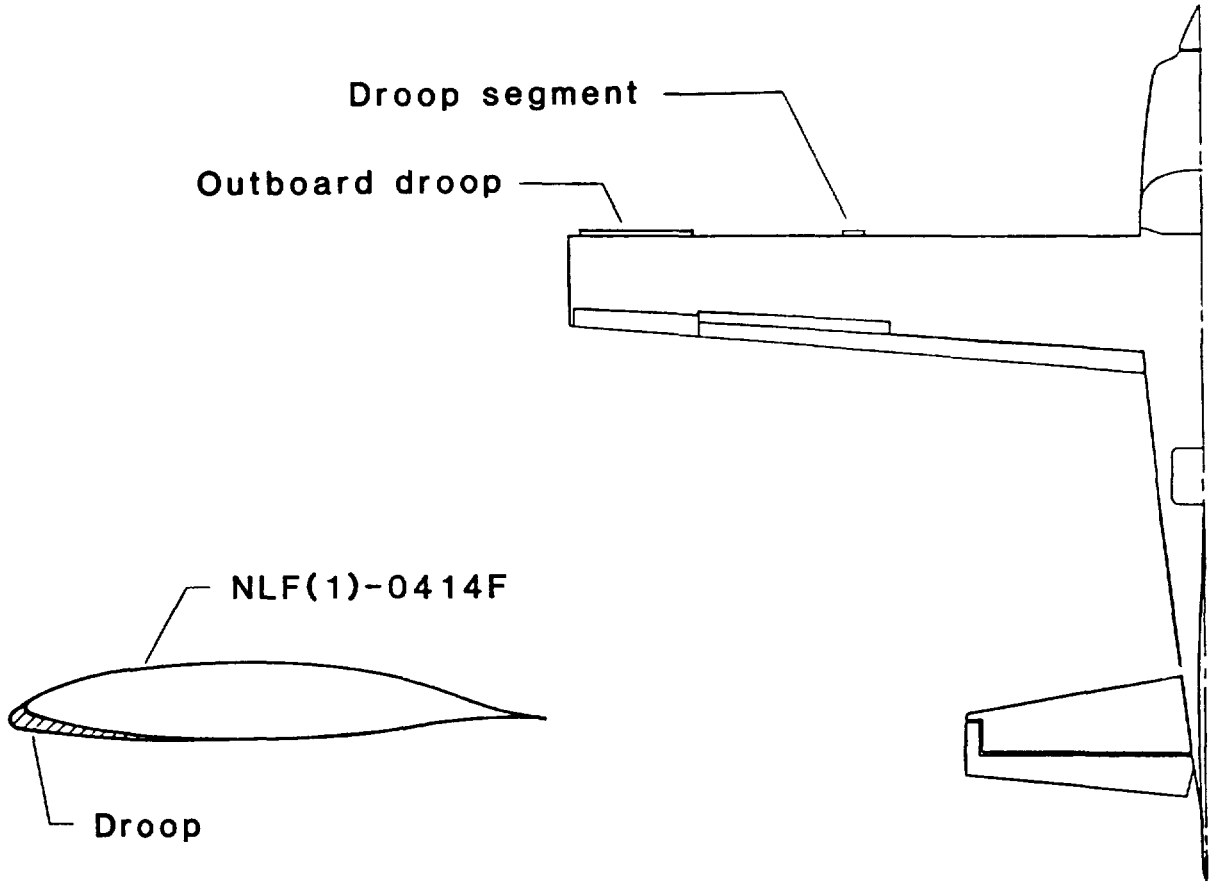

Figure 15

EFFECT OF OUTBOARD DROOP ON WING STALL CHARACTERISTICS

The effect of the outboard droop modification on the wing stall pattern is illustrated in figure 16. These sketches are based on flow visualization tests of the modified Cessna 210 in the 30- by 60-Foot Wind Tunnel. The sketches show that by 18° angle of attack the basic wing is almost completely stalled. With the outboard droop modification, however, attached flow was maintained at the wing tips up to about 28° angle of attack.

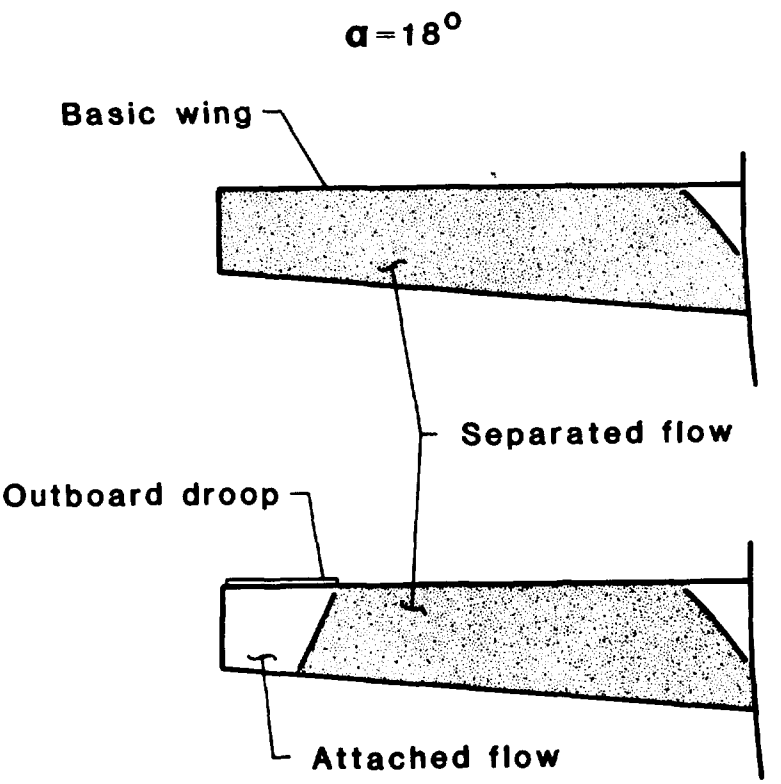

Figure 16

EFFECT OF OUTBOARD DROOP ON DAMPING IN ROLL

One criteria for assessing stall/departure resistance is the level of aerodynamic damping in roll. The effect of the outboard droop on the roll damping of the modified Cessna 210 was measured during sub-scale forced-oscillation tests and is presented in figure 17. It is noted that wing stall occurred at a lower angle of attack in these tests because of the lower test Reynolds number ($R = .65 \times 10^6$). The data show that the basic configuration exhibits highly unstable roll damping at the stall because of the negative lift-curve slope of the wing. The addition of the outboard droop is shown to significantly enhance these characteristics; however, unstable roll damping is still produced because of the rapid stall of the large inboard area of the wing.

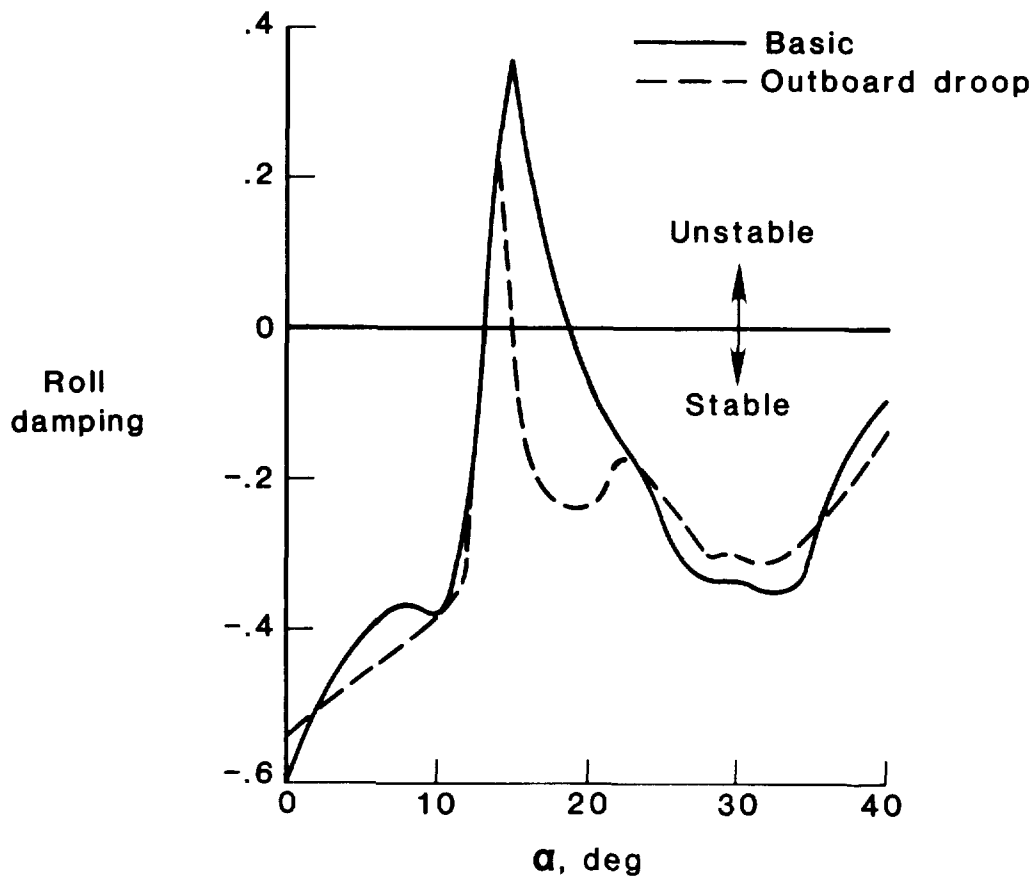

Figure 17

EFFECT OF DUAL SEGMENT DROOP ON WING STALL CHARACTERISTICS

The combined effect of the outboard droop and the inboard droop segment (called a dual segment droop or segmented droop) on the wing stall pattern is shown in figure 18 at 18° angle of attack. In this case, the inboard droop segment was found to act as a vortex generator and was effective in delaying the rapid stall of the inboard area of the wing.

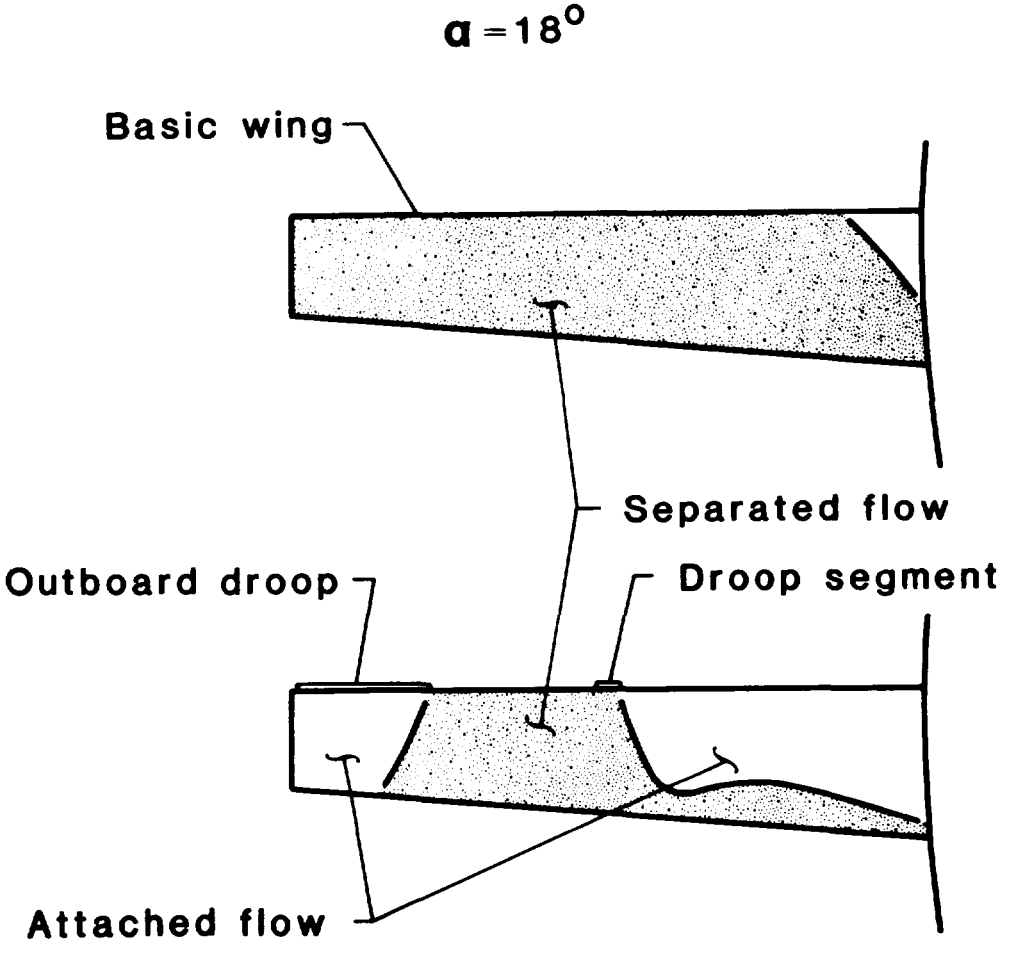

Figure 18

EFFECT OF DUAL SEGMENT DROOP ON DAMPING IN ROLL

The effect of the dual segment droop (segmented droop) on the roll damping characteristics are shown in figure 19. By delaying the rapid stall of the inboard area of the wing, the addition of the inboard droop segment was found to eliminate the unstable roll damping at the stall that was encountered with the outboard droop modification. Therefore, a combination of the outboard droop and the inboard droop segment was found to provide stable roll damping characteristics across the entire angle-of-attack range.

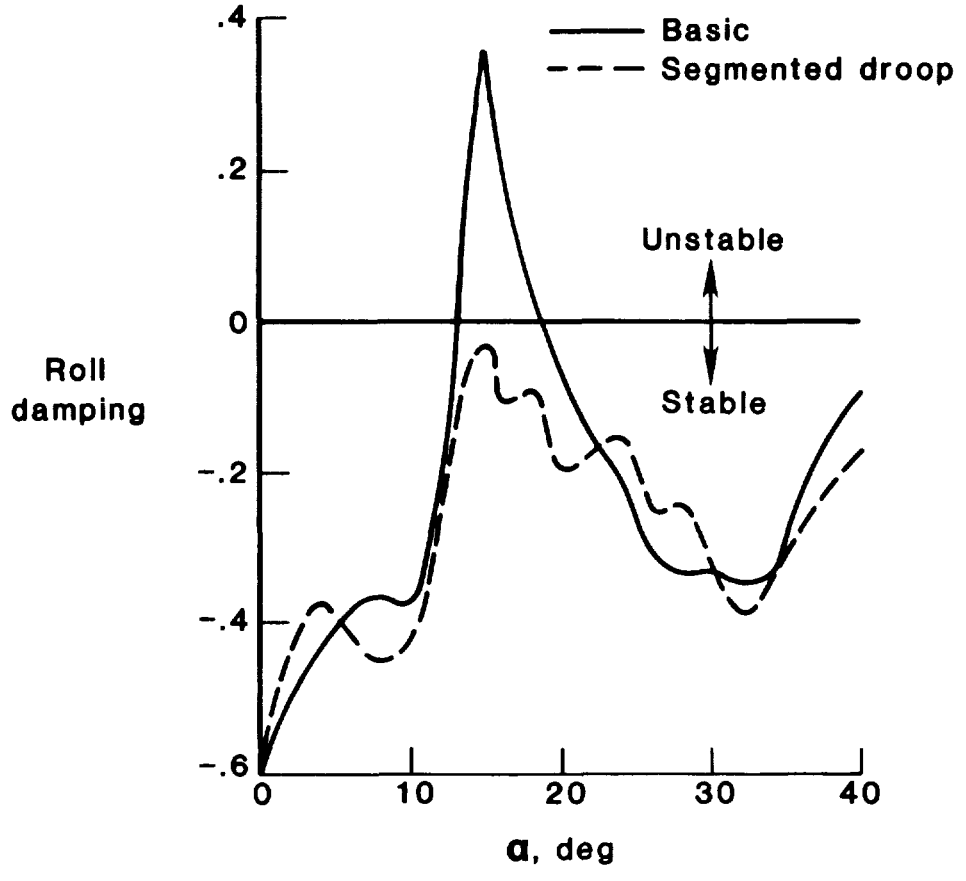

Figure 19

BOUNDARY LAYER TRANSITION WITH LEADING-EDGE MODIFICATIONS

A photograph of a sublimating chemical test with the leading-edge modifications in place is shown in figure 20. The photograph shows turbulent wedges emanating from the droop discontinuities and boundary layer transition occurring on the upper surface of the droop airfoil section at about 70-percent chord. Boundary layer transition was found to occur near the leading edge on the lower surface of the droop airfoil section; however, it is felt that more extensive laminar flow could be maintained on the lower surface by redesigning the droop airfoil section. In any case, the good laminar flow characteristics observed on the upper surface of the droop airfoil section would be expected to help minimize the drag penalty of the modifications.

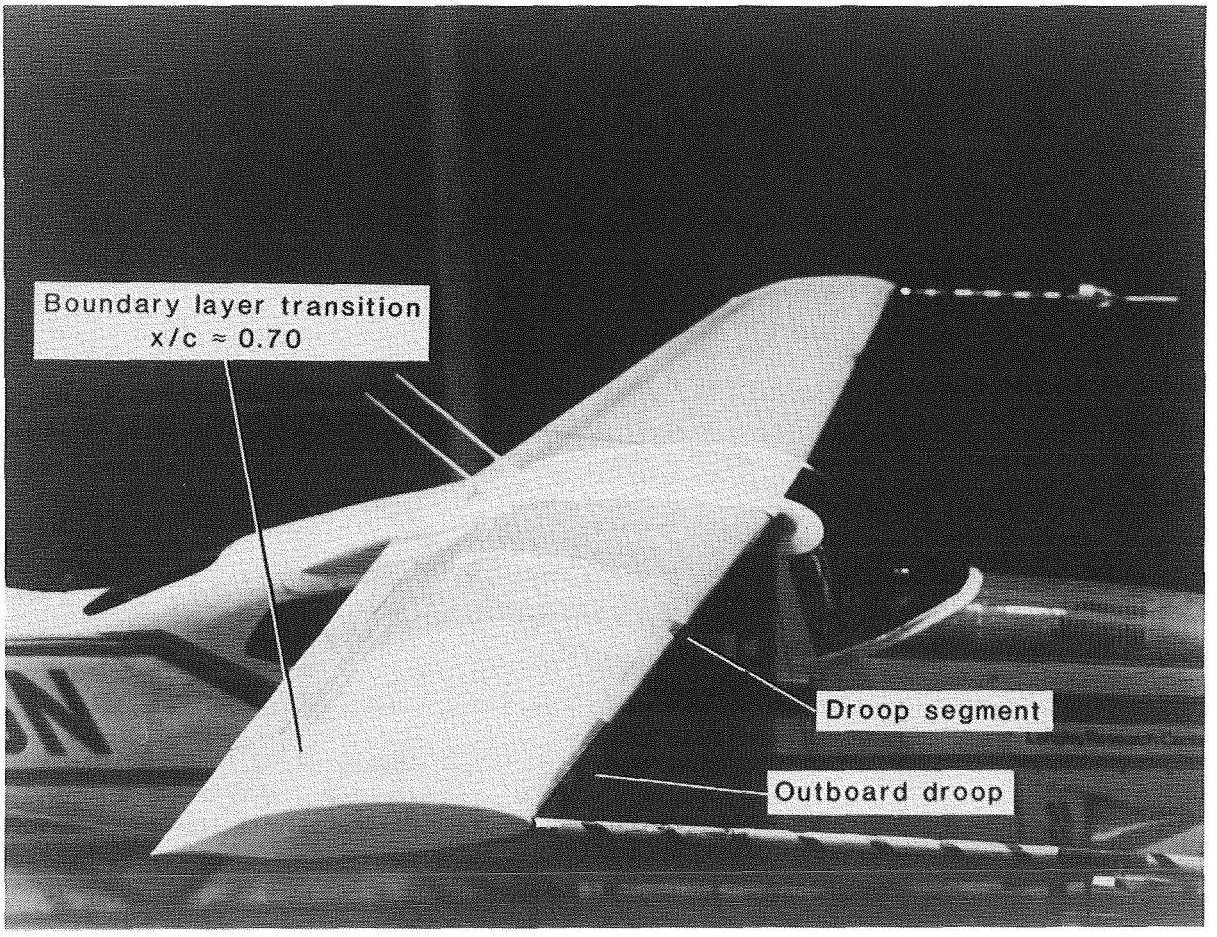

Figure 20

EFFECT OF LEADING-EDGE MODIFICATIONS ON CALCULATED CRUISE PERFORMANCE

The calculated effects of the leading-edge modifications on the cruise performance characteristics are presented in figure 21 using the same cruise conditions explained previously. The data show that the outboard droop modification would be responsible for about a 1.1-percent decrease in cruise speed whereas the segmented droop would be responsible for about a 2.8-percent decrease. The reason for the proportionately larger speed reduction with the addition of the small inboard droop segment is probably due to the addition of two discontinuities to each wing leading edge. However, additional tests have suggested the possibility of using a large vortex generator that only affects the wing upper surface, in place of the inboard droop segment. These tests, with the combination of the outboard droop and a large inboard vortex generator, predicted a cruise speed reduction only slightly more than with the outboard droop alone. This leading-edge configuration also produced wing stall patterns similar to the segmented droop configuration; however, roll damping data are not presently available for comparison. In any case, these cruise speed reductions are considered small compared to the potential stall/departure enhancement provided by the leading-edge modifications.

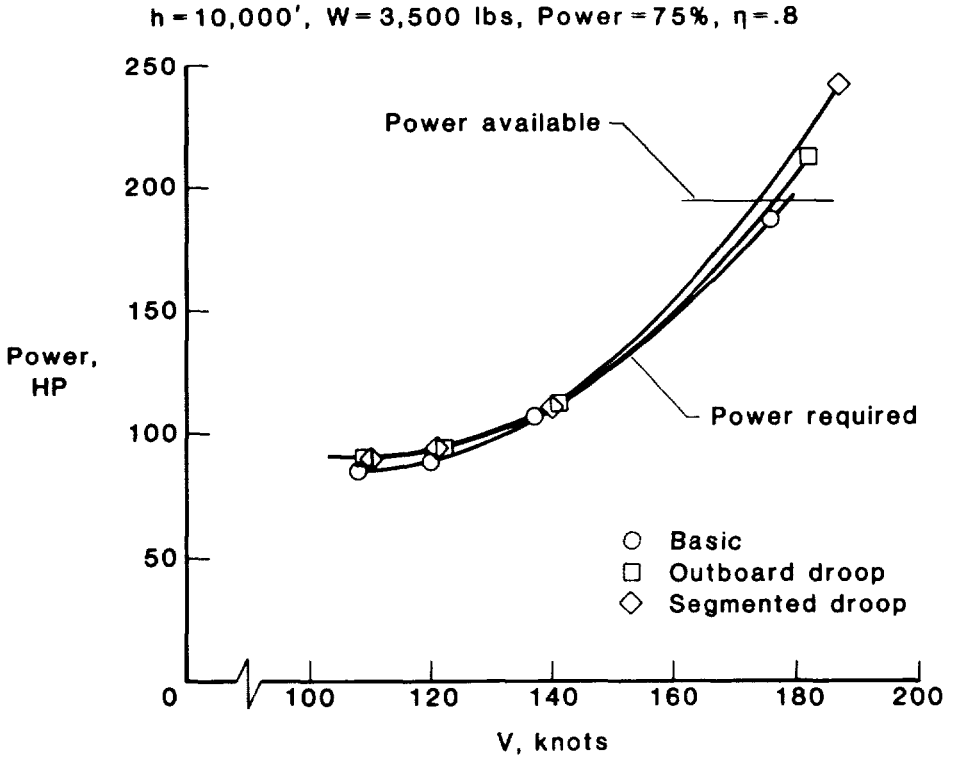

Figure 21

SUMMARY

The large performance gains predicted for the NLF(1)-0414F airfoil have been demonstrated in two-dimensional airfoil tests and in wind-tunnel tests conducted with a full-scale modified Cessna 210. The performance gains result from maintaining extensive areas of natural laminar flow, and have been verified by flight tests conducted with the modified Cessna 210 (see reference 8).

The lift, stability, and control characteristics of the modified Cessna 210 were found to be essentially unchanged when boundary layer transition was fixed near the wing leading edge. These characteristics are very desirable from a safety and certification standpoint where premature boundary layer transition (due to insect contamination, etc.) must be considered.

The leading-edge modifications were found to significantly enhance the roll damping characteristics of the modified Cessna 210 at the stall, and were therefore considered effective in improving the stall/departure resistance. Also, the modifications were found to be responsible for only minor performance penalties. A cooperative NASA/Cessna flight test program is planned to further investigate the effects of the leading-edge modifications on the modified Cessna 210.

- **Performance gains of NLF(1)-0414F airfoil demonstrated in wind-tunnel tests and verified in flight**
- **Lift, stability, and control characteristics not affected by transition from laminar to turbulent flow**
- **Leading-edge modifications improve the stall/departure resistance with only minor performance penalties**

Figure 22

REFERENCES

1. Viken, Jeffrey K.; Pfenninger, Werner; and McGhee, Robert J.: Advanced Natural Laminar Flow Airfoil With High Lift to Drag Ratio. Langley Symposium on Aerodynamics, Volume I, pp 401-414, NASA CP-2397, April 1985.

2. McGhee, Robert G.; Viken, Jeffrey K.; Pfenninger, Werner; and Harvey, W. D.: Experimental Results for a Flapped Natural-Laminar-Flow Airfoil with High Lift/Drag Ratio. NASA TM-85788, May 1984.

3. Viken, Jeffrey K.: Aerodynamic Design Considerations and Theoretical Results for a High Reynolds Number Natural Laminar Flow Airfoil. MS Thesis, George Washington University, January 1983.

4. Viken, J. K.; Campbell, R. L.; Viken, S. A. W.; Pfenninger, W.; and Morgan, H. L., Jr.: Design of the Low-Speed NLF(1)-0414F and the High Speed HSNLF(1)-0213 Airfoils with High-Lift Systems. NASA CP 2487, pp. 637-671. Natural Laminar Flow and Laminar Flow Control Symposium, NASA Langley Research Center, Hampton, Virginia, March 16-19, 1987.

5. Staff of Langley Research Center: Exploratory Study of the Effects of Wing Leading-Edge Modifications on the Stall/Spin Behavior of a Light General Aviation Airplane. NASA TP-1589, 1979.

6. DiCarlo, D. J.; Glover, K. E.; Stewart, E. C.; and Stough, H. P.: Discontinuous Wing Leading Edge to Enhance Spin Resistance. Journal of Aircraft, April 1985.

7. Stough, H. Paul, III; Jordan, Frank L., Jr.; DiCarlo, Daniel J.; and Glover, Kenneth E.: Leading-Edge Design for Improved Spin Resistance of Wings Incorporating Conventional and Advanced Airfoils. Langley Symposium on Aerodynamics, Volume II, pp. 141-157, NASA CP-2398, April 1985.

8. Befus, Jack; Nelson, E. Randel; Ellis, David R.; and Latas, Joe: Flight Test Investigations of a Wing Designed for Natural Laminar Flow. SAE-871044, April 1987.

N90-12542

WIND TUNNEL RESULTS OF THE HIGH-SPEED NLF(1)-0213 AIRFOIL

William G. Sewall, Robert J. McGhee,
David E. Hahne, and Frank L. Jordan, Jr.
NASA Langley Research Center
Hampton, Virginia

[redacted]

ABSTRACT

Wind tunnel tests have been conducted to evaluate a natural laminar-flow airfoil designed for the high-speed jet aircraft in general aviation (ref. 1). The airfoil, designated as the HSNLF(1)-0213, has been tested in two-dimensional wind tunnels to investigate the performance of the basic airfoil shape. A three-dimensional wing designed with this airfoil and a high-lift flap system is also being evaluated with a full-size, half-span model.

OUTLINE

The two-dimensional tests include low-speed tests in the Langley Low-Turbulence Pressure Tunnel (LTPT) at Mach numbers ranging from 0.10 to 0.30 to determine the extent of laminar flow possible at low speeds and also to measure the maximum lift of the basic airfoil (figure 1). The low-turbulence pressure tunnel is ideally suited for both of these items because of excellent flow quality and a unique force balance specifically designed for high-lift airfoils.

The high-speed characteristics were investigated in the Langley 6- by 28-Inch Transonic Tunnel to examine the cruise and climb performance at Mach numbers from 0.5 to 0.78.

The three-dimensional wing design has been recently tested in the Langley 30- by 60-Foot Tunnel with a half-span model that includes both a slotted flap and a fuselage shape. This investigation was conducted to determine the maximum lift for the flap system and to survey the boundary-layer characteristics at spanwise stations.

- 2-D tests, low speed, LTPT, M = .1 - .3
  - Laminar flow
  - Maximum lift
- High speed test, 6 × 28 T.T., M = .5 - .78
  - Cruise/climb performance
- 3-D tests in 30 × 60
  - Full-scale semi-span model
  - Actual flap system

Figure 1

AIRFOIL PROFILE

The shape of the HSNLF(1)-0213 airfoil shown in figure 2 represents a 13-percent thickness ratio which is designed for a cruise Mach number of 0.70, cruise lift coefficient of 0.26, and chord Reynolds number of 11 million.

These conditions allow laminar boundary layers back to 55-percent chord on the upper surface and 65-percent chord on the lower surface.

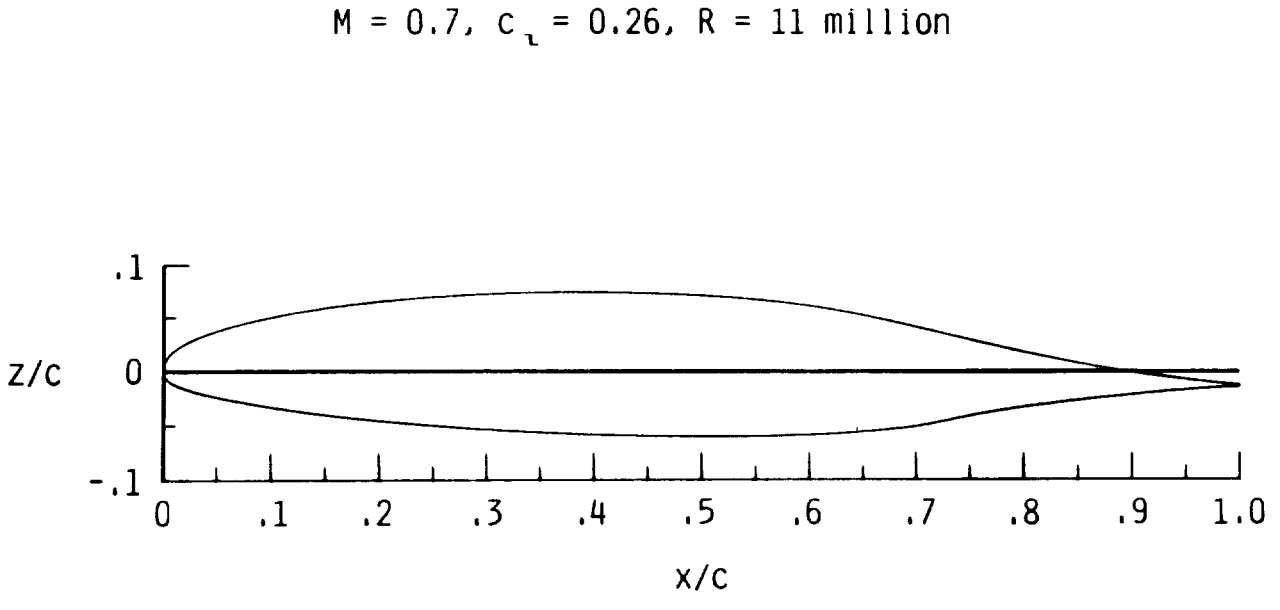

Figure 2

LOW-SPEED TESTS IN LTPT

The low-speed, two-dimensional airfoil tests were conducted in LTPT with a solid model supported by an external force balance (figure 3a) connected to the tunnel sidewalls. This balance provides the lift and pitching moment while drag measurements are determined from a wake survey probe, which is shown behind the model in figure 3b.

Boundary layers on the surfaces of the model were assessed with hot-film gages to determine laminar, transitional, or turbulent flows.

An estimation of the high-lift capability with a simple flap system was provided with a trailing-edge split flap that appears on the model lower surface in figure 3b. This split flap was deflected 60 degrees in a similar manner to airfoil experiments described in ref. 2.

- Solid model
- Force balance for lift and pitching-moment
- Wake survey probe for drag
- Hot-film gages to assess boundary layers
- Simulated split flap

Figure 3a

MODEL INSTALLATION IN LTPT

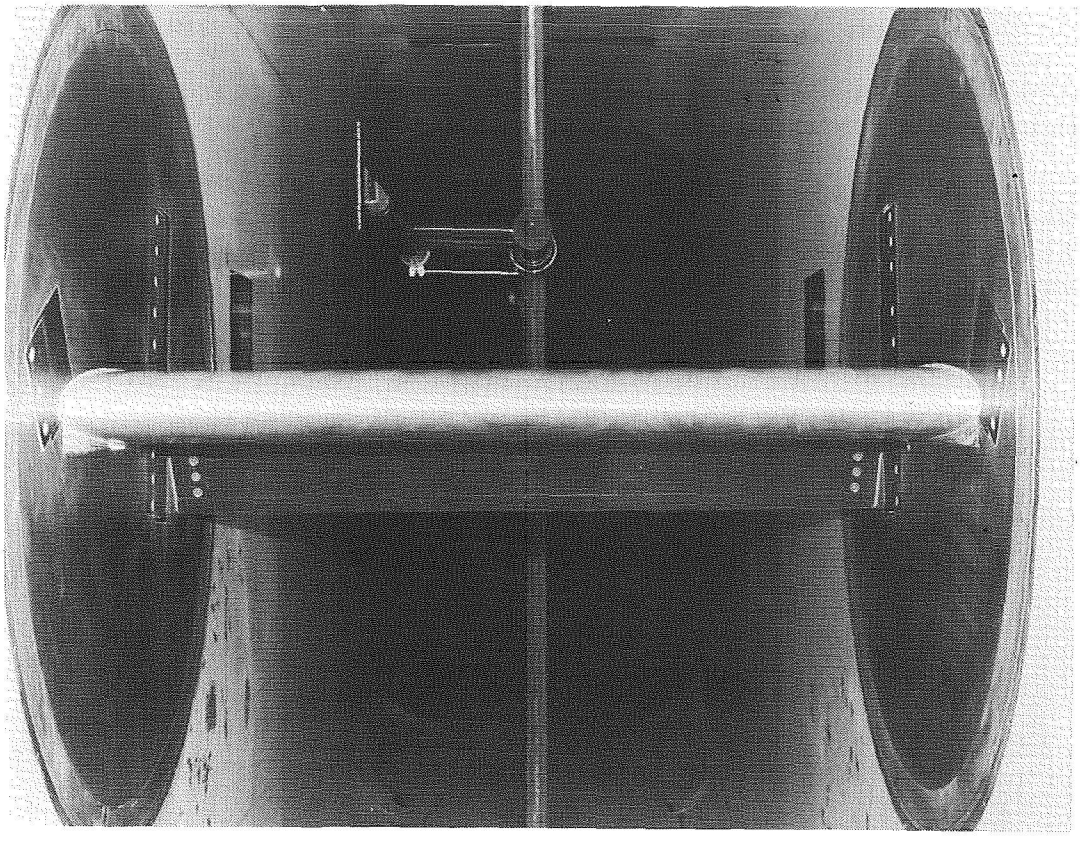

Figure 3b

MINIMUM DRAG

The two-dimensional, low-speed tests were conducted with both smooth model surfaces and fixed transition from thin spanwise strips of carborundum at 5-percent chord on the upper and lower surfaces. The minimum drag from these two surface conditions is shown in figure 4 in variation with the Reynolds number. The difference in drag levels is approximately 0.0040 to 0.0045 in drag coefficient values, which is due to the extensive laminar boundary layers on the smooth model.

For the low-speed tests, minimum drag occurred at lift-coefficient values of approximately 0.20.

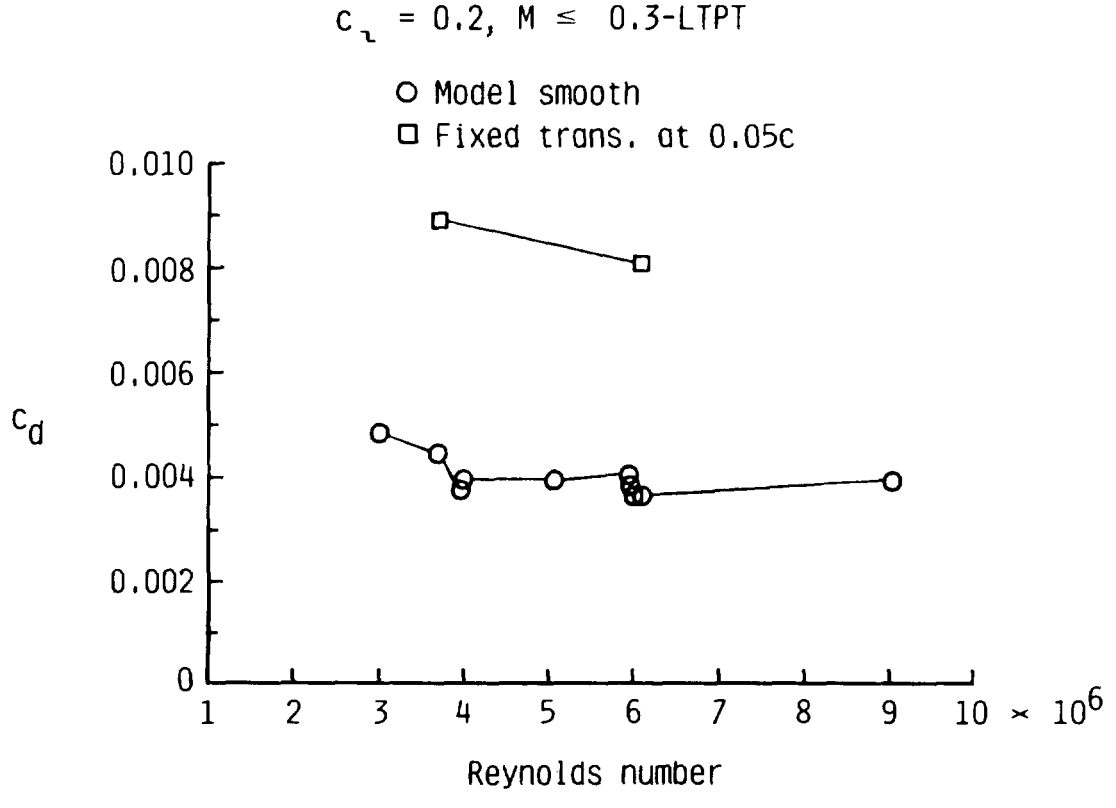

Figure 4

LOW-SPEED PERFORMANCE

Figure 5 presents the airfoil low-speed performance from the two-dimensional tests in LTPT with the variation of drag coefficient with lift coefficient. The chord Reynolds number is 9 million, and a range of lift coefficients between 0.08 and 0.20 provides the boundaries of the low-drag "bucket".

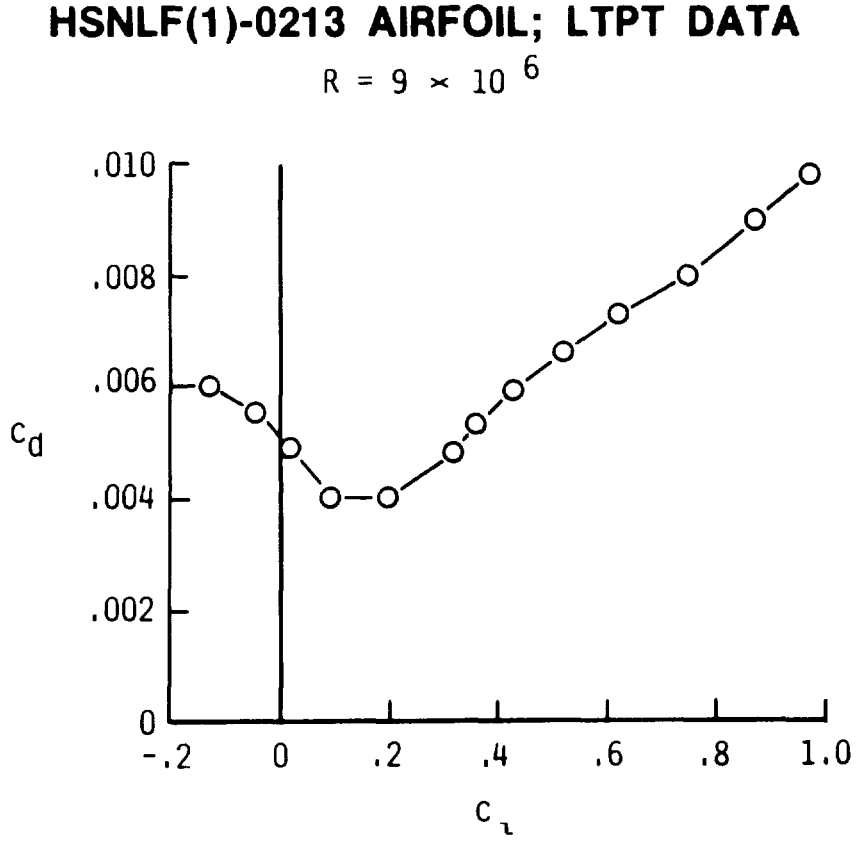

Figure 5

BOUNDARY-LAYER ASSESSMENT FROM HOT FILM

For the two-dimensional airfoil tests in LTPT, the various states of the boundary layers on the upper and lower surfaces of the model were assessed with hot-film gages. These flush-mounted devices allowed the determination of laminar, transitional, or turbulent flows and were mounted at 30-, 40-, 50-, and 60-percent chord on the upper surface and 40-, 50-, 60-, and 70-percent chord on the lower surface.

Figures 6a and 6b show the states of the boundary layers at these chord stations with varying lift coefficients. Both upper and lower surfaces are presented at Reynolds numbers of 3 and 9 million. The laminar boundary layers, denoted by the open circle symbols, diminish from the upper surface with increasing lift coefficient as the transition location moves upstream. The lower surface responds in the opposite manner by gaining more laminar flow. However, since the highest local flow velocities are on the upper surface, the skin friction for the turbulent boundary layers on the upper surface contributes the net increase in drag with increasing lift coefficient, as seen in figure 5.

At lift coefficients below 0.08, the transition point on the lower surface begins to move forward as lift coefficient decreases, and the drag increases in the same manner as seen for the higher lift coefficients ($c_\ell > 0.2$).

In several instances, the boundary layers on the same surfaces at the same lift coefficients will have different amounts of laminar flow at the two different Reynolds numbers. These differences are due to the higher turbulence levels in the facility at the higher Reynolds number, which in turn, causes earlier transition.

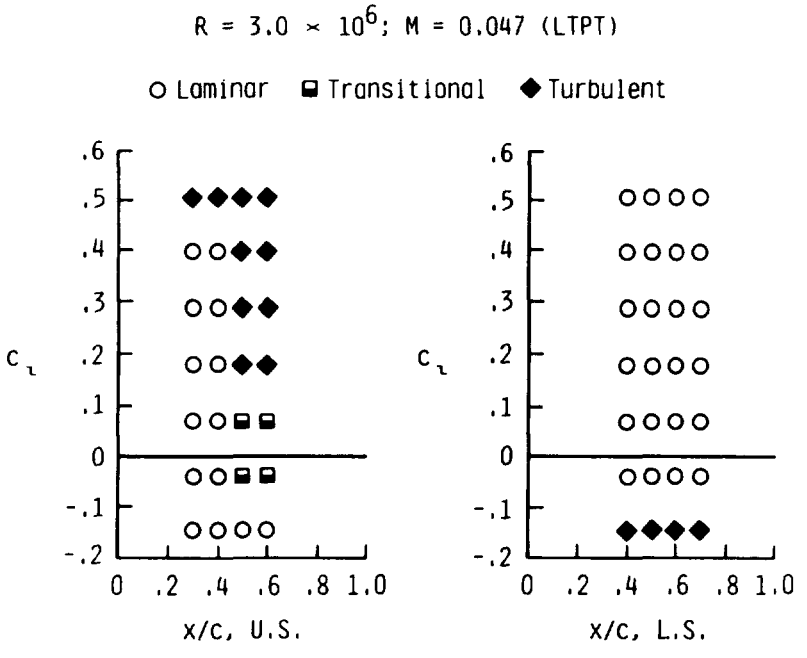

Figure 6a

BOUNDARY LAYER ASSESSMENT FROM HOT FILM

R = 9.0 × 10^6; M = 0.139 (LTPT)

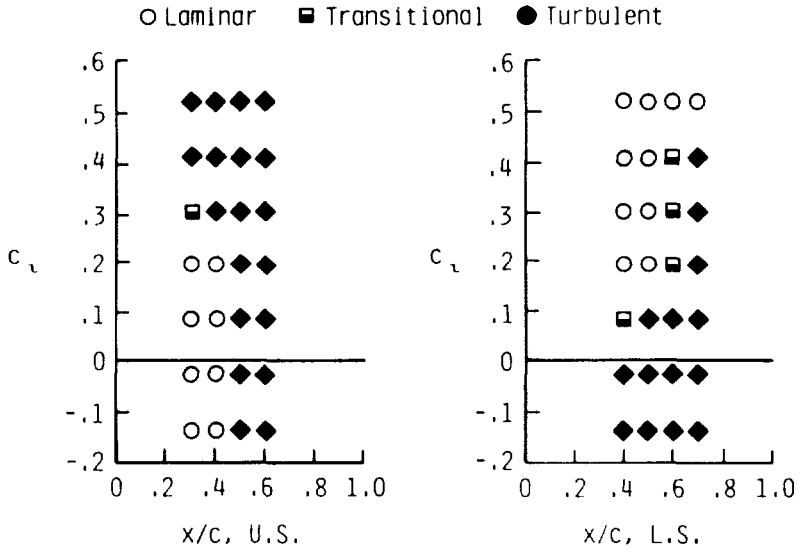

Figure 6b

MAXIMUM LIFT OF BASIC AIRFOIL

The maximum lift coefficient of the basic airfoil measured in the two-dimensional tests is presented in figure 7. Here, the variation of maximum lift coefficient with Mach number is provided for Reynolds numbers of 3, 4, and 6 million.

At a Reynolds number of 6 million, the maximum lift coefficient appears to decrease by almost 10 percent in value at the highest Mach number. The pressure tunnel allows independent variation of Mach number and Reynolds number to learn the true variation of maximum lift with either of these parameters.

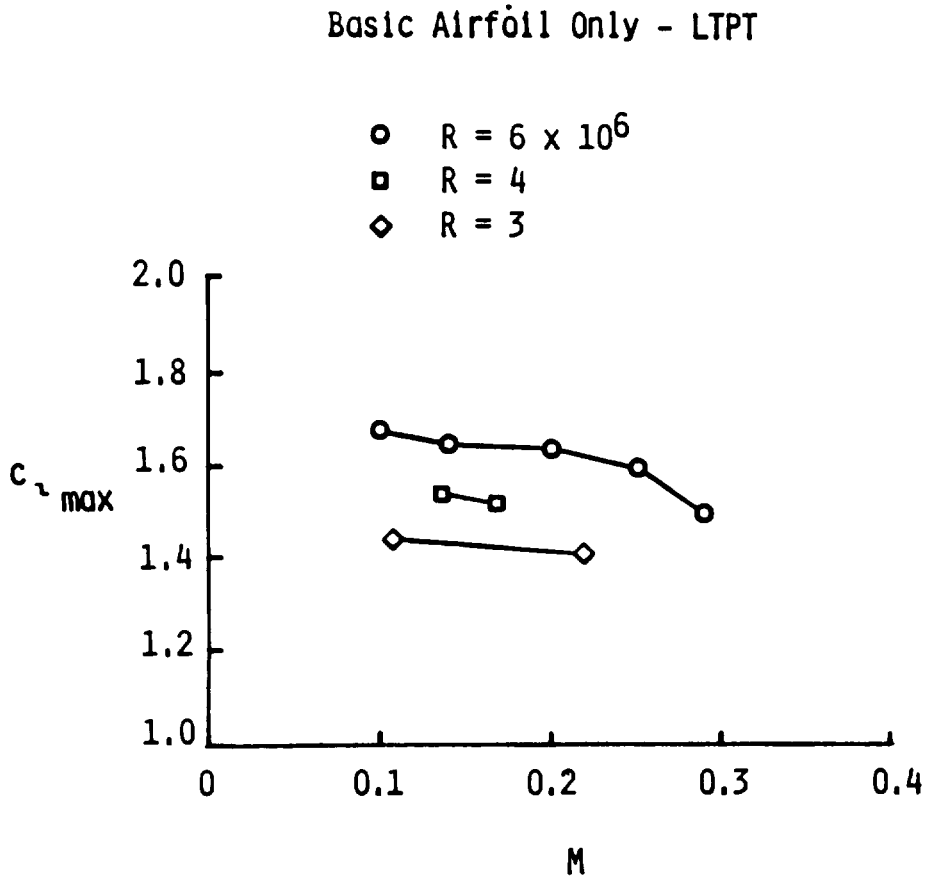

Figure 7

SPLIT-FLAP PERFORMANCE

To evaluate the capability of a simple high-lift device, a simulated split flap of 0.20 chord length was mounted on the lower surface of the airfoil model in LTPT. The split flap served as a baseline high-lift device in the testing reported in ref. 2 as well as this test.

This flap was deflected 60 degrees, and its effect is shown in figure 8 with the variation of lift coefficient with both angle of attack and pitching-moment coefficient. The split-flap provides a large increase in maximum lift coefficient, from 1.65 to 2.50, but also causes more negative pitching moment.

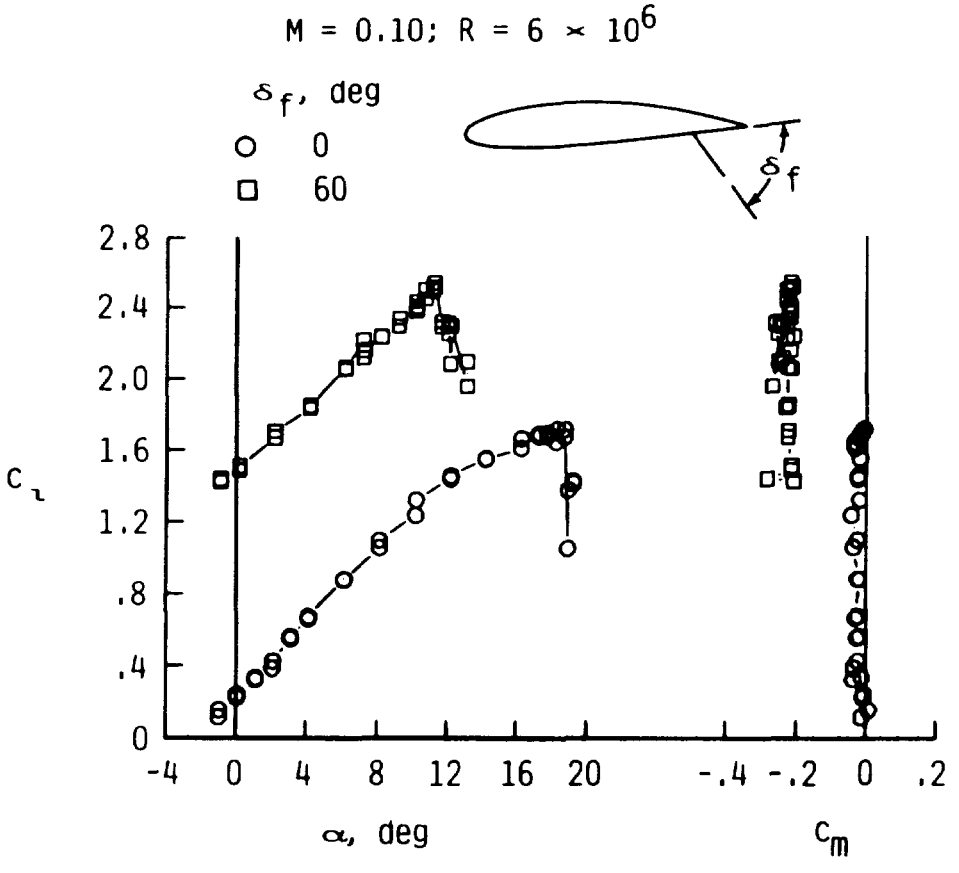

Figure 8

HIGH-SPEED TESTS IN 6- BY 28-INCH TRANSONIC TUNNEL

Evaluation of the airfoil performance at cruise and climb speeds was provided by two-dimensional tests in the Langley 6- by 28-Inch Transonic Tunnel (6x28 TT). The tests were conducted at Mach numbers ranging from 0.50 to 0.78 and at Reynolds numbers of 4 and 10 million. (**Figure** 9).

The model for these tests is shown in figures 10a and 10b as a solid shape with routing for chordwise surface pressure measurements. The measured pressure distributions were integrated along the chord to give normal force and pitching moment. Drag was measured by a traversing wake-survey probe.

The 6x28 TT is a blowdown facility and is unsuitable for testing natural laminar-flow airfoils. Drag measurements would therefore exceed the theoretical values by significant increments. However, these tests offered experimental pressure distributions at cruise and climb values of Mach number and Reynolds number which would help verify the airfoil design.

- Chordwise pressure distributions
- Wake survey probe for drag
- Blowdown facility
- Unsuitable for laminar flow

Figure 9

MODEL FOR HIGH-SPEED TESTS

The two-dimensional, high-speed airfoil tests were conducted on the model shown in figures 10a and 10b. A chordwise row of pressure orifices is located on each surface, and the routing associated with these orifices was located entirely on the lower surface to allow minimum surface disturbances on the upper surface.

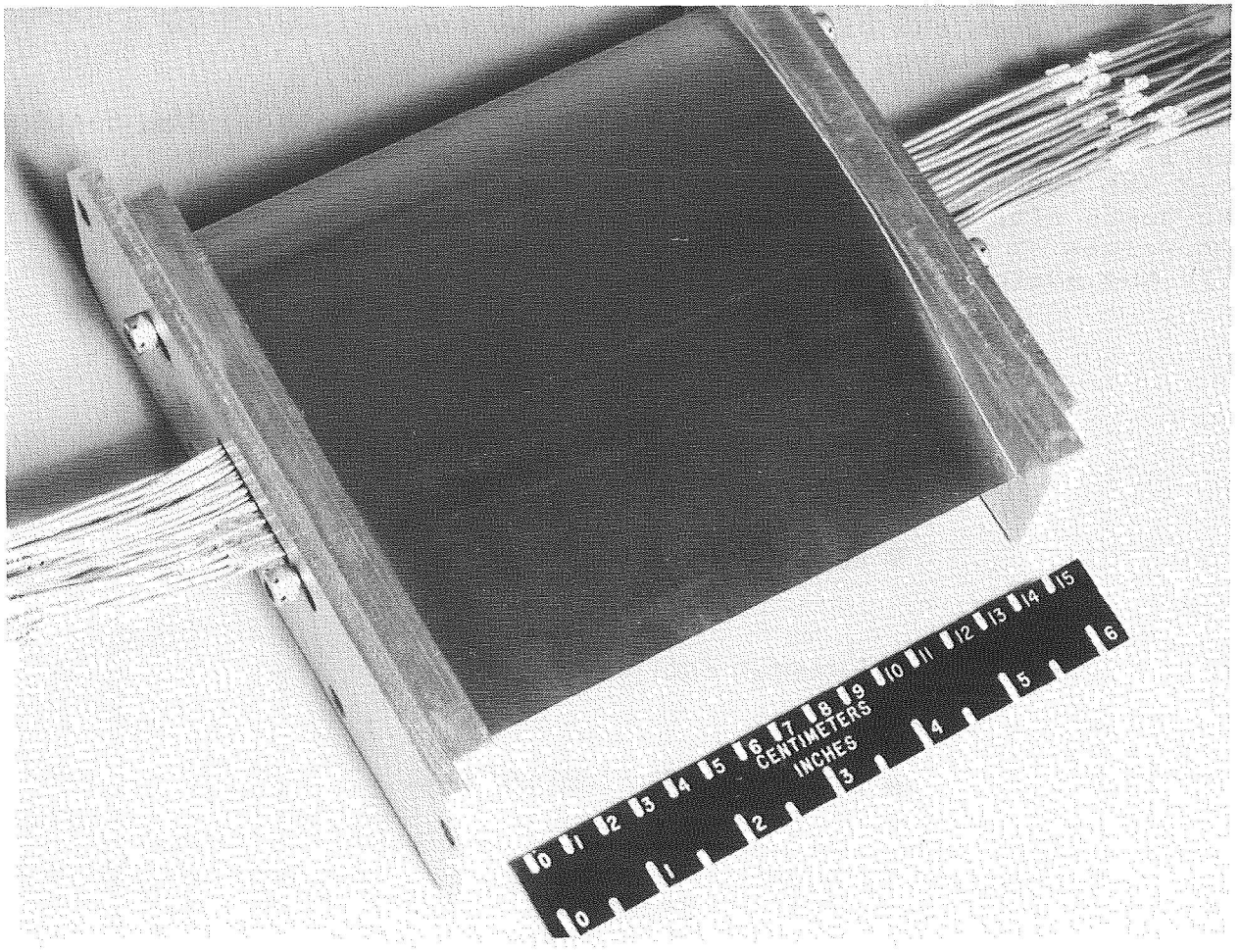

Figure 10a

MODEL FOR HIGH-SPEED TESTS

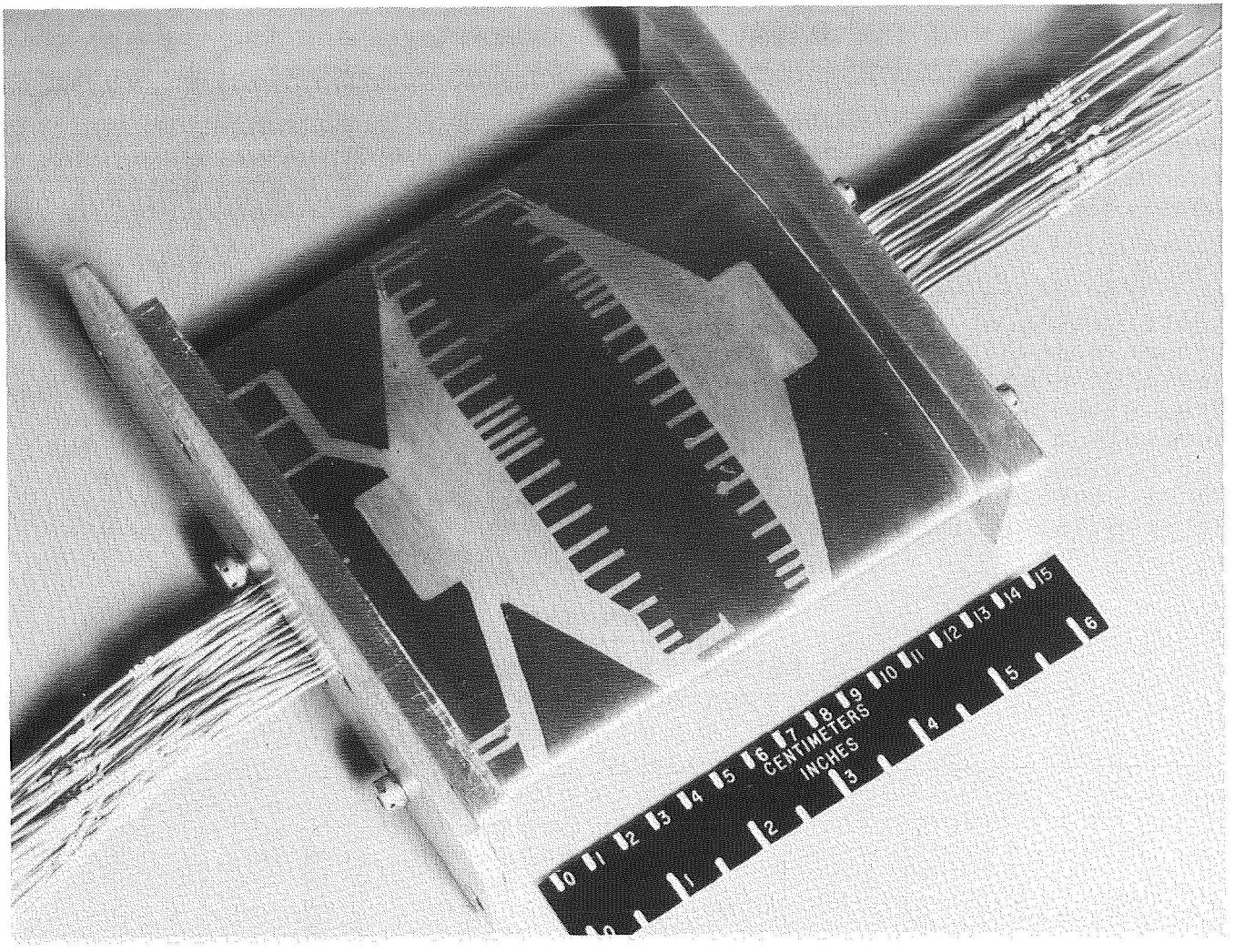

Figure 10b

TWO-DIMENSIONAL, HIGH-SPEED RESULTS

Results from the high-speed airfoil tests are shown in figure 11, which consists of the airfoil section characteristics for the smooth model, i.e., free transition, at the design Mach number of 0.70.

The section characteristics are given for three values of Reynolds number, ranging from 4 to 10 million, and indicate essentially identical behavior for the variation of normal-force coefficient with both angle of attack and pitching-moment coefficient.

For normal-force coefficients between 0.25 and 0.30, the drag coefficients at the 4.3 million Reynolds number still remain lower but become somewhat erratic. Drag levels at the 8.6 and 10.4 million Reynolds numbers have similar values to the low-speed data for minimum drag with fixed transition (see figure 4). This behavior indicates sufficient flow quality to allow some laminar boundary layers at the 4.3 million Reynolds number. At the higher Reynolds numbers, the tunnel turbulence level has probably increased to eliminate any substantial laminar flow.

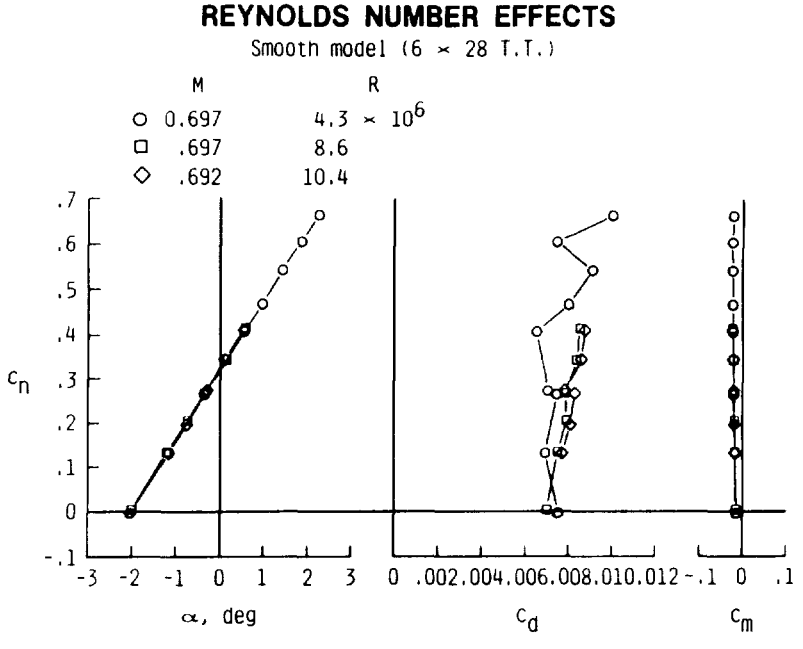

Figure 11

COMPARISON OF THEORY VERSUS EXPERIMENT

Figure 12 provides a comparison between the high-speed test data and the theory used in the design and analysis of the airfoil (ref. 1). The primary value of this comparison is the close agreement between the experimental and theoretical pressure distributions, which offers a major design verification. Without the proper pressure distribution, the extent of laminar flow on the airfoil would be unachievable.

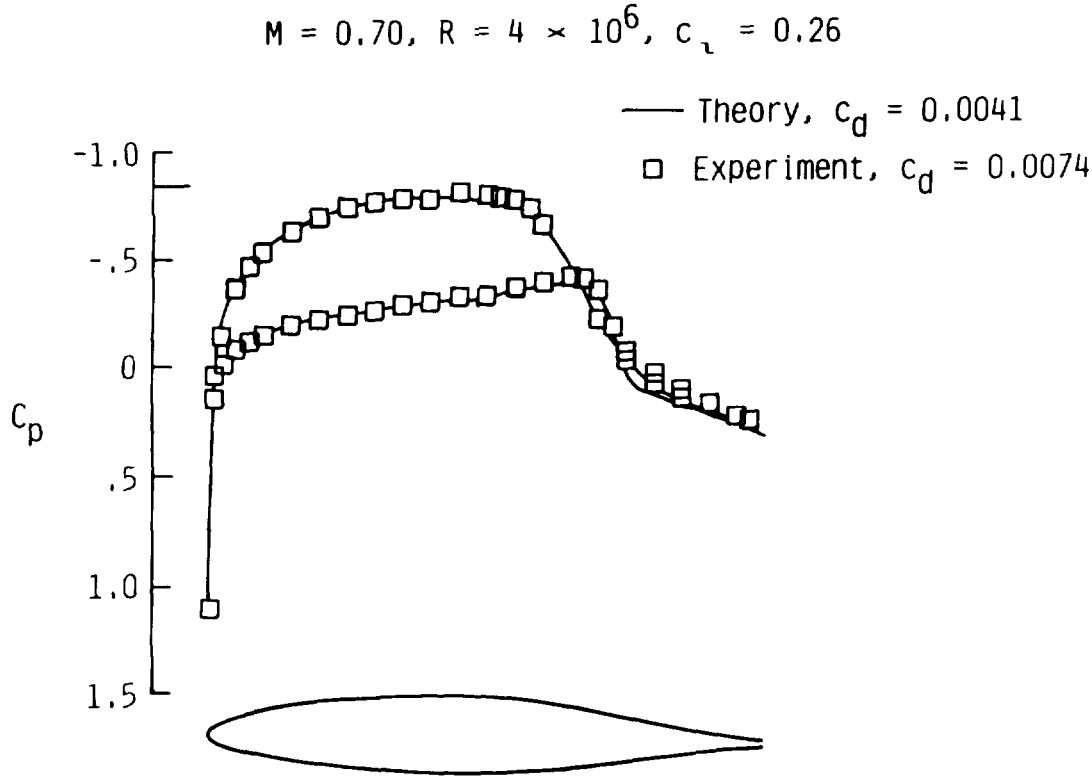

Figure 12

DRAG-RISE CHARACTERISTICS

Figure 13 illustrates the variation of drag coefficients with Mach number for the high-speed airfoil tests.

Test data were taken with fixed transition at 5-percent chord on upper and lower surfaces to investigate the airfoil performance without laminar flow at the near-design Reynolds number of 10 million. In comparison, the smooth model data at 4 million only had limited amounts of laminar flow due to the tunnel-flow quality.

The important aspects of the drag-rise characteristics in figure 12 are, first of all, that even limited amounts of laminar flow provide an increase in the drag-rise Mach number from 0.72 to 0.74. Also, even without laminar flow, where transition occurs near the leading edge, the drag-rise Mach number for this airfoil still exceeds the design Mach number 0.72 versus 0.70.

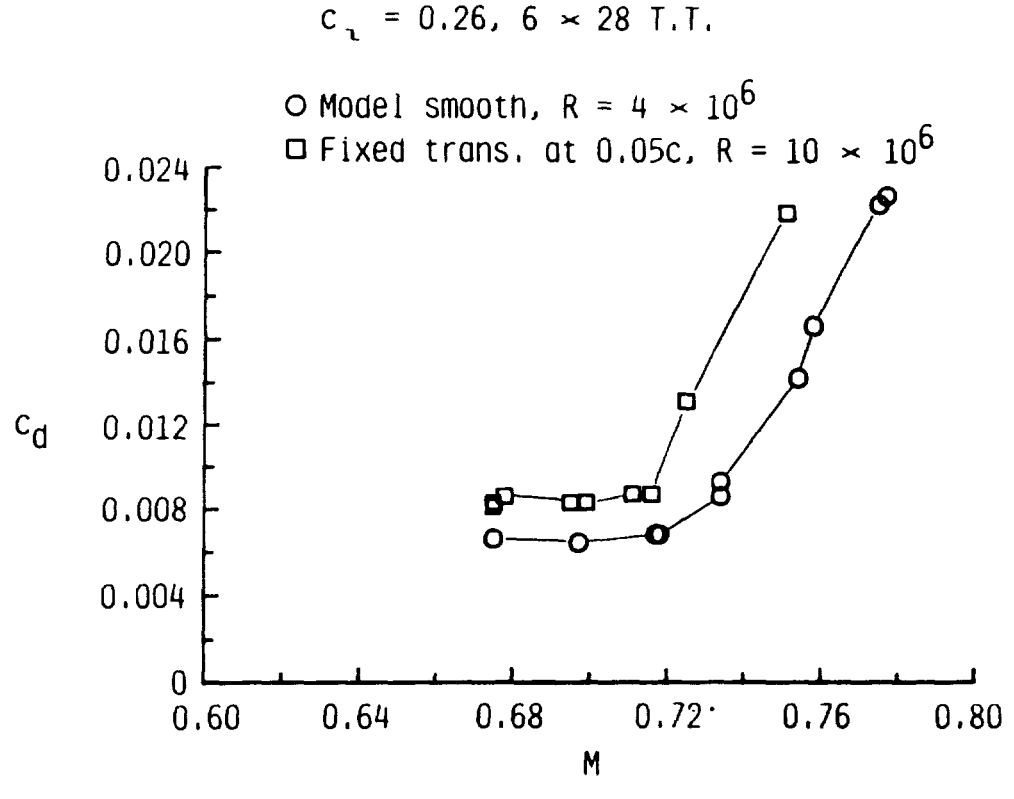

Figure 13

THREE-DIMENSIONAL TESTS IN 30 x 60 FOOT TUNNEL

Tests of a full-scale, semi-span model using the HSNLF-0213 airfoil section were conducted in the Langley 30- by 60-Foot Tunnel (figures 14a and 14b). The primary purpose was to evaluate the low-speed, high-lift characteristics of a three-dimensional wing using this NLF airfoil section. The tests were conducted at a Reynolds number of 3.7×10^6 based on mean aerodynamic chord and over an angle-of-attack range from -10° to 30°. In addition to force and moment measurements, pressure data, flow visualization, and hot-film data were obtained.

- Full-size semi-span model
- Actual flap system
- Force and moment data
- Hot film and flow visualization

Figure 14a

SEMI-SPAN MODEL IN THE 30 X 60 TUNNEL

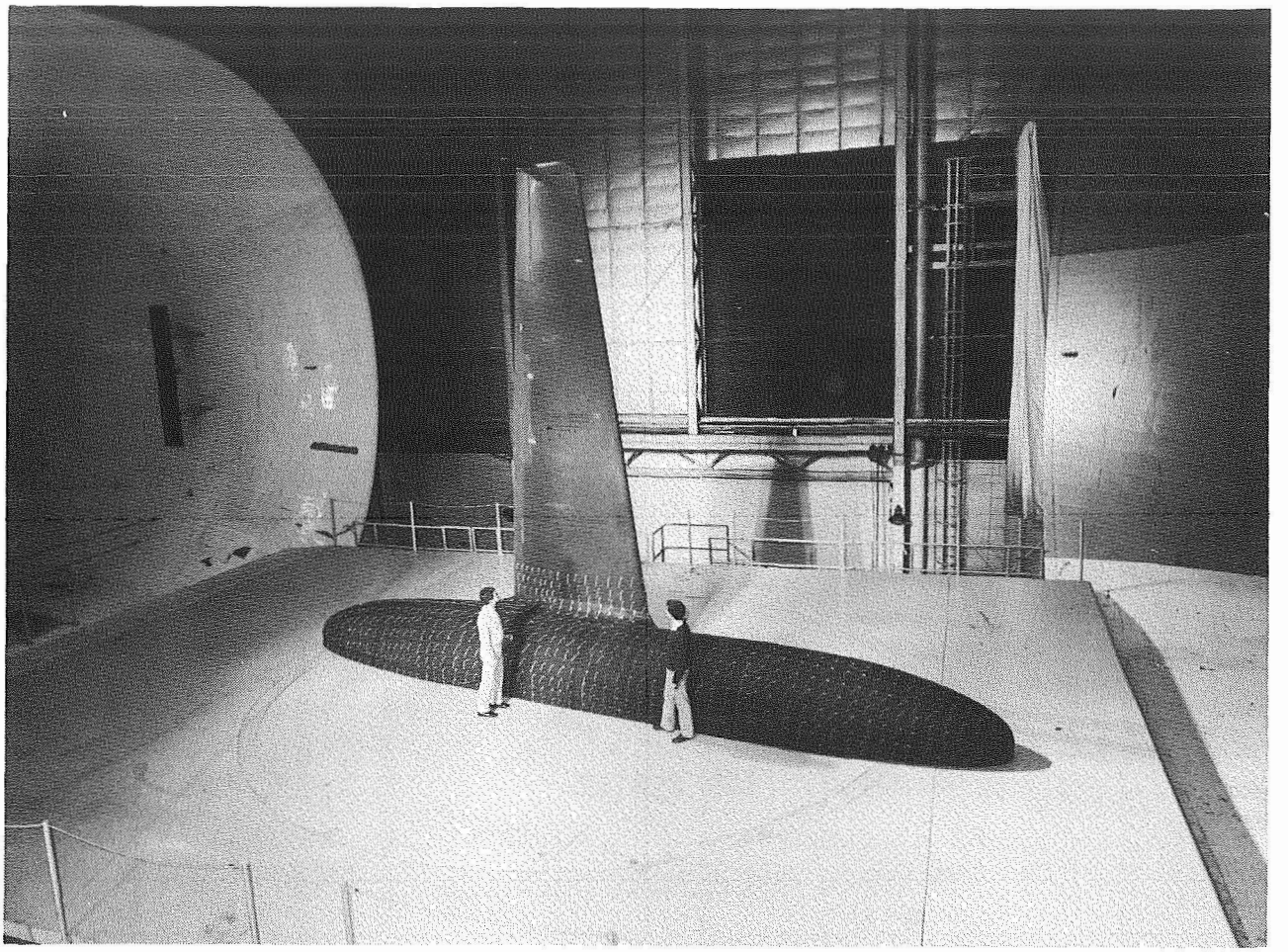

Figure 14b

SEMI-SPAN MODEL GEOMETRY

The model shown in figure 15 includes a body of revolution to simulate the presence of a fuselage near the wing. All force and moment data include the forces and moments acting on the fuselage. The fuselage is representative of a business jet fuselage in size and shape. Also included on the model are a deflectable aileron and spoiler to evaluate roll control and a multi-position flap to determine maximum lift for landing.

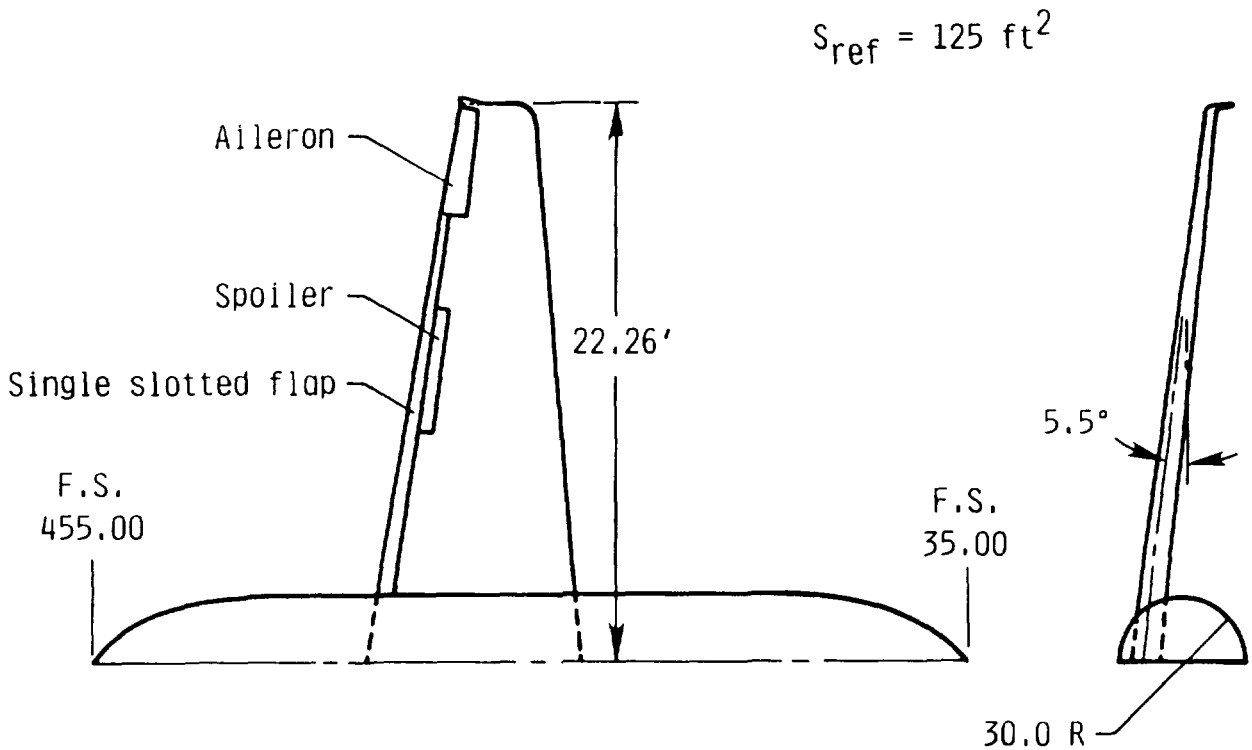

Figure 15

C-2

SLOTTED FLAP FOR SEMI-SPAN MODEL

Flap deflections are made by changing three brackets located on the lower surface of the wing. Deflections of 0°, 5°, 10°, 20°, 30°, and 40° are possible. In addition, at the 40° flap deflection, it is possible to vary both the gap and overlap of the flap. The flap is a 28-percent chord flap that extends from the wing root to a span location of 2y/b = 0.79. See figure 16.

Figure 16

EFFECT OF FLAP DEFLECTION ON LIFT

The lift characteristics for both 0° and 40° flap deflections are shown in figure 17. With the flap undeflected, a C_L of about 0.25 is achieved at $\alpha = 1^\circ$. This C_L is close to $C_L = 0.27$ predicted by the design techniques used in developing the twist distribution for the three-dimensional wing. For the undeflected flap configuration, a $C_{L_{max}}$ of 1.4 was achieved. Using the optimal gap and overlap settings with 40° of flap deflection increases $C_{L_{max}}$ to 2.6.

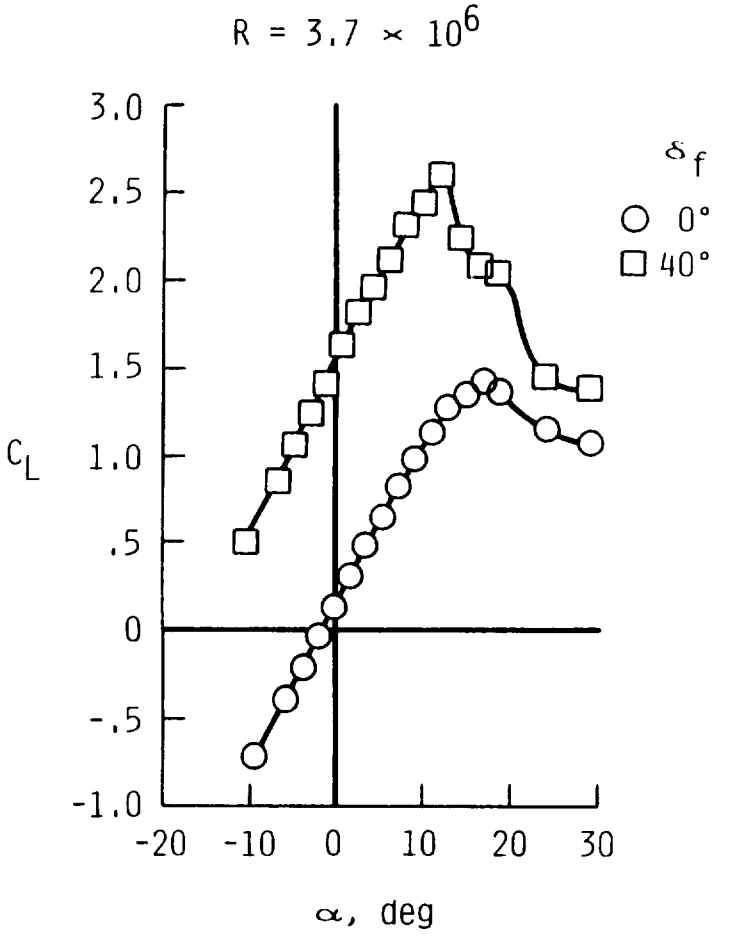

Figure 17

HOT-FILM GAGE INSTALLATION

In order to obtain data on the amount of laminar flow being achieved on the wing during the tests, six sets of hot-film sensors were placed on the wing (three sets on the upper surface, three sets on the lower surface). These sensors were placed at the 5-, 10-, 20-, 30-, 40-, 50-, 60-, and 70-percent chord locations in such a way that any turbulence generated by a sensor connection would not impact the sensors downstream (figure 18).

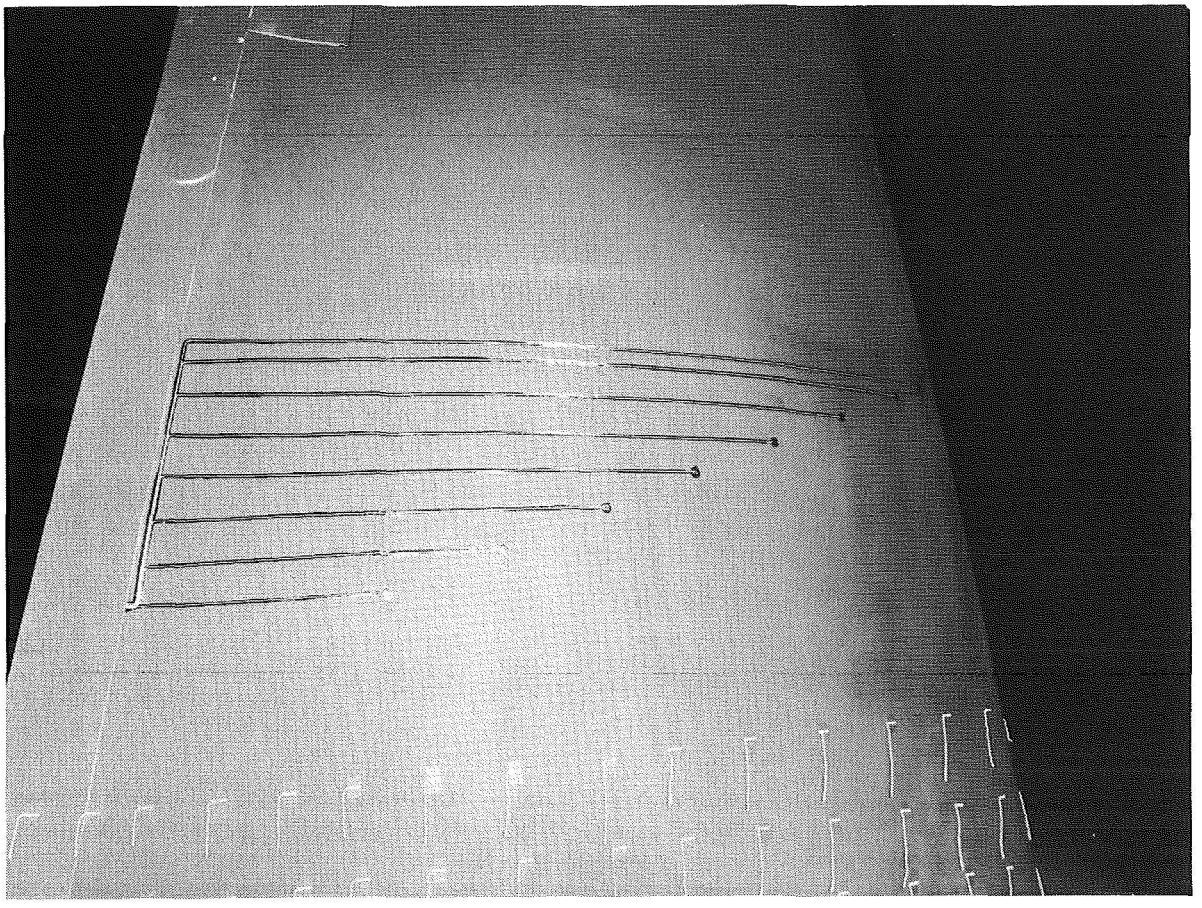

Figure 18

REGIONS OF LAMINAR AND TURBULENT BOUNDARY LAYERS

Hot-film data taken at $\alpha = 1^{\circ}$ at a Reynolds number of 3.0×10^{6} are presented in figure 19. The data indicate that the amount of achievable laminar flow increases from the wing root to the tip. Boundary-layer transition starts between 0.15 c and 0.25 c and becomes fully turbulent by 0.5 c to 0.7 c. Comparisons between previous tests results and flight data have indicated that while boundary-layer transition begins at a more forward chord location in the 30- by 60-foot tunnel, the chord station at which the boundary layer is 100-percent turbulent is generally similar.

$R = 3 \times 10^{6}$, $\alpha = 1^{\circ}$

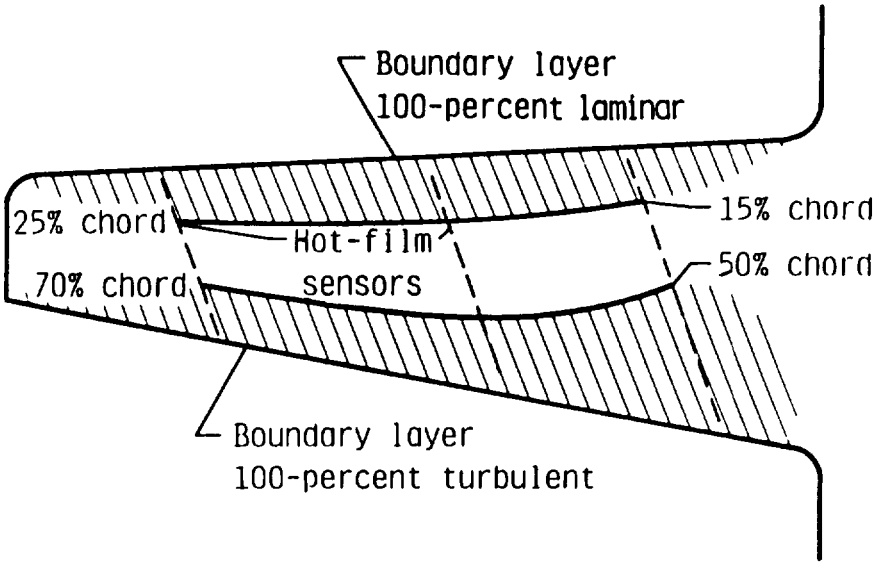

Figure 19

EFFECT OF BOUNDARY-LAYER TRANSITION ON DRAG

The net result of having a significant amount of laminar flow is a reduction in drag. This result is illustrated in figure 20 where boundary-layer transition was fixed at a chord station near the leading edge of the wing. With transition fixed at x/c = 0.05 on both the upper and lower surface, an increase in C_D of 0.003 is seen at C_L = 0.27. Data from two-dimensional tests indicated an increase in C_D of 0.004 for similar conditions. This difference can probably be attributed to the increased transition band noted earlier in the 30- by 60-foot tunnel data.

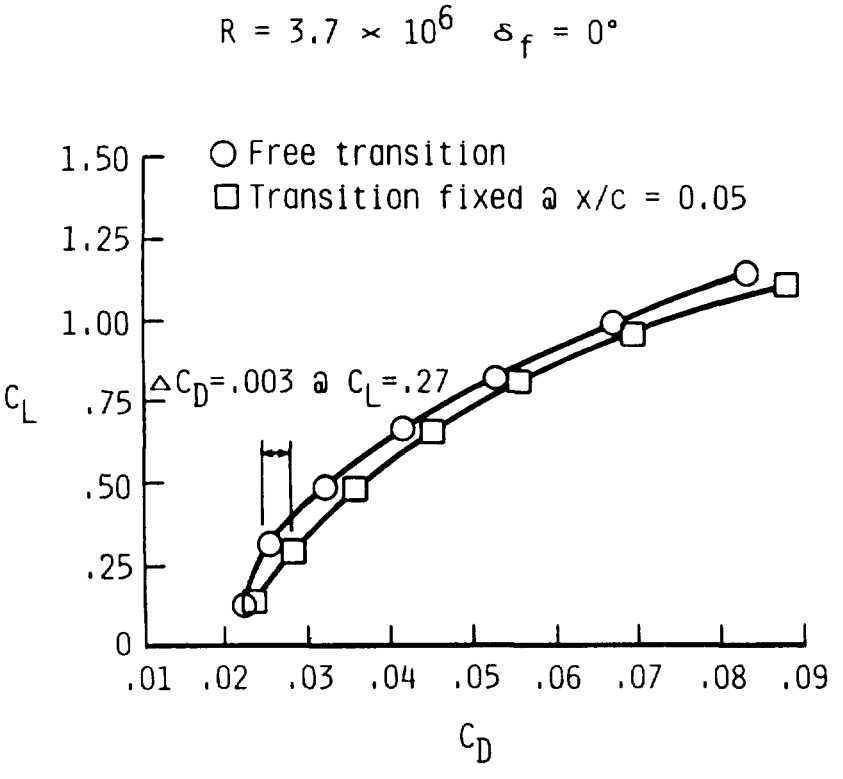

Figure 20

EFFECT OF BOUNDARY-LAYER TRANSITION ON LIFT

Of final concern is the effect of boundary-layer transition on the lift characteristics, which is shown in figure 21. Ideally, fixed transition would have no effect on lift. Test results, however, usually indicate some negligible reductions in C_L because of such things as a thickening of the boundary layer or slightly earlier separation than that for the wing with free transition. The data for this airfoil indicate a slight loss in lift near $C_{L_{max}}$ which is probably due to early separation. This reduction in C_L, however, is small and its effect on performance would be minimal.

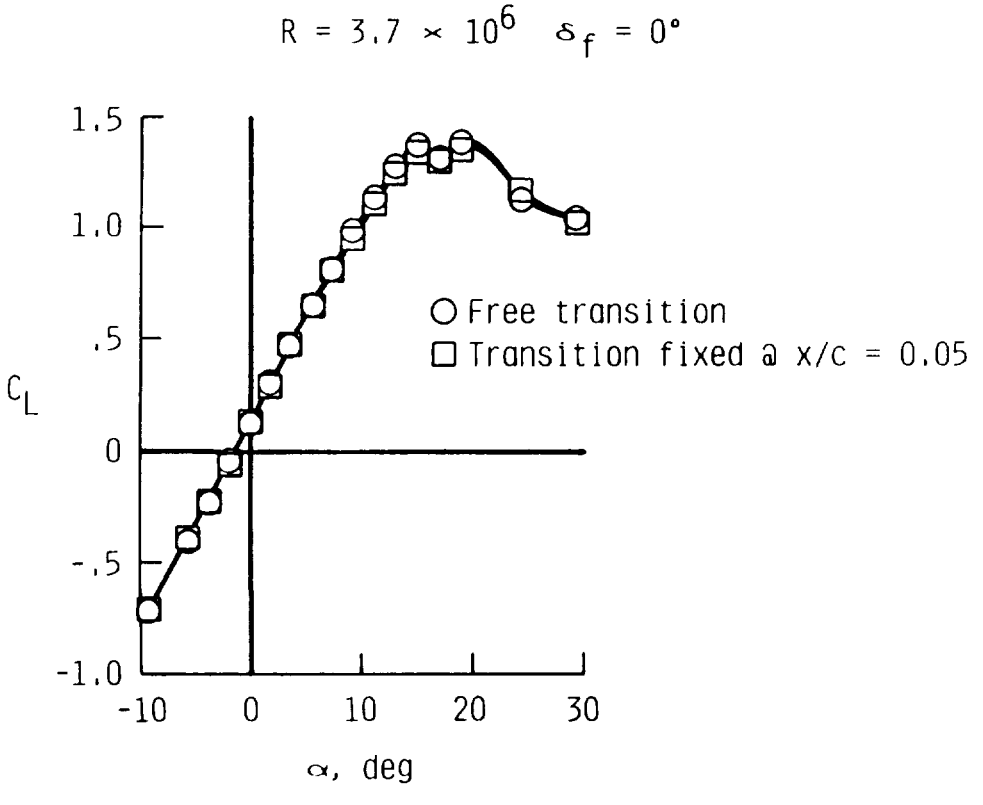

Figure 21

CONCLUSIONS

The two-dimensional airfoil tests on the HSNLF(1)-0213 airfoil demonstrated the following characteristics during the low-speed and high-speed tests (figure 22):

For the low-speed tests, the hot-film data showed laminar boundary layers back to 40-to 50-percent chord on the upper surface and 50- to 60-percent chord on the lower surface. The conditions for these observations were Reynolds numbers of 9 million, Mach numbers less than 0.30, and lift coefficient of 0.20, which resulted in a drag coefficient value of 0.0040.

The maximum lift in these tests for the basic airfoil ranged from 1.41 to 1.68 at Reynolds numbers of 3 and 6 million, respectively (M = 0.10). The simulated split flap increased the maximum lift coefficient to 2.5 at a Reynolds number of 6 million.

The high-speed tests primarily verified the design pressure distribution at the design Mach number of 0.70 and lift coefficient (0.26). In addition, the drag-rise Mach number with fixed transition near the leading edge (0.05 c) still exceeded the design Mach number (0.72 vs. 0.70). For the limited amount of laminar flow achieved with the Reynolds number of 4 million, the drag-rise Mach number increased to 0.74.

Three-dimensional tests on the full-size, semi-span model have evaluated the wing design with a slotted flap to determine the wing maximum lift coefficient and survey the boundary layer along the span. The basic wing (unflapped) obtained a maximum lift coefficient of 1.4 for both free and fixed transition at 0.05 c. With the 40° flap deflection, the maximum lift coefficient increased to 2.5 at the same Reynolds number of 3 million.

At the low angles of attack, hot-film data indicated laminar boundary layers back to 15-percent chord at the inboard station and 25-percent chord at mid-span and outboard stations. The semi-span model has shown drag coefficient values of 0.0030 lower for free transition than for fixed transition at 0.05 c, as compared to the 0.0040 increment observed in the two-dimensional, low-speed tests.

CONCLUSIONS

- 2-D test results
- Low speed
  - Laminar boundary layers exist on 40%-50% chord u.s. and 50%-60% l.s. with $c_d = 0.0040$ ($R = 9 \times 10^6$)
  - Basic airfoil $c_{l_{max}} = 1.44$, $R = 3 \times 10^6$ and 1.68, $R = 6 \times 10^6$ for $M = 0.10$
  - Split-flap $c_{l_{max}} = 2.5$, $R = 6 \times 10^6$ for $M = 0.10$
- High speed
  - Experimental and theoretical pressure distributions match
  - At $c_l = 0.26$, $M_{drag\text{-}rise} = 0.72$ at $R = 10 \times 10^6$, fixed trans.; $M_{drag\text{-}rise} = 0.74$ at $R = 4 \times 10^6$, free trans.
- 3-D test results
  - Basic $C_{L_{max}} = 1.4$ free or fixed trans., $R = 3.7 \times 10^6$
  - Slotted flaps at 40°, $C_{L_{max}} = 2.6$ free or fixed trans., $R = 3.7 \times 10^6$
  - Laminar boundary layers on u.s. back to 15% chord inboard, 25% chord mispan and outboard
  - Drag reduction free trans. vs. fixed trans. = 0.0030 3-D vs. 0.0040 2-D

Figure 22

REFERENCES

1. Waggoner, Edgar G.; Campbell, Richard L.; Phillips, Pamela S.; Viken, Jeffrey K.: Computational Design of Natural Laminar Flow Wings for Transonic Transport Application. Presented at the Langley Symposium on Aerodynamics, NASA CP-2398, vol.II, April 1985.

2. Abbott, Ira H.; Von Doenhoff, Albert E.; Stivers, Louis S., Jr.: Summary of Airfoil Data. NACA TR 824, 1945.

DESIGN AND TEST OF A NATURAL LAMINAR FLOW/ LARGE REYNOLDS NUMBER AIRFOIL WITH A HIGH DESIGN CRUISE LIFT COEFFICIENT

C. E. Kolesar
Boeing Military Airplane Company
Seattle, Washington

ABSTRACT

This paper reports on a Boeing aerodynamic research activity to design an airfoil for a large airplane capable of very long endurance times at a relatively low Mach number of 0.22. Airplane mission objectives and design optimization resulted in requirements for a very high design lift coefficient (C_l) and a large amount of laminar flow at high Reynolds number to increase the lift/drag ratio and reduce the loiter lift coefficient. Natural laminar flow was selected instead of distributed mechanical suction due to technology maturity differences when the study was performed. A design C_l of 1.5 was identified as the highest which could be achieved with a large extent of laminar flow.

A single element airfoil was designed entirely through a "synthesis" or inverse design process. This process utilized Boeing-developed inverse boundary-layer solution and inverse airfoil design computer codes to create an airfoil section that would achieve the performance goals and have reasonable off-design performance. This airfoil was designed to meet several criteria in addition to a 1.4 design C_l: a maximum C_l of 2.0, laminar flow on the lower surface from leading edge (L.E.) to trailing edge (T.E.) and laminar flow on the upper surface from L.E. to 0.30c followed by a forced transition. The design process and results, including airfoil shape, pressure distributions, and aerodynamic characteristics are presented in this paper.

A two-dimensional (2-D) wind tunnel model was constructed and subsequently tested in the 3 x 7.5 ft NASA Langley Low Turbulence Pressure Tunnel which enabled testing at the full scale design Reynolds number (RN) of 14×10^6. Model instrumentation included 53 static pressure orifices on the upper and lower surfaces at one spanwise station and a series of flush mounted hot-film gages used as boundary-layer laminar-to-turbulent transition detection devices. A comparison is made between theoretical and measured results to establish accuracy and quality of the airfoil design technique for the high lift/natural laminar-flow application.

INTRODUCTION

Boeing has been involved in the development of long endurance vehicles for many years. Design studies for a Continuous Patrol Aircraft (CPA) initiated in 1981 presented some unique challenges for the aerodynamic wing designer. The aircraft shown in Figure 1, was very large and was to be capable of enduring at low altitude for several days. The wing operated at relatively high Reynolds Number. A review of the literature indicated that while development work had been done for high lift/low drag sections at Reynolds numbers $\leq 1 \times 10^6$, there had been no airfoil sections designed suitable for the operating requirements of the CPA. Therefore, a parallel research and development study was initiated to design a high Reynolds number, long endurance airfoil.

The long endurance time required an airfoil design with the following characteristics:

- High lift (preferably without any flap deflection)
- Low drag
- Laminar flow to greatest extent possible (to minimize aircraft size)
- Reasonable stall characteristics

Furthermore, it was desired to advance beyond the empirical approach to airfoil selection, that is, modifying a base airfoil with trial and error redesigning in the wind tunnel. This study utilized Boeing-developed inverse boundary-layer solution and inverse airfoil design computer codes to create an airfoil section that would achieve the performance goals and still have reasonable off design performance.

LONG ENDURANCE CPA DESIGN
(CONTINUOUS PATROL AIRCRAFT)

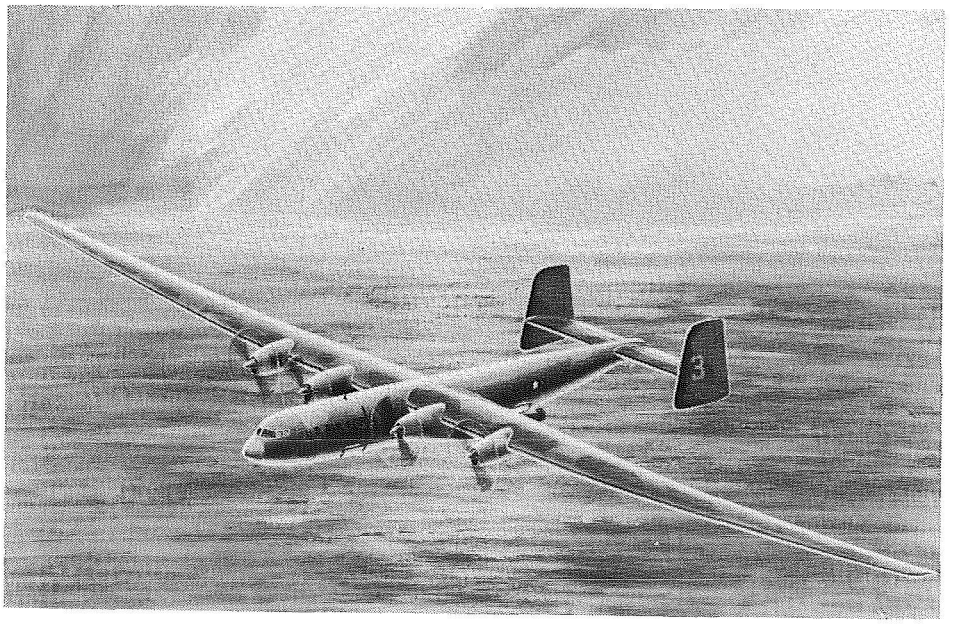

Figure 1.

Because the IR&D study was conducted in parallel with the CPA Program, most of the geometric and performance specifications for the 2-D airfoil reflect CPA mission specifications and requirements. As background for understanding the unusual design conditions, the following fundamental specifications were used from the CPA project:

- o Aspect Ratio: 21.6
- o Wing Area: 6000 ft^2
- o Span: 360 ft
- o Loiter Altitude: 5,000 ft
- o 145 kt endurance speed
- o Engine(s) type: turboprop

Figure 2 illustrates the high aspect ratio wing planform used for the CPA configuration and the design span loading for this wing geometry. This design study chose to formulate an airfoil for an outboard wing section (η=0.80) since this station represented the maximum required lift coefficient, and therefore was the critical airfoil for this loiter-design wing. The span loading curve integrates to a total airplane lift coefficient of 1.3.

WING PLANFORM AND SPANWISE LOADING

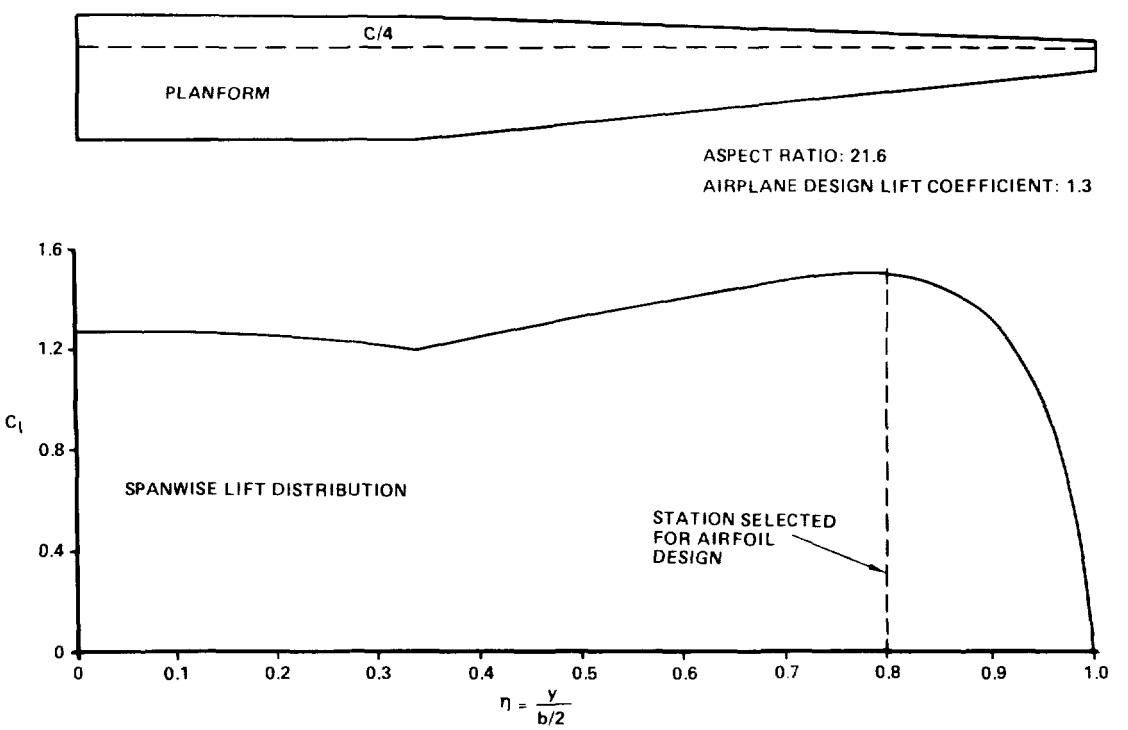

Figure 2.

AIRFOIL DESIGN REQUIREMENTS

Aspect Ratio and minimum drag coefficient (C_{D_O}) are well-known to have a significant effect on both the endurance parameter $(C_L^{3/2}/C_D)_{MAX}$ and the lift coefficient at which the maximum endurance parameter is reached. The endurance improvement and the important reduction in lift coefficient with extent of laminar flow as shown in Figure 3, provided an impetus for obtaining as much laminar flow on the wing as possible.

DESIGN LIFT COEFFICIENT FOR ENDURANCE

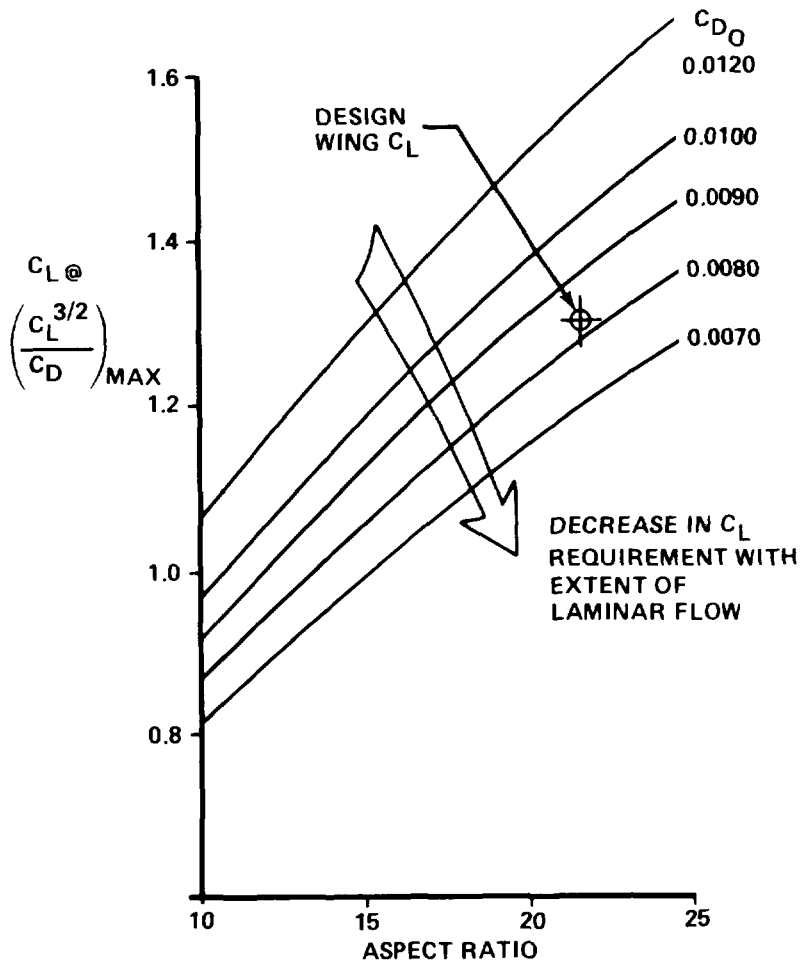

Figure 3.

AIRFOIL DESIGN REQUIREMENTS (CONCLUDED)

Based on the CPA design specifications, airfoil design criteria were selected. These are listed in Figure 4. A total airplane lift coefficient of 1.3 resulted in section design and maximum lift coefficients of 1.5 and 2.2 respectively at the aforementioned outboard wing station. These values will produce a 20 percent stall margin. Well into the design phase it became evident that these section coefficients were difficult to attain. Thus, a revision to section design and maximum lift coefficients of 1.4 and 2.0 was established as a more approachable goal.

A design goal to maximize the extent of laminar flow resulted in developing an airfoil which would sustain natural laminar flow from L.E. to T.E. on the lower surface and from L.E. to 0.3c on the upper surface. The upper surface extent was largely dictated by the chord distance required for velocity deceleration and pressure recovery.

The low endurance speed requirement in combination with a 5000 ft loiter altitude, resulted in a design Mach number of 0.22. This low Mach number enabled a large thickness ratio (18%) to be used in meeting the high design lift coefficient requirement.

AIRFOIL DESIGN CRITERIA

- DESIGN C_l=1.4
- MAXIMUM C_l=2.0
- MAXIMUM THICKNESS = 0.18 C
- RN=14 x 10^6
- MACH NO. = 0.22
- LAMINAR FLOW, UPPER SURFACE, L.E. TO 0.3 C
- LAMINAR FLOW, LOWER SURFACE, L.E. TO T.E.
- NO UPPER SURFACE SEPARATION
- REASONABLE STALL CHARACTERISTICS (NON-ABRUPT)
- REASONABLE OFF-DESIGN PERFORMANCE

Figure 4.

AIRFOIL DESIGN PROCESS

The airfoil was designed through a "synthesis" or inverse design process developed by Boeing. The process utilizes inverse boundary-layer solution and inverse airfoil design computer codes to create an airfoil section which can attain specified characteristics and achieve reasonable off-design performance. This method, briefly described herein, is described more comprehensively in Reference 1 along with a discussion of the background of the computer codes.

The design process begins with the inverse boundary-layer solution where desired boundary-layer characteristics, performance objectives, and constraints are specified. Through the synthesis process a corresponding viscous flow pressure distribution is developed and an airfoil shape is extracted that meets the specified requirements. Current computer codes used by Boeing to accomplish the two inverse solution processes are:

A427 — for airfoil pressure distribution design and parametric studies

A456 — for detailed geometry design and final performance evaluation (including the effects of separated flow)

The A427 program has the capability to generate a pressure distribution and corresponding "seed" airfoil given a set of boundary-layer characteristics, performance goals, and physical constraints. (Figure 5.)

- DEFINE AIRFOIL SPECIFICATIONS (X_r/C, T.E. C_p, ETC)
- SPECIFY BOUNDARY-LAYER H IN RECOVERY REGION
- DESIGN PRESSURE DISTRIBUTION USING INVERSE BOUNDARY-LAYER THEORY (A427)
- EXTRACT SEED AIRFOIL

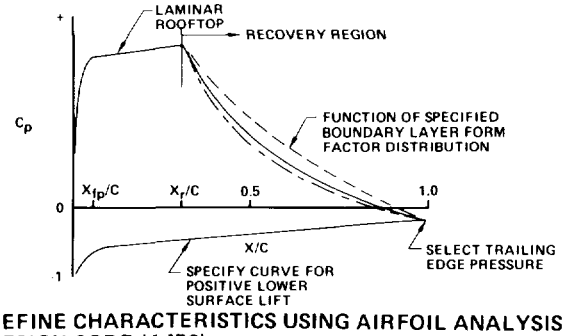

- REFINE CHARACTERISTICS USING AIRFOIL ANALYSIS AND DESIGN CODE (A456)
- EXTRACT FINAL AIRFOIL GEOMETRY (A456)

Figure 5.

AIRFOIL DESIGN PROCESS (CONCLUDED)

The Subsonic Airfoil Section System (A456) program is a general purpose 2-D, airfoil section analysis and design program. In the analysis mode the single element airfoil forces, moments, and boundary-layer characteristics are calculated at various angle of attack and flow conditions. Through the use of potential flow theory, boundary-layer theory, and separated flow modeling theory, the airfoil performance was predicted up to and beyond maximum lift. In the design mode the airfoil was reshaped to produce a desired pressure distribution.

Significant tasks involved in the iterative process of designing the airfoil are summarized in Figure 5. An important program input for designing the pressure recovery region is the boundary-layer form factor (H) distribution. Code A427 contains three forms of H distributions: a constant H, linear-increasing H, and exponentially increasing H. A linear-increasing H was selected to both maximize lift and soften the stall away from the sharp Stratford-type separation produced with a constant H distribution.

At the culmination of the design phase, an airfoil had been designed that analytically satisfied the required performance, achieved approximately 30 percent laminar flow on the upper surface, and was structurally practical. Figure 6 presents the airfoil contour and shows the amount of camber designed into the profile. This design phase was followed by a joint testing-verification effort between Boeing and NASA in which Boeing provided the 2-D airfoil and NASA contributed wind tunnel time and personnel at the Langley Low Turbulence Pressure Tunnel (LTPT).

GENERAL AIRFOIL CONTOUR

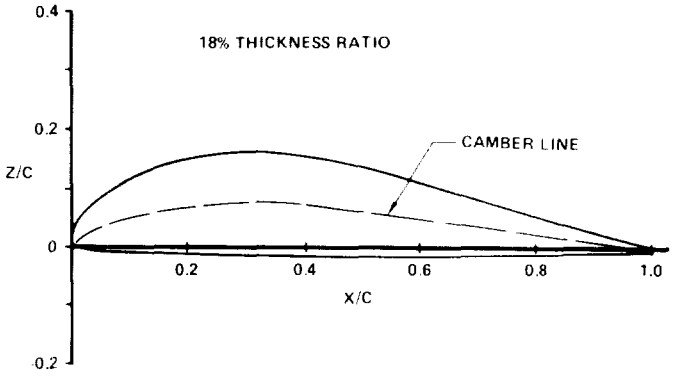

Figure 6.

TWO-DIMENSIONAL AIRFOIL MODEL

A solid aluminum airfoil section was built for testing in the NASA-Langley 2-D Low Turbulence Pressure Tunnel (LTPT). The installed model, shown in Figure 7, had a 32.0" chord and 36.0" span with a maximum thickness of 18 percent chord. The airfoil chord length was essentially limited by the largest length which could be physically accommodated on the end plates. It was recognized that the 32.0" chord would result in a high RN/ft at the design Reynolds number of 14×10^6. A 0.127c plain flap was built with options for three angular settings (excluding the nested position). Contour tolerances were kept to $\pm$.003" from the leading edge back to 0.75c and $\pm$0.006" from 0.75c to the trailing edge. A surface finish of 32 or better was specified. Surface waviness in the chordwise direction was to be no greater than 0.006" in 20". To prevent introducing flow disturbances, the airfoil was constructed with a minimum of joints or similar discontinuities. Figure 8 shows the two instrumentation cavities machined into the airfoil from the lower surface and the thick web retained to ensure structural rigidity. A thick flush contoured cover plate was fitted for bolting into a lower surface recess surrounding the two cavities. This cover plate and flap cove edges were the only visible surface discontinuities. These mating pieces were manufactured with special precautions to maintain the smoothest continuous contour possible. A tang at each end of the model was used to attach cirular end plates, which form part of the test section side walls, and in turn, flush mount the model on the left and right hand rotating inner drums of the pitching mechanism.

LTPT TEST 303-W3 AIRFOIL

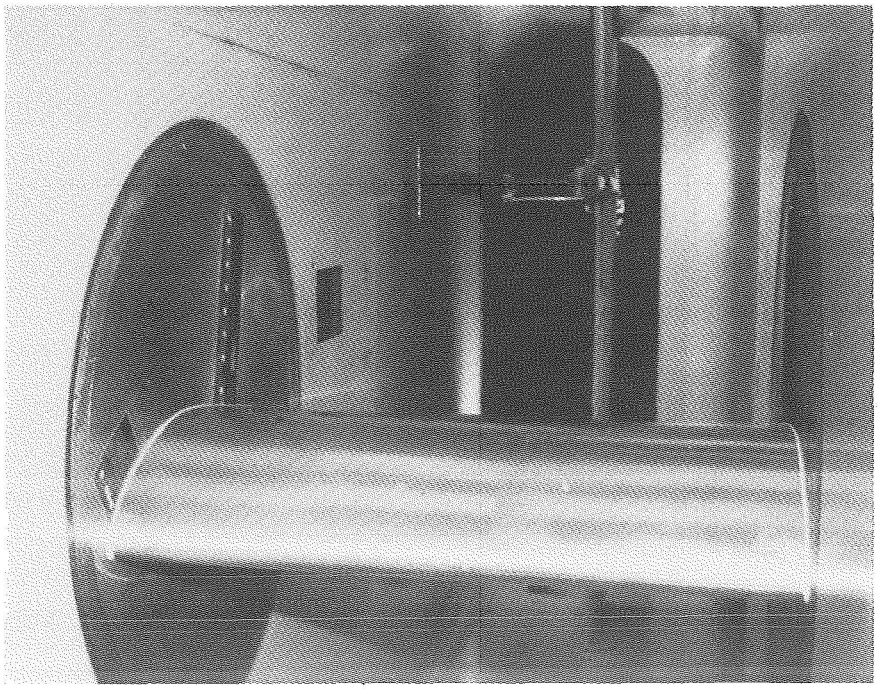

Figure 7.

MODEL VIEW SHOWING UNDERSURFACE
INSTRUMENTATION CAVITIES

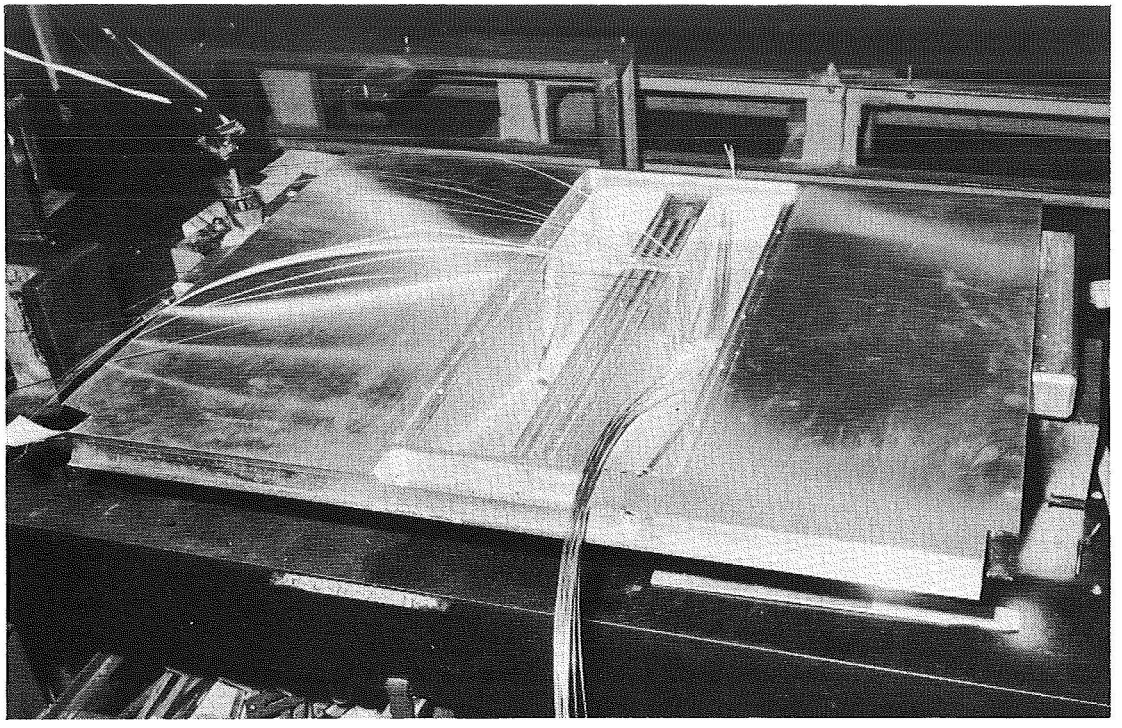

Figure 8.

INSTRUMENTATION

Pressure sensing instrumentation consisted of 53 static pressure orifices at one spanwise station: 32 on the upper surface and 21 on the lower surface. A slanted orifice pattern forward of 0.40c as shown in Figure 9 was utilized to preserve a smooth surface leading up to each forward orifice.

Flush mounted hot-film gages were used as boundary layer laminar-to-turbulent transition detection devices. By monitoring the root mean square (RMS) voltage of each hot-film sensor, in the natural or forced boundary-layer transition area of the upper surface, an indication of laminar flow, transition, or turbulent flow could be determined. Three types of output results were obtained for this test. First, a table of RMS voltage for each gage at each angle of attack was recorded. Second, this table was converted to integers of 1 to 4 representing the various boundary-layer stages from complete laminar through transition to full turbulent flow. Lastly, a plot of RMS voltage versus angle of attack for each gage was drawn giving an overall record of how a specific location changed from laminar to turbulent as angle of attack was increased. Ten hot-film gages were mounted flush in a slanted spanwise station pattern, covering the area from 0.17c to 0.44c on the upper airfoil surface, as illustrated in Figure 9.

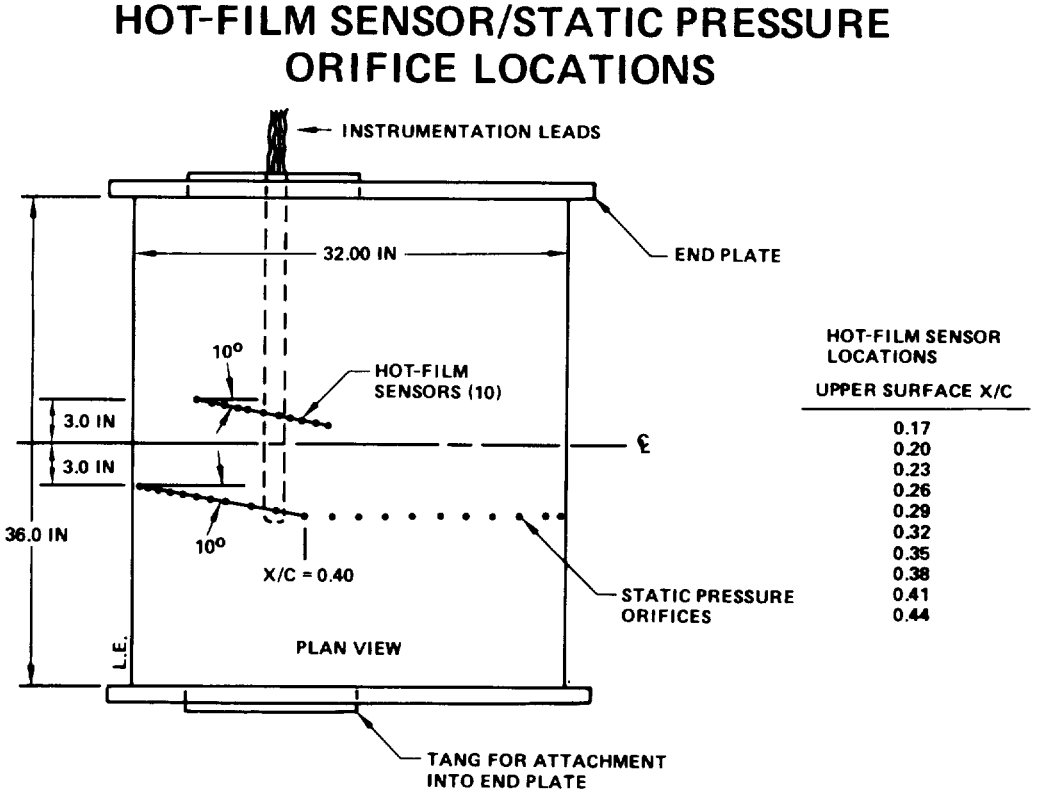

Figure 9.

TEST FACILITY

Two dimensional wind tunnel testing of the high lift/natural laminar airfoil was conducted at the NASA-Langley 3 ft x 7.5 Low Turbulence Pressure Tunnel (LTPT). This tunnel is designed to operate over a range of tunnel pressures from 160 psia to less than 1 psia, thereby providing full scale Reynolds number testing capability. The 2000 HP drive motor provides a speed capability of 0.46 Mach at 1 atm to 0.25 Mach at approximately a tunnel pressure of 120 psia.

Besides standard tunnel parameter values (Reynolds number, Mach number, angle of attack, etc.) data in coefficient form (C_l, C_d, and C_m) were obtained within an hour of completing a test run with the tunnel's data acquisition and data reduction system. Section lift coefficient was calculated by integrating the pressure measurements from the 53 static orifices located around the airfoil at one spanwise station. Section pitching moment coefficient was determined by summing the moments produced by the various measured static pressures about the 0.25c location.

Section drag coefficient was calculated from wake rake total pressure measurements. At each angle of attack, the sting mounted/remotely controlled/multi-probe rake was moved completely through the airfoil's wake. Drag profile plots showing the variation of drag coefficient with height as measured by each of the seven total pressure probes were obtained on-line. Section drag coefficient was calculated by integrating each of the drag profiles and then averaging. A limitation of the wake rake system was reached when the rake's traversing capability was exceeded by a wake depth expanded greatly by stall-generated flow separation. High loads due to turbulence intensity in a wake with airfoil flow separation at high static pressures was a second limitation. These drag measurement limitations prevented drag data acquisition at angles of attack beyond initial stall. The tunnel wake rake is visible in Figure 7.

CHORDWISE PRESSURE DISTRIBUTION

The theoretical chordwise pressure distributions selected to achieve the prescribed extent of natural laminar flow at the design section lift coefficient and Reynolds number of 1.4 and 14 x 10^6, respectively, is presented in Figure 10. The upper surface can be divided into four flow regions: 1. An acceleration region transisting into 2. A laminar roof with accelerating flow at the design conditions, 3. A forced transition region between 0.26 and 0.30c, and 4. A turbulent recovery region extending from 0.30c to the trailing edge. Note that a partial stagnation pressure recovery of about 0.25Cp was designed into the trailing edge area. The entire lower surface was designed to produce positive pressures to assist in achieving the high design lift coefficient. A continual flow acceleration is maintained from the leading edge to about 0.90c to aid in sustaining laminar flow. Figure 10 shows a close agreement over the entire upper and lower surface between theory and test data. However, theory does predict somewhat more positive pressure on the lower surface than was achieved.

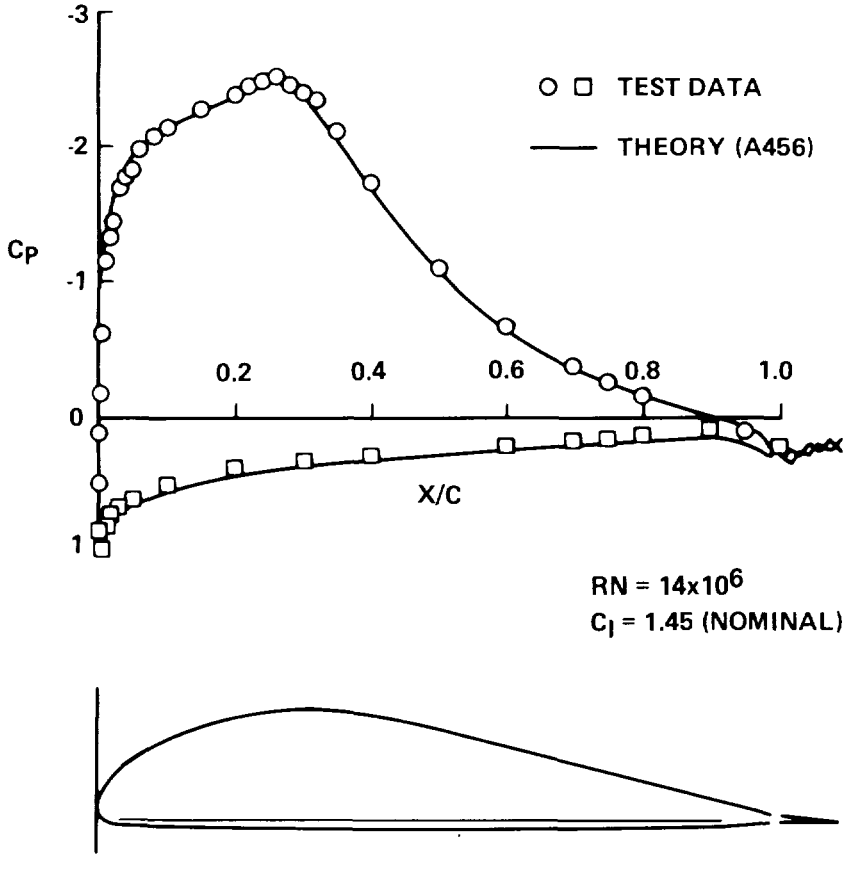

Figure 10.

CHORDWISE PRESSURE DISTRIBUTION (CONCLUDED)

One airfoil design criterion was reasonable off-design performance. Figure 11 presents three chordwise pressure distributions descending in lift coefficient from the design case at maximum endurance. That this goal was achieved in the lift component can be seen by noting the regular change in both upper and lower surface pressure coefficient over the entire chord (figure 11). Also note that a deceleration zone is present near the lower surface leading edge at $0.94C_l$. This characteristic along with a flat pressure coefficient over the lower surface is not favorable for maintaining laminar flow. This situation will become more unfavorable for laminar flow on the lower surface at smaller lift coefficients.

OFF-DESIGN PRESSURE DISTRIBUTIONS

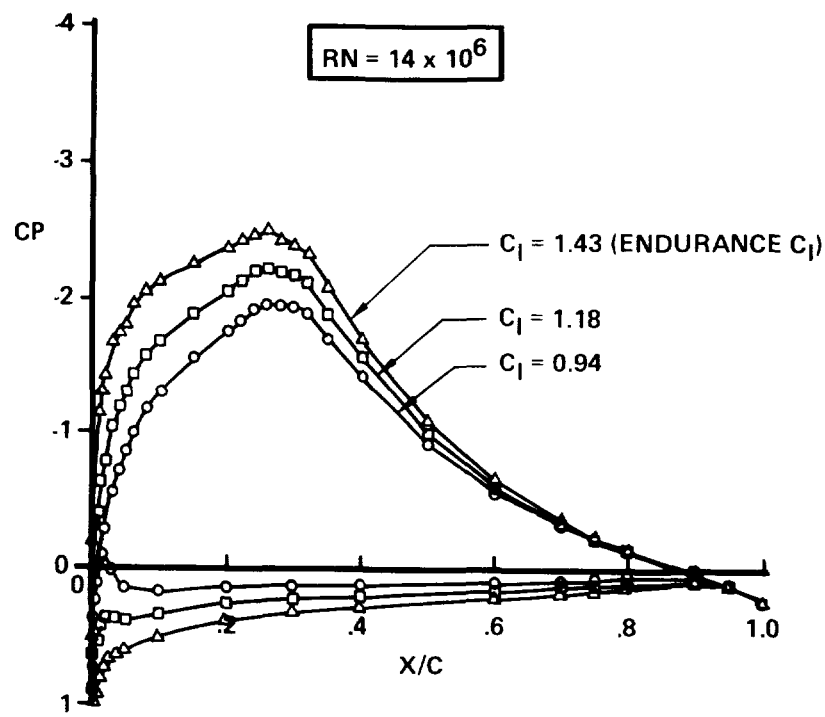

Figure 11.

BOUNDARY-LAYER ANALYSIS

The ten hot-film sensors installed in the upper surface from 0.17c to 0.44c were continuously monitored on scopes for signal content and permanent records were acquired, such as the two presented in Figure 12 where RMS voltage has been plotted as a function of angle of attack. Laminar flow is characterized by an almost zero RMS voltage. Transition is registered as a sharp rise in RMS voltage, a peak, and then a sharp decrease to a level indicative of fully turbulent flow. During the initial part of transition, the signal exhibits a laminar RMS voltage level mixed with bursts; in the second part the signal indicates turbulent flow mixed with bursts.

Prior to this test, experience level in using hot-film sensors as transition detectors was quite low. There was concern about sensor reliability, primarily due to their small size and fine wire leads. However, during the test this instrumentation was found to be trouble-free and rugged. If this had been known prior to the test, the lower surface would also have been instrumented.

HOT-FILM RESULTS

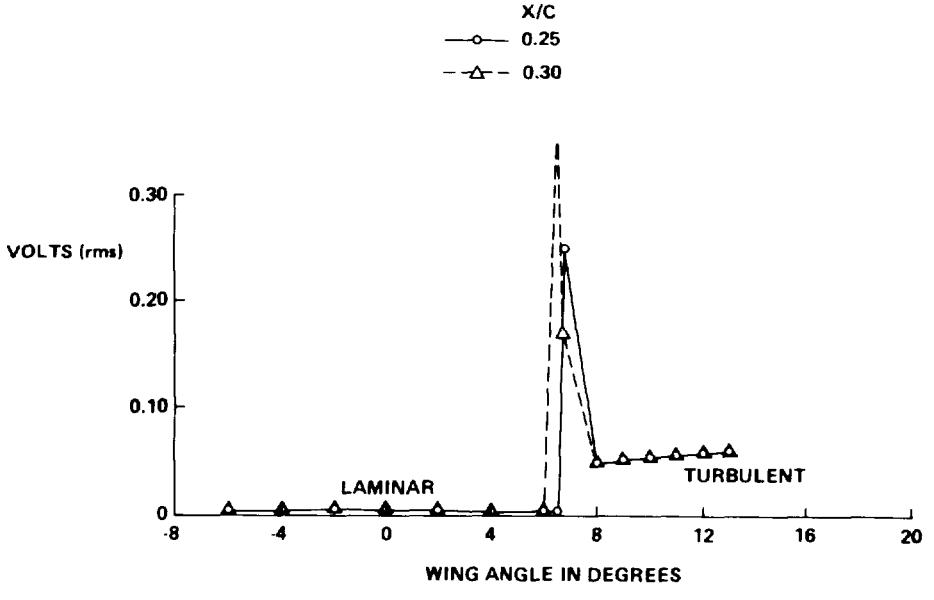

Figure 12.

Figure 13 presents hot-film data showing boundary-layer conditions as a function of chord during alpha sweeps at 14×10^6 and 12×10^6 Reynolds number. The data have been interpreted to establish chordwise extent of laminar flow and transition to fully developed turbulent flow. Note that the goal of obtaining laminar flow over the forward 30 percent chord was achieved. At 14×10^6 RN, the hot-film sensors indicated transition forward movement at 5.3^o alpha, an angle lower than predicted by theory. Transition forward movement was progressively delayed to higher alphas with decreasing Reynolds number. At 12×10^6 RN, Figure 13 shows that this movement occurs at 6.5^o alpha; at 10×10^6 RN, it is delayed to 10.5^o alpha.

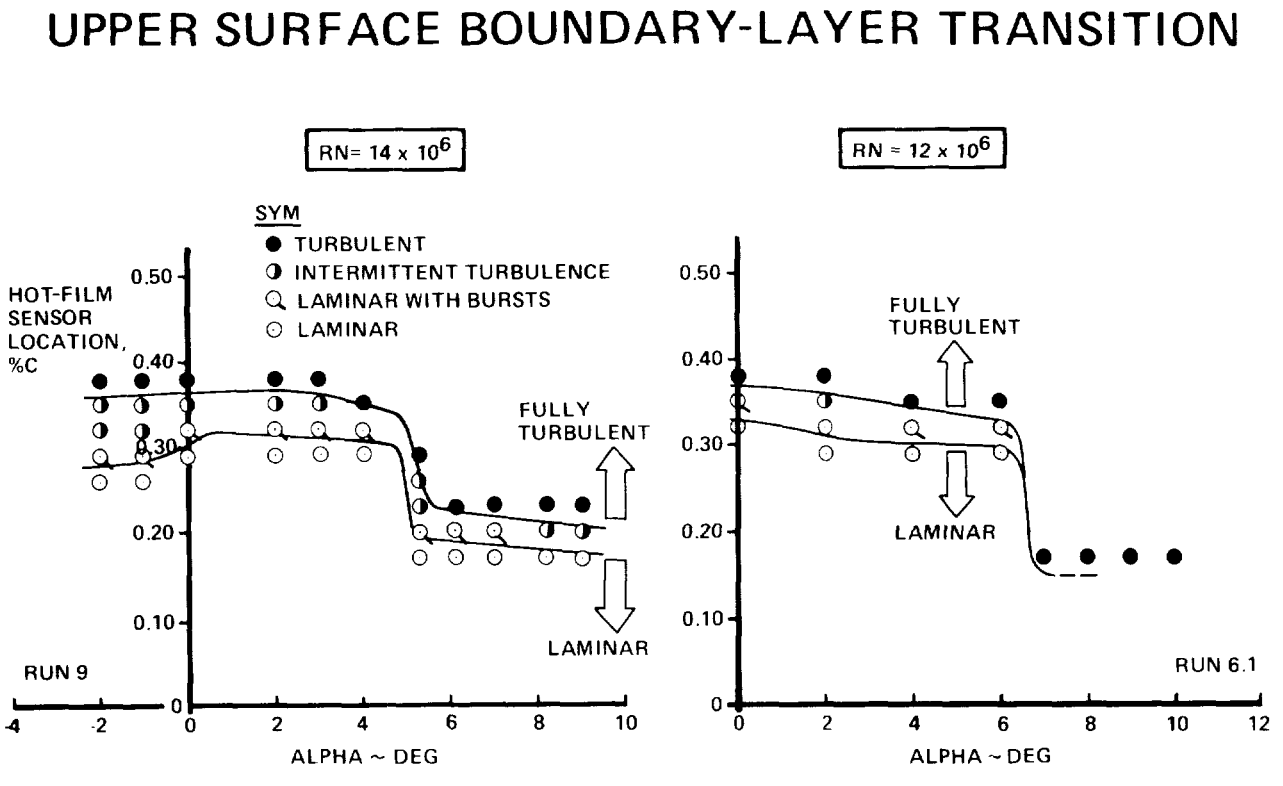

Figure 13.

REYNOLDS NUMBER EFFECTS

Figure 14 presents four lift curves obtained over a range of Reynolds numbers from $5x10^6$ to $14x10^6$. Note that whereas three of the pitch sweeps were performed close to the design Mach number of 0.22, the sweep for $14x10^6$ RN was conducted at 0.09 Mach. This deviation was caused by the practical necessity of relaxing the desired test Mach number to reduce tunnel pressurization pumping time.

Two characteristics of the lift curve can be observed: the decrease in lift curve slope with increasing Reynolds number and the decrease in maximum lift with increasing RN. An examination of chordwise pressure plots at 8^o alpha revealed higher negative pressure coefficients on the upper surface over the aft 80 percent chord at successively lower Reynolds number. At each test Reynolds number the stall was abrupt.

Measurement of an accurate maximum lift in a 2-D tunnel is a recognized problem due to boundary layer on the tunnel walls. During initial test runs, the impact of wall slot blowing using two blowing slots built into the model end plates (one forward and the second at 0.60c) was examined. Blowing did clean up initial flow separation in the corners between the aft wing surface and tunnel side walls, but only increased stall angle by 0.7^o before stall occurred evenly across the span. Since blowing only provided a modest improvement in stall angle and did not reduce stall abruptness, a decision was made to leave out slot blowing to materially reduce test time.

REYNOLDS NUMBER EFFECT ON LIFT CURVE

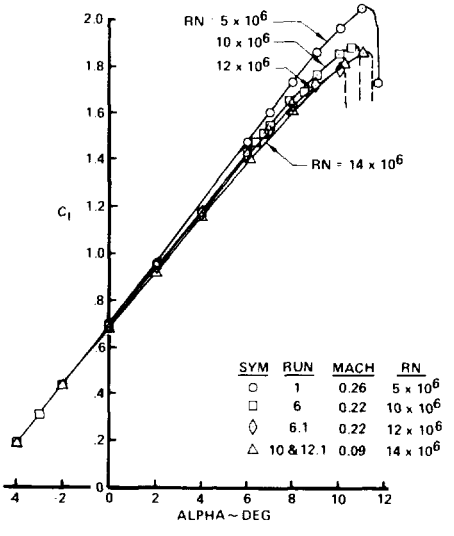

Figure 14.

Figure 15 presents the companion drag polars to the Figure 14 lift curves. The polars generally exhibit a flat drag over a range of lift coefficients from endurance levels down to the lowest test values, which is indicative of satisfactory off-design performance. Note the increase in drag at endurance level lift coefficients of 1.48 with 12×10^6 Reynolds number, for example. The departure in polar shape coincides with the forward movement in upper surface boundary-layer transition previously shown in Figure 13. At 4^o alpha, the drag level for both 10×10^6 and 12×10^6 RN curves closely match theory which includes laminar flow over the initial 30 percent of the upper surface and over almost the entire lower surface. The drag increase at 14×10^6 RN was a concern because it suggested premature transition on the lower surface.

REYNOLDS NUMBER EFFECT ON DRAG POLAR

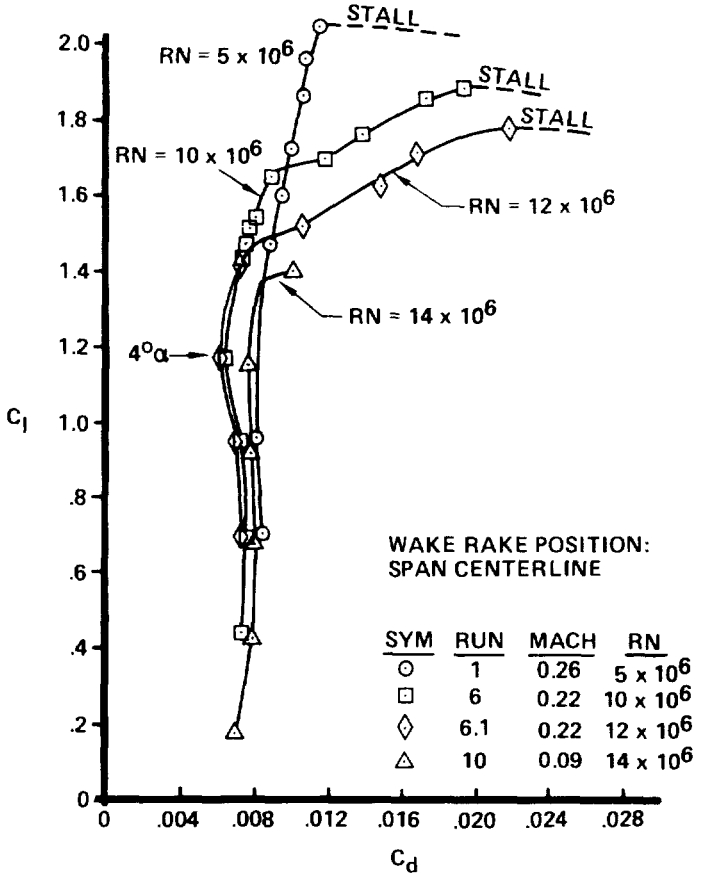

Figure 15.

LIFT AND DRAG COMPARISON WITH THEORY

The importance of properly locating instrumentation, and the care that must be taken in testing laminar-flow airfoils is illustrated in Figure 16. Two runs, increasing Reynolds number at a constant alpha of 4^{o}, were performed to investigate the unexpected high drag at $14x10^{6}$ RN and to obtain data for comparisons with theory. Upon examining the model it was observed that the wake rake was positioned behind the lower surface instrumentation cover plate during rake traverses. It was postulated that the access door with its edges and filled bolt head holes could trigger a premature transition on the lower surface. During the two RN runs, the wake rake was positioned at two different spanwise locations: behind the access door at the span centerline and the right hand side. Results presented in Figure 16 show two levels of drag. The lower drag level agrees with theory which includes the design goal of laminar-flow extent. The higher drag level, measured behind the access door, is consistent with a premise of turbulent flow being present over the entire lower surface. Test data shows that laminar-flow design goal could be maintained up to a Reynolds number of $18x10^{6}$ at an alpha of 4^{o}.

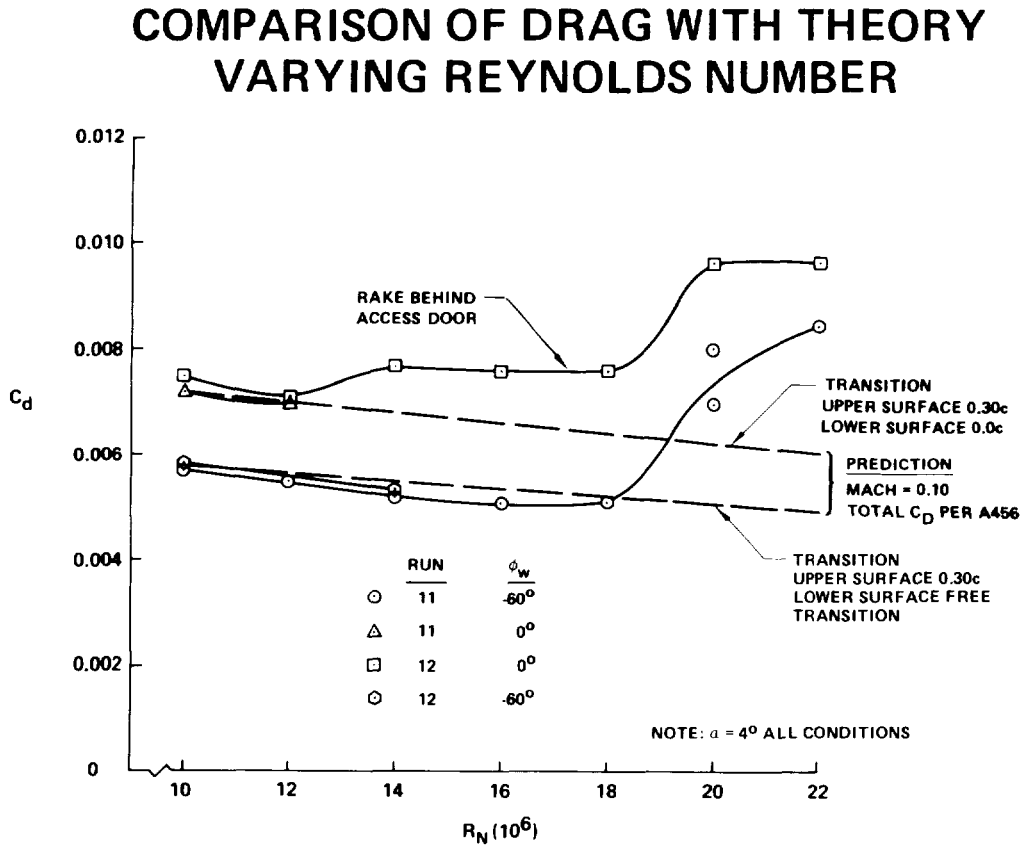

Figure 16.

The variation of drag with angle of attack at 14×10^6 Reynolds number, presented in Figure 17, shows that drag measured on the right hand side of the model (and not behind the access door) matches theory at angles of attack corresponding to endurance and cruise lift coefficients. A moderate drag increase above theoretical values occurred at 0° to 2° alpha. The increase is probably a result of pressure gradients developing on the lower surface that are unfavorable for sustaining laminar flow. This possibility was previously noted in discussing Figure 11 which presented off-design chordwise pressure distributions.

The drag departure from theory at 7° alpha, which should include a drag increment from upper surface transition forward movement, is in conflict with hot-film data presented in Figure 13 and shows transition forward movement occurring at 5.3° alpha. A question has been raised as to the validity of hot film sensors when they are used to detect boundary-layer transition at large values of Reynolds number per foot. The problem is that physical imperfections in the sensor installation could produce erroneous signals.

Data obtained from a trip strips-on run have also been plotted in Figure 17 to provide a reference for the drag levels achieved with natural laminar flow. These trip strips, installed at .025c upper surface and .035c lower surface were a dot-type configuration with a thickness determined to be only sufficient for tripping the boundary-layer at 14×10^6 Reynolds number. This was verified by comparing measured and predicted drag values.

COMPARISON OF DRAG POLAR WITH THEORY

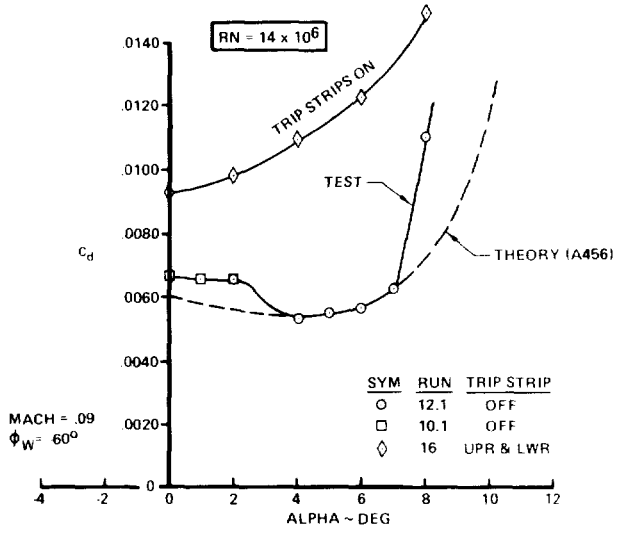

Figure 17.

LIFT AND DRAG COMPARISON WITH THEORY (CONCLUDED)

The lift curve acquired at 14×10^6 Reynolds number and 0.09 Mach number is presented in Figure 18 and compared with theory. There is some small deviation from theory in both angle for zero lift and lift curve slope; however, the most significant difference between theory and test is the stall region. Whereas theory predicted a maximum lift coefficient of 2.0 and a gradual stall with flow separation gradually progressing forward from the trailing edge, test data shows a lower maximum lift and a sharp stall. This stall characteristic is illustrated in Figure 19 which presents pre- and post-stall pressure distributions obtained at 14×10^6 Reynolds number. In 0.4^o of alpha, the airfoil stalled and separated flow has encompassed the aft 60 percent of chord. Peak pressures over the forward portion of the airfoil have decreased by 27 percent. Obviously, the airfoil design method did not incorporate the correct turbulent flow separation mechanism including wake modeling and/or did not correctly mathematically model the flow condition at the trailing edge. Consequently, the linear boundary-layer H distribution used in the pressure recovery region aft of 30 percent chord did not provide the desired soft stall for the highly cambered 18 percent thick section.

COMPARISON OF LIFT CURVE WITH THEORY

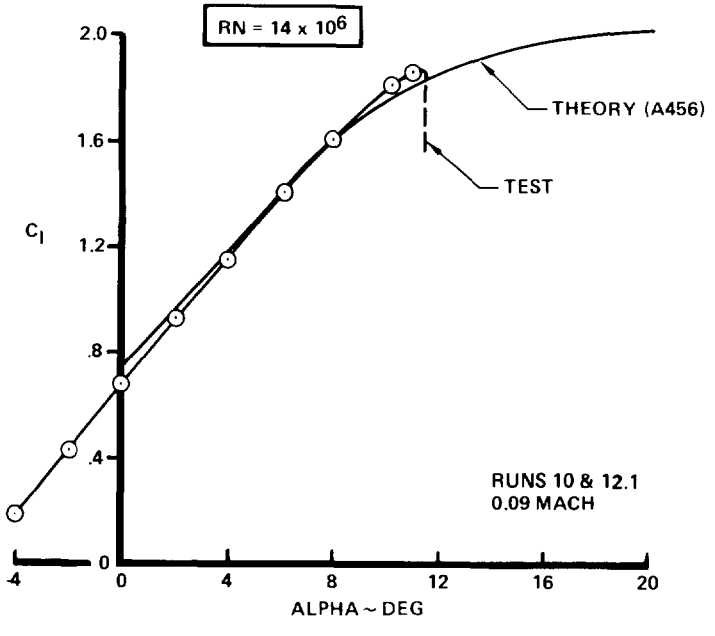

Figure 18.

CHORDWISE PRESSURE DISTRIBUTIONS: PRE-AND POST-STALL

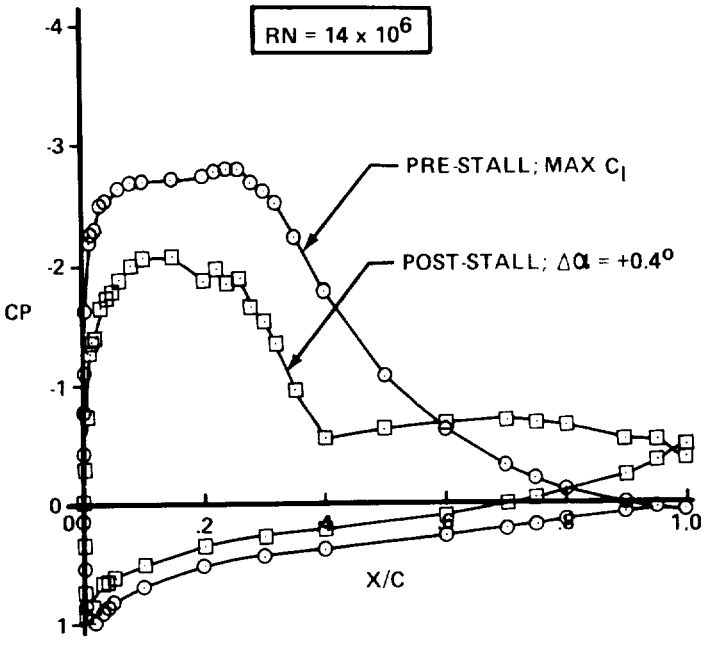

Figure 19.

LOW TRAILING EDGE FLAP DEFLECTION

A small 12.7 percent chord plain flap operating at low settings was proposed as a means of providing additional stall margin and modifying the wing stall pattern while incurring only a small drag penalty at cruise lift coefficients. The flap was designed to minimize contour deviations at both upper and lower flap cove trailing edges. The resultant small cavities were filled in for the zero flap angle testing. Figure 20 presents a comparison of flaps up and 5^{o} flap data for 14x10 Reynolds number. The lift curves show the flap produces a consistent lift increment, varying from 0.21 ΔC_l at 0^{o} alpha to 0.12 ΔC_l at stall. The maximum lift coefficient of 2.0 matches the design goal; however, the stall character did not deviate from the sharp stall recorded by the flaps up configuration.

Figure 20 also shows that the drag polar obtained with 5^{o} of flap deflection exhibits only a small variation in drag from the lowest angle of attack tested up to the design lift coefficient of 1.4. At this lift coefficient, the drag increment for the flap is 15 drag counts, which is attributed to a reduction in laminar flow on the lower surface. This reasoning followed an examination of hot-film sensor data. At $1.4C_l$ transition to turbulent flow occurred aft of 0.32c. Unlike data from flaps up runs, the 5^{o} flap polar shows a smooth, continuous and non-abrupt drag variation from 1.5 C_l up to stall where a typical large drag increase occurred.

LIFT AND DRAG CHARACTERISTICS WITH 5^{o} OF FLAP
RN = $14x10^{6}$

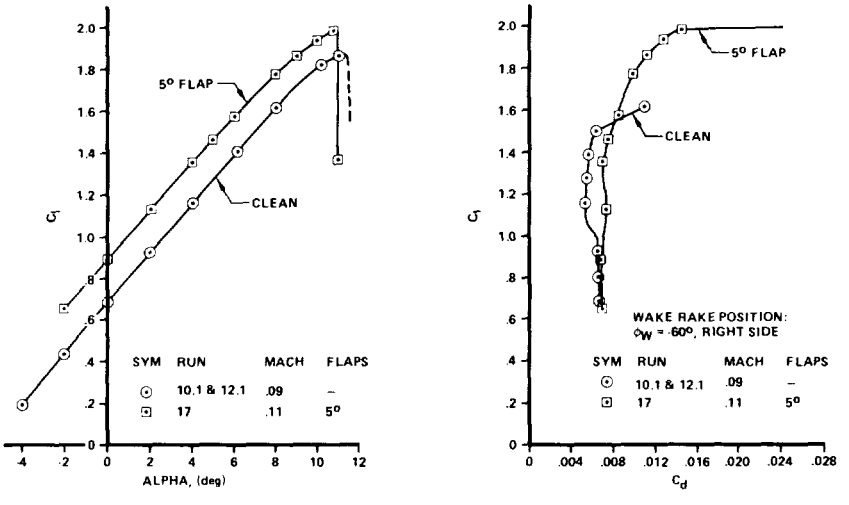

Figure 20.

CONCLUSIONS

Although limits of applicability of the design tools were pushed severely, the theoretically designed airfoil came very close to meeting the design goals. The predicted extent of natural laminar flow (over the forward 0.3c of the upper surface and over almost the entire lower surface) was obtained at the design goals of 1.4 C_l and 14×10^6 Reynolds number, good off-design airfoil performance was achieved at all tested lift coefficients below the endurance level, and a small plain flap at a low deflection can be used to improve stall margin for only a small drag penalty at cruise and endurance lift coefficients (Figure 21).

The major shortcoming of the computer codes was an inability to correctly model the stall character. Unlike theory that predicted a gradual stall with flow separation moving slowly forward from the trailing edge, test data showed a sharp stall with flow separation rapidly moving forward from the trailing edge up to 0.40c. This stall occurred at a lower than predicted stall angle, which resulted in a lower than predicted maximum lift coefficient. It is evident the current inverse airfoil design process does not mathematically model the correct flow separation mechanism for the type of thick airfoil tested. Additional airfoil analysis work is being performed with a revised A456 program, namely a modified wake-modeling procedure, to investigate stall predictions for the high camber/large thickness ratio class of airfoil. Data also showed that transition on the upper surface occurred earlier than predicted. The combination of a high design C_l and large Reynolds number did stretch the capability of the current airfoil design computer codes, and/or possibly the large test RN/ft created a problem.

- **THE PREDICTED EXTENT OF NATURAL LAMINAR FLOW WAS ACHIEVED AT THE DESIGN GOALS OF 1.4 C_l AND 14×10^6 RN**
- **GOOD OFF-DESIGN AIRFOIL PERFORMANCE IS AVAILABLE OVER A WIDE RANGE OF LIFT COEFFICIENTS**
- **A SMALL PLAIN FLAP AT 5^o CAN IMPROVE STALL MARGIN WITHOUT INCURRING MORE THAN A SMALL ENDURANCE DRAG PENALTY**
- **THE AIRFOIL DESIGN PROCESS DID NOT CORRECTLY MODEL STALL CHARACTER**

Figure 21.

REFERENCES

1. McMasters, John H., and Henderson, Michael L.: Some Recent Applications of High Lift Computational Methods at Boeing. Journal of Aircraft, Volume 20, No.1, January 1983.

ACKNOWLEDGMENTS

The author would like to thank Robert McGhee (NASA-Langley Research Center) for coordinating and conducting the test and then developing the test data, Victor R. Page (Boeing Military Airplane Company) for the majority of the airfoil design, and William M. Ralph (Boeing Military Airplane Company) for preparing the test report.

DESIGN AND TEST OF AN NLF WING GLOVE FOR THE VARIABLE-SWEEP TRANSITION FLIGHT EXPERIMENT

E. G. Waggoner, R. L. Campbell, P. S. Phillips, and
J. B. Hallissy
NASA Langley Research Center
Hampton, Virginia

[redacted]

VSTFE GLOVE TEST AND REDESIGN

The Applied Aerodynamics Group has been involved in design efforts supporting the F-14 Variable-Sweep Transition Flight Experiment (VSTFE). The VSTFE was formulated between NASA Ames-Dryden and NASA Langley Research Center to establish a data base on the effects of the interaction between cross flow (CF) and Tollmien-Schlichting (TS) instabilities on boundary-layer transition utilizing the F-14 aircraft as a test bed. The design effort involved modifying the F-14 wing outer-panel such that favorable pressure gradients could be generated over a wide range of flight conditions.

Background information relating to the initial computational glove design will be presented. The initial design relied extensively on both two- and three-dimensional transonic analysis methods applied in a "cut-and-try" manner. The initial design was tested in the National Transonic Facility (NTF) along with the baseline F-14 to verify the glove design and to obtain data supporting safety of flight issues. Based on the pressure data available from the NTF test a decision was made to redesign the inboard region of the glove to increase the envelope over which usable flight data could be obtained. The redesign process and two- and three-dimensional results from the redesign effort will be presented. Finally, a summary of the design and test results to date will be presented along with the status of the flight experiment.

* BACKGROUND

* NTF TEST RESULTS

* REDESIGN PROCESS

* RESULTS FROM REDESIGN EFFORT

* SUMMARY AND STATUS

F-14 VARIABLE SWEEP FLIGHT EXPERIMENT

An important question that must be answered in order to design wings which effectively utilize NLF relates to boundary-layer transition. It is known that for boundary layers in a three-dimensional flow environment, there is an interaction between cross flow (CF) and Tollmien-Schlichting (TS) instabilities that can cause transition to occur in an otherwise favorable environment (i.e., favorable pressure gradient, smooth surface, etc.), Hanks, 1984. In order to assist in identifying and quantifying the influence of the CF-TS interaction on wing-boundary-layer transition, data are needed for various combinations of favorable pressure gradients, Reynolds numbers, and sweep angles. This is the objective of the VSTFE. The F-14 aircraft was selected as the test bed aircraft because of its variable sweep capability, which would allow data to be taken over a wide range of sweep angles.

Objective: Obtain accurate in-flight measurement of boundary–layer transition location for wing pressure distributions, sweep angles, and flight conditions representative of future laminar–flow transport aircraft.

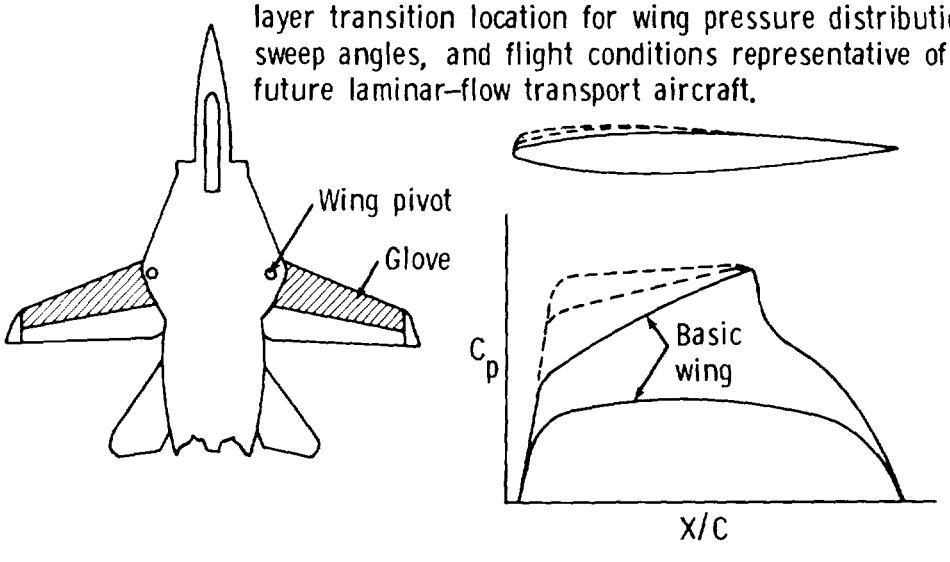

APPROACH

The approach of this flight experiment is to modify the wing outer panel by gloving on a foam and fiberglass contour so that favorable pressure gradients will be generated over a range of Mach numbers, sweep angles, and Reynolds numbers. Two different gloves were designed which correspond to an M = 0.70 and M = 0.80 design condition. NASA Langley was responsible for the M = 0.70 glove design, and Boeing Aircraft Company was responsible for the M = 0.80 glove design. Both gloves were to be flown simultaneously, one on each wing of the F-14, resulting in an asymmetric configuration. Hence, a maximum constraint on the rolling moment because of the asymmetric configuration was imposed on the design.

Glove Layout

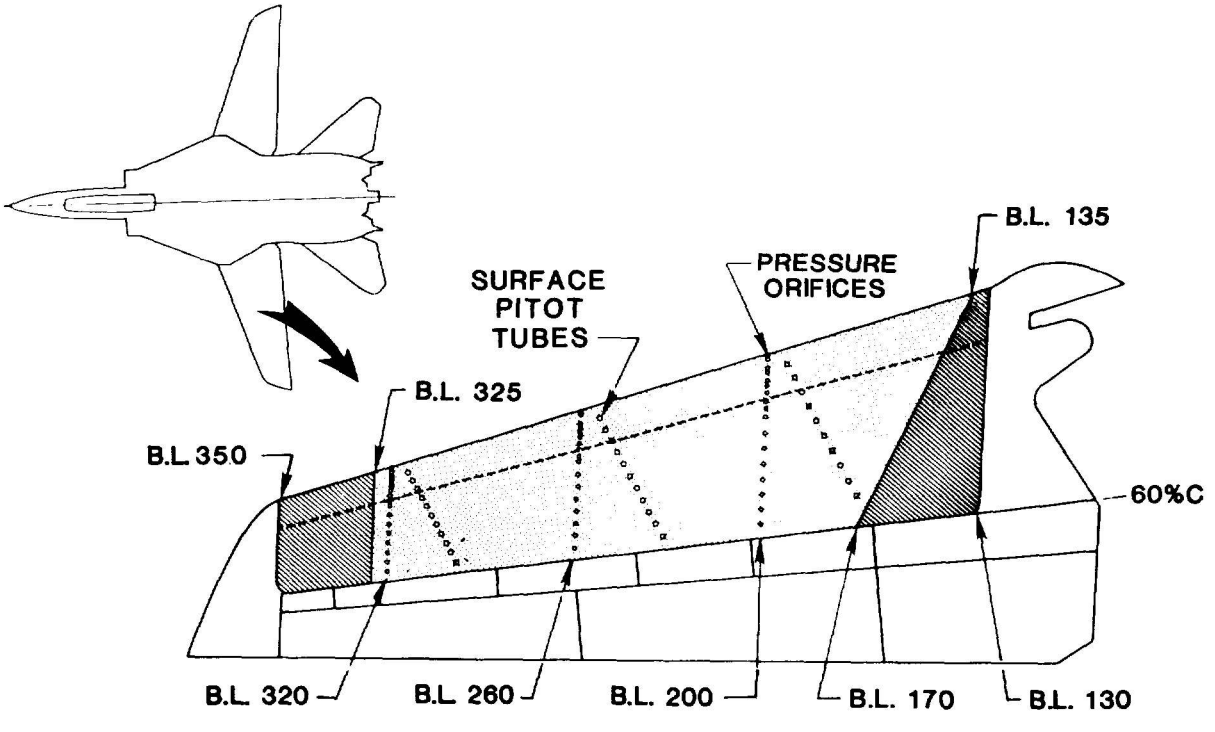

PROJECT PLAN

The project can be considered to consist of four phases: flight test of the "clean-up" glove, design of M = 0.7 and M = 0.8 gloves, wind tunnel testing of baseline and glove configuration, and flight test of the glove configuration. The "clean-up" glove corresponds to the contours of the basic F-14 wing. It was built up of foam and fiberglass and installed on the outer panel to demonstrate that acceptable tolerances could be maintained in the fabrication process and to obtain pressure and boundary-layer measurements in the flight environment.

Concurrent with the "clean-up" glove flight tests, two gloves were designed for M = 0.7 and M = 0.8 design points. The gloves were designed such that a neutral to slightly favorable pressure gradient was generated on the glove upper surface at the maximum test altitude, 35,000 feet, for 1 "g" flight conditions. This allowed more favorable gradients to be obtained for 1 "g" conditions at lower altitudes.

The designs and the baseline F-14 configuration were then to be tested in the NTF. The test would allow a verification of the designs and determination of changes in the performance and flying qualities of the modified configuration relative to the baseline F-14. Additionally, if any adverse effects were discovered during the data analysis, time would be available to modify the designs before the VSTFE configuration was to be flight tested.

Initially, both gloves were to be flight tested simultaneously on the F-14. However, the availability of the test-bed aircraft precluded the modification of both wing panels and completion of the flight test program. Based on the computational analysis and wind tunnel pressure data available for each of the designs, a decision was made to limit the flight test to the M = 0.7 design.

The final phase of the program is to install the glove design on the wing panel, perform the flight testing, and analyze the data. This is the only phase remaining to be completed.

* Fly "Clean-up" Glove
* Design gloves for M=0.7 and M=0.8 design points
* Conduct wind tunnel test on baseline and modified configurations
* Fly modified configuration

COMPARISON OF FLIGHT TEST AND COMPUTATIONS

A flight test of the F-14 was conducted to explore the test envelope for the VSTFE and to obtain wing pressure data on the basic aircraft (Moes and Meyer, 1985). From these data, four flight points were designated to be of primary interest. Three of the points correspond to corners of the flight envelope for the VSTFE, and the remaining point is an intermediate flight condition.

Analyses were made in the WBPPW (Boppe and Stern, 1980) and TAWFIVE (Melson and Streett, 1983) codes at the flight Mach number and measured angle of attack (Waggoner, et al., 1985). Overall, the comparisons are quite good. Several observations need to be made concerning the comparisons. First, the flight data showed a flow expansion at the leading edge followed by a compression that neither code predicted. This indicated that possibly the leading-edge slat deflected under load. Static loading corresponding to flight loads confirmed this. The differences seen in leading-edge expansions between the two codes are consistent with the code formulations. Shock resolution is much better in the WBPPW code results because of the denser grid in that region as compared to the TAWFIVE code. Additionally, the TAWFIVE code uses conservative differencing where WBPPW uses nonconservative differencing, which accounts for the discrepancy in shock location.

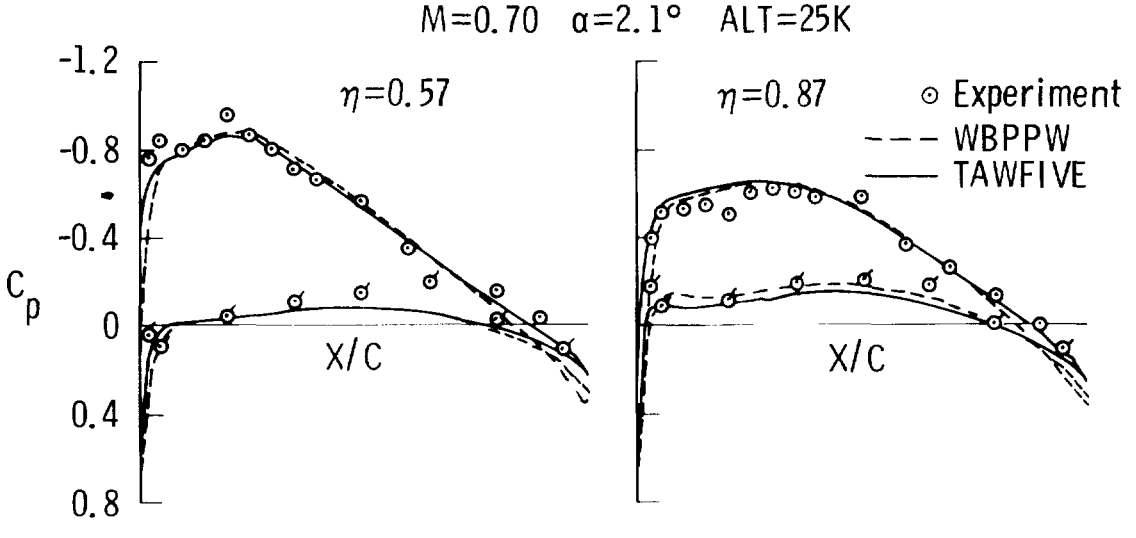

DESIGN CONSTRAINTS

The physical constraints on the modifications evolved with the design program. The final constraints and supporting rationale are as follows:

* The upper surface could be modified from the leading edge to the spoiler hinge line ($x/c = 0.60$) since the spoilers are used for low-speed roll control. Modifications on the lower surface were limited to the first 10-percent chord because of the glove fabrication method.
* The thickness of the glove at the spoiler hinge line must be less than 1.0 inch. This constraint was imposed to ensure spoiler effectiveness. For reference, the wing mean chord is 105.66 inches.
* The thickness of the glove was required to be a minimum of 0.65 inches. This constraint was required to minimize the possibility of the leading-edge slat deflecting under load.
* The rolling moment resulting from the asymmetric configuration was required to be less than 0.01 over the flight test envelope. This level of rolling moment could be counteracted by tail deflection, allowing the spoilers to remain undeflected during the test portions of the flight.

- Upper surface modification
  $0.0 \leqq x/c \leqq 0.60$
- Lower surface modification
  $0.0 \leqq x/c \leqq 0.10$
- Increment at spoiler hinge line less than 1.0 inch
- Increment over glove region a minimum of 0.65 inches
- Differential rolling moment less than 0.01

DESIGN AIRFOIL MEETING FINAL CONSTRAINTS

The design point selected corresponded to a "worst case" condition for the targeted Mach number (M = 0.70). This condition corresponded to the highest altitude, hence the largest lift coefficient for 1-g flight. If the sectional contours could be modified such that a slightly favorable gradient could be generated from the leading edge to the midchord region at this condition, then at lower altitudes there would be an even more favorable pressure gradient. Five defining stations were chosen to be recontoured using linear lofting between defining stations. These stations corresponded to the inboard and outboard extent of the glove and three intermediate defining stations. With two-dimensional analysis and design procedures, upper surface contours were defined which met the aerodynamic and physical constraints for each defining station. A favorable pressure gradient was observed from the leading edge to about midchord over a range of lift coefficients on the design airfoil.

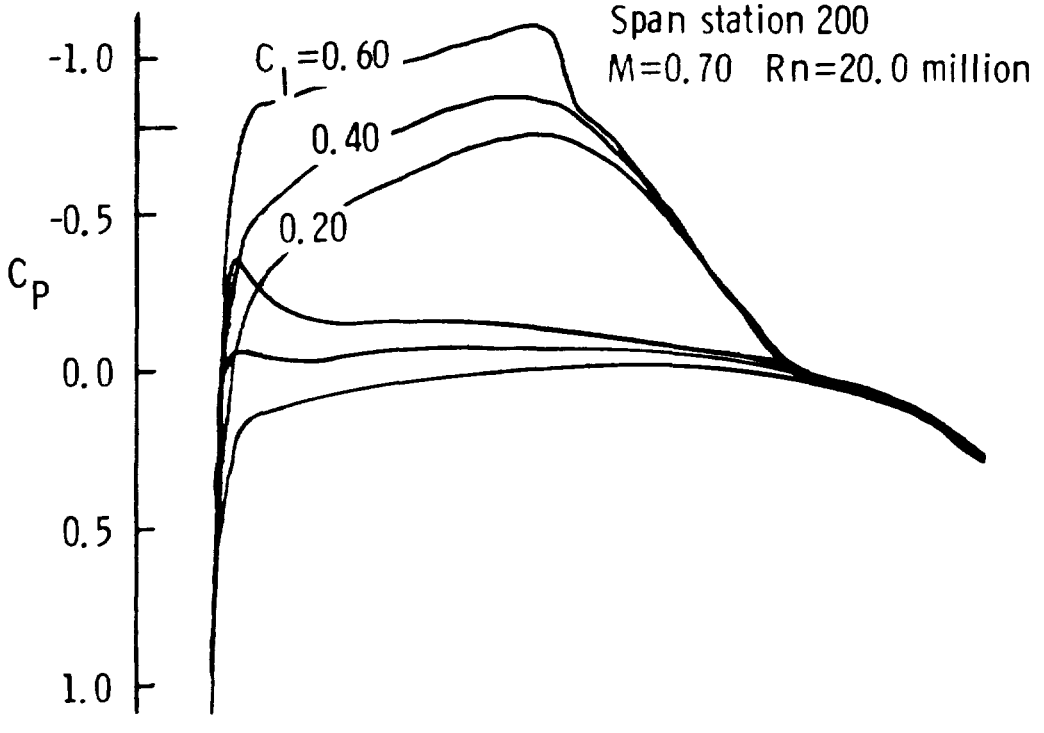

THREE-DIMENSIONAL ANALYSIS OF GLOVE DESIGN

Final computational verification of the design was realized by analyzing the entire configuration (fuselage, nacelles, strake, and outer panel) in the TAWFIVE code. Results show that the design objectives were met over the range of lift coefficients corresponding to the altitudes of interest at M = 0.70. Presented below are the results for the high altitude case at the design Mach number. The results show a neutral pressure gradient on the upper surface at the most inboard span station and slightly favorable pressure gradients at the two outboard span stations.

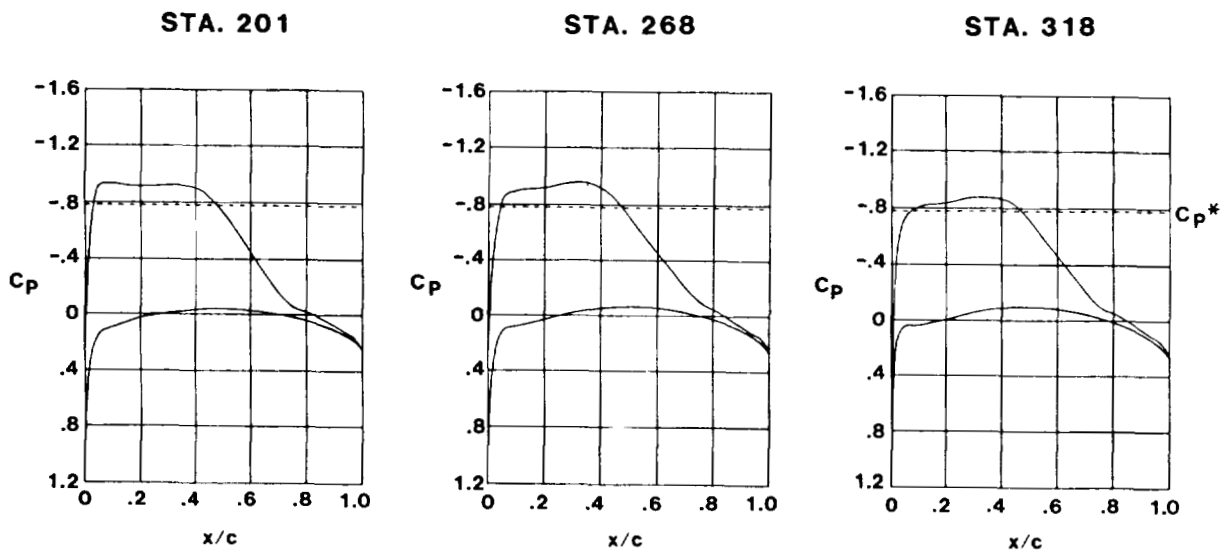

CALCULATED N-FACTORS FOR THE ORIGINAL GLOVE DESIGN

Boundary-layer disturbance growth was analyzed using the method of Mack, 1979. The M = 0.7 glove design was analyzed at three conditions to assess its operating range and usefulness in obtaining transition data (Rozendaal, 1986). The conditions were:

a. Level flight, M = 0.7, 25,000 feet
b. Level flight, M = 0.7, 35,000 feet
c. Level flight, M = 0.8, 35,000 feet

The data show that for the three conditions a wide variation in CF and TS N-factors is available. Near its design point the glove shows a predominance of TS growth at low CF N-factors. At lower altitudes at the design Mach number, the glove produces moderate growth in the CF instability mode and rapid growth in the TS mode. At M = 0.8, the instability growth is most noticeable in the CF mode. These data indicate the range of instability interactions available from the M = 0.7 glove design pressure distributions.

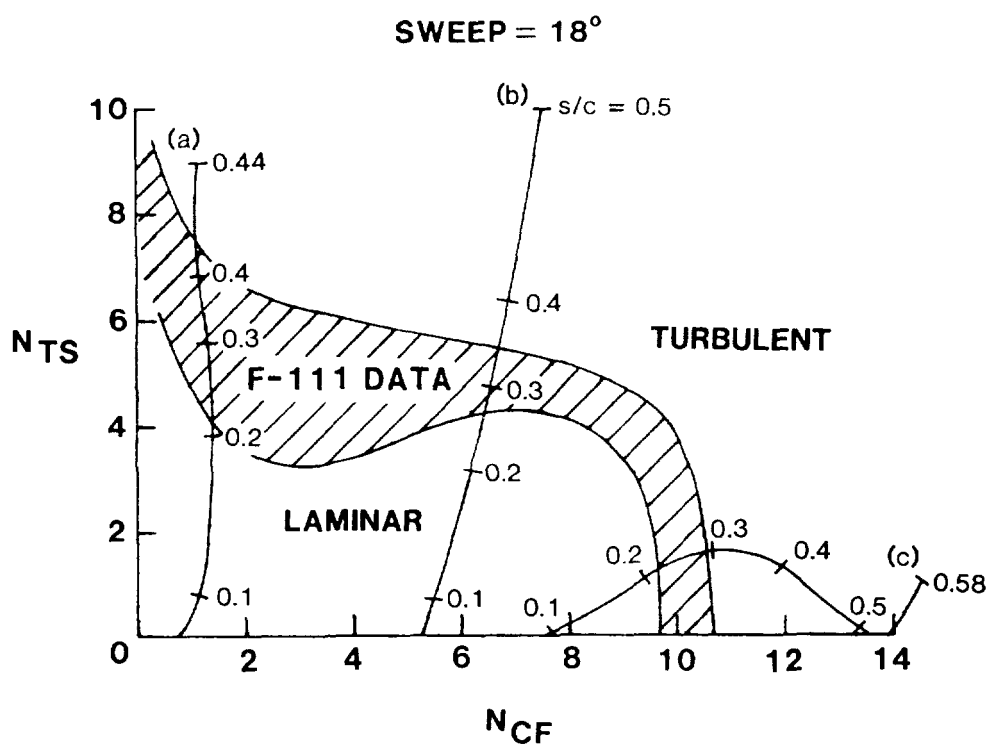

NTF WIND TUNNEL TEST

After the designs were completed, the glove designs and the F-14 baseline configuration were tested in the NTF. There were two primary objectives for the test entry. The first was to determine the incremental changes in the performance and flying qualities of the VSTFE configuration relative to the baseline. This involved comparing performance and stability and control data on each configuration over the anticipated flight test envelope. Two areas of significant interest were the levels of rolling moment generated on the asymmetric VSTFE gloved configuration and maximum lift generated at approach speeds. Analysis of the data indicated that the increments between the two configurations were minimal.

The second objective was to verify the computational designs. The glove designs had pressures available at locations corresponding to the flight test instrumentation. The experimental pressures could be compared to the computational predictions at these locations. Any discrepancies between the computed and experimental pressures could then be assessed and resolved if necessary.

OBJECTIVES:

* SAFETY OF FLIGHT—INCREMENTAL CHANGES
  * Performance
  * Stability and Control
  * Rolling Moment
  * $C_{L_{MAX}}$ at Approach Speeds
* VERIFICATION OF COMPUTATIONAL PREDICTIONS

ENVELOPE:

* $M = 0.2$——0.9
* $\Lambda_{LE} = 20^{\circ}$—$35^{\circ}$

COMPARISON OF THEORETICAL AND EXPERIMENTAL PRESSURE DISTRIBUTIONS AT M = 0.7

Experimental wing pressure distributions for the original glove are compared with theoretical results from the TAWFIVE 3-D transonic code in the figure below. The Mach number of 0.7 and angle of attack of 2.95 degrees represent the high-altitude, level-flight design condition for the flight experiment. The analysis code was first run matching the experimental angle of attack. While the overall correlation was good, the suction peak and the slight adverse pressure gradient that occur near the leading edge in the experimental data were not predicted. Often in comparing potential flow calculations with experimental data it is found that the codes underpredict the lift levels and must be run at an angle of attack slightly higher than the experiment to achieve good correlation. Therefore, additional calculations were made with the angle of attack increased to 3.25 degrees. These results more closely matched the experimental pressure levels and gradients near the leading edge, so this angle of attack was chose for any further analytical or design work. It is interesting to note that the theory and experiment matched fairly well aft of 58 percent chord where the glove ended abruptly in an aft-facing step on the wind tunnel model, but was smoothly faired into the basic wing for the computations.

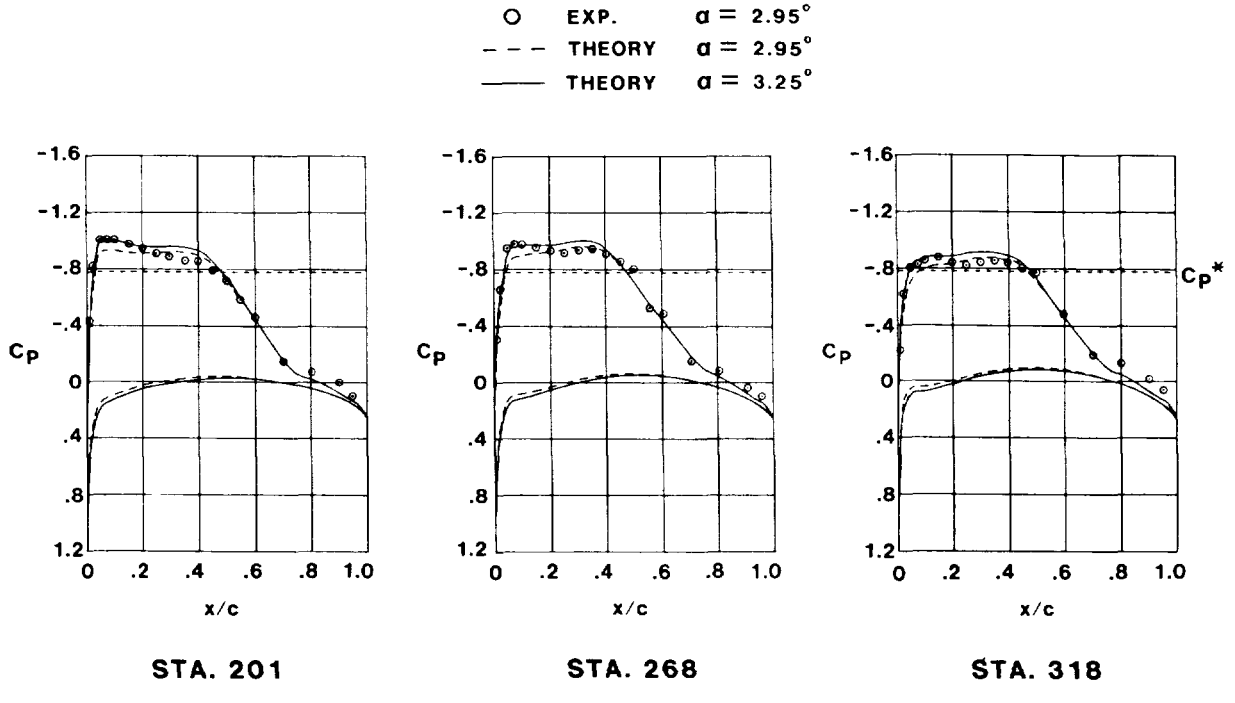

THEORETICAL PRESSURE DISTRIBUTION AT STATION 134

The original plan for instrumentation on the glove had pressure orifice rows located at span stations 200, 260, and 320. It was decided that an additional row of orifices should be installed at station 160 to take advantage of the larger chord (and thus larger Reynolds numbers) in this region as well as to provide a more complete description of the glove pressures. The experimental pressure data indicated that the upper surface pressure distributions at the inboard stations were slightly more adverse than the relatively flat distributions of the outboard stations due to the increased upwash from the strake. If this trend continued for the stations inboard of 200, the original glove design would probably not allow any significant transition location data to be obtained in this region. Since the wind tunnel model did not have any instrumentation in this area of the glove, computational results were used to evaluate this concern.

The calculated pressure distribution for station 134 near the inboard edge of the glove is shown in the figure below. A fairly strong leading-edge peak is present, and the following adverse gradient would probably cause the laminar flow to undergo transition to turbulent flow very rapidly. Since early transition at this station could contaminate the flow at station 160, a redesign effort for the inboard portion of the glove was initiated.

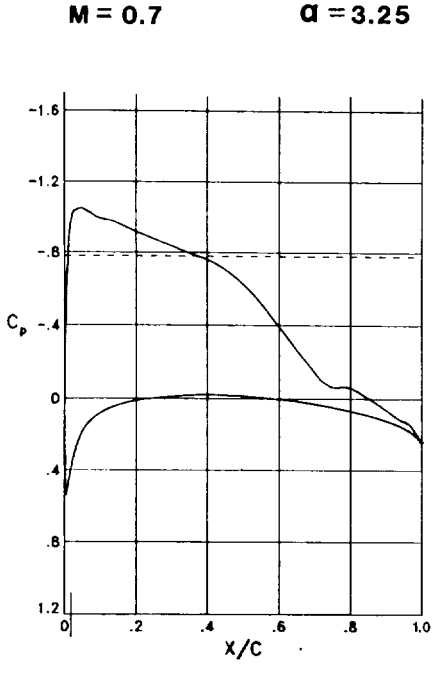

INBOARD GLOVE REGION MODIFICATION

Based on the NTF test results and the good correlation of the theoretical and experimental data, it was felt that some very useful data could be obtained on the inboard portion of the glove if the original design constraints were relaxed to allow some additional design work. The objective of the new design was to eliminate the adverse gradient over the inboard part of the glove so that the entire upper surface of the glove would have a favorable-to-neutral pressure gradient in the leading-edge region at the high altitude, M = 0.7 design point. Since there would not be an opportunity to verify a new design in the wind tunnel due to time constraints, it was decided to modify only the region of the glove inboard of station 200.

In order to reduce the leading-edge pressure peak, the leading edge of the glove had to be drooped for better alignment into the oncoming flow. This necessitated relaxing several of the design constraints in this region. The glove overhang region was extended to 4 inches ahead of the basic wing leading edge and the minimum allowable glove thickness was reduced to 0.25 inches to enable the drooped sections to fit over the existing wing. The match point for the glove to fair into the lower surface was also extended to 30 percent chord to minimize any concavity that might occur.

OBJECTIVE:

* Remove adverse pressure gradient in leading edge region over entire glove at high altitude, M = 0.7 design point

CONSTRAINTS:

* Minimal change to tested geometry
* Overhang region extended to 4 inches
* Minimum thickness relaxed to 0.25 inch inboard of span station 200
* Lower surface modification extended to 30% chord

REDESIGN PROCESS

The redesign of the inboard glove region utilized a three-step approach. The first stage was a parametric study of leading-edge camber or droop distributions, using the NYU airfoil code (Bauer, et al., 1975) to calculate the pressure distributions. From this study, airfoils having favorable gradients in the leading-edge region with as little disturbance as possible to the rest of the pressure distribution would be selected. The second step involved modifying these airfoils using an airfoil design code to obtain favorable upper surface pressure gradients extending from the leading edge to about midchord and to minimize lower surface leading edge pressure peaks caused by the droop. (The airfoil design code could not be used for the droop design since at that time it required a fixed leading edge point.) The final airfoils generated by the design code were then evaluated in the three-dimensional flow environment using the TAWFIVE code. This third step in the process included runs at conditions throughout the flight envelope as well as the design point.

* Parametric study to define leading-edge camber distribution

* Application of 2–D design code

* Evaluation with 3–D analysis code

PARAMETRIC STUDY OF CAMBER DISTRIBUTION

Incremental camber distributions were added to the leading-edge region of two airfoil sections from the inboard region of the glove. The camber distribution was generated using a polynomial equation similar to the camber equation for the NACA four-digit airfoils, but modified to produce leading-edge droop and no camber change at the match point. The magnitude of the droop was varied from one to four percent chord. Two types of polynomials were tried: quadratic, which matched the ordinate of the original camber line; and cubic, which matched both the ordinate and slope of the original camber line. The chordwise extent of the droop was also varied, up to a maximum value of 30 percent chord.

The results of this study indicated that the four percent droop cases gave too strong a pressure peak at the leading edge on the lower surface and just ahead of the match point on the upper surface. The one percent droop had small disturbances at these locations, but the upper surface favorable gradient was fairly weak and would probably become adverse in the three-dimensional flow case. The cubic polynomial camber airfoils had slightly smoother pressure distributions than the quadratic camber airfoils. The effect of increasing the chordwise extent of the droop was to strengthen the favorable gradient of the upper surface while reducing the pressure peak at the match point. Based on these results, the airfoils having the two percent cubic camber distribution extending over the first thirty percent of the chord were chosen for further modification by the airfoil design code.

* Maximum camber at leading edge (droop)

* Order of polynomial fit for camber distribution

* Chordwise extent of modification

Analysis of 3 x 2 x 3 Matrix

Redesigned Camber Distribution

TWO-DIMENSIONAL DESIGN CODE

The airfoils chosen from the parametric camber study were further modified using an airfoil design code developed at NASA Langley. This code is based on the NYU analysis code (Bauer, et al., 1975) and modifies an airfoil contour to achieve a target pressure distribution. The design method begins by calculating the pressure distribution for the initial airfoil shape and comparing it to the target pressures. The airfoil shape is then modified based on the differences in these pressures using a design algorithm similar in concept to the ones used by Barger and Brooks (1974) and Davis (1979). This algorithm relates the difference in the predicted and target pressure coefficients to the surface curvature in subsonic and mildly supersonic flow regions. For regions with stronger supercritical flow (local Mach numbers greater than 1.15), a term that relates surface slopes to pressure coefficients is also included. The changes in surface slopes and curvatures are then used to modify the initial airfoil, and the resulting airfoil is analyzed by the NYU code. This predictor/corrector approach is repeated until the pressures and airfoil shape converge.

Target pressures for the design were defined in a three-step process. Analysis pressure distributions were obtained on the drooped airfoils. Next the undesirable flow expansion ahead of the droop match point (30-percent chord) on the upper surface was eliminated by reducing the maximum pressure coefficient near the leading edge. Finally, the strength of the favorable pressure gradient behind the match point was increased to help maintain airfoil thickness. The code required approximately 4 design cycles to achieve the target pressures.

* Based on Garabedian and Korn analysis code

* Modifies contour to achieve a specific pressure distribution

* Predictor/corrector design algorithm

  * Subsonic $-\Delta C_p = f(\text{surface curvature})$

  • Supersonic $-\Delta C_p = f(\text{surface curvature, surface slope})$

TWO-DIMENSIONAL PRESSURE DISTRIBUTIONS FOR GLOVE AIRFOIL AT STATION 130

Calculated two-dimensional pressure distributions are shown in the figure for the airfoil at station 130 at various stages of the design effort. The dashed line represents the pressure distribution for the original glove at two-dimensional conditions that are equivalent to the high altitude design point. The two-dimensional Mach number was calculated using simple sweep theory, and the angle of attack was adjusted to give a pressure distribution that closely matched the one from the three-dimensional code. The results for the airfoil from the camber study show that the leading-edge peak on the upper surface was eliminated, but a peak formed instead just ahead of the match point. This pressure distribution was modified to create the target pressures that were input into the airfoil design code. The final airfoil results (solid line) matched the targets everywhere except near sixty percent chord on the upper surface. This difference was caused by the constraint that the airfoil could only be modified ahead of sixty percent on the upper surface and thirty percent on the lower surface.

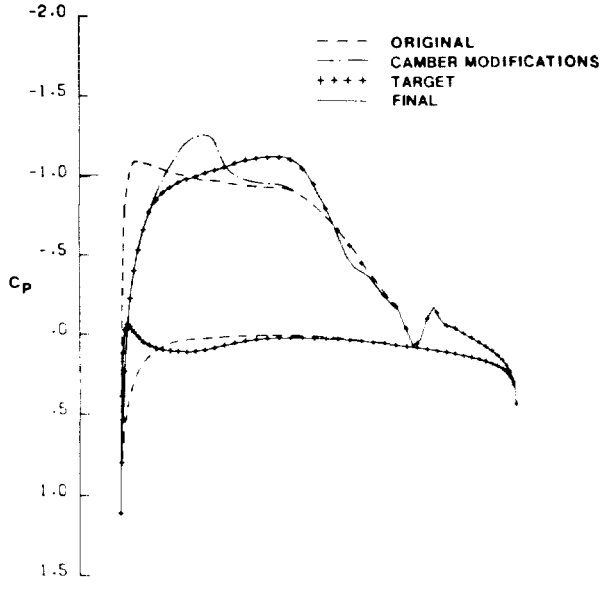

FINAL AIRFOILS

The final airfoils from the redesign process are shown in the figure. The drooped airfoils at stations 130 and 164 are overlaid on the original glove designs while the glove airfoil at station 200, which was not redesigned, is compared to the basic wing airfoil. The leading-edge extension and droop for the new gloves is evident, and the need to relax the minimum glove thickness can be seen at station 130, where the modified glove undercuts the original glove (though it is still outside the basic wing). The new glove sections have a slightly greater maximum thickness, but are still within the original constraint for the step size at the end of the glove on the upper surface.

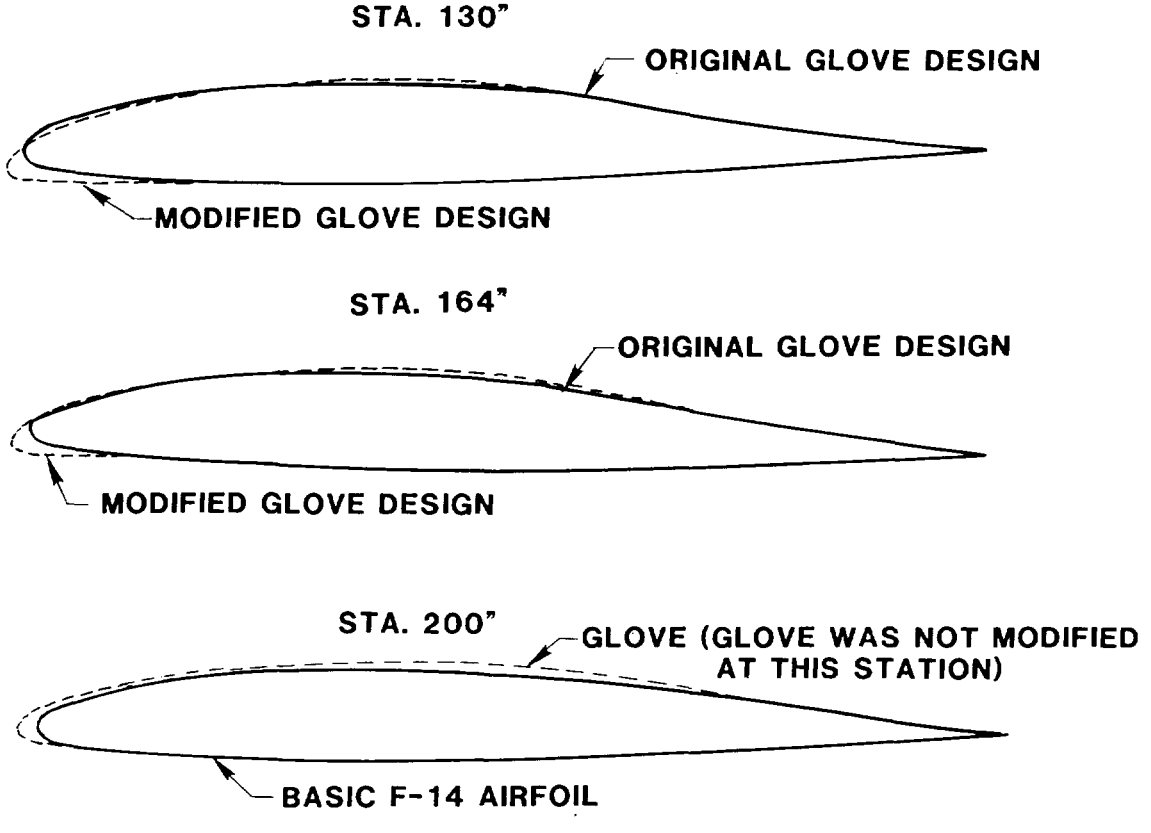

THREE-DIMENSIONAL ANALYSIS OF MODIFIED GLOVE - M = 0.7

Analysis of the modified glove design was performed at the design condition and other flight conditions throughout the flight envelope. Results are presented below for the M = 0.7, high altitude design point and compared against results from the original design. Note that at the most inboard station presented, span station 134, the adverse pressure gradient was reduced but not eliminated. However, the pressure peak was reduced at the leading edge on the upper surface. Moving outboard to station 167, note that the modified glove exhibits a neutral pressure gradient while the pressure expansion and slightly adverse gradient evident in the original design has been eliminated. The pressure distributions from the two designs are virtually indistinguishable from station 234 outboard. Hence, the modifications have allowed useful data to be obtained over a wider range of flight conditions than were available from the original glove design.

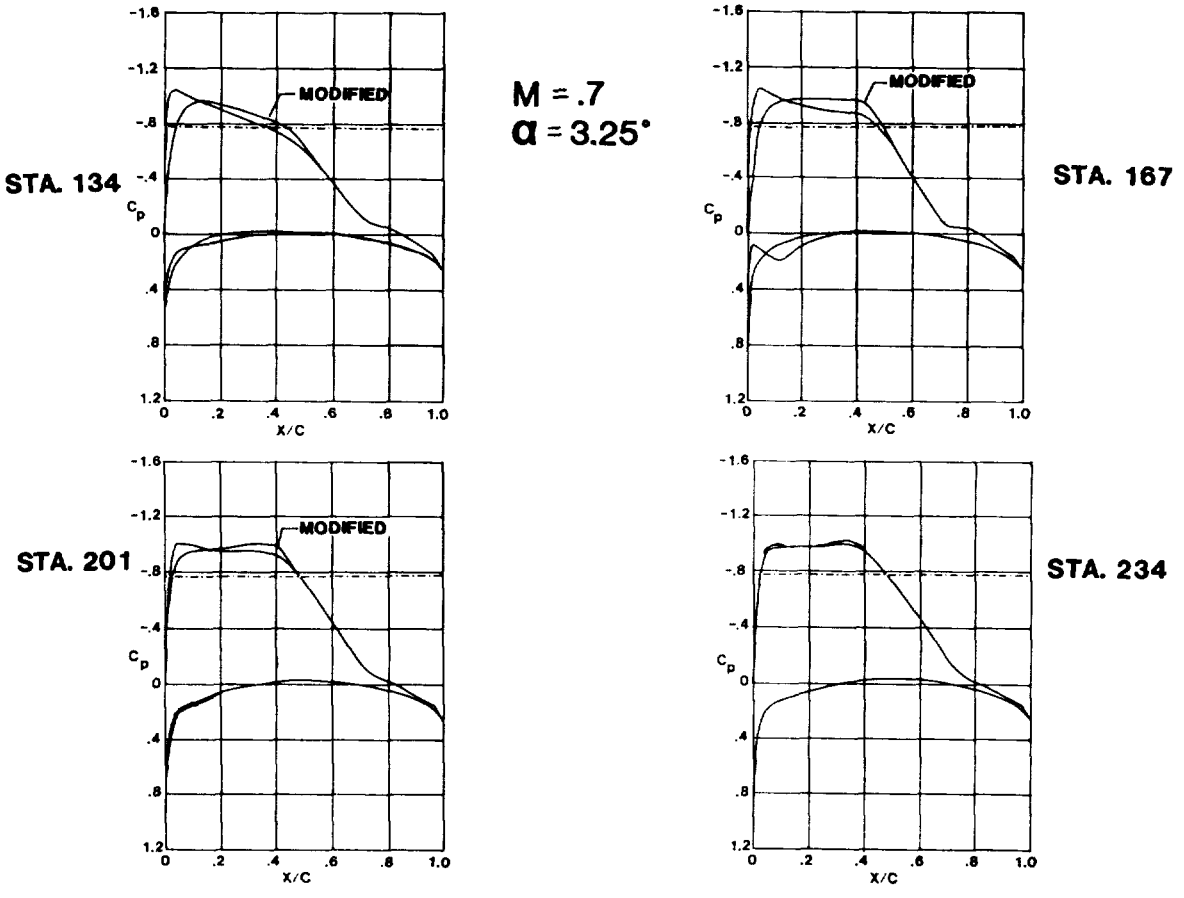

THREE-DIMENSIONAL ANALYSIS OF MODIFIED GLOVE - M = 0.8

The data presented in the figure below represent the pressure distributions at the worst case condition in the proposed flight envelope, level flight at M = 0.8 and 35,000 feet. The concern at this condition is related to the shock strength causing boundary-layer separation over the aft part of the wing. Although the shocks seem relatively strong at this condition, they are no stronger than the shocks on the baseline F-14 configuration at comparable conditions. No other adverse effects are observed in the inboard pressure distributions for the modified gloved configuration.

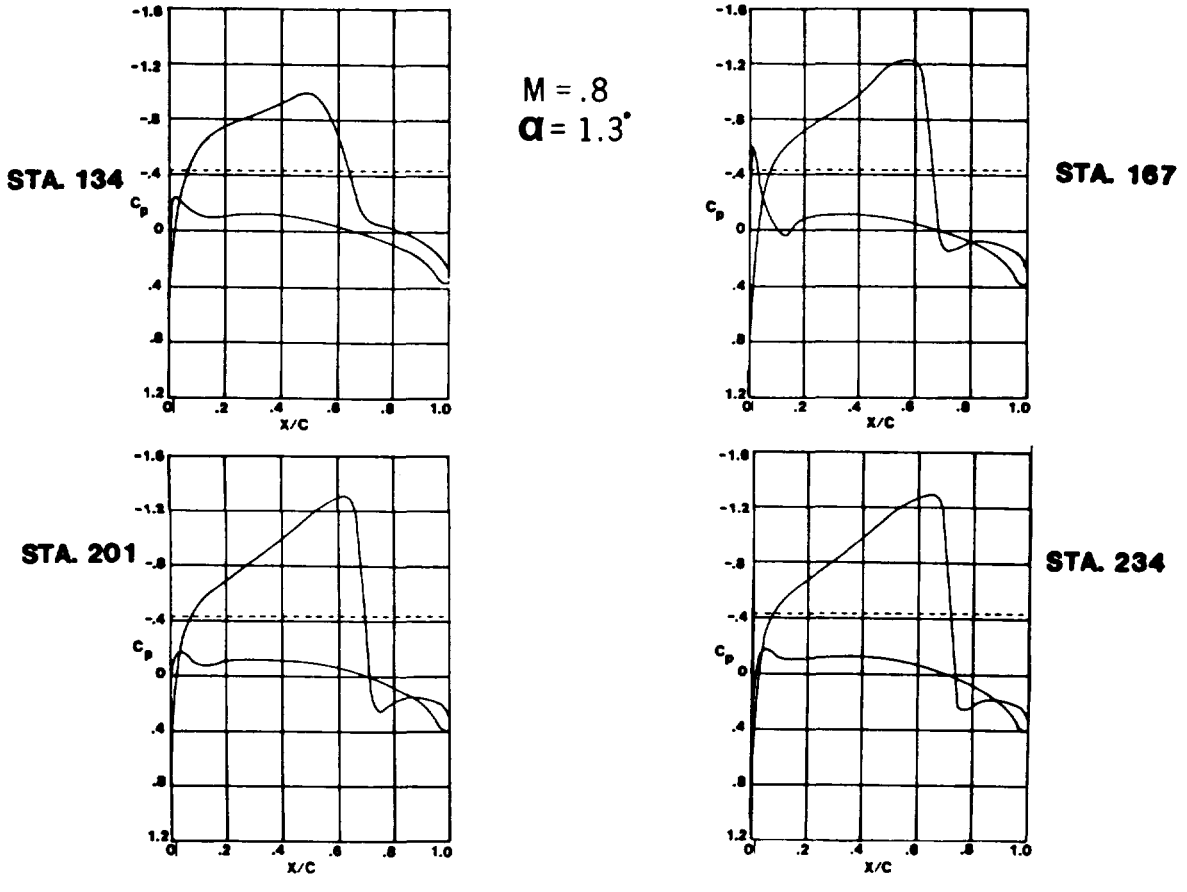

SUMMARY

Gloves for M = 0.7 and M = 0.8 design points have been computationally designed and analyzed at conditions over the proposed flight test envelope. The resulting computational pressure distributions have been analyzed in a boundary-layer stability code. These results indicate that the available pressure distributions offer a wide range of combinations of CF and TS N-factors.

The glove designs along with the baseline configuration were tested in an entry into the National Transonic Facility. Analysis of the force and moment data showed no significant differences in the performance and stability and control characteristics between the baseline and gloved configurations. The rolling moment constraint was met over the entire flight test envelope for the gloved configuration. In addition, there were only minor differences in the maximum lift coefficient at approach speeds for the two configurations.

Pressure distributions from the NTF test confirmed the design pressure distributions were achieved. However, it was decided that with minor modifications to the inboard region of the glove, useful available data could be significantly increased by adding another row of pressure orifices at span station 167. The inboard glove region was successfully redesigned, and the modified glove was analyzed over the proposed flight envelope.

* Initial gloves computationally designed
* NTF force and moment data showed no significant differences between baseline and VSTFE configurations
  * Performance
  * Stability and Control
  * Rolling Moment
  * $C_{L_{MAX}}$ at Approach Speeds
* Pressure distributions from NTF test confirmed target design
* Inboard glove region successfully redesigned

STATUS

The clean-up glove flight test has been completed and the data are being analyzed. The newly designed modified glove contour has been built up on the F-14 wing, and the wing has been reinstalled on the aircraft. Flight test instrumentation is now being checked out for the modified glove. Flight testing is scheduled to resume in late Spring of 1987.

* Clean–up glove flight test completed

* Modified glove contour has been installed on wing

* Flight test scheduled to resume May 1987

REFERENCES

Barger, R.L.; and Brooks, C.W.: A Streamline Curvature Method for Design of Supercritical and Subcritical Airfoils. NASA TN D-7770, September 1974.

Bauer, F.; Garabedian, P.; Korn, D.; and Jameson, A.: Supercritical Wing Sections II. Lecture Notes in Economics and Mathematical Systems, Volume 108, 1975.

Davis, W.H.: Technique for Developing Design Tools from the Analysis Methods of Computational Aerodynamics. AIAA Paper 79-1529, July 1979.

Hanks, G.W.; et al.: F-111 Natural Laminar Flow Glove Flight Test Data Analysis and Boundary Layer Stability Analysis. NASA CR-166051, January 1984.

Mack, L.M.: On the Stability of Boundary Layers on a Transonic Swept Wing. AIAA Paper 79-0264, January 1979.

Melson, N.D.; and Streett, C.L.: TAWFIVE: A User's Guide. NASA TM-84619, September 1983.

Moes, T.R.; and Meyer, R.R.: In-Flight Wing Pressure Distributions for the F-14A Aircraft. NASA TM- 85921, June 1985.

Rozendaal, R.A.; Variable Sweep Transition Flight Experiment (VSTFE) Parametric Pressure Distribution Boundary Layer Stablilty Study and Wing Glove Design Task. NASA CR-3992, June 1986.

Waggoner, E.G.; Campbell, R.L.; Phillips, P.S.; and Viken, J.K.: Computational Design of Natural Laminar Flow Wings for Transonic Transport Application. NASA CP-2398, Volume II, April 1985.

THE DESIGN OF AN AIRFOIL FOR A HIGH-ALTITUDE, LONG-ENDURANCE REMOTELY PILOTED VEHICLE

Mark D. Maughmer
The Pennsylvania State University
University Park, Pennsylvania

Dan M. Somers
NASA Langley Research Center
Hampton, Virginia

AIRFOIL/AIRCRAFT DESIGN INTEGRATION

Whereas the airfoil to be used on a new aircraft was once chosen from a catalog of possibilities as the compromise which most closely matched the design requirements, the state of airfoil design is now at such a level that each new vehicle should have an airfoil tailored specifically to the intended mission. The role of the airfoil designer in this case is as it has always been, that is, to achieve the required lift for the least possible drag. It should not be inferred, however, that the best airfoil design is accomplished by maximizing the section lift-to-drag ratio. Instead, by making use of modern airfoil design technologies, the designer arrives at the most suitable airfoil for a particular aircraft by trading off the conflicting goals of achieving low section profile-drag coefficients through laminar-flow management, for example, against attaining high maximum lift coefficients which reduce the wetted-area drag by allowing a reduction in the required wing area. These types of trade-offs make it clear that in order to achieve the highest levels of aircraft performance possible, the airfoil design process should be integrated, as shown in the flow diagram of Fig. 1, with that of the aircraft. In tailoring the airfoil to match the aircraft, the most significant element in this diagram is the airfoil/aircraft design iteration loop. Clearly, the more closely the baseline airfoil data used in the preliminary design process match the mission requirements, the fewer the iterations necessary in the design loop.

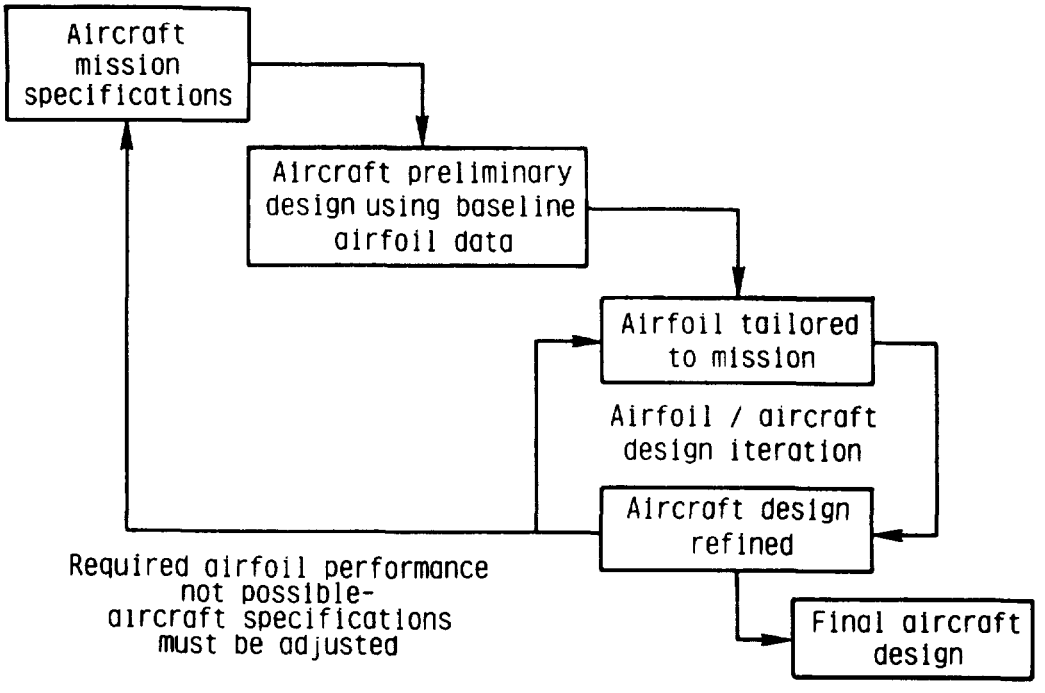

Figure 1

TYPICAL SPECIFICATIONS FOR A HIGH-ALTITUDE,
LONG-ENDURANCE REMOTELY PILOTED VEHICLE

Currently, there is interest in the development of high-altitude, long-endurance remotely piloted vehicles for a number of proposed missions, including communications relaying, weather monitoring, and providing cruise missile targeting information. The preliminary design and sizing of such vehicles is complicated however, by the fact that data regarding suitable airfoils are limited. This is due to the fact that such vehicles, unlike those for which the majority of airfoils have been developed in the past, operate at fairly high lift coefficients and at relatively low Reynolds numbers. Thus, to provide realistic airfoil performance information for preliminary design purposes, a generic airfoil has been designed for the aircraft having the specifications given in Fig. 2. These specifications are representative of the aircraft proposed for the missions noted.

Wing span = 25m (82 ft)

Gross weight = 2000 kg (4400 lbs)

Empty weight = 1000 kg (2200 lbs)

Payload = 150-500 kg (330-1100 lbs)

Operational altitude = 20,000 m (66,000 ft)

Endurance $\approx$ 90 hrs.

Range $\approx$ 32,000 km (20,000 mi)

Figure 2

DESIGN GOALS

Based on performance studies of the aircraft having the specifications given in Fig. 2, the airfoil design requirements for the section located at the mean aerodynamic chord emerged. These requirements are summarized in the form of the section drag polar presented in Fig. 3. The design goal is to achieve the lift coefficients required for the key operational points noted in the figure, and to achieve them with the lowest possible profile-drag coefficients. Thus, the desired polar is of the form shown, but moved to the left as far as possible for the given width of the laminar "bucket". In addition, subject to the other design constraints, it is desirable to achieve a reasonably high maximum lift coefficient for take-off and landing performance.

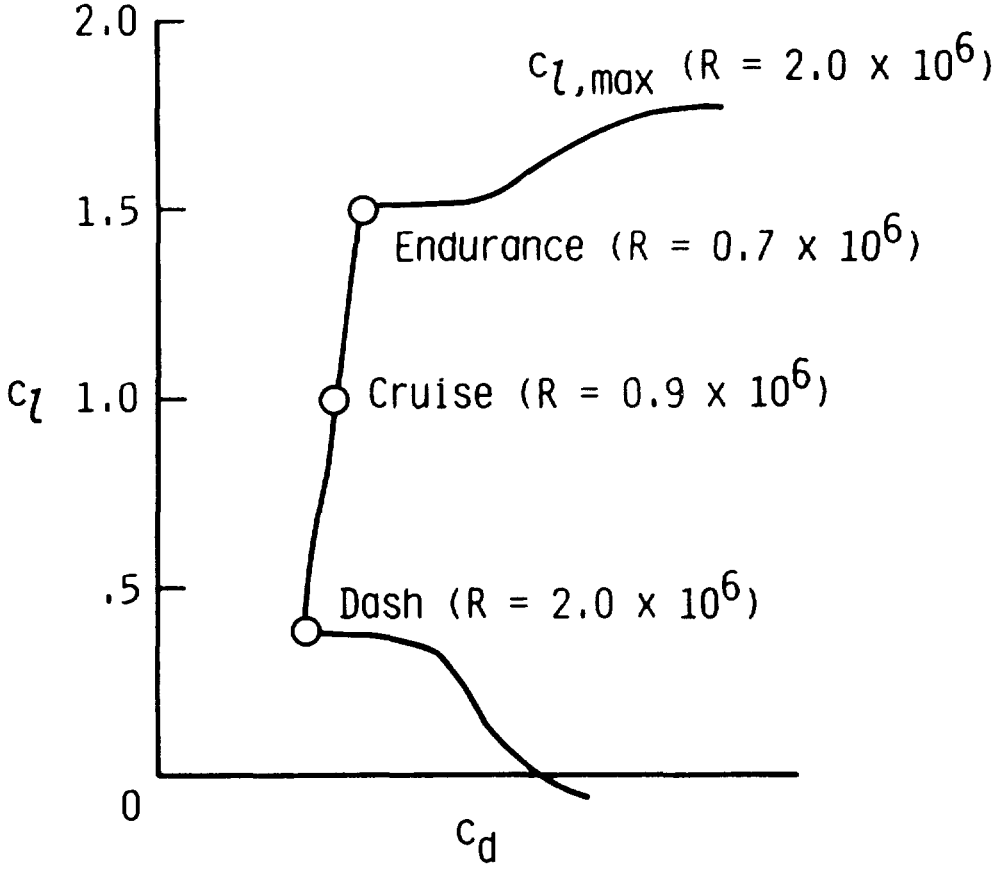

Figure 3

FIGURE OF MERIT

In order that the most suitable airfoil for a given aircraft results, it is necessary to direct the design process using some means of quantitatively comparing different candidate airfoils. On first consideration, it might be thought that the airfoil having the highest of the so-called endurance parameter, $c_\ell^{3/2}/c_d$, would offer the best aircraft endurance performance; however, because of the impact of the airfoil on such things as wing area, tail size, and so forth, selection of the airfoil having the highest endurance parameter does not insure that the aircraft will have the highest three-dimensional endurance parameter, $C_L^{3/2}/C_D$. In fact, it was found that in order to maximize the aircraft endurance, the airfoil should be designed such that the figure of merit, given in Fig. 4, is maximized. The figure of merit provides a quantitative means of trading off the gain due to decreasing wetted-area wing drag by increasing the maximum lift coefficient against that of decreasing the section profile-drag coefficient. It should be noted that, if the appropriate operational lift coefficient for which the profile drag is minimized is considered, this figure of merit is the same as that used to design an airfoil for general aviation applications.[1]

- Reduce wing profile drag
  - Decrease wing area by increasing $c_{l,max}$
  - Reduce section profile drag at operational c_l
- Maximize $\left\{ \dfrac{c_{l,max}}{c_d \text{ @ } c_l = 1.5} \right\}$

Figure 4

APPLICATION OF THE FIGURE OF MERIT

As an example of how the figure of merit given in the preceding figure might be used, consider the drag polars of two candidate airfoils as depicted in Fig. 5. The airfoil having performance represented by the solid line has a lower profile-drag coefficient over most of the flight range, while the airfoil represented by the dashed line has a higher maximum lift coefficient which allows the required wing area to be less, and thereby reduces the wetted-area drag. While the two polars are very different, it is entirely possible that the two airfoils have the same maximum section endurance parameters or lift-to-drag ratios. Thus, while it is clear that one of the two must offer better aircraft endurance, it is not at all clear which one it is. The figure of merit, however, provides a quantitative means which allows the proper selection to be made.

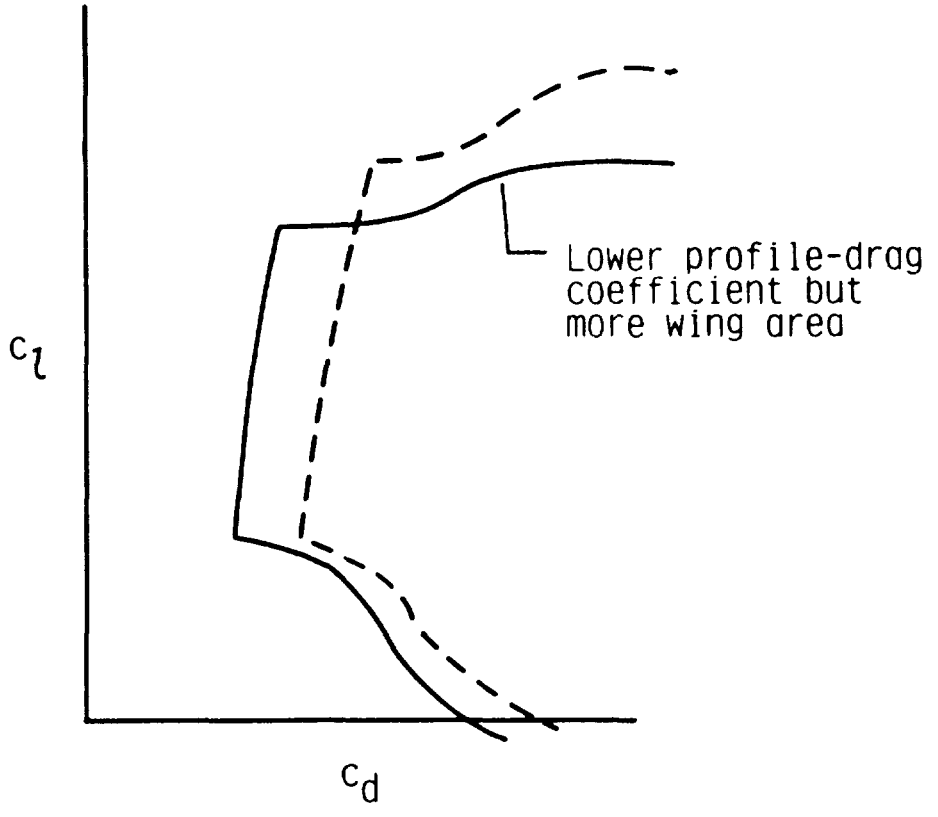

Figure 5

ADDITIONAL DESIGN CONSIDERATIONS

In addition to the design considerations already noted, the constraints indicated in Fig. 6 were imposed. A single-element airfoil was decided on because performance calculations indicated the penalty for carrying the additional weight of a flap system over such a long period of time could not be justified. To keep the trim drag within reasonable limits, it was decided that the airfoil pitching moment coefficient should be no more negative than indicated. Finally, although resulting in a severe limitation on the achievable $c_{\ell,max}$, the constraint was imposed that the maximum lift coefficient should not depend on surface contamination. Thus, take-off and landing performance would be unaffected by rain, bugs, dirt, and so forth, on the wings.

1. No flaps
2. $c_{m,o}$ no more negative than -0.20
3. $c_{l,max} \neq f$(surface contamination)

Figure 6

THE UPPER-SURFACE VELOCITY DISTRIBUTION USED FOR THE ACHIEVEMENT OF $c_{\ell,max}$ INDEPENDENT OF SURFACE CONTAMINATION

In order to achieve $c_{\ell,max}$ independent of surface contamination, the upper-surface velocity distribution was designed to behave as indicated in Fig. 7. The idea is to have the velocity distribution corresponding to $c_\ell = 1.5$, which is the upper limit of the low-drag range, such that the boundary-layer transition is "on the verge" of moving forward from its location just at the start of the main pressure recovery. Thus, for lower angles of attack, the pressure gradients are such that transition will be confined to the ramp just upstream of the main pressure recovery. For higher angles of attack, however, the resulting unfavorable pressure gradients will cause transition to move rapidly toward the leading edge. Thus, the maximum lift coefficient does not depend on a long run of laminar flow. The pressure peaks over the forward portion of the airfoil required to achieve this behavior, however, tend to limit the maximum lift coefficient that can be produced.

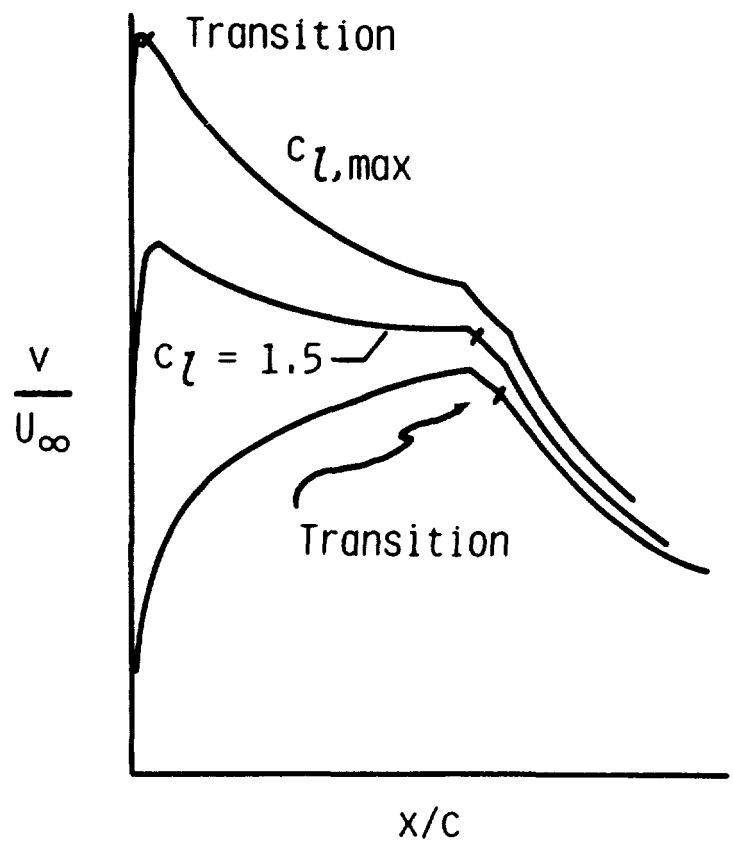

Figure 7

SEPARATION RAMP

In order to operate at the relatively high lift coefficients required by the high-altitude, long endurance mission, the level of the upper-surface velocity distribution must be fairly high. In recovering to free-stream conditions over the aft portion of the airfoil, however, the low operational Reynolds number severely limits the amount of adverse pressure gradient that can be negotiated by the turbulent boundary layer without separation problems. One method of obtaining the lift needed while controlling the extent of upper-surface separation is through the use of the separation ramp (shown in Fig. 8), originally credited to F. X. Wortmann. While some separation is present at angles of attack within the operating range of interest, the ramp limits the amount of separation to less than ten-percent chord. It is not until the angle of attack is near that corresponding to the maximum lift coefficient that the separation point is able to move upstream of the ramp and onto the main pressure recovery.

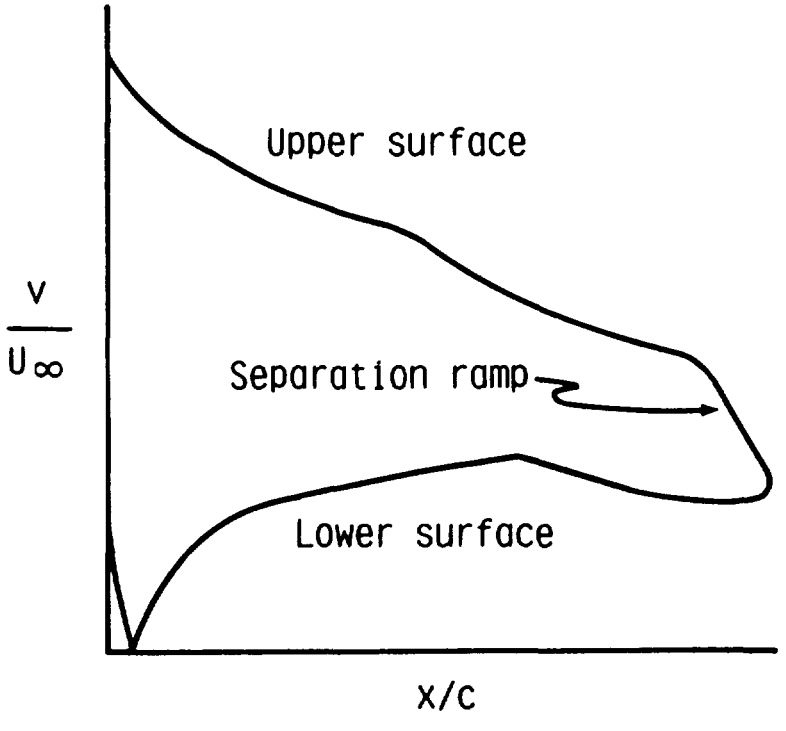

Figure 8

DESIGN METHODOLOGY

Once the design goals were firmly established, the actual design was carried out using the Eppler program.[2,3] Most design methodologies develop the airfoil for a given condition, then explore off-design, and if found unacceptable, modify the design-point solution until acceptable off-design performance is achieved. The Eppler method, however, is unique in that the airfoil is designed to satisfy the entire performance envelope from the onset. This is possible because the method allows different parts of the airfoil to be designed for different operating conditions. For example, as shown in Fig. 9, the upper surface of the airfoil is designed primarily to the upper limit of low-drag range of the polar, corresponding to the high-altitude long-endurance operating point, while the lower surface was designed to the lower limit of the low-drag range, corresponding to the dash requirements.

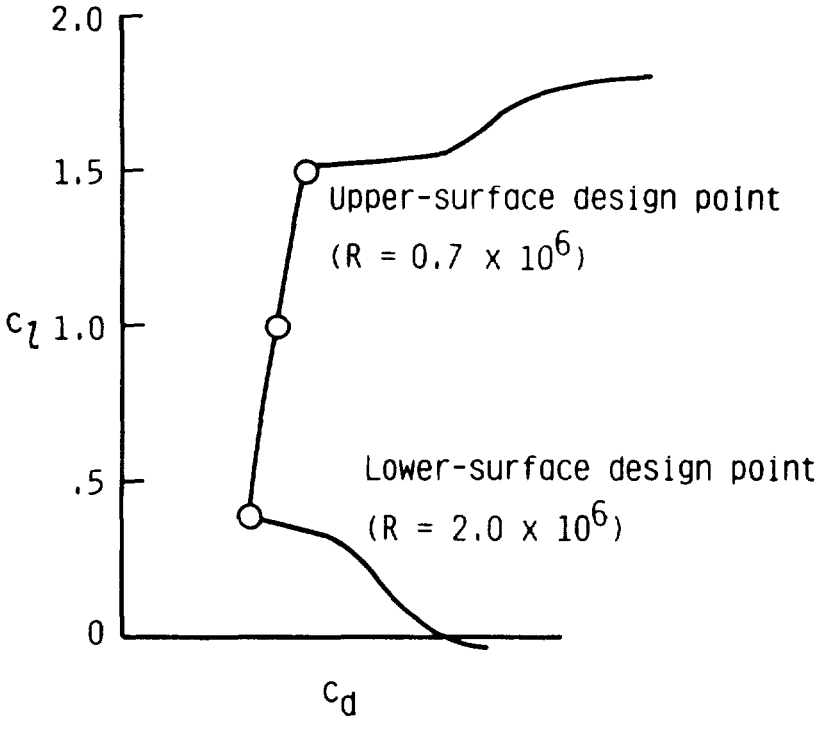

Figure 9

DESIGN FOR DESIRED BOUNDARY-LAYER DEVELOPMENT

It is notable that, unlike most methods which design for a given velocity distribution, the Eppler program makes it possible to go one step beyond this and design an airfoil which achieves a desired boundary-layer development. As an example of the process, consider the program-generated plot, presented in Fig. 10, of Reynolds number based on momentum thickness against the boundary-layer shape factor. Indicated in the figure are the empirically determined criteria for transition and turbulent separation. Also shown for reference are the shape factors corresponding to a laminar separation, stagnation, and the Blasius solution for the boundary layer over a flat plate. The curves plotted in the figure represent the boundary-layer developments at two angles of attack near the upper-surface design condition. Both developments begin at the leading-edge stagnation point and rapidly move toward laminar separation. The development at α = 14.79 degrees closely follows the laminar separation criterion and intersects the transition curve at a point on the airfoil corresponding to the start of pressure recovery. The boundary-layer development which is shown for a slightly higher angle of attack intersects the laminar separation line almost immediately, and transition near the leading edge by means of a laminar separation bubble is indicated. This particular development provides for the rapid forward movement of transition for lift coefficients greater than 1.5 and thereby satisfies the requirement that the maximum lift be independent of surface contamination. The desired boundary-layer development on the lower surface is obtained similarly.

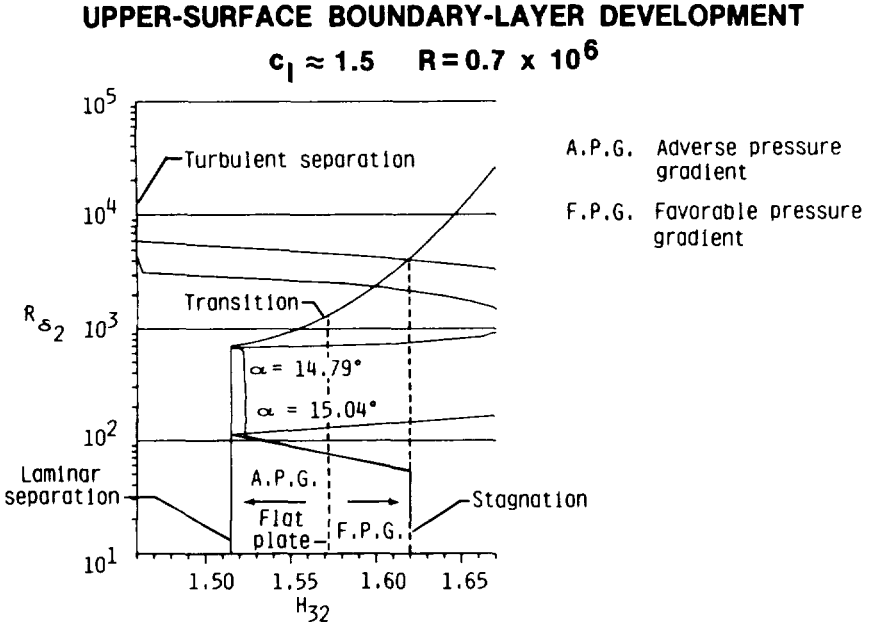

Figure 10

HIGH-ALTITUDE, LONG-ENDURANCE AIRFOIL
AND INVISCID VELOCITY DISTRIBUTIONS

The high-altitude, long-endurance airfoil which was designed is presented in Fig. 11. Also included in the figure are the inviscid velocity distributions corresponding to the key design lift coefficients for this airfoil.

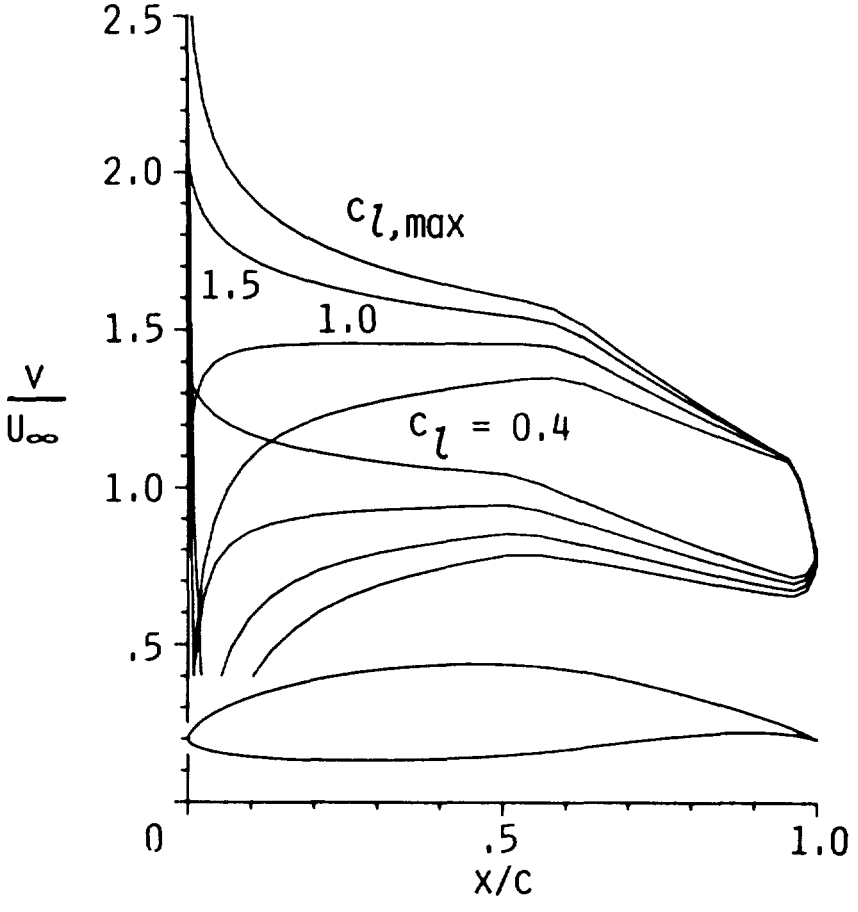

Figure 11

SECTION CHARACTERISTICS
$R = 0.7 \times 10^6$

The performance of the airfoil is summarized in the program-generated plots presented in Fig. 12. The results shown correspond to the long-endurance Reynolds number. Comparing these results with the requirements shown in Fig. 3, it is clear that all the design goals have been satisfied. The small triangles on the drag curves indicate lift coefficients for which a laminar separation bubble is predicted that is significant enough to alter the drag coefficients given. It should be noted, however, that the laminar-separation-bubble warnings occur outside the operating range for the airfoil for this Reynolds number.

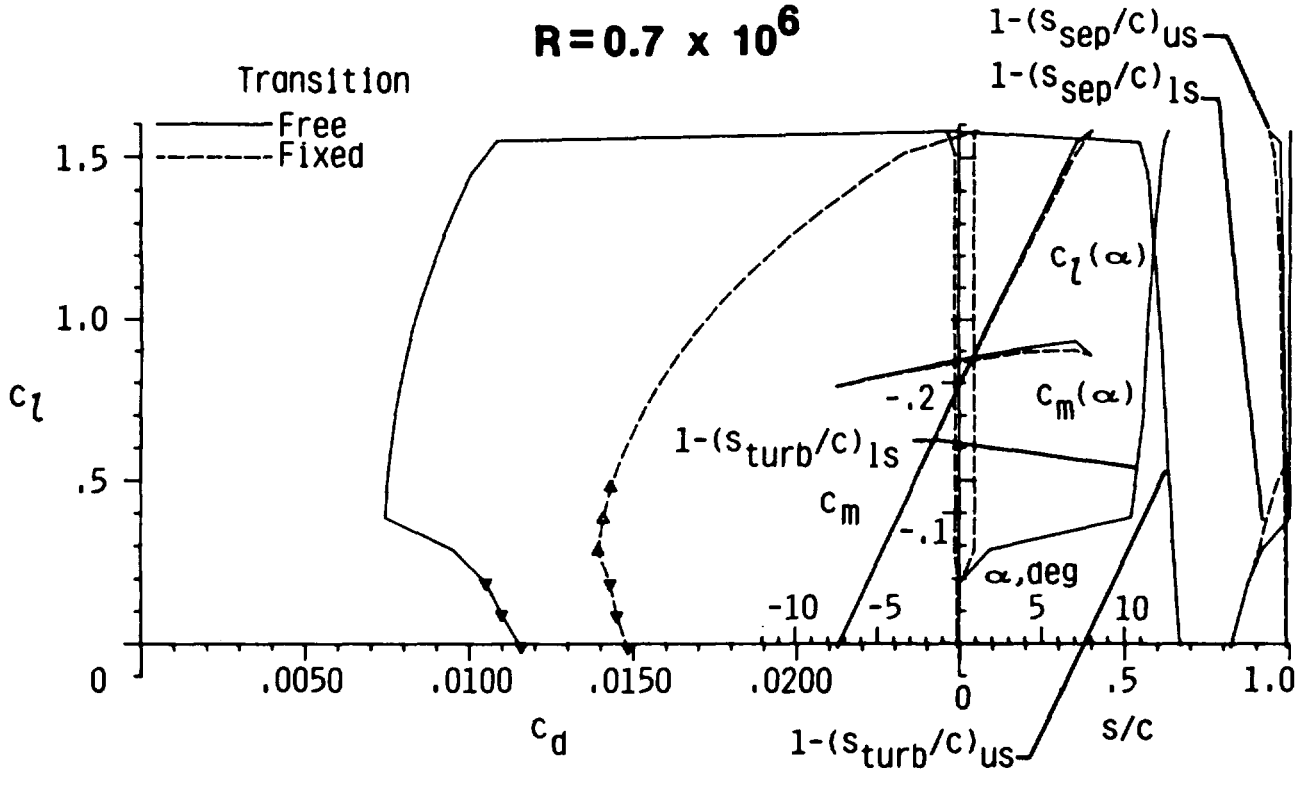

Figure 12

SECTION CHARACTERISTICS
$R = 2 \times 10^6$

The section characteristics for the Reynolds number corresponding to take-off and dash conditions are given in Fig. 13. Of most significance is the fact that the transition-free and transition-fixed polars merge at high lift coefficients. Thus, because the transition point on the upper surface has already moved to the leading edge, the behavior of the airfoil at high lift coefficients is independent of surface contamination which, otherwise, would influence the location of transition. Based on a long-term calibration of the program calculations against wind-tunnel and flight data, a maximum lift coefficient of 1.8 is expected for this airfoil.

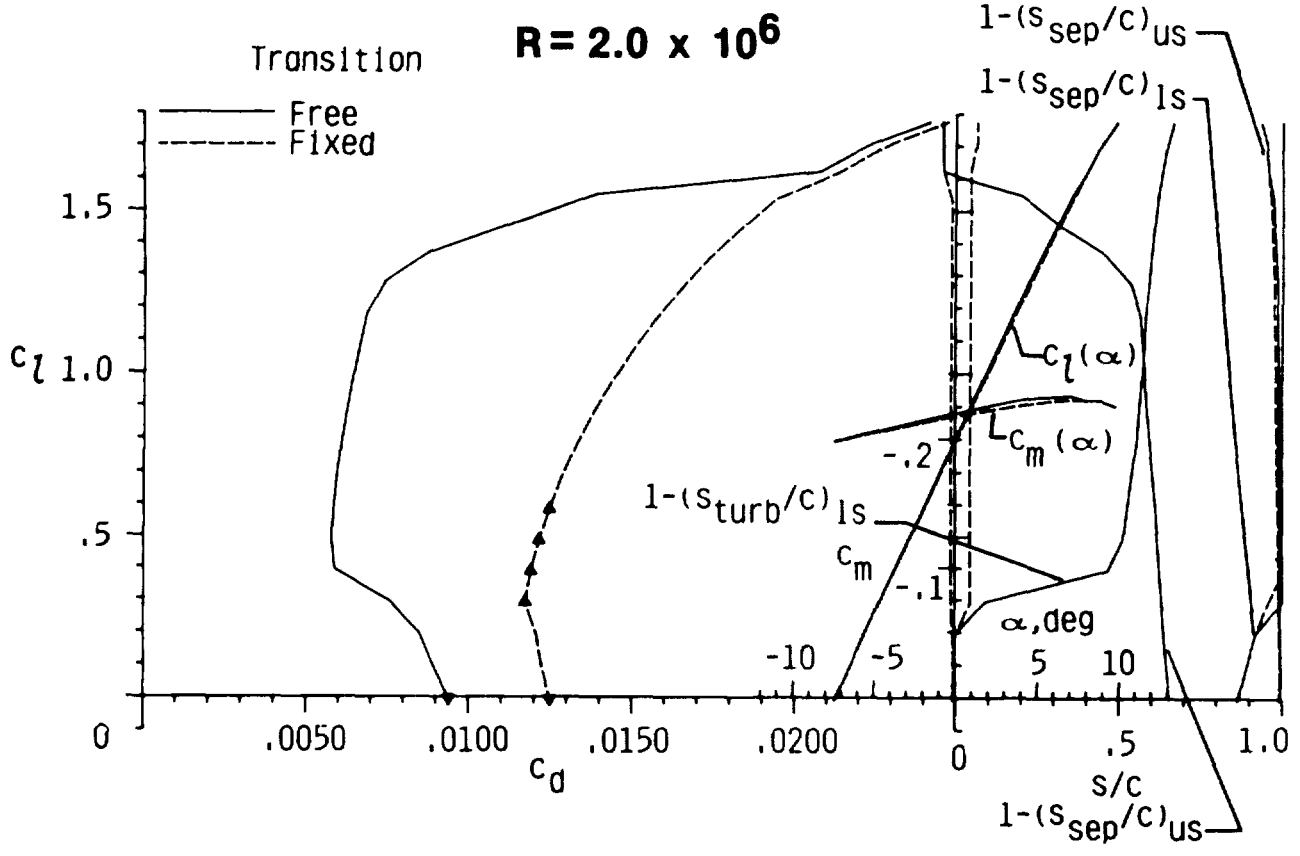

Figure 13

VEHICLE PERFORMANCE COMPARISON

To demonstrate the relative importance of the airfoil performance to that of the overall aircraft, a performance comparison is presented in Fig. 14 for two aircraft which are identical in all respects except for the airfoil utilized on the main wing. The first column results are for the aircraft having an NACA 23015 airfoil, while the second column results are for the vehicle having the new high-altitude, long-endurance airfoil, the NASA NLF(1)-1015. The thirty-percent improvement in endurance and fourteen-percent in range clearly indicate that the potential benefits offered by the new airfoil are significant. While further iteration of the airfoil/aircraft design would result in even better overall performance, the airfoil designed provides realistic, performance data which should facilitate the meaningful preliminary design and sizing of high-altitude, long-endurance remotely piloted vehicles.

	NACA 23015	NLF(1)-1015
Endurance	72 hrs.	93 hrs. (+ 30%)
Range	18,000 mi	21,000 mi (+ 14%)

Figure 14

CONCLUSIONS

The contributions of the airfoil design effort reported in this paper are summarized in Fig. 15.

- Demonstrated importance of integrating airfoil and aircraft designs
- Provided realistic airfoil data to aid future high-altitude, long-endurance aircraft preliminary design
- Developed test case for further validation of Eppler program
- Designed boundary layer -- not pressure distribution or shape
- Achieved substantial improvement in vehicle performance through mission-specific airfoil designed utilizing multipoint capability of Eppler program

Figure 15

SYMBOLS AND ABBREVIATIONS

C_D drag coefficient

C_L lift coefficient

c airfoil chord

c_d section profile-drag coefficient

c_ℓ section lift coefficient

c_m section pitching moment coefficient taken about quarter-chord point

$c_{m,o}$ section quarter-chord pitching-moment coefficient at zero lift

H_{32} boundary-layer shape factor, δ_3/δ_2

R Reynolds number based on free-stream conditions and airfoil chord

s arc length along airfoil surface

s_{sep} arc length along which boundary layer is separated

s_{turb} arc length along which boundary layer is turbulent, including s_{sep}

U_∞ free-stream velocity

v local velocity on airfoil

x airfoil abscissa

α angle of attack relative to zero-lift line, deg

δ_2 boundary-layer momentum thickness

δ_3 boundary-layer energy thickness

Abbreviations:

ls lower surface

us upper surface

REFERENCES

1. Somers, Dan M.: Design and Experimental Results for a Flapped Natural-Laminar-Flow Airfoil for General Aviation Applications. NASA TP-1865, 1981.

2. Eppler, Richard; and Somers, Dan M.: A Computer Program for the Design and Analysis of Low-Speed Airfoils. NASA TM-80210, 1980.

3. Eppler, Richard; and Somers, Dan M.: Supplement To: A Computer Program for the Design and Analysis of Low-Speed Airfoils. NASA TM-81862, 1980.

757 NLF GLOVE FLIGHT TEST RESULTS

L. J. Runyan, G. W. Bielak, R. Behbehani,
A. W. Chen, and R. A. Rozendaal
Boeing Commercial Airplane Company
Seattle, Washington

OBJECTIVES AND APPROACH

A major concern in the application of a laminar flow wing design to commercial transports is whether laminar flow can be sustained in the presence of the noise environment due to wing-mounted turbofan engines. To investigate this issue, a flight test program was conducted by Boeing under contract to NASA Langley using the Boeing 757 flight research airplane with a portion of the wing modified to obtain natural laminar flow (Refs. 1 and 2).

Prior to this flight-test program, there were no extensive measurements of the noise field on the wing of a commercial transport with wing-mounted high-bypass-ratio engines. There also were no flight measurements of the effect of such a noise field on laminar boundary-layer transition. Therefore, the flight test had two primary objectives. The first was to measure the noise levels on the upper and lower surface of the wing for a range of flight conditions. The second was to investigate the effect of engine noise on laminar boundary-layer transition. In order to achieve these objectives, the wing was instrumented with an array of microphones, and a Natural Laminar-Flow (NLF) glove was installed on the right hand wing just outboard of the nacelle. The noise field on the wing and transition location on the glove were then measured as a function of the engine power setting at a given flight condition. (Figure 1).

(NASA Contract NAS1-15325)

Objectives

- **Define noise environment on wing**
- **Investigate effect of engine noise on laminar boundary layer transition**

Approach

- **Install NLF glove outboard of engine**
- **Measure noise field and transition location as function of engine power**

Figure 1

NATURAL LAMINAR FLOW GLOVE INSTALLATION

The objective of the glove design was to obtain enough natural laminar flow to allow the effect of engine noise on the extent of laminar flow to be observed. The extent of natural laminar flow that is obtained with a given pressure distribution is a strong function of leading edge sweep. Lower leading edge sweep results in longer laminar runs. However, lower leading edge sweep has some adverse effects. The bending load due to the overhang increases with decreasing leading edge sweep. The asymmetry of the airplane also increases, which results in possible reduction of the flight envelope. The final choice of the leading edge sweep was 21 deg, which limited the airplane to 2.0-g operations.

The glove location was chosen to be immediately outboard of the No. 2 engine at slat No. 7. This location gives the glove maximum engine noise exposure. The glove was designed with the constraint that it have straight spanlines within the prime test region in order to facilitate its manufacture. It also was designed with the constraint that it match the existing wing at x/c = 0.35 in order to minimize the size of the glove.

Because the glove was considered to be a relatively small departure from the existing 757 wing, for which both wind tunnel and flight data are available, no wind tunnel testing was considered necessary to substantiate the aerodynamic design. The availability of accurate transonic aerodynamic codes was also a factor in the decision to dispense with testing. (Figure 2).

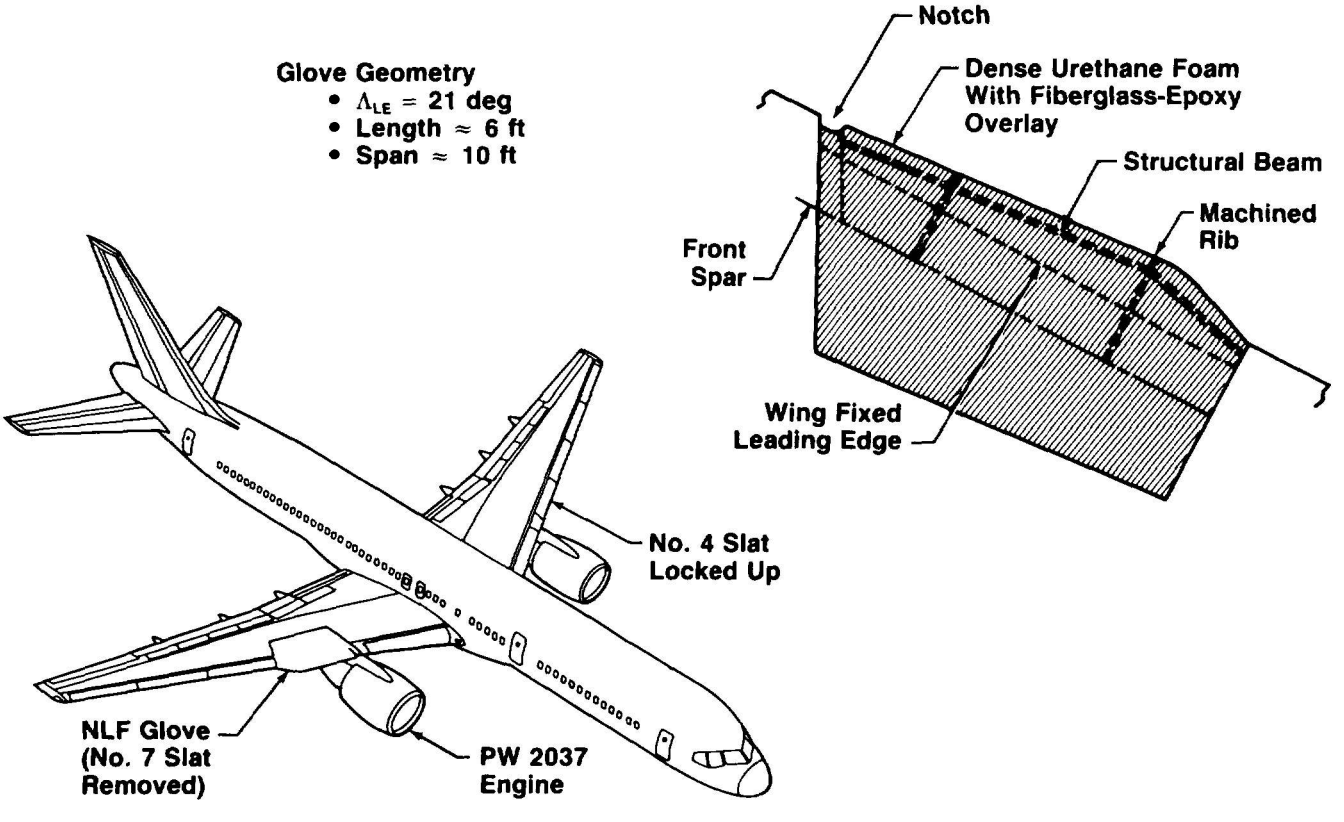

Figure 2

ACOUSTIC INSTRUMENTATION

Eight microphones were mounted on each surface of the wing. One additional microphone was mounted just above the attachment line near the outer edge of the glove. On the forward part of the wing where the boundary layer is thin, the transducers were bonded directly to the wing surface and faired smoothly to the surface using Magic Bond. Each surface-mounted transducer was modified by inserting a 0.016-in wire in the unit's vent tube to provide desired response characteristics. The microphones located further back on the wing were mounted on a probe. The probe height above the wing surface was chosen so that the microphone would be slightly above the boundary layer as calculated for the glove design condition (M = 0.80, altitude = 40,000 ft). The vent tube of each of the probe-mounted transducers was modified by inserting a 0.008-in wire to provide satisfactory response characteristics.

The microphone locations were chosen to survey the entire wing with a limited number of transducers. It was also desired to use a denser distribution of microphones in the NLF glove region for the investigation of sound effects on laminar flow. The microphone placement on the glove recognized that the microphones would trip the laminar boundary layer. Their locations were chosen so that the turbulent wedge emanating from them would not interfere with any of the hot films. (**Figure** 3).

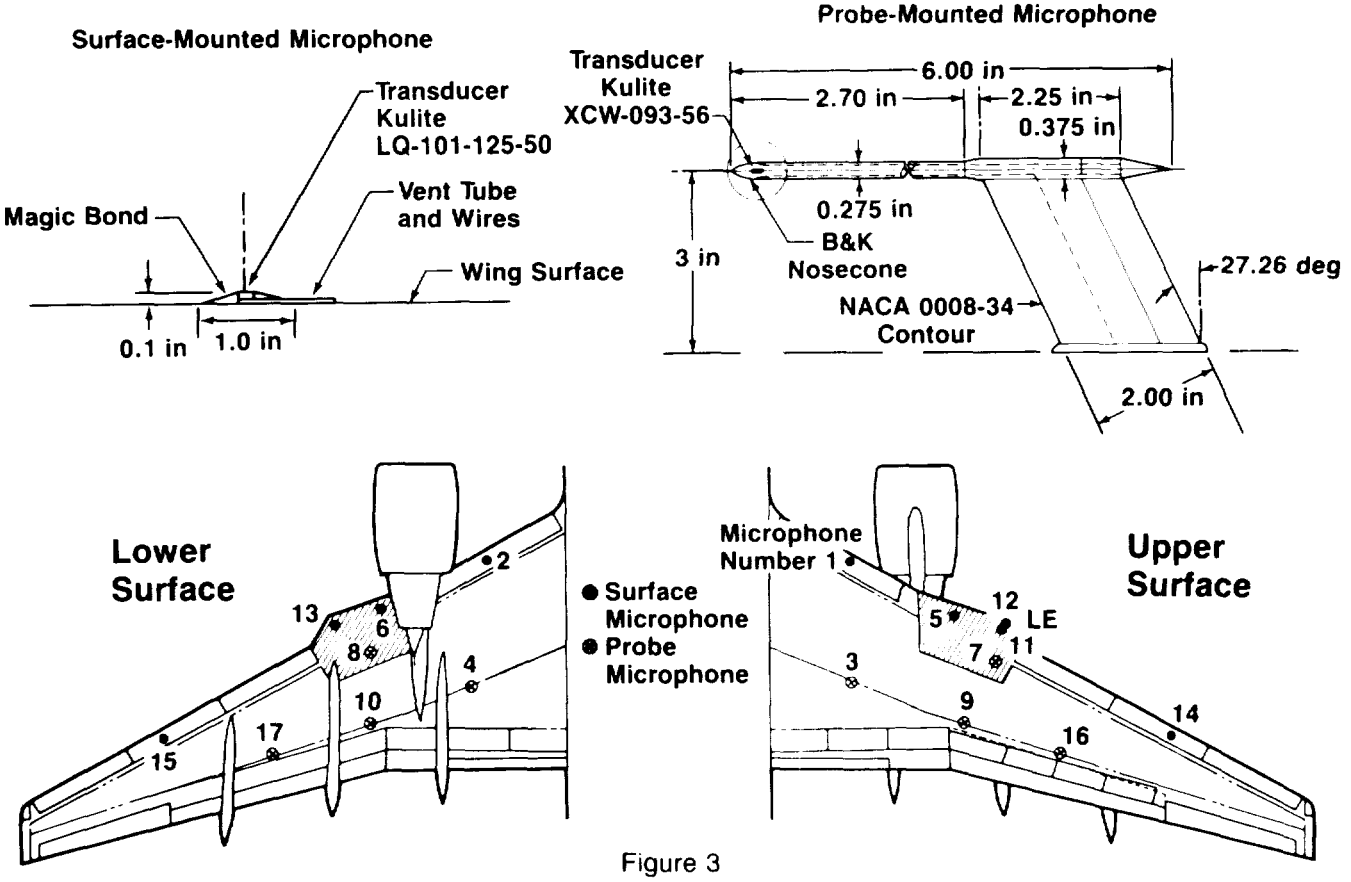

Figure 3

NLF GLOVE INSTRUMENTATION

In addition to the noise-measuring instruments, glove pressure distributions were measured with separate upper and lower surface "strip-a-tube" belts, and the state of the boundary layer was determined by surface hot-film sensors. Two separate pressure belts were used for each glove surface so there would be no chance of contaminating the attachment line flow with a belt wrapped around the leading edge. The pressure belts were carefully faired to the glove surface to minimize the effect of their presence on the measured pressures. The number of available data channels limited the pressure measurements to one section at a time. Therefore, only the pressure belts at the inboard section were used for the first two flights, and only the outboard belts were used for the last two flights. By closely matching the test conditions, measurements from the two sets of flights with different instrumentation layouts could be combined.

The ten hot-film sensors installed on each surface of the glove were staggered 15 deg from a streamwise line so the disturbances created by upstream sensors would not affect the response of downstream sensors. The choice of this angle was based, in part, on transonic analyses that determined the streamline pattern on the glove. On the first two flights the films were placed in a long row to get an accurate chordwise determination of the transition point near the middle of the glove. For the last two flights the sensors were repositioned based on results from the first flights, so the spanwise extent of laminar flow could be determined. (Figure 4).

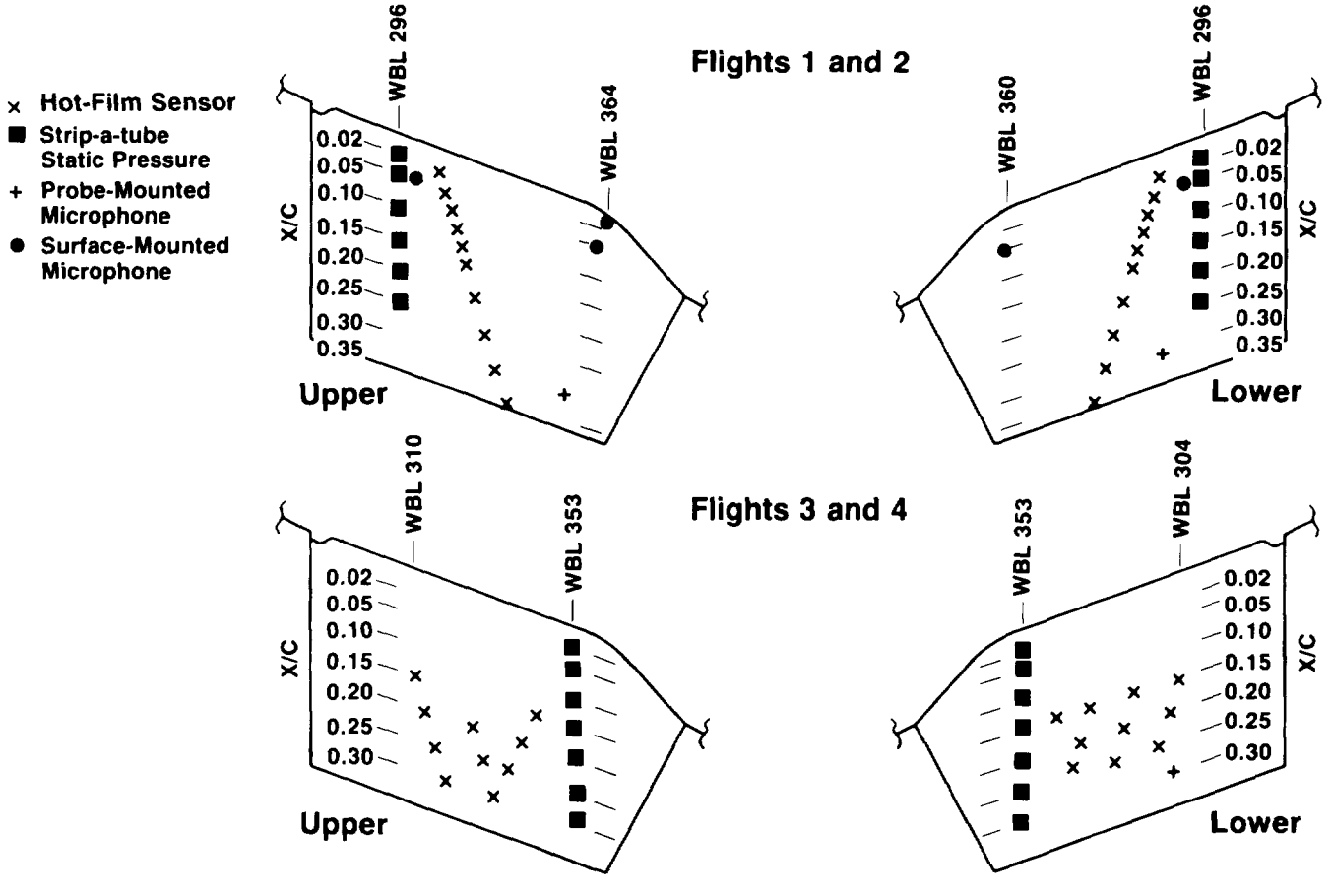

Figure 4

TRANSITION SENSING SYSTEM

The hot-film sensors used for this test were 50-Ohm nickel gages made by Micromeasurement. The electronics that controlled the gages was designed and fabricated at Boeing, and maintained the gages at a constant voltage. The fluctuating current signal from each gage was converted to a voltage and recorded on magnetic tape during each test point interval and also displayed continuously on oscilloscopes. The rms value from each hot film was also recorded.

The oscilloscope displays were used by the test engineer on the flights to determine the boundary-layer state in real time at each of the hot-film locations. The traces exhibited by the hot films fell into four quite distinct categories. A laminar trace was nearly flat with an rms signal value of about 10 mV. The next development was an intermittent signal burst superimposed on the laminar signal. This was interpreted as being discrete bursts of turbulence moving past the gage. These intermittent bursts eventually replaced the laminar signal as the boundary layer moved into its transitional phase. The transitional signal had rms values of several hundred millivolts. As the boundary layer became fully turbulent, the signal settled down from the wildly fluctuating transitional trace to a steady state fluctuation having an rms value around 50 mV. (Figure 5).

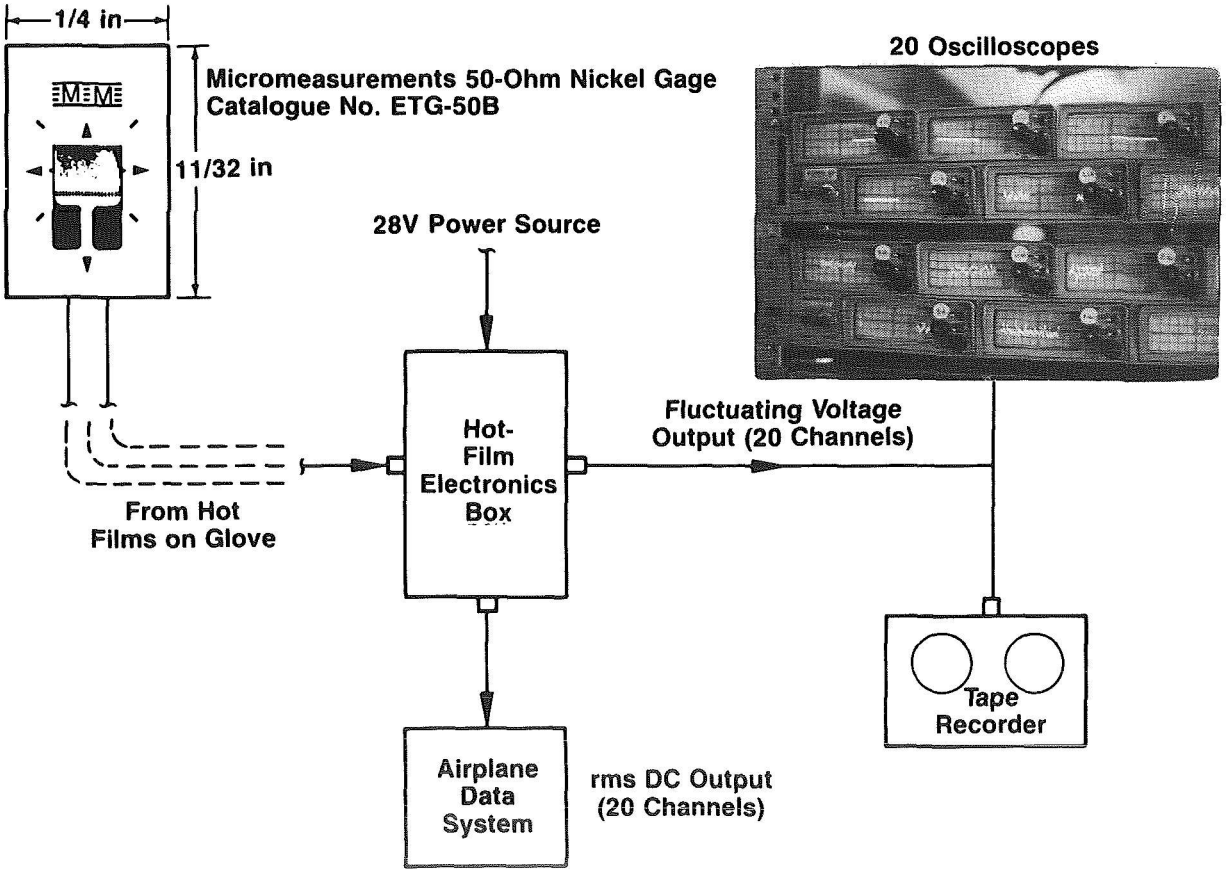

Figure 5

INSECT PROTECTION COVER

Because the glove was flight tested in June, it was necessary to protect the test area from insect impingement that would result in contamination of the laminar flow. The technique used was similar to that used successfully in the King Cobra flight-test program (Ref. 3). The leading-edge area was covered with paper during takeoff and climb. The paper used was similar to butcher paper in strength and thickness, with a thin film of wax on the side next to the glove surface. To remove the paper, a heavy nylon rip cord was led under the leading edge of the cover to its outboard end and then back through a small paper envelope attached to the outside leading edge of the cover. The cord was attached to the cover at its inboard end and was protected from the airflow by the envelope. The cord was run into the cabin through a 0.25-in copper tube that was secured to the wing and body surfaces. After the airplane climbed above 5000 ft, the cord was pulled, ripping the paper into two halves that flew away. The ripping mechanism did not work as planned on the first two flights because of initial problems with the routing of the copper tube and the strength of the rip chord. "Roller-coaster" type maneuvers had to be used to shake off the paper. On flight 3, the ripping mechanism worked as planned. On all 3 of those flights there was no evidence of insect contamination, indicating that the cover did provide the desired protection. (Figure 6).

Figure 6

INSECT IMPINGEMENT ON UNPROTECTED GLOVE

The glove was not protected during flight 4 since the primary purpose of that flight was to obtain pressure data. Laminar flow sensor data taken on the flight indicated a loss of laminar flow in some areas of the glove relative to the flight 3 results. It was suspected that this was due to insect contamination, although this could not be visually confirmed in flight. After landing, an inspection of the glove leading edge showed that seven insects had hit the glove in the vicinity of the attachment line. It is not known how many of these were picked up during takeoff and climbout. However, this evidence, together with the reduced extent of laminar flow in some areas of the glove, indicates that the cover served its essential purpose on the three flights for which it was used. (Figure 7).

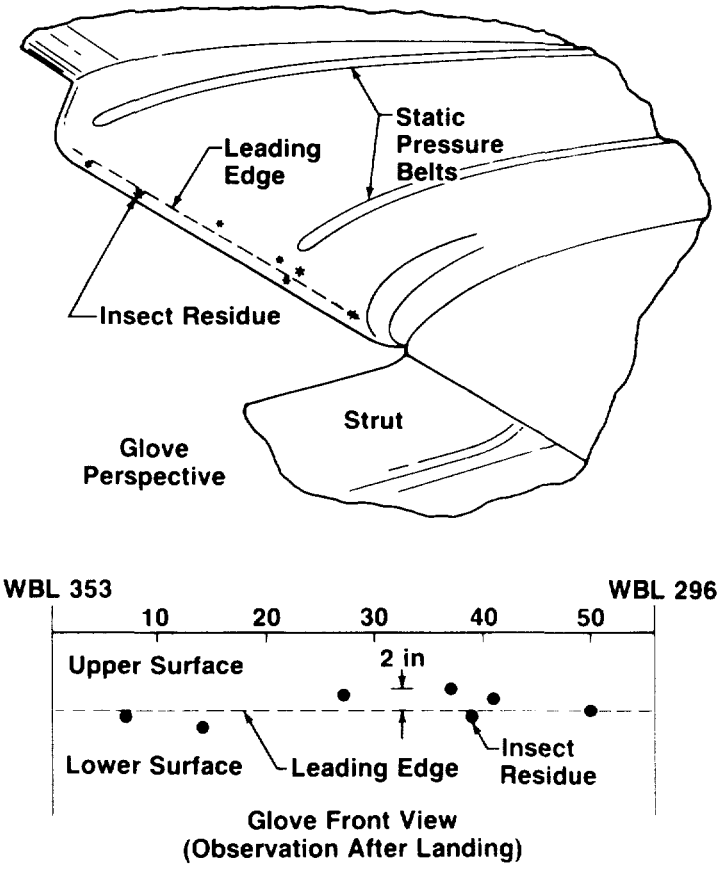

Figure 7

MACH ALTITUDE CONDITIONS TESTED

The design point of the NLF glove was M = 0.8 and an altitude of 40,000 ft. At this condition it was expected that a significant extent of laminar flow would be achieved on the upper and lower surface of the glove simultaneously. However, it was also expected that the condition for maximum extent of laminar flow on the upper surface would be obtained at a condition different from that of the lower surface, both of which would differ from the design condition. Furthermore, it was necessary to study the effects of Reynolds number, Mach number, lift coefficient, and sideslip on the extent of laminar flow. The effect of altitude and Mach number on the measured noise levels was also desired. Therefore, a wide range of Mach-altitude conditions were tested, as shown in Figure 8. The Mach numbers tested ranged from 0.63 to 0.83, and the altitudes ranged from 25,000 ft to 41,000 ft. The most important Mach numbers were 0.8 and 0.7, and the most important altitudes were 39,000 ft and 35,000 ft.

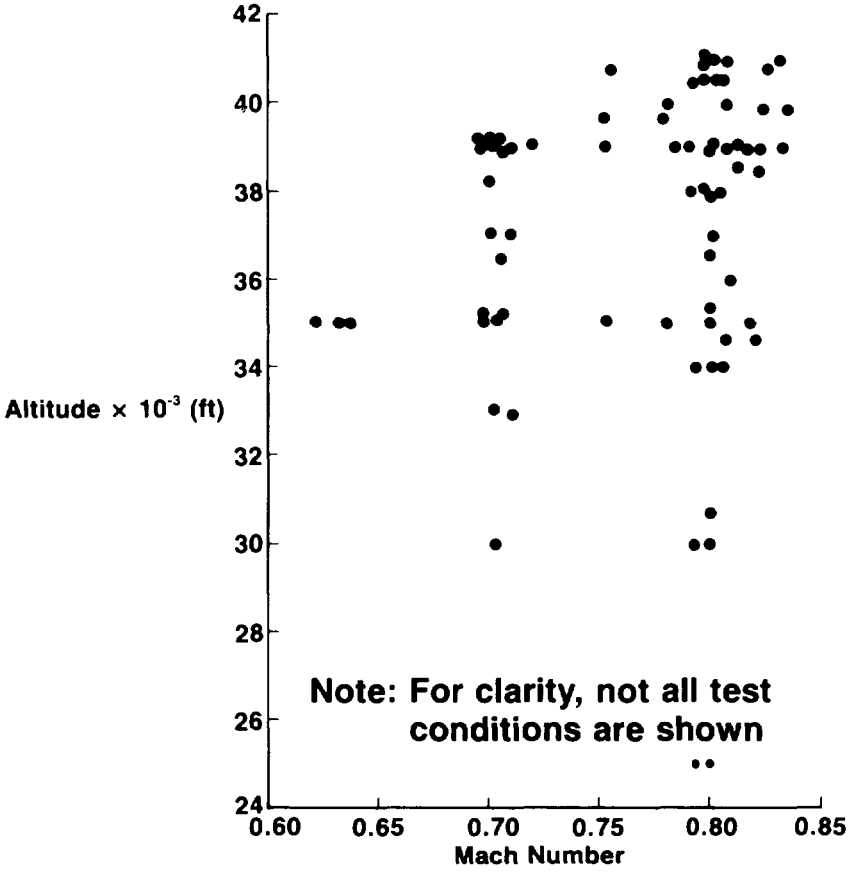

Figure 8

OASPL DISTRIBUTION ON 757 WING

Figure 9 shows the overall sound pressure level (OASPL) distribution measured on the wing for a cruise engine power setting at an airplane Mach number of 0.81 and an altitude of 39,000 ft. The upper surface noise levels range from 111 dB to 131 dB. The lower surface noise levels range from 121 dB to 136 dB. This data is presented to give an overview of the noise levels measured. The flight-test program resulted in a large data base of this type of noise data for a large range of flight conditions and engine power settings. In addition, the spectral characteristics of the noise at each microphone location were measured.

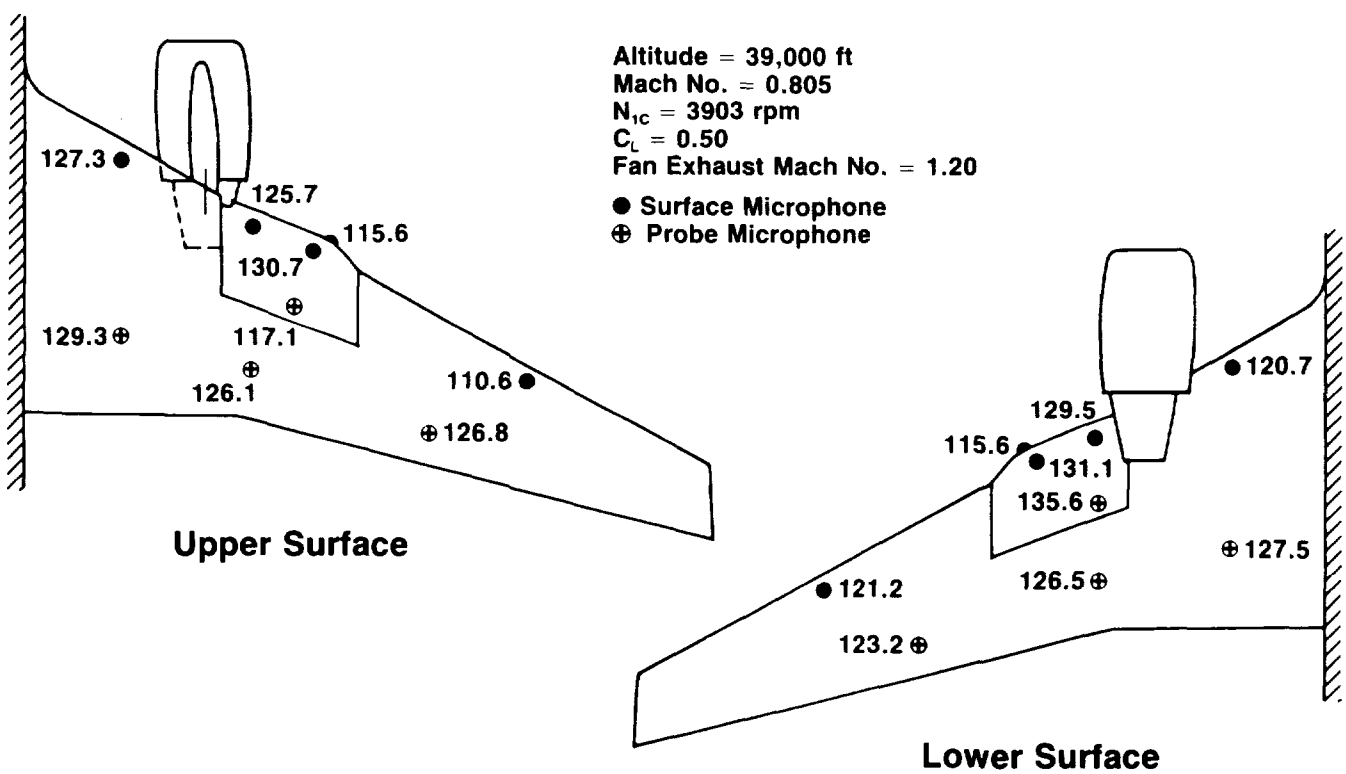

Figure 9

NORMALIZED OASPL VERSUS FAN MACH NUMBER
(Forward Surface Microphones)

Figure 10 shows the relationship of the noise overall sound pressure level (OASPL) to engine power condition (M_{FAN} = fan exhaust jet fully expanded Mach number) for one forward surface microphone on the upper surface and one on the lower surface. Curves are shown for airplane Mach numbers from $M_{AP} \simeq 0.63$ to $M_{AP} \simeq 0.82$. A clear engine power dependence, with very little airplane Mach number dependence, is seen for the lower surface microphone. This engine power dependence indicates a dominance of engine noise. The point labeled "nacelle spillage" is believed to result from turbulent airflow from the engine nacelle impinging on the wing. For this condition the engine was at idle with the airplane in a slight dive to maintain speed.

The upper surface microphone generally does not show an engine power dependence but does show an airplane Mach number dependence. Except for the "nacelle spillage" point the highest noise levels were observed for the lowest airplane speed condition. The engine noise is apparently shielded from the microphone by the wing surface. The pressure fluctuations that the microphone is responding to are probably related to turbulent flow over the microphone.

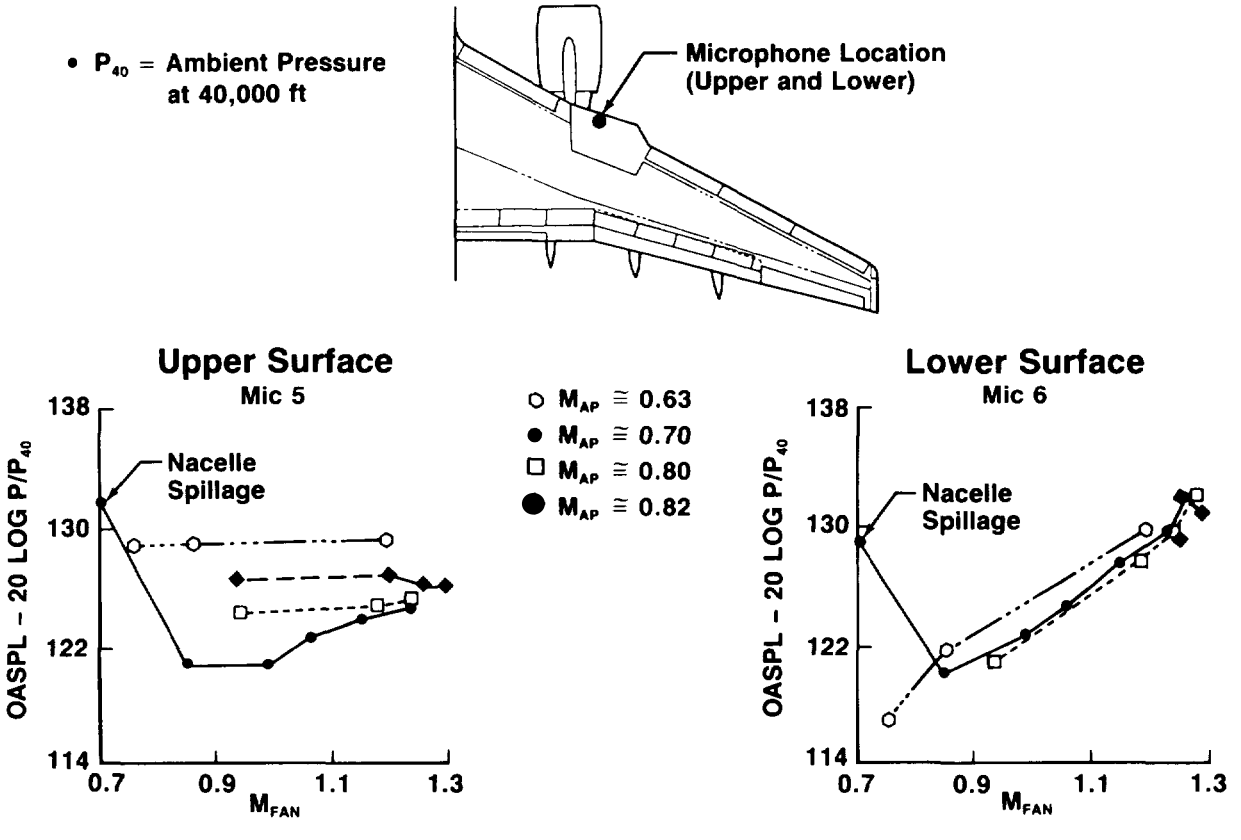

Figure 10

NOISE CHARACTERISTICS AT NLF GLOVE UPPER SURFACE LEADING EDGE MICROPHONE

For the higher Mach number conditions ($M_{AP} \approx 0.8$) the boundary layer on the upper glove surface was found to be laminar back to 20% to 30% chord. The high noise levels measured by microphone 5 therefore suggest that the microphone or microphone fairing was causing the local boundary layer to become turbulent near the microphone. The noise level initially decreases as C_L increases. The airplane mach number decreases for the higher C_Ls so that a M_{AP} dependence is possibly influencing the data to some degree. For $C_L \geq 0.62$ the noise level begins to increase with C_L. For these points the hot-film data indicated that the laminar boundary layer transition point was very close to the glove leading edge. The increased noise level is probably related to this transition. It is interesting to note that the one-third octave spectrum shape for the low Mach number/high C_L points at microphone 5 (lower left of Figure 11) is quite different from the higher Mach number cases (lower right of Figure 11). It appears that the boundary-layer transition resulted in lower frequency noise than that due to the microphone-generated turbulence.

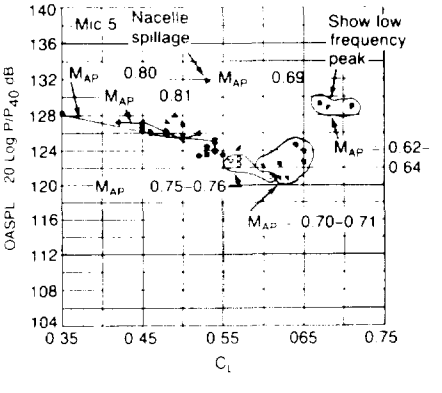

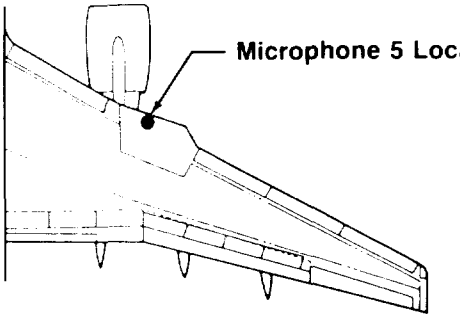

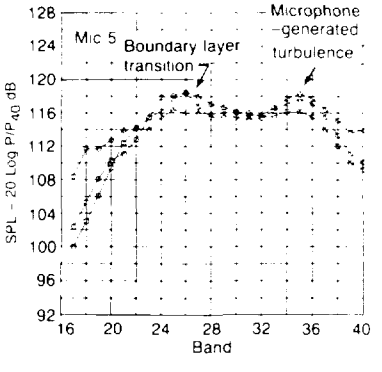

Cond		M_{AP}	M_{FAN}	C_L
221	○	0.63	0.76	0.68
220	□	0.62	0.86	0.71
219	◇	0.64	1.19	0.67

Hot Film rms Voltage - V

Cond	x/c 5%	x/c 7.5%
221	0.032	0.039
220	0.033	0.041
219	0.036	0.041

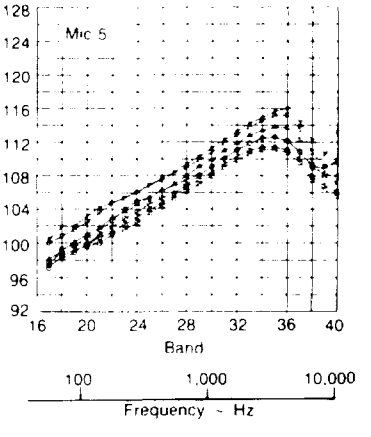

Cond		M_{AP}	M_{FAN}	C_L
236	○	0.71	0.85	0.62
237	□	0.71	0.99	0.63
218	◇	0.70	1.05	0.62
217	◇	0.71	1.06	0.60
233	△	0.70	1.06	0.65
232	▷	0.70	1.15	0.65
231	▽	0.70	1.23	0.64

Hot Film rms Voltage - V

Cond	x/c 5%	x/c 7.5%
236	0.006	0.089
237	0.005	0.087
218	0.006	0.030
217	0.010	0.034
233	0.006	0.033
232	0.006	0.034
231	0.005	0.038

Figure 11

ENGINE NOISE SPECTRA ON LOWER WING SURFACE

Figure 12 shows narrow band spectra for two microphones on the lower surface of the wing. Measurements for a range of engine power conditions at an airplane Mach number of approximately 0.8 and an altitude of approximately 40,500 ft are shown. Tones identifed as originating from the engine fan (1F, 2F, 3F and 4F—fan blade passing harmonics) and turbine (T4 and T5—fourth and fifth stage low pressure turbine blade passing frequency tones) are clearly seen. Other tones and higher frequency broadband maxima are not identifiable as engine related. The low frequency (500 Hz-1000 Hz) broadband noise peak that increases with engine power (M_{FAN}) is believed to be due to the interaction of jet exhaust turbulence and shocks.

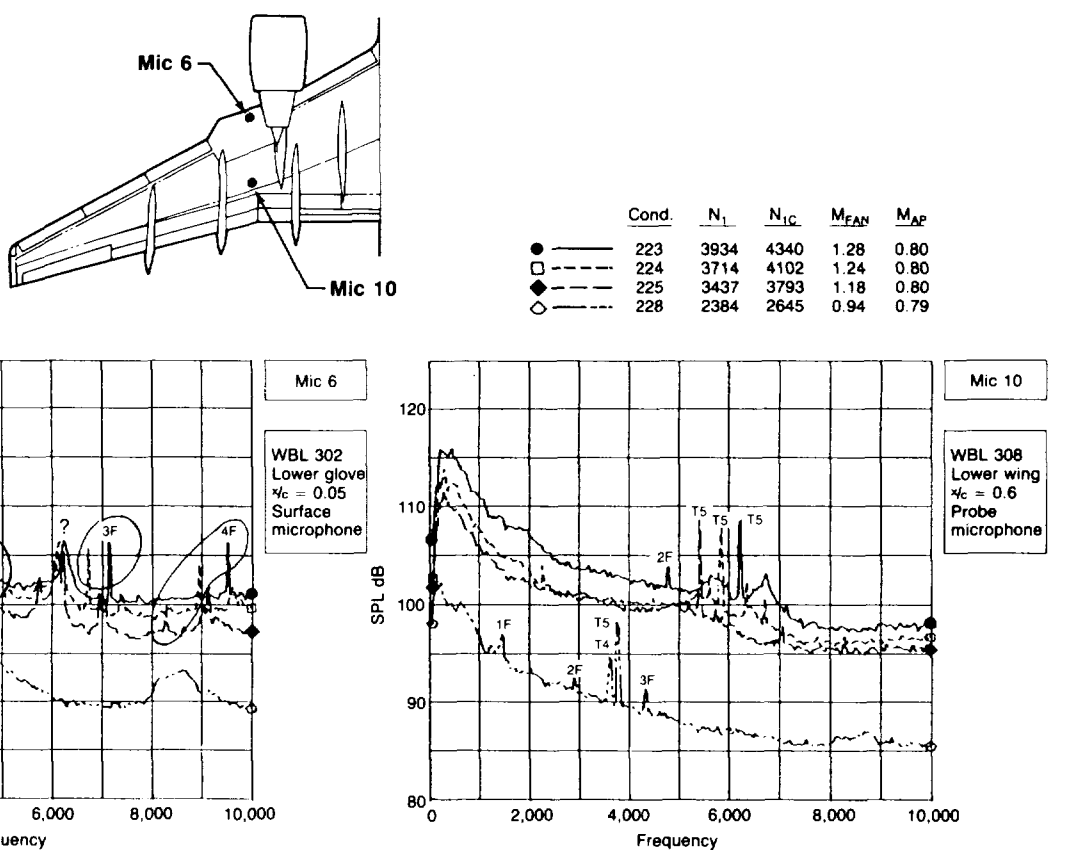

Figure 12

NORMALIZED OASPL VERSUS FAN MACH NUMBER
(Aft Probe Microphones)

The aft probe microphones indicate, as did the forward surface microphones, that there is very little engine power dependence of the noise levels on the upper surface, but a strong engine power dependence on the lower surface. Also, the upper surface data shows a strong airplane Mach number dependence, while the lower surface data shows very little airplane Mach number dependence. (Figure 13).

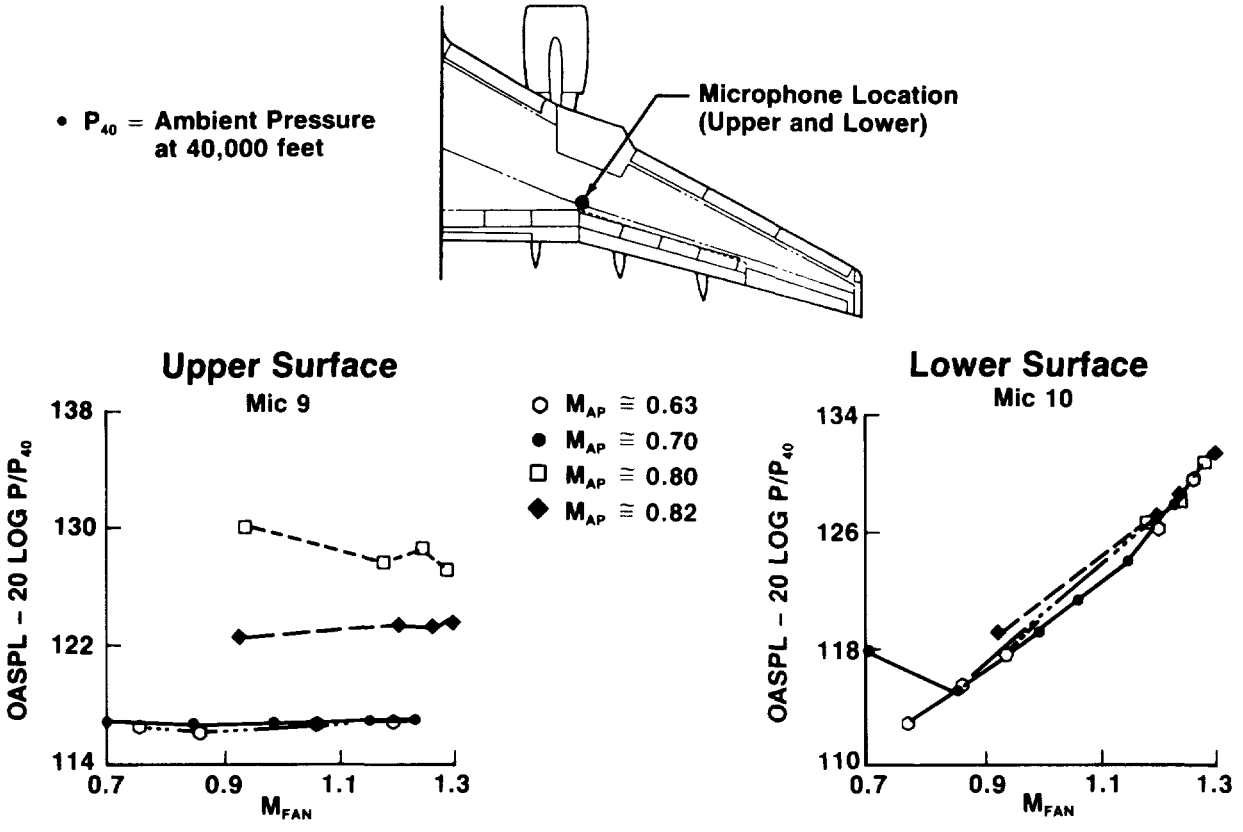

Figure 13

EFFECT OF SHOCK LOCATION ON UPPER SURFACE NOISE

The effect of the wing shock location on the upper wing microphone noise spectra measurements is shown in Figure 14. As the airplane Mach number is increased from 0.70 to 0.80, the wing shock is shown to move from just forward of microphone 7 to just forward of microphone 9. For both microphones, maximum noise levels are observed when the shock is just forward of the microphone. At microphone 7 the one-third octave spectrum peaks in a much higher frequency range than for microphone 9. This is probably related to the thinner boundary layer thickness at microphone 7. The high noise levels observed may be due to boundary layer turbulence directly or sound generated by the shock wave interacting with the turbulent boundary layer. The increased thickness of the boundary layer behind the shock may have been sufficient to cause high levels of boundary-layer pressure fluctuations at the elevated probe microphone as the shock gets closer and stronger with increasing airplane Mach number.

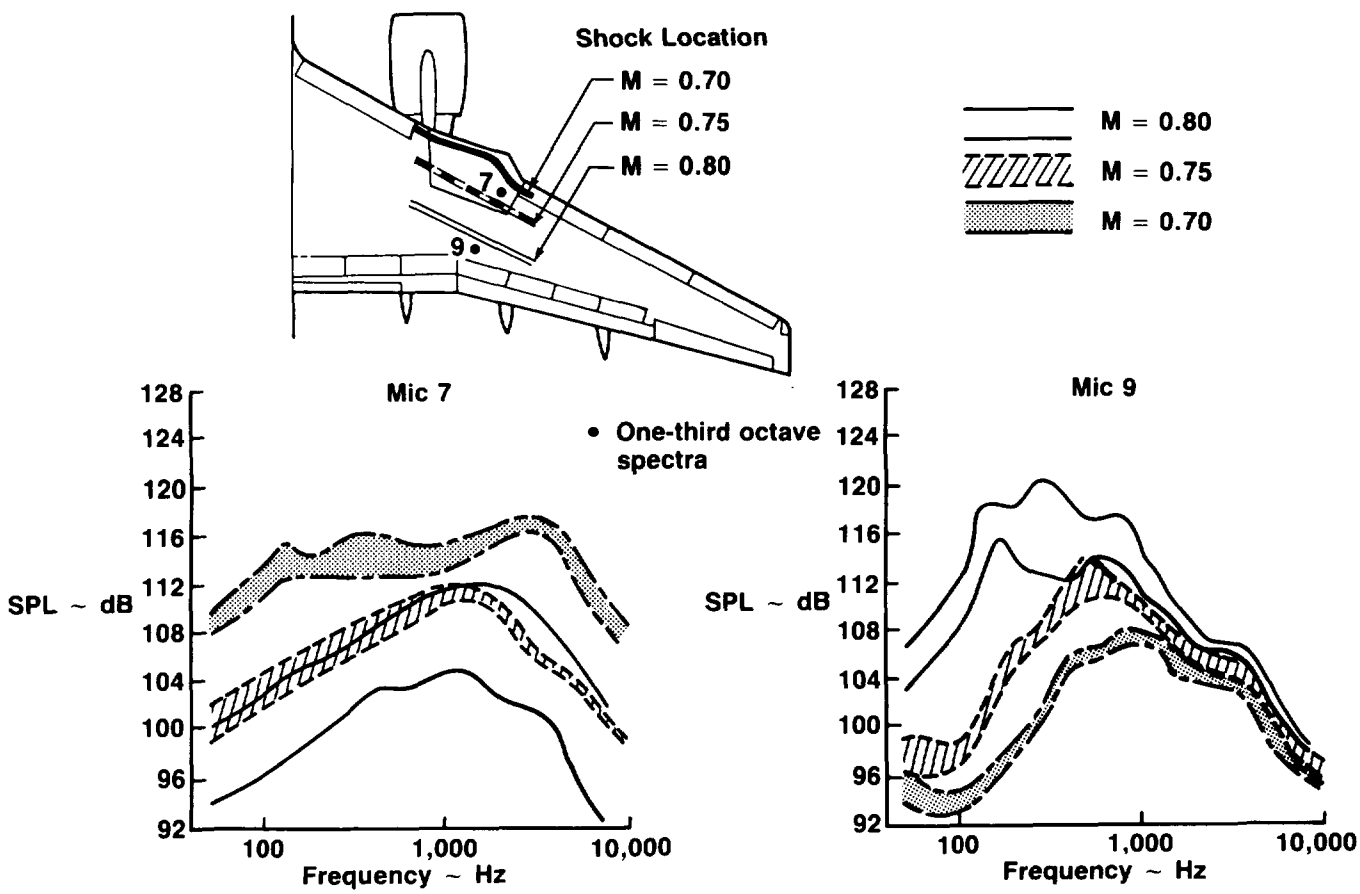

Figure 14

MICROPHONE 10 MEASURED OASPLs VERSUS LOCKHEED PROCEDURE PREDICTIONS

Predictions of the noise measured by the microphones mounted on the lower wing surface were made using near-field engine noise and airframe noise prediction methods incorporated into a computer program by the Lockheed-Georgia Company under contract to NASA. A description of these methods can be found in Reference 4. Predicted noise levels for various engine and airframe noise sources are compared to measured noise levels for microphone 10 in Figure 15. For one plot the predictions were made using the forward motion corrections incorporated into the computer program. High values for the trailing-edge airframe noise component resulted at all microphones with these forward motion corrections. The fan jet shock broadband noise component is seen to be well predicted at the microphone shown using the forward motion corrections. However, for the leading-edge microphones this component over-predicted the data by as much as 40 dB. As a result, predictions were calculated with the forward motion corrections not applied. This resulted in much lower predictions for the trailing-edge noise at all microphones. The fan jet shock broadband noise prediction increased for the aft probe microphones, as shown, and decreased for the forward microphone locations. Overall it is felt that more accurate predictions resulted without the forward motion corrections.

At the higher engine power conditions the predictions indicate that the measured noise is predominately due to the fan jet shock broadband source. The predicted dependence of the noise from this source on fan exhaust Mach number as well as airplane Mach number is consistent with the measurements. For fan exhaust mach numbers less than one, the fan jet shock noise source no longer contributes to the engine noise. The predictions shown indicate a dominance of turbine noise for these conditions, but narrowband data indicates lower frequency broadband noise to be dominant. The prediction method would not give jet mixing predictions for microphones close to the engine but predicted jet mixing results at the other microphones led to the conclusion that jet mixing noise was not an important source. The source of the broadband noise floor at lower engine power settings was not identified.

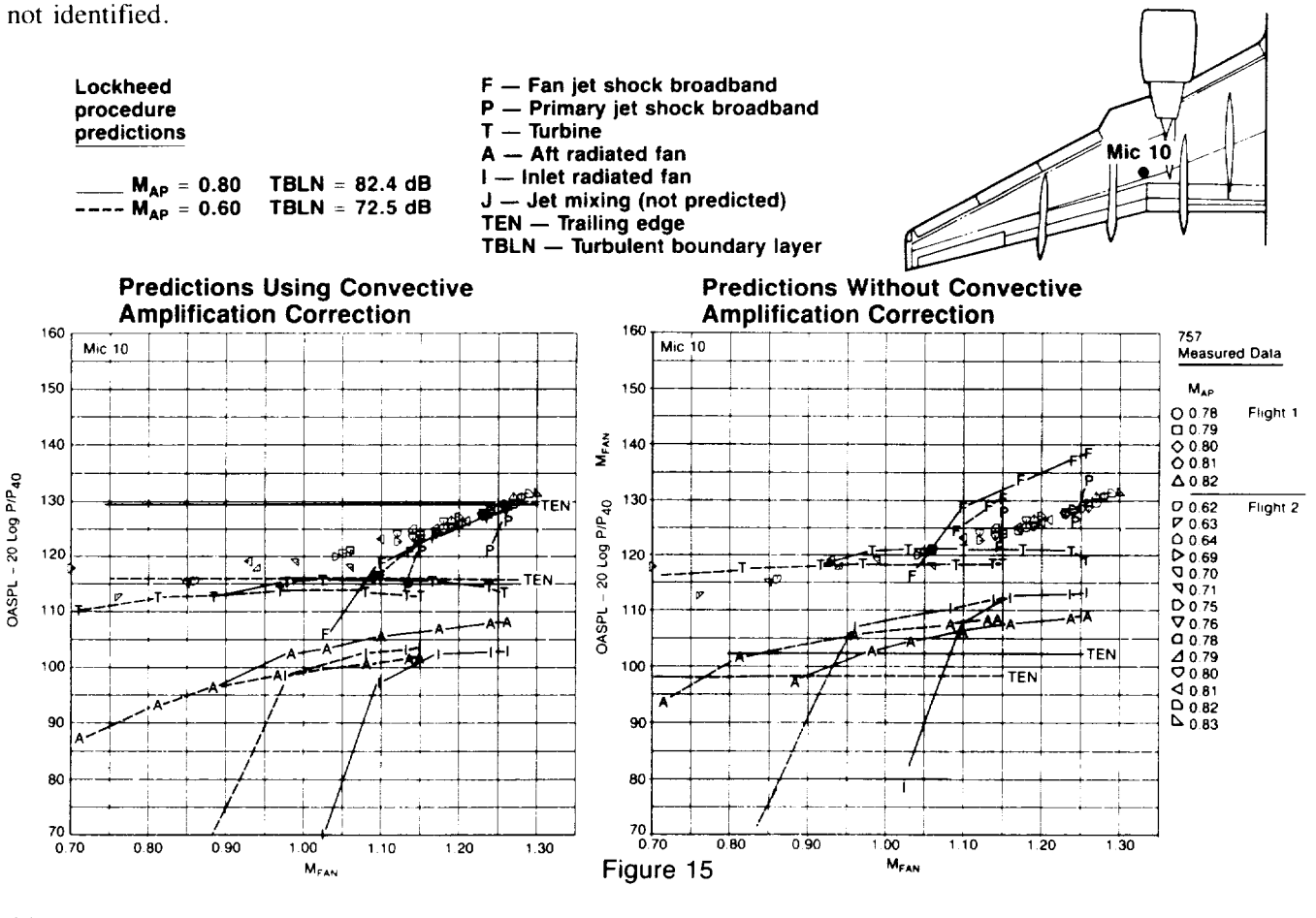

Figure 15

MEASURED EXTENT OF LAMINAR FLOW

The glove design condition was chosen so that a significant extent of laminar flow could be obtained on the upper and lower surface simultaneously. Figure 16 shows that at this condition the upper surface had about 28% chord laminar flow (4.7 ft) in the inboard portion of the test area, while the lower surface had about 18% chord laminar flow (3.0 ft). The decreased extent of laminar flow on the outboard portion of the upper surface was due to a peak in the pressure distribution in that area at about 5% chord. This peak was not predicted by the transonic analysis program used to design the glove. This was probably due to the difficulty of modeling the rapid planform changes occurring at the outboard edge of the glove.

The maximum extent of laminar flow on the upper surface (29% chord) occurred at a high Mach number condition. The extent of laminar flow was only slightly more than at the design condition. The maximum extent of laminar flow on the lower surface (27% chord) occurred at a low Mach, high C_L, high sideslip condition. The high sideslip resulted in an effective sweep reduction that was beneficial in reducing cross-flow instability on the lower surface. High sideslip was less beneficial on the upper surface because it increased the peakedness of the pressure distribution.

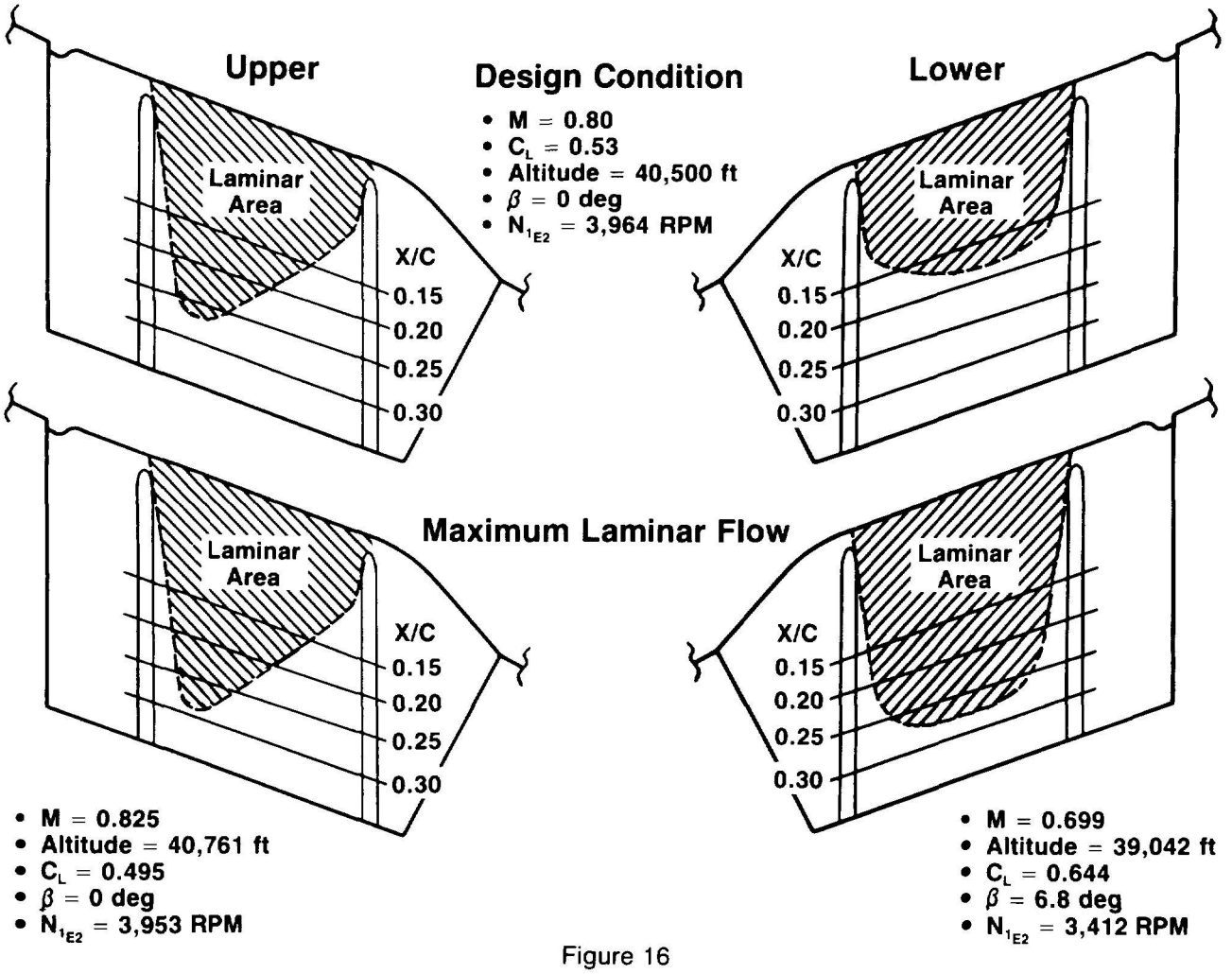

Figure 16

EFFECT OF LIFT COEFFICIENT AND MACH NUMBER ON EXTENT OF LAMINAR FLOW

As shown in Figure 17, at the design Mach number of 0.8, both the upper surface and the lower surface performed best at high lift coefficients. The decrease in extent of laminar flow at low lift coefficients was probably due to increased cross-flow instability resulting from the decreased flow acceleration near the leading edge at the low lift coefficients. Also, the lower lift coefficients corresponded to lower altitudes and, therefore, higher Reynolds number.

The upper surface extent of laminar flow exhibited a strong Mach number dependency. The greatest extent of laminar flow occurred at the highest Mach number. As the Mach number decreased, a forward pressure peak developed along the entire span of the glove that moved the transition location forward. On the lower surface the greatest extent of laminar flow was obtained at Mach numbers between 0.75 and 0.78. The Mach number dependency on the lower surface was not as strong as on the upper surface.

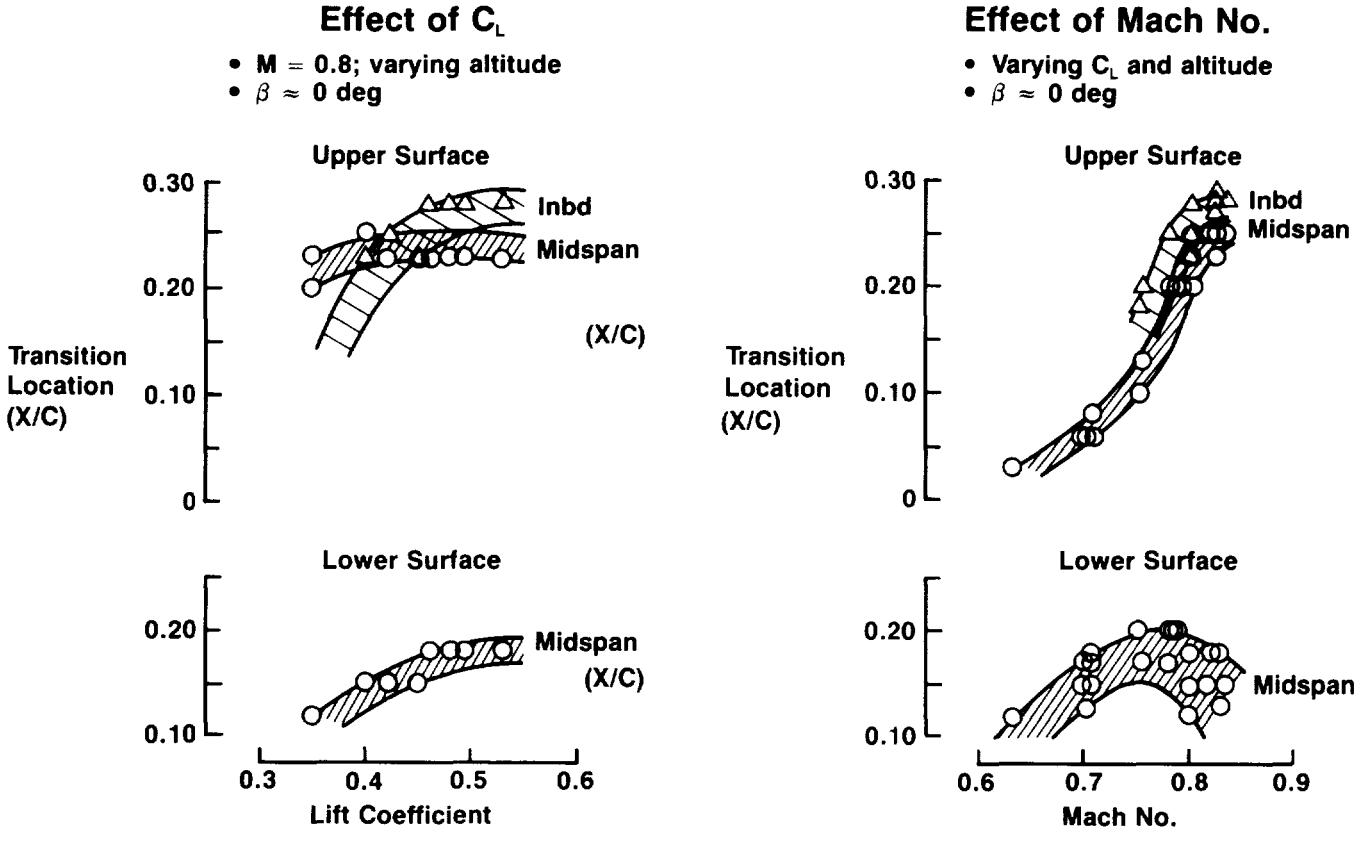

Figure 17

EFFECT OF ENGINE POWER SETTING ON EXTENT OF LAMINAR FLOW

One of the primary objectives of the flight program was to determine the influence of engine noise on transition. As discussed previously, the noise measurements indicated that aerodynamic noise is dominant on the upper surface of the wing. Therefore, it is not surprising that there does not appear to be a clear correlation between the measured upper surface transition location at a given flight condition and the engine power setting, as shown in Figure 18. The M = 0.70, C_L = 0.64 case does show a small forward shift in the transition location at the high power settings. However, as discussed earlier, there does not appear to be any noticeable change in engine noise on the upper surface at this Mach number with changes in engine power setting. Therefore, the small change in extent of laminar flow (the hot film at 7.5% chord went from turbulent to transitional) at this condition may have actually been due to small differences in lift coefficient between the low and high power settings.

The lower surface noise measurements, discussed previously, showed that engine noise is dominant at all flight conditions. As shown in Figure 18, the lower surface transition location does show a greater sensitivity to the engine power setting than was the case for the upper surface. At most flight conditions, there was 2% to 3% less laminar flow at the high power settings than at the low power settings.

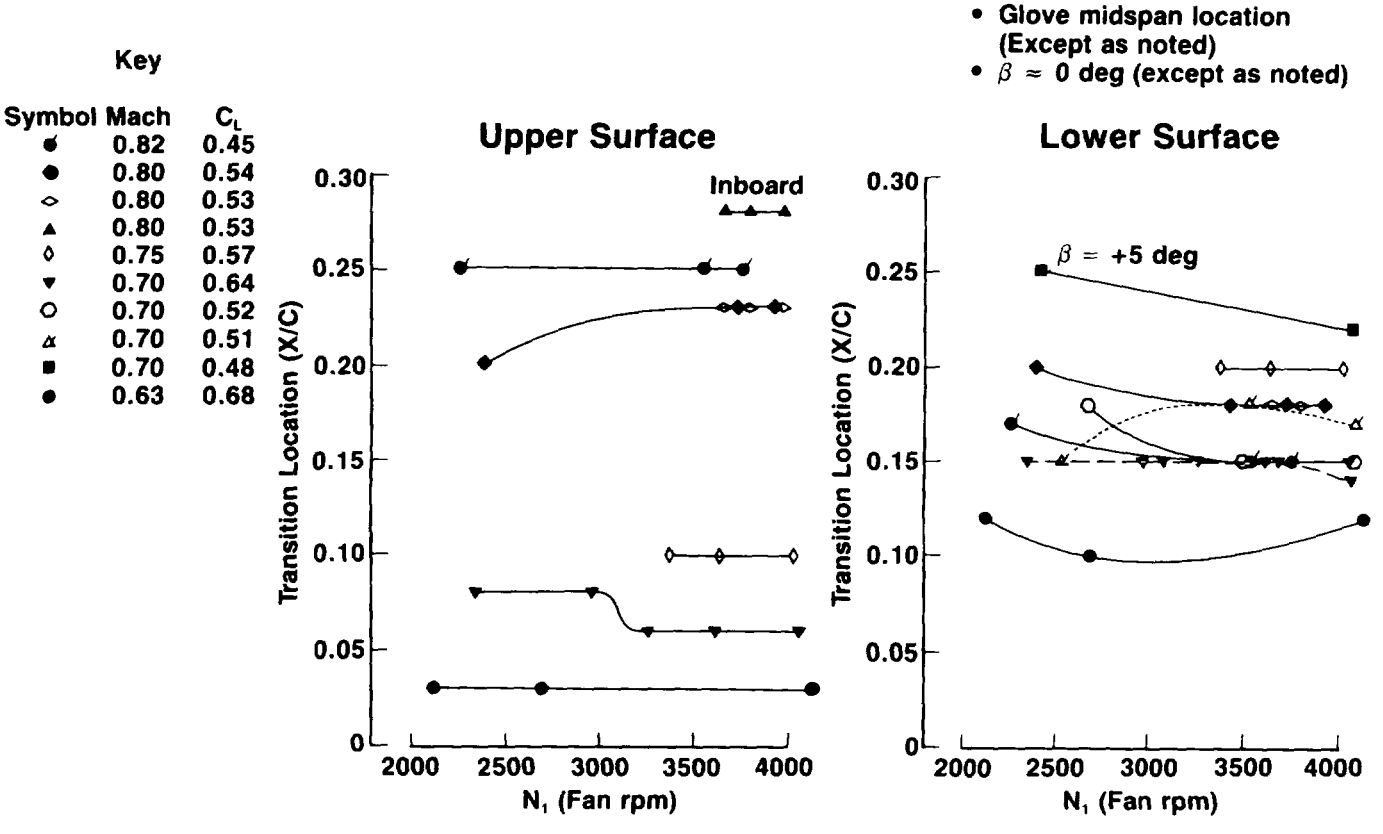

Figure 18

BOUNDARY-LAYER STABILITY ANALYSIS INPUT DATA

The 757 NLF glove provides a new source for empirical calibration of boundary-layer transition methods. Transition prediction methods based on linear boundary layer stability theory are currently the most widely used. Therefore, linear boundary-layer stability analysis was applied to twenty-one 757 flight data cases. The first step in the analysis of a given case was to generate the boundary-layer data, which consist of the velocity and temperature profiles. Figure 19 shows a typical set of flight data from which input data to the boundary-layer code (which was a Boeing infinite yawed wing compressible boundary-layer program) was generated. This flight data consisted of: 1) the isobar pattern, based on measured pressures at the inboard and outboard locations of the glove, together with guidance from the isobars predicted by the transonic analysis code; 2) the transition location, based on the hot film data; and 3) the pressure distribution at the chosen spanwise analysis station, interpolated from the measured inboard and outboard pressures in conjunction with the isobar pattern. For most cases, WBL 308.5 was the chosen analysis station. For the upper surface, this was usually the location of greatest laminar flow extent. It also was close to the inboard pressure measurement station, which minimized interpolation uncertainties.

The sample isobars shown in Figure 19 are typical of many of the upper surface cases analyzed. It can be seen that the isobar sweep in the leading edge region is much lower than that aft of 10% chord. Because of this, two separate infinite yawed wing analyses were made, each with a sweep angle representative of one of the two regions. The two solutions were then "patched" together in the vicinity of 10% chord.

- **Infinite Yawed Wing Boundary–Layer Analysis**
- **Upper Surface; WBL 308.5**
- **Flight 3, Condition 16 (Outbd Cp)**
- **Flight 2, Condition 233 (Inbd Cp)**
- **M∞ = 0.804, Alt = 40,483 ft**
- **Re_c = 25.5 x 10^6**

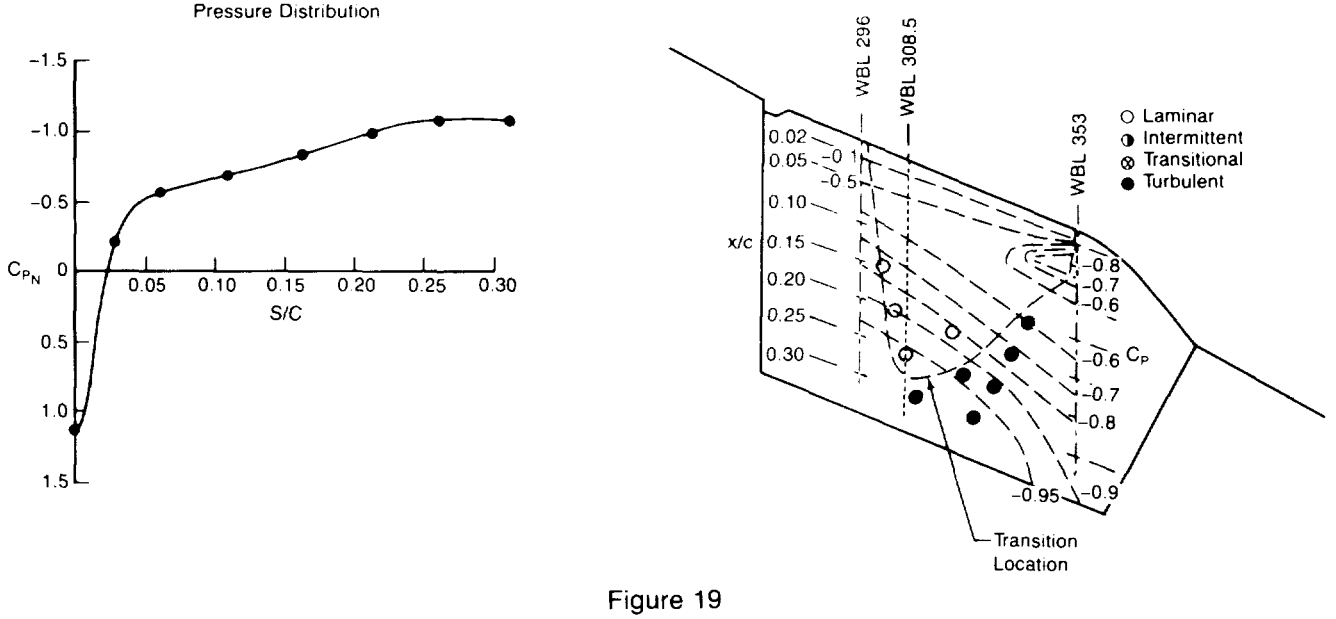

Figure 19

BOUNDARY LAYER STABILITY RESULTS

The calculated velocity and temperature profiles served as input data to the Boeing stability code (a modified version of the Mack code). This program solves the boundary-layer stability equations for three-dimensional, linearized, parallel flow in the spatial mode. For each flight condition both Tollmien-Schlichting (T-S) and cross flow (C-F) instabilities were analyzed. T-S amplification factors (NTS) were determined by keeping wave angle and frequency fixed. For crossflow amplification factors (NCF) the frequency was kept fixed at zero and the wave angle varied in accordance with the irrotationality condition (Ref. 5) for a fixed spanwise wave number component. A range of wave numbers was then analyzed to obtain the envelope of C-F disturbances. Sample results for these disturbance growths are shown in Figure 20. These results were then used to plot a trajectory curve on the NTS versus NCF plane, as shown.

The desired result is the N-factor combination at the measured transition location, indicated by the band near the end of the trajectory curve, the ends of which represent the location of the last laminar and first turbulent hot films. The figure also includes the F-111 transition data band, calculated in a previous study by applying the same method to flight data obtained by NASA on an NLF glove on the F-111 airplane (Ref. 6). This F-111 data band is the transition criterion that has been used at Boeing for the last several years.

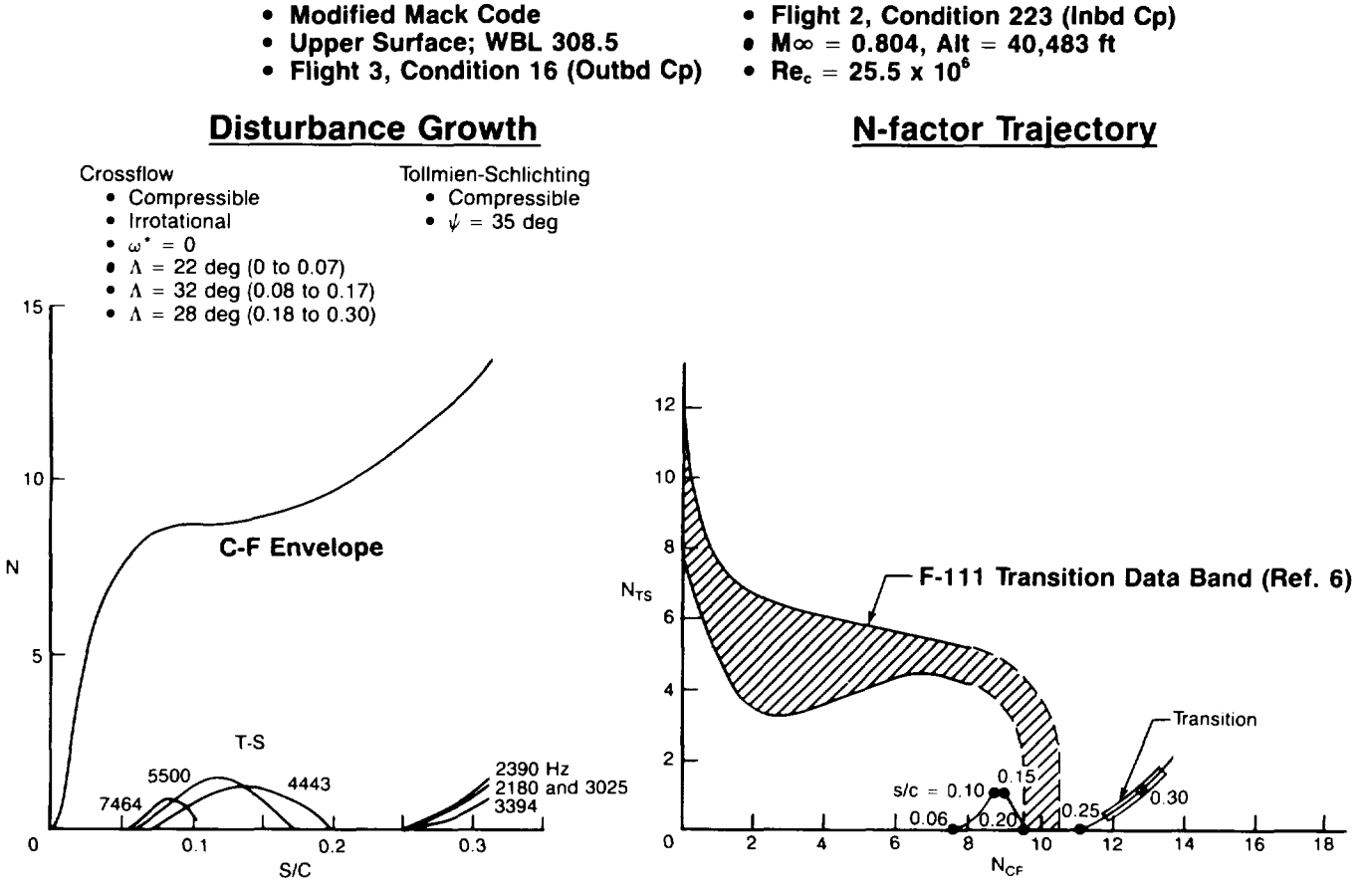

Figure 20

TOLLMIEN-SCHLICHTING TRANSITION N-FACTOR VERSUS CROSS-FLOW TRANSITION N-FACTOR

From the accumulated flight test data, a total of twenty-one cases were analyzed by the stability code. The final results, showing the values of NCF and NTS at transition (based on the middle of the transition uncertainty band), were all combined on a single plot, shown in Figure 21. Also included are the points from the previous F-111 calculations, which tend to fall in a different region of the diagram. The F-111 results had not provided any guidance in the low NTS, high NCF region of the diagram. Since this is where the bulk of the 757 data falls, the two sets of data complement each other. In the region of overlap between the two sets of data, there is fairly good agreement between the results. A band enclosing all of the F-111 data points and most of the 757 points provides a new transition criterion. Two of the 757 points below the band were not included because the degree of uncertainty in the measured pressures was higher for these cases than for the other cases. The 757 point above the band was not included simply because it lies outside of the region where the rest of the data lies. Excluding it tends to make the band more conservative.

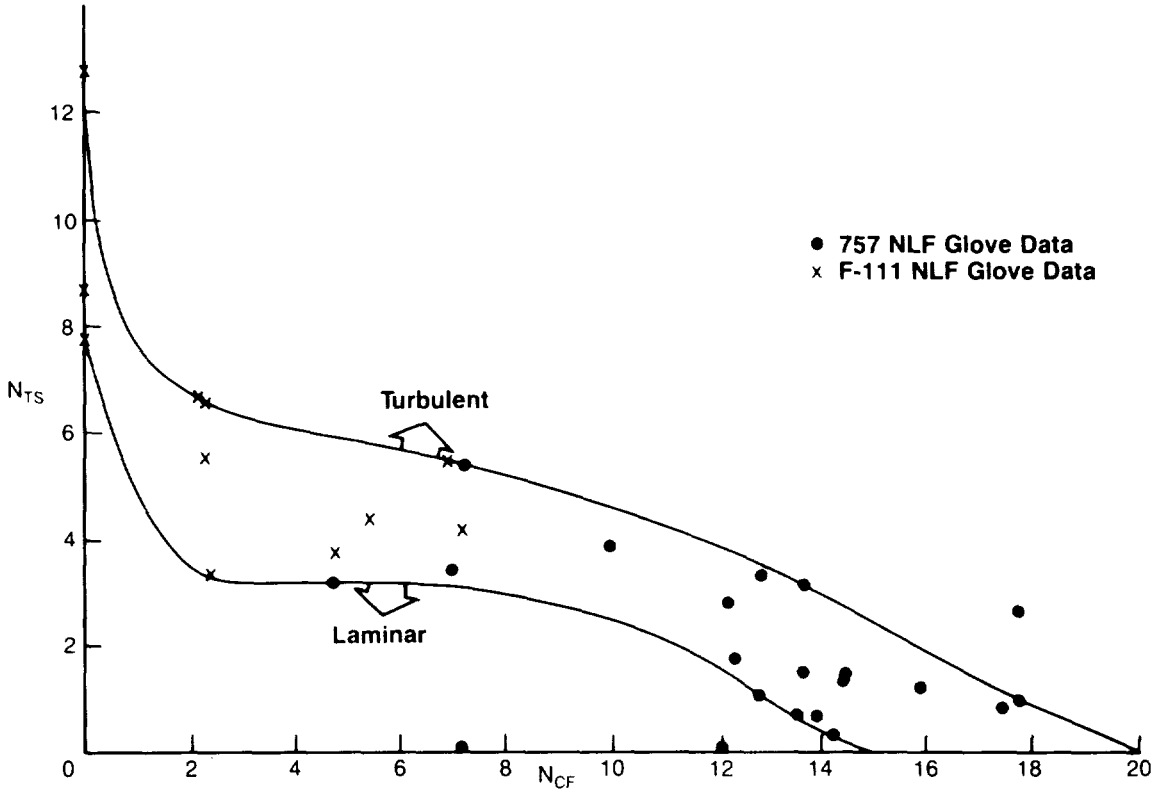

Figure 21

SUMMARY OF RESULTS

As a result of the 757 wing noise survey and NLF glove flight test, there now exists a large data base of near-field inflight noise measurements on the wing of a commercial transport with wing-mounted high-bypass-ratio engines. The data is for a wide range of airplane Mach numbers and altitudes and engine power settings. The data shows that aerodynamic noise is the dominant noise source on the upper surface and engine noise is the dominant noise source on the lower surface. At cruise, (M = 0.8, 39,000 ft) the upper surface OASPLs are 115 dB to 130 dB and the lower surface OASPLs are 120 to 140 dB.

The transition and noise measurements on the NLF glove show that there is no apparent effect of engine noise on the upper surface transition location. On the lower surface, the transition location moved forward 2% to 3% chord at most conditions from the engine's low-power setting to the high-power settings. Since the effect of noise on the extent of laminar flow is dependent upon the particular wing design, the lower surface noise effect may be larger for other wing designs.

A boundary layer stability analysis of 21 of the 757 flight data cases showed that cross-flow disturbances were the dominant cause of transition at most flight conditions. The results of this analysis provide additional calibration data for linear stability-based transition prediction methods. (Figure 22).

- **Wing noise environment**
  - **First large data base of near-field inflight noise measurements**
  - **On upper surface**
    - **Aerodynamic noise is the dominant source**
    - **OASPLs at cruise are 115 dB to 130 dB**
  - **On lower surface**
    - **Engine noise is the dominant source**
    - **OASPLs at cruise are 120 dB to 140 dB**
- **Effect of engine noise on transition location**
  - **No effect on upper surface**
  - **Small effect on lower surface (2% to 3% chord)**
  - **Lower surface effect may be larger for other wing designs**
- **Boundary layer stability analysis**
  - **Cross-flow disturbances were dominant cause of transition at most flight conditions**
  - **Analysis of 21 757 flight cases provides additional calibration data for transition prediction**

Figure 22

REFERENCES

1. "Boeing Commercial Airplane Company: Flight Survey of the 757 Wing Noise Field and Its Effects on Laminar Boundary Layer Transition," Volume I—Program Description and Data Analysis, NASA CR 178216, March 1987.

2. "Boeing Commercial Airplane Company: Flight Survey of the 757 Wing Noise Field and Its Effects on Laminar Boundary Layer Transition," Volume II—Data Compilation, NASA CR 178217, March 1987.

3. Smith, F. and Higton, D. J., "Flight Test on King Cobra, FZ.440 To Investigate the Practical Requirements for the Achievement of Low Profile Drag Coefficients on a Low Drag Airfoil," R&M No. 2375, H.M.S.O., London, 1950.

4. Tibbets, J. G., "Near Field Noise Prediction for Aircraft in Cruising Flight—Methods Manual," NASA CR 159105, August 1979.

5. Mack, L. M., "On the Stability of the Boundary Layer on a Transonic Swept Wing," AIAA Paper No. 79-0264, 1979.

6. Runyan, L. J., Navran, B. H., and Rozendaal, R. A., F-111 Natural Laminar Flow Glove Flight Test Data Analysis and Boundary Layer Stability Analysis," NASA CR-166051, January 1984.

N90-12547

F-14 VSTFE AND RESULTS OF THE CLEANUP FLIGHT TEST PROGRAM

Robert R. Meyer and Bianca M. Trujillo
NASA Ames Research Center
Dryden Flight Research Facility
Edwards, California

Dennis W. Bartlett
NASA Langley Research Center
Hampton, Virginia

[redacted]

VARIABLE-SWEEP TRANSITION FLIGHT EXPERIMENT

Flight transition data applicable to swept wings at high subsonic speeds are needed to make valid assessments of the potential for natural laminar flow or laminar-flow control for transports of various sizes at various cruise speeds. NASA initiated the variable-sweep transition flight experiment (VSTFE) to help establish a boundary-layer transition data base for use in laminar-flow wing design. The carrier vehicle for this experiment is an F-14 aircraft, which has variable-sweep capability. The variable-sweep outer panels of the F-14 aircraft are being modified with natural laminar-flow gloves to provide not only smooth surfaces but also airfoils that can produce a wide range of pressure distributions for which transition location can be determined at various flight conditions and sweep angles. As indicated in figure 1, the current plan is to fly two gloves in the program: glove I, which is a cleanup or smoothing of the basic F-14 wing, and glove II, which has been designed to provide specific pressure distributions at Mach 0.7 (ref. 1). A glove III was also designed for Mach 0.8 (ref. 2) but will probably not be flown (NASA expects to lose custody of the F-14 aircraft before glove III can be flown). The majority of the glove I flight tests have been completed, and glove II flight tests are planned for spring and summer of 1987. This paper briefly describes the VSTFE program and presents some preliminary glove I flight results.

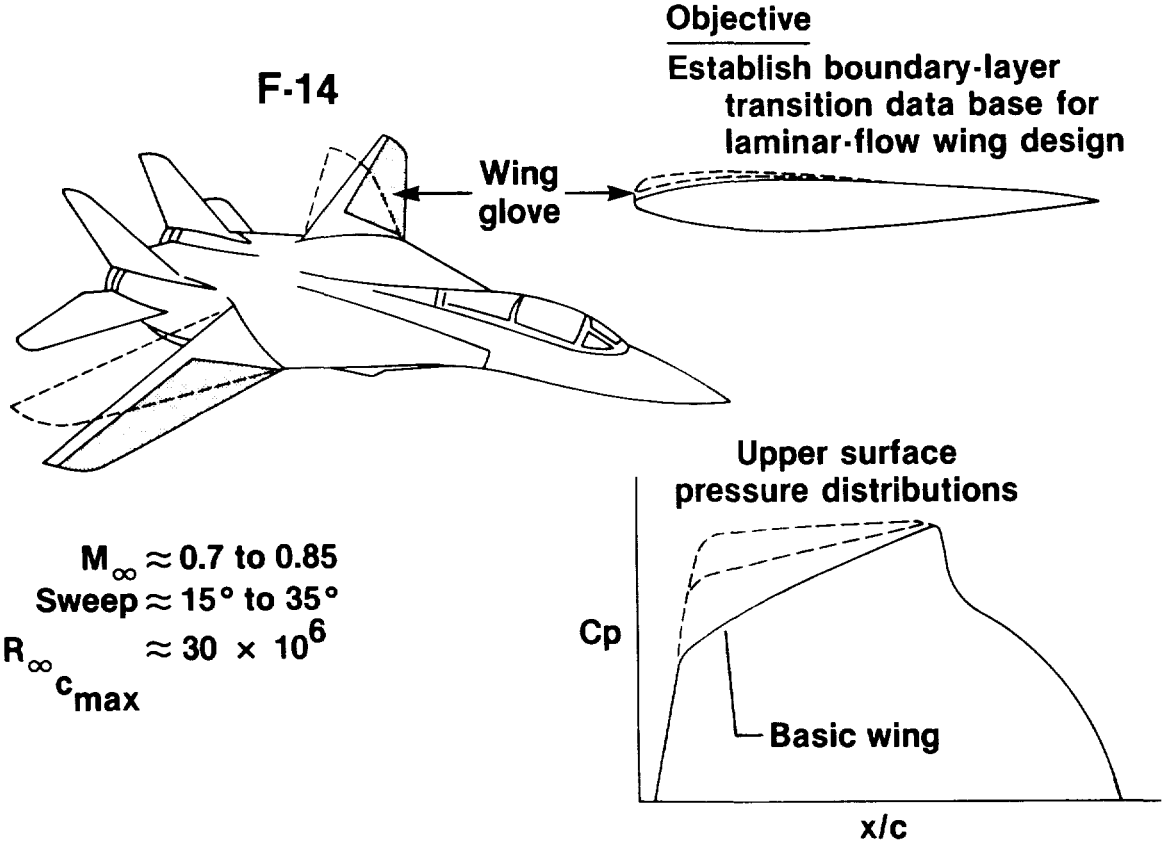

Figure 1

F-111/TACT NLF GLOVE

The catalyst for the present VSTFE program was the encouraging results from an earlier NASA flight test program, the F-111/TACT natural laminar flow (NLF) experiment (refs. 3 and 4). The NLF flight test program provided the first definitive flight results on the effects of wing sweep on boundary-layer transition. A complete supercritical NLF airfoil was "gloved" around the right wing panel of the F-111/TACT aircraft (fig. 2). This glove, made of foam and fiberglass, had a span of approximately 6 ft and a chord of 10 ft. Although the glove was designed for a 10° sweep, data were obtained at sweep angles as high as 26°. At sweep angles near 10°, transition occurred at about 55-percent chord (transition Reynolds numbers of about 15×10^6), but for a 26° sweep, transition occurred in the 10- to 20-percent chord range. In addition to providing transition data, this program helped develop the construction techniques for making large contour modifications to metal wings from foam and fiberglass (ref. 5).

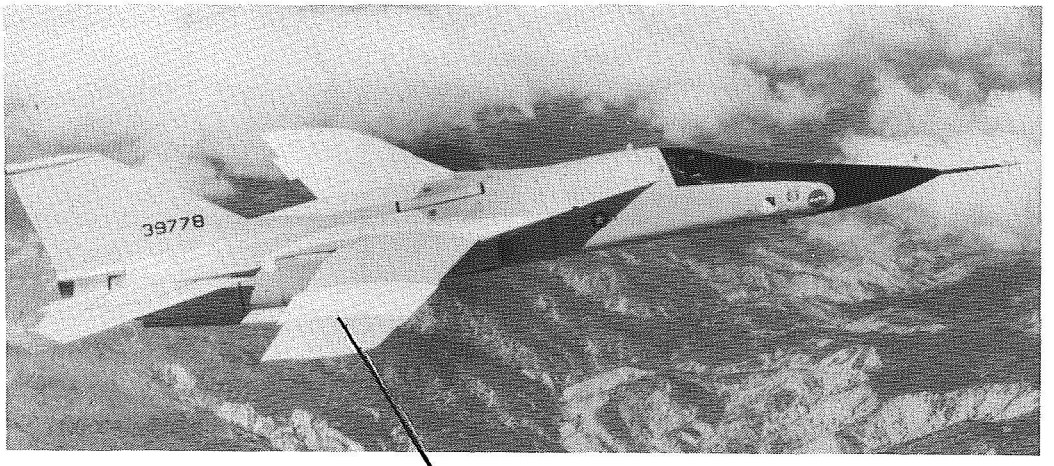

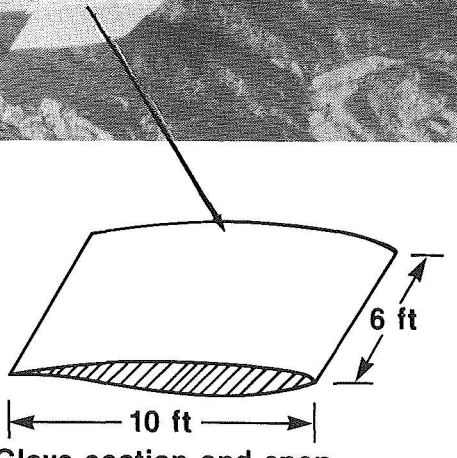

Glove section and span

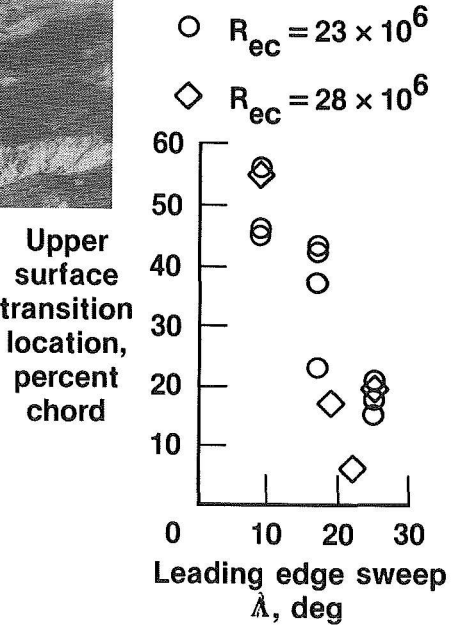

Figure 2

F-111/TACT NLF ENHANCEMENT OF BOUNDARY-LAYER STABILITY PREDICTION METHODS

In the past, semiempirical transition prediction methods have been enhanced by correlating boundary-layer stability theory with experimentally obtained transition data from the F-111/TACT NLF flight test program (refs. 3 and 6). The computational approaches generally utilize linear noninteracting boundary-layer stability analysis conducted for the Tollmien-Schlichting (T-S) and cross-flow (C-F) disturbances. The natural log of the most amplified disturbance growth, or N factor, of each type is then correlated to empirically derived limits to assess the likelihood of transition.

In one approach, (refs. 3, 6, and 7), analytically derived T-S N factors and C-F N factors for stationary disturbances are correlated with experimentally derived transiton locations obtained from F-111/TACT NLF results. The resultant S-shaped (cross-hatched) region in figure 3 indicates the combined T-S and C-F N-factor values for which transition is determined to occur. Consequently, this method predicts that transition will occur when any combination of T-S and C-F N factors reaches the values defined by the S-shaped region in figure 3.

Prior to the F-111/TACT NLF flight experiment, it was suggested (ref. 8) that a linear coupling existed between T-S and C-F disturbances. The relationship between the linear coupling and the S-shaped F-111/TACT NLF criteria indicates that the adverse effect of wing sweep is not as severe at higher sweep angles as had been originally assumed.

Another approach (ref. 9) also uses linear noninteracting boundary-layer stability theory. However, the calculations are conducted for stationary and nonstationary C-F and T-S disturbances, and transition is presumed to occur when growth of either disturbance has reached a certain N factor. Some previous correlations (refs. 10 and 11) with experimental data indicate that the value of N at transition should be in the range of 9 to 12 if all variables are taken into account.

The F-111/TACT NLF experiment was originally designed for a leading-edge sweep of 10°. The data were obtained for only one airfoil shape, and data defining the lower right-hand portion of the S-shaped curve were limited. More follow-on variable-sweep experimental data were needed for different airfoil shapes. Unfortunately, the F-111 aircraft used for the previous experiment was committed to another program and was unavailable for laminar-flow experiments. Consequently, another variable-sweep aircraft was sought.

Figure 3

F-111/TACT NLF ENHANCEMENT OF BOUNDARY-LAYER STABILITY PREDICTION METHODS

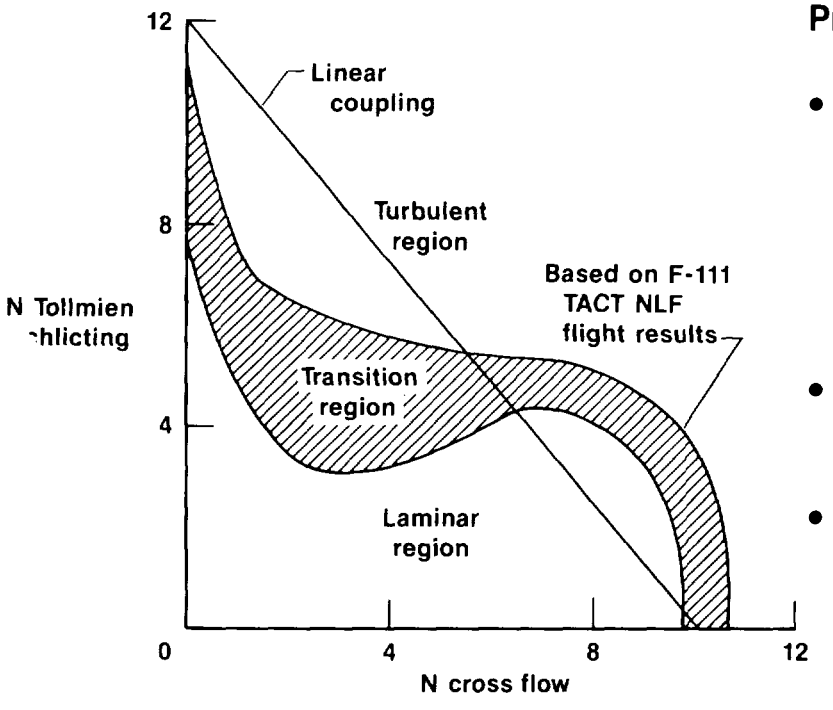

Problem

- F-111/TACT NLF originally designed for 10° leading-edge sweep but most data obtained at 20° and 25° leading-edge sweep
- Data on lower portion of curve limited
- Different airfoil shapes needed to be evaluated

F-14 VSTFE AIRCRAFT DESCRIPTION

An F-14 aircraft was chosen as the carrier vehicle for the VSTFE program, primarily because of its variable-sweep capability, Mach and Reynolds number capability, availability, and favorable wing pressure distribution (ref. 12). A laminar-flow glove (glove I) was installed on the upper surface of the left wing panel (fig. 4). The standard radome on the aircraft was replaced with a flight test radome that incorporated a flight-test-quality pitot-static probe equipped with alpha and beta vanes (ref. 13). The cockpit of the aircraft was equipped with a special display that allowed for trajectory guidance signals to be uplinked and displayed to the pilot in real time (ref. 14). With the laminar-flow glove installed, the wing sweep capability was restricted to a range of 20° to 35° leading-edge sweep, and the flaps and slats were locked in an up position. The basic aircraft glove vanes were disabled for these flight tests. A 15° leading-edge sweep was simulated by sideslipping the aircraft 5° at 20° sweep, resulting in an equivalent sweep of 15°.

F-14A provides

- **Variable sweep**
- **Mach/Reynolds number envelope**
- **Favorable wing pressure distribution**

"Cleanup" glove (Glove I) installed on left wing upper surface leading edge

Sweep range

- **20° to 35°**
- **Simulate 15° with $\beta = 5°$**

Slats and flaps locked in up position

Figure 4

GLOVE I CONSTRUCTION

Glove I was installed to provide an equivalent "sailplane finish" on the existing F-14 wing. It was determined that the extra thickness of the glove would have only a minor influence on the pressure distribution shape or thickness/chord ratio. The glove wraps around the wing leading edge (disabling leading-edge slats), extends aft to just forward of the spoiler hinge line (approximately 60-percent chord), and covers most of the span (fig. 5). The glove was constructed by applying a constant-thickness foam and fiberglass surface over the existing wing skin (a method similar to that described in ref. 5). The glove was approximately 0.65 in thick, initially consisting of one layer of fiberglass, 0.5 in of polyurethane foam, six layers of fiberglass, and a finish of polyester body filler and paint. During the flight envelope verification flights, small surface cracks developed in the glove. These cracks probably resulted from lateral stick rap maneuvers performed for structural excitation during the flutter clearance phase of the flight test. To repair these cracks, one additional layer of fiberglass was applied over the surface of the glove. The final glove incorporated this one additional layer of fiberglass and a finish of polyester body filler and paint.

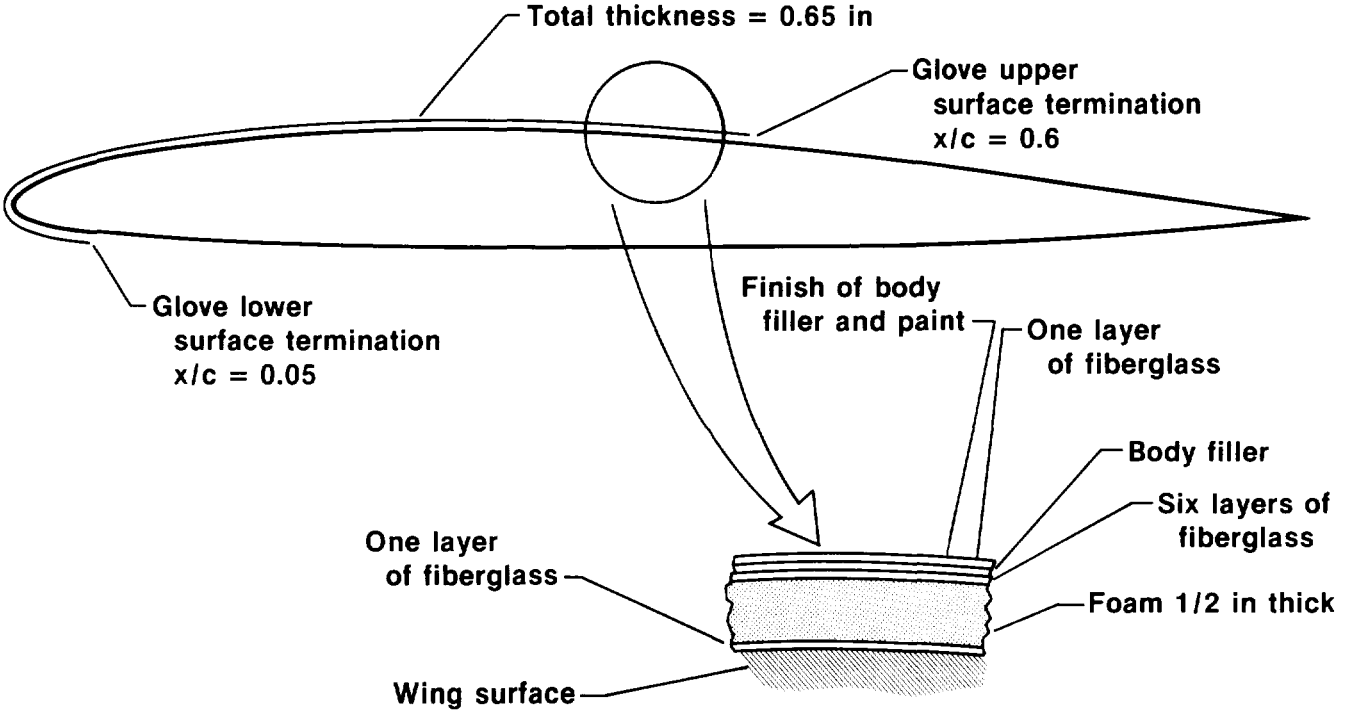

Figure 5

GLOVE I WAVINESS MEASUREMENTS

Figure 6 presents surface curvature measurements for three wing stations on glove I. These measurements were taken with the wing unloaded (zero load) and with the wing jacked from the lower surface to simulate a 1-g loaded condition, which was the condition for most of the flight tests. The measurements were obtained with a mechanical deflection dial gauge having support feet 2-in apart. The dial gauge was equipped with a wheel from which the distance along the glove surface could be determined. The outputs from both the dial gauge and the wheel were automatically plotted when the unit was manually moved across the surface. Because of the long chord lengths involved, two people were required to make the measurements; this resulted in an apparent roughness at the gauge "handoff" locations. In general, the glove is not as smooth in the simulated 1-g loaded condition as in the unloaded condition; however, even for this case, the wave amplitudes are within 0.002 in/in, the criterion specified for glove construction.

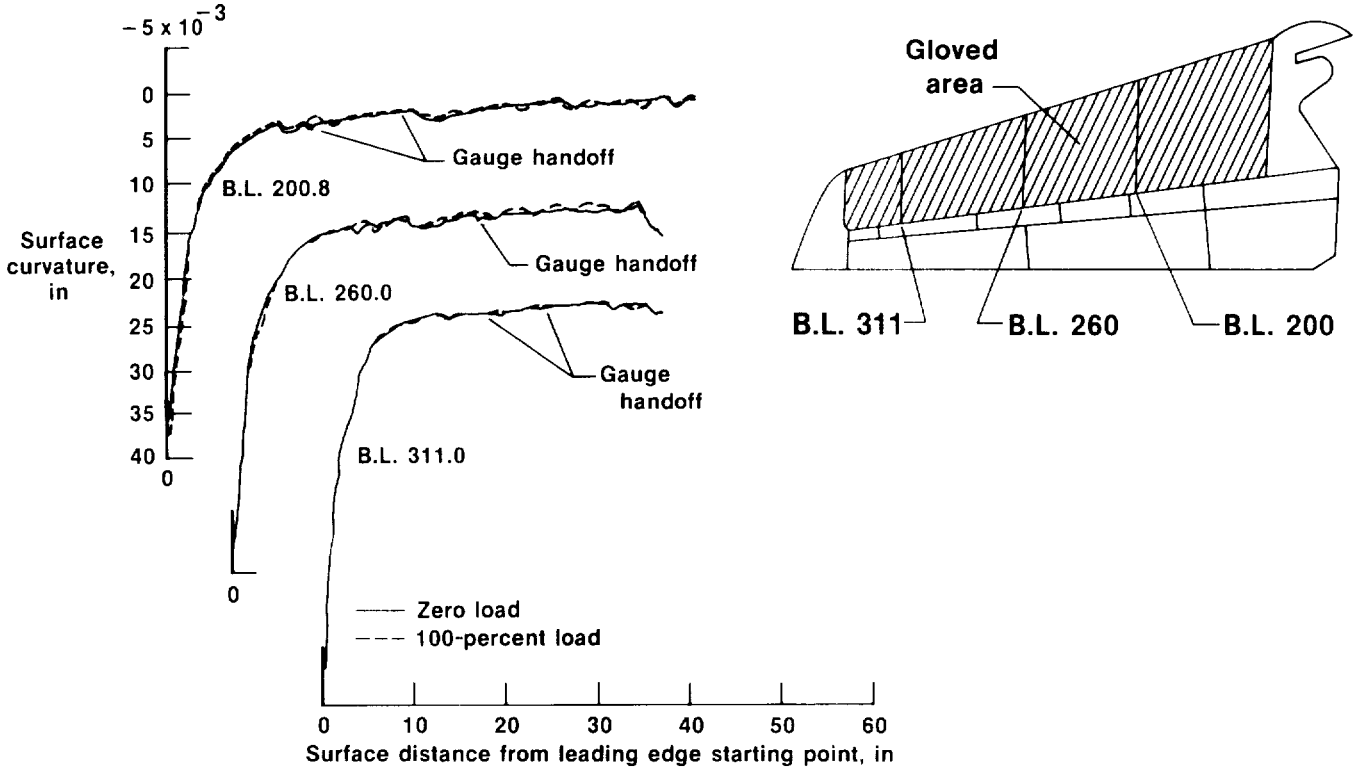

Figure 6

GLOVE I PLANFORM AND INSTRUMENTATION

The glove was instrumented as shown in figure 7. All signals from the instruments were recorded onboard the aircraft, and most were downlinked to a ground station for real-time display and recording. Data from the pitot tubes, dynamic transducers, strain gauges, skin temperature gauges, or accelerometers are not discussed in this paper. The three rows of surface pressure orifices were located at butt line stations of 200, 260, and 320. The orifices were drilled through the glove surface into small cavities built into the glove. Pressure lines were routed internally through the glove to lower surface wing compartments, where the transducers were located. Each boundary-layer rake consisted of 20 pitot tubes distributed along a 4-in strut, which was slanted 30° from the surface of the glove. Pressure lines were routed internally through the glove to the lower surface wing compartments.

The locations of the five hot-film gauges varied from flight to flight. Each was oriented streamwise to the flow for a wing sweep of 20°. To alleviate interference between the hot-film gauges, they were placed along a line oriented 30° to each orifice row (30° to the streamline at 20° sweep). Electrical wires from the hot-film gauges were routed externally along the glove surface to wing compartments. Additionally, the output signals were monitored in real time in the F-14 cockpit using an intercom audio system. This system allowed the pilot to affect transition location through the modification of either flight path or wing sweep.

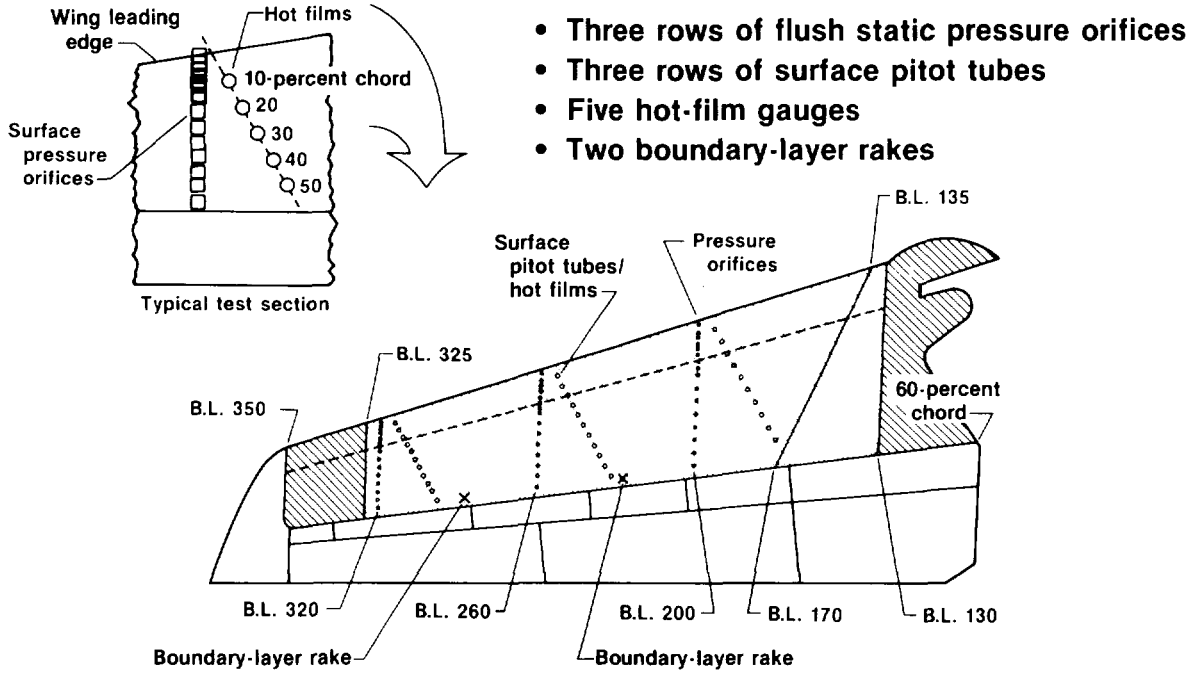

Figure 7

FLIGHT TEST ENVELOPE

Initial flights were designed to clear an operating envelope that was free from flutter and to obtain an airspeed calibration. Flutter data were obtained during stable Mach number and altitude conditions using control raps and natural turbulence for vehicle excitation. Airspeed calibration data were obtained from an acceleration-deceleration method and tower flybys (refs. 15 and 16). Maximum airspeed limit on the aircraft with the glove installed was 450 knots indicated airspeed or Mach 0.9, whichever occurred first (fig. 8). Reynolds number could be varied from approximately 1.0×10^6 ft^{-1} to 4.0×10^6 ft^{-1}, or a minimum and maximum chord Reynolds number of 5.0×10^6 to 34.0×10^6, respectively.

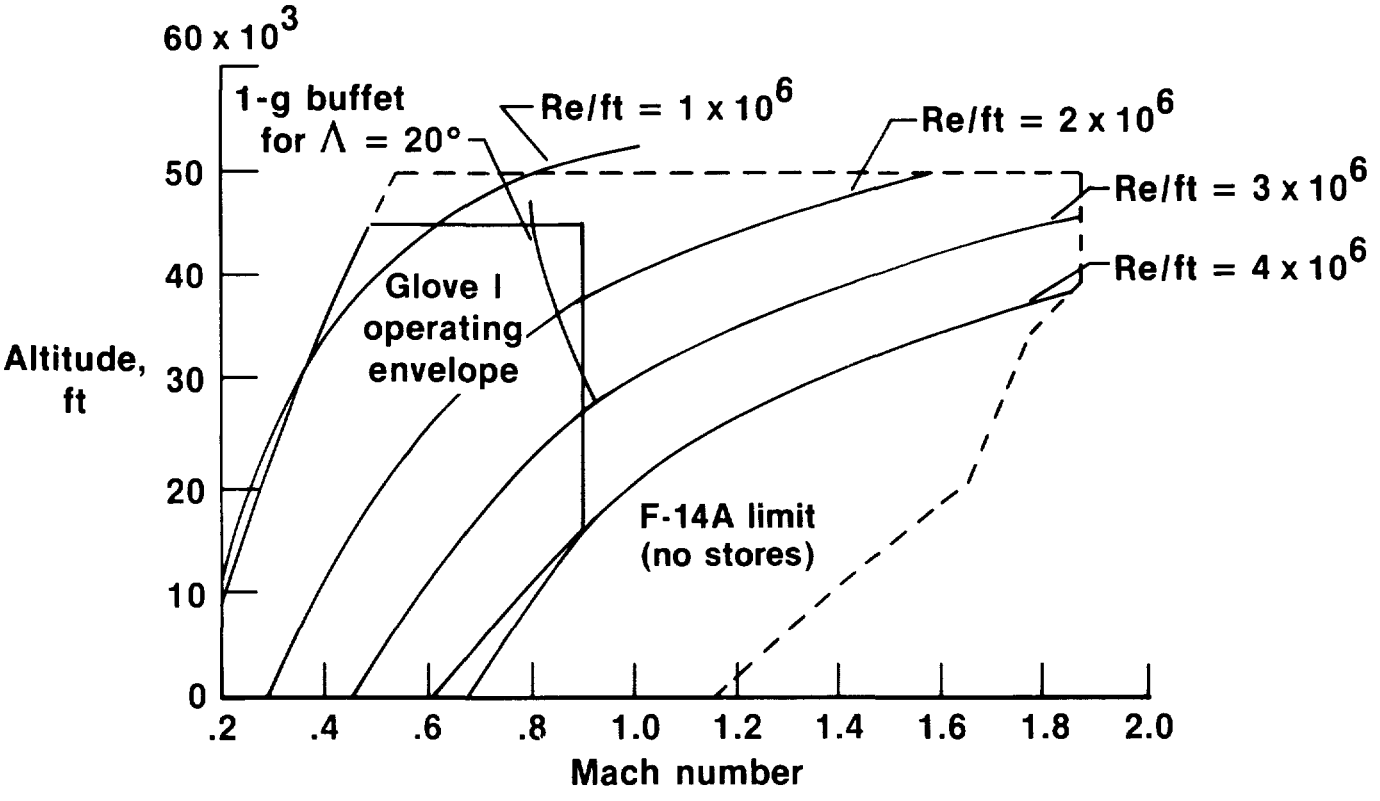

Figure 8

TYPICAL FLIGHT TEST MANEUVERS AND
UPPER SURFACE PRESSURE DISTRIBUTIONS

Laminar-flow data flights were conducted within the cleared envelope. First, coarse-resolution survey flights were conducted, followed by more detailed surveys to establish transition location as a function of wing sweep, angle of attack, Mach number, and Reynolds number (altitude). Maneuvers performed during the coarse-resolution survey flights consisted primarily of trim points and level turns. The level turns were used to obtain data at greater than 1-g trim angle of attack, particularly at low altitudes (high dynamic pressure). Figure 9 presents typical butt line (B.L.) 260 (middle test section) pressure distributions at trim angle of attack and Mach numbers of 0.7 and 0.8. The most notable characteristic is the change in the leading-edge pressure gradient $\Delta CP/\Delta(x/c)$ and pressure distribution shape with Mach number. At Mach 0.7 the gradient is less steep and becomes mildly adverse near 30-percent chord (x/c = 0.3), whereas at Mach 0.8 the favorable pressure gradient is much steeper and extends to 50-percent chord (x/c = 0.5), where a shock wave occurs. One undesirable characteristic of the pressure distribution at Mach 0.7 is the formation of an adverse pressure gradient near the leading edge with increasing angle of attack. This adverse gradient precludes laminar flow aft of the leading edge region. However, it was possible to alleviate these undesirable characteristics by performing a pushover maneuver, as described in the discussion of figure 10.

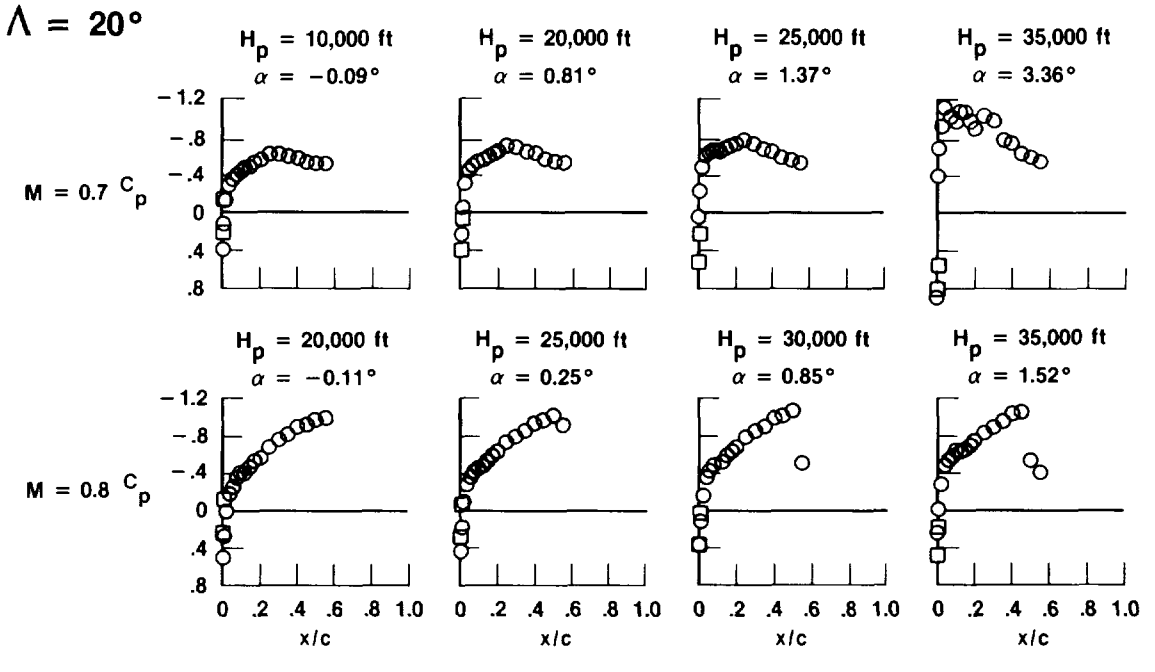

Figure 9

PUSHOVER MANEUVER

At certain combinations of Mach number, wing sweep, and altitude, it was necessary to perform a pushover maneuver to obtain a suitable pressure distribution on the glove. A smooth pushover maneuver that fulfilled these requirements was developed. Figure 10 shows typical time histories of angle of attack, altitude, and Mach number during such a pushover maneuver. For this example, trim angle of attack was approximately 2.0°, and desired angle of attack was 0.5°. The maneuver was started with a pullup at a flight condition slightly below the desired altitude and slightly above the test Mach number. The pull-up was followed by a pushover to the desired angle of attack, and conditions were maintained for approximately 10 sec before a recovery pullout was initiated. The ability to develop and perform this maneuver was attributed primarily to the real-time cockpit display.

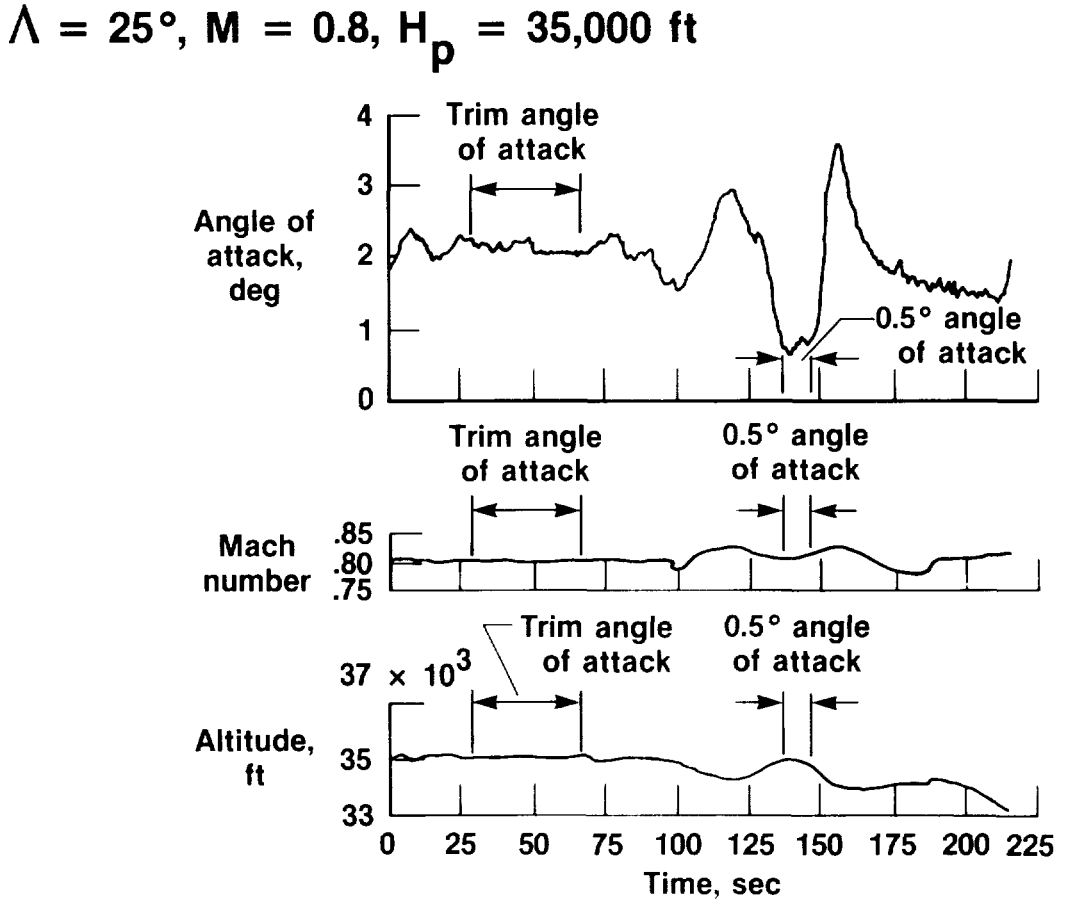

Figure 10

HOT-FILM ANEMOMETER AND PRESSURE DISTRIBUTION RESULTS

Hot-film anemometer interpretation was the primary method for determing transition location. Typically the hot-film gauges were located at 10-, 20-, 30-, 40-, and 50-percent chord on a particular test section. Outputs were plotted on a strip chart as functions of time. Two types of time histories were obtained: One consisted of low-frequency response plots displayed in real time in the ground station. The other consisted of high-frequency response plots that were made postflight. Signals originating in areas of laminar flow were of lower amplitude or quieter than those originating in areas of turbulent flow (fig. 11). Additional indicators were spikes in the output signal; spikes in a direction of positive voltage indicated a mostly laminar signal with occasional turbulent bursts, and spikes in a direction of negative voltage indicated a mostly turbulent signal with occasional laminar bursts. Maximum occurrence of these spikes was at peak transition, or the region where the flow is most unstable. The real-time ground station plots were generally acceptable for determining transition location; however, in some cases the high-frequency response plots were needed for clarification.

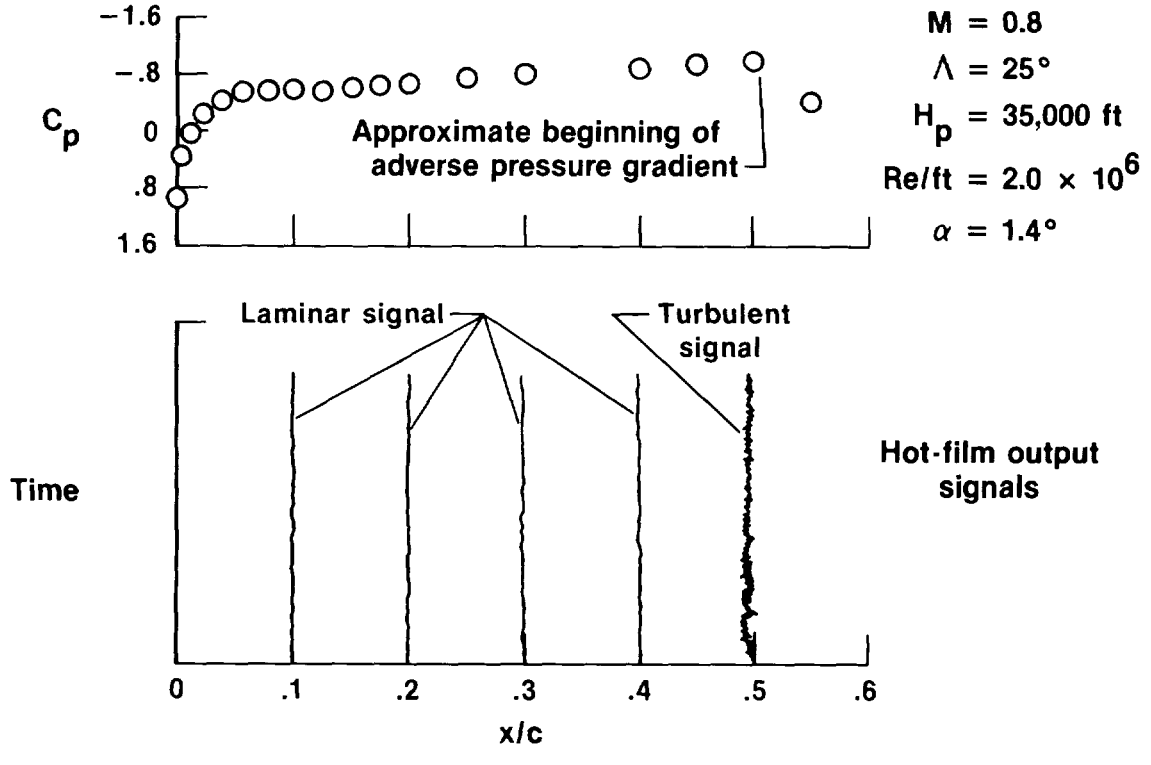

Figure 11

DETERMINING TRANSITION LOCATION
FROM BOUNDARY-LAYER MEARUREMENTS

Boundary-layer profile measurements were used as a secondary source for determining approximate transition location and as a source for determining skin-friction-related parameters. Transition location was determined by measuring the boundary-layer thickness δ as a function of angle of attack for a given sweep angle, Mach number, and altitude at various forced transition locations. Comparing the clean wing results (natural transition) with the calibration data (where transition was forced with grit strips using the method described in ref. 17) provided an indication of the extent of laminar flow achieved on the test section (fig. 12).

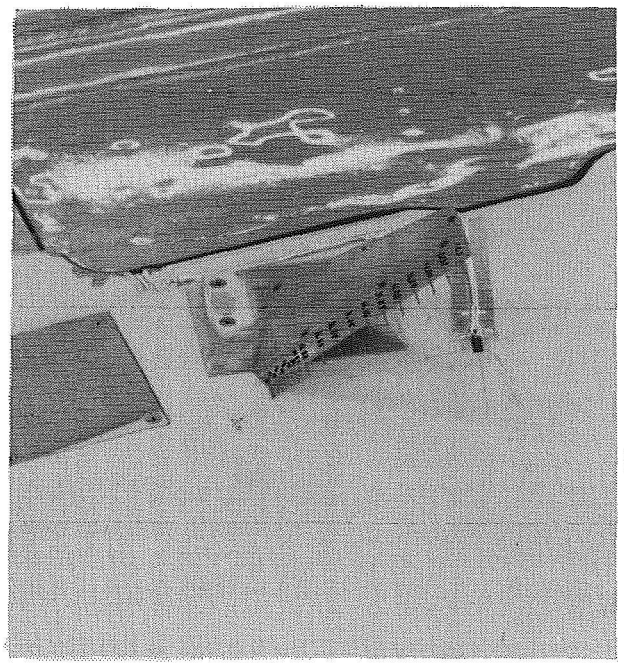

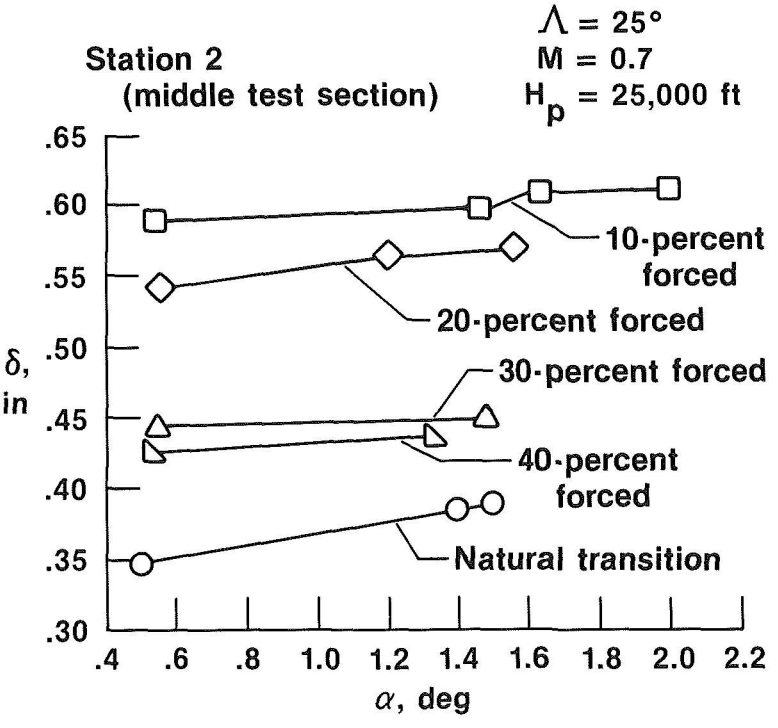

Figure 12

FLOW VISUALIZATION RESULTS

A flow visualization technique utilizing liquid crystals provided encouraging results. The technique was similar to that described in reference 18; a liquid crystal chemical in an oil base was applied with a brush to the wing glove surface prior to takeoff. However, the chemicals used in this case were primarily sensitive to shear. These chemicals provided results over a wider altitude and speed range than the temperature-sensitive chemicals used in reference 18.

For the flow visualization flights, the middle test section (station 2) was refinished with black paint to provide contrast with the liquid crystals. Photographs of the liquid crystal patterns were taken from a chase aircraft flying in close formation. Figure 13 presents a photograph of the liquid crystal patterns on the middle test section along with pressure distribution and hot-film anemometer traces for Mach 0.7, an altitude of 20,000 ft, and an equivalent wing sweep of 15°. The contrast change appears in the photo at 35-percent chord, indicating an abrupt change from laminar to turbulent flow. A wedge-shaped pattern emanates from the leading-edge region near the outboard portion of the test section. The wedge is a small region of turbulent flow believed to be caused by a surface discontinuity, such as dirt or an insect impact. The wedge is located forward of the 30-percent chord hot-film gauge with the edge of the wedge near the 20-percent chord hot-film gauge. The photographic observations are consistent with information from the pressure distribution and hot-film anemometer traces. The pressure distribution shows an adverse pressure gradient beginning at about 30-percent chord, indicating that the laminar boundary layer exists approximately 5-percent chord beyond the beginning of the adverse gradient. The hot-film anemometer traces indicate a laminar signal at 10-percent chord, an intermittent (but mostly laminar) signal at 20- and 30-percent chord, and a turbulent signal at 40- and 50-percent chord. The intermittent signal probably results from the turbulent wedge.

FLOW VISUALIZATION RESULTS

$\Lambda = 20°$, $\Lambda_{equiv} = 15°$, $\beta = -5°$, $M = 0.7$, $H_p = 20{,}000$ ft

$\alpha = 0.7°$

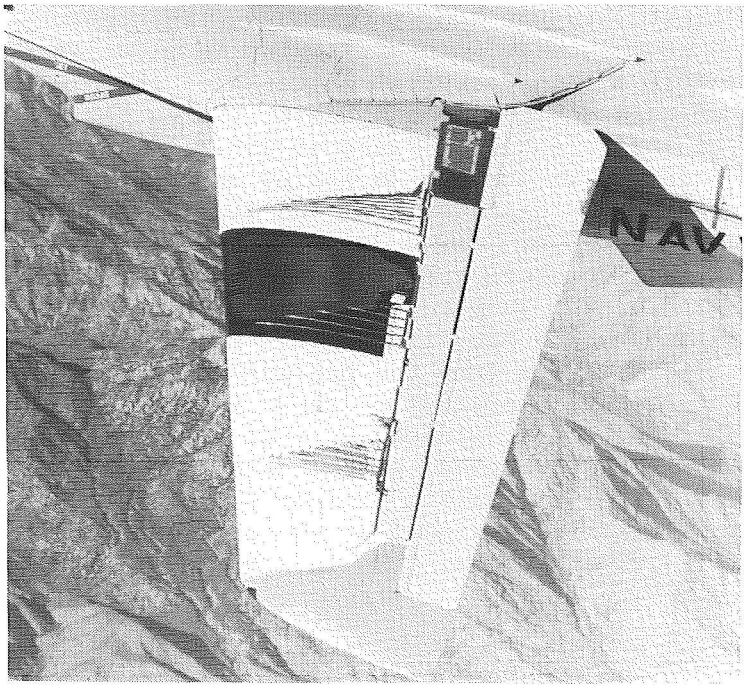

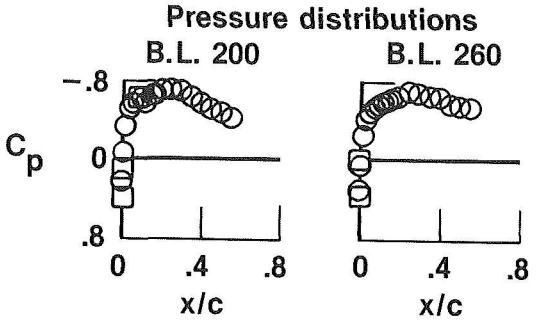

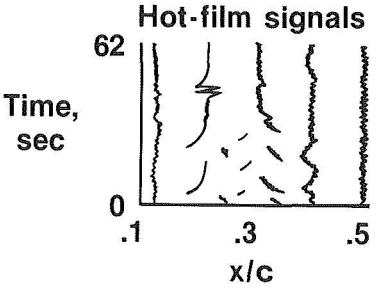

Figure 13

FLOW VISUALIZATION RESULTS

Figure 14 presents another photograph of the liquid crystal patterns on the middle test section with the corresponding pressure distribution and hot-film anemometer trace for Mach 0.8, an altitude of 25,000 ft, and a wing sweep of 20°. The contrast change in this photograph occurs in a sawtooth pattern between 10- and 20-percent chord. This indicates spanwise variation from laminar to turbulent flow. The pressure distribution shows a favorable pressure gradient existing to about 50-percent chord, indicating that the laminar boundary layer undergoes transition forward of the adverse gradient, which is the likely result of cross flow. The hot-film anemometer traces indicate a laminar signal at 10-percent chord and turbulent signals at 20-, 30-, 40-, and 50-percent chord. The traces are consistent with the liquid crystal pattern.

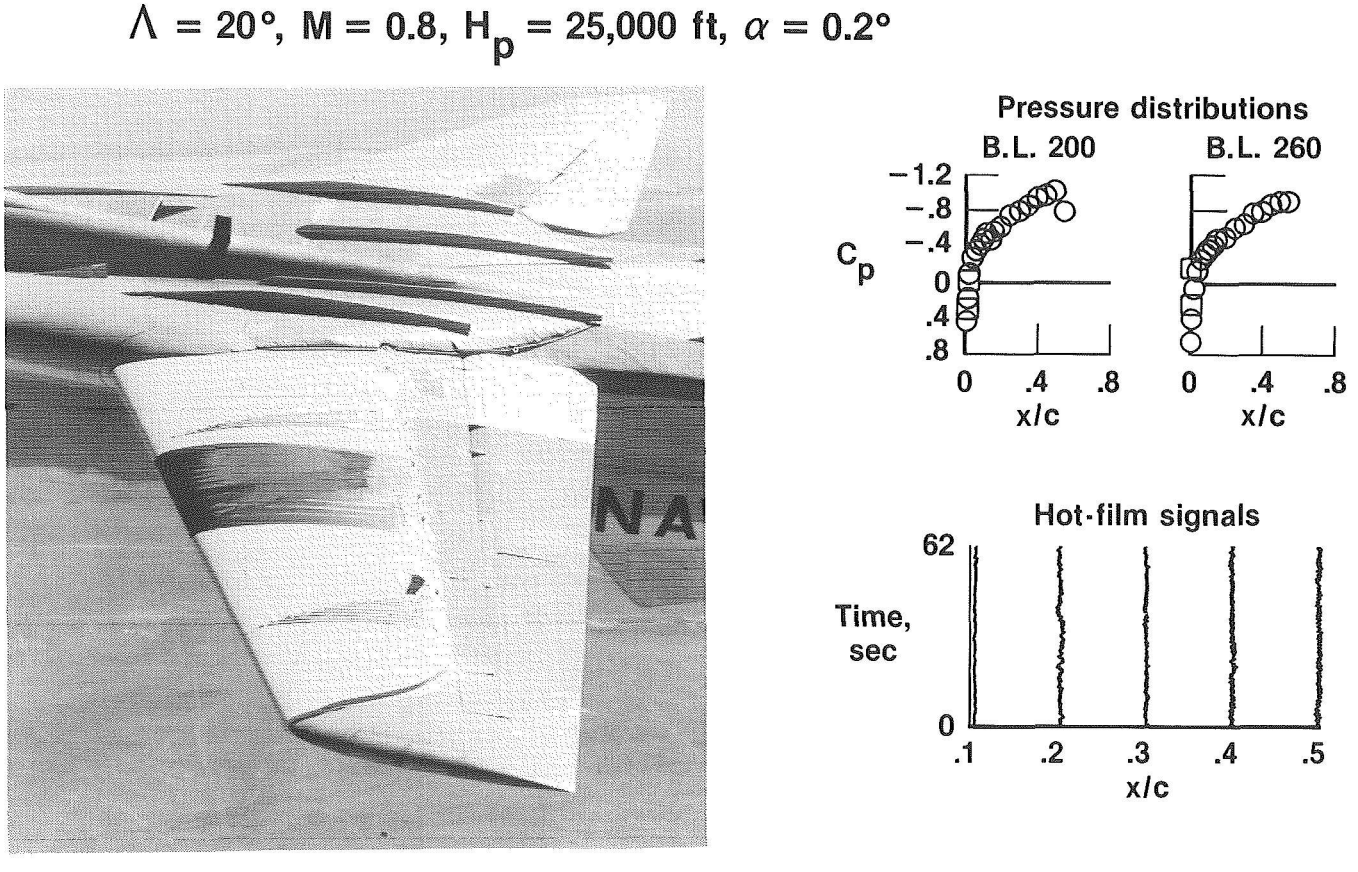

Figure 14

TYPICAL DETERMINATION OF TRANSITION LOCATION

Using hot-film anemometer and boundary-layer measurements, transition location was plotted as a function of angle of attack. Figure 15 shows a typical transition location plot at Mach 0.7, an altitude of 35,000 ft, and a wing sweep of 20° for the three test sections of the glove. The chord location of the beginning of the adverse gradient, shown as a dashed line in the figure, was obtained from analysis of data such as those presented in figure 9. For the middle and outboard test sections (stations 2 and 3), transition occurred at 40- to 50-percent chord ($x/c = 0.4$ to 0.5) for angles of attack below about 1.75°. The scatter in the data at station 2 for the more aft transition location ($x/c = 0.4$) was typically ±5-percent chord. It is interesting to note that transition occurred approximately 10-percent chord aft of the adverse pressure gradient on the middle and outboard test sections. The most aft transition on the inboard section occurred at slightly greater than 30-percent chord ($x/c = 0.3$). On all three test sections the data indicate a forward movement of transition location with increasing angle of attack. This is attributed to the previously mentioned localized adverse pressure gradient that occurs with increasing angle of attack. For example, at the middle test section (station 2), for this Mach number and wing sweep, a strong adverse pressure gradient formed at about 20-percent chord for 1.75° angle of attack, moving the transition location to about the 20-percent chord ($x/c = 0.2$) location.

It should be noted that the Mach 0.8 pressure distribution, as shown in figure 9, provided a favorable pressure gradient extending to about 50-percent chord ($x/c = 0.5$), where a shock wave occurred. The position and steepness of the adverse leading-edge gradient could be controlled in flight with Mach number, within the range of the Mach 0.7 and 0.8 pressure distributions shown in figure 9.

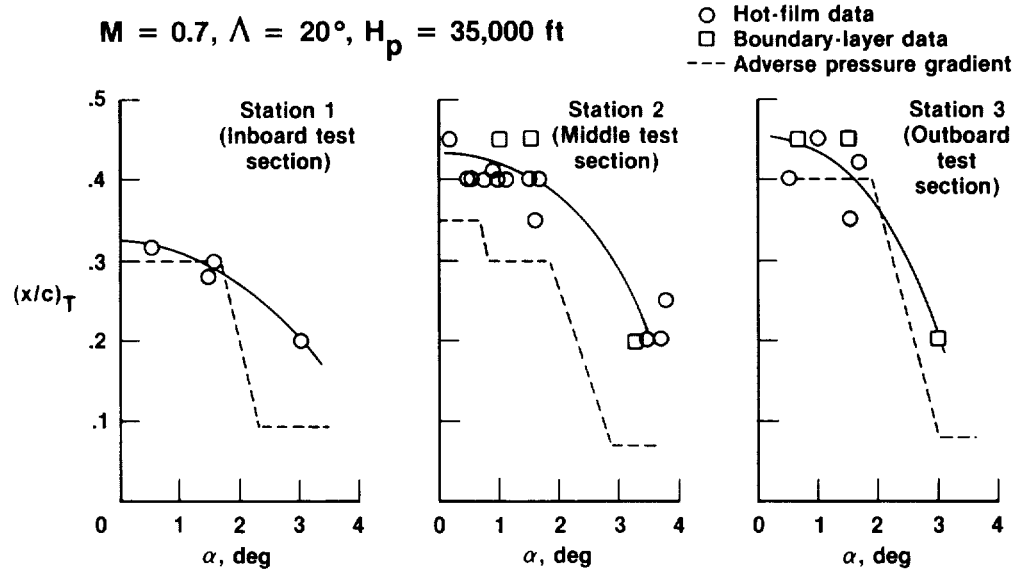

Figure 15

EFFECT OF WING SWEEP ON
TRANSITION LOCATION AT MACH 0.7

Figure 16 presents the most aft or optimum* transition location as a function of wing sweep for two altitudes at Mach 0.7. The data were obtained from results typical of those presented in figure 15 at the angle of attack at which the most aft transition occurred. For example, at 35,000 ft for the middle and outboard test sections (stations 2 and 3), the transition location varied from 45-percent chord at 20° wing sweep, to 35-percent chord at 35° wing sweep. For the inboard test section (station 1), transition location varied from 32-percent chord at 20° wing sweep to 10-percent chord at 35° wing sweep. The more forward transition location on the inboard test section is attributed to a less favorable pressure distribution and increased chord Reynolds number.

*Optimum refers to the most aft transition location observed from hot-film anemometer and boundary-layer measurements at these condtions (Mach number and wing sweep), but not necessarily the most aft obtained at other conditions (other Mach numbers and wing sweeps).

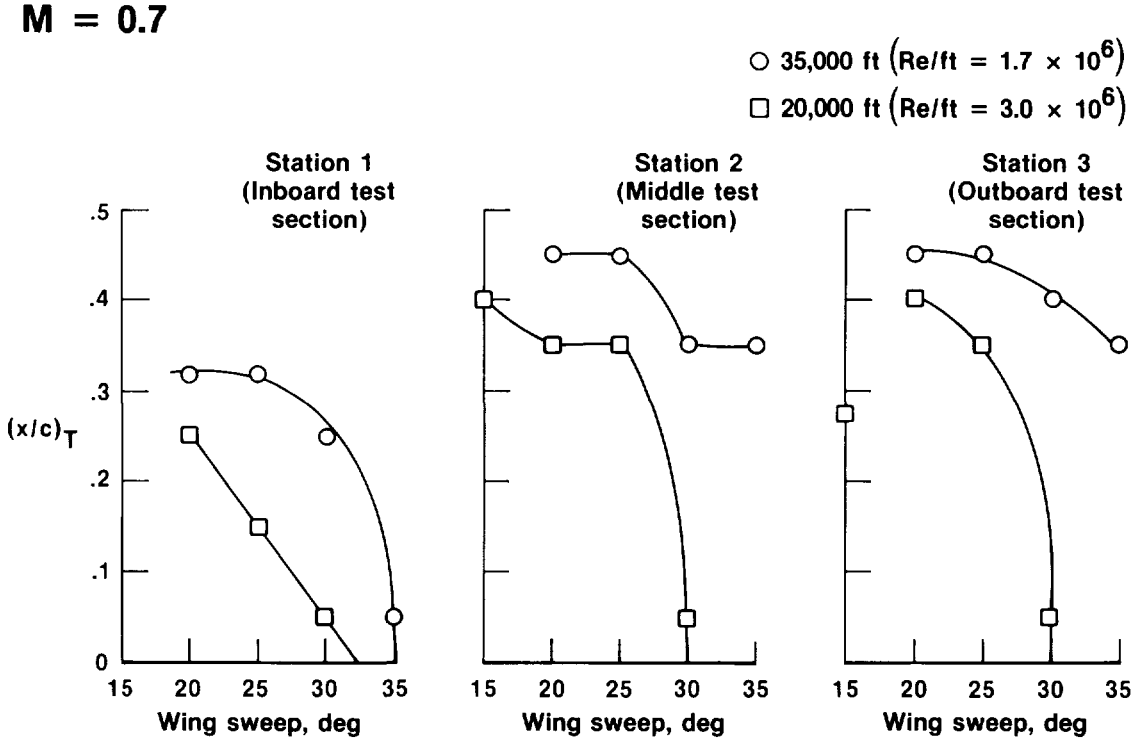

Figure 16

EFFECT OF WING SWEEP ON
TRANSITION LOCATION AT MACH 0.8

Figure 17 presents optimum transition location as a function of wing sweep for two altitudes at Mach 0.8. The results are generally similar to those presented in figure 16, with the exception that wing sweep has a more pronounced effect on transition location. For example, on the middle test section (station 2) transition is aft of 50-percent chord at 20° wing sweep and moves forward to 10-percent chord at 35° wing sweep. The increased effect of sweep is attributed to the steeper leading-edge pressure gradient at Mach 0.8, which increases the likelihood of cross-flow-type disturbances.

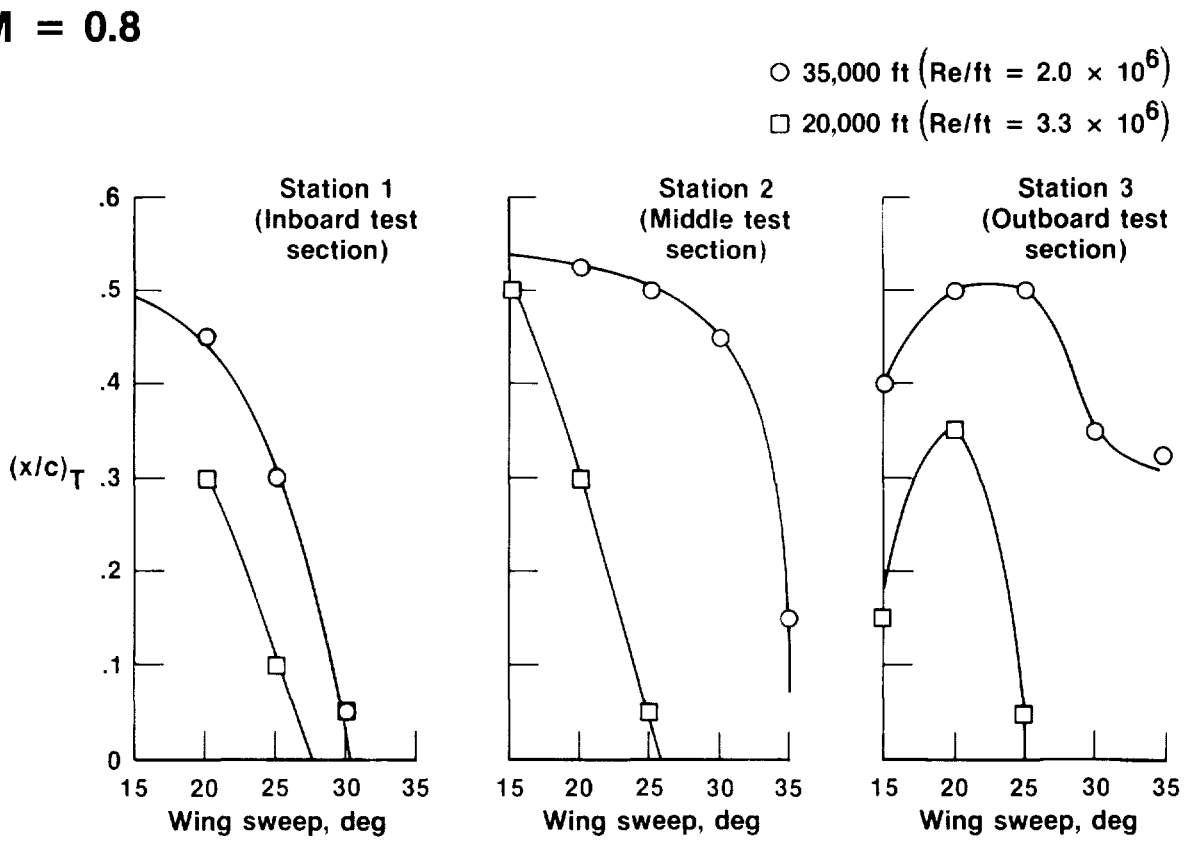

Figure 17

TRANSITION REYNOLDS NUMBER
AS A FUNCTION OF WING SWEEP

Figure 18 presents transition Reynolds number as a function of wing sweep at Mach 0.7 and 0.8. Maximum transition Reynolds number of approximately 13 × 10^6 occurs on the middle test section at a wing sweep of 15° for both Mach 0.7 and 0.8 data. It is interesting to note that transition Reynolds number decreases almost linearly with wing sweep at Mach 0.8. This is attributed to the highly favorable pressure gradient at this Mach number. The extent of this highly favorable pressure gradient (fig. 9) and the fact that transition occurred forward of the adverse pressure gradient are probably due to Reynolds-number-related phenomena, such as cross-flow disturbances. For the Mach 0.7 data, transition Reynolds number decreases in a nonlinear fashion with wing sweep. This is attributed to the less favorable pressure gradient at Mach 0.7 and to the more forward location of the adverse gradient, conditions that allow transition to occur sometimes because of the adverse gradient and sometimes because of Reynolds-number-related phenomena in the favorable gradient, such as cross-flow disturbances.

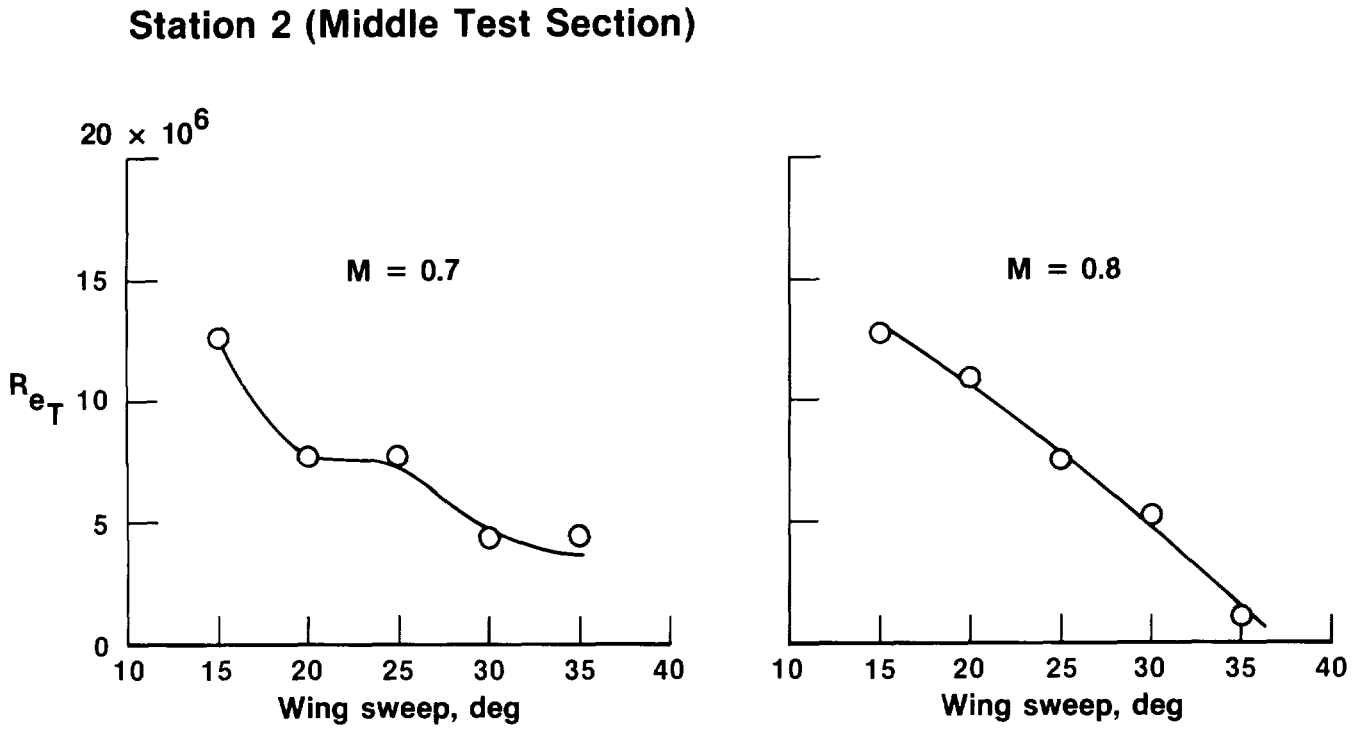

Figure 18

VISCOUS DRAG REDUCTION

Another interesting parameter available from the boundary-layer profile measurements is momentum thickness, which is an indicator of the viscous losses in the boundary layer. Figure 19 presents momentum thickness θ as a function of transition location at Mach 0.7 and a wing sweep of 20°. These data were obtained during boundary-layer rake calibration by forcing transition at known locations (see discussion of fig. 12). Maximum reductions in viscous losses were obtained at the higher altitudes (35,000 ft), as might be expected. For the outboard test section, θ varies from 0.033 at a transition location of 45-percent chord to 0.078 at a transition location of 10-percent chord. This change in θ results in a 58-percent reduction in viscous drag on the first 55-percent chord of the upper surface. Two qualifying statements apply to this viscous drag reduction: First, this experiment was not intended to be a complete airfoil test; that is, only the forward 60-percent portion of the upper wing surface is gloved, and these results indicate an optimum reduction on the upper surface of only one test section. Second, these results were not attained at working lift coefficients; that is, the pushover maneuver was required to attain the conditions that would provide extensive laminar flow. However, there is no reason to expect that an airfoil contoured specifically for high-altitude lift coefficients could not attain comparable amounts of laminar flow at working, or cruise, lift coefficents.

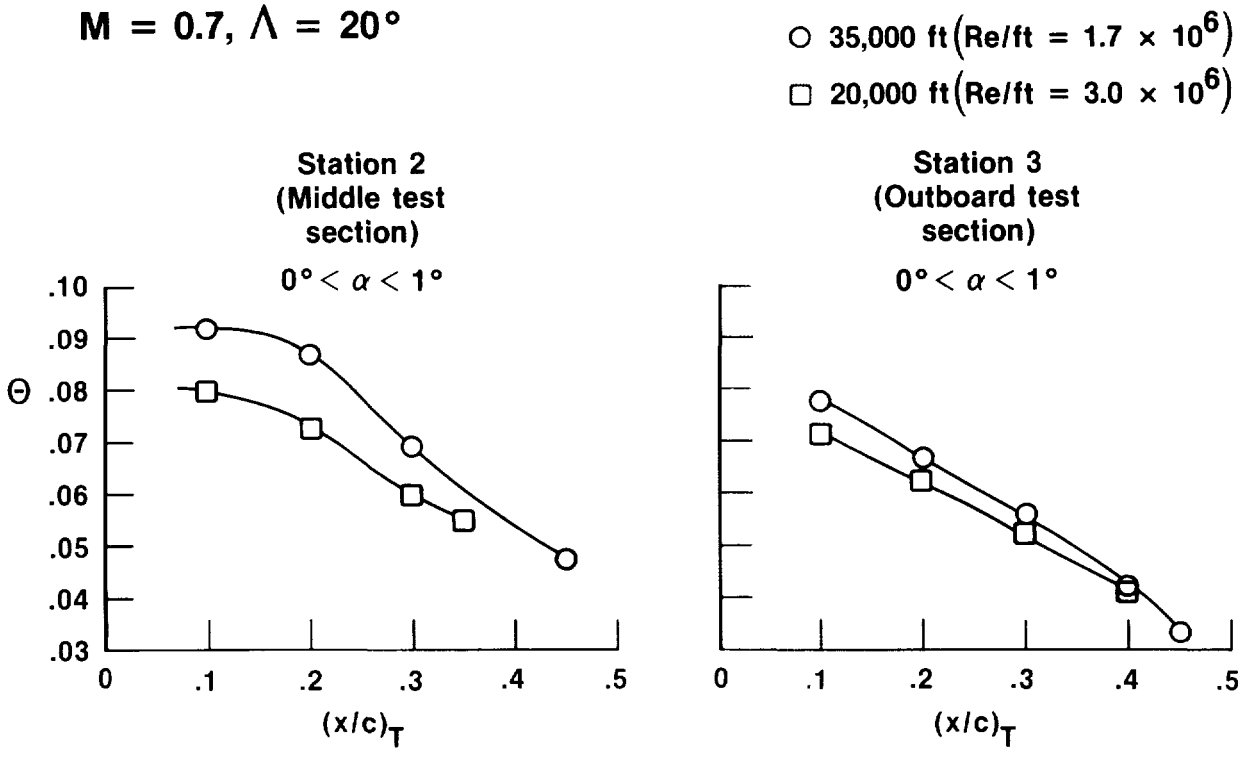

Figure 19

TYPICAL CASES FOR DETAILED ANALYSIS

During the course of the glove I flight tests, interesting results often occurred. An example is shown in figure 20, which presents three pressure distributions for a wing sweep of 30°, along with transition locations obtained from hot-film anemometer data. It is interesting to note the significant change in transition location as a result of small changes in angle of attack. For example, at an angle of attack of 0.8°, transition is between 20- and 30-percent chord; a change of approximately 1.5°, to an angle of attack of 2.3°, moves transition aft to between 40- and 50-percent chord. This change in transition location is attributed to the change in the leading edge pressure gradient, as shown in figure 20. The change in leading edge pressure gradient most likely changes the amplification of cross-flow disturbances.

Nineteen of these interesting cases, including those discussed here, have been selected and made available for detailed analysis. These cases will be discussed in detail in another paper from this conference (ref. 6).

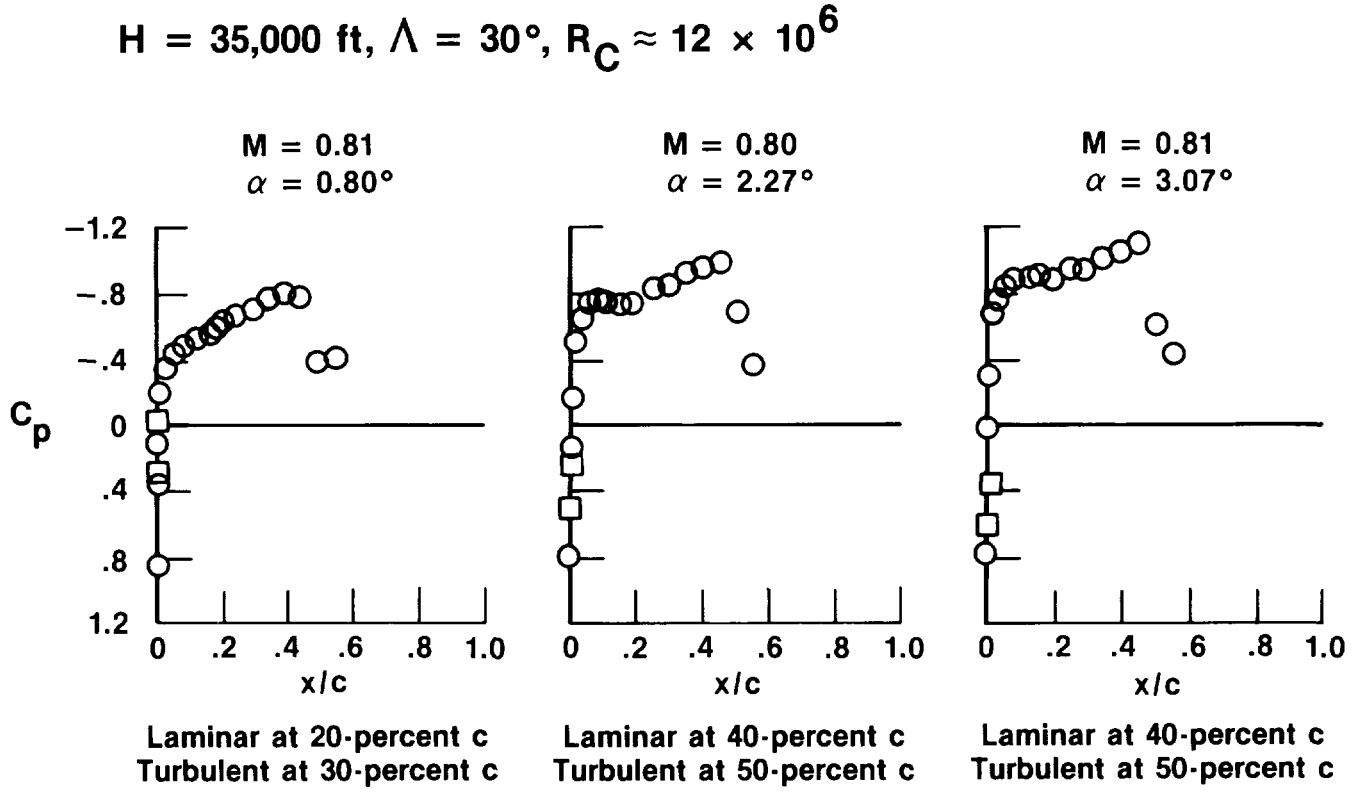

Figure 20

Concluding Remarks

- Majority of Glove 1 (cleanup) flight test have been completed
- VSTFE construction, instrumentation, and test techniques have been established
- Transition location from various methods correlate
- Preliminary results indicate a maximum transition Reynolds number of approximately 13×10^6 at 15° sweep and 5×10^6 at 35° sweep
- 19 cases selected for detailed analysis
- F-14 and associated real-time capability have proved to be a valuable laminar flow research facility
- Glove 2 will be tested

REFERENCES

1. Waggoner, E.; Campbell, R.; Philips, P.; and Hallissy, J.: Design and Tests of an NLF Wing Glove for the Variable Sweep Transition Flight Experiment. NASA CP 2487, pp. 753-776. NLF and LFC Research Symposium, Langley Research Center, Hampton, Virginia, Mar. 16-19, 1987.

2. Rozendaal, Rodger A.: Variable Sweep Transition Flight Experiment (VSTFE) - Parametric Pressure Distribution Boundary Layer Stability Study and Wing Glove Design Task. NASA CR-3992, 1986.

3. Runyan, L. James; Navran, Brent H.; and Rozendaal, Rodger A.: F-111 Natural Laminar Flow Glove Flight Test Data Analysis and Boundary Layer Stability Analysis. NASA CR-166051, 1984.

4. Meyer, Robert R., Jr.; and Jennett, Lisa A.: In-Flight Surface Oil-Flow Photographs With Comparisons to Pressure Distribution and Boundary-Layer Data. NASA TP-2395, 1985.

5. Bohn-Meyer, M.; and Jiran, Fred: The Use of Techniques to Modify Airfoils and Fairings on Aircraft Using Foam and Fiberglass. AIAA-81-2445, Nov. 1981.

6. Rozendaal, R.: VSTFE - Stability Code Development and Clean-Up Glove Data Analysis. NASA CP 2487, pp. 845-859. NLF and LFC Research Symposium, Langley Research Center, Hampton, Virginia, Mar. 16-19, 1987.

7. Mack, L.M.: On the Stability of Boundary Layer on a Transonic Swept Wing. AIAA-79-0264, Jan. 1979.

8. Hybrid Laminar Flow Control Study, Final Technical Report. NASA CR-165930, 1982.

9. Hefner, Jerry N.; and Bushnell, Dennis M.: Status of Linear Boundary Layer Stability Theory and the e^n Method, With Emphasis on Swept-Wing Applications. NASA TP-1645, 1980.

10. Malik, M.R.; and Poll, D.I.A.: Effect of Curvature on Three-Dimensional Boundary-Layer Stability. AIAA J., vol. 23, no. 9, 1985, p. 1362.

11. Malik, Mujeeb R.; Wilkinson, Stephen P.; and Orszag, Steven A.: Instability and Transition in Rotating Disk Flow. AIAA J., vol. 19, no. 9, Sept. 1981, p. 1131

12. Moes, Timothy R.; and Meyer, Robert R., Jr.: In-Flight Wing Pressure Distributions for the F-14A Aircraft. NASA TM-85921, 1985.

13. Richardson, Norman R.; and Pearson, Albin O.: Wind-Tunnel Calibrations of a Combined Pitot-Static Tube, Vane-Type Flow-Direction Transmitter, and Stagnation-Temperature Element at Mach Numbers From 0.60 to 2.87. NASA TN D-122, 1959.

14. Meyer, R.R., Jr.; and Schneider, Cdr. E.T.: Real-Time Pilot Guidance System for Improved Flight Test Maneuvers. AIAA-83-2747, Nov. 1983.

15. DeAnda, Albert G.: AFFTC Standard Airspeed Calibration Procedures. Air Force Flight Test Center. AFFTC-TIH-81-5, June 1981.

16. Johnson, J. Blair; Larson, Terry J.; and Ficke, Jules M.: Digital Program for Calculating Static Pressure Position Error. NASA TM-86726, 1987.

17. Braslow, Albert L.; and Knox, Eugene C.: Simplified Method for Determination of Critical Height of Distributed Roughness Particles for Boundary-Layer Transition at Mach Numbers From 0 to 5. NACA TN-4363, 1958.

18. Gall, P.D.; and Holmes, B.J.: Liquid Crystals for High-Altitude In-Flight Boundary Layer Flow Visualization. AIAA-86-2592, Oct. 1986.

VARIABLE-SWEEP TRANSITION FLIGHT EXPERIMENT (VSTFE) - STABILITY CODE DEVELOPMENT AND CLEAN-UP GLOVE DATA ANALYSIS

R. A. Rozendaal
Boeing Commercial Airplane Company
Seattle, Washington

THE GOAL OF THE VSTFE

The Variable Sweep Transition Flight Experiment (VSTFE) was initiated in 1983 by NASA to establish an improved boundary-layer transition data base for swept wings. An earlier flight experiment using the F-111 (ref. 1) had also investigated the effect of sweep and Reynolds number on transition, but was compromised by a very limited span laminar-flow glove and a crude method for determining transition location. The VSTFE addresses these shortcomings by using natural laminar-flow (NLF) gloves which span nearly all of the variable-sweep portion of the F-14 wing and hot-film gauges to sense the state of the boundary layer.

Data from the VSTFE flight tests will be analyzed using linear stability theory to determine the growth of disturbances on the wing. The disturbance growth results from many different flight conditions will then be correlated with the transition locations measured at those conditions to form a transition criterion. This criterion will then be available for use with the linear stability theory to design laminar-flow wings for future aircraft. The establishment of a reliable transition criterion for swept wings is one of the principal goals of the VSTFE.

As part of the process of establishing a reliable transition criterion, NASA contracted with Boeing to improve and expand the capability of using linear stability theory to determine disturbance growth in typical swept wing laminar boundary layers. This paper describes some of the details of this improved stability analysis system and shows disturbance growth results for eleven cases from the VSTFE clean-up glove flight test.

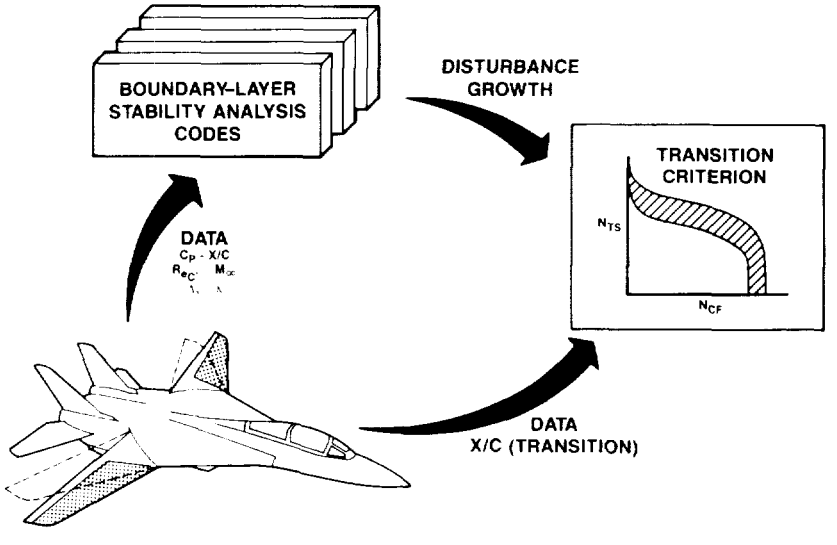

BACKGROUND ON LINEAR STABILITY THEORY

To develop an improved laminar boundary-layer stability analysis procedure, two existing computer codes were examined: COSAL, a temporal stability analysis technique using matrix solution methods (ref. 2), and MACK, a method which can solve for temporal or spatial stability using numerical integration through the boundary layer (ref. 3). After considerable work with both methods, the MACK code was chosen for use in the new stability system.

The mathematical development of the linear stability theory used in the MACK method parallels that for the Orr-Sommerfeld equation, but compressibility is included and the spanwise dimension is added. Disturbances in the boundary layer are characterized as having some wave length, λ, frequency, ω, wave direction relative to the local external flow, ψ, and a spatial growth rate, dN/ds. N is the exponent of "e" in describing disturbance growth as disturbance amplitude at some point = e^N (amplitude of that disturbance when it first starts to be amplified). The introduction of the disturbance into the compressible, 3-D boundary layer equations results in an eighth order system of equations with four unknowns: λ, ω, ψ, dN/ds. Typically, wave length or frequency and wave orientation are chosen by the user, and the other two unknowns are solved for. This is an eigenvalue problem since only certain combinations of the unknowns will solve the system. In the MACK method guesses for the eigenvalues start an iterative solution process which uses the Newton-Raphson procedure to refine the eigenvalues until the system of equations is solved to within some adequate tolerance.

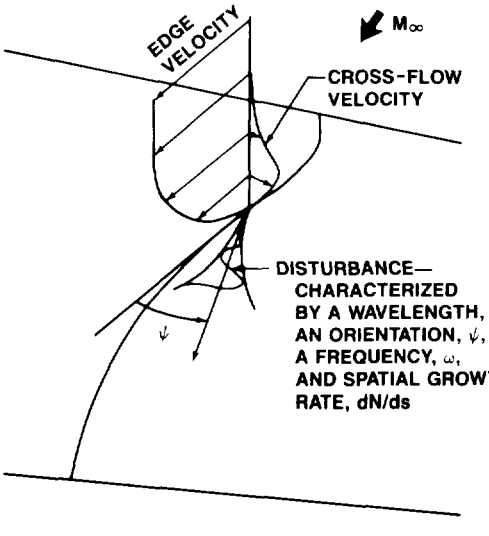

- BASIC DEVELOPMENT SIMILAR TO ORR-SOMMERFELD BUT:
  - 3D BOUNDARY LAYERS CAN BE EXAMINED
  - COMPRESSIBILITY INCLUDED
- INSTEAD OF FOURTH ORDER, WE GET AN EIGHTH ORDER SYSTEM OF EQUATIONS WITH FOUR UNKNOWNS (ψ, ω, λ, dN/ds)
- TYPICALLY, WE CHOOSE TWO (ψ AND λ OR ω) AND SOLVE FOR THE OTHER TWO
  - THIS IS AN EIGENVALUE PROBLEM
- SOLVED BY NUMERICAL INTEGRATION FROM OUTER FLOW TO WALL, CHANGING FREE PARAMETERS UNTIL WALL BOUNDARY CONDITIONS ARE MET

PHILOSOPHIES OF DETERMINING DISTURBANCE GROWTH

In general, the stability characteristics of a 3-D laminar boundary layer at a point on a wing involve a wide range of possible disturbance frequencies and orientations. To calculate the growth of all disturbances which may be important in causing transition, the engineer must choose some philosophy to apply in integrating the disturbance growth rate, dN/ds, with respect to distance from the attachment line.

One philosophy used presently (refs. 1 and 4) investigates two classes of disturbances, those more or less aligned with the local external flow (called Tollmien-Schlichting (TS) disturbances), and those nearly perpendicular to the local external flow (called cross-flow (CF) disturbances). This philosophy involves choosing a wave angle at which to analyze the TS disturbances. The angle is usually chosen to give the greatest growth throughout the range of important frequencies. In addition, this philosophy considers the zero frequency (stationary) cross-flow disturbances to be the most important in causing transition and calculates the growth of stationary cross-flow waves for which the component of spanwise wavelength is constant. This is the "irrotational" method described by Mack (ref. 3).

Another philosophy of calculating disturbance growth does not distinguish between TS and CF wave classes but calculates the growth of disturbances of different frequencies at whatever wave angle gives the maximum growth rate at each point on the wing.

As shown on the following figure, both philosophies just described require only a partial knowledge of the boundary-layer stability characteristics. The latest improvement to the stability analysis procedure automatically determines stability characteristics over a wide enough range of wave angles and frequencies so either of these philosophies, or perhaps a different one, can be used to calculate disturbance growth, N, from dN/ds (a function of ψ, ω) at each point on the wing. In addition, the whole procedure of calculating the boundary layer, analyzing the stability, and integrating the disturbance growth is combined into one system of programs, making better use of the analyst's time.

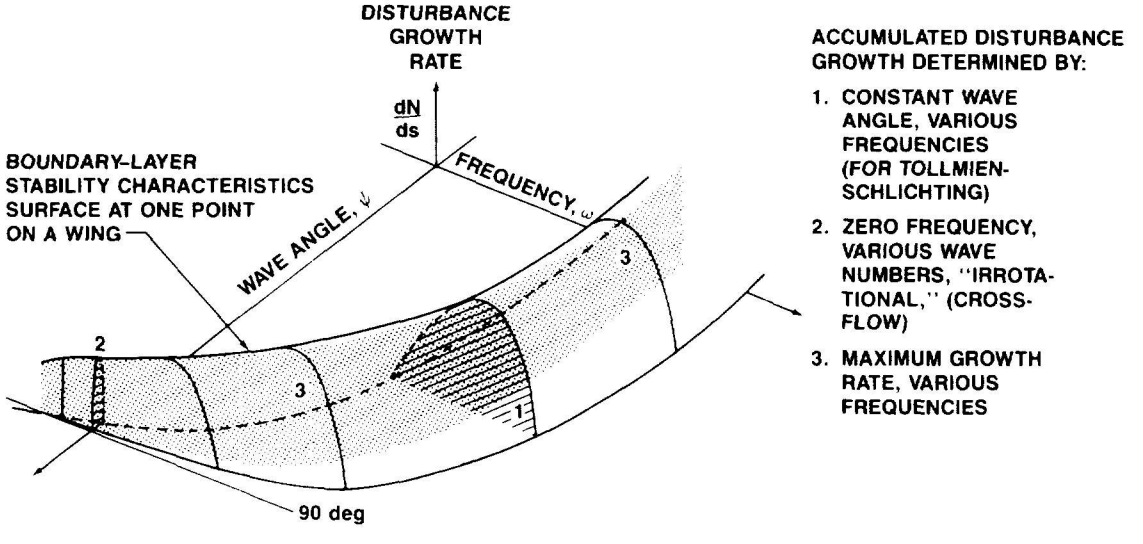

THE UNIFIED STABILITY SYSTEM

The laminar boundary-layer stability analysis procedure, as modified under the VSTFE, consists of eight computer codes and is called the Unified Stability System (USS). A master program sets up the job control statements to carry out the calculations desired by the user. Three programs set up the input for the boundary-layer analysis, carry out the analysis, and prepare the boundary-layer information for the stability codes. The boundary-layer analysis uses a finite difference method and can account for conventional or inverse taper.

Two different computer programs are used to calculate the boundary-layer stability. The solution procedure in both is almost identical, but one is tailored to analyze low wave angle disturbances, $\leq$ 70 degrees, and the other the high wave angles, 72 $\leq \psi \leq$ 91 degrees.

The final disturbance growth integrations (finding N from $dN/ds = f(\psi, \omega, x/c)$), are also done by two programs. One handles the TS disturbances, and the other calculates N_{CF} using the "irrotational" approach or N using the "maximum amplification" approach.

Numerous files are generated by these programs. Some only transfer information between programs, but several are available to the user for detailed examination of the boundary layer or its stability characteristics.

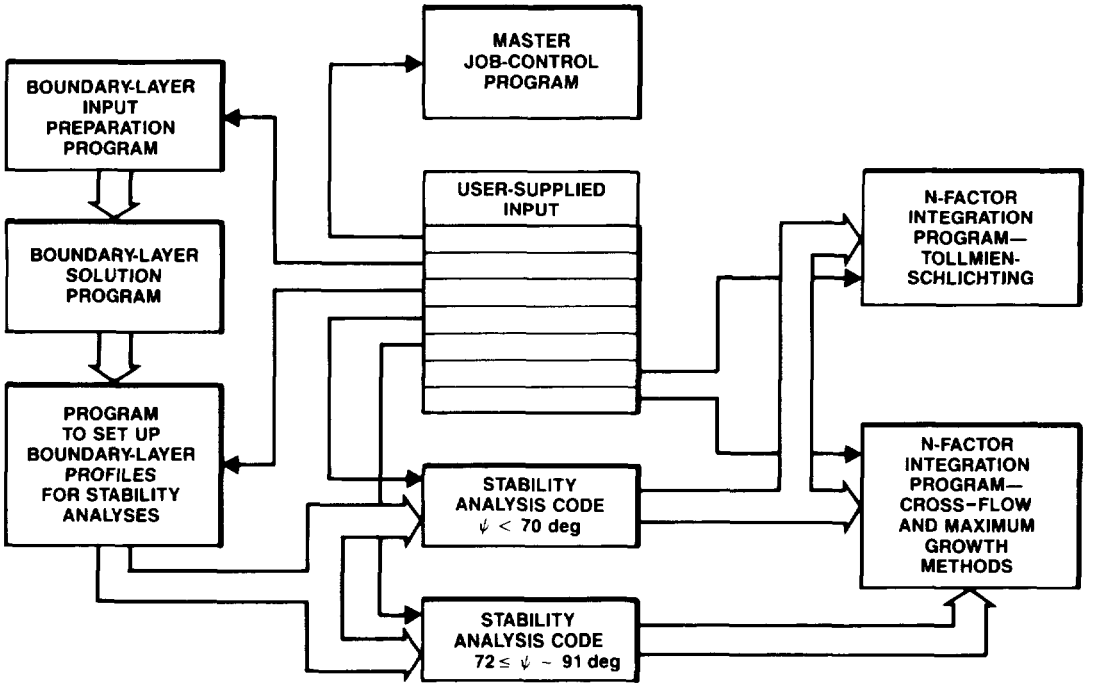

CHECK-OUT CASES FOR THE USS

The accuracy of the USS has been verified by comparing it to results of Mack (ref. 3) for two classic boundary layers: Blasius and Falkner-Skan. For both cases the boundary-layer analysis code was used to generate the boundary-layer profiles, so the check out includes the generation of the profiles, as well as the stability analyses. The Blasius boundary layer with a length Reynolds number of $(1200)^2$ was used for verification of the program which analyzes stability at lower wave angles. The graph below shows the comparison of nondimensional disturbance growth rate at two wave angles and three frequencies.

For high wave angles a Falkner-Skan profile with $\beta = 1.0$, $\theta = 45$ degrees, and length Reynolds number of 400^2 was used to verify the USS. The comparisons of neutral curve and maximum nondimensional amplification rate are shown below for wave angles from 72 to 85 degrees.

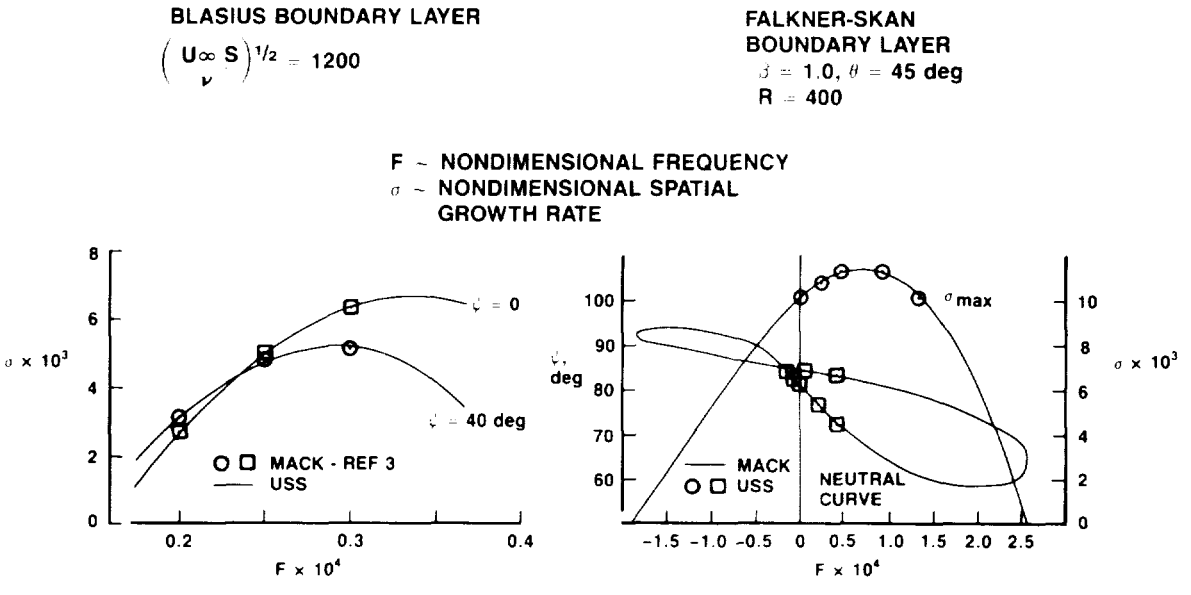

DETERMINING USS INPUT FROM THE F-14 DATA

The F-14 aircraft used for the VSTFE flight testing has three rows of static pressure orifices on the clean-up glove to measure the wing pressure field. A staggered row of hot-film gauges was placed between each of the static pressure rows to determine the boundary-layer state.

The sketch below helps show how the static pressure and hot-film data were used to determine the pressure distribution used in the stability analyses. The hot-film data showed not only the chordwise location of transition but also a spanwise location. The spanwise location was used to 1) find the local chord length used to calculate chord Reynolds number, and 2) interpolate the pressure data for determining C_p - x/c. Leading-edge sweep was known for each flight condition, and the three rows of pressure data were enough to get a good approximation of the isobar pattern, which determined the taper to use for the stability analyses. If too much scatter was present in the interpolated pressure distribution, a judicious hand-smoothing was done.

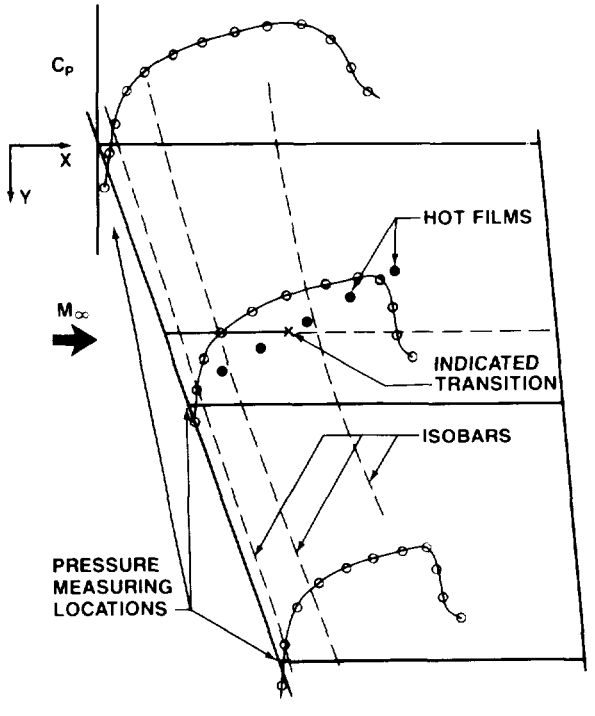

- HOT FILMS GIVE X/C AND SPANWISE LOCATION OF TRANSITION
- C_p - X/C AND LOCAL CHORD LENGTH TO USE FOR BOUNDARY LAYER AND STABILITY ANALYSES COME FROM INTERPOLATION AT SPAN WHERE TRANSITION OCCURRED
- SWEEP AND TAPER ARE FROM LEADING-EDGE SWEEP AND ISOBARS

STABILITY CHARACTERISTICS FOR A TYPICAL SWEPT WING CASE

Boundary layers on swept wings often have velocity profiles which are considerably different from the Blasius or Falkner-Skan profiles used as check-out cases for the USS. One of the cases from the VSTFE clean-up glove flight tests can be used to illustrate this. This case has a region of adverse pressure gradient near the nose followed by a second favorable gradient, and the resulting cross-flow profiles change dramatically.

As shown below, at 12.5 percent chord the boundary layer nearest the surface has responded to the adverse pressure gradient ahead of that point and switched from negative to positive cross flow. The disturbance growth characteristics show that the strong growth of cross-flow disturbances (ψ near 90 degrees), which was present near the leading edge, is largely damped at this position. A small "island" of growth is still present near 90 degrees, but the disturbances with lower wave angles have the most rapid growth at this position. This trend continues into the negative wave angle region.

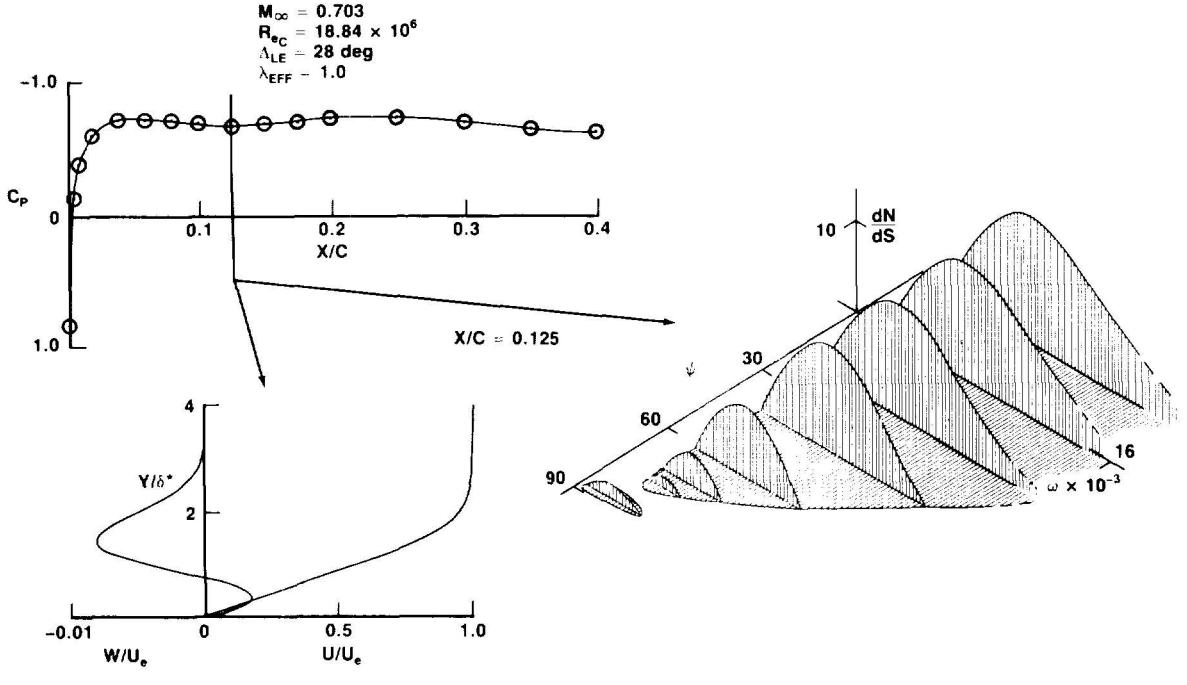

STABILITY CHARACTERISTICS FOR A TYPICAL SWEPT WING CASE (continued)

Continuing from the previous figure, as the boundary layer moves from 12.5 to 15 percent chord, the pressure gradient has gone from adverse to favorable, and the cross flow near the surface has all returned to negative values. The stability graph shows the substantial decrease in TS disturbance growth rates at this wing station, and the cross-flow region is still mostly stable. Note, however, that there is an indication of the unstable region at wave angles higher than 90 degrees for negative frequencies. One can also consider these to be disturbances of positive frequency at wave angles near 270 (-90) degrees. This region becomes more significant for cross-flow profiles with positive components, as found in regions in which an adverse pressure gradient predominates. The USS is not presently tailored to investigate this wave angle region because in most swept wing situations presently being investigated, the disturbances with wave angles between $-50 < \psi < 91$ degrees experience the most growth, and hence, are likely to be the cause of transition.

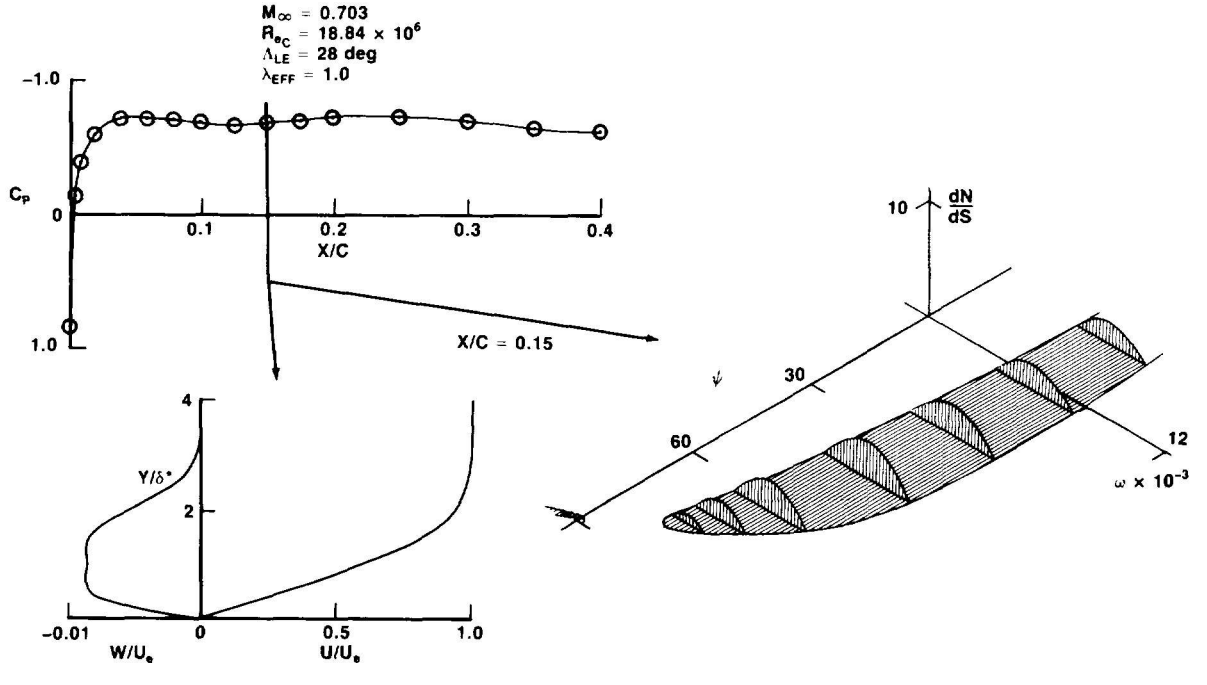

STABILITY CHARACTERISTICS FOR A TYPICAL SWEPT WING CASE (concluded)

When the boundary layer has moved to 33.8 percent chord in our example case, it has been in the second region of adverse pressure gradient for about 8 percent chord. The velocity profile parallel to the external flow now exhibits an inflection point and is close to separation (Falkner-Skan β for this profile is very near the separation value). Most of the cross-flow velocity is now positive.

The stability characteristics show that the TS disturbances have the greatest growth rates, and this behavior extends over a frequency range large enough so the automatic frequency ranging in the USS doesn't capture the complete unstable area. At the cross-flow wave angles, the disturbance growth rate surface goes through a saddle point and starts increasing rapidly again as the $\psi > 90$, $\omega < 0$ region is entered.

For the flight condition which has just been discussed, hot-film sensors indicated a transition of the boundary layer at 30 percent chord.

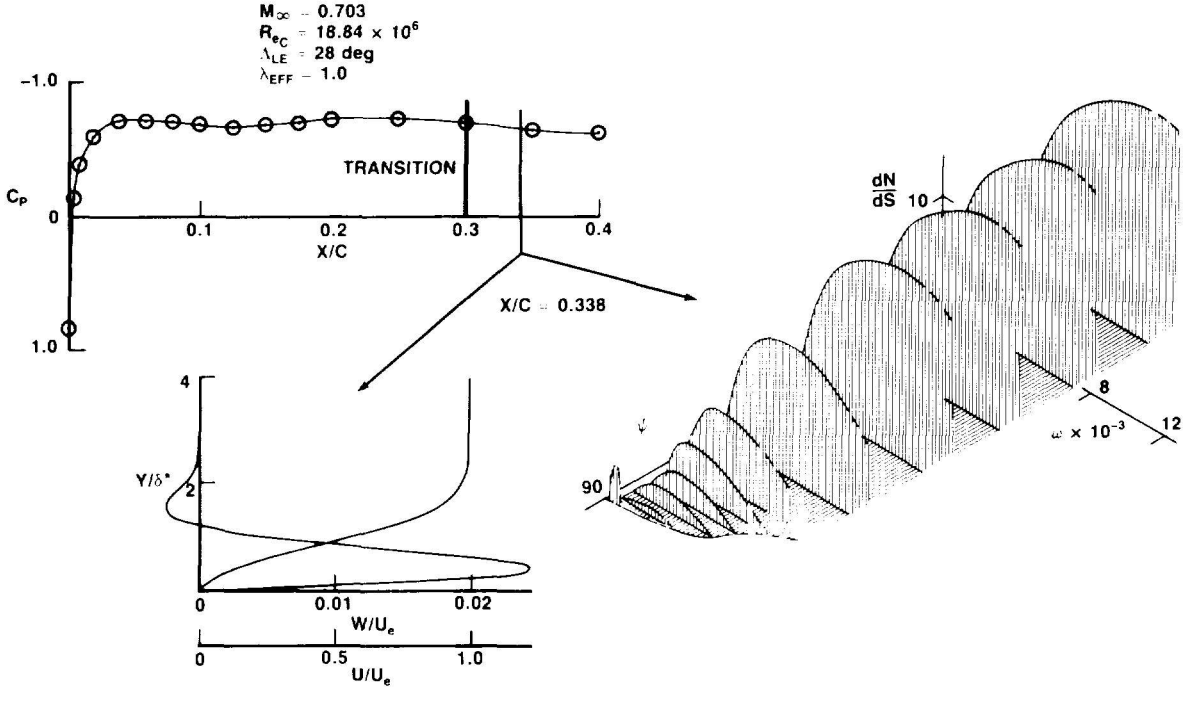

N-FACTOR GROWTH FOR THE TYPICAL SWEPT WING CASE

The N-factor growth for the case introduced in the previous figures is shown below. The maximum TS growth occurs for disturbances at 30 degrees wave angle and frequencies between about 5500 and 15000 Hertz. Maximum growth for these TS disturbances takes place where there are adverse pressure gradients.

The cross-flow N-factor envelope is formed by disturbances which have a spanwise component of wave number between 450 and 1700. In terms of wavelength these are between 0.044 and 0.167 inches. These zero-frequency, stationary disturbances show very strong damping at about 15 percent chord. Note that the cross-flow velocity profile at 15 percent chord had an unusual flat feature. Cross-flow disturbances tend to be amplified in favorable gradient regions and damped by adverse gradients, at least until the final recompression area of the wing is reached. This behavior is opposite to that of TS disturbances.

The N-factor as calculated using the wave angle for maximum amplification is also shown below. The envelope of maximum growth for this method is formed by disturbances with frequencies between about 4200 and 8000 Hertz. The wave angles which have the maximum growth rates are in the 90 degree (cross-flow) range near the leading edge but then move into the low (TS) range in the second adverse pressure gradient, eventually moving into the negative angle region (wave fronts advancing in a direction inboard of the local edge velocity).

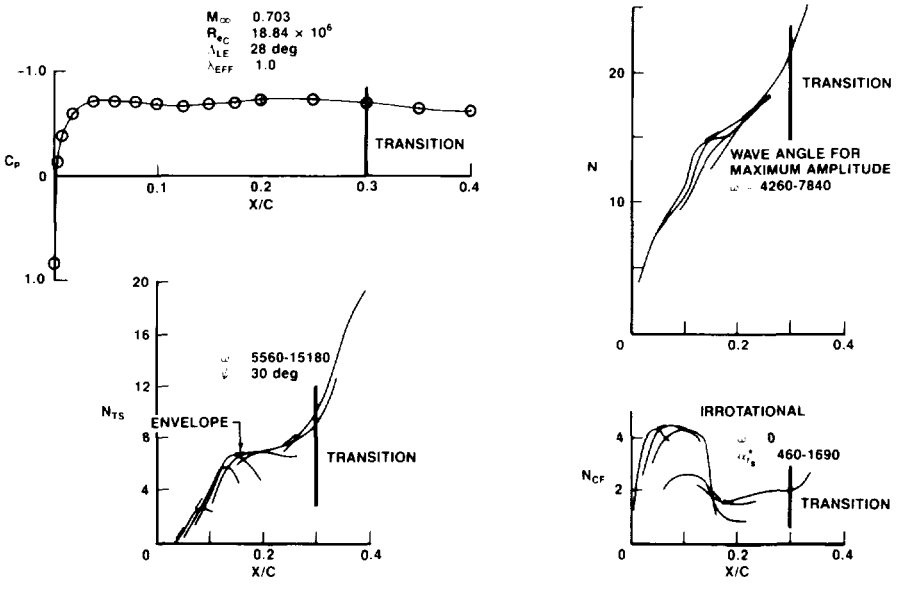

N-FACTOR GROWTH FOR A CASE WITH HIGH CROSS FLOW

Disturbance growth for another VSTFE case, one with considerably different flight conditions, is shown on this figure. For this case the cross-flow disturbances are dominant due to a strong favorable pressure gradient, even though the wing sweep is relatively low. This case illustrates a problem that can arise using a transition criterion which involves both N_{TS} and N_{CF}. In finding TS disturbance growth using a constant wave angle which gives the maximum growth, one may find that that wave angle is not in what is usually considered the TS region, but in the cross-flow region instead. This serves as a reminder that the original consideration of two classes of disturbances was just a simplification used in an attempt to predict transition in a swept wing. This problem does not negate the practice of using both TS and CF N-factors in predicting transition, but probably necessitates a change to considering the TS region to be below some wave angle, for example, between $\pm$ 50 degrees.

The disturbance growth philosophy which uses the wave angle for maximum growth likewise has weaknesses for use in defining a transition criterion. For the case shown on the previous figure the N-factor calculated by that method was near 21 at transition. Although for the present case that method predicts 16 to 19 at transition, other cases analyzed at Boeing predicted N-factors up to 30 at transition using the maximum amplification method.

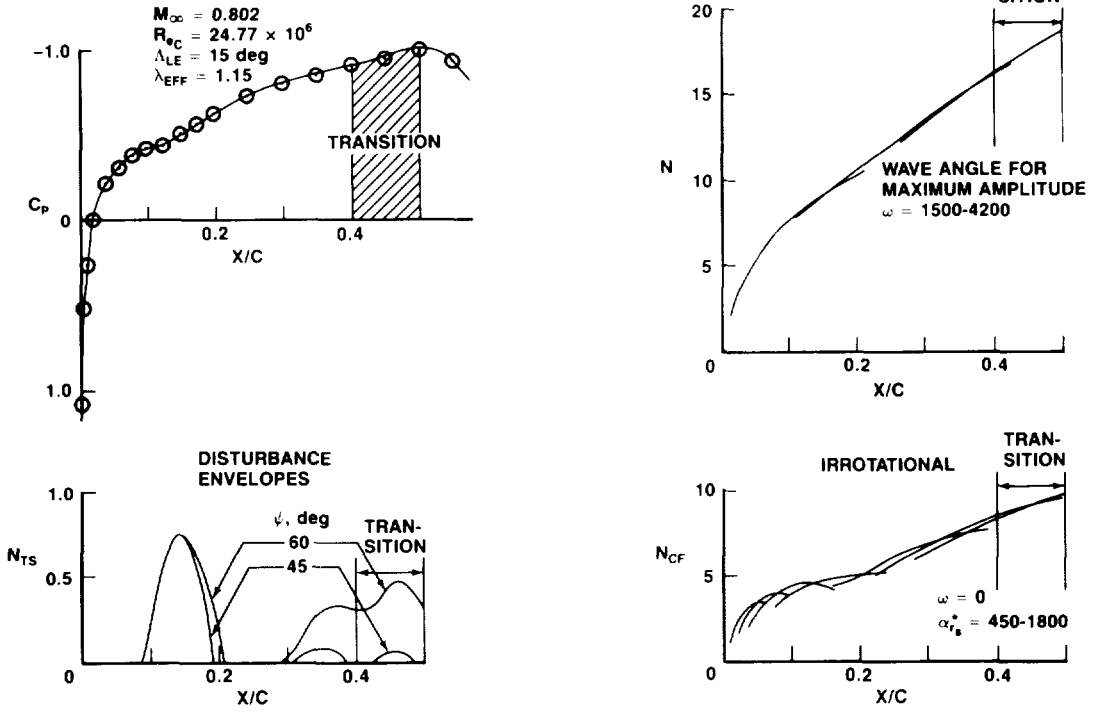

CLEAN-UP GLOVE DISTURBANCE GROWTH AT TRANSITION

Eleven cases from the VSTFE clean-up glove flight tests have calculated TS and CF disturbance growth in the area of transition plotted below. By varying flight conditions and wing sweep, the stability characteristics varied from almost exclusively CF dominant to mostly TS dominant. The traces shown below are for transition as detected by the hot-film sensors. Four of these cases had transition at one of the hot-films, so the N-factors for those cases are shown as a point rather than a line between the last laminar-indicating and the first turbulent-indicating hot-film. The length of the lines represents the N-factor change in 10 percent chord.

Despite the use of improved transition sensing methods, the disturbance growth traces from the VSTFE clean-up glove flight tests give a much broader N_{CF} - N_{TS} region at transition than the F-111 data. Several factors could be involved in this scatter: 1) Data from both tests involve uncertainties, not all of which are well understood, 2) The F-111 data may result in a generally pessimistic TS N-factor at transition, and 3) The use of the N_{CF}-N_{TS} graph may not collapse the transition points to a narrow band. A careful review of the clean-up glove data will show which cases have data with the least uncertainty. When analyzed, these may show less scatter.

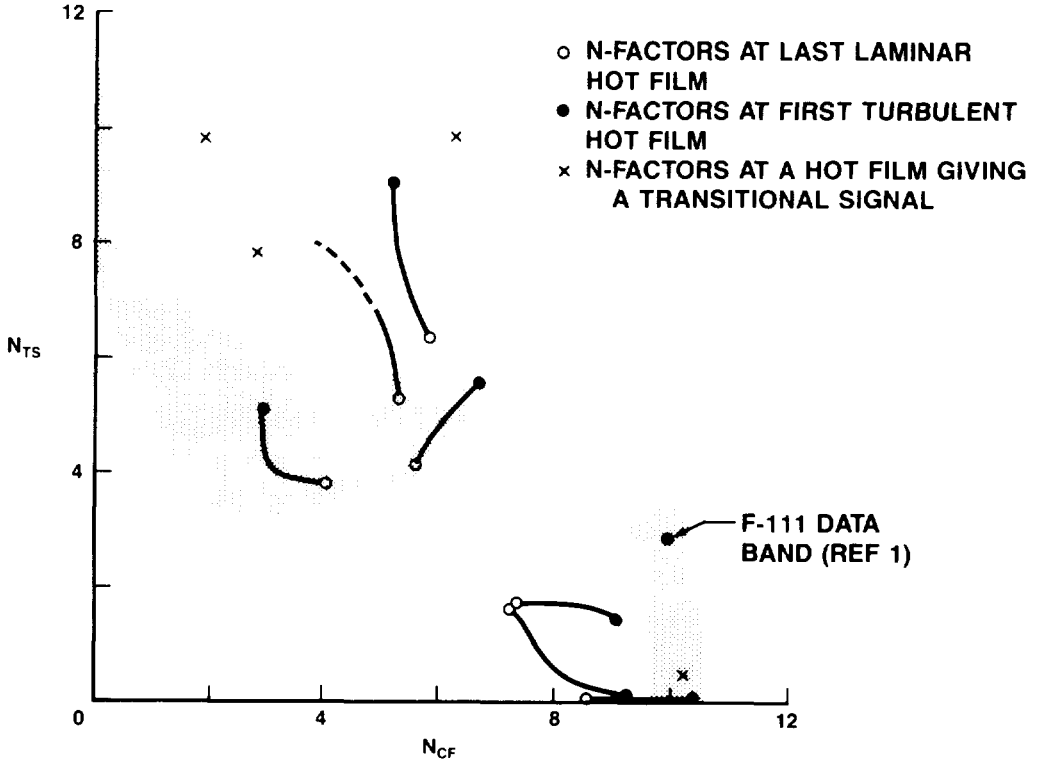

CONCLUSIONS FROM THE VSTFE CLEAN-UP GLOVE ANALYSES AND RECOMMENDATIONS

The primary goal of the VSTFE is to establish an improved swept wing transition criterion. The development of the Unified Stability System gives the aerodynamicist a way of quickly examining disturbance growth for a wide variety of laminar boundary layers, but the philosophy to be used in relating disturbance growth to transition and the accuracy of the data to use in the correlation are problems requiring more work.

The disturbance growth traces shown on the previous graph are too scattered to define a transition criteria to replace the F-111 data band, which has been used successfully by Boeing to design NLF gloves. Still, a careful review of the clean-up glove data may yield cases for which the transition location is known more accurately. Liquid crystal photographs of the clean-up glove show much spanwise variation in the transition front for some conditions, and this further complicates the analyses. Several high quality cases are needed in which the transition front is well defined and at a relatively constant chordwise station. Before liquid crystal coatings can be used to establish this information, it must be verified that they do not affect transition themselves.

The question of how best to correlate disturbance growth with transition location should not be addressed until high quality transition data are available. Since one glove remains to be tested in the VSTFE, this program can still meet its goals.

CONCLUSIONS

- VSTFE CLEANUP GLOVE EXHIBITED GROWTH OF DISTURBANCES OF WIDELY VARYING CHARACTERISTICS
- TRANSITION LOCATION NOT LOCATED ACCURATELY ENOUGH ON CLEANUP GLOVE FLIGHTS
- USE OF THE USS CAN GIVE RAPID INSIGHT TO QUITE COMPLEX STABILITY CHARACTERISTICS
- DISTURBANCE GROWTH PHILOSOPHIES PRESENTLY USED DON'T RESULT IN A SATISFYING TRANSITION CRITERION

RECOMMENDATIONS

- REVIEW CLEANUP GLOVE DATA FOR CASES WHERE TRANSITION WAS ACCURATELY KNOWN; ANALYZE THESE CASES
- CONDUCT TESTS ON THE NEXT VSTFE GLOVE WITH IMPROVED TRANSITION SENSING, WHICH GIVES GOOD CHORDWISE AND SPANWISE RESOLUTION

REFERENCES

1. Runyan, L. James; Navran, Brent H.; and Rozendaal, Rodger A.: F-111 Natural Laminar Flow Glove Flight Test Data Analysis and Boundary Layer Stability Analysis. NASA CR-166051, 1984.

2. Malik, M. R.; and Orszag, S. A.: Efficient Computation of the Stability of Three-Dimensional Compressible Boundary Layers. AIAA Paper 81-1277, 1981.

3. Mack, Leslie M.: Boundary-Layer Linear Stability Theory. AGARD Report No. 709, 1984.

4. Rozendaal, Rodger A.: Variable Sweep Transition Flight Experiment (VSTFE) - Parametric Pressure Distribution Boundary Layer Stability Study and Wing Glove Design Task. NASA CR-3992, 1986.

EXPERIMENTAL AND NUMERICAL ANALYSES OF LAMINAR BOUNDARY-LAYER FLOW STABILITY OVER AN AIRCRAFT FUSELAGE FOREBODY

Paul M. H. W. Vijgen
University of Kansas
Lawrence, Kansas

Bruce J. Holmes
Head, Flight Applications Branch
NASA Langley Research Center
Hampton, Virginia

INTRODUCTION

Fuelled by a need to reduce viscous drag of airframes, significant advances have been made in the last decade to design lifting surface geometries with considerable amounts of laminar flow. Advances in production techniques and materials have allowed lifting surface geometries to be within required tolerances for laminar flow. Both availability of linear and nonlinear computational boundary-layer stability analysis methods and several recent swept-wing flight tests utilizing advanced transition instrumentation have resulted in definition of a geometric and aerodynamic matrix for applicability of natural laminar flow over swept and unswept wings.

In contrast to the present understanding of practical limits for natural laminar flow over lifting surfaces, limited experimental results are available examining applicability of natural laminar flow over axisymmetric and nonaxisymmetric fuselage shapes at relevantly high length Reynolds numbers. This briefing will show the drag benefits attainable by realizing laminar flow over nonlifting aircraft components such as fuselages and nacelles. A status report is presented on a flight experiment being conducted in cooperation with Cessna Aircraft Company in Wichita, Kansas, to investigate transition location and transition mode over the forward fuselage of a light twin-engine propeller-driven airplane.

Possible application areas for natural laminar flow over nonlifting aircraft components are given in Figure 1.

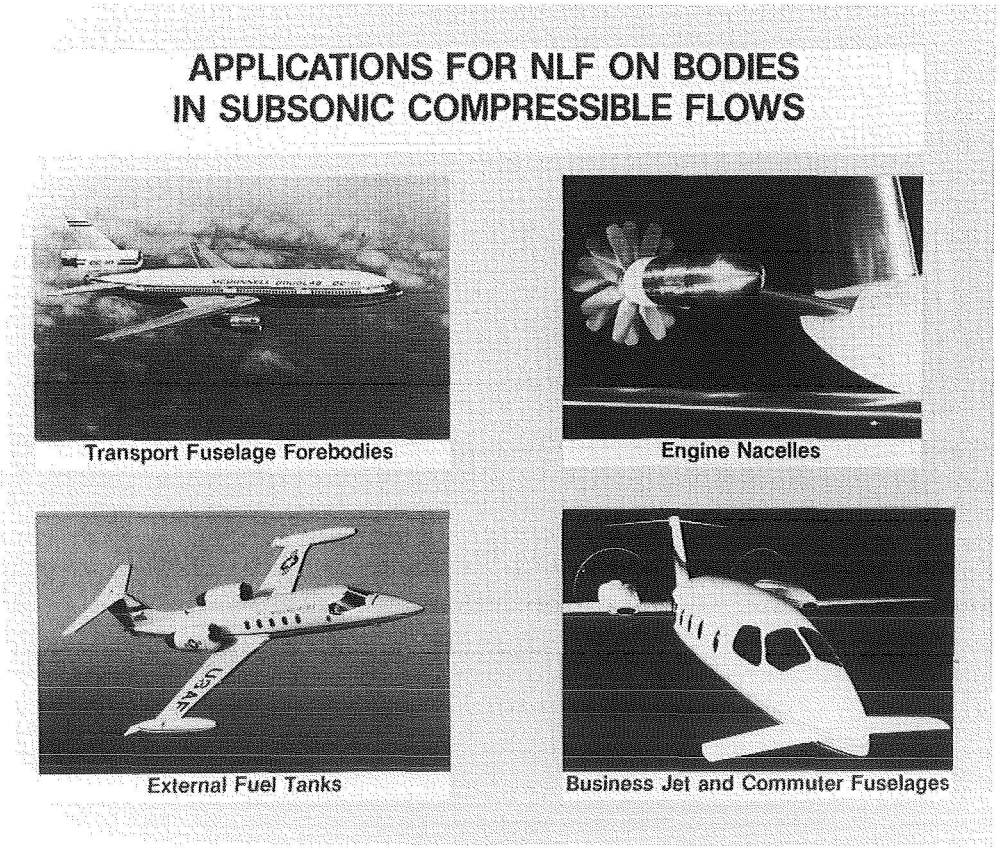

Figure 1

INTRODUCTION (CONTINUED)

Application of laminar flow to lifting surfaces of transports will increase the relative contribution of the turbulent fuselage to aircraft viscous and total drag (see Figure 2), thus presenting a stimulus to reduce viscous drag of the fuselage. In reference 1 an estimate is presented of the decrease in total aircraft drag when a laminar boundary layer is realized over the above indicated fuselage area. The geometry of the forward fuselage of a typical transport aircraft provides a favorable accelerating pressure gradient from the nose up to the beginning of the cylindrical cabin section on the sides and bottom of the fuselage and after the windshield on top of the fuselage (see reference 2). Additional benefits of a laminar run over the initial portion of the fuselage are a reduction in turbulent drag over the remainder of the fuselage (and possible greater ease of scaling large-eddy break-up devices for turbulent drag reduction) and relief of the wing-fuselage interaction problem. Axisymmetric nacelles of recently introduced high-bypass unducted-fan engines and external fuel tanks can be shaped to sustain large amounts of laminar flow, particularly at compressible flight speeds. Significant runs of laminar flow are predicted in reference 3 for business-jet and commuter-type fuselages when appropriate body shaping is available. At compressible flight conditions (M = 0.60 and up) as much as 30- to 40-percent of the fuselage length is predicted to be capable of sustaining a sufficiently stable laminar boundary layer (reference 1).

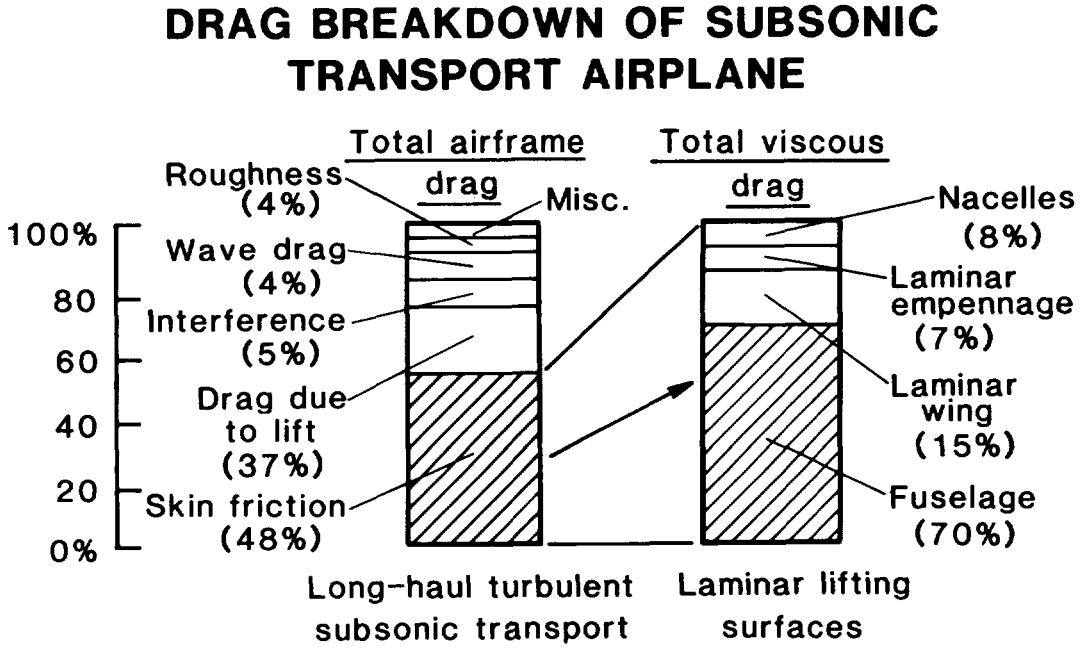

Figure 2

BENEFITS OF NATURAL LAMINAR FLOW

Drag benefit for maintaining laminar flow over the first 30 percent of an advanced business-jet type fuselage can amount to 7-percent in total (viscous and induced) aircraft drag (Figure 3). By comparison, realization of laminar flow over 40 to 50 percent of wing chord results in 12-percent total drag reduction. These drag reductions are compared to fully turbulent configurations. Reference 4 presents a detailed assessment of performance and operating cost improvements for achieving laminar flow over different components of a typical commuter aircraft. Figure 3 also indicates a 2-percent drag reduction for maintaining a laminar boundary layer over turbofan engine nacelles. Reference 5 presents a status report of a flight experiment investigating stability of the laminar boundary layer over a turbofan nacelle under varying acoustical environments.

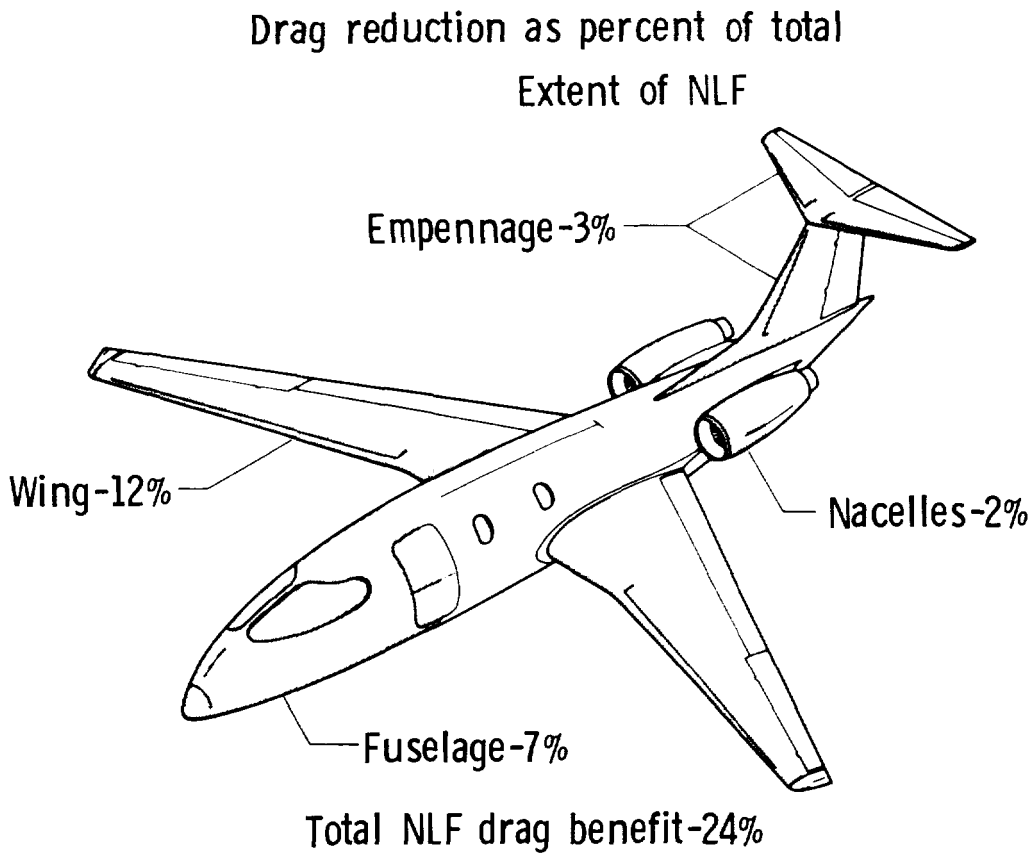

Figure 3

NLF BODY DESIGN CONSIDERATIONS

Figure 4 presents a road map of transition mechanisms that can affect the stability and extent of natural laminar flow over a fuselage. The stability of a laminar boundary layer (in absence of suction or wall cooling) is derived from the magnitude of pressure gradients along the body surface in axial and circumferential directions at a given unit Reynolds number and free-stream Mach number. Energy from sound and turbulence in the environment can be entrained into the laminar boundary layer and lead to increased amplification growth of disturbances in the laminar layer (receptivity problem). Manufacturing excrescences on the fuselage surface can induce strong destabilizing disturbances in the boundary layer, resulting in immediate transition (bypass mechanism), and can generate large local pressure gradients which allow sound and turbulence to be entrained (receptivity).

- Body shape for axial and circumferential pressure gradients (Tollmien-Schlichting and crossflow instabilities)
- Noise and turbulence environment (receptivity)
- Manufacturing tolerances (bypasses)

    - Reynolds number
    - Mach number (flow compressibility)

Figure 4

PAST INCOMPRESSIBLE BODY TRANSITION EXPERIMENTS

Past experimental transition results are mainly available for axisymmetric incompressible (underwater) body shapes. Wind-tunnel results at high subsonic Mach number (Reference 6) pertain to low length Reynolds numbers. Figure 5 presents the measured extent of natural laminar flow (expressed as a transition Reynolds number based on axial length) as a function of the body fineness ratio F_R, defined as ratio of body length to body diameter for incompressible conditions. A decrease of body fineness ratio leads to an increase in axial pressure gradients for a body with constant internal volume. Figure 5 shows that a large increase in the amount of laminar flow is obtained when fineness ratio is reduced. Reference 7 presents results of some of the low-fineness-ratio findings indicated in this figure. Fuselages of business-jet and commuter type aircraft are characterized by fineness ratios of 5 to 9. Figure 5 also shows that limited experimental results are available for axisymmetric shapes in this design area. However, some of the forebody shapes tested are typical for underwater applications. No experimental results are available for nonaxisymmetric geometries at relevant length Reynolds numbers to define practical limits for NLF design factors given in Figure 4.

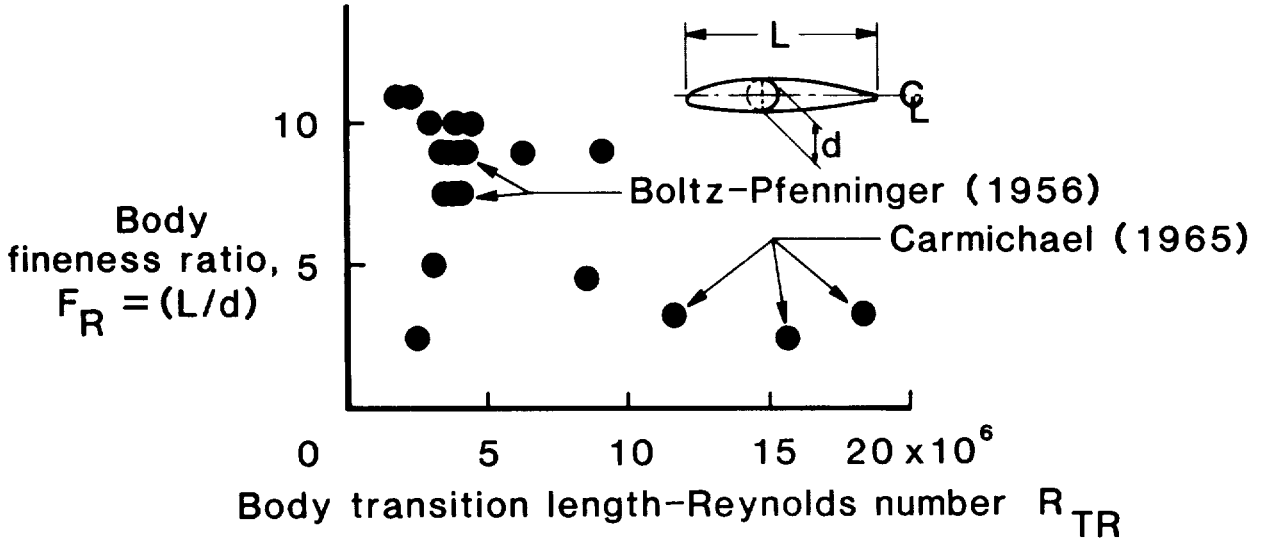

Figure 5

NASA/CESSNA T-303 NLF FUSELAGE FLIGHT EXPERIMENTS

To investigate the extent and stability of laminar flow over a practical nonaxisymmetric fuselage a flight-test program has been started in cooperation with Cessna Aircraft Company using a Cessna T303 "Crusader" light twin-engine propeller-driven aircraft (Figure 6). Preliminary analysis of axial pressure gradients over the original fuselage forebody indicated a strong potential for laminar flow in cruise and climb conditions. The indicated nose surface constitutes about 5 percent of the total fuselage wetted area. The production-quality forebody (painted black in Figure 6 for flow-visualization observations) required smoothing with body filler and subsequent sanding of rivet lines and lap joints to prevent premature transition. Proximity of the propeller propulsion system to the forebody allows study of possible effects of propeller and engine noise on mode and location of transition over the fuselage nose. Figure 6 also shows the wing-mounted boom for static and total reference pressures and angle-of-attack and angle-of-sideslip indicators.

Figure 6

T-303 NLF FUSELAGE FLIGHT EXPERIMENT

Installed transition instrumentation on the T303 forebody is given in Figure 7. Pressure port lines along 7 meridian lines measure the pressure field over the nose and possible streamtube effects in the proximity of the propeller plane. Location of transition and extent of the transition process is measured by 3 lines of staggered surface hot films, one line on top, port and starboard side of the fuselage nose respectively. The signal-to-noise characteristics of these high-impedance hot films will allow spectral analysis of the signal to identify energy distribution in the frequency domain of each hot film. To identify and quantify the external environment to which the laminar boundary layer is subjected, 3 flush mounted microphones are installed in the nose area and a single-wire free-stream-turbulence probe is mounted near the port wing tip. Engine and propeller power and RPM settings are also measured by the onboard data system.

- 7 surface pressure port lines (140 ports)
  - Nose pressure distribution
  - Propeller streamtube effect
- 39 staggered M&M 50Ω hot films
  - Boundary-layer intermittency
  - Spectral content (T.S. Frequencies)
- 3 Flush mounted B&K microphones
  - Acoustic environment
- TSI freestream turbulence probe
  - Turbulence environment
- Propellers and gas generator RPM and power settings

Figure 7

BOUNDARY-LAYER STABILITY ANALYSIS OVER NONAXISYMMETRIC FUSELAGE FOREBODY

Computational assessment of stability of the laminar boundary layer over the fuselage forebody is carried out along the steps indicated in Figure 8. Inviscid surface pressure distributions are determined for the complete fuselage geometry. Using a quasi-axisymmetric approach the laminar boundary-layer development is determined using a finite-difference scheme. Streamwise Tollmien-Schlichting (T.S.) stability is determined using the boundary-layer profiles calculated by the finite-difference method. In the present briefing only an assessment of the T.S. stability is presented. A full three-dimensional analysis of stability of the laminar boundary layer (i.e., including the effect of boundary-layer cross flow) will be commenced as soon as the required computational tools are available to the authors.

- Inviscid pressure distribution
- Axisymmetric-analogue approach
  - Quasi-axisymmetric boundary-layer analysis
  - Tollmien-Schlichting stability analysis
- Full three-dimensional approach
  - 3-D boundary-layer analysis
  - Tollmien-Schlichting and crossflow stability analysis

Figure 8

T303 FUSELAGE FOREBODY ANALYSIS

Figure 9 shows the inviscid pressure distribution over the T303 forebody as predicted by the VSAERO panel method (Reference 8) at the indicated flight conditions. The pressure contour plots show a moderately favorable pressure gradient (flow acceleration) in the axial direction from the nose (stagnation area) towards the windshield. On top of the fuselage a pressure recovery near the windshield can be observed resulting in an adverse axial pressure gradient towards the windshield. A moderate pressure gradient is predicted in the circumferential direction from the symmetry line to the side of the fuselage. These circumferential gradients will induce curvature of the streamlines and can result in boundary-layer cross flow and possible cross-flow instability.

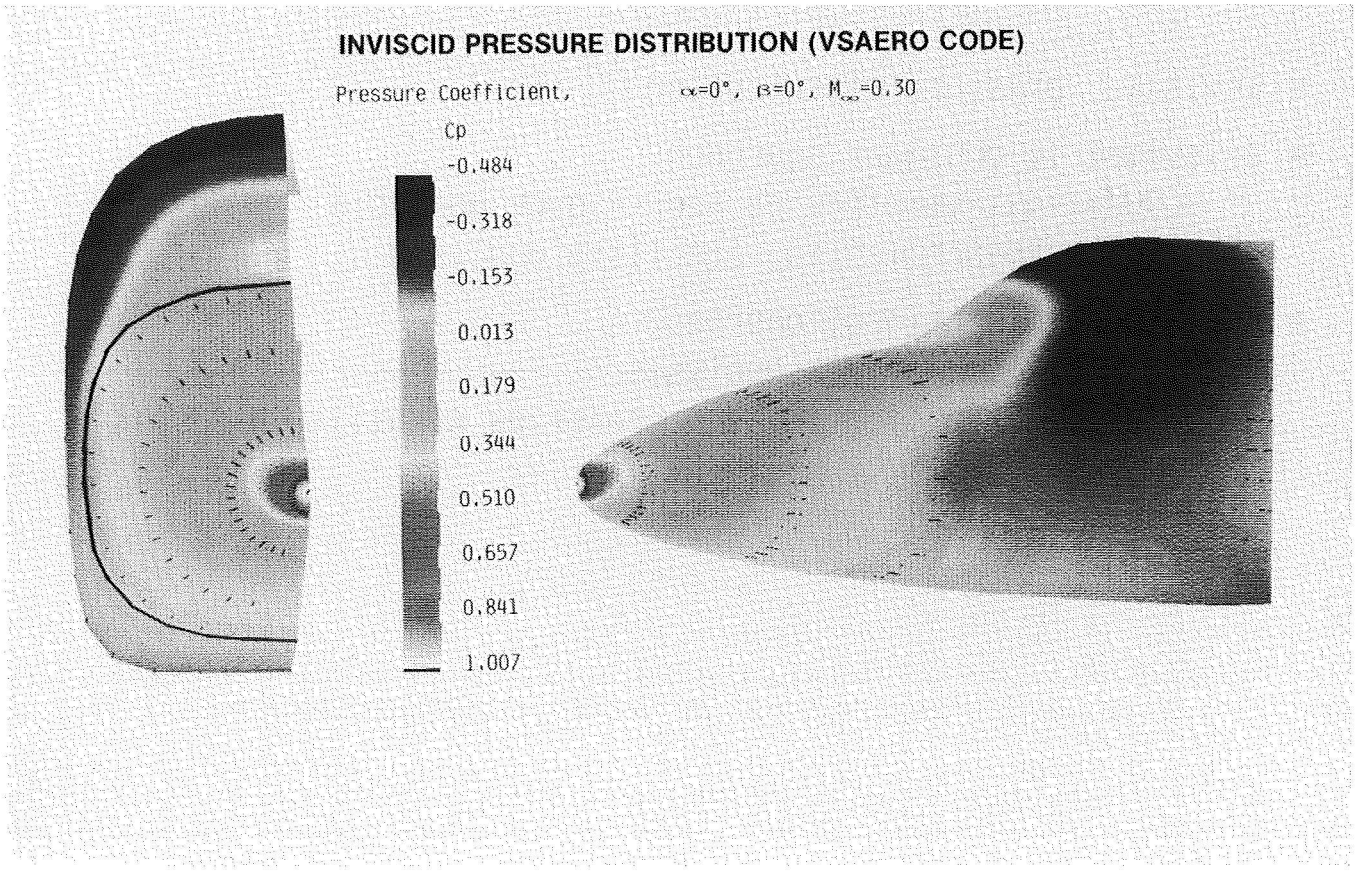

Figure 9

T303 NLF FUSELAGE FLIGHT EXPERIMENT
COMPARISON OF MEASURED AND CALCULATED PRESSURE DISTRIBUTIONS

Figure 10a presents a comparison of the VSAERO prediction and the measured pressure distribution along meridians at 0 and 45 degrees radials at zero angles of attack and sideslip. Figure 10b gives the comparison for the pressure lines on both sides of the fuselage. A good agreement can be observed between the measurements and the calculations for this flight condition. The effect of a surface wave near the radome joint at FS 44.0 along the 0 degrees radial can be observed in the measured pressure distribution (Figure 10a). The effect of the propellers and propeller-rotation direction on the pressure distribution can be seen in Figure 10b. The rotation sense of both propellers is counter clockwise when looking from the nose to the tail of the fuselage. Consequently, a local acceleration and deceleration is measured near the propeller plane on the port side and starboard side respectively, due to superposition of the propeller-induced flowfield over the basic flowfield over the nose.

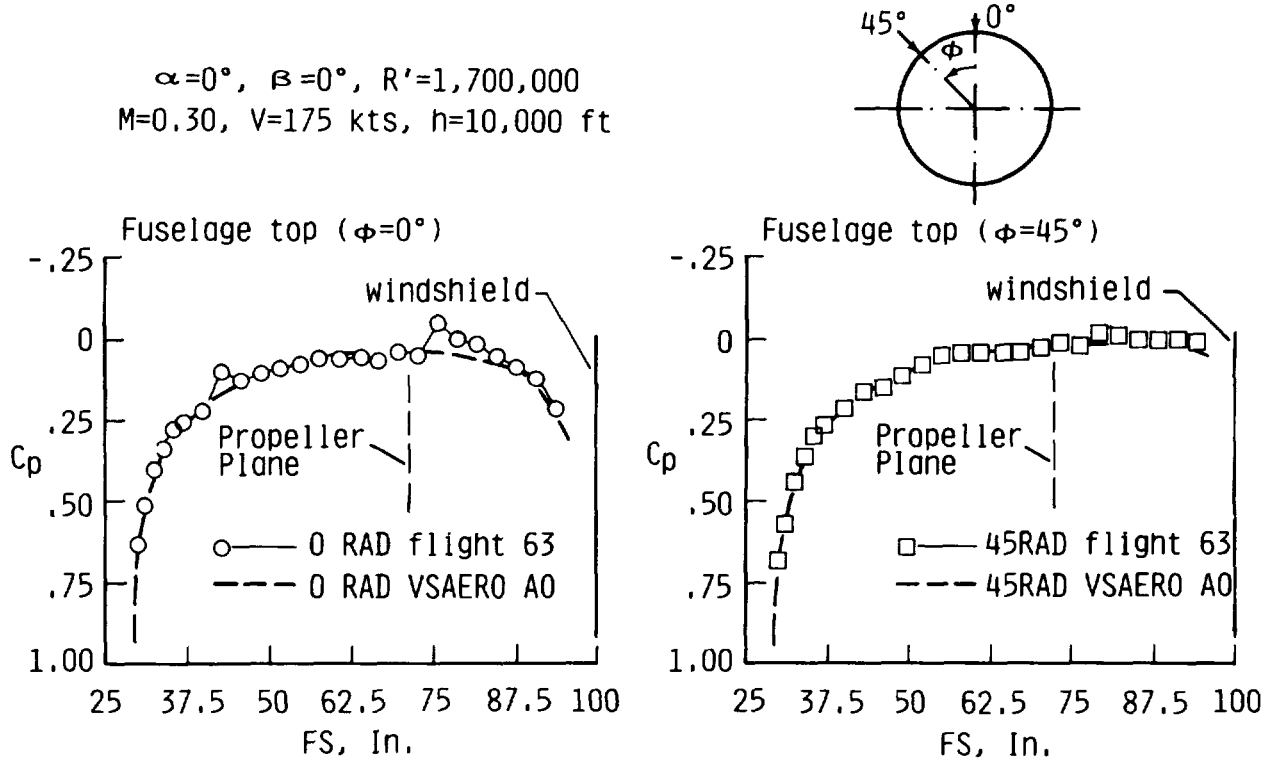

Figure 10a

T303 NLF FUSELAGE FLIGHT EXPERIMENT

Comparison Measured and Calculated Pressure Distributions

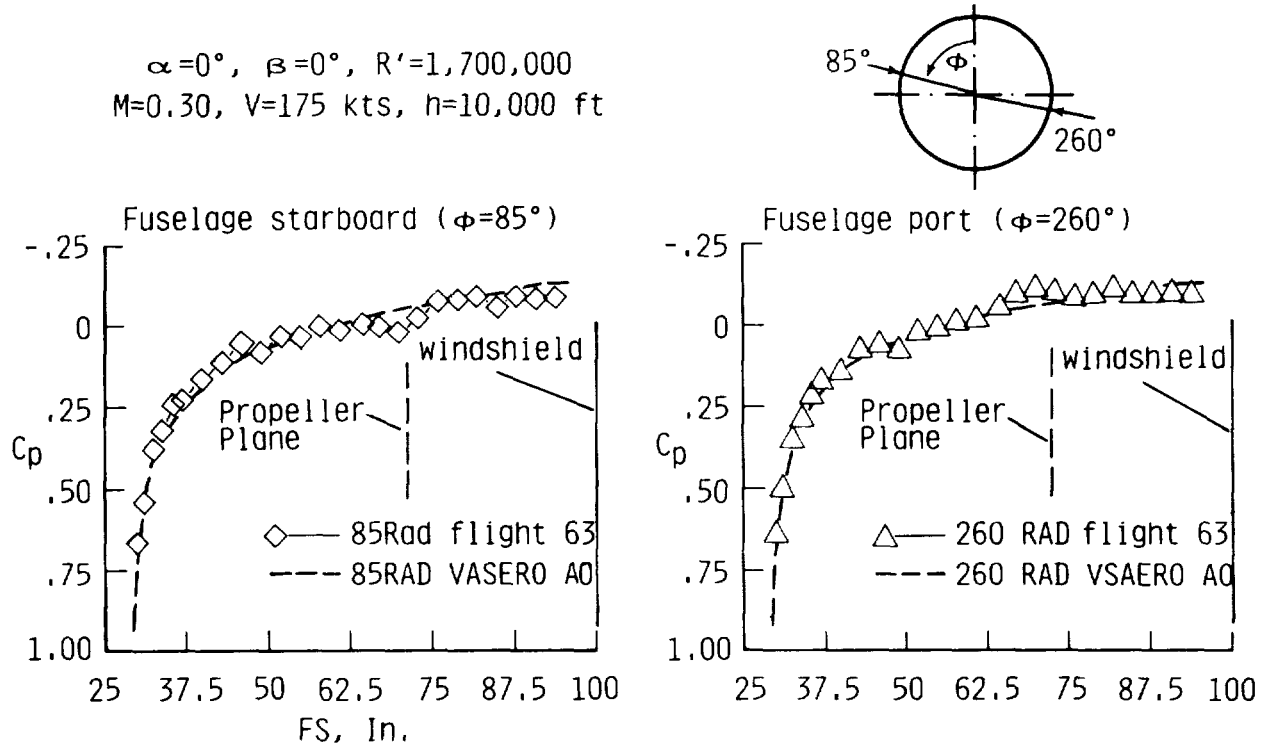

Figure 10b

T303 FUSELAGE FOREBODY ANALYSIS
INVISCID CROSS-FLOW VELOCITY DISTRIBUTION (VSAERO CODE)

Figure 11 shows the VSAERO prediction of inviscid surface velocities in circumferential directions for two angles of attack (zero sideslip) over the nonaxisymmetric T303 fuselage. At zero angle of attack a line of zero cross flow can be observed near the 45 degree radial position. In the area on top of the fuselage nose between this line and the vertical symmetry plane a circumferential (negative) cross flow towards the symmetry plane is predicted. For radial positions to the left of this line the inviscid circumferential flow is positive. Existence of reversal of inviscid cross-flow vectors presents formidable numerical problems for three-dimensional boundary-layer solvers, as discussed in Reference 9. An increase in angle of attack (see right side of Figure 11) results in an increase in magnitude of circumferential velocities and a shift of the reversal location to the lower quadrant of the fuselage nose. The magnitude of inviscid cross flow and its potential effects on three-dimensional boundary-layer stability can be assessed to first order by relating the magnitude of inviscid cross flow predicted for the fuselage to the cross-flow magnitude over a swept wing. An inviscid cross-flow velocity v_R/U_{inf} = .250 occurs in the leading-edge region of a wing with 15 degrees sweep. From previous laminar-flow experiments on swept wings it is known that cross flow becomes the dominant instability phenomenon only if wing leading-edge sweep is larger than 20 to 25 degrees.

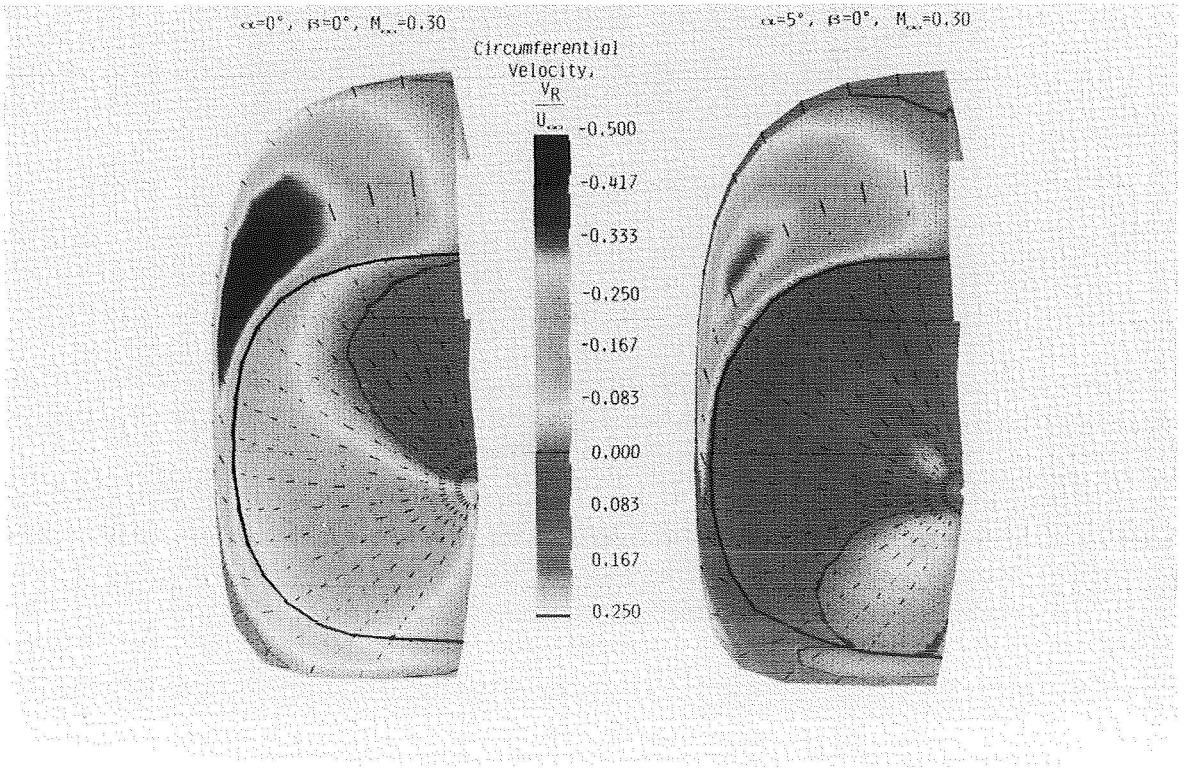

Figure 11

Figure 12a and 12b show the extent of laminar flow and the location of the transition front as indicated by the residue of sublimating chemical (naphthalene) at V = 170 kts at 10,000 ft. On top of the fuselage nose transition occurs about 12 inches ahead of the propeller plane (Figure 12b). Identification of transition extent on the port side of the fuselage was impossible due to roughness transition near the nose during this flight (see figure 12a). Transition extent on the starboard fuselage side (not shown here) is similar to the location on top. Note the effect of sweep of the leading edge of the masking-tape strips, used as coordinate system references, on transition: transition as evidenced by a turbulent wedge occurs 1 to 2 inches behind the beginning of the tape, suggesting a relieving effect on the roughness height as perceived by the laminar boundary layer due to the sweep angle (See Reference 10).

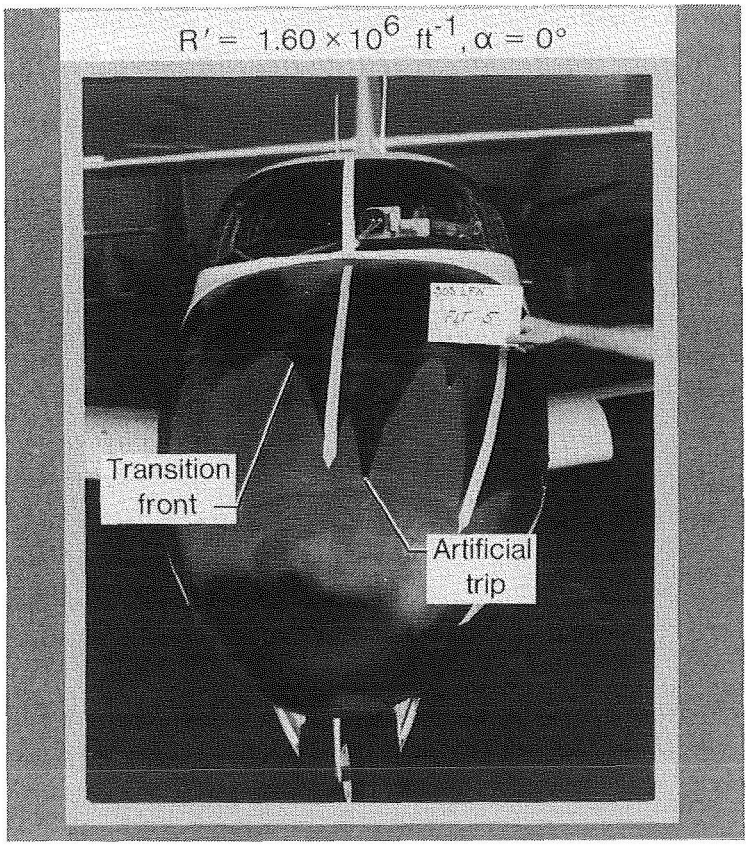

Figure 12a

Figure 12b

T303 FUSELAGE FOREBODY ANALYSIS
TOLLMIEN-SCHLICHTING STABILITY ANALYSIS - AXISYMMETRIC ANALOGUE APPROACH

For three streamlines over the top, side, and lower quadrant of the fuselage forebody (indicated as S1, S2 and S3 respectively in Figure 13), boundary-layer development has been calculated using an axisymmetric analogue approach. For each streamline, an equivalent axisymmetric body shape is defined using axial and radial coordinates of the streamline as meridian. This approach is justified in the absence of strong streamline divergence and boundary-layer cross flow (Reference 11). The axisymmetric boundary-layer development along each streamline is calculated using a modified version of Harris's method (Reference 12). Using a spectral method (Reference 13), the incompressible linear Tollmien-Schlichting stability of the laminar boundary layer is determined for each streamline along the body surface for a range of disturbance frequencies at the indicated unit Reynolds number. Figure 13a shows the frequency envelopes for the three streamlines as function of axial nose distance. Most amplified T.S. disturbance frequencies range from 1750 to 3000 Hz for the given flight condition. By comparison, the fundamental propeller and generator turbine frequencies are approximately 100 Hz and 800 Hz, respectively. A logarithmic amplification factor ("n-factor") of 9 is predicted in the region of the propeller plane at R' =1,400,000 at zero angle of attack (Figure 13a). Using the e^n-stability method as a transition prediction tool, and n=9 as criterion for transition onset, transition due to T.S. instability is expected to start near the propeller plane in the absence of exterior disturbances (noise of appropriate frequency and energy levels, free-stream turbulence, and manufacturing imperfections). The observed transition front at a slightly higher unit Reynolds number in Figure 12 corresponds to a calculated "n-factor" of about 6 to 8 in Figure 13a.

Figure 13b shows the calculated T.S. amplification factors along streamlines at an angle of attack of 5 degrees. An "n-factor" of 9 is predicted to occur slightly ahead of the propeller plane over the top of the fuselage forebody, while a lower T.S. instability growth is predicted over the lower quadrant of the nose due to an increased favorable axial pressure gradient at positive angle of attack.

T303 FUSELAGE FOREBODY ANALYSIS

Tollmien-Schlichting Stability Analysis,
Axisymmetric Analogue Approach

M=0.30, R'=1,400,000, α=0°, β=0°
Forebody streamlines (VSAERO)

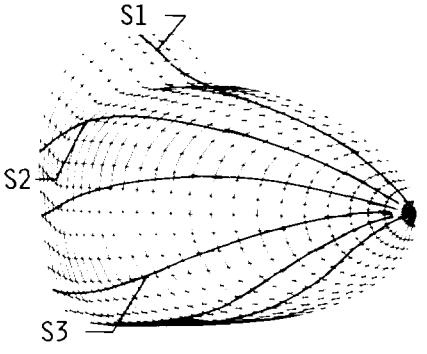

T.S. amplification (Harris-Sallyf)

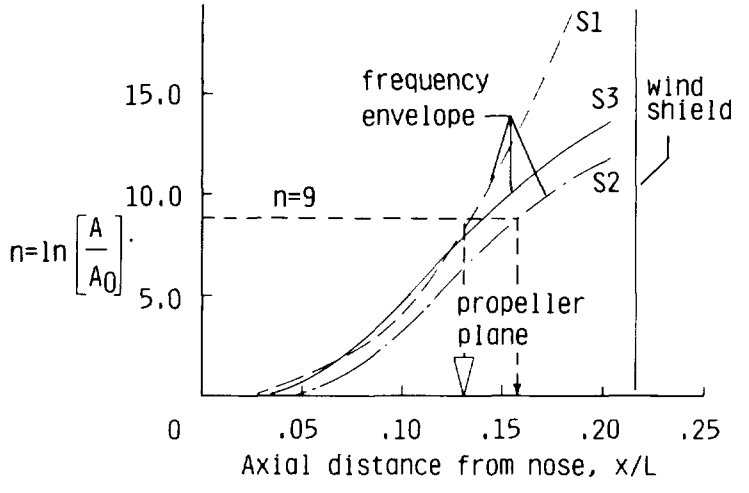

Figure 13a

Tollmien-Schlichting Stability Analysis,
Axisymmetric Analogue Approach

M=0.30, R'=1,400,000, α=5°, β=0°
Forebody streamlines (VSAERO)

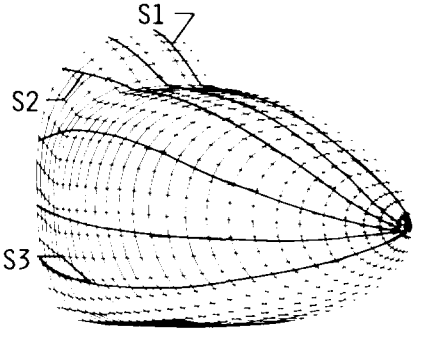

T.S. amplification (Harris-Sallyf)

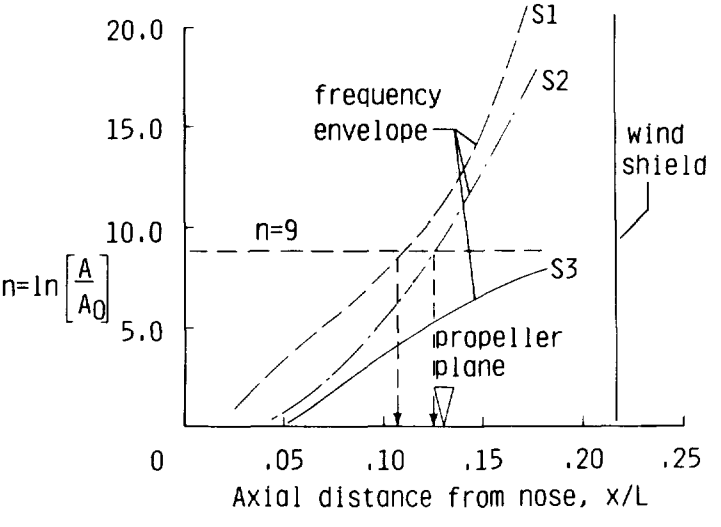

Figure 13b

T303 NLF FUSELAGE FLIGHT EXPERIMENT
HOT-FILM BOUNDARY-LAYER TURBULENCE INTERMITTENCY

Figure 14a and 14b show the observed turbulent intermittency of the hot-film signals over the top and starboard side of the fuselage nose respectively for a flight condition similar to the one shown in Figure 13 (R'=1,700,000). Hot-film intermittency shows transition to occur about 1 foot upstream of the propeller plane (transition location being defined here by 50-percent intermittency) in agreement with the flow visualization pattern. Note a reduction in intermittency from 65 to 50 percent downstream of the propeller plane (indicated by the solid symbol in the intermittency plot) in this flight condition on both top and side of the fuselage nose. The local favorable pressure gradient immediately behind the propeller plane (see Figure 10a and 10b) might explain the observed reduction in turbulence intermittency. Higher turbulent intermittency for the third hot film in both arrays is attributed to turbulent contamination of the previous hot film and its lead wires in the staggered array.

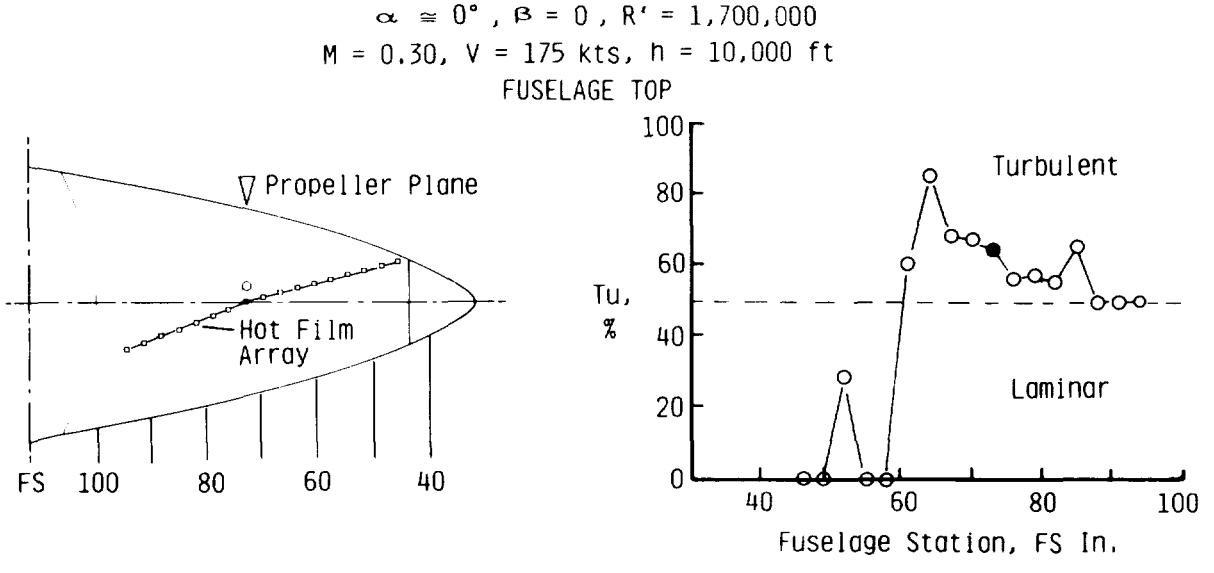

Figure 14a

T303 NLF FUSELAGE FLIGHT EXPERIMENT

Hot Film Boundary-Layer Turbulence Intermittency

$\alpha \cong 0°$, $\beta = 0$, $R' = 1{,}700{,}000$

$M = 0.30$, $V = 175$ kts, $h = 10{,}000$ ft

FUSELAGE STARBOARD SIDE

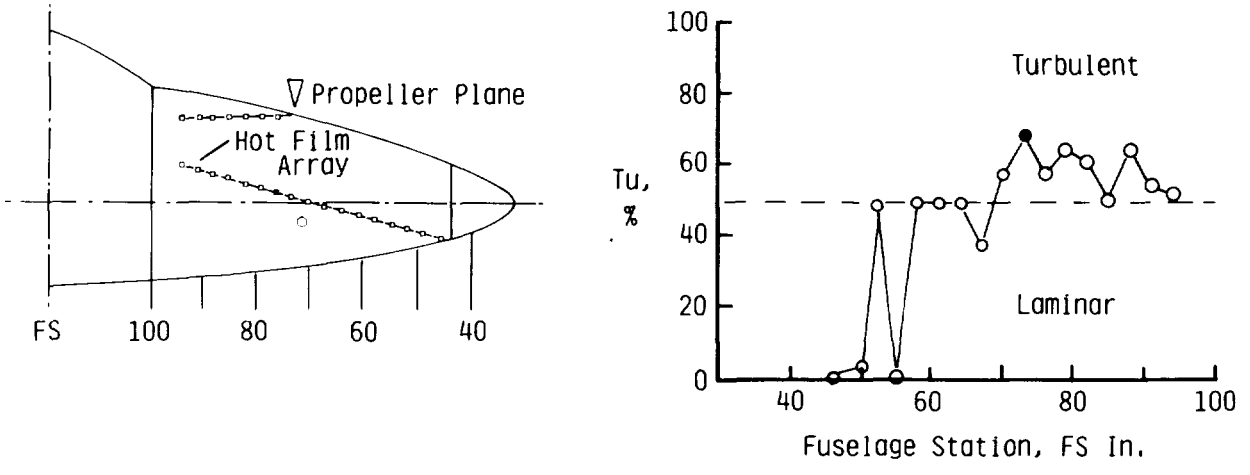

Figure 14b

T303 NLF FUSELAGE FLIGHT EXPERIMENT
HOT-FILM BOUNDARY-LAYER TURBULENCE INTERMITTENCY

Turbulent intermittencies obtained for both hot-film arrays are shown for a reduced unit Reynolds number R' = 800,000 at zero angle of attack in Figure 15a and 15b. Decrease in Reynolds number for this flight condition results in a large increase in laminar run on both top and side of the fuselage. Transition onset is indicated to occur behind the propeller plane, while intermittencies in the turbulent boundary layer beyond FS 90 grow to levels over 80 percent, in contrast to the levels indicated in Figures 14 at the higher unit Reynolds number.

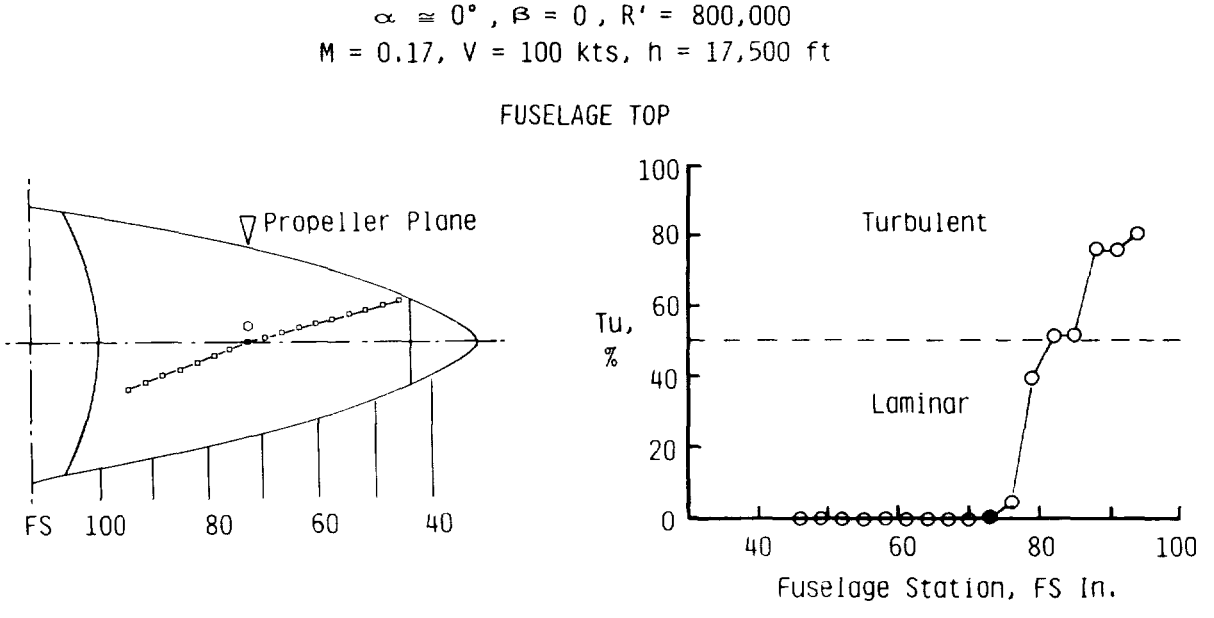

Figure 15a

T303 NLF FUSELAGE FLIGHT EXPERIMENT

Hot Film Boundary-Layer Turbulence Intermittency

$\alpha \cong 0°$, $\beta = 0$, $R' = 800{,}000$

$M = 0.17$, $V = 100$ kts, $h = 17{,}500$ ft

FUSELAGE STARBOARD SIDE

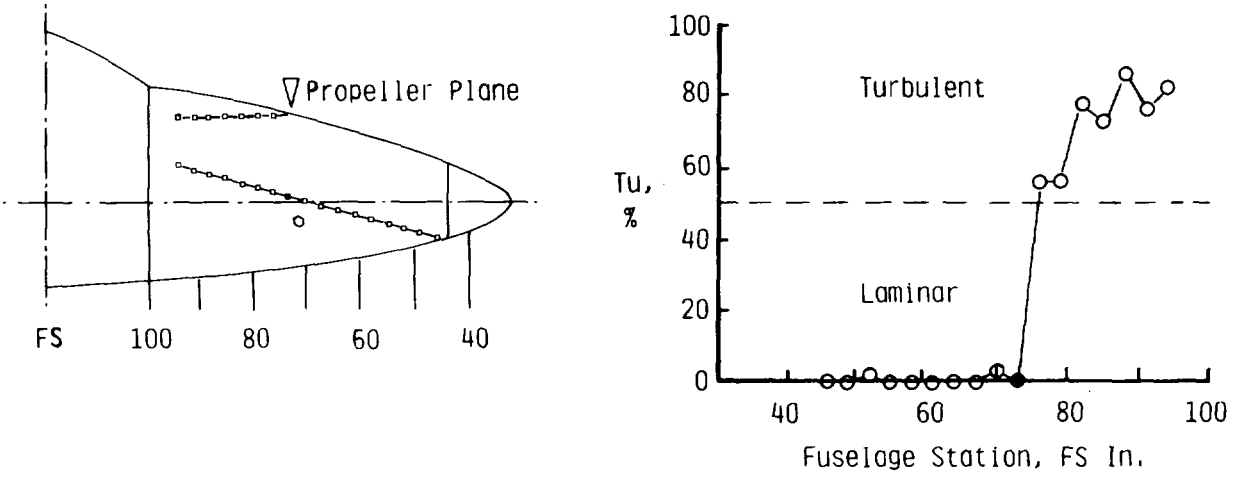

Figure 15b

T303 NLF FUSELAGE FLIGHT EXPERIMENT
PRELIMINARY FLIGHT-TEST RESULTS
CONTINUATION FLIGHT-TEST PROGRAM

The results from only a limited number of flights and initial data reduction are summarized in Figure 16a. Continuation of the flight program is planned to explore the location and mode of transition on this nonaxisymmetric fuselage shape under varying flight conditions as indicated in Figure 16b. The prototype airplane used in this program allows for extended glide flight with wind-milling propellers and stopped generators. Study of transition location without streamtube and noise effects of the propellers and generators provides an opportunity to assess acoustic receptivity phenomena in the boundary layer under study. Subsequent analysis of microphone and hot-film signals in time and frequency domain is planned to help understanding of the transition process under varying flight conditions. Analysis of stability of the laminar boundary layer over the fuselage nose using a full three-dimensional method can determine in detail the significance of cross flow in the location of transition as measured with the hot films.

Preliminary Flight Test Results

- Agreement pressure distribution calculation with measurement at α=0° (β=0°)
- Observed extent of laminar boundary layer at α=0° (β=0°) is 2.5 to 4.5 ft along surface: R_{TR} = 2.0-5.0 million
- Calculated T.S. amplification factor is 6-9 in observed transition range

Figure 16a

Continuation Flight Test Program

- Planned flight matrix
  $-2° < \alpha < 7.5°$
  $-10° < \beta < 10°$
  $750{,}000 < R' < 2{,}500{,}000$
  Propeller/generator power setting/RPM
  (including glide flights)
- Spectral analysis hot film and microphone signals
- Identification transition mode(s)

Figure 16b

EFFECT OF FLIGHT ALTITUDE ON UNIT REYNOLDS NUMBER

The transition observations over the nonaxisymmetric fuselage shape obtained in this flight program are obtained at low Mach numbers (0.20 to 0.35) and flight altitudes from 5,000 to 20,000ft, resulting in unit Reynolds numbers of 750,000 to 2,500,000 per foot (Figure 17). Typical flight conditions of subsonic (and supersonic) transports occur at comparable unit Reynolds numbers, however, at considerably higher flight altitudes and Mach numbers. As demonstrated in Reference 1 for a business-jet type body shape, Tollmien-Schlichting stability of the axisymmetric laminar boundary layer is greatly increased when Mach number increases to 0.80 as compared to incompressible conditions. Transition length Reynolds numbers of 20 million (see Figure 5) and higher seem possible at high-subsonic flow conditions when the favorable effect of flow compressiblity on boundary-layer stability is included. Study of effects of nonaxisymmetry and noise on transition location over a practical fuselage shape, which are investigated in the present flight program, is relevant to assess the achievability of substantial amounts of sufficiently stable laminar flow over the geometries indicated in Figure 1.

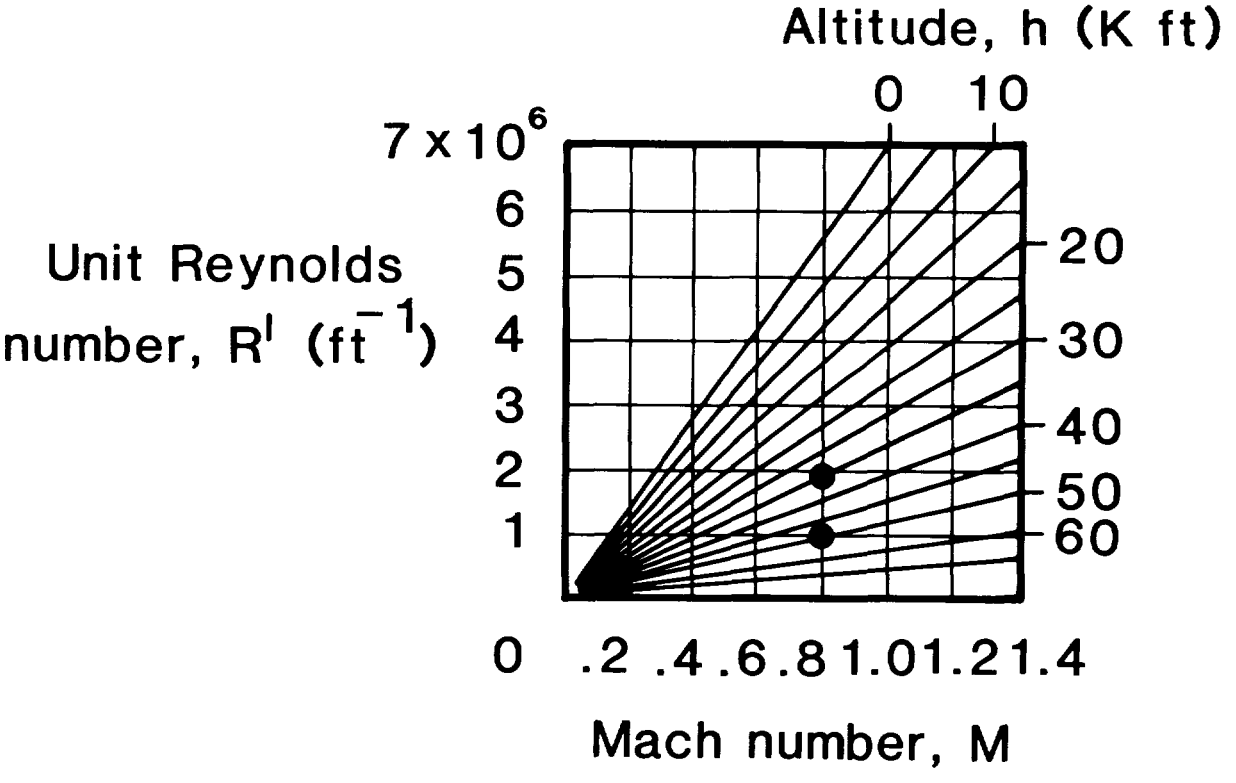

Figure 17

RESEARCH NEEDS FOR LAMINAR FLOW OVER FUSELAGES

The present study is the first flight investigation of stability of natural laminar flow over a practical nonaxisymmetric fuselage shape under varying free-stream conditions. Figure 18 indicates areas where further work is needed to understand the transition process over nonaxisymmetric fuselage geometries and to define application limits for laminar flow over body shapes in a fashion similar to the limits currently emerging for laminar flow over swept and unswept lifting surfaces. Detailed microscopic boundary-layer development and boundary-layer stability measurements are needed on bodies at sufficiently high length Reynolds numbers in a large low-turbulence ground facility as well as in flight to assess adequacy of boundary-layer and boundary-layer stability calculation methods. Similarly, wind-tunnel and flight experiments are required to investigate the stability of laminar flow over nonaxisymmetric bodies at subsonic and supersonic flight conditions. Only very limited studies of effects of manufacturing imperfections on the stability of laminar flow over fuselage geometries have been published. Waviness and step tolerances derived for wing-like geometries (Reference 10) need to be assessed for fuselage geometries which in general are characterized by axial pressure gradients that are less favorable than pressure gradients present over wings.

- Development and application of 3-D boundary-layer and boundary-layer stability codes for fuselage geometries
- Detailed 3-D boundary-layer measurements on bodies at high Reynolds numbers
- Body experiments at compressible flow conditions
- Study of NLF manufacturing tolerances for body geometries

Figure 18

REFERENCES

1. Vijgen, P. M. H. W., Dodbele, S. S., Holmes, B. J., and Van Dam, C. P., "Effects of Compressibility on Design of Subsonic Natural Laminar Flow Fuselages," AIAA 4th Applied Aerodynamics Conference, San Diego, June 1986. AIAA Paper 86- 1825CP.

2. Georgy-Falvy, D., "Effect of Pressurization on Airplane Fuselage Drag," J. of Aircraft, Vol. 2, No. 6, 1965, pp. 531-537.

3. Dodbele, S. S., Van Dam, C. P., Vijgen, P. M. H. W., and Holmes, B. J., "Shaping of Airplane Fuselages for Minimum Drag", AIAA 24th Aerospace Science Meeting, Reno, 1986. AIAA Paper 86-0316, also: J. of Aircraft, Vol. 24, No. 5, May 1987, pp. 298-304.

4. Williams, K.L., Vijgen, P. M. H. W., and Roskam, J. R., "Natural Laminar Flow and Regional Aircraft," SAE Paper 850864, 1985 SAE General Aviation Aircraft Meeting & Exposition, Wichita, Kansas. Published in SAE Transactions, Vol. 4, 1985.

5. Hastings, E., Schoenster, J., Obara, C., Jones, M., Dodbele, S., Faust, G., and Mungur, P., "The NLF Nacelle Flight Experiment", Symposium on Natural Laminar Flow and Laminar Flow Control Research, NASA CP 2487, 1987, pp. 887-921.

6. Boltz, F.W., Kenyon, G.C., and Allen, C.Q., "The Boundary-Layer Transition Characteristics of Two Bodies of revolution, a Flat Plate and an Unswept Wing in a Low-Turbulence Wind Tunnel," NASA Technical Note D-309, April 1960.

7. Carmichael, B. H., "Underwater Vehicle Drag Reduction Through Choice of Shape," AIAA Second Propulsion Joint Specialist Conference, June 1966, AIAA Paper 66-657.

8. Maskew, B., "Prediction of Subsonic Aerodynamic Characteristics - A Case for Low-Order Panel Methods," J. of Aircraft, Vol. 19, No.2, 1982, pp. 157-163.

9. Harris, J., and Iyer, V., "Numerical Solutions of the Compressible 3-D Boundary-Layer Equations for Aerospace Configurations with emphasis on LFC," Symposium on Natural Laminar Flow and Laminar Flow Control Research, NASA CP 2487, 1987, pp. 517-545.

10. Holmes, B.J., Obara, C.J., Martin, G.L., and Domack, "Manufacturing Tolerances for Natural Laminar Flow Airframe Surfaces," SAE Paper 850863, 1985 SAE General Aviation Aircraft Meeting & Exposition, Wichita, Kansas.

11. Cooke, J.C., and Hall, M.G., "Boundary Layers in Three Dimensions", in Progress in Aeronautical Sciences, Volume 2, Boundary Layer Problems, Ed. by A. Ferri, Pergamon, 1962.

12. Harris, J.E., and Blanchard, D.K., "Computer Program for Solving Laminar, Transitional, or Turbulent Compressible Boundary-Layer Equations for Two-Dimensional and Axisymmetric Flow," NASA TM-83207, Feb. 1982.

13. Srokowski, A.J., and Orszag, S.A., "Mass Flow Requirements for LFC Wing Design", AIAA Paper 77-1222, 1977.

STATUS REPORT ON A NATURAL LAMINAR-FLOW NACELLE FLIGHT EXPERIMENT

Summary
Earl C. Hastings, Jr.

Nacelle Design
G. K. Faust and P. Mungur

Nacelle Aerodynamic Performance
Clifford J. Obara and S. S. Dodbele

Effects of Acoustic Sources
James A. Schoenster and Michael G. Jones

[redacted]

SUMMARY

Earl C. Hastings, Jr.
Langley Research Center
Hampton, Virginia

SUMMARY

EXPERIMENT DESCRIPTION

The natural laminar-flow (NLF) nacelle experiment is part of the Langley Research Center viscous drag reduction program, and has the dual objectives of studying the extent of NLF on full-scale nacelles in a flight environment and the effect of acoustic disturbance on the location of transition on the nacelle surface. It is a cooperative experiment between the General Electric Company, the Low-Speed Aerodynamics Division, and the Acoustics Division of Langley Research Center. Each of these organizations has contributed to this paper.

This flight experiment is being conducted in two phases. In Phase I, which has been completed, an NLF fairing was flown on a full-scale Citation nacelle to develop the experiment technique and establish feasibility. Results of Phase I are presented in references 1 and 2. In the Phase II configuration shown in the photograph, full-scale, flow through, NLF nacelles are being evaluated. The nacelles are located below the right wing of an experimental NASA OV-1 aircraft. One controlled noise source is located in an underwing pod outboard of the nacelle, and a second is located in the nacelle centerbody. Several NLF nacelle geometries will be flown during Phase II. The data presented here are for the shape defined as GE2 in Section II. Tests are now being conducted with a thicker shape (defined as GE3), but those data are not available at this time.

Phase II Configuration

The measurements of primary interest are the static pressure distribution and transition location on the nacelle surface, and the fluctuating pressure levels associated with the noise sources. (These measurements are discussed in more detail in later sections of the paper.) Data are collected in straight and level flight, with the noise sources off, and with various combinations of acoustic frequencies and sound pressure levels. The test unit Reynolds number is about 1.8×10^6 per foot. During data acquisition, the right hand aircraft engine is feathered to reduce propeller interference effects.

RESULTS

The results of the Phase II tests to date indicate that on shape GE2, natural laminar flow was maintained as far aft as the afterbody joint at 50 percent of the nacelle length. An aft facing step at this joint caused premature transition at this station. No change was observed in the transition pattern when the noise sources were operated. Computations of surface pressures, using a low-order surface-panel method, showed reasonable agreement with the measured pressure distributions, although the magnitude differed somewhat from the measured values.

NACELLE DESIGN

G. K. Faust and P. Mungur
General Electric Company
Cincinatti, Ohio

[redacted]

NATURAL LAMINAR-FLOW NACELLE CONCEPT

The external cowlings of engine nacelles on large turbofan-powered aircraft are attractive candidates for application of natural laminar flow. These nacelles usually have shorter characteristic lengths than other candidate surfaces such as wings and fuselages and therefore have lower characteristic Reynolds numbers. Also, since nacelles are not required to provide lift, they can be shaped to have pressure distributions favorable to laminar flow without too much concern for lift and moment characteristics that necessarily influence the design of natural laminar-flow wings.

The figure on the right shows the natural laminar flow nacelle (NLF) concept. On the typical conventional nacelle, shown on the left, the flow accelerates to a curvature-induced velocity peak near the lip and then decelerates--at first quite rapidly--over the remainder of the nacelle length. Transition occurs near the start of the deceleration, so turbulent flow with high friction coefficient exists over most of the nacelle length. On the other hand, the natural laminar flow nacelle is contoured to have an accelerating flow over most (about 70%) of its length, so transition is delayed, and a relatively lower friction drag exists over most of the nacelle.

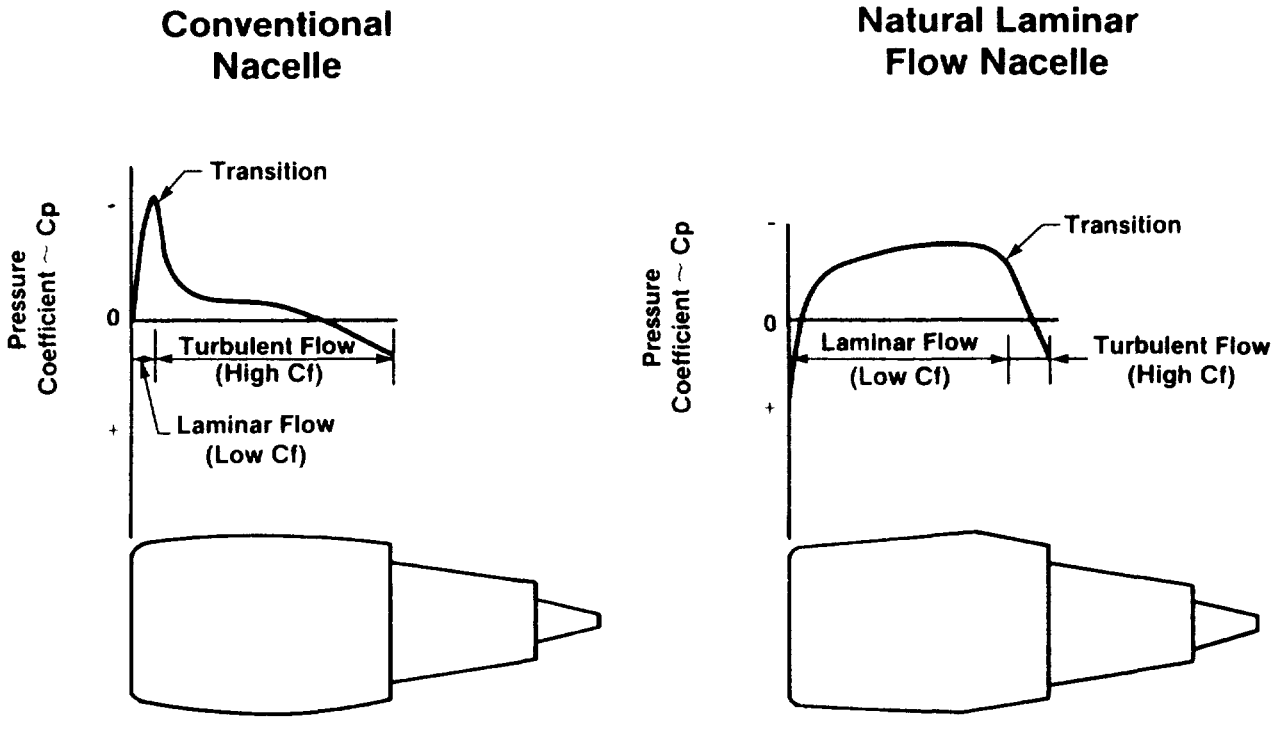

MOTIVATION FOR LAMINAR FLOW NACELLE

The motivation for development of the LFN is a potential 40 to 50 percent reduction in nacelle friction drag. For a large commercial transport with wing-pylon mounted engines, this reduction is equivalent to a 1 to 2 percent reduction in total aircraft drag and cruise fuel burn.

- **Reduction in Nacelle Friction Drag** **40% to 50%**
- **Reduction in Aircraft Total Drag** **1% to 2%**
- **Reduction in Cruise Fuel Burn** **1% to 2%**
- **One 747 Uses Approximately 13,000,000 Gallons/Year**

BACKGROUND WIND TUNNEL TESTS

Several wind tunnel tests have been undertaken by General Electric to explore NLF nacelle design parameters. Two proof-of-concept tests were run in the NASA Langley 16-Foot Transonic Tunnel. The left photograph shows a test model of an isolated NLF nacelle. The right photograph shows a test of an NLF nacelle installed on a high wing transport model. The tests validated the estimated drag reduction and indicated that installation effects did not adversely affect the reduction.

The contouring required to achieve natural laminar flow results in a sharper external lip than that on a conventional nacelle. Therefore, the NLF nacelle must operate at higher mass flow ratio to avoid a lip velocity peak that would cause transition. For the same throat area, the NLF nacelle must then have a lower internal contraction ratio, so the internal lip is also sharper. There is, of course, a reason for blunt lips on conventional nacelles. These lips allow the inlet to operate separation-free with acceptable recovery and distortion at off-design, cross-wind, and engine-out conditions. Achieving good off-design performance and operability is the greatest challenge facing the NLF nacelle designer.

Approaches to the off-design challenge have included tests in ONERA wind tunnels of a nacelle with internal lip suction and a nacelle with translating lip. These models are shown in the two photographs on the next page.

Isolated NLF Nacelle

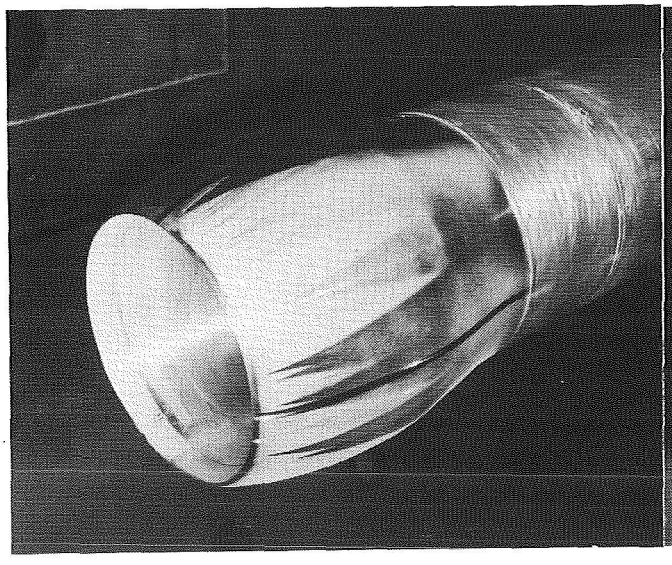

NLF Nacelle on High Wing Transport Model

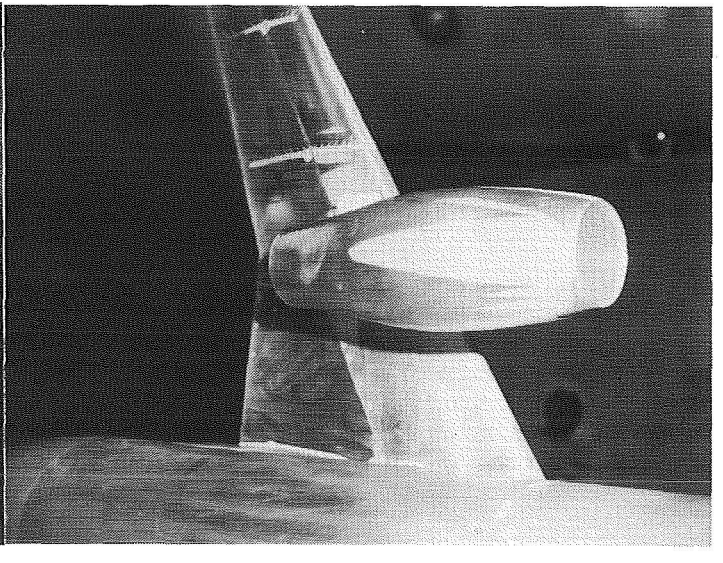

NACELLE WITH INTERNAL LIP SUCTION

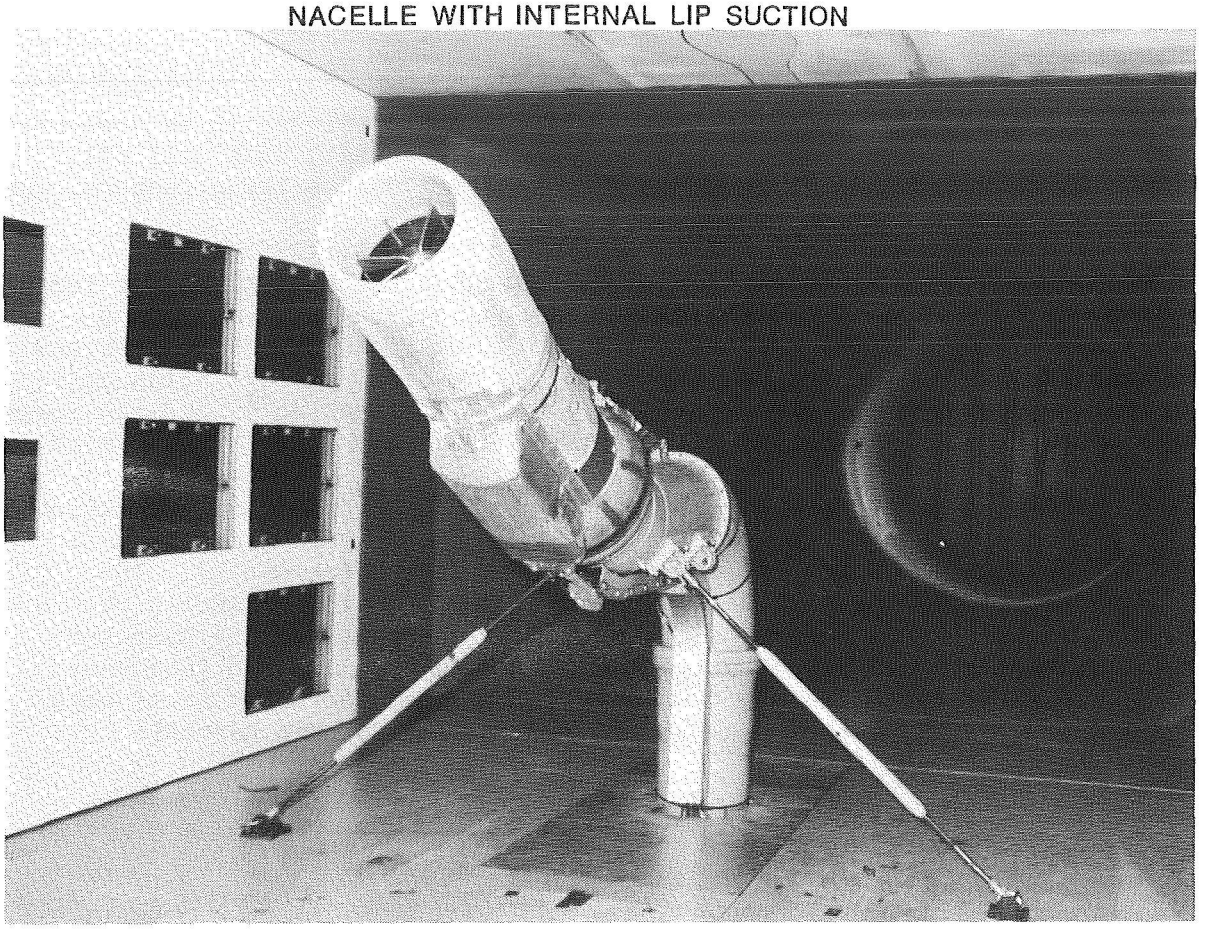

NACELLE WITH TRANSLATING LIP

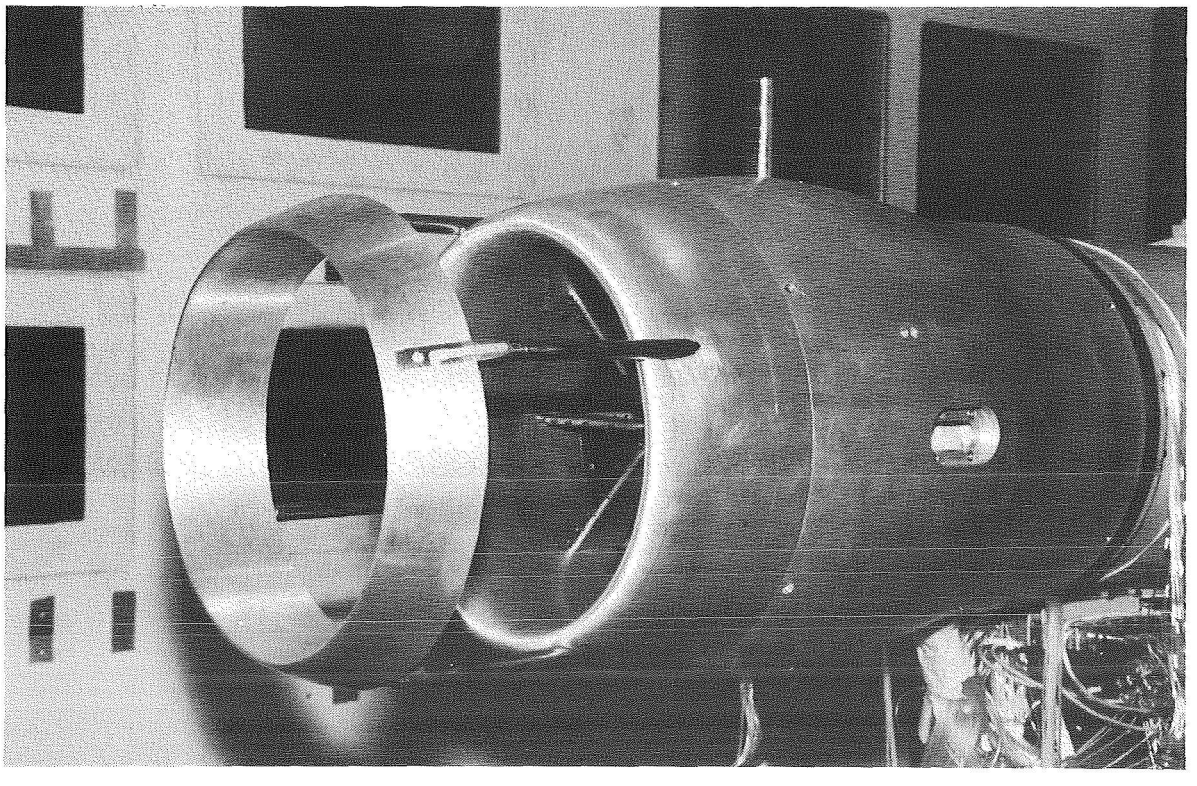

Given the difficulties associated with sharp-lip inlets, it is desirable to use the bluntest lip (less favorable pressure gradient) that will still maintain laminar flow in the presence of prevailing destablizing factors. One such destablizing factor is noise.

Many wind tunnel experiments have demonstrated the sensitivity of laminar boundary layers to acoustic disturbances of appropriate frequencies and amplitudes. These disturbances excite Tollmien-Schlichting (T-S) waves and have been shown to lower the critical Reynolds number. Amplification of T-S waves is the primary type of instability in the accelerating, two-dimensional flow over a smooth NLF nacelle in the low-turbulence, cruise flight regime.

Potential noise sources in flight include both airframe and propulsion system components as shown below. However, flight experiments of acoustic effects on laminar flow are few and not definite in their results. The results of a preliminary analytical stability study of a NLF nacelle at cruise are shown in the figure on the next page. This figure shows the computed neutral stability curve as a function of chordwise distance and frequency normalized by the blade passing frequency. The study indicated there were regions where T-S waves may be amplified by the dominant and harmonic frequencies of the engine's fan.

POTENTIAL CRUISE NOISE SOURCES

PROPULSION SOURCES

- FAN
- COMPRESSOR
- TURBINE
- CORE/COMBUSTION
- JET

AIRFRAME SOURCES

- TURBULENT BOUNDARY LAYERS
- TRAILING EDGES AND WAKES
- ATMOSPHERIC DISTURBANCES
- OSCILLATING SHOCKS
- SEPARATED FLOWS
- IMPINGING FLOWS
- CAVITIES
- PROJECTIONS
- PANEL VIBRATIONS

TURBOFAN STABILITY ANALYSIS

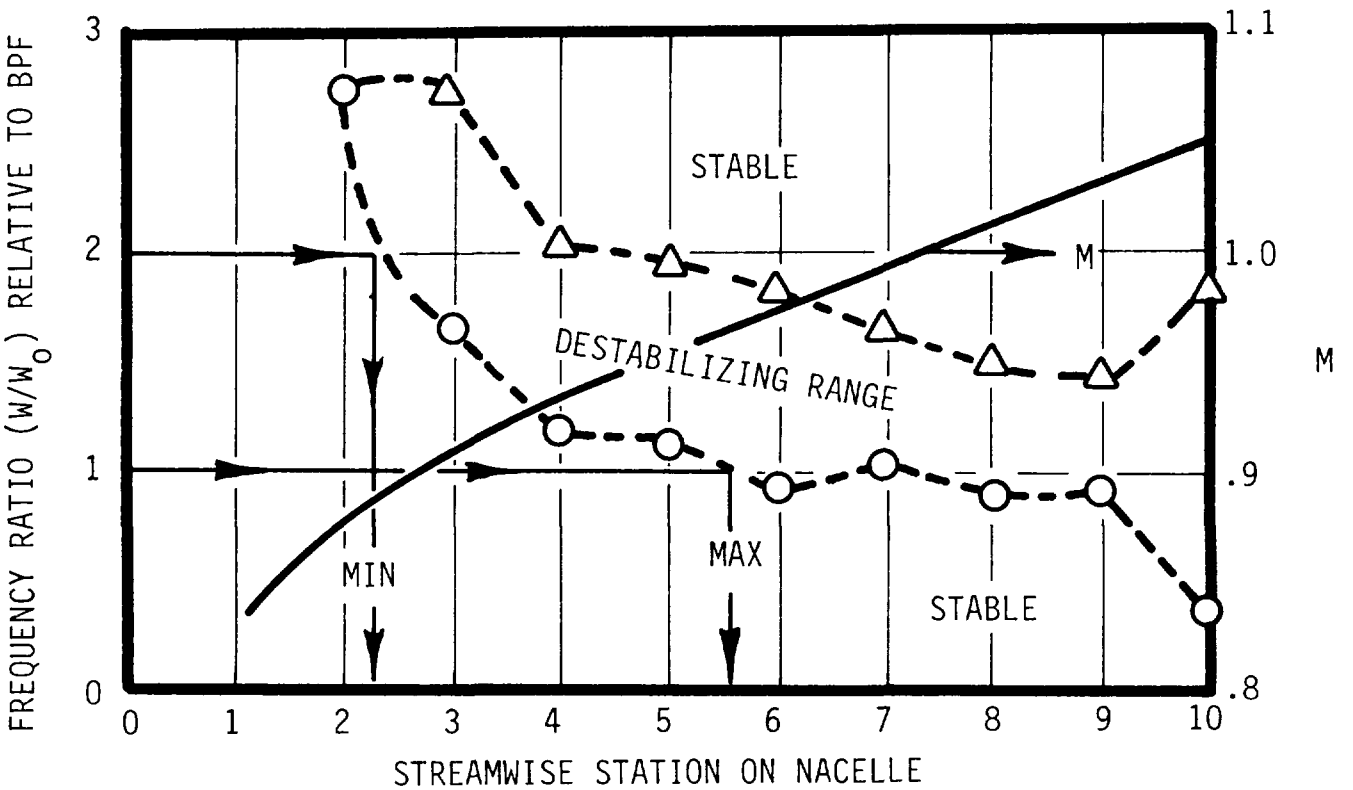

WHY A FLIGHT TEST?

In wind tunnel tests of NLF nacelles, as with many other wind tunnel transition tests of aircraft components, there is concern about the application of results to the full-scale flight environment as shown in the left figure. The need to study acoustic effects adds further uncertainties.

Although full scale testing of the NLF nacelle concept in its intended flight environment is technically feasible, economic considerations and the desire to obtain fundamental acoustic transition data in a controlled noise environment prompted the decision to conduct a low-speed flight test. A joint NASA-GE program to conduct the test with Langley's OV-1B airplane was initiated.

Conducting a low-speed flight test in a controlled noise environment reflects the decision to obtain fundamental acoustic transition data for use in developing prediction techniques, but makes the application of the results to the full scale NLF nacelle at cruise less straightforward. For instance, the favorable effects of compressibility on laminar flow are not addressed by the test.

As shown in the figure on the right, the allowable flight conditions (limited by structural considerations) of the OV-1B with the laminar flow nacelle (LFN) provide unit Reynolds numbers in the range of those for large subsonic transports.

OV-1B with LFN

WIND TUNNEL CONCERNS

- REYNOLDS NUMBER
- TURBULENCE
- NOISE SIMULATION
- INSTRUMENTATION NOISE

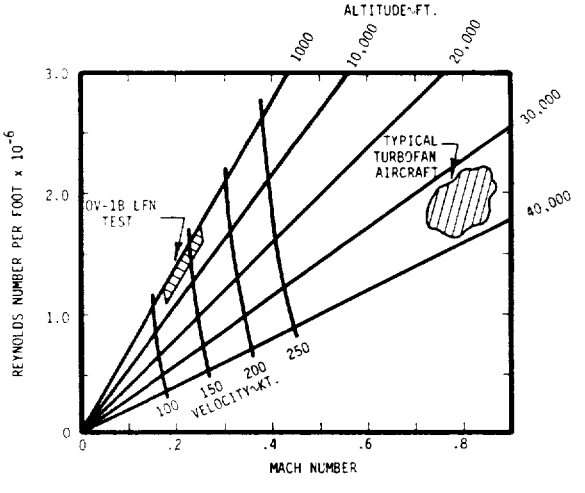

TEST VEHICLE CONFIGURATION

The Grumman OV-1B Mohawk is an Army reconnaissance aircraft powered by two Lycoming T53 turboprop engines. The research aircraft modified for NLF nacelle testing is shown in this figure.

The flow-through NLF nacelle is mounted on the external store pylon below the right wing. The mounting structure allows the nacelle to be locked at various pitch and yaw angles relative to the aircraft.

A noise source consisting of a JBL compression driver and exponential horn is located in the nacelle centerbody. A second noise source and a video camera are located in a pod outboard of the nacelle.

Installation Schematic of NLF Nacelle and Noise Source on OV-1B

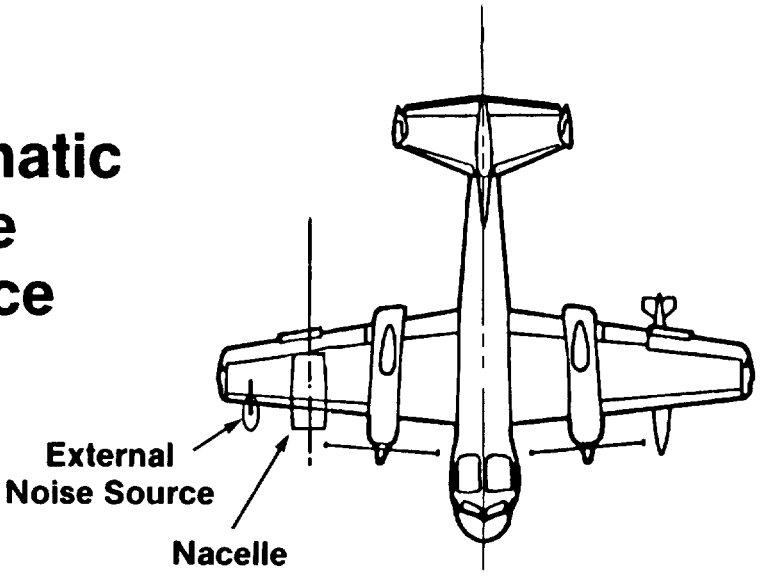

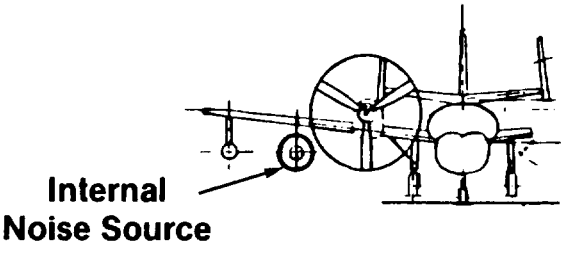

OVERVIEW OF NACELLE AERO-ACOUSTIC DESIGN

The objective of the aero-acoustic design was to determine a nacelle shape and corresponding pressure distribution that would provide enough sound-induced amplification of T-S waves to influence transition location. Due to the limited sound pressure level available from the controllable noise sources, it was important to design for adequate amplification while avoiding designs with so much amplification that free-stream turbulence would cause uncontrolled transition. Toward this end, three nacelles were designed.

This figure shows an overview of the design methodology. An incompressible flow code was first used to compute the pressure distributions on candidate nacelle shapes chosen from a family of super ellipses. The pressure distribution was then evaluated for regions of instability. To avoid the expense of running boundary-layer and stability codes, the initial screening made use of available stability characteristics of Falkner-Skan flows. From the calculated pressure distribution and Falkner-Skan parameter, the distribution of critical Reynolds number was determined. A comparison of critical and actual Reynolds numbers identified shapes that had a range of potential unstable regions. Final selection was then based on boundary layer stability calculations and empirical data as discussed below.

OV-1B LFN DESIGN PROCEDURE

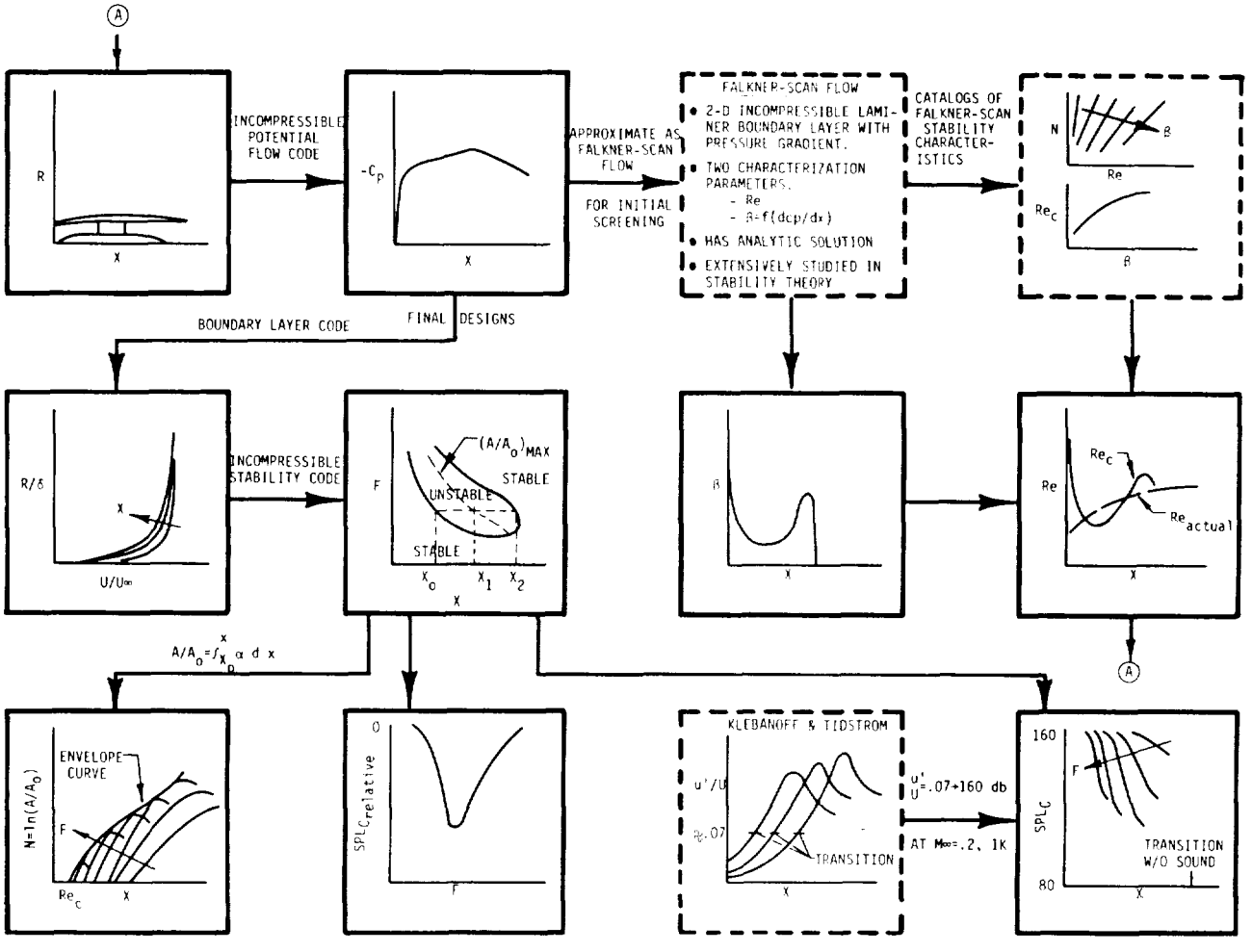

STABILITY ANALYSIS

The chordwise amplification spectra were evaluated with an incompressible stability code. Boundary-layer parameters required for input to this code were calculated with the VBGLP code of NASA TM-83207. The left figure shows instability regions, and the right figure shows integrated amplification spectra for three pressure distributions. These distributions correspond to the three final nacelle shapes denoted GE1, GE2, and GE3 in order of most to least stable. These shapes were selected by using the integrated amplification factors to evaluate critical Sound Pressure Level (SPL) spectra and the influence of SPL on transition location.

Instability Regions

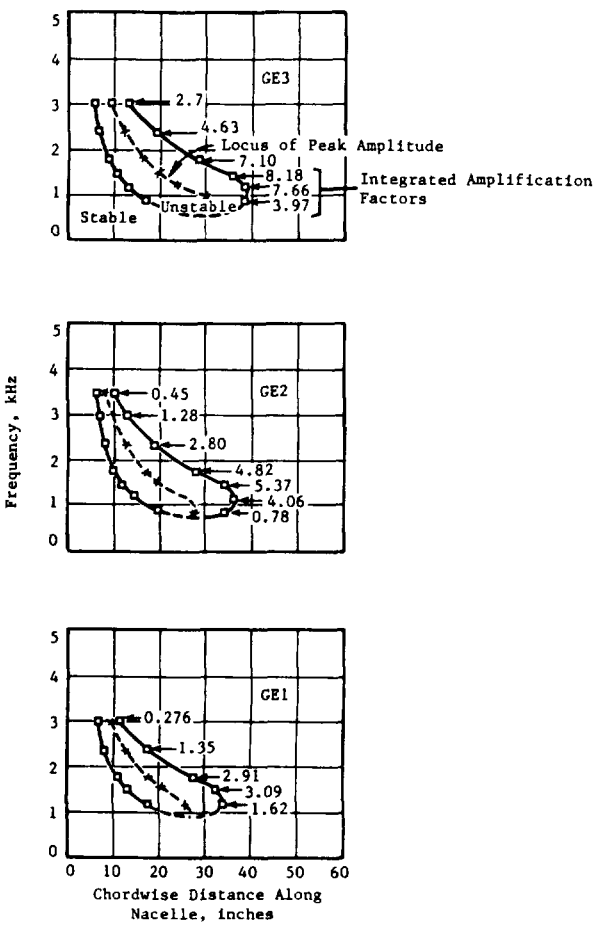

Pressure Distributions

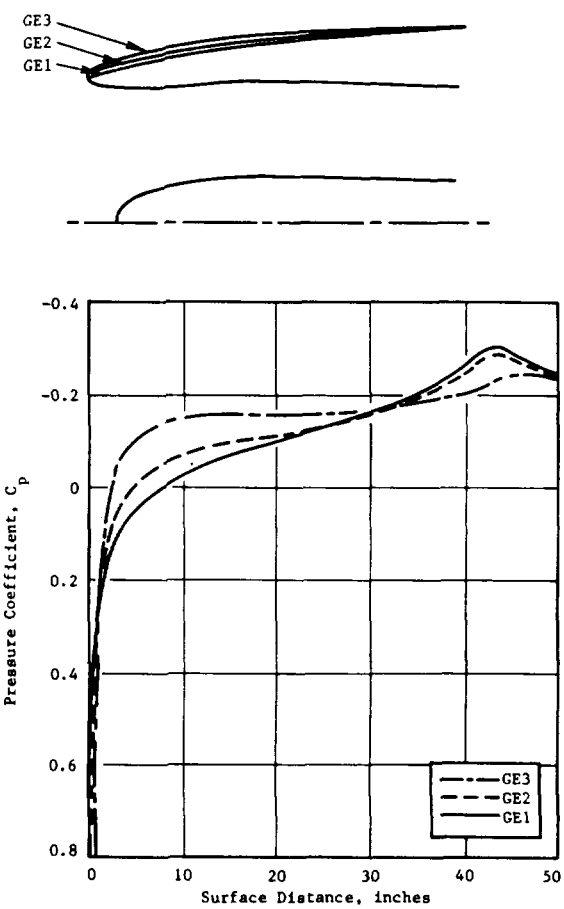

ESTIMATE OF CRITICAL SPL AND TRANSITION LOCATION

The critical SPL is defined as the minimum sound pressure required to move the transition location upstream. Since the boundary-layer amplification is frequency dependent, the critical SPL will also be frequency dependent. Its evaluation requires knowledge of the normalized acoustic receptivity of the boundary-layer wave which is in fact a vortical wave. It is defined as the ratio of the normalized fluctuating velocity associated with sound induced vorticity (boundary-layer wave) to the amplitude of the acoustic pressure field. Analytically, as shown by Mungur and Swift (Ref. 1), this is a function of the mean velocity profile, the acoustic wave number, and the directionality of the sound wave. It can vary from 0 (no coupling) to 1 (fully coupled).

Another quantity of relevance is the critical fluctuating velocity above which transition occurs. Based on the measurements of Klebanoff and Tidstrom (Ref. 2), seven percent of the free-stream velocity appears to trigger the transition. The fluctuating boundary layer velocity may now be written in the form:

$$\frac{u'(\zeta, \omega)}{U_o} = N \left(\frac{P}{P_{ref}}\right) \rho c \left(\frac{Uref}{U_o}\right) e^{A(\zeta, \omega)}$$

ESTIMATE OF CRITICAL SPL AND TRANSITION LOCATION (cont'd)

The previous equation allows determination of the critical SPL spectrum in terms of the integrated amplification (A) and the acoustic receptivity (N) with (u'/Uo) = 0.07. Such a spectrum is shown in the figure below for all three nacelles with N = 1. This shows that if full coupling is possible, nacelles GE2 and GE3 should be responsive to SPL between 90 and 115 dB, whereas nacelle GE1 should be unconditionally stable for SPL < 130 dB.

It is the objective of the test to search for such initial SPL spectra. If the acoustic receptivity is less than 1, then higher SPL will be required to move transition upstream. It is for this reason that the third nacelle (GE3) was also fabricated. Nacelle GE1 was designed to shown the feasibility of achieving full laminar flow.

Upstream movement of the transition location for SPL above the initial SPL may be computed from the same above equation with $A(\zeta, \omega)$ becoming variable. Some results are shown in the figure on the next page.

Critical SPL Spectrum

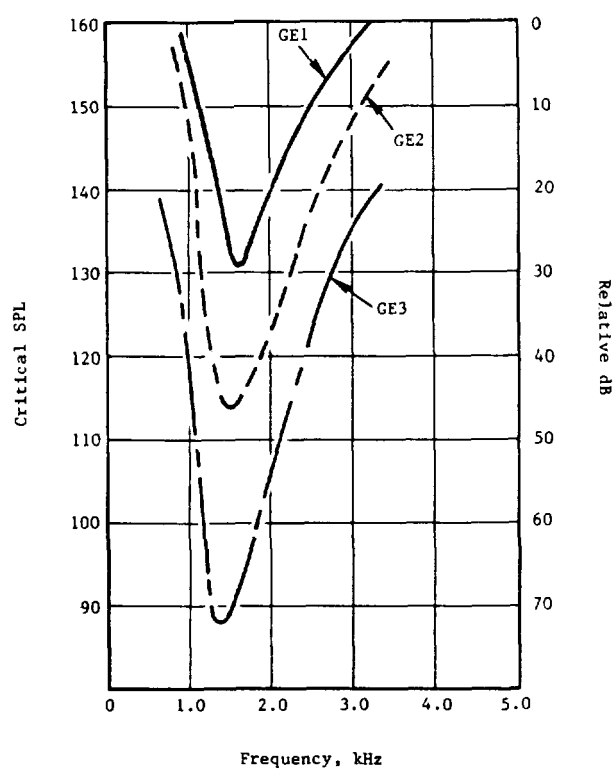

PREDICTED TRANSITION LOCATION

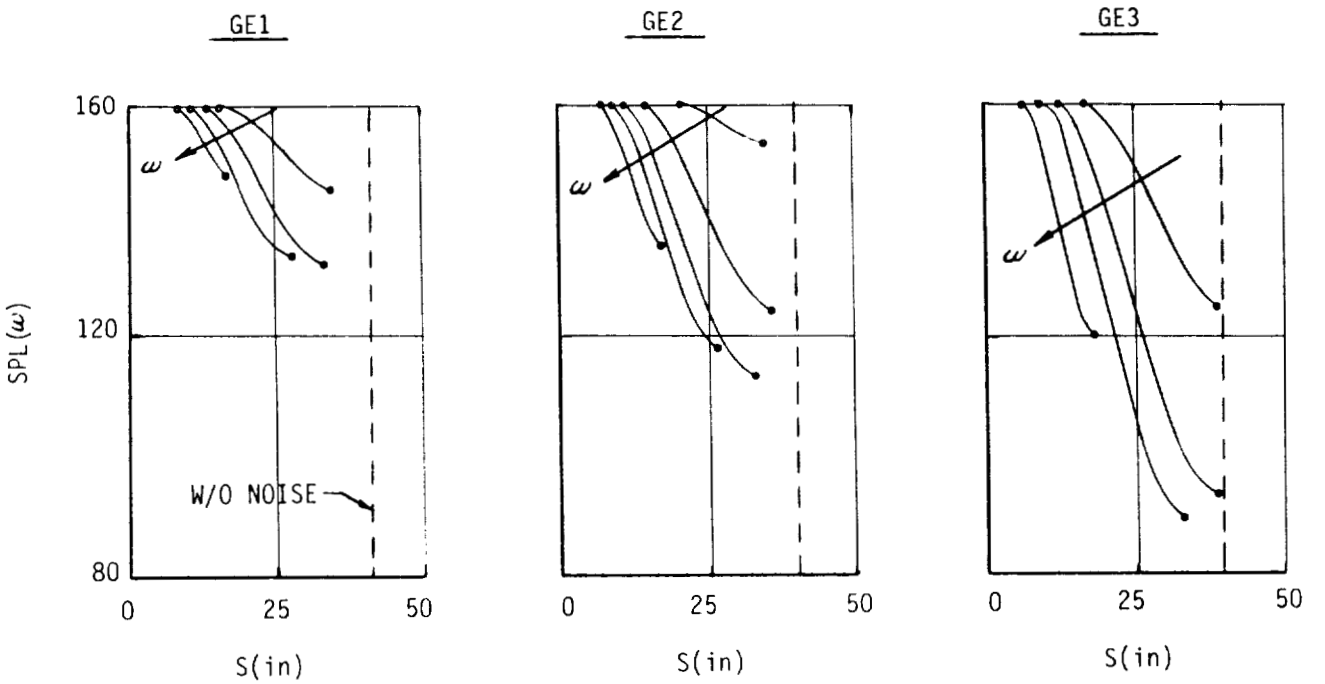

NACELLE STRUCTURE

The fiberglass and aluminum structure consists of an aft nacelle and three interchangeable forebodies. The main nacelle is designed with seven longitudinal spars and eight radial bulkheads attached to a main structural tube (which forms the inner flow surface of the nacelle) with screws and a structural damping adhesive. The outer fiberglass skins were fastened to the spars and bulkheads with buried rivets. The centerbody containing the internal noise source is attached to the main nacelle by four instrumented struts. A fairing on the inboard side of the nacelle houses the instrumentation tray. The external flow surfaces were sprayed with an epoxy coating and a silicone wax. Surface roughness is less than 16 microinches and surface waviness heights are less than $.008/\lambda$ where the allowable wavelength, λ, is less than four inches. A photograph of the three removable forebodies is shown below.

Removable Forebodies

Measurement parameters include (1) sound pressure levels using fluctuating pressure transducers on the external surface, inside the duct inlet, and on the noise source horn, (2) static pressure measurements on the external surface and inside the duct, and (3) total pressure measurements with rakes inside the duct and at the aft end of the afterbody.

Two methods for determining transition location will be used. Data from the hot-film sensors will be recorded on magnetic tape for later analysis of transition location, and a video camera in the outboard pod will be used to photograph liquid crystals and sublimating chemicals on the nacelle surface. These pictures will be displayed in the cockpit and recorded on a video cassette recorder for post-flight analysis.

The hot-film sensor was developed by NASA Langley and DISA Electronics. It consists of eight individual sensors embedded in a plastic strip. A list of primary measurements is shown in the table on the left, and a photograph of the installed hot-film sensor is shown on the right.

List of Primary Measurements

Measurement	Quantity/Description
Static pressures	142 on external surface (4 rows) and 12 inside duct
Sound pressure levels	9 on external surface, 4 inside duct and 2 on centerbody
Total pressures	24 inside duct and 14 in boundary layer rakes
Transition location	Liquid crystals and sublimating chemicals for flow visualization and hot-film anemometers

Installed Hot-Film Sensors

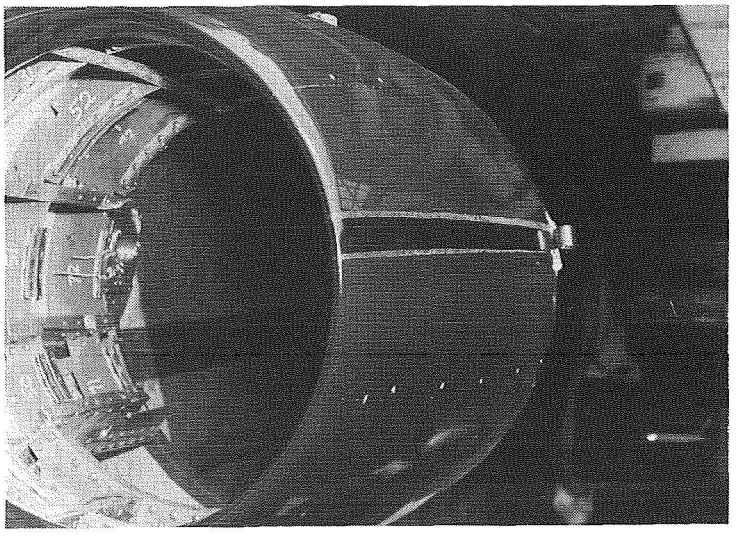

The aerodynamic design of the nacelles was based on axisymmetric flow. In order to obtain the design pressure distributions in the presence of the wing/pylon flow field, the nacelles are mounted to the pylon by a mechanism that allows their pitch and yaw positions to be changed.

The VSAERO panel-method code from AMI Inc. was used to obtain an initial estimate of the correct orientation. These figures show the panel model and computed streamline paths for two nacelle orientations. The analysis shows that ten degrees downward pitch combined with four degrees nose-in yaw is one orientation that results in nearly axial flow over the instrumented (outboard) nacelle surface.

Computational Panel Model

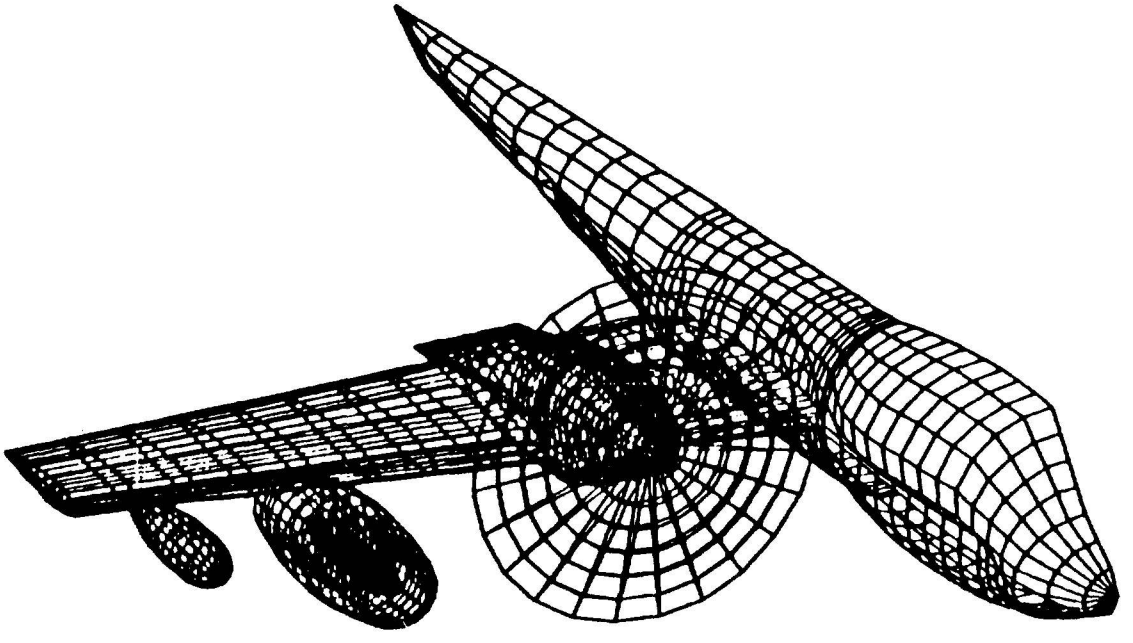

Calculated Results, 0° Pitch

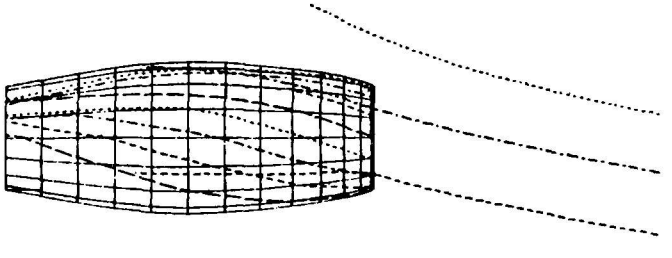

Calculated Results, Pitch Down 10°

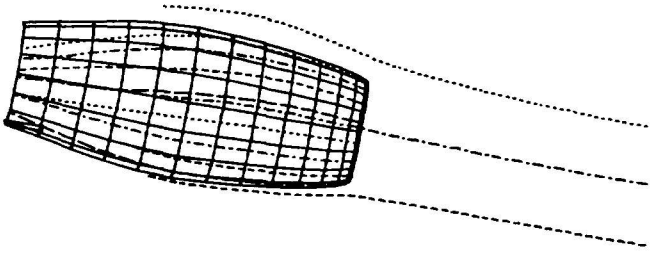

NACELLE AERODYNAMIC PERFORMANCE

Clifford J. Obara
PRC Kentron, Inc.
Hampton, Virginia

S. S. Dodbele
Vigyan Research Associates
Hampton, Virginia

MEASURED TRANSITION LOCATION USING SUBLIMATING CHEMICALS

The boundary-layer transition location was measured on nacelle shape GE2 using the sublimating chemical flow visualization technique. This technique involves coating the surface with a thin film of volatile chemical solid, which, during exposure to free-stream airflow, rapidly sublimates in the turbulent boundary layer as a result of high shear stress and high mass transfer near the surface. Transition is indicated because the chemical coating remains relatively unaffected in the laminar region due to lower shear and low mass transfer (Reference 1). The slow response time of the chemical in a laminar boundary layer allowed for two test conditions during the same flight. The aircraft was first flown at the desired airspeed and altitude with the noise source off. Once a pattern had developed, the noise source was turned on to the desired setting and a new chemical pattern was sought. In this fashion a direct comparison of the effect of the noise could be determined.

The photograph shows a chemical pattern for test conditions of V = 163 knots, h = 1300 ft, R = 1.8×10^6 ft^{-1}, and M = 0.25. The transition location occured at 50% of the nacelle length along the forebody to afterbody joint, which had a significantly high aft-facing step to cause the premature transition. Turbulent wedges caused by dirt particles are evident on the forebody. The same flight conditions were held after the noise source was set to 1500 Hz and 80 volts (132 dB). No effect of this added disturbance could be visualized in the sublimating chemical pattern. In addition, other noise source settings showed no effect on the transition location.

MEASURED PRESSURE DISTRIBUTION

The surface pressure distribution was measured under the same flight conditions as those flown for the flow visualization tests (V = 163 knots, h = 1300 ft, R = 1.8×10^6 ft^{-1}, and M = 0.25). There are 4 radial rows of pressure ports of which 2 have 60 pressure ports each (50° and 150°), while the remaining rows have 10 each (90° and 210°). Early flight tests attempted to match the measured pressure distributions with the desired pressure distribution as determined during the nacelle design process. Although an exact match was not made, the pressure gradients were kept similar, forsaking a uniform flow over the entire nacelle surface.

The measured distribution is shown in the diagram along with the design pressure distribution. The pressures remain favorable up to 50% length location over the entire surface. The pressure distribution for the 50° row has a steeper gradient probably caused by the proximity to the wing. Within the region of primary interest (90° to 150° radially) the measured pressure distribution agrees fairly well with the design distribution. It was decided that this distribution would provide the best response to any acoustic disturbance that might alter the location of boundary-layer transition.

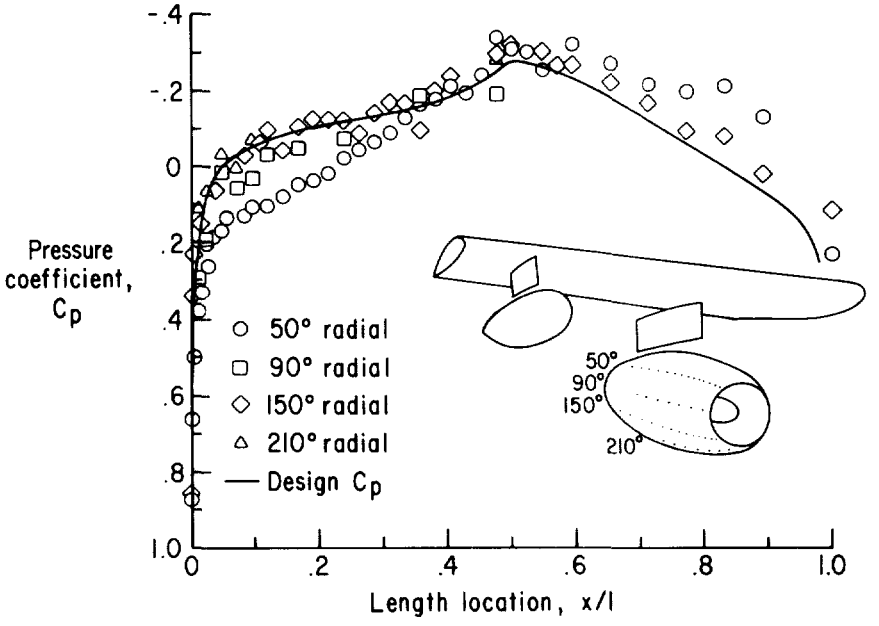

COMPUTATIONAL PANEL GEOMETRY FOR OV-1 AIRCRAFT WITH NLF NACELLE

Pressure distributions for the NLF nacelle shape GE2 were calculated for the same flight conditions. The predictions were made using a low-order surface-panel method (Reference 2). The method is based on piecewise constant doublet and source singularities, and can take into account the effects of compressibility. Using this three-dimensional surface-panel code, the nacelle, instrument pod, support pylons, and wing were modeled as shown in the diagram. The wake from the configuration was also modeled using the panel code, but is omitted in the diagram for the sake of clarity. The wing was modeled by using 8 panels in the chordwise direction (upper and lower surface combined) and 8 panels in the spanwise direction. The pylons were modeled by 12 lengthwise (left and right surface) and 5 vertical panels. As many contour details as possible were retained in the model of the nacelle, including the flow-through feature of the nacelle. More panels were used on the nacelle surface than on the wing to obtain detailed aerodynamic pressures and boundary-layer flow characteristics. The nacelle was modeled by 22 panels characteristics along the length (inner and outer surfaces) and 25 circumferential panels. The centerbody was modeled by 14 panels along its length and 8 panels circumferentially.

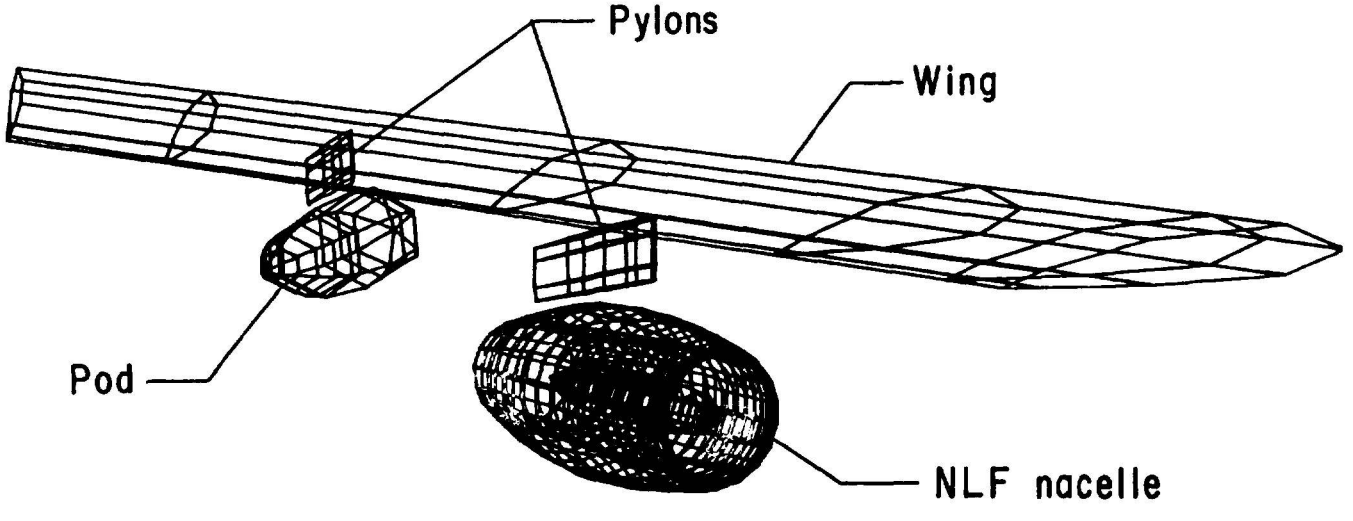

PREDICTED PRESSURE DISTRIBUTION

The predicted pressure distribution is presented in this figure for the 90° and 150° radial rows. A comparison is made to the previously presented measured pressure distributions. The data show that for the two rows the agreement between the measured and predicted pressures is reasonable in terms of the pressure gradient; however, the magnitude differs somewhat. This difference is most dramatic beyond about 35% of the nacelle length.

The panel code of Reference 2 has an additional capability of computing the boundary-layer development using integral methods. Therefore, this method was also able to predict boundary-layer transition location on the nacelle surface (using the Granville transition criterion). Transition is predicted to occur at 61% of the nacelle length for both the 90° and 150° radial rows. Since the measured transition location on shape GE2 occurred at the forebody to afterbody joint (50% of the length), it can be speculated that the predicted transition location would have agreed well with the natural transition location flight.

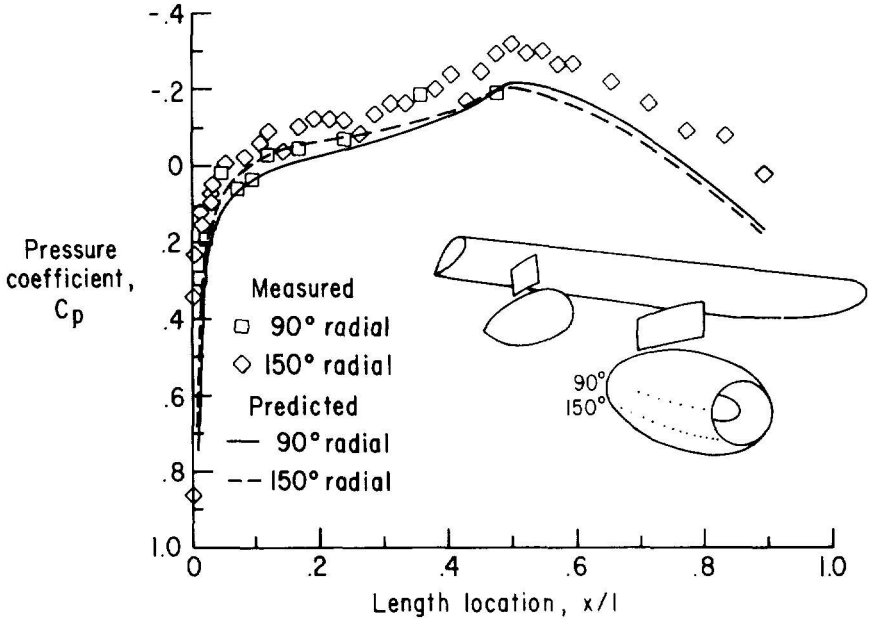

INSTABILITY WAVE GROWTH RATES USING THE PREDICTED PRESSURE DISTRIBUTIONS

In order to understand the transition on the nacelle further, a laminar boundary-layer stability analysis for the 90° and 150° pressure rows was performed. This analysis used a method based on incompressible linear stability theory (Reference 3). The method used detailed boundary-layer profiles for several lengthwise stations on the nacelle, computed by the boundary-layer program described in Reference 4. The stability code is designed to compute the Tollmien-Schlichting (T-S) wave growth rates. The "n-factor" (or logarithmic disturbance amplitude ratio) serves as a measure of the growth of T-S waves within the laminar boundary layer. The disturbances analyzed in the boundary-layer stability calculations are periodic pressure fluctuations in the laminar boundary layer caused by rotational vorticity waves moving downstream very close to the surface. The effect of coupling between these T-S waves, and irrotational acoustic waves generated by an outside source is not considered in this analytical method.

This diagram shows n factors plotted for the two pressure rows previously defined (90° and 150°). As shown, the laminar boundary layer remains stable or at low growth rates ($n<6.0$) up to about 55% of the nacelle length. Further calculations could not be completed because of the predicted beginning of laminar separation. Although not always a direct comparison, the frequencies that dominate maximum amplification are in the range of frequencies selected for the noise source.

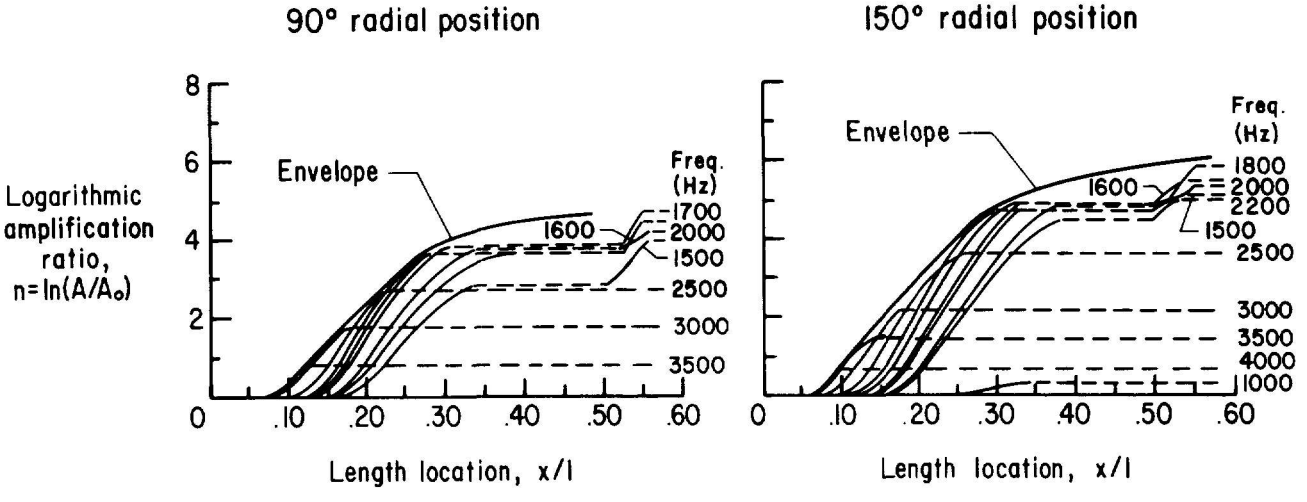

N90-12553

EFFECTS OF ACOUSTIC SOURCES

James A. Schoenster
Langley Research Center
Hampton, Virginia

Michael G. Jones
PRC Kentron, Inc.
Hampton, Virginia

ACOUSTIC FLIGHT EXPERIMENT ON THE GE LAMINAR FLOW NACELLES

As discussed in the prior sections, this experiment is being primarily conducted to determine the effect of acoustics on the laminar flow on the side of a nacelle. A flight test was designed to meet this goal (section II) and a brief review of the purpose is shown in the figure. A nacelle with a significant length of laminar flow is mounted on the wing of the OV-1. Two noise sources are also mounted on the wing: One in the center body of the nacelle; the second in a wing-mounted pod outboard of the nacelle. Thse two noise sources allow for a limited study of the effect of source direction in addition to control of the acoustic level and frequency. To determine the range of most sensitive Tollmien-Schlichting frequencies, a stability analysis using the pressure coefficient distribution along the side of the nacelle is performed. Then by applying these frequencies and varying the acoustic level, a study of the receptivity of the boundary layer to the acoustic signal, as determined by the shortening of the length of laminar flow, may be conducted. Initial tests on GE nacelle number 2 did not provide any indication of sensitivity to acoustics, probably because the flow was laminar past the attachment joint, and transition was not caused by Tollmien-Schlichting growth but rather the bypass mechanism of the joint. It was for this reason that the change to GE nacelle number 3, which was designed to have less laminar flow, was made.

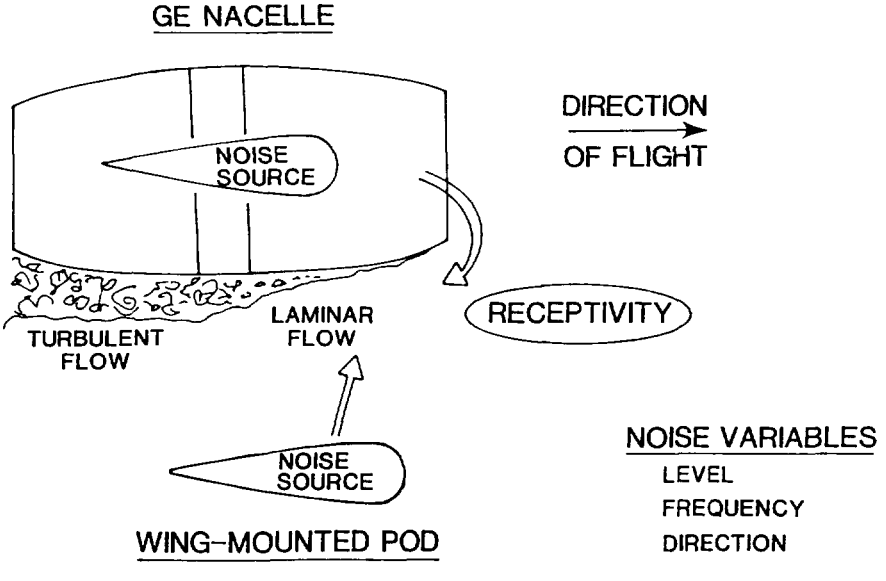

NOISE SOURCES ON THE OV-1 AIRCRAFT

As noted, two noise sources were added to the OV-1 aircraft. One was enclosed in an external pod outboard of the nacelle, and the second was mounted internal to the nacelle in the centerbody section. Both noise sources consisted of JBL compression drivers, model 2483, with a throat diameter of 2 inches. They were designed to operate in the 0.3 to 6Khz range with 120 watts of power. The speakers were custom designed to fit into the area available and were not the most efficient speaker that could be used with the drives. The mouths of the horns were covered with a low-resistance, honeycomb-stiffener wire mesh screen to minimize aerodynamic turbulence. The addition of the screen was estimated to provide less than 1dB of sound pressure attenuation.

The horn/driver system was controlled by an audio oscillator with discrete step outputs and a high power audio amplifier. The oscillator controls were located in a area accessable from the co-pilots seat and were monitored online. Either one or both of the sources could be operated at one frequency per run.

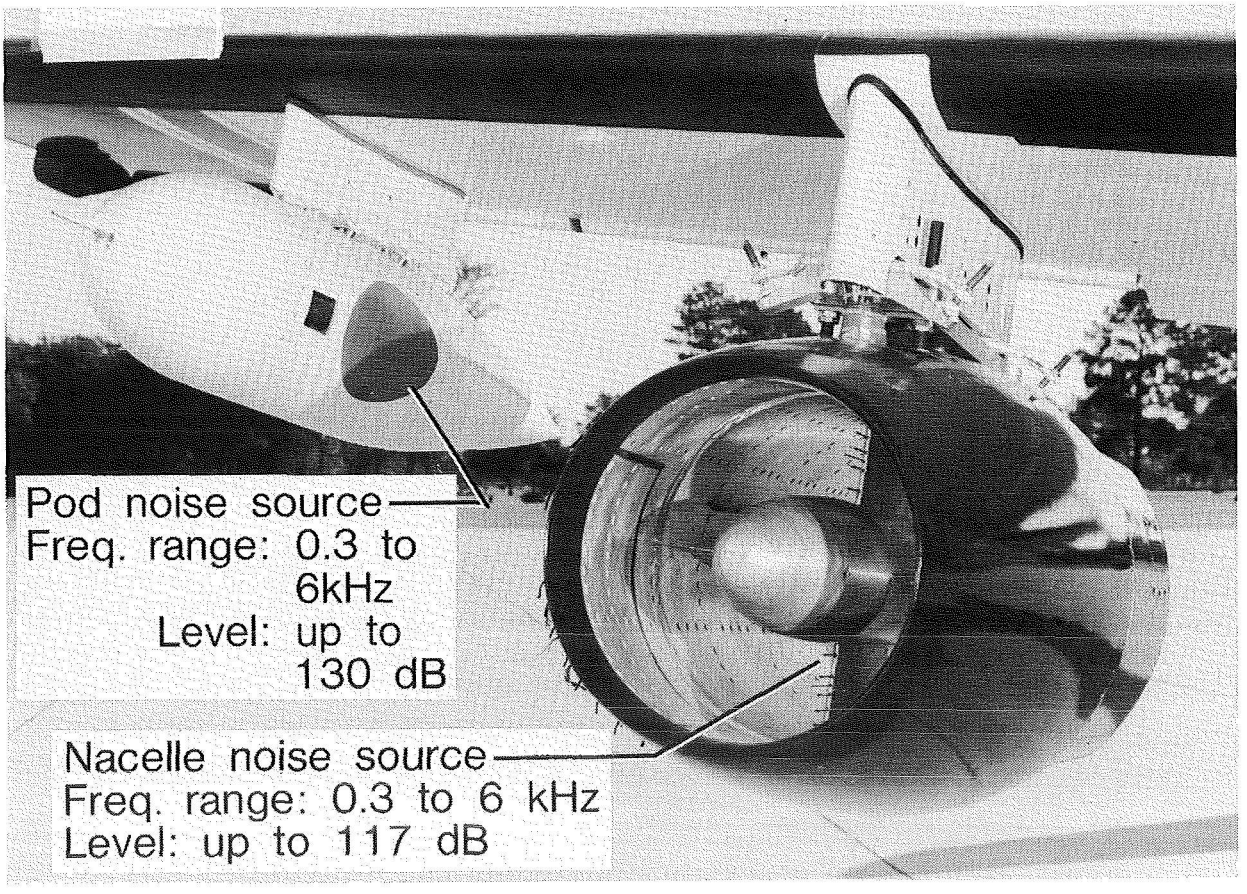

SPECTRA ON SURFACE OF NACELLE

Shown in the figure is the spectra obtained by a surface-mounted, fluctuating-pressure transducer in flight at 1500 feet. The pod noise source was tuned to 1500 Hz. It may be seen that the broadband noise in the range of zero to 5 kHz varies from about 105 dB to 90 dB while the applied tonal signal at 1500 Hz is about 128 dB, 15 dB above the broadband signal. Control of these signals in flight varies from 0.3 to 6 kHz with the levels adjustable up to 130 dB for the pod source and 117 dB for the nacelle source, depending on the frequency.

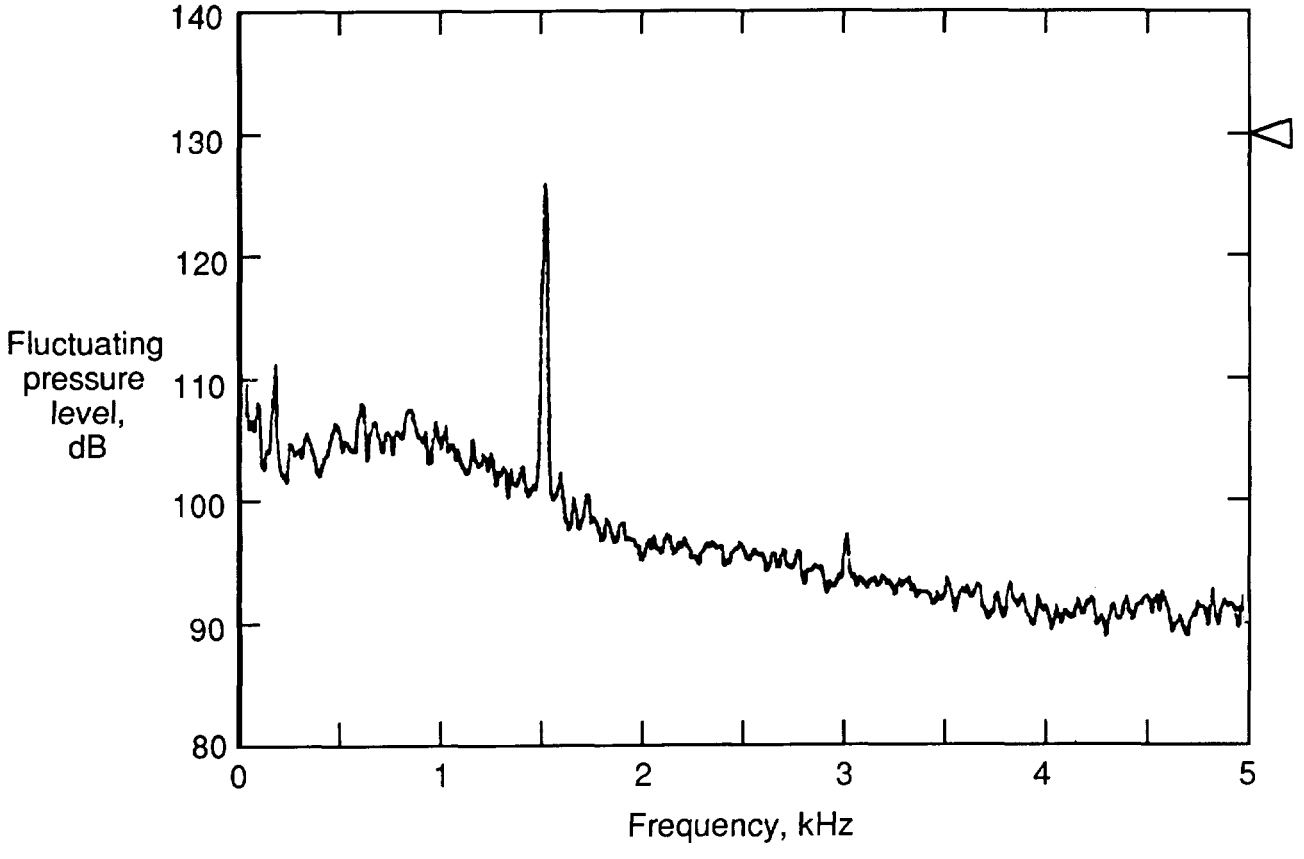

NOISE LEVELS ON THE NACELLE SURFACE

Several fluctuating-pressure measuring tranducers were mounted on the surface of the nacelle to determine the noise field from the two sources. One row of five tranducers (shown schematically) as "X" on the figure were mounted at 92° from the top of the nacelle at chord stations, x/c, equal to 0.06, 0.13, 0.21, 0.33, and 0.45. A pair of tranducers was also mounted a 152° at chord stations 0.06 and 0.13. The figures show the measured distributions for for the nacelle source and the pod source at the maximum output and 1,500 Hz. The maximum level at the leading edge (x/c = 0.06) for the nacelle source at 1,500 Hz was 117 at 92° and 116 dB at 152°. The pod source provided a maximum level of 124 dB and 122 dB at the same locations under similar conditions. These levels could be reduced in selected increments and as may be seen in the figures the distribution along the length of the nacelle is completely different for each source.

1500 Hz 80 v nacelle input

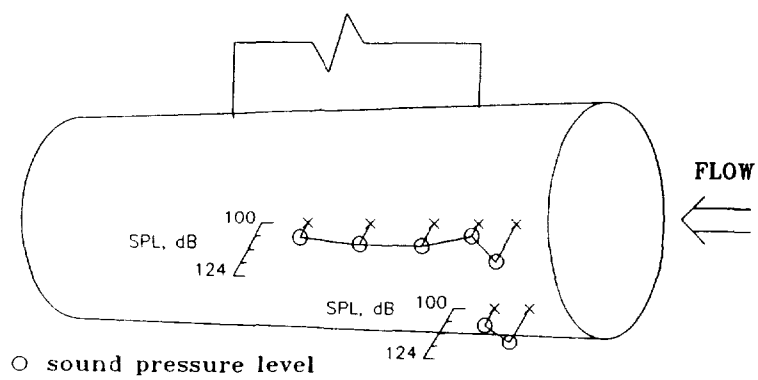

○ sound pressure level
× transducer location

1500 Hz 80 v pod input

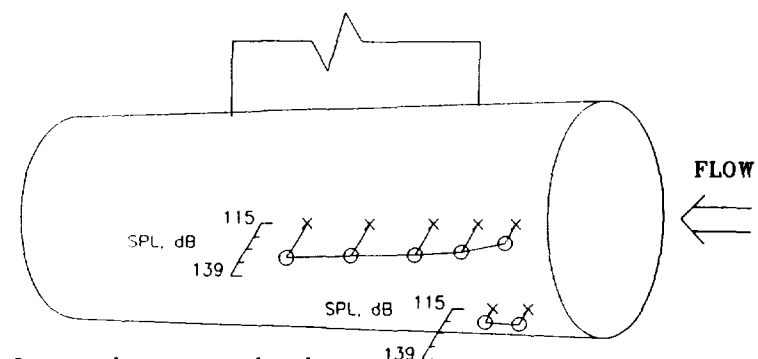

○ sound pressure level
× transducer location

PRESSURE COEFFICIENT FOR THE GE-3 NLF NACELLE

The predicted pressure coefficient, C_p, for the GE-3 nacelle (from Section II) is shown again in this figure. This nacelle was designed to allow for the Tollmien-Schlichting (TS) waves to grow to the largest value of the three nacelles. The relatively flat curve provides a favorable pressure gradient up to about 45% chord. To determine a range of most sensitive TS frequencies, this curve was input to a Cebeci code (reference 1) to obtain boundary-layer profiles for use in the stability analysis.

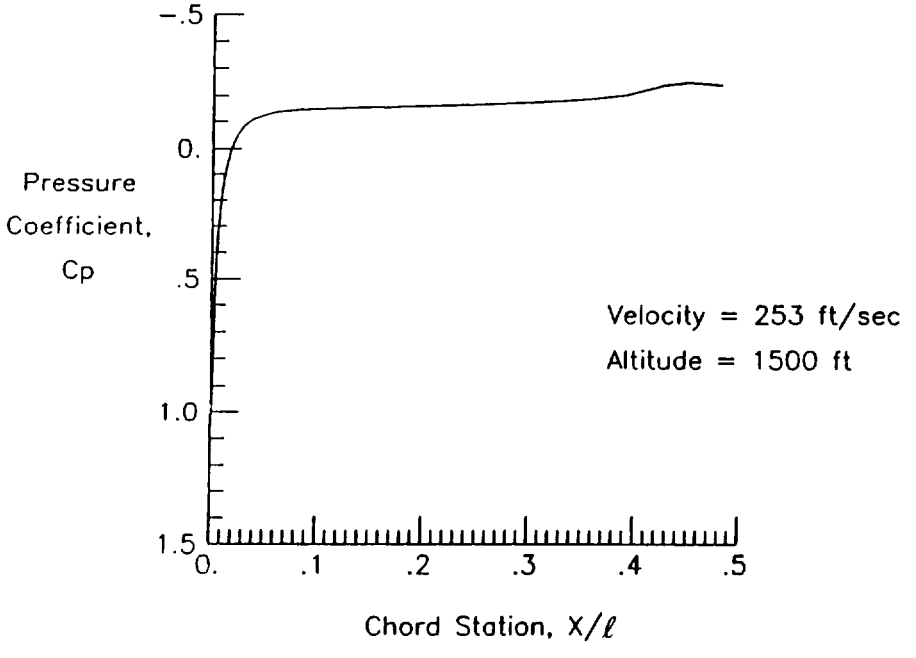

TOLLMIEN-SCHLICHTING AMPLIFICATION FACTORS

Using the envelope method of the SALLY (Stability Analysis which is Local, Linear and Incompressible) program (reference 2) amplification factors for the flight test conditions shown by the C_p analysis of the prior figure were calculated. These factors for four frequencies 1,300 Hz, 1,500 Hz, 1,800 Hz and 2,000 Hz are shown in this figure, indicating the growth rate as a function of chord length. Maximum values reach about nine which would indicate that the laminar flow may be very close to transitioning without any external distrubance (e^n method, reference 3). While it is recognized that frequency and amplitude are not sufficient by themselves to determine if an acoustic signal will cause a higher level TS wave (i.e. therefore causing transition prior to "natural" transition) it was anticipated that a high enough level would have some effect. Therefore, a frequency of 1,500 Hz at the maximum output level was selected to determine if "premature" transition would take place in flight.

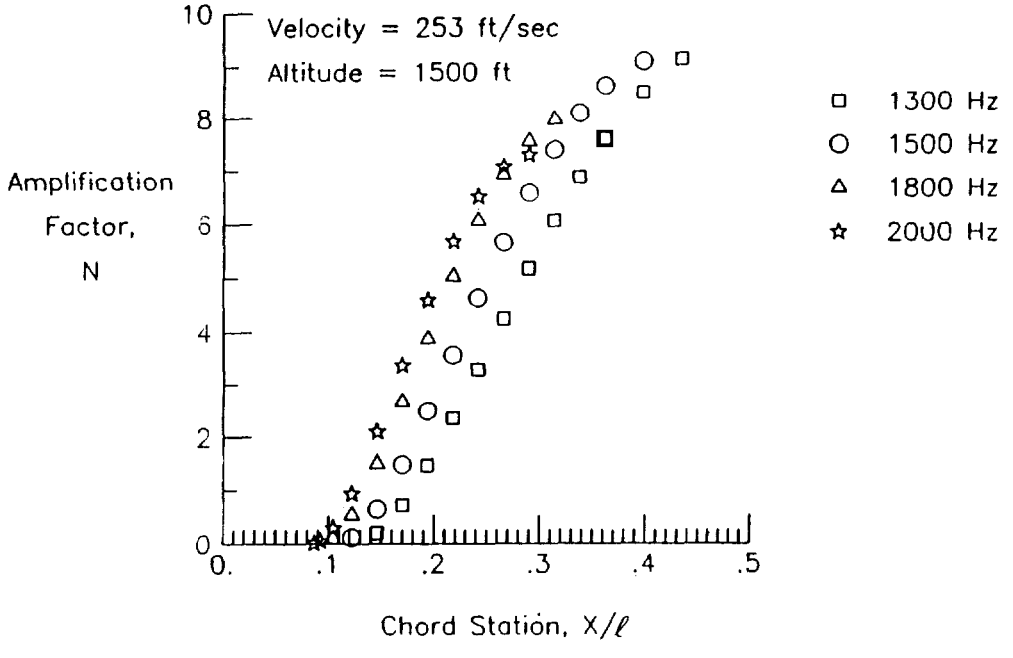

REFERENCES

I. Summary

1. Obara, C. J.; Hastings, E. C.; Schoenster, J. A.; Parrott, T. L.; and Holmes, B. J.: "Natural Laminar Flow Flight Experiments on a Turbine Engine Nacelle Fairing." AIAA Paper 86-9756, April 1986.

2. Hastings, E. C.; Schoenster, J. A.; Obara, C. J.; and Dodbele, S. S.: "Flight Research on NLF Nacelles: A Progress Report" AIAA Paper 86-1629, June 1986.

II. Nacelle Design

1. Swift, G.; and Mungur, P.: "A Study of the Prediction of Cruise Noise and Laminar flow Control Noise Criteria for Subsonic Air Transports," NASA CR-159104, October 1978.

2. Klebanoff, P. S.; and Tidstrom, K. D.: "Evolution of Amplified Waves Leading to Transition in a Boundary Layer with Zero Pressure Gradient," NASA TN D-195, 1959.

III. Nacelle Aerodynamic Performance

1. Obara, C. J.: Boundary-Layer Flow Visualization for Flight Testing. Natural Laminar Flow Aircraft Certification, NASA CP-2413, 1986.

2. Maskew, B: Prediction of Subsonic Aerodynamic Characteristics - A Case of Low-Order Panel Methods. Journal of Aircraft, vol. 19, no. 2, February 1982, pp. 157-163.

3. Srokowski, A. J.; and Orszag, S. A.: Mass Flow Requirements for LFC Wind Design. AIAA Paper 77-1222, August 1977.

4. Kaups, K.; and Cebeci, T.: Compressible Laminar Boundary layers with Suction on Swept and Tapered Wings. Journal of Aircraft, vol. 14, no. 7, July 1977, pp. 661-667.

IV. Effect of Acoustic Sources

1. Kaupe, Kalle; and Cebeci, Teincer: Compressible Laminar Boundary Layers with Suction on Swept and Tapered Wings. Journal of Aircraft, vol. 14, no. 7, July 1977, pp. 661-667.

2. Srokowski, Andrew J.; and Orsyag, Stephen A.: Mass Flow Requirements for LFC Wing Design. AIAA Paper 77-1222, Aug. 1977.

3. Hefner, Jerry W.; and Bushnell, Dennis M.: Status of Linear Boundary-Layer Stability Theory and the e^n Method, With Emphasis on Swept-Wing Applications. NASA TP-1645, April 1980.

SUPERSONIC LAMINAR-FLOW CONTROL

D. M. Bushnell
NASA Langley Research Center
Hampton, Virginia

M. R. Malik
High Technology Corporation
Hampton, Virginia

[redacted]

BENEFITS
LAMINAR-FLOW CONTROL FOR SUPERSONIC CRUISE

Detailed, up-to-date systems studies of the application of laminar-flow control (LFC) to various supersonic missions/vehicles, both civilian and military, are not yet available. However, various first order looks at the benefits are summarized on the figure and in references 1-4. The bottom line is that laminar-flow control may allow development of a viable second generation SST. This follows from a combination of reduced fuel, structure, and insulation weight permitting operation at higher altitudes, thereby lowering sonic boom along with improving performance. The long stage lengths associated with the emerging economic importance of the "Pacific Basin" are creating a serious and renewed requirement for such a vehicle.

- Civilian/SST
  - Key to viable second generation SST ALA OSTP National Aeronautical R&D goals
  - Increased range/payload
  - Lower fuel weight/usage
  - Lower skin temperature (reduced Stanton number, recover factor) 0 (100° F) reduction for $M \sim 3$, increases material options
  - Reduced thermal/sound insulation for cabin (reduced skin temperature, P'_w), reduced air conditioning load
  - Increased altitude/lower sonic boom
  - Lower cost, reduced landing/take-off speeds
- Military
  - All of above plus reduced I. R. signature

HIGH-SPEED TRANSITION PHYSICS

Before discussing supersonic laminar-flow control, it is reasonable to briefly examine the transition physics which must be altered to prolong the laminar boundary-layer state. This physics is summarized on the figure and in reference 5. Of particular importance is the existence, known for more than 20 years, of a second (inviscid) instability mode at higher Mach numbers. Conventional wisdom holds that, in the absence of cross flow, compressibility and wall cooling are stabilizing. This is not so in some speed ranges due to the second mode physics. The dominant fact of life in supersonic LFC is the presence and importance of the cross-flow instability mode, engendered by the large sweep angles necessitated by wave-drag reduction/control.

Three fundamentally different boundary-layer instability modes

I "T-S" modes		II Cross-flow mode	III Concave curvature (Taylor-Gortler) mode
● First mode (viscous)	● Second mode (inviscid)	● Inflectional instability	● Induced by wall or streamline longitudinal concave curvature
● Dominant up to $M_E \sim 4$	● Dominant beyond $M_E \sim 4$	● Characteristic of 3-dimensional B.L.s.	● Low Re_T
● Damped by cooling	● Amplified by cooling	● Low Re_T	
● Moderate to high Re_T	● Relatively high Re_T at high M		

Note: Swept leading edges (attachment lines) constitute a separate case

TRANSITION BEHAVIOR
EXISTING SUPERSONIC CRUISE AIRCRAFT

Another preparatory phase to the consideration of supersonic LFC is an examination of transition occurrence/behavior on contemporary large supersonic vehicles. As summarized on the figure most of these vehicles were designed more than 20 years ago, and their surface condition is not consistent with extensive laminar flow. The prime difficulty is the occurrence and often dominance of thermal stresses and their impact upon obtainable surface smoothness/waviness. Newer technologies, such as super plastic formed diffusion bonded titanium (SPFDB) may allow design and fabrication of surfaces consistent with supersonic laminar-flow control (refs. 6 and 7).

- XB-70
- X-15
- SR-71

50's and early 60's technology

Surfaces have steps, gaps, joints, waviness (for thermal stress relief)

- B-58
- Concord and "Concordski"
- MIG 25 Foxbat

Surface irregularities, combined with cross flow, induces early transition (within inches of leading edge)

- Outlook for smooth, low waviness skins for modern supersonic cruise machines good via molded sandwich skins made of thermoplastics or SPFDB titanium

ALTERNATIVE CONTROL TECHNIQUES
LFC FOR SUPERSONIC CRUISE

Much of the available research literature for supersonic LFC is summarized in references 8-11. The prime design driver in supersonic LFC is the prevalence of large cross flow. This tends to negate "natural" laminar flow except in very specialized circumstances/body areas. Therefore, the laminar-flow control approach of choice for supersonic/hypersonic speeds is suction. As will be shown herein, wall cooling has only a secondary influence upon cross flow, even at high speeds. Therefore, unless some other technique (other than large sweep) can be found to reduce wave drag at supersonic/hypersonic conditions, "natural" and hybrid LFC will be extremely difficult at high speeds.

- General consideration
  - Supersonic flow implies large sweep for wave-drag reduction, this results in boundary-layer cross flow and consequent destabilization upon imposition of $-DP/DX$, $\therefore$ "natural" laminar flow restricted to body-nose regions only
- Suction
  - Usual approach of choice for $M > 1$ LFC, handles cross flow, (slot suction thus far)
- Wall temperature
  - Small cross-flow regions only (also $-DP/DX$)
    - $M < 4$, first mode, cooling ($R_{x_{Tr}} \rightarrow 34 \times 10^6$ at $M \sim 4$ on body of revolution, CCCP)
    - $M > 4$, second mode, heating

MACH NUMBER INFLUENCE UPON LFC/STABILITY PROBLEM

In general, LFC becomes both easier and harder as speed increases. LFC is easier due to somewhat reduced roughness sensitivity caused by outward movement of the critical layer and lower wall region Reynolds numbers and harder because increased suction levels are required due to the same outward movement of the critical layer and increased cross flow. The very limited high-speed cross-flow stability computations available thus far indicate that increasing Mach number may further stabilize the boundary layer for this mode, but this effect is generally overcome by the increasing cross flow/sweep at higher M. See reference 12 for the high Mach number Gortler case.

- First and second mode "T-S" disturbances (Tollmien-Schlichting)
  - Up to M ~ 4 (1st mode)
    - Amplification rate decreases
    - Wave angle increases
    - Absolute roughness sensitivity decreases

    } With Mach number
  - Beyond M ~ 4 (2nd mode)
    - High frequency transverse waves most unstable
    - Critical layer moves to outer part of boundary layer/further decrease in roughness sensitivity
    - Two-dimensional boundary layers extremely hard to trip
- Gortler mode
  - Increasing Mach number stabilizing
  - Suction/wall cooling less effective (for stabilization) as M increases
- X-flow mode
  - Weak dependence upon Mach number

EFFECT OF SUCTION ON THE SECOND-MODE INSTABILITY

The second (inviscid) instability mode becomes important in the high supersonic/low hypersonic range, and these higher modes dominate the non-cross-flow/non-Gortler boundary-layer transition problem thereafter. The stability results shown on this figure (method of ref. 13) are among the first for the second mode control case and indicate that suction is still highly stabilizing for these disturbances.

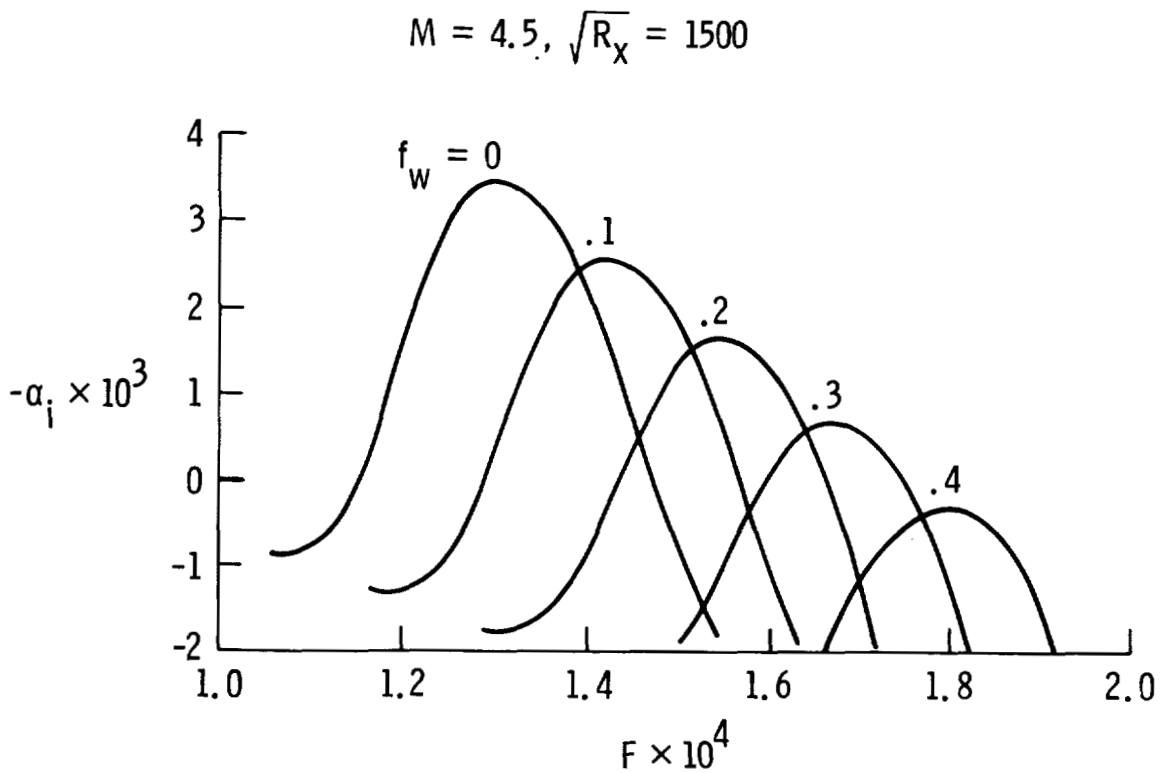

EFFECT OF PRESSURE GRADIENT ON THE
SECOND-MODE INSTABILITY

This figure is a companion to the previous figure and indicates that favorable pressure gradient is also stabilizing for second-mode instabilities. Therefore, in the absence of significant cross flow, natural laminar flow would still be an LFC option, even at high Mach number. However, pressure gradients in the presence of sweep exacerbate the cross-flow problem, which is one of the major reasons that natural laminar flow was dropped in the late 1940's with the advent of the jet engine and higher speeds/swept wings.

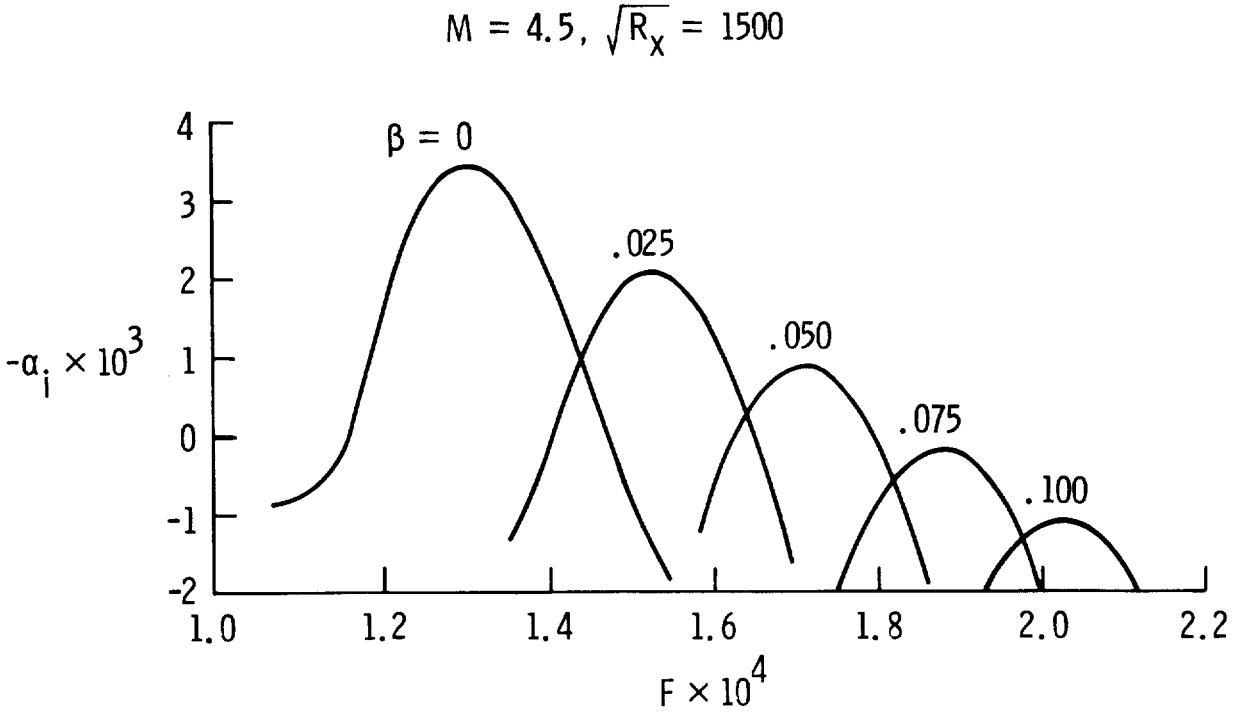

EFFECT OF COOLING ON T-S GROWTH RATES IN A TWO-DIMENSIONAL BOUNDARY LAYER

These calculations, carried out using the method of reference 13, elucidate the dramatic difference in the effect of wall cooling upon instability growth rates for first- and second-mode disturbances. These results have been known to the stability theory community for many years but usually still come as a surprise to the design community. See reference 14 for corresponding experiments and the next chart for the influence of cooling upon the cross-flow mode.

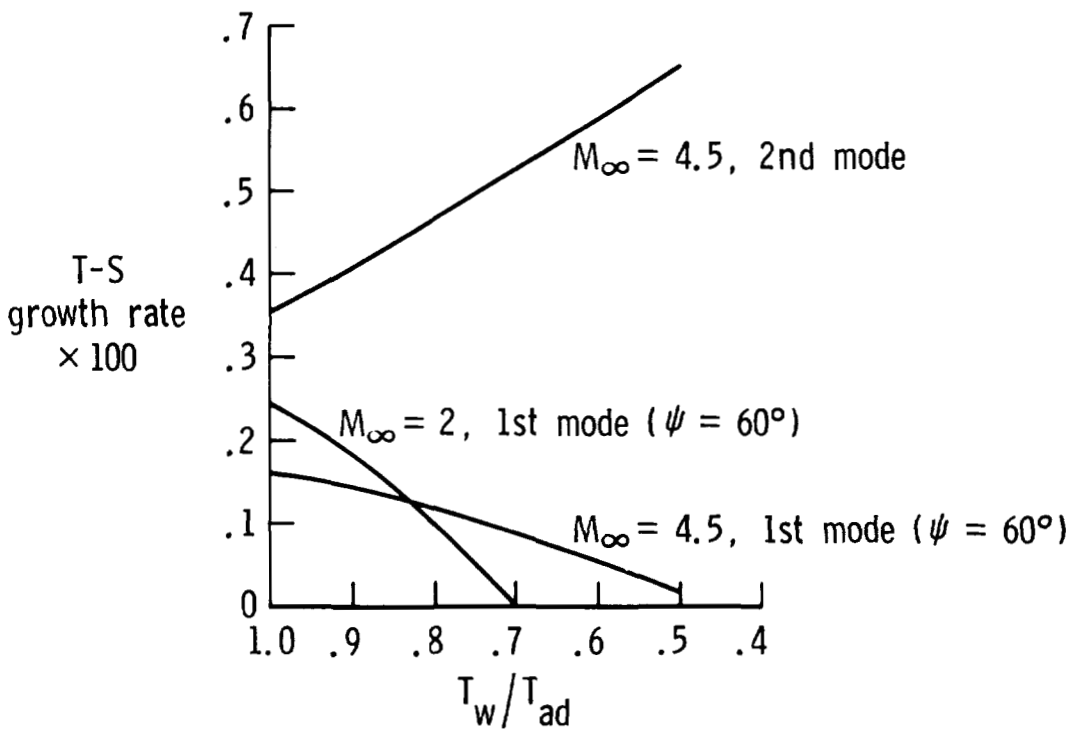

GROWTH RATES FOR STATIONARY CROSS-FLOW VORTICES ON A 60° SWEPT CYLINDER AT $M_\infty = 3.5$

The disturbance growth rates are seen to be only weakly dependent upon wall cooling for the high supersonic case. This result is in agreement with previous research at near transonic conditions (ref. 15) and indicates that, even if cryogenic fuel were utilized, suction would still be required for laminar-flow control on highly swept supersonic configurations.

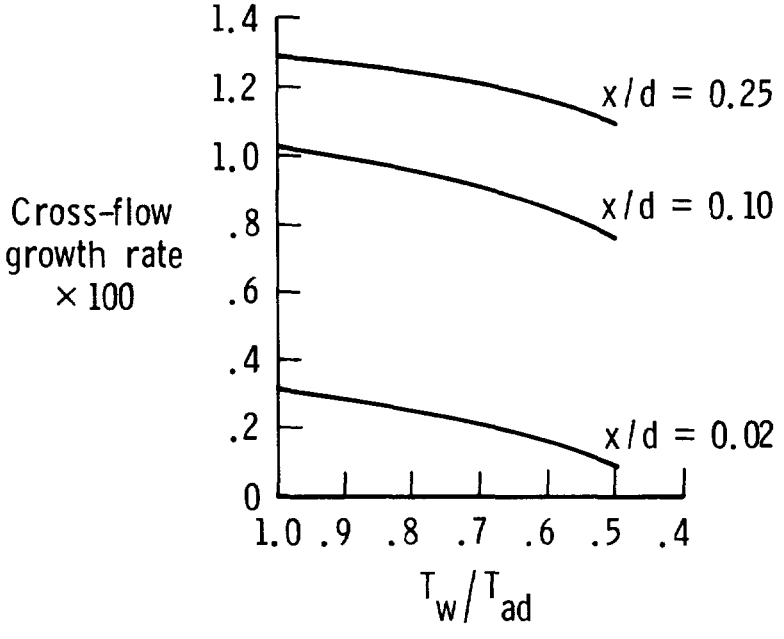

MACH NUMBER EFFECT ON CRITICAL ROUGHNESS REYNOLDS NUMBER

As in conventional LFC applications, a smooth, relatively wave-free surface is a necessary (but obviously not sufficient) condition for LFC. For the non-cross-flow case the "second mode" disturbance growth occurs farther from the wall (compared to the low-speed case) and therefore the "smoothness" requirement is far less stringent as the figure indicates (from ref. 16). Note that the criteria shifts in the expected region, above Mach 4 where the second mode growth rates begin to exceed those from the first mode. Unfortunately, while definitive information is lacking, what information is available indicates that the roughness criteria for the cross-flow mode remains quite stringent, generally even more restrictive than for the two-dimensional low-speed case.

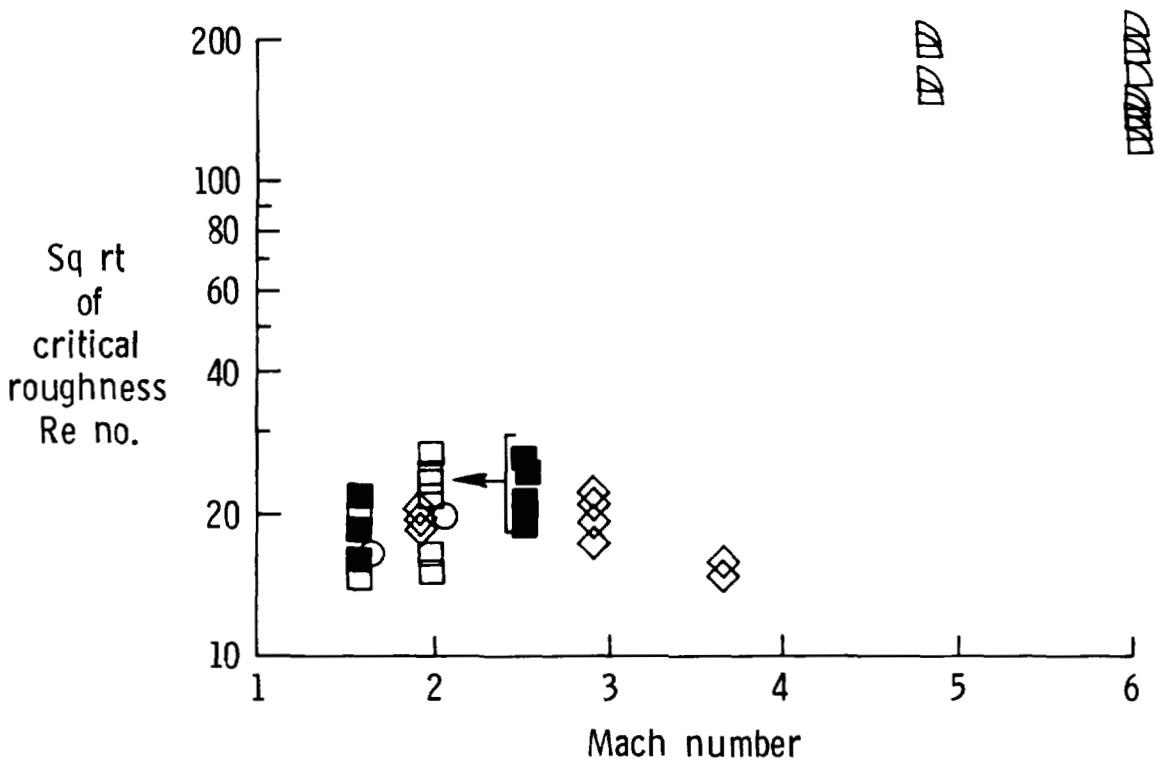

APPLICATION OF THE E^N METHOD TO SUPERSONIC LFC DESIGN

As discussed in reference 17 the e^N approach (see also ref. 13) constitutes the current best bet for LFC design and transition prediction. The basic idea is to integrate the growth rates of the most unstable wave between inception of instability and the location of transition and to represent the growth factor (final to initial amplitude) as e^N where N is determined from comparison with experimental transition loci. As noted on the figure the various comparisons with supersonic data indicate values for N in the same range as for the lower speed flows, 9 to 11. In LFC design the disturbance must remain small (linear) for ease of control, and therefore maximum N values the order of 5 to 7 are usually employed.

- N value calibrations, $M > 1$
  - Gortler mode ($M \rightarrow 3.5$, quiet wind tunnel wall)
  - Cross flow (F-106 wing, F-15 wing, swept cylinder in quiet wind tunnel)
  - T-S, first mode (cones, quiet wind tunnel and flight up to $M \sim 3.5$)
  - Second mode (inferred from matching flight transition data on cones)
- Conclusion from all of these cases is that an N of 9 to 11 usually corresponds to transition occurrence
- Utilization of e^N for LFC necessitates applying sufficient control to keep disturbances linear (N small)

TRANSITION ON SHARP CONES

This plot indicates that the e^N approach can be extended into the hypersonic regime. The bottom curve is a best fit through available wind tunnel data (not shown) and, due to large acoustic disturbances in ground facilities, the bottom curve indicates lower transition Reynolds numbers than the flight data (which are shown). The e^{10} theory line corresponds to the filled symbols (adiabatic wall case). Most of the flight data points above the curve below Mach 4 are for cold wall, and because this is first mode "territory", the transition levels are higher (as would be predicted by the e^{10} theory for the cold wall case). At higher Mach number the flight data are also cold wall, but now, in 2nd mode territory, this is destabilizing, and therefore the data are below the adiabatic line shown.

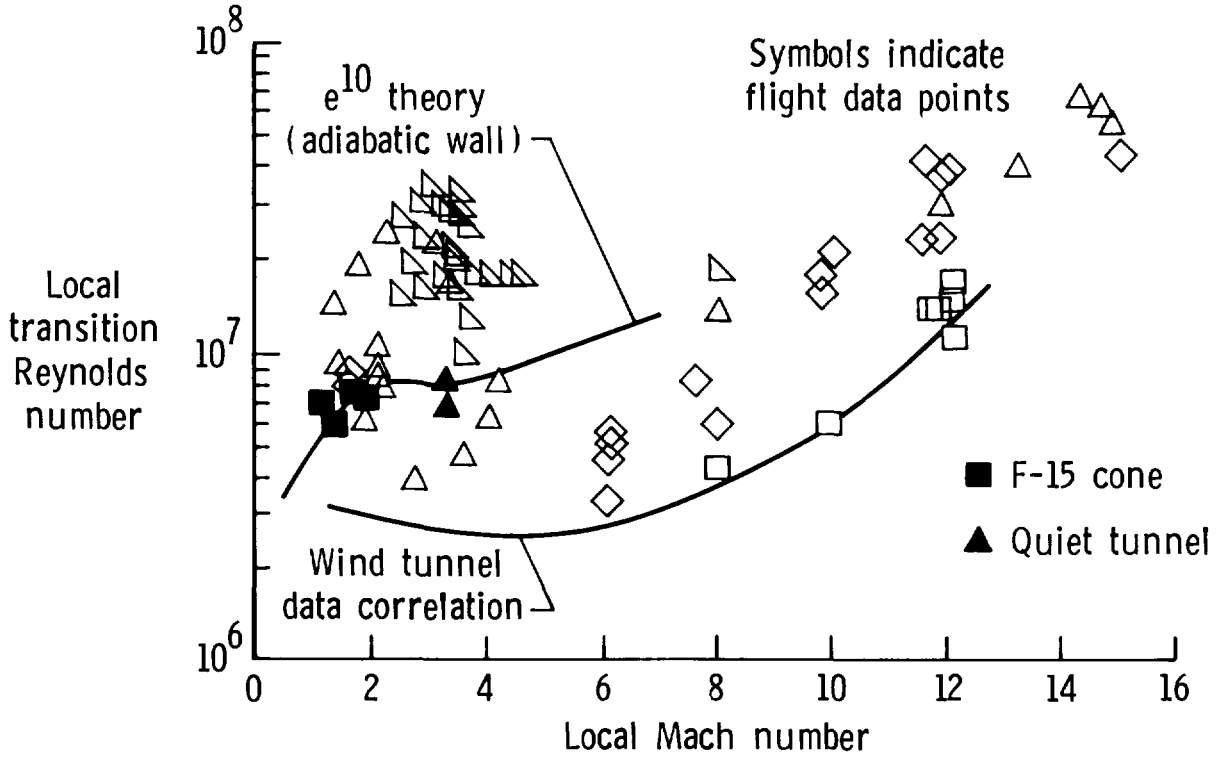

LFC SUPERSONIC SUCTION EXPERIMENTAL DATA BASE

An active supersonic suction LFC research program existed coincident with and following the Air Force-Northrop X-21 program for transonic LFC. This work is documented in references 8 and 18-21. A summary of the key experimental results are shown on the figure. Note that the experiments covered a wide range of flow disturbance conditions (two-dimensional, axisymmetric, swept) and even considered the problem of laminarization through incident shock waves. The cogent results from these works are summarized on the following charts.

Mostly Northrup/Pfenninger*/AEDC Tunnel A

Model	Mach number	Reynolds number with laminar flow (using suction)
● Flat plate (with and without reflective shock wave, $P_2/P_1 \sim 1.1$)	2.5 - 3.5	25.7×10^6
● 6° half-angle cone	5 - 8	30×10^6
● Axisymmetric model, cylindrical afterbody (with and without reflective shock, $P_2/P_1 = 1.16$)	2.5 - 3.5	51×10^6
● 36° swept wing, 3.0% T/C, biconvex	2.5 - 3.5	25×10^6
● 50° swept wing, 2.5% T/C, biconvex	2.5 - 3.5	17×10^6
● 72.5° swept wing	1.99 - 2.25	9×10^6

* W. Pfenninger (Analytical Services and Materials, Inc., Hampton, Virginia) was instrumental in this work.

TOTAL DRAG FOR SUPERSONIC LFC - AXISYMMETRIC FLOW, $M_\infty = 3$

This sample result from the Northrop work indicates the increasing and increased importance of the suction drag component. Turning the flow into and along the body in supersonic flow produces a train of shock waves, thereby producing additional wave drag. Also, required suction rates are generally higher in the supersonic case due to critical layer movements and increased cross flow.

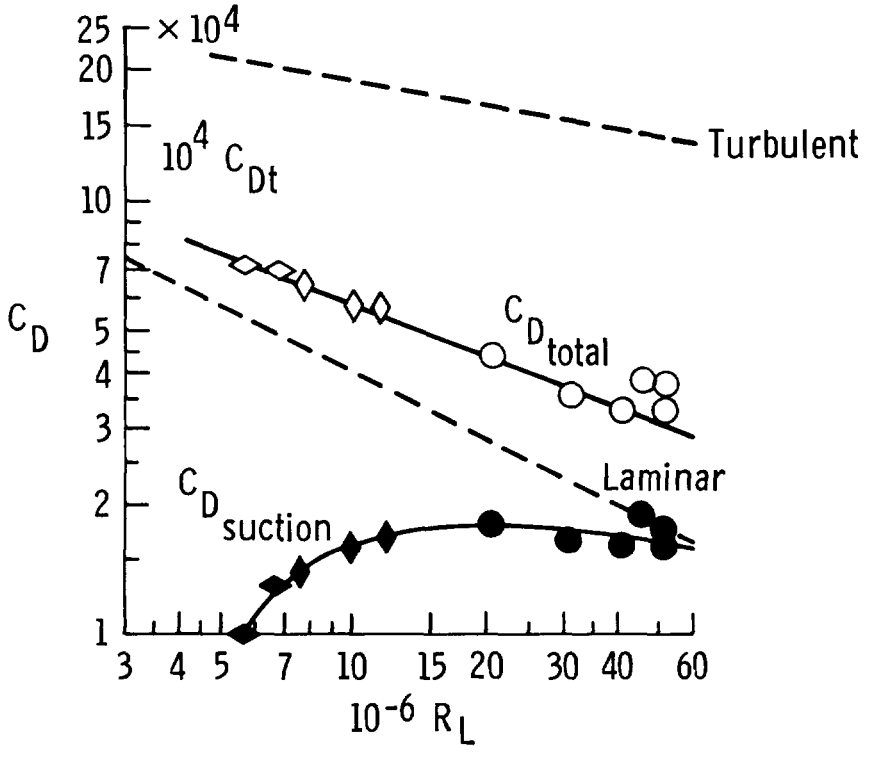

RESULTS, SUMMARY OF "LESSONS LEARNED" SUPERSONIC SUCTION LFC EXPERIMENTS

This figure and the following summarize many of the major results from the extensive Northrop (Pfenninger) research in supersonic suction LFC. This work was conducted in conventional (noisy) ground facilities. In spite of this, in most cases laminar flow was obtained using suction up to the maximum performance limits of the facility (total pressure, model size) i.e., these studies obtained/proved LFC at huge unit Reynolds and in the presence of large stream disturbance levels. In the analogous low-speed case LFC was extremely difficult, if not impossible, in high disturbance tunnels even at reasonable unit Reynolds numbers. It should be noted that increasing difficulty in attaining LFC was encountered with increasing sweep/cross flow.

- Overall drag (C_F + suction) 0 (25% to 60%) of turbulent level
- Required suction rates increase with sweep and Mach number, i.e., suction drag greater for supersonic LFC (for 2-D case, $(V_W)/(U_E) \sim .001$ vs. .0003 for low speed)
  - Caused by (a) increased cross flow (increased sweep), and (b) outward movement of critical layer
- Slot sizes (for R/ft up to order of magnitude greater than flight applic.) of .004" to .008", approximately 1/2" spacing, .003", .080" spacing on highly swept wing
- Slot width < 20% of "sucked height"
- Sucked height per slot < momentum thickness
- For most tests, R_X with laminar flow was limited by tunnel size/ pressure, i.e., absolute limits for supersonic LFC are considerably in excess of demonstrated capability
- These excellent results obtained in noisy, high-stream disturbance conventional M > 1 tunnels (subsonic LFC not even attainable in high disturbance subsonic tunnels)
- For axisymmetric bodies even small incidence (1°) can be highly destabilizing due to large induced cross flow
- Spanwise contamination locus on lower surface of swept wing may necessitate laminarization of wing fuselage junction

EFFECT OF TURBULENCE LEVEL ON
TRANSITION REYNOLDS NUMBER

This figure indicates the improved performance obtained in the supersonic case compared to conventional (lower speed) studies. Possible reasons for this improved performance include (a) decreased boundary-layer receptivity/internalization for acoustic as opposed to vortical disturbances of the same relative intensity, and (b) decreased stream disturbance/roughness coupling due to the reduced roughness sensitivity/lower wall Reynolds number.

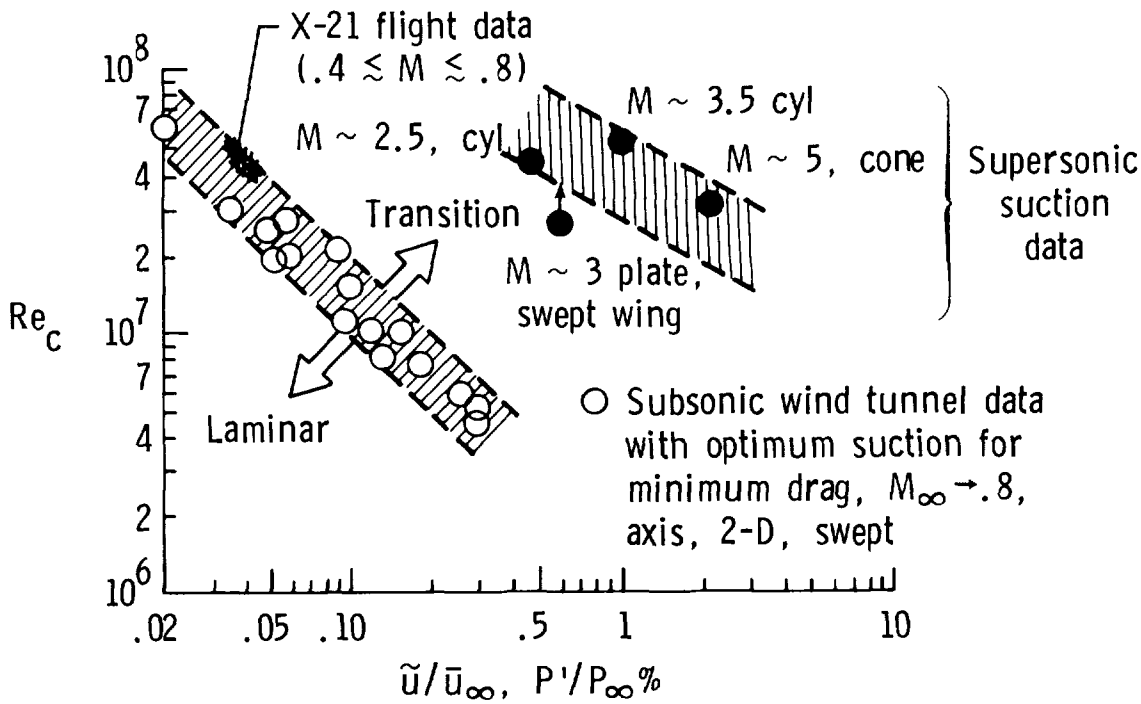

DISTRIBUTION OF HEAT TRANSFER COEFFICIENT ALONG
STAGNATION LINE OF A SINGLE SLOTTED FIN

This figure, taken from reference 22, corresponds to stagnation line heating data for a highly swept fin upstream and downstream of a single chordwise slot. The slot allows natural stagnation line boundary-layer bleed, which in this case, is sufficient to "relaminarize" an initially turbulent swept attachment line. Such fixes for the attachment line contamination problem are well known for low speeds, but this experiment at Mach 8 indicates that the process also works at high speeds.

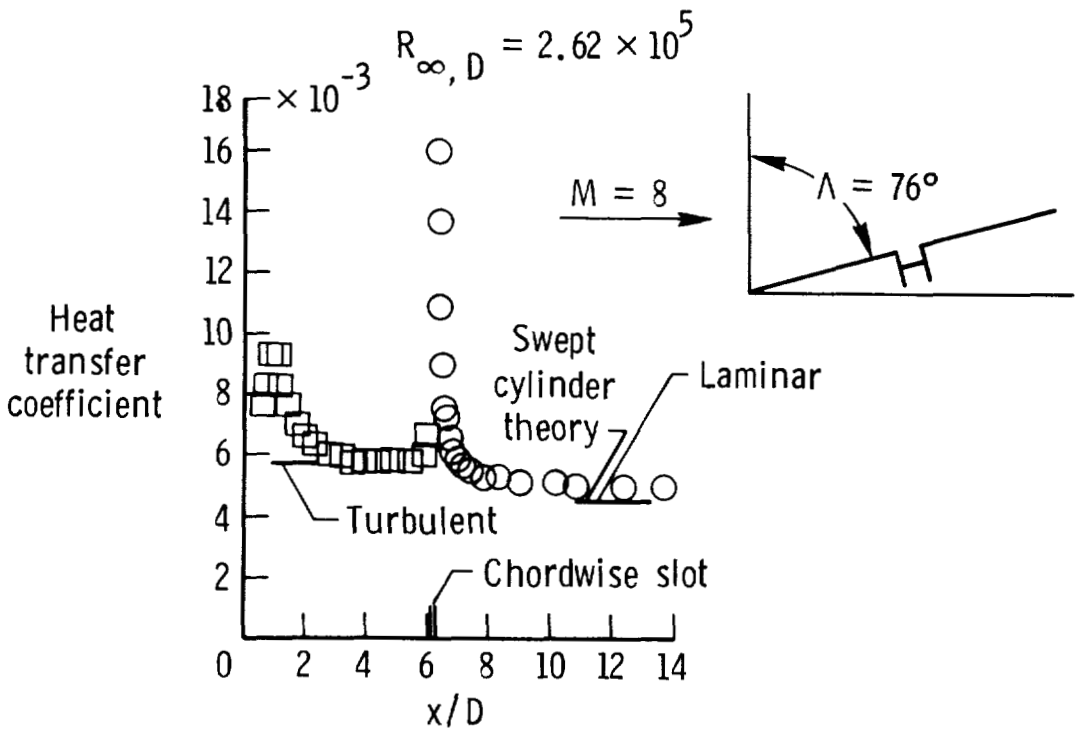

APPLICATION ISSUES FOR SUPERSONIC (SUCTION) LFC

The major issues are as indicated. Supersonic specific problems include maintenance of smoothness and waviness conditions in the presence of large thermal stresses, suction penalty minimization, and duct volume/sealing management. Passive efflux (in liu of suction pumps) may be of particular importance for the supersonic case where the bodies approach wave-rider designs. Allowing bleed through the wing (bottom to top) would simultaneously (a) provide LFC on the bottom surface, (b) provide turbulent C_f reduction on the top surface, and (c) reduce wave drag by reducing the strength of the upper surface closure shock, all at nearly minimal system weight and duct volume (depending upon detailed structural design). A possible added benefit would be a reduction of thermal stresses through a tendency to make the entire wing structure more nearly isothermal.

- Minimization of suction drag penalty required for reasonable "return on investment"
- Aerodynamic heat transfer induces high temperatures/thermal stresses which can severely compromise
    - Surface smoothness/waviness
    - Suction duct sealing
- SPFDB honeycomb titanium with electron beam perforations appears to constitute a "best bet" surface
- Suction duct volume requirements are in opposition to the thin wing requirement for wave drag reduction

Suction options include (a) active and (b) passive (bleed)

- Passive efflux can
    - Reduce turbulent drag
    - Reduce wave drag (increase δ^*)

ALTERNATIVE CONFIGURATION APPROACHES
- SUPERSONIC CRUISE LFC -

A basic design decision for supersonic LFC is whether to reduce wave drag but increase LFC difficulty/cross flow by increasing sweep or to reduce sweep, increase wave drag, but simultaneously improve the LFC design problem. In fact, for the nearly zero pressure gradient attached shock flat wing case, the cross flow may be reduced sufficiently to allow wall cooling to become a major LFC factor.

Blunt subsonic leading edges

- Λ large
- Low wave drag
- Large cross flow, makes suction LFC difficult
  - High suction rates required
  - Increased sensitivity to roughness including suction surface geometry (partially plugged slots, perforations)

Sharp supersonic leading edges

- Λ moderate
- High wave drag
- Smaller cross flow, makes suction LFC "easier"
  - Lower suction rates
  - Reduced roughness sensitivity
  - Wall cooling (for SST speed range) an adjunct/alternative control technique (cryo fuel)

SUPERSONIC LFC - BOTTOM LINES

Essentially, supersonic LFC is attainable. Considerable detailed research remains, but there are presently no known "stoppers", and many benefits. The porous surface suction technology must obviously be worked. All of the previous research employed slotted surfaces, and such research should be carried out in low-disturbance facilities for maximum "intellectual" return on investment, i.e., improved understanding of disturbance growth physics and control thereof.

- Aerodynamically, supersonic LFC is attainable, perforated surface physics/efficiency still to be determined
- Critical issues for application include
  - Minimization of suction drag penalty to maximize net drag reduction
    - Approaches include improved slot pressure recovery, passive bleed rather than active suction, cross-flow minimization
    - Necessitated by increased suction requirements due to high sweep/cross flow and High M
  - Duct volume, heated air handling/sealing

SUGGESTED RESEARCH TOPICS FOR SUPERSONIC LFC

This chart provides some suggestions for fluid physics research applicable to supersonic LFC. The possibility that some of the "unit Reynolds effect" observed in flight may be due to disturbances engendered by atmospheric particle-shock interaction is particularly intriguing (see refs. 23 and 24). Also, as noted previously, the suction process creates myriad flow field shocks which should tend to amplify the existing disturbance field in the boundary layer. Information on this process is required for suction surface optimization.

- Perforated surface suction with and without cross flow, experiments and theory especially at large sweep angle/cross flow
- Disturbance amplification through shocks
  - Impinging
  - Suction generated
- Disturbances induced by atmospheric particle/bow-shock interactions
- Further theory/analysis for steps, gaps, waviness, roughness (and combinations) with and without cross flow at high speed

References

1. Driver, Cornelius; and Maglieri, Domenic J.: The Impact of Emerging Technologies on an Advanced Supersonic Transport. Proceedings of the 15th Congress of the International Council of the Aeronautical Sciences, London, UK, Semptember 1986, pp. 213-220.

2. Gasich, Welko E.: Application of Laminar Flow Control to Transport Aircraft. Aerospace Engineering, October 1961.

3. The Laminar Flow Control Presentation for the Aeronautical Division, May 3-4, 1962. III. Laminar Flow Control Aircraft Application Studies. "Supersonic Transport Aircraft," pp. 114-118. Northrop Report 62-105.

4. Craven, A. H.; and Hopkins, H. L.: On the Application of Boundary Layer Control to a Slender Wing Supersonic Airliner Cruising at M = 2.2. The College of Aeronautics, Cranfield, Report No. 157.

5. Morkovin, M. V.: Understanding Transition to Turbulence in Shear Layers. Air Force Office of Scientific Research. AFOSR-TR-83-0931, Final Report, October 1976-December 1982.

6. McQuilkin, F. T.: Feasibility of SPF/DB Titanium Sandwich for LFC Wings. NASA Contractor Report, 165929, June 1982.

7. Ecklund, R. C.; and Williams, N. R.: Laminar Flow Control Control SPF/DB Feasibility Demonstration. NASA Contractor Report 165818, October 1981.

8. Bushnell, Dennis M.; and Tuttle, Marie H.: Survey and Bibliography on Attainment of Laminar Flow Control in Air Using Pressure Gradient and Suction, Volume I. NASA Reference Publication 1035, September 1979.

9. Tuttle, Marie H.; and Maddalon, Dal V.: Laminar Flow Control (1976-1982) A Selected, Annotated Bibliography. NASA TM 84496, August 1982.

10. Lysenko, V. I.; and Maslov, A. A.: The Effect of Cooling on Supersonic Boundary-Layer Stability. J. Fluid Mech., Vol. 147, 1984, pp. 39-52.

11. Kuz'minskiy, V. A.: Effect of Cooling of the Wing Surface on the Transition of Laminar Boundary Layer into the Turbulent at Supersonic Speeds of Flow. Uchenyye Zapiski TSAGI, Vol. 12, Nr. 1, 1981, pp. 1-178.

12. El-Hady, Nabil M.; and Verma, Alok K.: Instability of Compressible Boundary Layers Along Curved Walls with Suction or Cooling. Presented at the AIAA/ASME 3rd Joint Thermophysics, Fluids, Plasma and Heat Transfer Conference, June 1982, St. Louis, MO. Paper No. AIAA 82-1010.

13. Malik, M. R.: COSAL - A Black-Box Compressible Stability Analysis Code for Transition Prediction in Three-Dimensional Boundary Layers. NASA CR-165925, 1982.

14. Lysenko, V. I.; and Maslov, A. A.: Transition of a Supersonic Laminar Boundary Layer on a Cooled Flat Plate. Comptes Rendus Proceedings, Vol. 2., Eighth Canadian Congress Congress of Applied Mechanics, June 1981.

15. Lekoudis, S.: The Stability of the Boundary Layer on a Swept Wing With Wall Cooling. Presented at the AIAA 12th Fluid and Plasma Dynamics Conference, July 1979, Williamsburg, VA. AIAA Paper No. 79-1495.

16. Braslow, Albert L.: A Review of Factors Affecting Boundary-Layer Transition. NASA TN D-3384, August 1966.

17. Bushnell, Dennis M.; and Malik, M. R.: Application of Stability Theory to Laminar Flow Control - Progress and Requirements. Proceedings of the Symposium on the Stability of Time Dependent and Spatially Varying Flows held August 19-23, 1985, NASA Langley Research Center, Hampton, VA, Springer-Verlag, pp. 1-17.

18. USAF and Navy Sponsored Northrop LFC Research Between 1949 and 1967. Special Course on Concepts for Drag Reduction, Belgium, 1977, AGARD Report No. 654, pp. 3-4 - 3-23.

19. Burchfield, C. G.: Boundary-Layer Suction Experiments on a 6-Deg Half-Angle Cone at Mach Numbers 5 through 8. Arnold Engineering Development Company. AEDC-TR-66-230, November 1966.

20. Summary of Laminar Boundary Layer Control Research, Volume II. Northrop Corp., Technical Documentary Report ASD-TDR-63-554.

21. Goldsmith, E. L.; Evans, N. A.; and Smith, G. V. F.: The Effect of Combined Boundary-Layer Suction and Base Bleed on the Drag of a 10 Degree Cone at M = 2.58. Royal Aircraft Establishment Technical Report 67218, August 1967.

22. Bushnell, Dennis M.; and Huffman, Jarrett K.: Investigation of Heat Transfer to Leading Edge of a 76° Swept Fin With and Without Chordwise Slots and Correlations of Swept-Leading-Edge Transition Data for Mach 2 to 8. NASA TM X-1475, December 1967.

23. Holden, M. S.: Studies of Boundary Layer Transition and Surface Roughness Effects in Hypersonic Flow. Calspan Technical Report, AFOSR-TR-84-0251.

24. Pearce, Blaine E.; Sullivan, R. E.; and Donaldson, C. duP.: Cloud Particle Induced Boundary Layer Transition on Hemispherically Blunted Bodies in Supersonic Flight. Aeronautical Research Associates of Princeton, Inc. Report No. 460, 1981.

DESIGN AND FABRICATION REQUIREMENTS FOR LOW NOISE SUPERSONIC/HYPERSONIC WIND TUNNELS

I. E. Beckwith
NASA Langley Research Center
Hampton, Virginia

F.-J. Chen and M. R. Malik
High Technology Corporation
Hampton, Virginia

PROPOSED SUPERSONIC LOW-DISTURBANCE TUNNEL

A schematic diagram of the new proposed Supersonic Low-Disturbance Tunnel at NASA Langley is shown in figure 1. Existing high pressure air and vacuum systems will be used. The specifications and design of two high quality air filters for the new facility are based on experiences and data in the pilot tunnel (ref. 1). Aerodynamic analysis and engineering details of the 8-ft diameter settling chamber and other tunnel components are given in reference 2. The tunnel is designed to accommodate nozzles of various lengths with Mach numbers ranging from 2 to 6. The first nozzle to be operated in the tunnel will be the Mach 3.5 rapid expansion, two-dimensional nozzle illustrated in the lower part of figure 1. The two-stroke model injector is required to place the model into the quiet test core in the upstream part of the uniform flow test rhombus. A 1/3-scale version of this nozzle has been developed and tested extensively in the Pilot Low-Disturbance Tunnel at NASA Langley (refs. 1-4). The techniques for obtaining laminar boundary layers on the nozzle walls, which is the key requirement for quiet test section flow, will be presented in the next several figures.

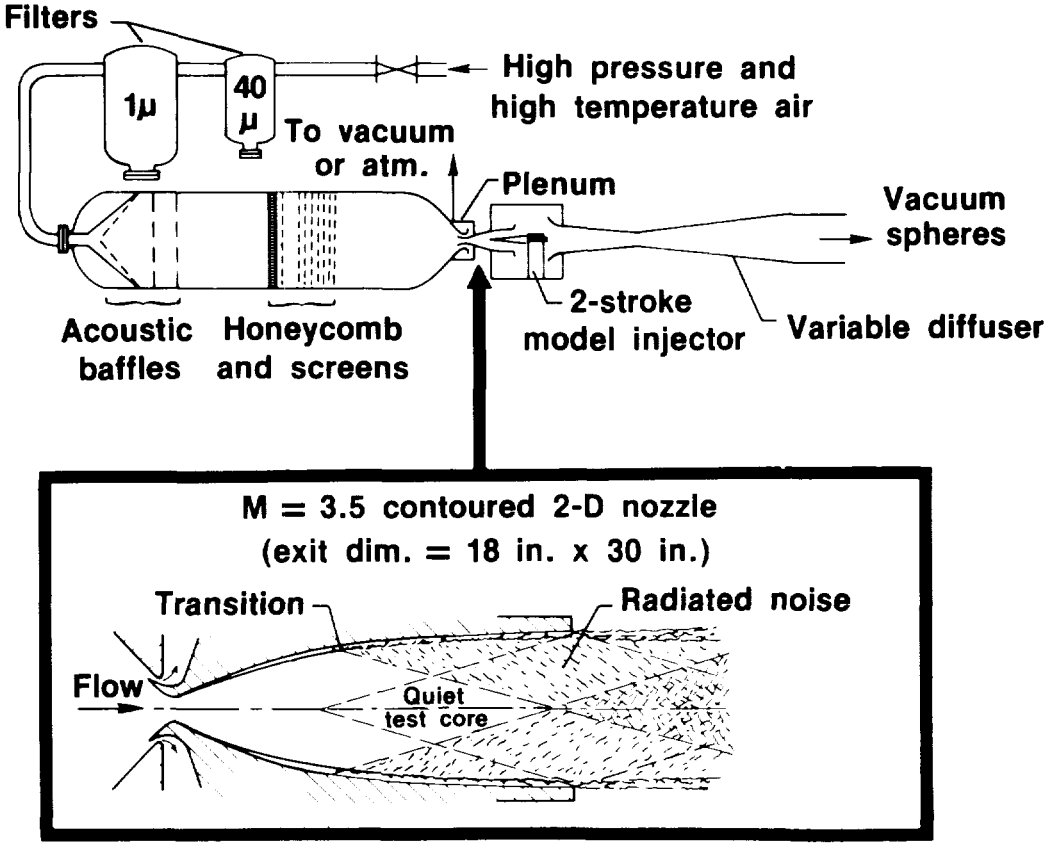

Figure 1

QUIET TEST CORE IN M_∞ = 3.5 RAPID EXPANSION NOZZLE

The dominant source of test-section disturbances in conventional supersonic/hypersonic tunnels is the acoustic radiation from eddies in the turbulent boundary layers on the nozzle walls. In supersonic flow, this noise is in the form of finite-strength wavelets which are propagated along Mach lines. Hence, as illustrated in figure 2, the location of transition onset in the wall boundary layers is sensed with a hot-wire probe at any point along a Mach line extended downstream from that location which is then the "acoustic origin" for the onset of radiated noise in the nozzle flow field. As the unit Reynolds number is increased, transition moves upstream along the contoured walls in this nozzle. The quiet test core region then becomes smaller and tends to approach some minimum size of streamwise length ΔX and height ΔY. When the nozzle walls are very clean and highly polished, the minimum value of ΔX is about 4.5-inches (refs. 1 and 2). At high Reynolds numbers, the sidewall boundary layers are generally turbulent. For these conditions, radiation from the side walls is minimized by the large width of the nozzle (see lower part of fig. 2) and the small local Mach numbers ($M_e < 2.5$) at the acoustic origin locations. The large width of the quiet test core, ΔZ, allows the testing of swept wings and models at large angle of attack.

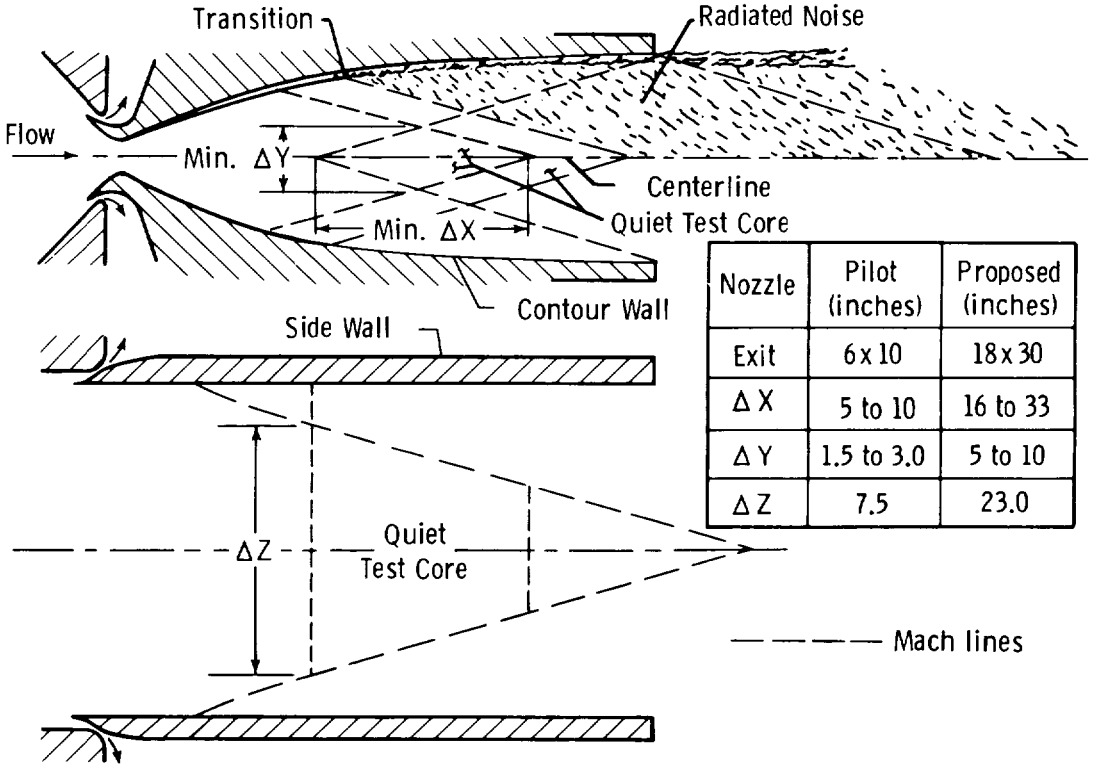

Nozzle	Pilot (inches)	Proposed (inches)
Exit	6x10	18x30
ΔX	5 to 10	16 to 33
ΔY	1.5 to 3.0	5 to 10
ΔZ	7.5	23.0

Figure 2

TRANSITION REYNOLDS NUMBERS ON SHARP CONES

Local Reynolds numbers at transition onset, Re_T, determined from recovery temperatures measured on a sharp tip 5° half-angle cone in the pilot tunnel are plotted against local unit Reynolds number, Re, in figure 3 (see refs. 3 and 4). For values of Re/in < 8×10^5, these data are in the range of atmospheric flight data which are much higher than conventional wind-tunnel data due to the high-stream noise levels in these latter tunnels (sources of these flight and conventional wind-tunnel data are given in ref. 3). The cone used in the quiet tunnel tests was 15-inches long, and for these lower values of Re/in, transition usually occurred on the cone well downstream of the acoustic origin boundary of the quiet test core. Analysis and correlation of these results (refs. 3 and 5) indicate that the cone boundary layer is much more sensitive to wind-tunnel noise in the vicinity of the neutral stability point than further downstream. For Re/in > 8×10^6, the transition Reynolds numbers decrease more or less rapidly towards the levels for previous conventional wind-tunnel data depending on the nozzle wall finish. The effect of surface finish on wall transition and quiet test core sizes in the pilot nozzle and the corresponding quantitative requirements on the wall finish will be considered next.

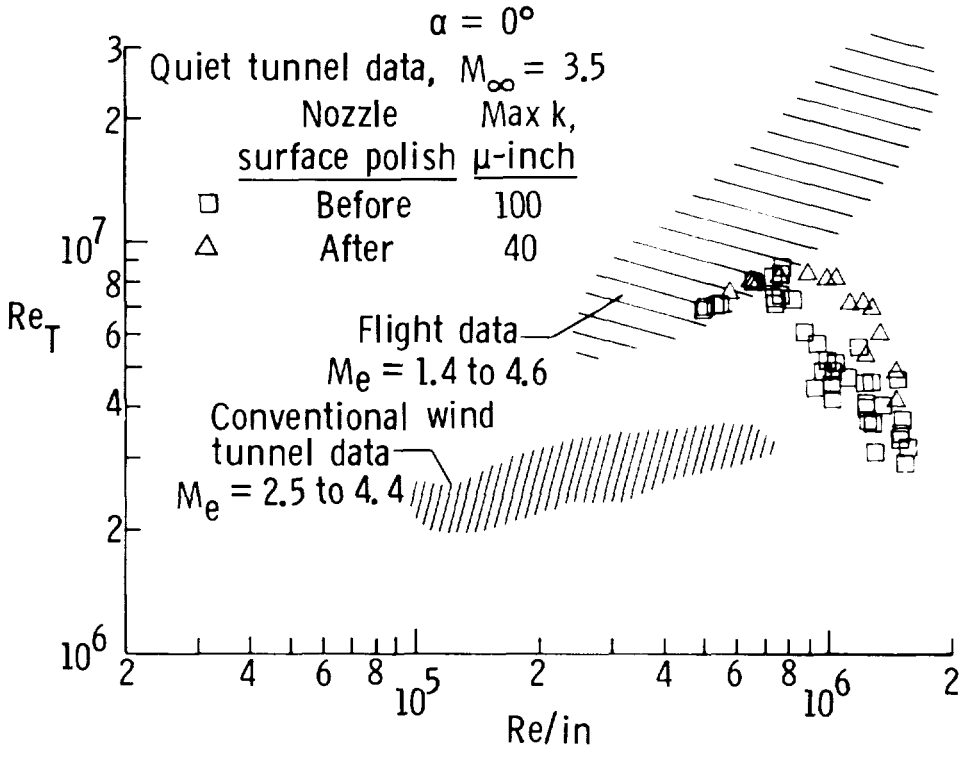

Figure 3

EFFECT OF TRANSITION ON QUIET TEST CORE LENGTH

Figure 4 shows how the axial distance from the throat to transition on the nozzle wall, X_T, is related to the length of the quiet test core, ΔX. Values of these parameters and corresponding free-stream Reynolds numbers based on ΔX are given in the table for large values of $R_\infty/in > 9 \times 10^5$ and for different surface finish conditions. The original blocks were made of 17-4 PH stainless steel with a nominal surface finish of 4 to 6 rms μ-inches. After more polish work was completed the finish was improved to about 1 rms μ-inch and the values of ΔX then approached the "minimum" values observed for this very good surface finish with the corresponding much larger values of $R_{\infty,\Delta X}$. As part of an attempt to improve this finish a new set of blocks was machined from 15-5 PH vacuum remelt stainless steel. The before-polish data on these blocks indicates that ΔX was very small or zero. After preliminary polish work, the value of ΔX for $R_\infty/in \approx 10 \times 10^5$ was increased by a factor of about 7 times. However, at $R_\infty/in = 12.5 \times 10^5$ there was still no usable quiet test core. To understand the reasons for these poor results, we will consider next the effects of known roughness magnitudes and characteristics on nozzle-wall transition.

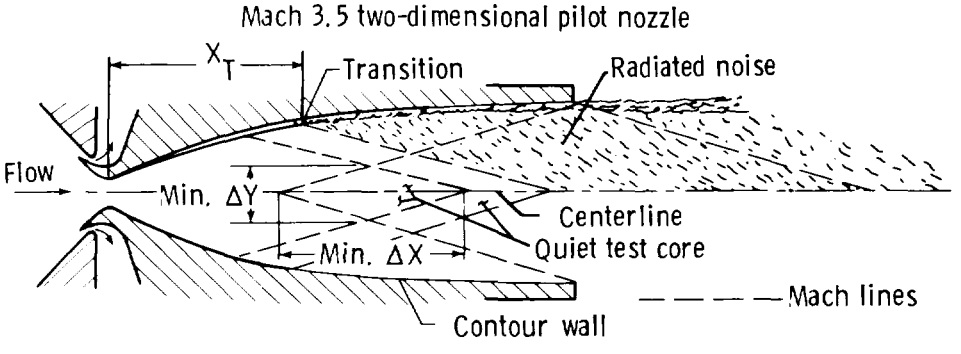

	$R_\infty/in. \times 10^{-5}$	X_T, inches	Quiet ΔX, inches	$R_{\infty,\Delta X} \times 10^{-6}$	
Original blocks	10.2	1.7	2.5	2.6	Before Polish
	15.0	.9	.5	.8	
	10.4	2.7	4.6	4.8	After Polish
	15.5	2.6	4.5	7.0	
New blocks	10.0	1.0	0.7	0.7	Before
	15.1	0.6	0	0	
	9.3	2.9	4.9	4.6	After
	12.5	0.4	0	0	

Figure 4

EFFECT OF SURFACE DAMAGE ON TRANSITION ASYMMETRY

The surface finish of the new Mach 3.5 two-dimensional nozzle blocks has been monitored throughout the polish work with scanning micro-video-recording equipment developed by Dr. L. M. Weinstein at NASA Langley. The effects of any observed surface defects on nozzle-wall boundary-layer transition can then be determined from hot-wire surveys of free-stream disturbances. Results of such surveys obtained after the preliminary polish work (fig. 4) are shown in figure 5. These surveys were made in the vertical centerplane of the nozzle along the centerline (Y = 0) and 1/2-inch above the centerline (Y = 1/2-inch) as illustrated in the upper part of the figure. In the lower part of the figure, values of the rms pressure normalized by the mean static pressure, $\tilde{P}/\bar{P}$, (the "noise level") from the hot-wire data are plotted against the axial distance from the throat for three unit Reynolds numbers. The criterion used to locate transition is where the noise levels rise above low "laminar" values to $\tilde{P}/\bar{P}$ = 0.1 percent. In the upper part of the figure, the asymmetrical locations of transition on the top (No. 1) and bottom (No. 2) blocks are shown for the surveys at $R_\infty/in = 3.7 \times 10^5$. The arrow indicates where transition would have been detected at Y = 1/2-inch for symmetrical locations on the two blocks. The three arrows in the lower part of the figure indicate where transition would be for the surveys at Y = 1/2-inch if X_T was the same on both blocks for the three unit Reynolds numbers. At the highest unit Reynolds number of 9.6×10^5/in, transition asymmetry is more pronounced and $(X_T)_{Y=0}$ = 6.2-inches which corresponds to X_T = 1.1-inch on the wall of block No. 2. This location of transition is well upstream of its location at the slightly smaller value of $R_\infty/in = 9.3 \times 10^5$ in figure 4 where X_T = 2.9-inches. This rapid forward movement of transition with increasing unit Reynolds number and the consistently larger values of X_T on block No. 1 than block No. 2, as well as the complete loss of laminar flow at $R_\infty/in = 12.5 \times 10^5$ (fig. 4) are caused by different surface defects on the two blocks as shown in the next two figures.

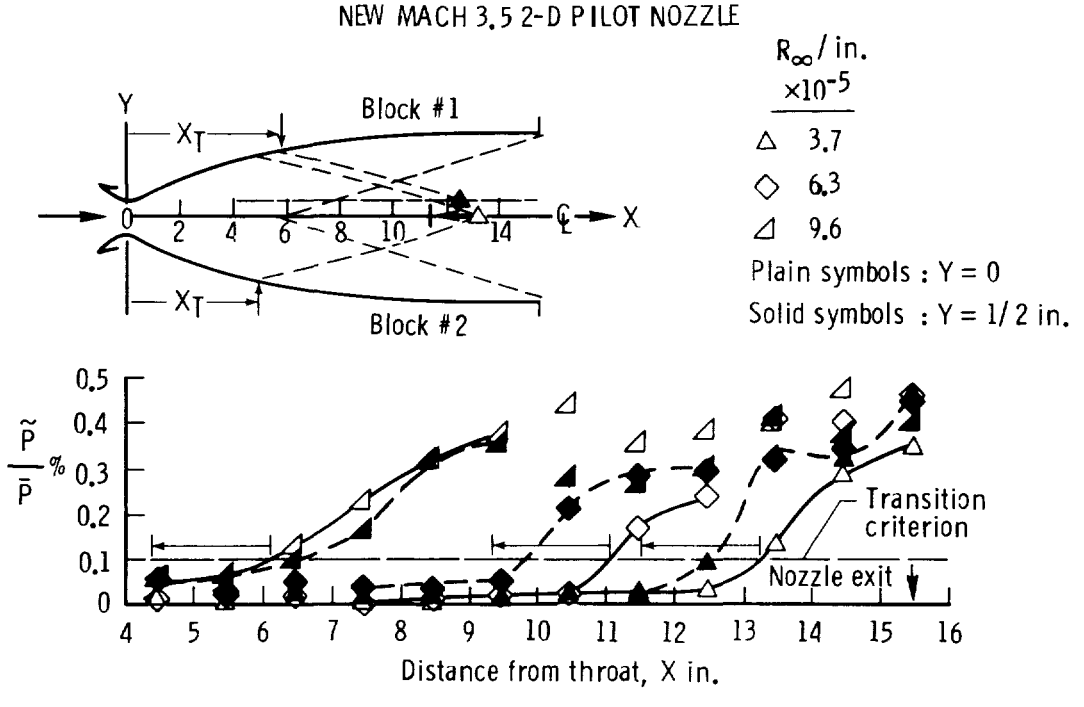

Figure 5

POLISH RESULTS ON NEW MACH 3.5 TWO-DIMENSIONAL NOZZLE
BLOCK NO. 1

Figure 6 shows four microphotographs which illustrate the gradually improved surface finish as the diamond polish grit is reduced in size from 15 microns down to 1/4-micron. A typical pattern of pits located at X = .7-inch from the throat and at Z = 5.1-inches from the sidewall on block No. 1 is shown. Most of these pits are probably caused by micro-inclusions (air bubbles) in the metal. The larger pits in the photographs are .002 to .004-inch long with depths up to about 120 μ- inches measured with a micro-deflection transducer attached to the scanning video microscope. A large amount of data obtained with a commercial profilometer on these blocks indicates that some of the smaller pits are only 20 to 30 microinches deep and that the number and size of the pits decreases as the throat region is approached.

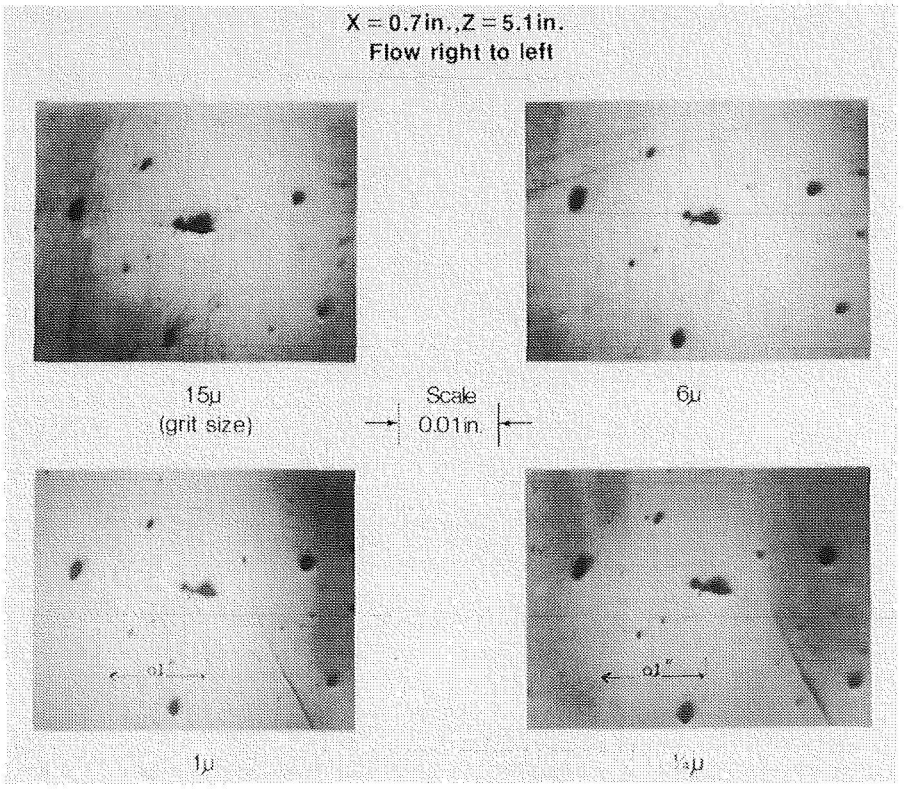

Figure 6

DAMAGE TO SURFACE FINISH FROM POLISH CONTAMINANTS

Figure 7 shows two microphotographs and corresponding profilometer traces of typical contaminant scratches which were visible to the naked eye and were observed only on block No. 2. These scratches, as well as many pits (fig. 6), were present during the test runs used for figures 4 and 5. The scratches shown in figure 7 are only 30 to 35 micro-inches deep at the location of the profilometer stylus tracks. However, they are close to the throat and are aligned across the flow direction. (The laminar boundary-layer thicknesses for $R_\infty = 10 \times 10^5$/inch at these two locations of X = .1 and .3-inch were only .002 and .003-inch, respectively). We conclude from these results and the transition asymmetry shown on figure 5 where X_T was consistently smaller on block No. 2 than block No. 1, that scratches of this type and depth are more dangerous than pits (fig. 6) to the required maintenance of laminar boundary layers on these nozzle walls.

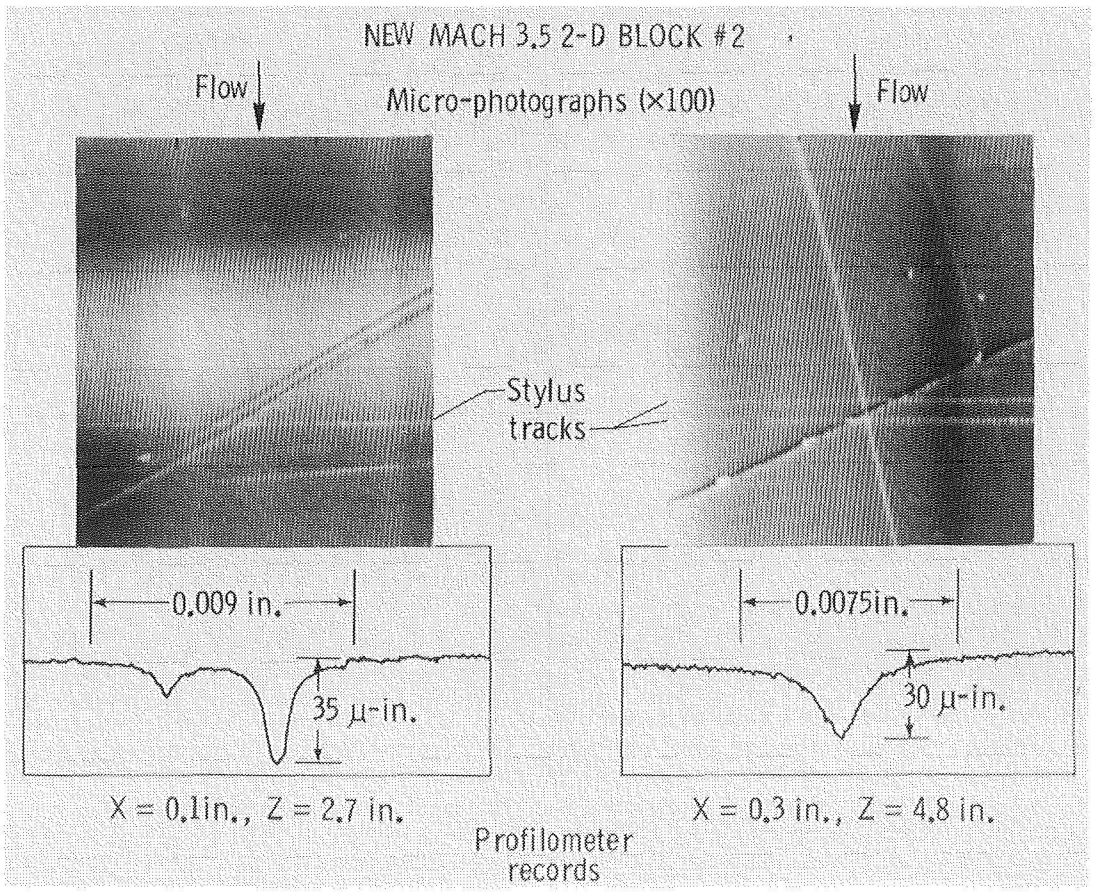

Figure 7

ALLOWABLE SURFACE ROUGHNESS

A review of profilometer roughness measurements on both the original and new Mach 3.5 two-dimensional contoured nozzle blocks is presented in figure 8. The maximum peak-to-valley roughness defects, k, obtained from profilometer measurements on these blocks before and after polish work are plotted against the axial distance from the throat. Typical data at different distances from the sidewall are shown. These data may be compared with the calculated variations of k obtained from numerical solutions for the local laminar boundary-layer profiles using the computer code of reference 6 for the two values of R_∞ shown and for the two values of roughness "height" Reynolds numbers of $R_k = 42$ and 12. This type of roughness Reynolds number, defined as the local Reynolds number evaluated at the distance from the surface of y = k, has been used historically to characterize the effects of both isolated and distributed roughness particles on transition. Early examples are given in reference 7 where critical values of R_k for transition on flat plates and cones varied from about 260 to 625 for the Mach number range from 1.6 to 3.7. The critical values of R_k on these blocks are apparently much smaller, presumably due to the different type of roughness and the different flow conditions such as pressure gradients and instability mechanisms. Nevertheless, it may be concluded from detailed flow and roughness data in references 1-4 and the results in figures 4-7 herein, that $R_k \approx 10$ is required to maintain laminar boundary layers on the contoured walls in this type of nozzle. For this application, k is defined as the maximum peak-to-valley profilometer measurement of local surface defects. However, all scratches of the type shown in figure 7 must be removed during the final polishing work.

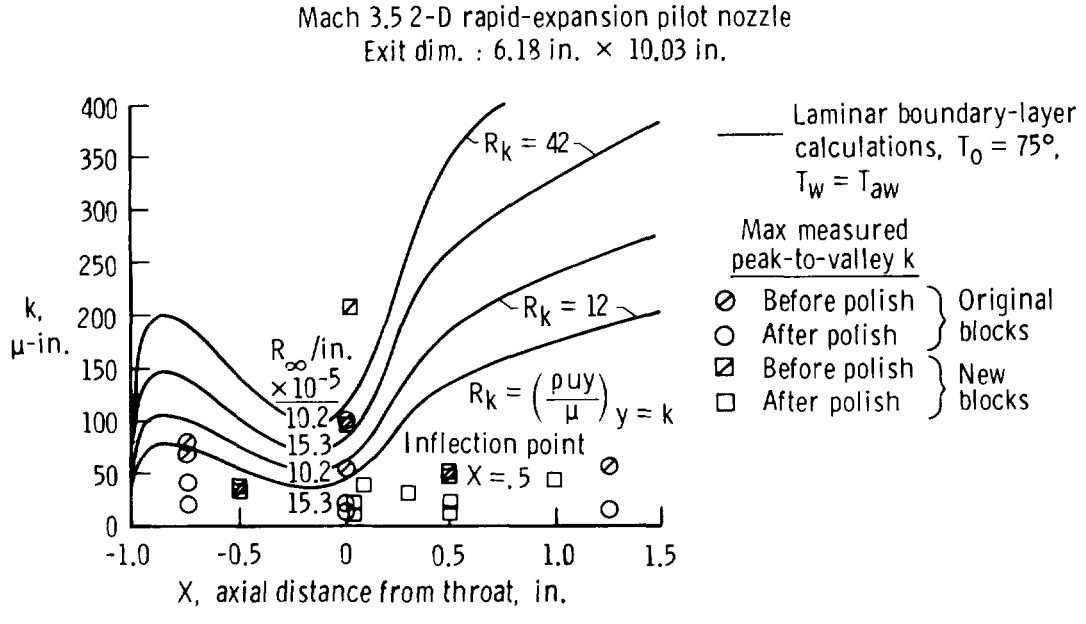

Figure 8

GÖRTLER VORTICES IN M=3.5 TWO-DIMENSIONAL NOZZLE

In order to apply transition results from the present nozzles to the design of different nozzles at other flow conditions or to more general supersonic configurations, it is essential to understand the transition mechanisms involved and to develop theoretical models that can be used for predictive purposes. An early start to understanding the mechanisms was reported in reference 8, but satisfactory models depended on the successful application of linear stability theory by Dr. Malik to the correct local flow conditions (refs. 4, 9 and 10). The principal results of this work were to show that transition in these nozzles for Mach numbers from 3 to 5 was generally caused by the Görtler instability mechanism in the concave curvature regions of the nozzles rather than Tollmien-Schlichting waves, provided that the nozzle walls were maintained clean and polished, and boundary-layer removal slots at the nozzle entrance were used. A brief review of some of that work will now be presented with applications to the design of advanced nozzles that promise much longer quiet test regions than achieved to date.

Figure 9 shows flow vectors calculated by the stability theory for Görtler vortices (the mean flow direction is into the page) in the Mach 3.5 two-dimensional pilot nozzle at R_∞ =5.1 x 10^5/in, where the experimental location of transition on the wall was at $X_{w,T}$ = 3.6-inches from the throat. The laminar boundary-layer thickness at this point was 0.019-inch and maximum amplification was calculated when the ratio of Görtler wavelength to boundary-layer thickness, λ/δ, was taken as 0.82 as shown on the right side of the figure. These conditions gave N = 9.6 as the integral of the local amplification rates from the wall inflection point to transition.

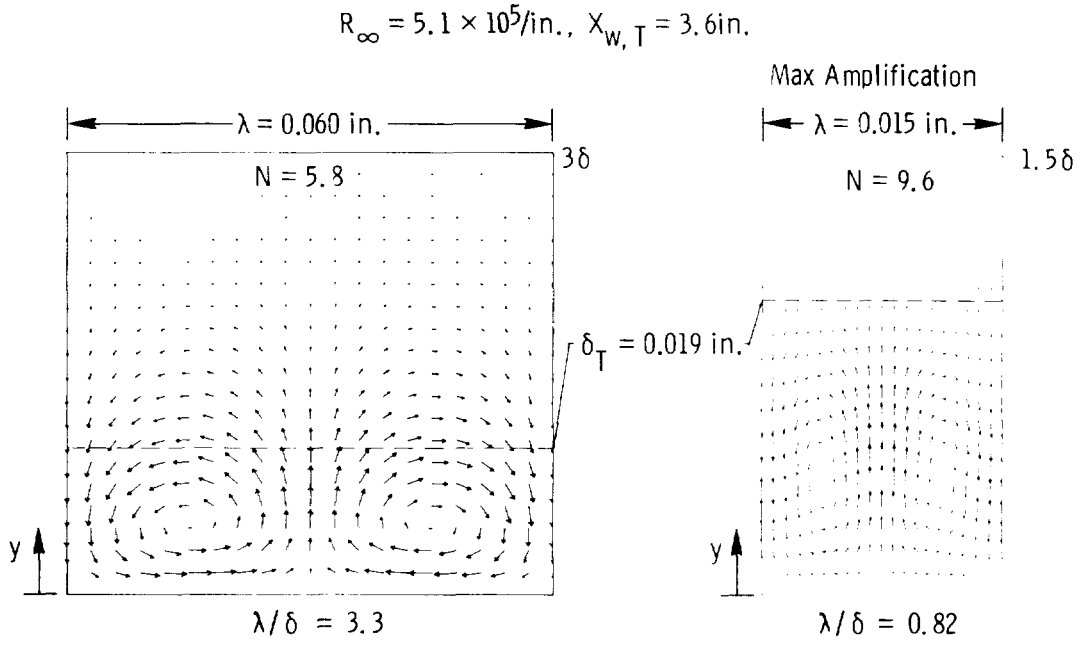

Figure 9

EFFECT OF GÖRTLER VORTEX WAVELENGTH ON AMPLIFICATION TO TRANSITION

Figure 10 shows that the N-factors for maximum amplification to transition of the Görtler vortices in this nozzle varied from about 9 to 11 over the entire range of test Reynolds numbers and measured transition locations, $X_{w,T}$. These transition locations were observed only when the nozzle walls were clean and polished and with the bleed valve open (ref. 4). The calculated maximum amplification always occurred within the narrow wavelength range of $.75 < \lambda/\delta < .95$. Similar results were obtained in two rapid-expansion axisymmetric nozzles for test section Mach numbers of 3 and 5 (ref. 10).

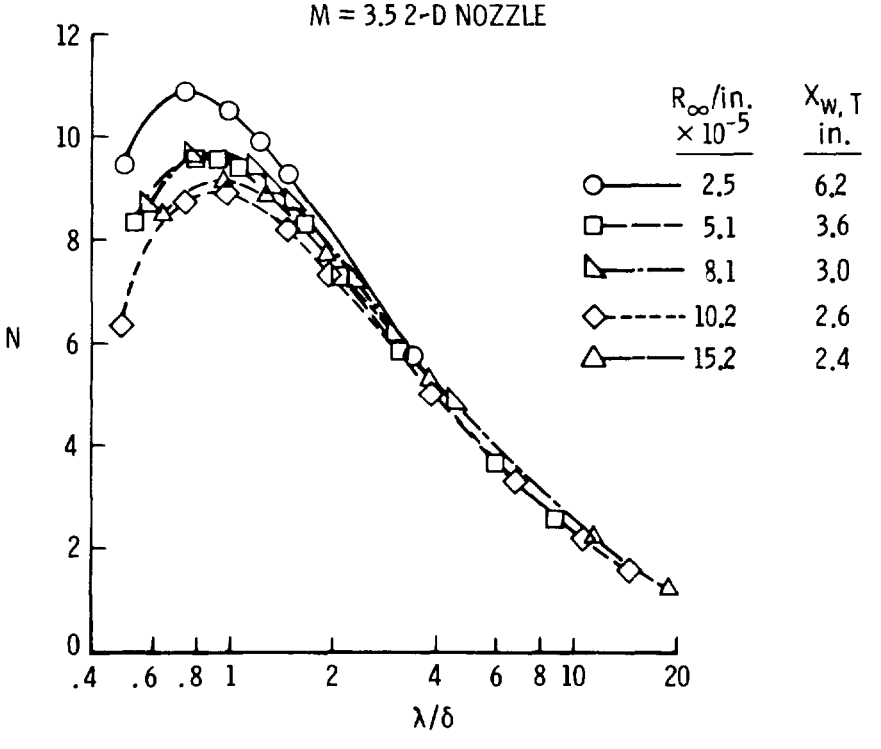

Figure 10

MACH 3.5 AXISYMMETRIC-LONG NOZZLE

After it was established that Görtler vortices were the dominant cause of transition in these slotted nozzles, techniques for modifying the onset and amplification of the vortices were developed (ref. 4, 9, and 10). The most practical technique was to insert a section of radial flow in the expansion region of the nozzle. This technique is used to minimize the concave wall curvature by moving the inflection point far downstream which delays the onset of the Görtler instability and reduces the vortex growth rates because of smaller streamwise increases in boundary-layer thicknesses.

Figure 11 illustrates the application of this technique to the aerodynamic design of a new Mach 3.5 axisymmetric nozzle which is now being fabricated. The value of the N-factor used to predict the location of transition ($X_{w,T}$) was taken as N = 9.2. At the largest value of R_∞/in = 15.5 x 10^5, the value of N for amplification of Tollmien-Schlichting (TS) waves was only 2.3. Therefore, if the surface finish determined by the criteria of $R_k \simeq 10$ can be obtained, and if the extremely small tolerances on wall radius and waviness based on our test results of a Mach 3 rapid-expansion axisymmetric nozzle (ref. 10) can be achieved, this new nozzle should provide the large values of $R_{\infty,\Delta X}$ shown.

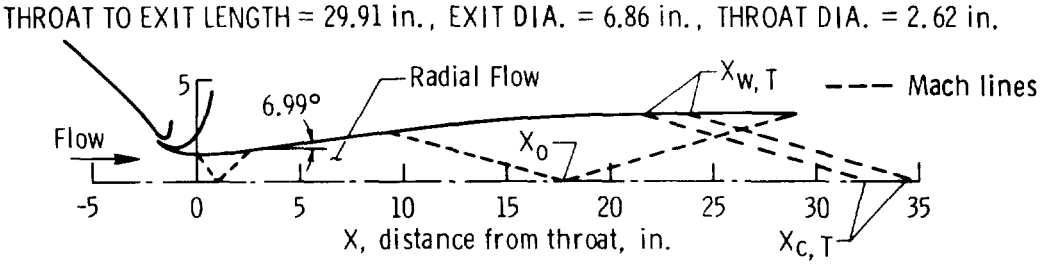

Transition predicted for Görtler N = 9.2, T_0 = 530°R

P_0 psia	R_∞/in. $\times 10^{-6}$	$X_{w,T}$ inches	$X_{c,T}$ inches	$\Delta X = X_{c,T} - X_0$, in.	$R_{\infty,\Delta X}$ $\times 10^{-6}$	TS N
100	1.03	23.57	34.89	17.09	17.6	
150	1.55	21.21	32.40	14.60	22.6	2.3

Figure 11

COMPARISON OF TRANSITION REYNOLDS NUMBERS WITH $R_{\Delta X}$

Experimental values of $R_{\Delta X}$ for three nozzles are compared with flight data for transition Reynolds numbers, R_T, on cones in figure 12. The Mach 3 axisymmetric rapid-expansion nozzle (ref. 10) was fabricated by electroforming nickel onto a stainless steel mandrel. The final surface finish of the mandrel was examined with an interference microscope. The space between each fringe was 10.75 micro-inches, or half the wavelength of the green mercury light used. The maximum peak-to-valley defects as determined from the fringe deviations on micro-interferograms at 6 random locations on the mandrel was approximately 15 μ-inches. The electroformed nickel surface of the nozzle duplicated that of the mandrel and resulted in the highest quality finish on any of the 6 nozzles tested to date. The measured values of $R_{\Delta X}$ were also higher than for the other nozzles. At the highest test unit Reynolds number of $R_\infty = 1.6 \times 10^6$/in, $R_{\Delta X} = 10.1 \times 10^6$ for the Mach 3 nozzle. The calculated value of the N-factor at the corresponding measured location of transition was N = 5.9 (ref. 10). The effects of different surface finishes, as shown in figure 8, on $R_{\Delta X}$ for both the original and new Mach 3.5 two-dimensional, rapid expansion (R.E.) blocks are also shown in figure 12. Note that the new blocks with maximum k = 40 μ-inches, resulted in the highest levels of $R_{\Delta X}$ for R_∞/in < 6×10^5/inch. However, for R_∞/in > 9.3×10^5 the extent of laminar flow decreased rapidly due to the influence of damage scratches such as those shown in figure 7. The predicted values of $R_{\Delta X}$ for the new axisymmetric-long Mach 3.5 nozzle are in the range of flight data for R_T. This indicates that most of the laminar boundary layer preceding transition on slender test models would be exposed to the extremely low "laminar" noise levels below .05 percent.

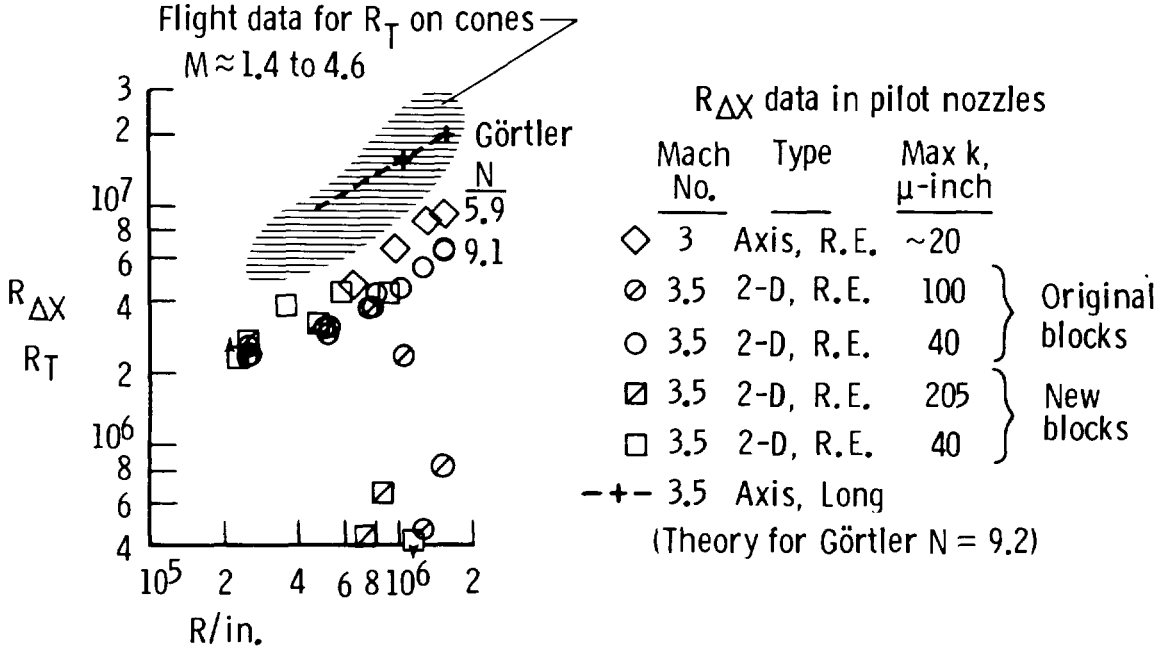

Figure 12

ALLOWABLE SURFACE ROUGHNESS

As a guide for the surface finish specifications on the new Mach 3.5 axisymmetric-long nozzle, values of k have been computed for the same test conditions used for the surface finish assessment of the Mach 3.5 two-dimensional nozzle (fig. 8). Again, values of R_k = 42 and 12 were used as shown in figure 13. For R_k = 12 and at the highest unit Reynolds number this figure indicates that the maximum allowable peak-to-valley roughnesses for this nozzle are increased somewhat to about 50 μ-inches as compared to 40 μ-inches on the two-dimensional nozzle. However, the region where k < 150 μ-inches is required, extends over a total axial distance of about 5.4-inches compared to a corresponding distance of only 1.7-inches on the two-dimensional nozzle.

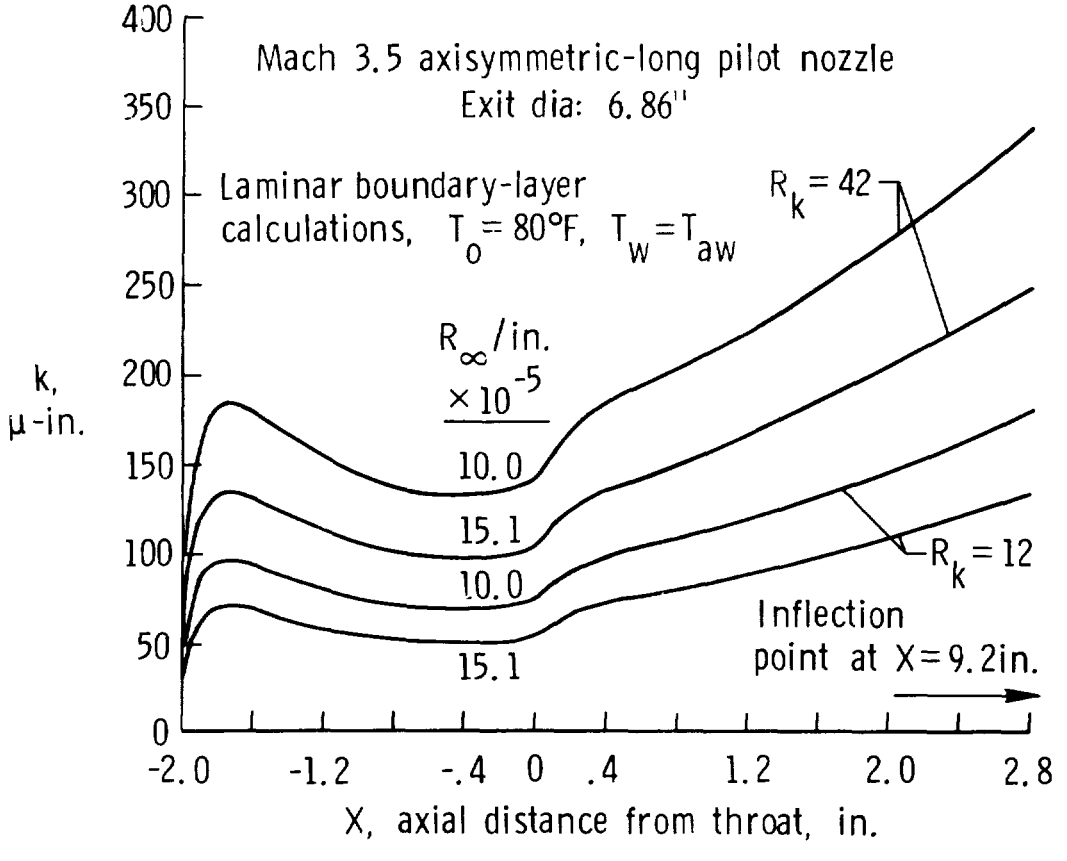

Figure 13

MACH 6 LOW-DISTURBANCE PILOT NOZZLE

A new Mach 6 long-axisymmetric nozzle has been designed using the same radial flow techniques and N-factor criteria as for the new Mach 3.5 axisymmetric nozzle (fig. 11). The engineering design for this nozzle, which will be tested in an existing facility at NASA Langley, is now completed. The contour outline and predicted quiet test core is shown in the upper part of figure 14. The high value of $R_{\infty,\Delta X} = 13.2 \times 10^6$ at $R_\infty/in = 5.1 \times 10^5$ was predicted using N = 9 for transition due to the Görtler instability. At this transition point the value of N for the first mode TS instability was 3.6. In spite of the higher local Mach numbers, the first TS mode was still dominant over the second mode in this calculation. In the lower part of figure 14, the projected performance of the new Mach 6 nozzle, in terms of $R_{\Delta X}$, is compared with Mach 6 transition onset data on cones in atmospheric flight and in conventional wind tunnels. The wind-tunnel data are from references 11 and 12 for 5° and 10° semi-apex angle, sharp tip cones at $M_\infty \approx 6$. (The data from reference 12 were adjusted to represent transition onset.) The flight data are from figure 4 in reference 13 for cones at $M_e \approx 6$. The corresponding cross-hatched region in figure 14 is based partly on interpolations along the correlation curves presented in reference 13. Also shown in figure 14 below are experimental values of $R_{\Delta X}$ and corresponding values of N-factors for a Mach 5 axisymmetric, rapid-expansion nozzle tested at NASA Langley (refs. 8 and 10). Again, these comparisons indicate that the new Mach 6 nozzle should provide sufficiently high values of $R_{\Delta X}$ to simulate flight noise levels and transition Reynolds numbers.

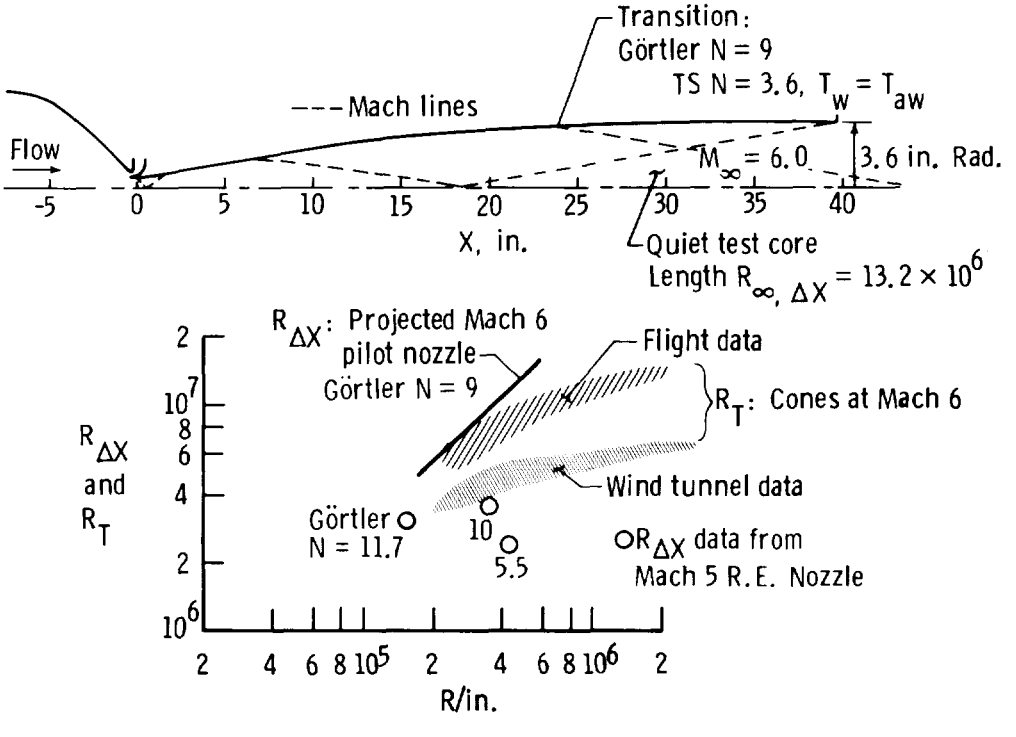

Figure 14

ALLOWABLE SURFACE ROUGHNESS

The values for local roughness Reynolds numbers of R_k = 42 and 12 have again been used to calculate allowable peak-to-valley roughnesses for the new Mach 6 axisymmetric-long pilot nozzle. The results are shown in figure 15 for two unit Reynolds numbers corresponding to stagnation pressures of 150 and 300 psia at the stagnation temperature of 820°R. Thus, for R_k = 12 and $R_\infty/in = 5.1 \times 10^5$, values of k < 30 μ-inches are required in the throat region. This surface finish can be achieved based on our experiences with the Mach 3 axisymmetric nozzle (fig. 12).

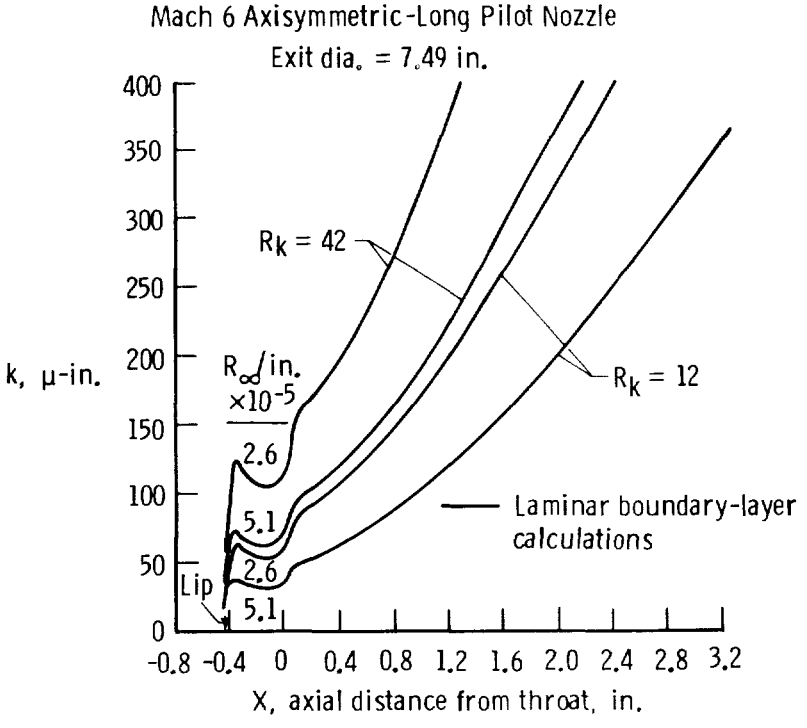

Figure 15

CONCLUSIONS

1. Large width two-dimensional rapid expansion nozzles guarantee wide quiet test cores that are well suited for testing models at large angle of attack and for swept wings. Hence, this type of nozzle will be operated first in the new proposed large scale Supersonic Low-Disturbance Tunnel.

2. Test results indicate that the surface finish of pilot nozzles is critical. The local roughness Reynolds number criteria of $R_k \simeq 10$ will be used to specify allowable roughness on new pilot nozzles and the new proposed tunnel.

3. Experimental data and calculations for M = 3.0, 3.5, and 5.0 nozzles give N-factors from 6 to 10 for transition caused by Görtler vortices.

4. The use of $N \simeq 9.0$ for the Görtler instability predicts quiet test cores in the new M = 3.5 and M = 6.0 axisymmetric-long pilot nozzles that are 3 to 4 times longer than observed in the test nozzles to date. The new nozzles utilize a region of radial flow which moves the inflection point far downstream and delays the onset and amplification of the Görtler vortices.

REFERENCES

1. Creel, Theodore R.; Beckwith, Ivan E.; and Chen, Fang-Jenq: Nozzle Wall Roughness Effects on Free-Stream Noise and Transition in the Pilot Low-Disturbance Tunnel. NASA Technical Memorandum 86389, September 1985.

2. Beckwith, I. E.; Chen, F.-J.; and Creel, T. R., Jr.: Design Requirements for the NASA Langley Supersonic Low-Disturbance Wind Tunnel. AIAA Paper No. 86-0763-CP, March 1986.

3. Beckwith, Ivan E.; Creel, Theodore R., Jr.; Chen, Fang-Jenq; and Kendall, James M.: Free-Stream Noise and Transition Measurements on a Cone in a Mach 3.5 Pilot Low-Disturbance Tunnel. NASA Technical Paper 2180, September 1983.

4. Beckwith, I. E.; Malik, M. R.; and Chen, F.-J.: Nozzle Optimization Study for Quiet Supersonic Wind Tunnels. AIAA-84-1628, June 1984.

5. Chen, Fang-Jenq; Beckwith, Ivan E.; and Creel, Theodore R., Jr.: Correlations of Supersonic Boundary-Layer Transition on Cones Including Effects of Large Axial Variations in Wind-Tunnel Noise. NASA TP-2220, January 1984.

6. Harris, Julius E.; and Blanchard, Doris K.: Computer Program for Solving Laminar, Transitional, or Turbulent Compressible Boundary-Layer Equations for Two-Dimensional and Axisymmetric Flow. NASA Technical Memorandum 83207, February 1982.

7. Braslow, Albert L.: A Review of Factors Affecting Boundary-Layer Transition. NASA TN D-3384, August 1966.

8. Beckwith, Ivan E.; and Holley, Barbara B.: Gortler Vortices and Transition in Wall Boundary Layers of Two Mach 5 Nozzles. NASA Technical Paper 1869, August 1981.

9. Beckwith, Ivan E.; Malik, M. R.; Chen, F.-J.; and Bushnell, D. M.: Effects of Nozzle Design Parameters on the Extent of Quiet Test Flow at Mach 3.5. Laminar-Turbulent Transition, IUTAM Symposium Novosibirsk 1984, Editor: V. V. Kozlov, Springer-Verlag, Berlin, Heidelberg, 1985.

10. Chen, F.-J.; Malik, M. R.; and Beckwith, I. E.: Instabilities and Transition in the Wall Boundary Layers of Low-Disturbance Supersonic Nozzles. AIAA-85-1573, July 1985.

11. Stainback, P. Calvin: Hypersonic Boundary-Layer Transition in the Presence of Wind-Tunnel Noise. AIAA Journal, Vol. 9, No. 12, December 1971, pp. 2475-2476.

12. Pate, S. R.: Measurements and Correlations of Transition Reynolds Numbers on Sharp Slender Cones at High Speeds. AIAA Journal, Vol. 9, No. 6, June 1971, pp. 1082-1090.

13. Beckwith, I. E.: Development of a High Reynolds Number Quiet Tunnel for Transition Research. AIAA Journal, Vol. 13, No. 3, March 1975, pp. 300-306.

THE EFFECTS OF WALL SURFACE DEFECTS ON BOUNDARY-LAYER TRANSITION IN QUIET AND NOISY SUPERSONIC FLOW

E. L. Morrisette and T. R. Creel, Jr.
NASA Langley Research Center
Hampton, Virginia

INTRODUCTION

The design of supersonic vehicles with laminar-flow control and vehicles such as the Space Shuttle requires information on allowable transition tolerances to fabrication defects such as discrete surface roughness and waviness. The existing data base for the effect of waviness on transition consists primarily of the World War II data of Fage,[1] the studies of Carmichael[2] for the X-21 program, and the lone supersonic work of Howard and Czarnecki[3] in the early 60's. A relatively large data base on the effects of discrete roughness on transition exists for subsonic and supersonic speeds. The existing supersonic wind-tunnel transition data are "contaminated" by wind-tunnel noise emanating from the turbulent boundary layers on the nozzle walls. The present paper will compare roughness and waviness transition data obtained in a "quiet" Mach 3.5 supersonic wind tunnel (Langley Research Center's Supersonic Low-Disturbance Pilot Tunnel[4]) with those obtained in conventional "noisy" flows. See figure 1.

- WAVINESS AND ROUGHNESS CRITERIA REQUIRED FOR M > 1 LFC
  - E^N APPROACH ONLY VALID FOR NEGLIGIBLE ROUGHNESS/WAVINESS
  - WHAT IS DEFINITION OF NEGLIGIBLE?
- ONLY ONE WAVINESS M > 1 STUDY AVAILABLE AND IS IN A "NOISY" GROUND FACILITY
- ALL ROUGHNESS (M > 1, GROUND FACILITY) STUDIES IN NOISY FACILITIES
- PRESENT PAPER:
  - CONDUCTED WITH AND WITHOUT FACILITY NOISE
  - COVERS RELATIVELY WIDE RANGE OF WAVE PARAMETERS
  - INCLUDES INITIAL STUDIES OF ROUGHNESS VS. WAVE EFFECTS

Figure 1

WAVY WALL CONE MODELS

The models used in this study were all 5° half-angle sharp cones with surface finishes better than 5 μ-in. rms and tip diameters less than 0.002 inches. A smooth wall cone instrumented with thermocouples along two rays, 180° apart, was used for comparison with the wavy wall cone data and for the tests with discrete roughness. The surface profiles of the 8 wavy wall cones are shown with exagerated vertical scales. The wavelengths were chosen to fall into the range of the most amplified Tollmein-Schlichting waves for flow over sharp tip smooth cones at the present tunnel operating conditions. For all wavy cones, the waves start 2-inches from the tip of the model and extend to the rear of the 15-inch long cones (figure 2).

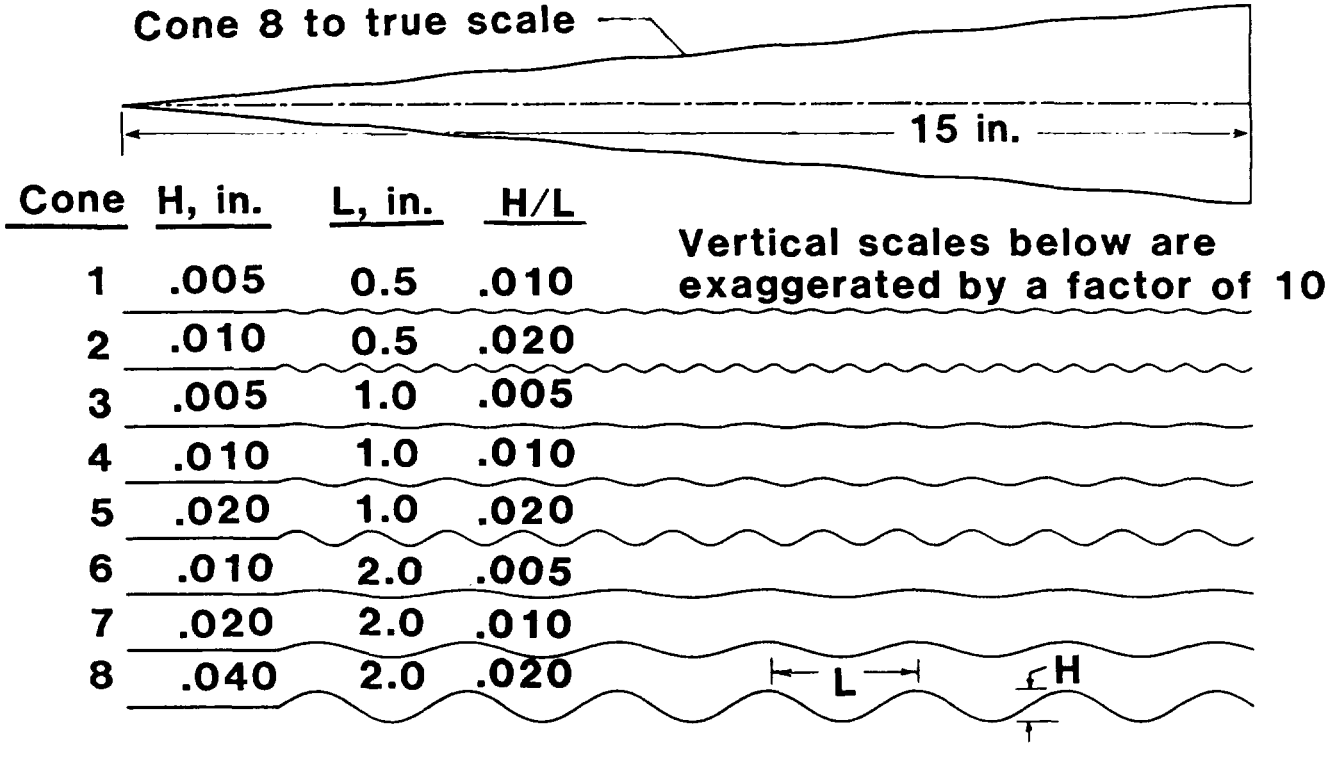

Figure 2

CONE PRESSURE AND PRESSURE GRADIENT DISTRIBUTIONS

Figure 3 shows the surface profiles of the 8 wavy wall cones along with the non-dimensionalized pressures and the pressure gradients calculated from supersonic small disturbance theory. Each of the scales shown applies to the plots for each of the eight cones. The minimiums and maximums in pressure are functions of H/L; the maximums and minimums in pressure gradient are proportional to H/L^2. Cone 2 is seen to have the most severe pressure gradients and cone 6 the mildest gradients. While there is a step increase in pressure at the start of the waves, the pressure rise for the worst case corresponds to the pressure rise of only a 3-degree turn.

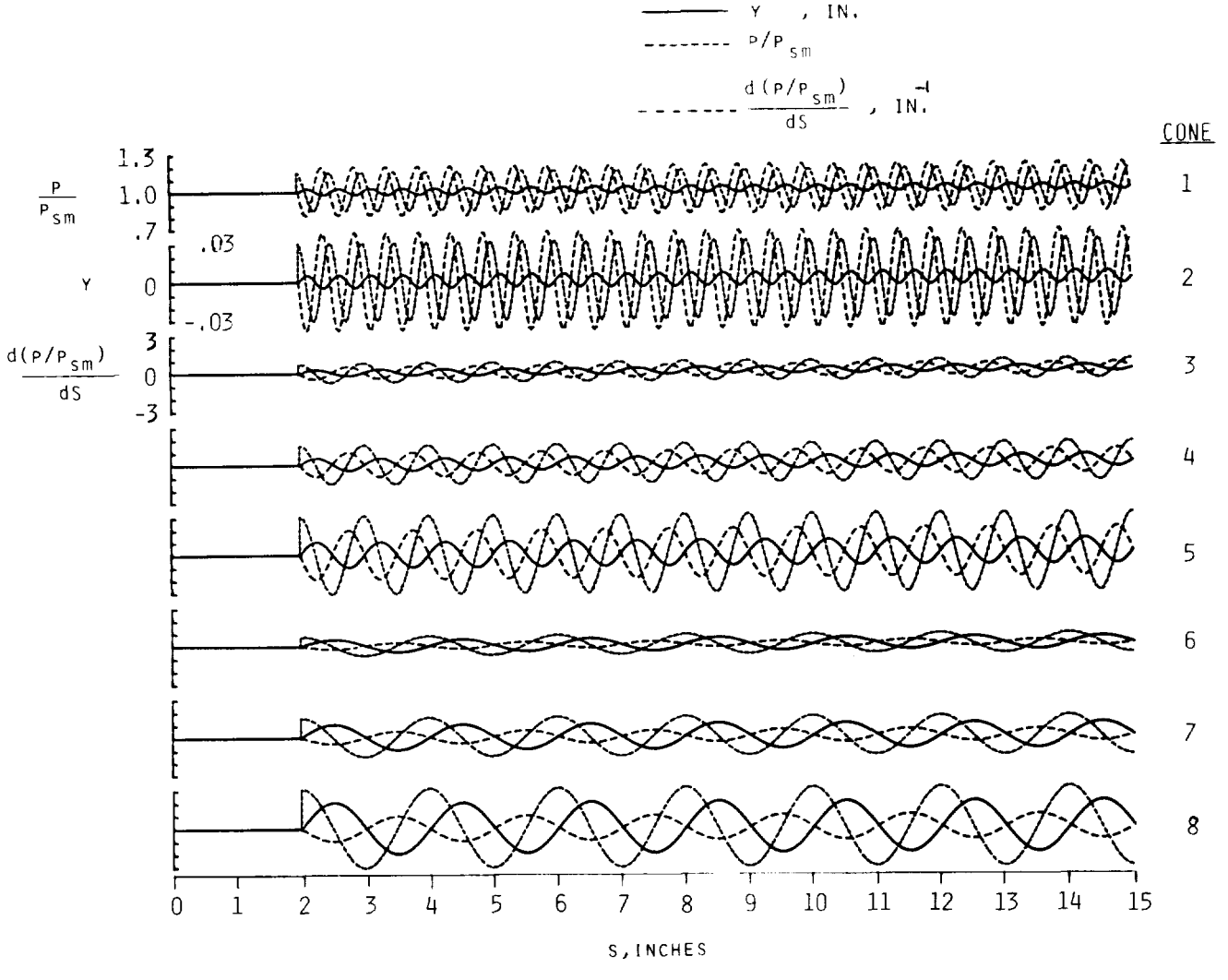

Figure 3

TRANSITION DETECTION TECHNIQUES

Transition on the wavy cones was obtained by using a fixed surface pitot tube and increasing the tunnel total pressure until transition was detected. Figure 4 shows typical variations of the pitot pressure for various pitot positions along the cone surface. In all cases the pitot tube was located at the peak of a wave and no effort was made to determine the patterns of transition movement between peaks. The location of transition was taken at the value of total pressure where there was a sharp increase in pitot pressure. Transition on the smooth cone was determined with recovery temperature distributions measured with thermocouples as well as with pitot tube data. Transition for the recovery temperature distribution was taken at the location of sudden increase in recovery temperature. The recovery temperature and pitot tube techniques gave similar transition Reynolds numbers.

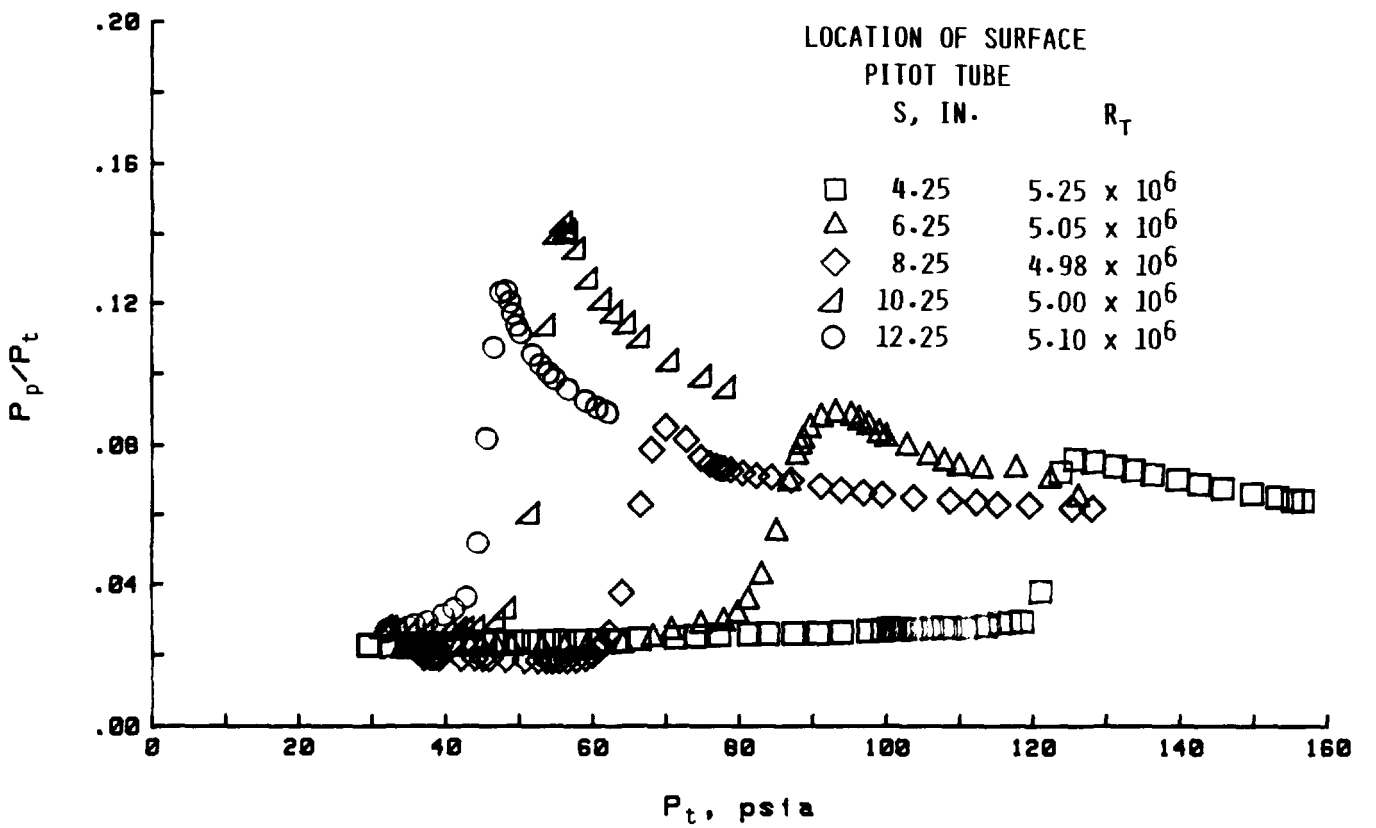

Figure 4

TRANSITION REYNOLDS NUMBERS
WAVY WALL CONES - QUIET FLOW

Figure 5 shows the transition Reynolds numbers as a function of unit Reynolds number for the cones in "quiet flow." The outlined area shows data obtained on smooth cones and the solid line ($R_T = 8 \times 10^6$) is used as a data fairing for comparison with the wavy wall cone data. The waves on all of the cones cause a reduction in transition Reynolds number. In general the data follow the trend of the smooth cone data but at a lower level. At the higher unit Reynolds numbers it is expected that wavy wall cone data would approach the smooth wall data since the smooth wall transition locations are approaching the location of the start of the waves on the wavy wall cones.

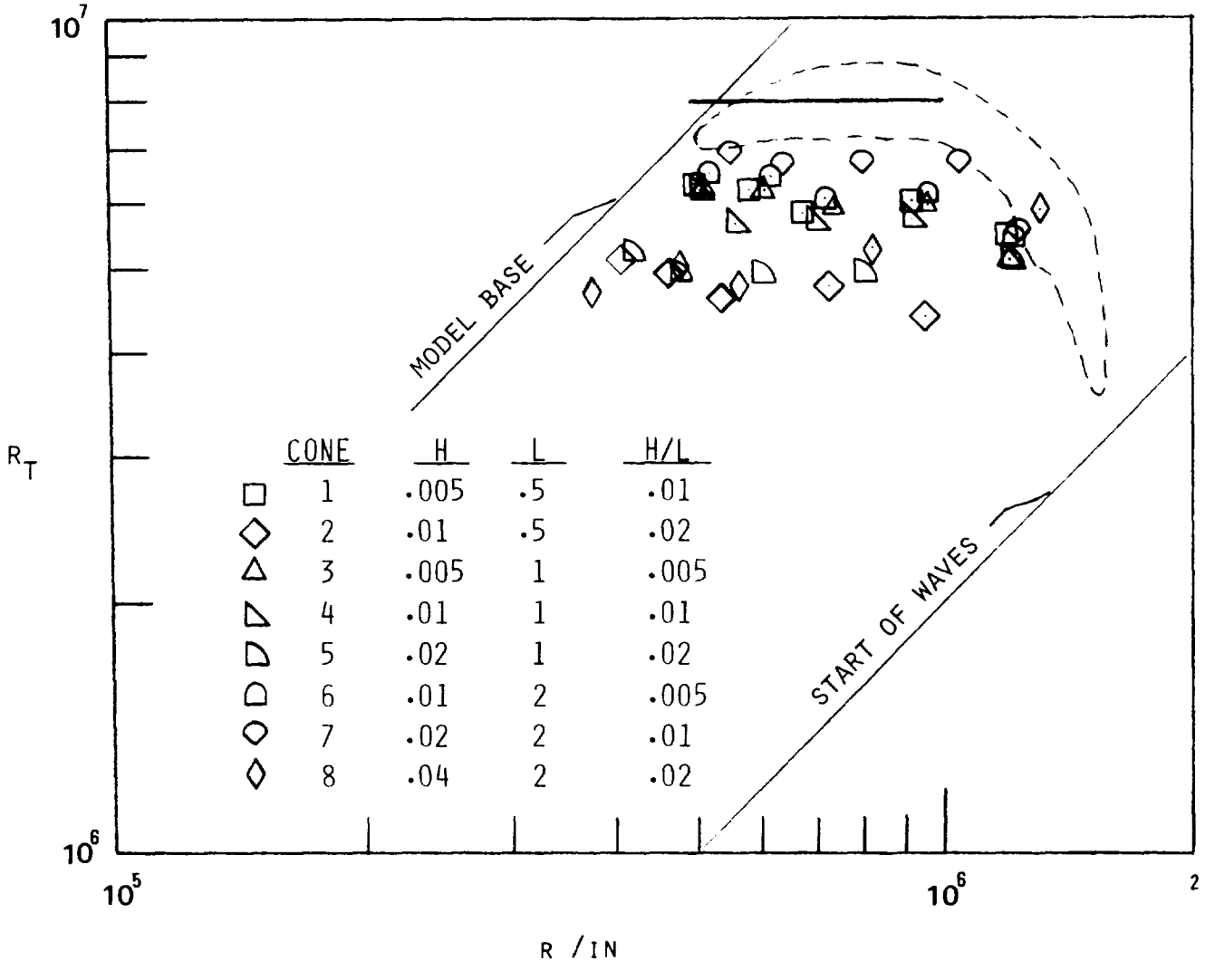

Figure 5

TRANSITION REYNOLDS NUMBERS
WAVY WALL CONES - NOISY FLOW

Figure 6 shows the transition Reynolds numbers for data obtained in a "noisy" flow. The data trends are similar to those of the "quiet" flow data (figure 5) but at much lower levels. The wavy wall cone data merge with the smooth wall data above a unit Reynolds number of 5×10^5 per inch where a peak in free-stream noise[4] causes a rapid forward movement in transition location on all of the models.

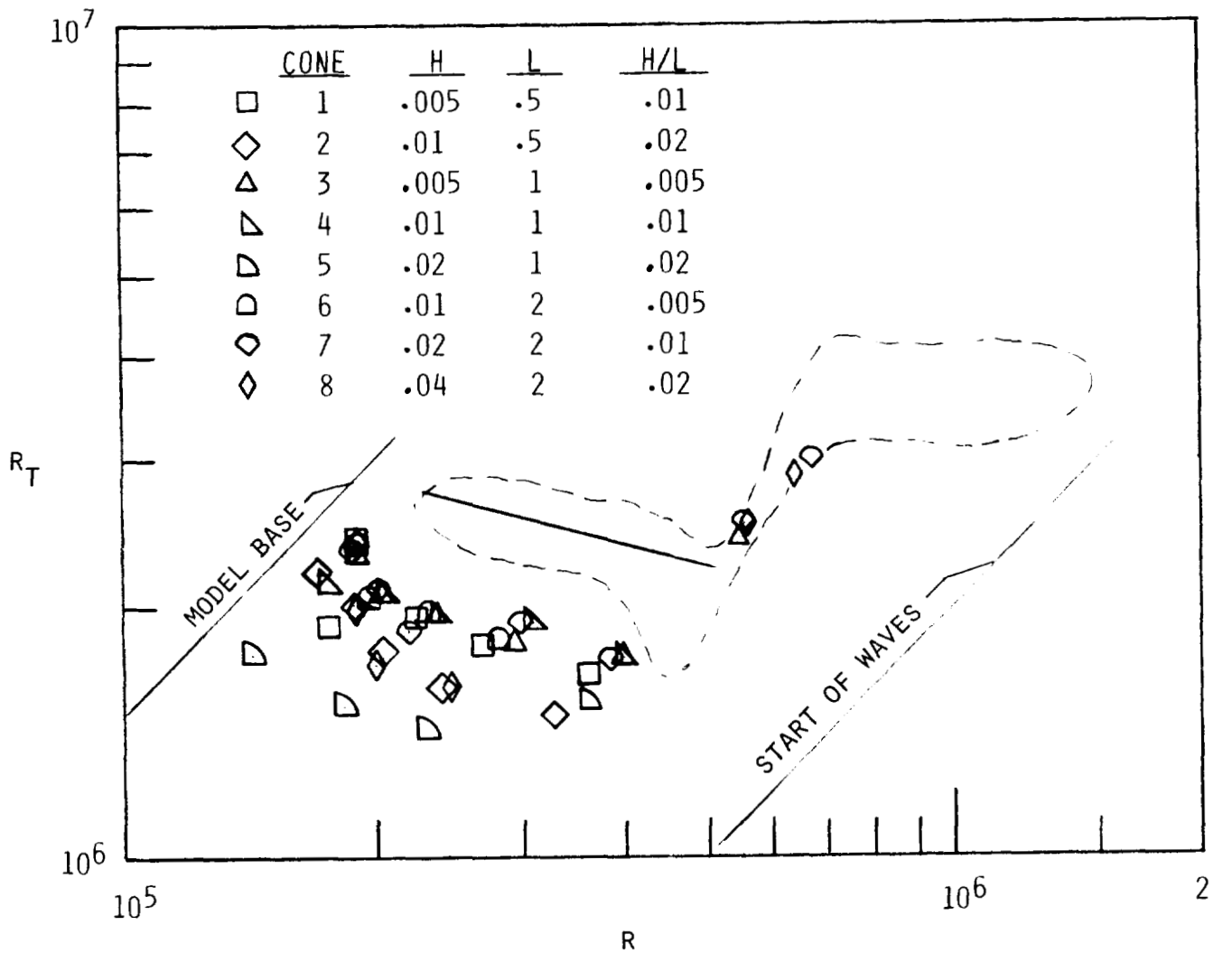

Figure 6

TRANSITION REYNOLDS NUMBERS AS A FUNCTION OF H/L

To better show the effects of the waves, the transition Reynolds numbers are plotted as a function of H/L for constant values of unit Reynolds number. Data for two unit Reynolds numbers in "quiet" flow and one in "noisy" flow are plotted from fairings of the data of figures 5 and 6. Figure 7 shows that the change in transition Reynolds number is primarily a function of H/L. The height of the waves and the number of waves seem to have no obvious effect on the present transition Reynolds number data.

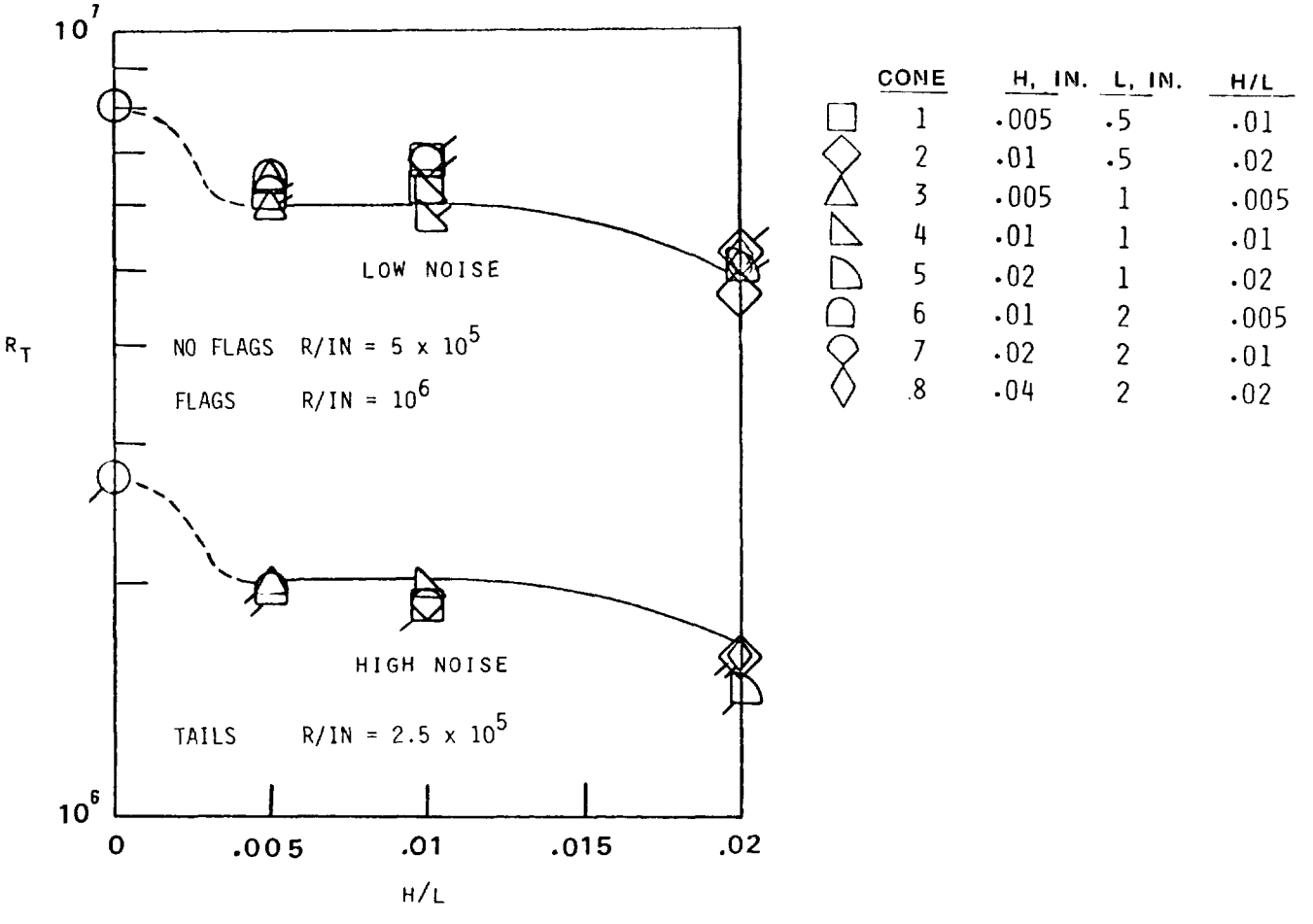

Figure 7

PERCENTAGE CHANGE IN TRANSITION POSITION
AS A FUNCTION OF H/L
QUIET FLOW

The "quiet" flow data of figure 7 are plotted in figure 8 in the form of transition distances normalized by the smooth cone transition distances, thus showing the percentage change in transition location as a function of H/L ratio.

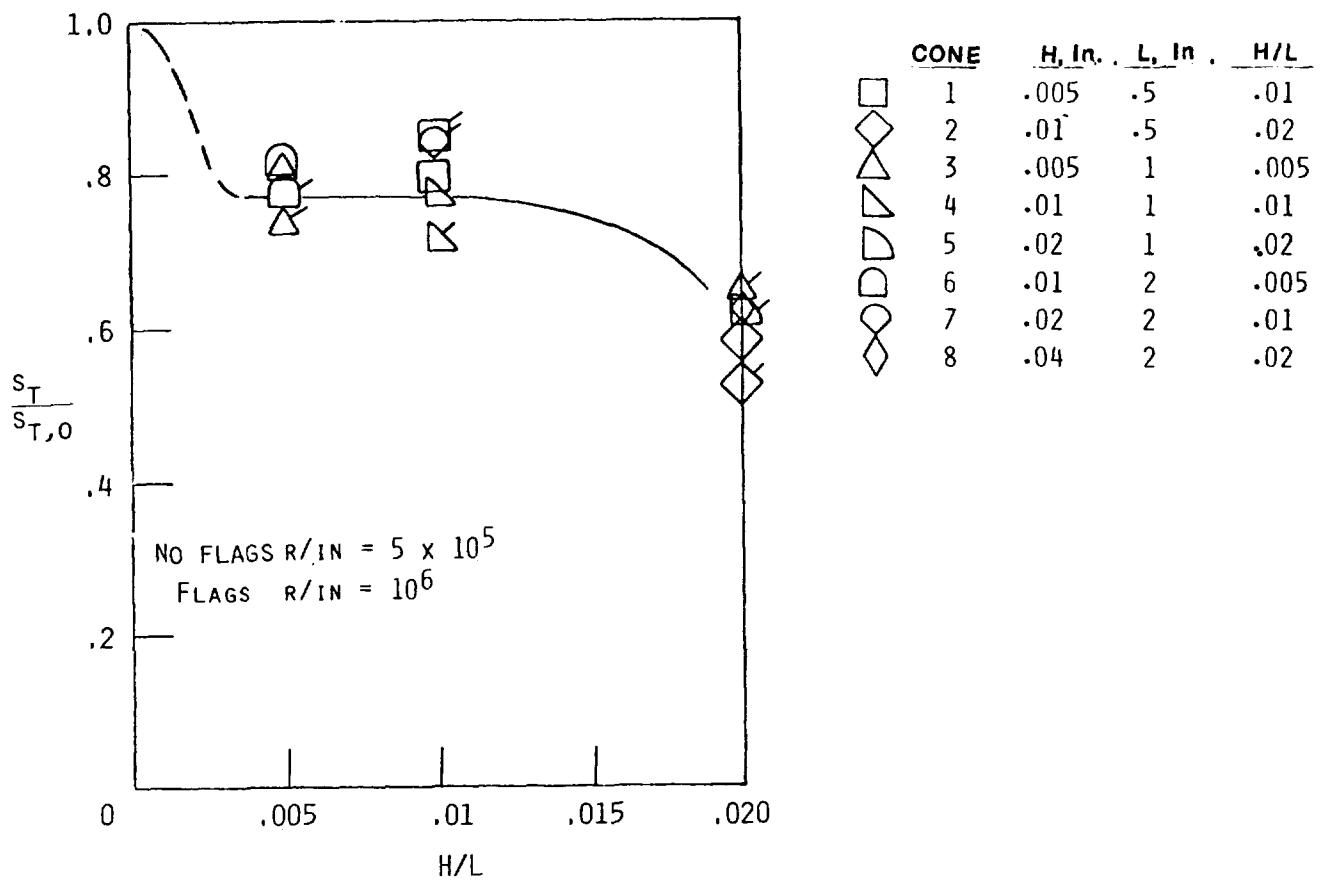

Figure 8

PERCENTAGE CHANGE IN TRANSITION POSITION
AS A FUNCTION OF H/L
NOISY FLOW

Figure 9 shows the "noisy" flow data of figure 7 plotted in the form of transition distances normalized by the smooth cone transition distances. A comparison of figures 8 and 9 indicates that a given H/L causes approximately the same percentage change in transition for both quiet and noisy flows. This result offers hope that trends in data obtained in conventional wind tunnels may be usable.

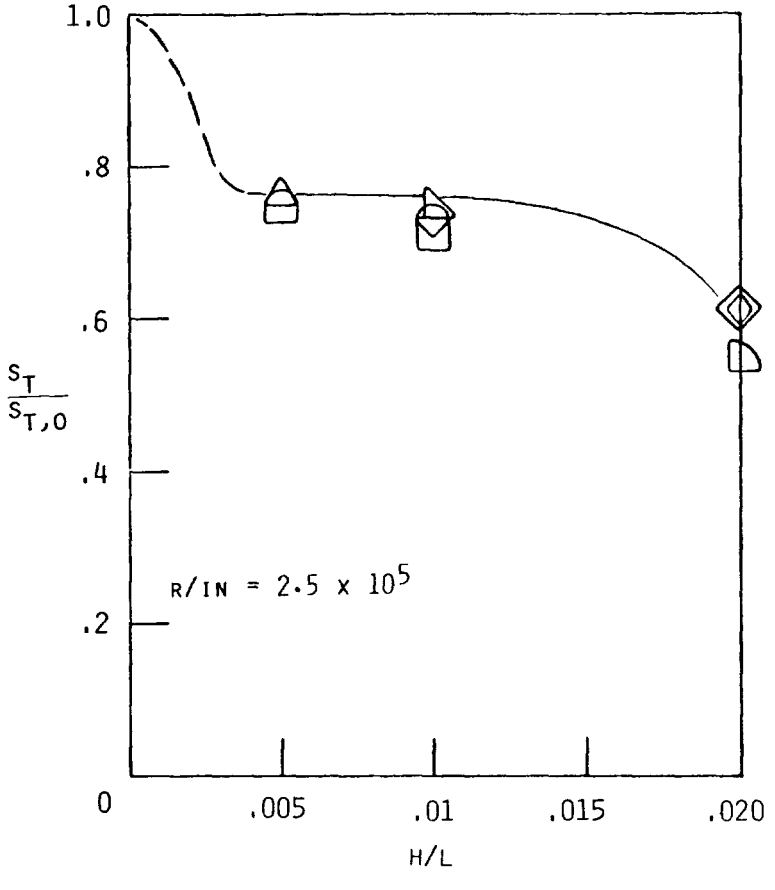

	CONE	H, IN.	L, IN.	H/L
□	1	.005	.5	.01
◇	2	.01	.5	.02
△	3	.005	1	.005
◺	4	.01	1	.01
▱	5	.02	1	.02
▢	6	.01	2	.005
◇	7	.02	2	.01
◇	8	.04	2	.02

Figure 9

TRANSITION POSITION ON SMOOTH CONE

Figure 10 shows the transition position on the smooth cone as a function of unit Reynolds number for both quiet and noisy flows. The upper limit to the data is the length of the cone, while the lower limit is determined by the maximum unit Reynolds number in the quiet flow and the start of the instrumentation on the cone for the noisy flow. The regional transition reversal at a unit Reynolds number of about 5×10^5 in the noisy flow is caused by a peak in radiated noise in the nozzle.

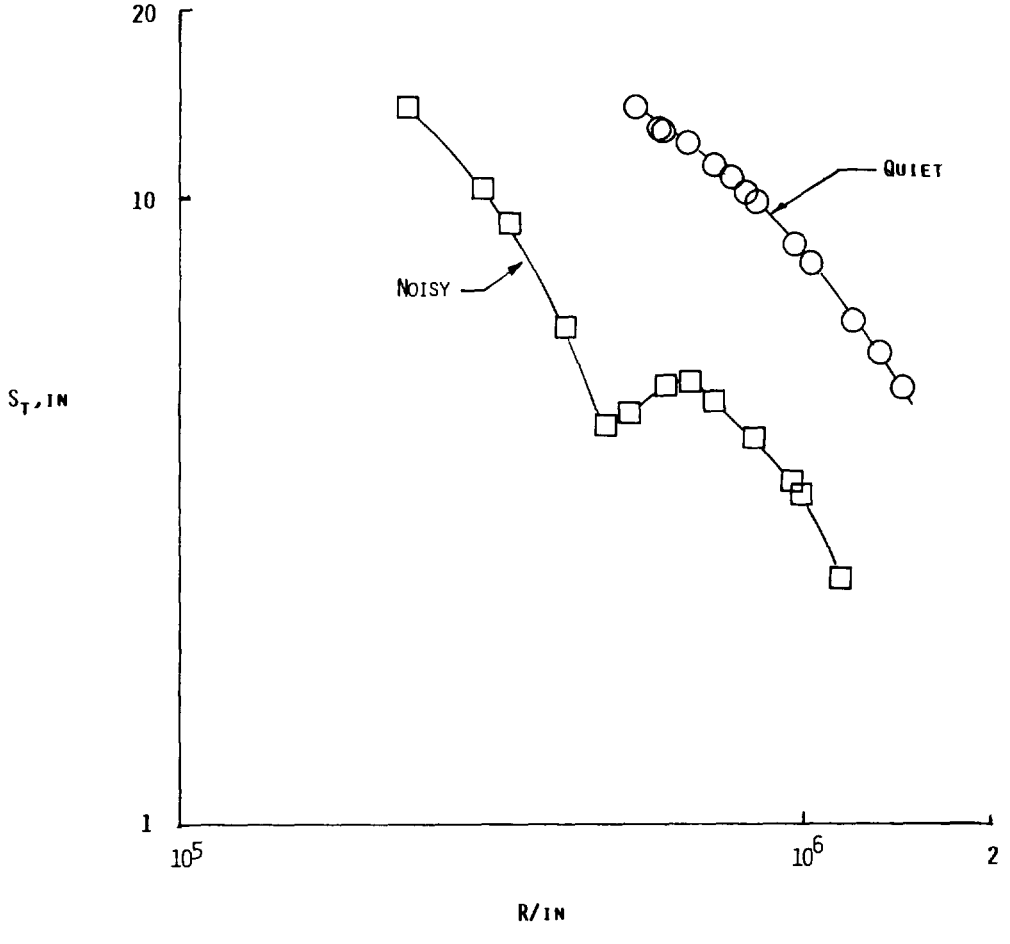

Figure 10

TRANSITION ON CONE WITH ROUGHNESS PARAMETER DEFINITIONS

Figure 11 shows a typical effect of discrete three-dimensional roughness (spheres) on transition position. As the unit Reynolds number is increased, the transition position follows the smooth cone value until at some value of Reynolds number there is a sudden forward movement of the transition position. This unit Reynolds number and height of the roughness determine the critical roughness Reynolds number. Further increases in unit Reynolds number will bring transition close to but at a discrete distance from the roughness. The value at which further increases in unit Reynolds number cause no significant further forward movement in transition determines the effective roughness Reynolds number. While vehicle manufacturers are more interested in critical values, the data base is much larger for values of effective roughness Reynolds number which are mainly of interest to the experimentalist for use in tripping the boundary layer on models. For the present study, critical roughness Reynolds numbers can only be obtained for the range of unit Reynolds numbers at which the smooth cone transition data is available while effective values can be determined on the entire unit Reynolds number range.

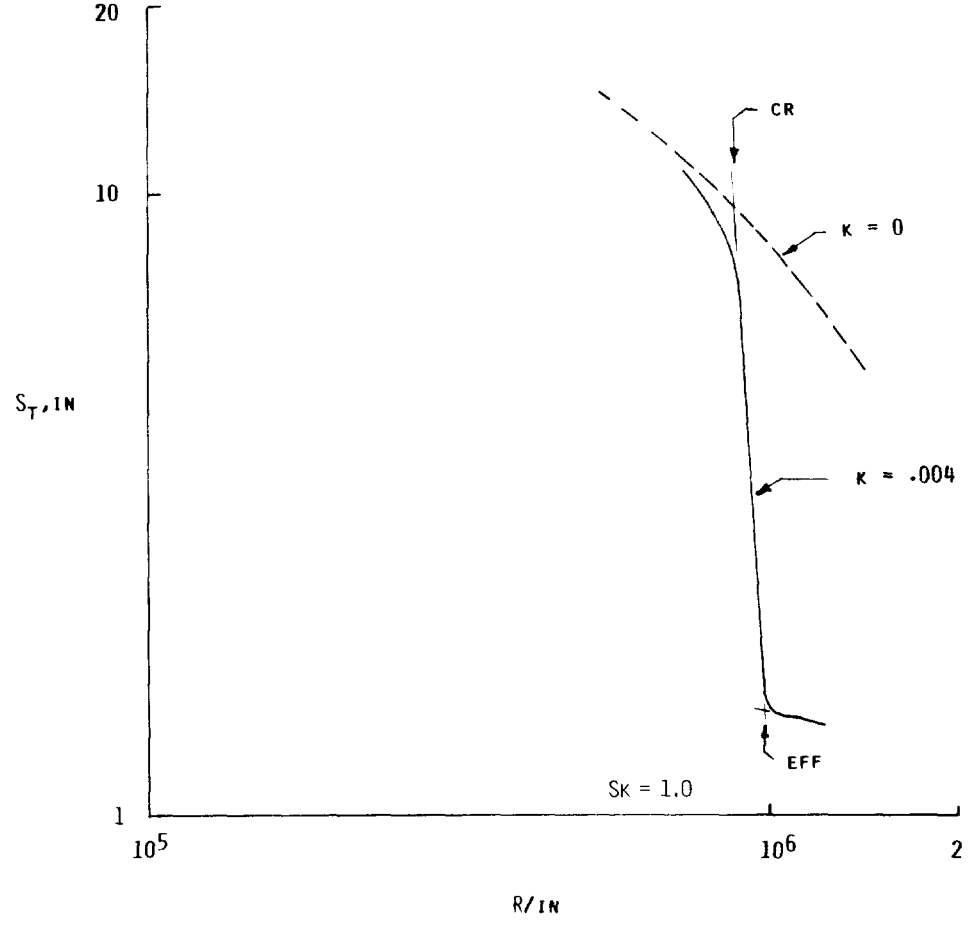

Figure 11

EFFECTIVE ROUGHNESS REYNOLDS NUMBER CORRELATION
VAN DRIEST DATA

Figure 12 shows the data and correlation of Van Driest[5] for effective roughness Reynolds numbers as a function of roughness position Reynolds number on cones. The solid symbols represent the data calculated using the Reynolds number at the edge of the boundary layer ($R_k = k\rho_e u_e/\mu_e$), and the open symbols are the data calculated using the undisturbed conditions inside the boundary layer at the height of the roughness ($r_k = k\rho_k u_k/\mu_k$). The line $r_k = 600$ is a widely used value of effective roughness Reynolds number for subsonic to low supersonic speeds. The solid lines are Van Driest's correlation for cones:

$$R_{k,eff} = 32.8\ (1 + \frac{\gamma - 1}{2} M_e^2)\ R_{S_k}{}^{.25}$$

and show excellent agreement with the data. The ease of calculation makes the Van Driest correlation the method of choice. The present study falls in the range of Mach numbers covered by Van Driest, and both sets of data were obtained on sharp 10° cones.

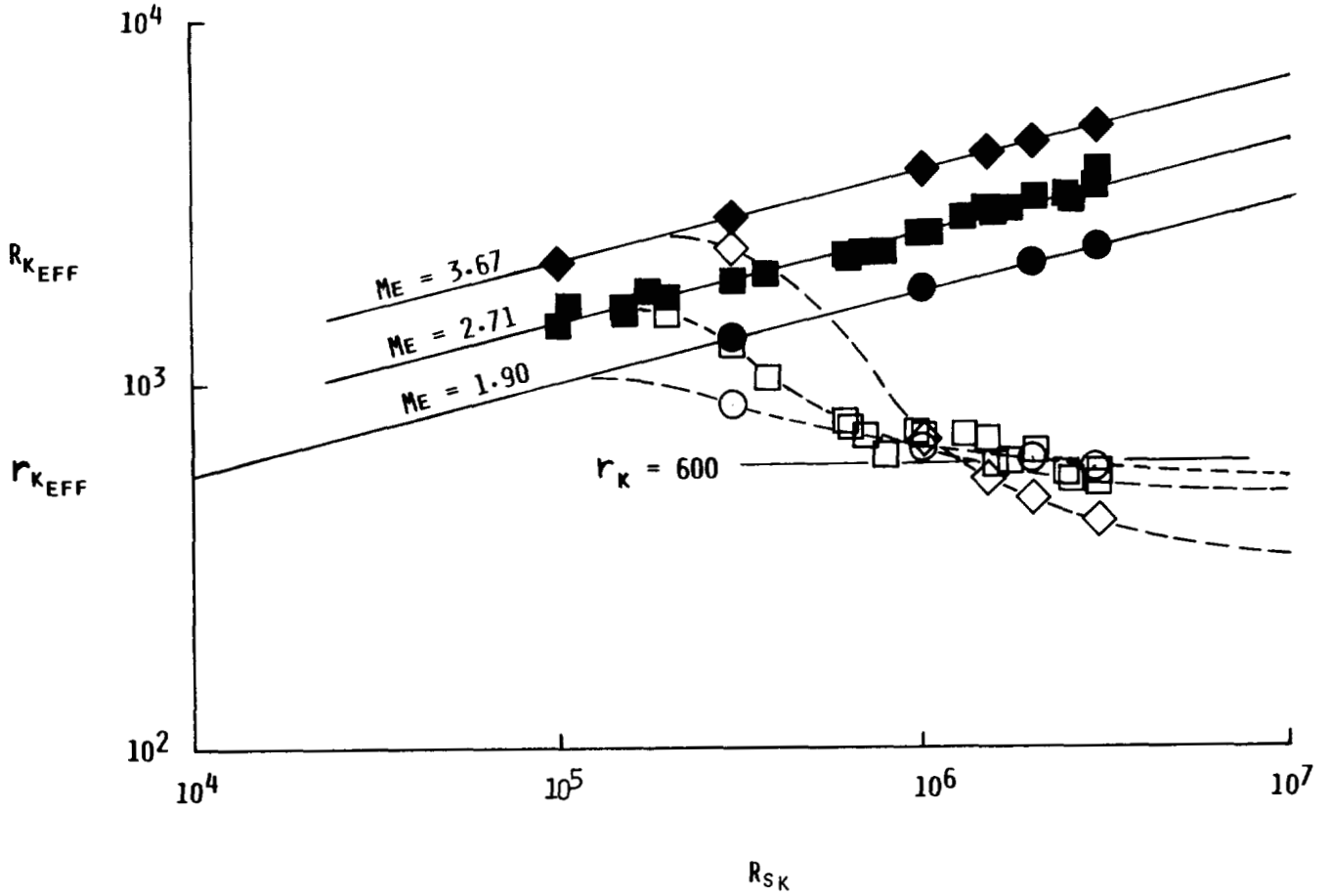

Figure 12

ROUGHNESS REYNOLDS NUMBER CORRELATIONS
QUIET TUNNEL DATA

Figure 13 shows the data of the present study in the form of effective and critical roughness Reynolds numbers as a function of the roughness position Reynolds number. The solid line is the Van Driest correlation for the local cone Mach number, and the dashed lines are fairings of the quiet and noisy effective values. Both quiet and noisy values are above the Van Driest correlation line, but neither shows significant differences. The "quiet" flow data are about 20 percent higher than the correlation and 10 percent higher than the noisy flow data. The few data points for critical values of roughness Reynolds numbers seem to indicate the same percentage difference in quiet and noisy flows and somewhat less influence of position Reynolds number on the value. These very preliminary data indicate that the existing data base may be usable and conservative.

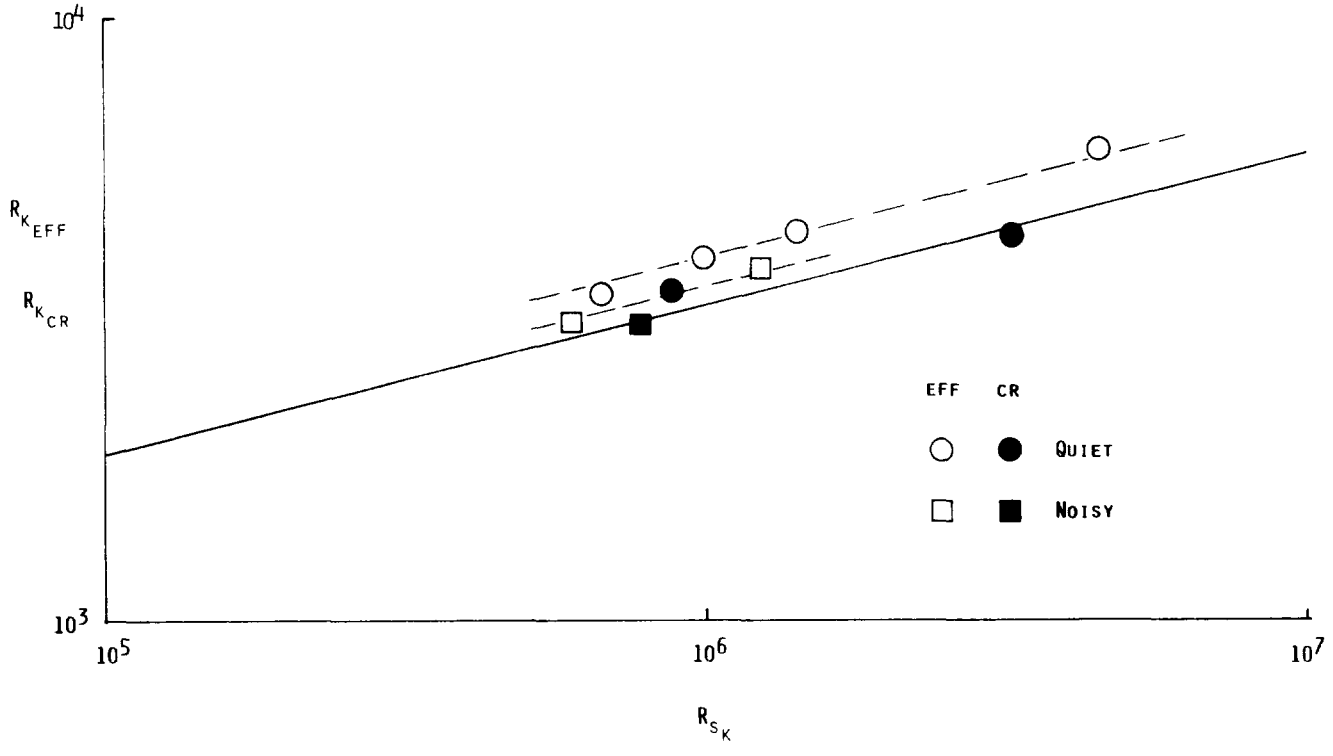

Figure 13

CONCLUSIONS

Waviness

1. Effect of sinusoidal waves on transition is mainly a function of wavelength-to-height ratio - H/L.

2. The effect of waves on transition was much less than a single trip wire of similar height.

3. No waves were found which did not affect transition; no lower critical size was found.

4. A given wave caused the same percentage change in transition in quiet and noisy flows.

Discrete Roughness

1. Effect of noise on effective roughness Reynolds numbers is small (< 20 percent).

2. Effect of noise on critical roughness Reynolds numbers appears small based on very preliminary data.

3. Existing data base may be usable and conservative.

REFERENCES

1. Fage, A.: The Smallest Size of a Spanwise Surface Corrugation Which Affects Boundary-Layer Transition on an Airfoil. Reports and Memoranda No. 2120, British Aeronautical Research Committee, Vol. I, 1943, pp. 261-279.

2. Carmichael, B. H.: Surface Waviness Criteria for Swept and Unswept Laminar Suction Wings. Report No. NOR-59-438 (BLC-123), Northrop Corp, August 1959.

3. Howard, P. W.; and Czarnecki, K. R.: Effect of Fabrication-Type Surface Roughness on Transition on Ogive-Cylinder Models at Mach Numbers of 1.61 and 3.01. NASA TN D-1933, July 1963.

4. Beckwith, I. E.; Creel, T. R., Jr.; Chen, F.-J.; and Kendall, J. M.: Freestream Noise and Transition Measurements on a Cone in a Mach 3.5 Pilot Low-Disturbance Tunnel. NASA TP-2180, September 1983.

5. Van Driest, E. R.; and McCauley, W. D.: The Effect of Controlled Three-Dimensional Roughness on Boundary-Layer Transition at Supersonic Speeds. Journal of Aerospace Sciences, Vol. 27, No. 4, April 1960, pp. 261-271, 303.

EXPERIMENTAL AND THEORETICAL INVESTIGATION OF BOUNDARY-LAYER INSTABILITY MECHANISMS ON A SWEPT LEADING EDGE AT MACH 3.5

T. R. Creel, Jr.
NASA Langley Research Center
Hampton, Virginia

M. R. Malik
High Technology Corporation
Hampton, Virginia

I. E. Beckwith
NASA Langley Research Center
Hampton, Virginia

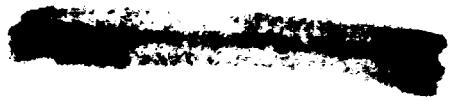

OUTLINE

The figure below gives a brief outline of the experimental and theoretical investigation of boundary-layer instability mechanisms on a swept leading edge at Mach 3.5.

- REVIEW OF TRANSITION MECHANISMS ON SWEPT-LEADING EDGES
- SWEPT-CIRCULAR CYLINDERS TESTED IN MACH 3.5 PILOT QUIET TUNNEL
  - MEASURED RECOVERY TEMPERATURES
  - OIL FLOW STUDIES
- COMPARISON OF THEORY AND EXPERIMENT
- REVIEW OF STABILITY THEORY

TWO MECHANISMS GENERALLY CAUSE TRANSITION IN THE
LEADING-EDGE REGION OF SWEPT WINGS

Spanwise contamination and cross-flow instability are outlined in the figure below.

1. SPANWISE CONTAMINATION

SOLVED IN THE EARLY '60's BY:

STRONG LOCAL SUCTION, LEADING-EDGE SUCTION FENCES, X-21

PROTRUDING FAIRED BUMP ATTACHED TO THE WING LEADING EDGE
BRITISH HANDLEY PAGE

2. CROSS-FLOW INSTABILITY

FIRST OBSERVED BY GRAY AS REGULARLY SPACED STREAKS IN SURFACE COATINGS

STREAKS CAUSED BY CO-ROTATING VORTICES RESULTING FROM THE INFLECTIONAL INSTABILITY OF THE CROSSFLOW BOUNDARY-LAYER PROFILES IN THE UPSTREAM REGIONS OF SWEPT WINGS

PHOTOGRAPH OF SWEPT-CYLINDER MODELS

The models consisted of .030-inch thick stainless steel cylindrical shells 1/2- and 1-inch outside diameters with both ends sealed and cut-off parallel with the free-stream flow direction as illustrated by the photograph. Chromel-alumel thermocouple wires of .010-inch diameter were spot welded to the inside surface of the shells at 1/4-inch intervals along the entire length of the attachment lines. The surfaces of the models were maintained clean and polished with a finish of less than 10 rms micro-inches.

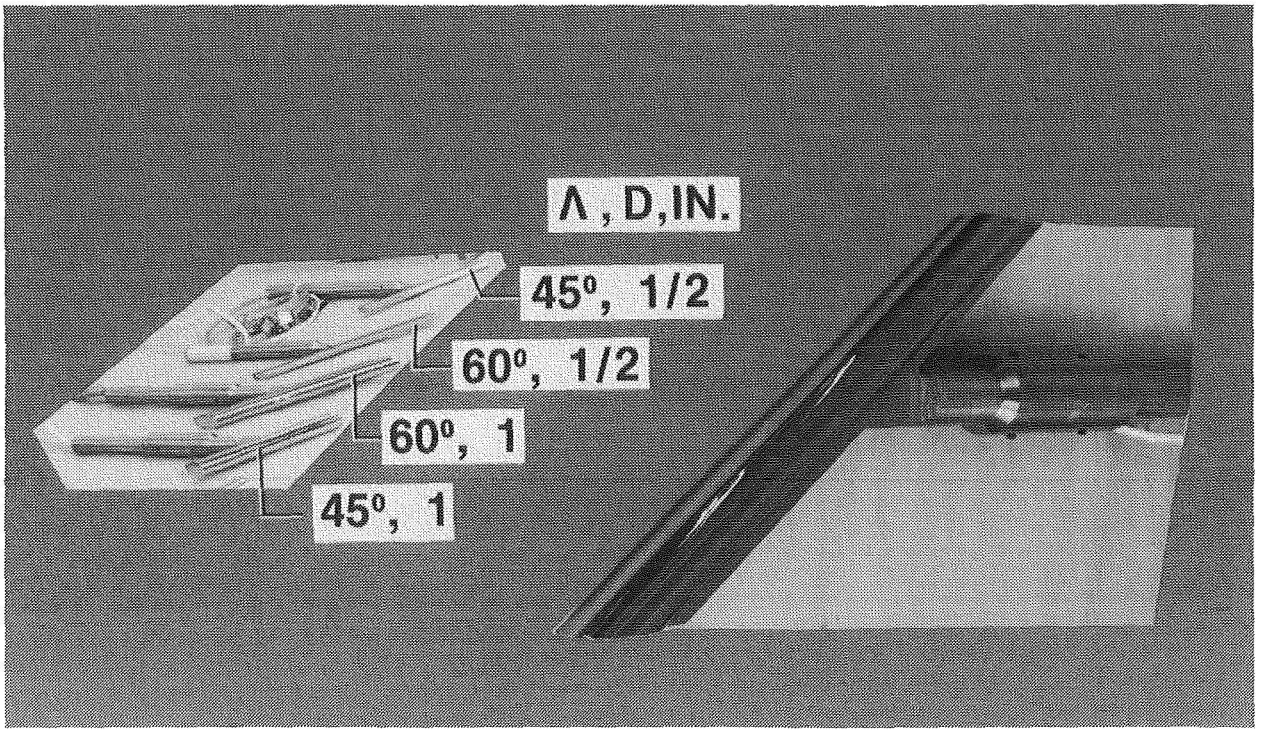

ONE-INCH DIAMETER SWEPT CYLINDERS IN MACH 3.5
PILOT LOW-DISTURBANCE TUNNEL

The models are shown mounted in the nozzle at upstream and downstream positions with respect to the quiet test core. In the upstream "quiet" test position and with the bleed valve open, the forward tips of the models were located 5.8-inches downstream from the nozzle throat (see ref. 1). For $R_\infty = 3 \times 10^5$ about 85 percent and 70 percent of the attachment line spans on the $\Lambda = 45°$ and 60° models, respectively, were exposed to the extremely low noise levels. As unit Reynolds number is increased, transition moves upstream on the nozzle walls and thus the corresponding location of increasing noise measured along the centerline also moves upstream. This results in a greater percentage of the attachment line span being exposed to high noise levels. In the downstream "noisy" test position and with the bleed valve closed, the entire model was exposed to noise levels ranging from .2 to .5 percent.

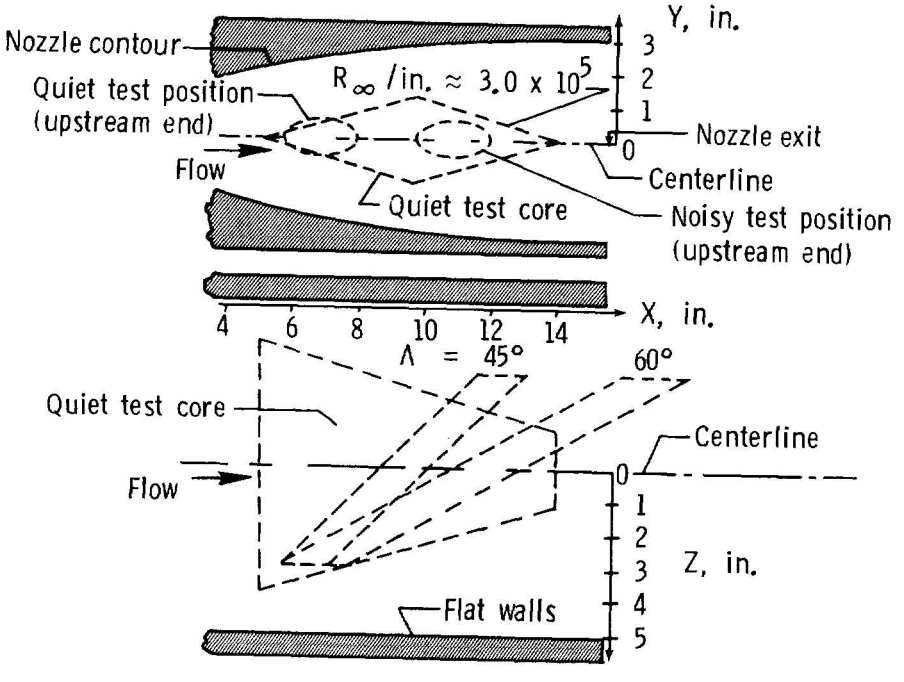

TRANSITION ON THE ATTACHMENT LINE

Recovery factors obtained at both low and high noise conditions for $\Lambda = 60°$ are summarized here where r is plotted against $R_{\infty,D}$ for selected values of s from several runs (Ref. 1). The trip height is k=.004 inch and the trip was located at s=6 inches for these data. The results for no trip (circle symbols and s = 5 in.) and also upstream of the trip (square symbols and s = 5 in.) show transition at $R_{\infty,D} \simeq 7.5 \times 10^5$ for both low and high noise (flagged symbols). This transition Reynolds number is in agreement with Poll's criteria (Ref. 2). However, downstream of the trip (s = 10 in.) transition occurs at lower values of $R_{\infty,D} \simeq 3$ or 4×10^5 depending on the tunnel noise. Clearly, the tunnel noise appears to enhance the effect of the trips but has no effect when there is no trip.

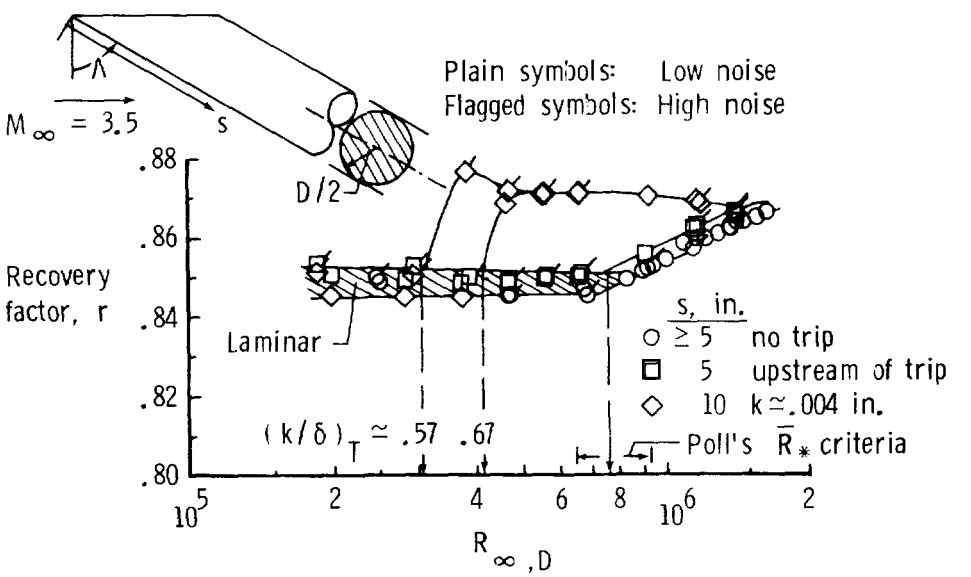

TRANSITION ON THE ATTACHMENT LINE

Typical effects of tunnel noise and a trip on attachment line transition for the $\Lambda = 45°$ model are shown in the figure. Data without a trip and with a trip height (h) = .002-inches are presented for a Reynolds numbers range of $2 \times 10^5 < R_{\infty,D} < 1.7 \times 10^6$. The trip was located at s = 5.5 inches for these data. The high tunnel noise enhances the effect of the trip for $5 \times 10^5 < R_{\infty,D} < 6.5 \times 10^5$. Upstream of the trip (s = 5 in.) or with no trip, transition occurred at $R_{\infty,D} \simeq 7 \times 10^5$ independent of tunnel noise. This value of $(R_{\infty,D})_T$ is somewhat smaller than Poll's $\bar{R}_*$ criteria (Ref. 2) for no end disturbances in low-speed flow and is also somewhat smaller than the Bushnell/Huffman supersonic criteria of $(R_{\infty,D})_T > 8 \times 10^5$ (Ref. 3).

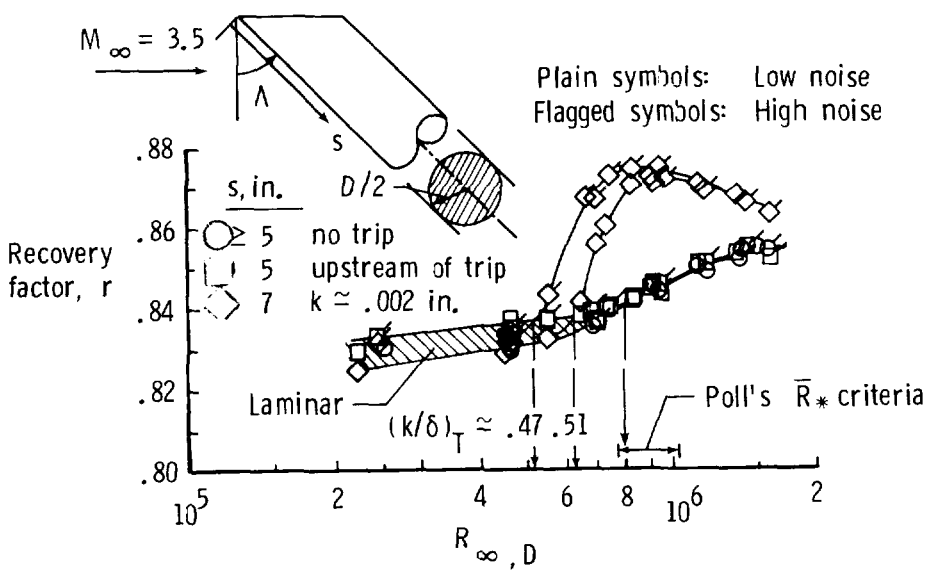

EFFECTS OF TRIP HEIGHT AND NOISE ON ATTACHMENT-LINE TRANSITION

To facilitate comparisons with Poll's data for trip wires in low-speed flow (Ref. 2), the local reference temperature parameters $\bar{R}_*$ and k/η_* are plotted for all the present transition-onset data for the $\Lambda = 45°$ and $60°$ models and D = 1-inch. The trend of $(\bar{R}_*)_T$ with $(k/\eta_*)_T$ are similar to those of Poll with respect to the effects of "critical" roughness heights. These critical roughness heights correspond to the values of k/η_* where the transition Reynolds numbers are first reduced significantly as k/η_* is increased. Thus, for $\Lambda = 45°$, the critical values are $k/\eta_* \approx 1.4$ and 1.6 for high and low noise, respectively. For $\Lambda = 60°$, the critical values are $k/\eta_* \approx 0.85$ and 0.95 for high and low noise, respectively. These latter values may be compared with Poll's critical values for $\Lambda \approx 60°$ of $d/\eta = 0.6$ to 0.8. Poll's subcritical values of $\bar{R}_T$ were approximately 600 to 750, depending on the distance from the trip. It is apparent that the present subcritical values of $(\bar{R}_*)_T$ for both sweep angles and the critical k/η_* values for $\Lambda = 60°$ agree reasonably well with Poll's values for $\Lambda = 60°$.

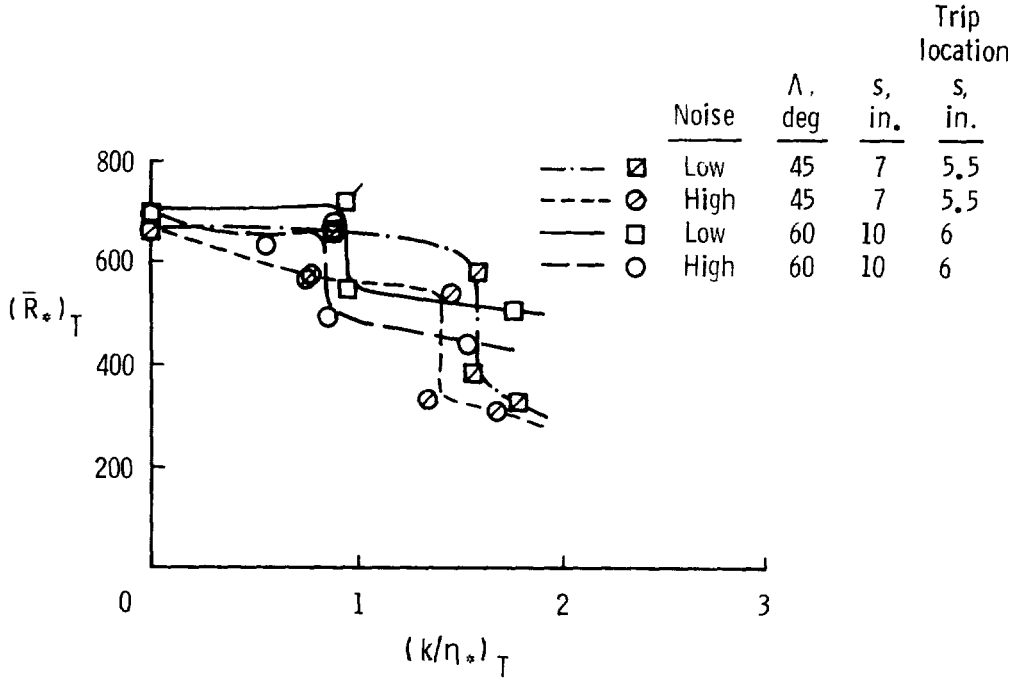

OIL FLOW PATTERNS WITH TRIP (K = .004-IN.) AT
S = 6-IN. $\Lambda = 60°$, D = 1-IN., $R_{\infty,D} = 4.6 \times 10^5$

Typical photographs of oil flow patterns on the $\Lambda = 60^0$ model are shown in this figure. Also shown is a small trip (identified in the picture, of height h = .004-inch, which results in $k/\delta = .7$) fixed to the attachment line at 6-inches from the upstream tip of the model. For this run, the wavelength of the vortices measured from the more closely spaced oil-flow streaks, increased from $\lambda = .03$ to .04-inch as the angular distance from the attachment line is increased from $\theta = 70°$ to 90°. Normalized by the attachment boundary-layer thickness, these values give $\lambda/\delta_s = 5$ to 7 for this Reynolds number of $R_{\infty,D} = 4.6 \times 10^5$.

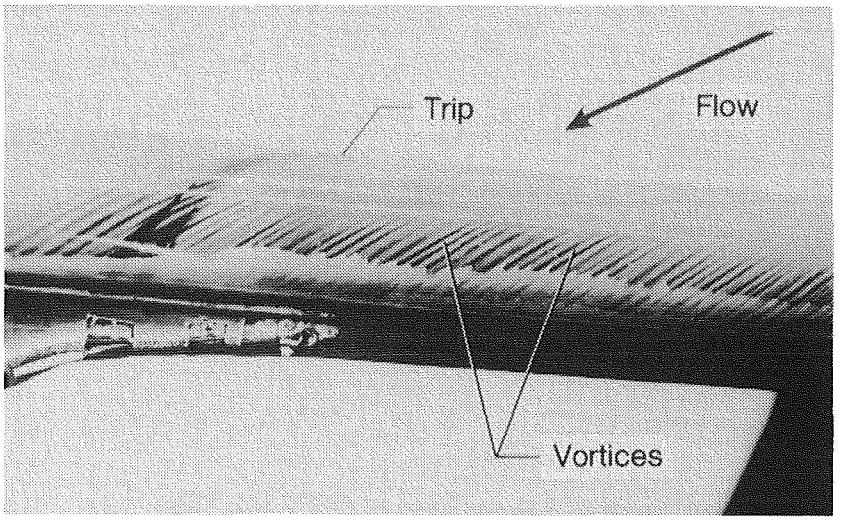

OIL FLOW PATTERNS DOWNSTREAM OF TRIP

This figure shows more of the downstream part of this model for the same run. The wide streaks have been completely obliterated downstream of the trip by turbulent boundary-layer flow.

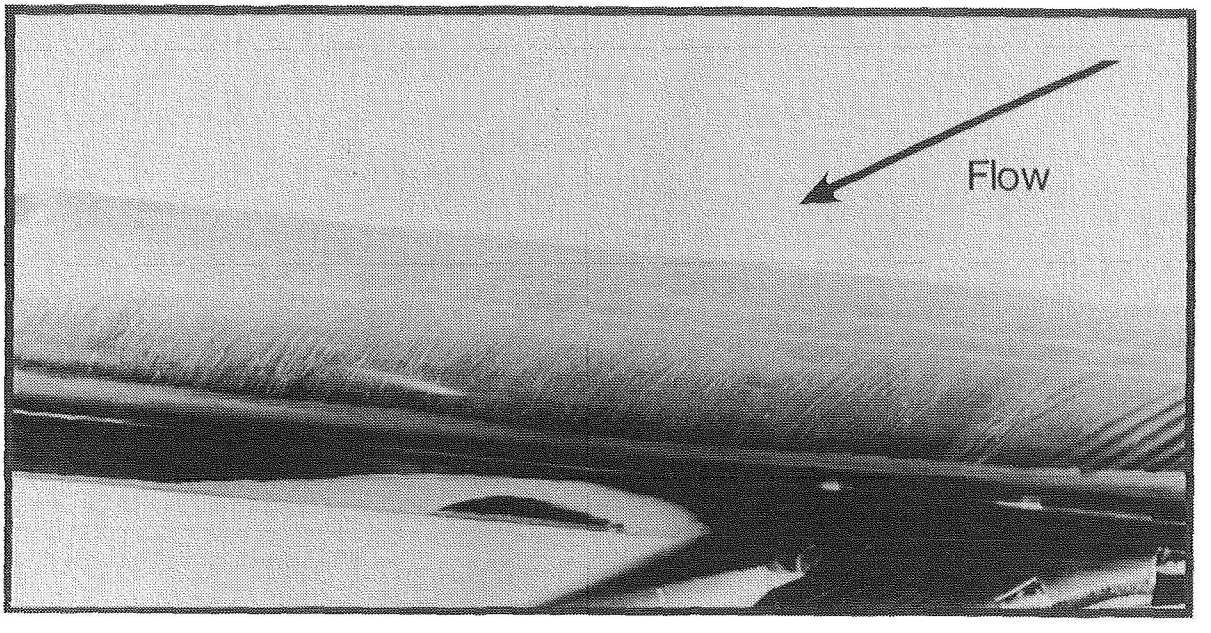

COMPARISON OF THEORY AND EXPERIMENTS

The stability of three-dimensional boundary-layer flow on the 60° swept cylinder was examined for $R_{\infty,D} = 4.6 \times 10^5$. Compressible linear stability equations were solved by the method used in reference 4. Computed wavelength of the most amplified stationary cross-flow disturbances is plotted in the figure as a function of the azimuthal angle θ from the attachment line. The figure also contains wavelength values measured on the oil flow photographs. Both the magnitude of the wavelength and its variation with θ are well predicted by the theory.

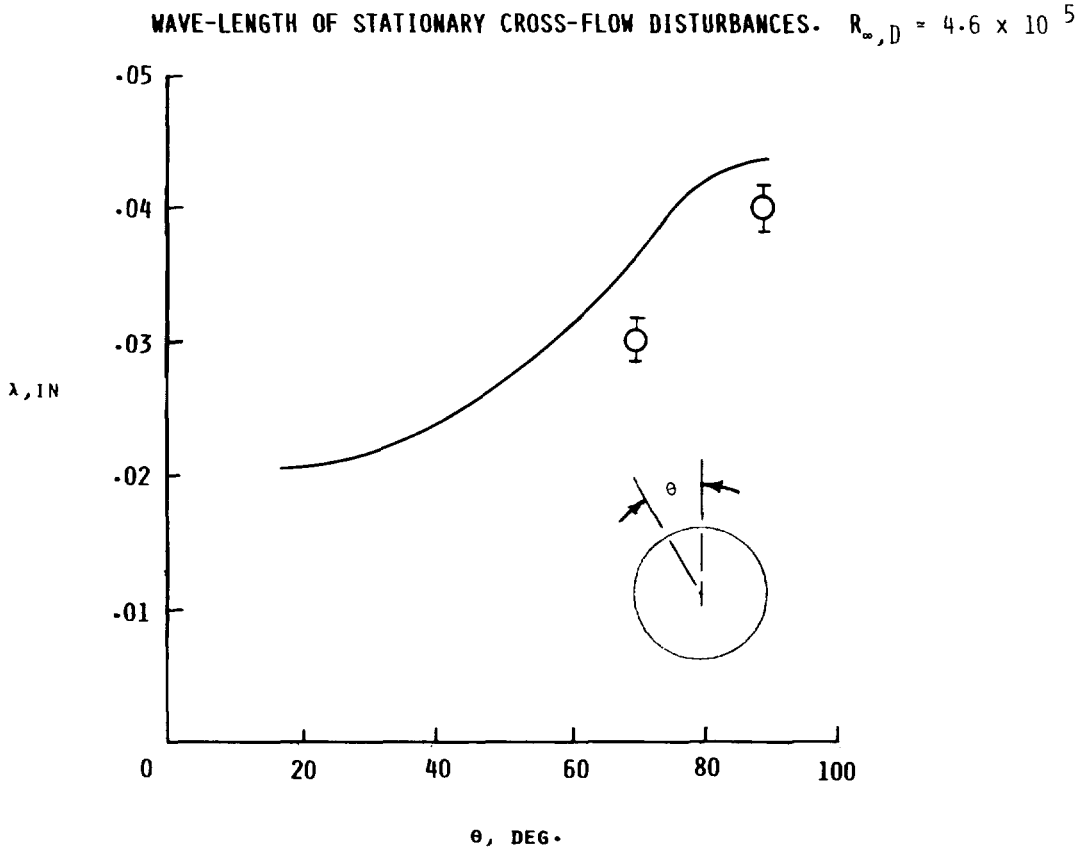

INSTABILITY OF BOUNDARY LAYER ON SUPERSONIC SWEPT ATTACHMENT LINE

The instability of a boundary layer at the attachment line of a swept cylinder was theoretically investigated. The results of this investigation are documented below.

- CALCULATIONS USING COMPRESSIBLE LINEAR STABILITY THEORY PERFORMED FOR $\Lambda = 60^0$ AND $M_\infty = 3.5$
- BOUNDARY LAYER SUBJECT TO TOLLMIEN-SCHLICHTING TYPE INSTABILITY
- OBLIQUE WAVES WITH WAVE ANGLES AROUND 60° ARE MOST AMPLIFIED
- COMPUTED CRITICAL REYNOLDS NUMBER IS $R_\theta = 240.$
- WALL COOLING IS STABILIZING. EXAMPLE: THE CRITICAL REYNOLDS NUMBER DOUBLES IF $T_W/T_{AD} = .8$
- ATTACHMENT LINE BOUNDARY LAYER SUBJECT TO FINITE AMPLITUDE SUBCRITICAL INSTABILITY. DISTURBANCES SUCH AS WALL ROUGHNESS MAY CAUSE PREMATURE TRANSITION

INSTABILITY OF BOUNDARY LAYER IN SWEPT LEADING-EDGE REGION

The figure below outlines the results regarding the instability of a boundary layer on the attachment line of a swept cylinder at Mach = 3.5.

- COMPRESSIBLE LINEAR STABILITY ANALYSIS OF THE THREE-DIMENSIONAL BOUNDARY LAYER HAS BEEN PERFORMED BOTH FOR THE STATIONARY AND NON-STATIONARY WAVES
- CROSS-FLOW VELOCITY PROFILE DOWNSTREAM IN ATTACHMENT LINE HAS INFLECTION POINT AND THUS IS SUBJECTED TO INVISCID (RAYLEIGH) INSTABILITY
- COMPUTATIONS SHOW THAT NON-STATIONARY WAVES AMPLIFY MORE THAN THE STATIONARY ONES

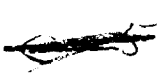

CONCLUSIONS

1. Transition is affected by wind-tunnel noise only when roughness is present.

2. Local $\bar{R}_*$ Reynolds number and k/η_* are useful correlation parameters for a wide range of free stream Mach numbers.

3. Stability theory is in good agreement with the experimental cross-flow vortex wavelength.

REFERENCES

1. Creel, T. R.; Beckwith, I. E., and Chen, F.-J.: Transition on Swept Leading Edges at Mach 3.5. Accepted for publication in the Journal of Aircraft. October 1987.

2. Poll, D. I. A.: Transition Description and Predictiion in Three-Dimensional Flows. Agard-R-709, June, 1984.

3. Bushnell, D. M., and Huffman, J. K.: Investigation of Heat Transfer to a Leading Edge of a 76° Swept Fin With and Without Chordwise Slots and Correlations of Swept-Leading-Edge Transition Data For Mach 2 to 8. NASA TMX-1475, 1967.

4. Malik, M. R.: COSAL - A Black-Box Compressible Stability Analysis Code for Transition Prediction in Three-Dimensional Boundary Layers. NASA CR-165915, 1982.

SUPERSONIC BOUNDARY-LAYER TRANSITION ON THE LaRC F-106 AND THE DFRF F-15 AIRCRAFT

Part I: Transition Measurements and Stability Analysis
F. S. Collier, Jr. and J. B. Johnson

Part II: Aerodynamic Predictions
O. J. Rose and D. S. Miller

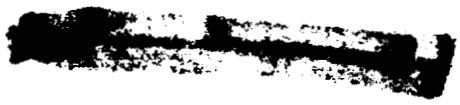

PART I: TRANSITION MEASUREMENTS AND STABILITY ANALYSIS

F. S. Collier, Jr.
High Technology Corporation
Hampton, Virginia

J. B. Johnson
NASA Ames-Dryden Flight Research Facility
Moffett Field, California

NOTATION

SYMBOLS

F	-	frequency (Hertz)
H,h	-	altitude (feet)
M	-	Mach number
C_p	-	pressure coefficient = $P-P_\infty/q_\infty$
C_q	-	suction coefficient = $(\rho V)_w/(\rho U)_\infty$
N	-	N-factor
x/c	-	chord fraction
c	-	chord (feet)
U,V	-	velocity (ft/sec)
q	-	dynamic pressure (lb_f/ft^2)
p	-	pressure (lb/ft^2)
Re	-	Reynolds number = Ul/ν
l	-	characteristic length (feet)
α	-	angle of attack (degrees)
Λ	-	sweep angle (degrees)
ρ	-	density ($slugs/ft^3$)
ν	-	kinematic viscosity (ft^2/sec)

SUBSCRIPTS

∞	-	free-stream condition
w	-	wall condition
t	-	transition
cf	-	crossflow

INTRODUCTION

Because of renewed interest in the supersonic flight regime and the recent success with laminar flow techniques at subsonic speeds, there is a developing interest in examining laminar flow control for increased fuel efficiency at high speeds. However, flight data in the area of supersonic boundary-layer transition phenomena is scarce. In late 1985, a limited window of opportunity of about 6 months existed where the Langley F-106 and the Dryden F-15 aircraft were available for flight tests. Two exploratory supersonic flight tests were conducted to expand upon the supersonic boundary-layer transition data base. The objectives of these cursory flight tests were to explore boundary-layer transition measurement techniques and to identify future experiments. In addition, for future design considerations, there was a need to obtain transition data to evaluate existing stability theory criteria at supersonic speeds and to use measured aerodynamic pressure data to evaluate full potential flow codes in the supersonic regime. This latter point will be discussed in Part II of this paper.

Primary

- Explore boundary layer transition at supersonic cruise
- Develop experience in supersonic transition measurement techniques
- Identify future experiments

Secondary

- Obtain transition data to evaluate existing stability theory criteria at supersonic speeds
- Use measured aerodynamic pressure data to evaluate full potential flow codes in supersonic regime

APPROACH

These exploratory supersonic flight tests were conducted utilizing surface cleanup gloves on the right wing and vertical tail of the Langley F-106 and the right wing of the Dryden F-15 test aircraft. Each glove was instrumented with surface pressure orifices and hot films to obtain measured pressure and transition data during flight. The measured transition data was correlated with compressible, linear, boundary-layer stability theory which is considered by many as the state-of-the-art transition prediction method. The measured pressure data was used to evaluate a non-linear, inviscid, full potential code which is described in more detail in Part II of this report.

- Perform exploratory supersonic flight tests using surface cleanup gloves
  - F-15
  - F-106
- Correlate results with computations
  - COSAL; compressible, linear boundary layer stability theory
  - NCOREL; non-linear, full potential, inviscid code

DRYDEN F-15 TEST AIRCRAFT

The flight experiment was conducted using an F-15 twin engine fighter type aircraft with a wing leading-edge sweep of 45 degrees. The F-15, normally used for propulsion tests at NASA Ames-Dryden Flight Research Facility, has the ability to reach speeds in excess of Mach 2. Data from previous flight experiments showed that the F-15 wing produces a pressure distribution which under ideal conditions may yield small amounts of laminar flow. A photograph of the F-15 with the foam and fiberglass test section on the right wing is shown in the figure below.

INSTRUMENTATION LAYOUT AND TEST CONDITIONS

Two separate instrumentation systems were used for the flight experiment. Quantities such as Mach number, altitude, and angle of attack were obtained from the aircraft's main instrumentation system. The main system employed two absolute pressure transducers to measure total and static pressure from the flight test Pitot static probe mounted on a noseboom.

The instrumentation system for the test section consisted of a 32 port electronic scanivalve, five temperature compensated hot-film anemometers, and an absolute pressure transducer. The electronic scanivalve was used to measure pressures from the two rows of 15 flush static pressure orifices and the absolute pressure transducer measured the pressure on the backside of the scanivalve. The temperature compensated hot-film anemometers, similar to the system described in reference 1, were used to measure transition location. Temperature compensated hot-film anemometers were used because previous experience at supersonic speeds showed that uncompensated anemometers were sensitive to the local total temperature, thereby affecting the overall sensitivity of the anemometers between flight conditions. The temperature compensated anemometers eliminate this problem. The locations of the hot-film sensors for the first phase of the flight tests were 5%, 10%, 15%, 20%, and 15% chord. The hot-film sensors were at 1%, 2%, 4%, 10%, and 15% chord for the second phase of flight tests.

Test points were flown at Mach numbers ranging from 0.7 to 1.8 and altitudes between 20,000 feet and 55,000 feet. Angle of attack ranged from -1 to 10 degrees. The unit Reynolds number ranged from 1.2 to 4.0 million/foot. In order to vary angle of attack and hold Mach number and altitude constant, constant G-loading turns were flown.

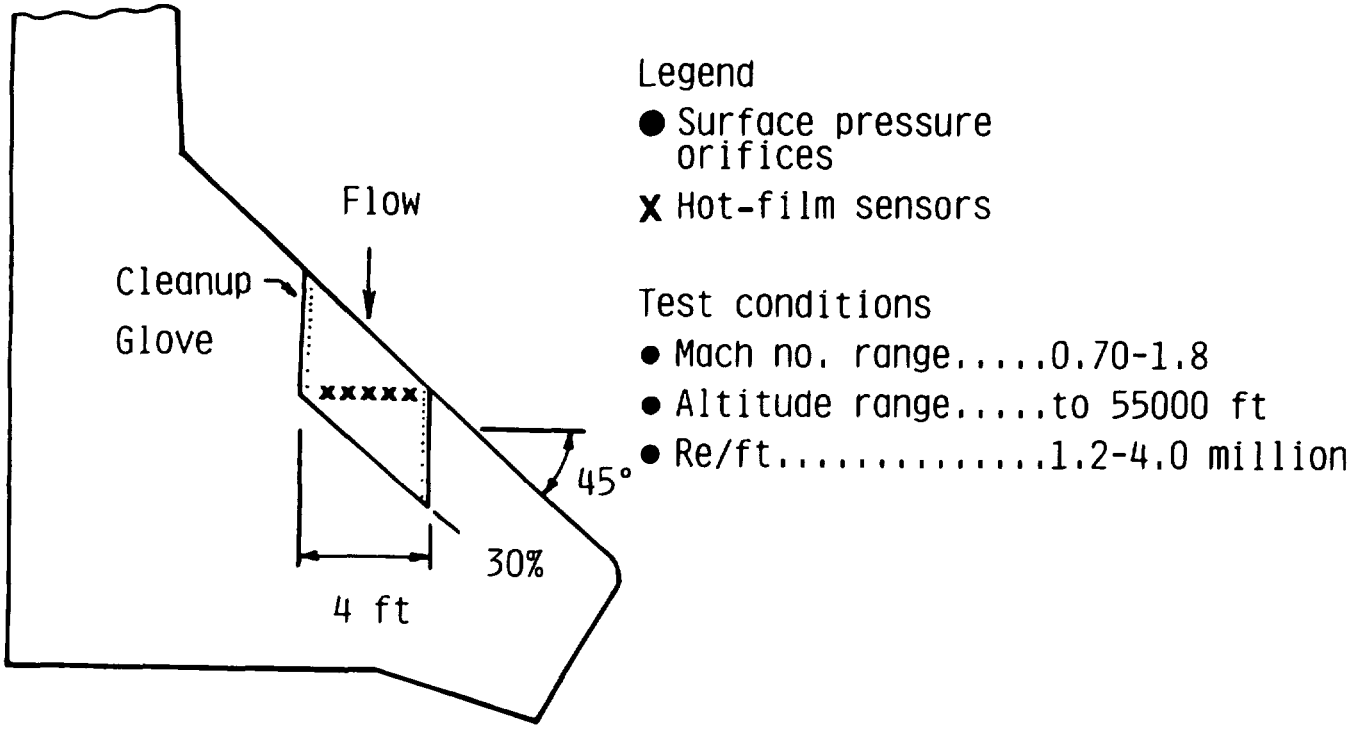

FOAM AND FIBERGLASS TEST SECTION

The foam and fiberglass test section was placed on the right wing of the F-15 to eliminate the possible effects of surface imperfections. The test section retained the existing airfoil shape but added approximately 1/4 inch thickness. The glove was 4 feet wide and extended past 30% chord. It was constructed using one layer of unidirectional fiberglass under 1/8 inch thick polyethylene foam covered with four layers of bidirectional fiberglass. The surface consisted of body filler and polyester paint. The waviness did not exceed 0.00075 inch/inch.

The test section configuration was changed during the latter part of the flight experiment. A notch/bump was added to the inboard side of the leading edge of the test section to eliminate the possible effects of leading-edge contamination.

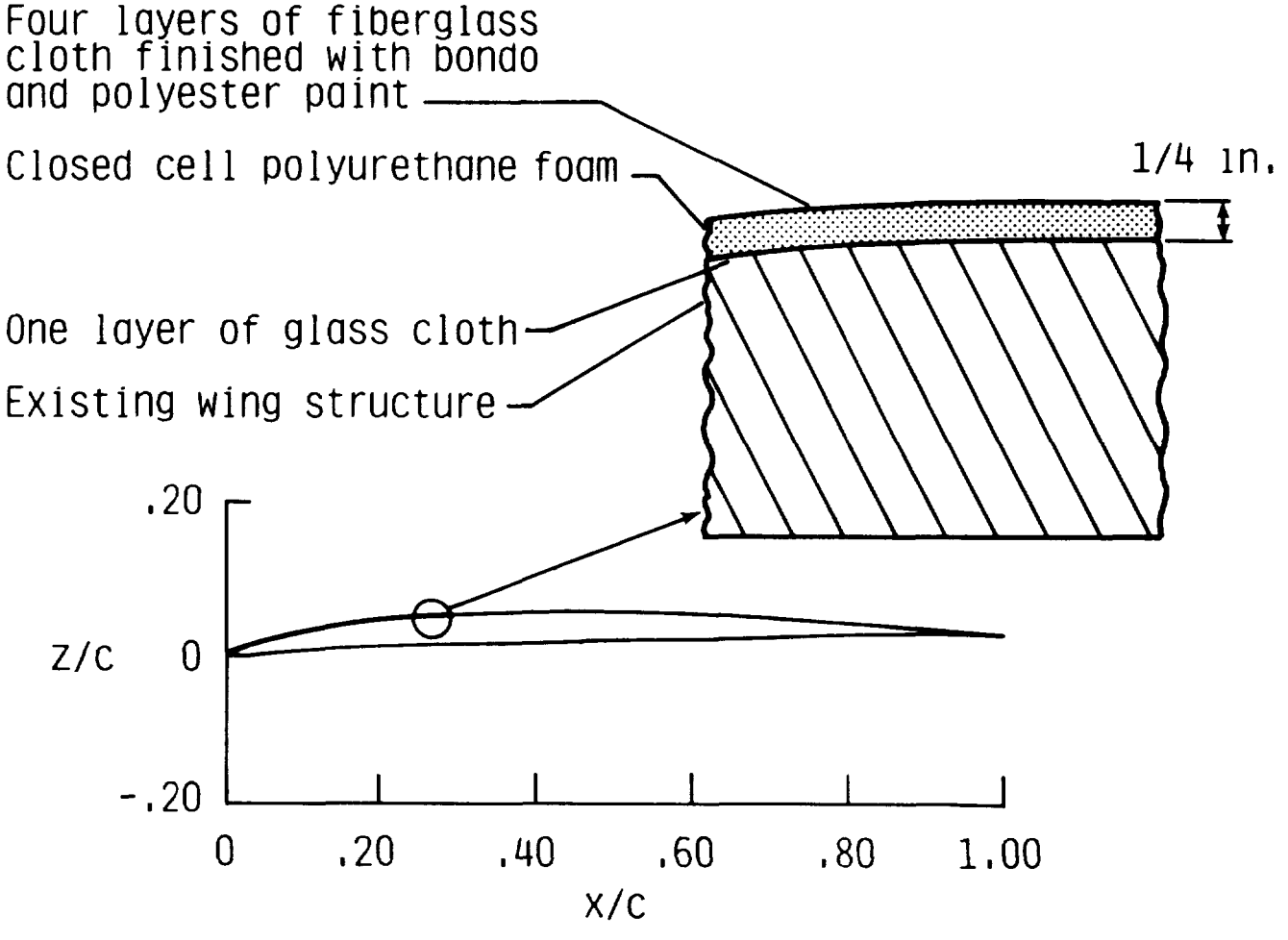

STABILITY ANALYSIS OF THE F-15 SUPERSONIC BOUNDARY-LAYER TRANSITION FLIGHT EXPERIMENT RESULTS

Shown in the figure below are four test points from the flight test. On the left, the pressure distributions as a function of chord fraction are presented for Mach numbers ranging from 0.90 to 1.76, Reynolds numbers ranging from 13 to 18 million, and angles of attack from about 3 to 9 degrees. The differences in the levels of the pressure distributions are mainly due to an angle of attack effect. Test points away from the 1-G loading condition were acquired in constant G windup turns and were considered very nearly steady state. On the right, the corresponding cross-flow N-factor results are presented as calculated from the compressible linear stability theory code COSAL. The envelope method was used and the cross-flow disturbances were assumed to be stationary (zero frequency). As can be seen from the figure, at M=0.98 and M=1.16, the cross-flow N-factor at transition was 10.5 and 11, respectively. These results are in agreement with previous subsonic transition correlations that transition should occur where the N-factor is in the range of 9-12. On the other hand, for M=0.90 and M=1.76 the cross-flow N-factors were about 6 at transition. There may be several explanations for this result. The above analysis was conducted for zero frequency disturbances and without the effects of surface curvature included. It is known that travelling disturbances (non-zero frequencies) can be more highly amplified, which could result in higher N-factors at transition. Conversely, convex surface curvature has a stabilizing effect on the disturbances. It is possible that, with further analysis which takes into account the aforementioned effects, the N-factors at transition might fall into the expected range of 9-12.

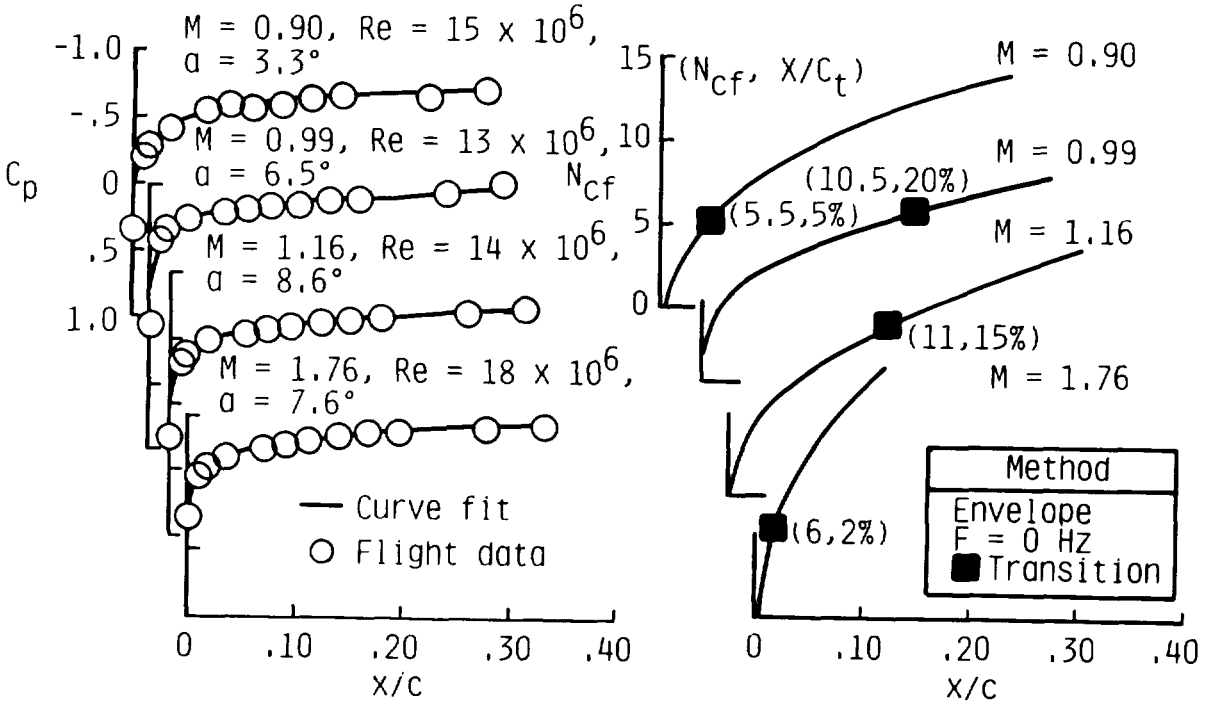

CROSS-FLOW REYNOLDS NUMBER AT TRANSITION

Another method that has been used in the past for correlating boundary-layer transition data is that of comparing the computed value of the cross-flow Reynolds number at the point of transition with previous data. Presented in the figure below is the cross-flow Reynolds number at transition as a function of sweep for a series of previous incompressible investigations as compiled by Poll (Ref. 2). The results of the present investigation show good agreement with past results.

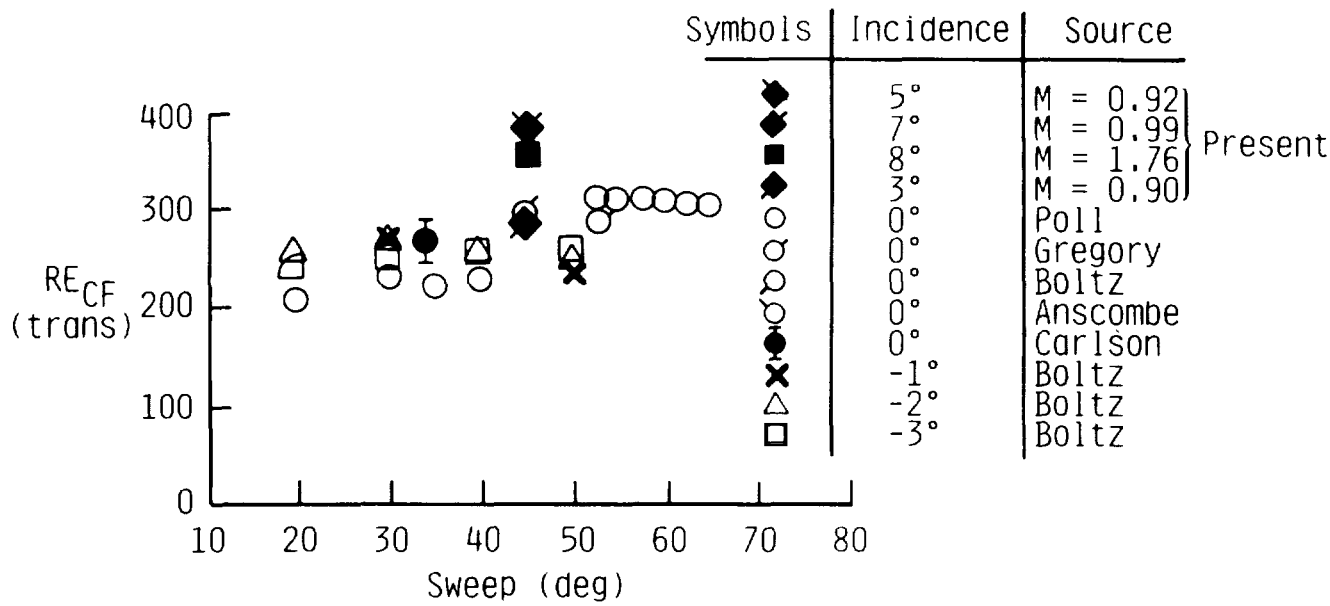

F-106 SUPERSONIC BOUNDARY-LAYER TRANSITION FLIGHT TEST

At Langley Research Center, the F-106 aircraft was utilized to conduct an exploratory supersonic boundary-layer transition flight experiment. A schematic of the F-106 is shown in the figure below. Surface clean-up gloves were mounted on the right wing which has a sweep of 60 degrees and the vertical tail which has a sweep of 55 degrees. The gloves were constructed by laminating alternate layers of fiberglass and epoxy over the existing wing. The final layer was sanded, primed, and sprayed with lacquer to achieve a very smooth finish. The gloves added approximately 0.10 inch thickness to the existing surfaces. During the flight tests, the Mach number ranged from 0.80 to 1.80, and the altitude varied from 30,000 to 50,000 feet resulting in unit Reynolds numbers in the range of 1.6 to 5.2 million per foot. The angle of attack varied from about 3 degrees up to 14 degrees. Because of fuel and supersonic air space limitations, data had to be collected in either a slowly varying acceleration or deceleration mode.

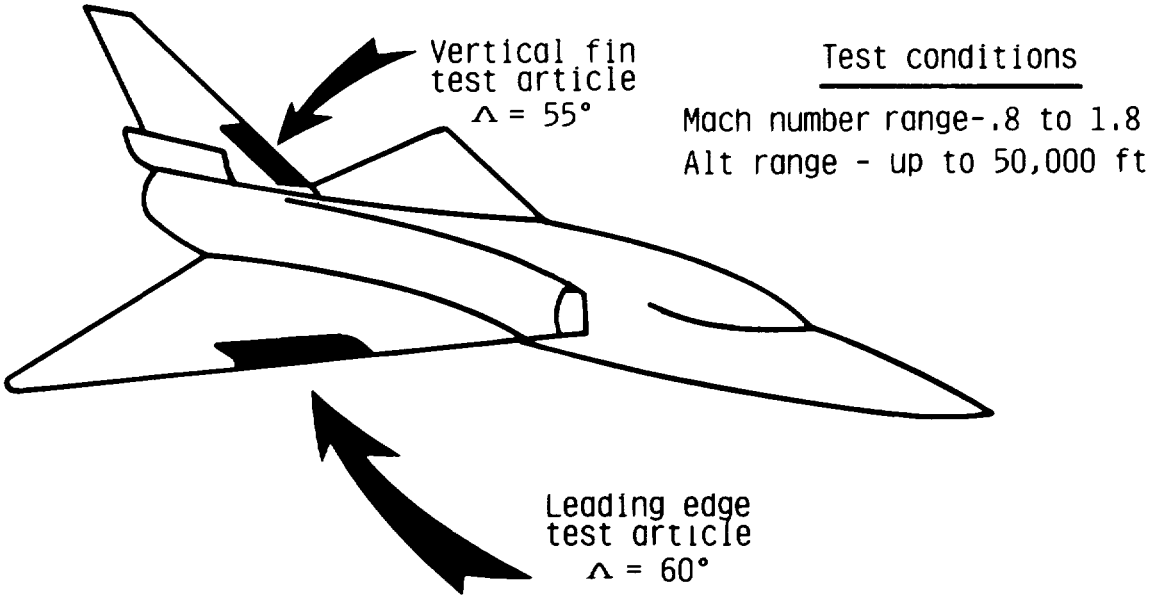

F-106 WING GLOVE

The surface clean-up glove on the right wing of the F-106 is shown in the figure below. The glove has a span of about 3 feet and extends beyond 20% chord. Surface pressure measurements were made in two rows on the wing. The inboard row consists of 18 flush taps on the glove followed by a Strip-A-Tube pressure belt with 12 taps. The outboard row consists of 20 flush orifices on the glove followed by a 10 tap Strip-A-Tube belt. The inboard and outboard pressure rows were oriented in the streamwise direction and were located at fractional semispan locations of about 0.5 and 0.6, respectively. A set of eight hot-film sensors are mounted on the glove for transition detection purposes. The hot-film sensors were mounted so that they were normal to the leading edge. The first hot film was located approximately 0.5 inch from the leading edge with others following at intervals of 1.5 inches. Since attachment line contamination was anticipated for this flight test, a Gaster bump was built onto the leading edge near the inboard edge of the glove to alleviate this problem. The best location of the bump was uncertain because of the unknown migration of the attachment line throughout the flight as flight conditions change. Its effectiveness was thus somewhat uncertain.

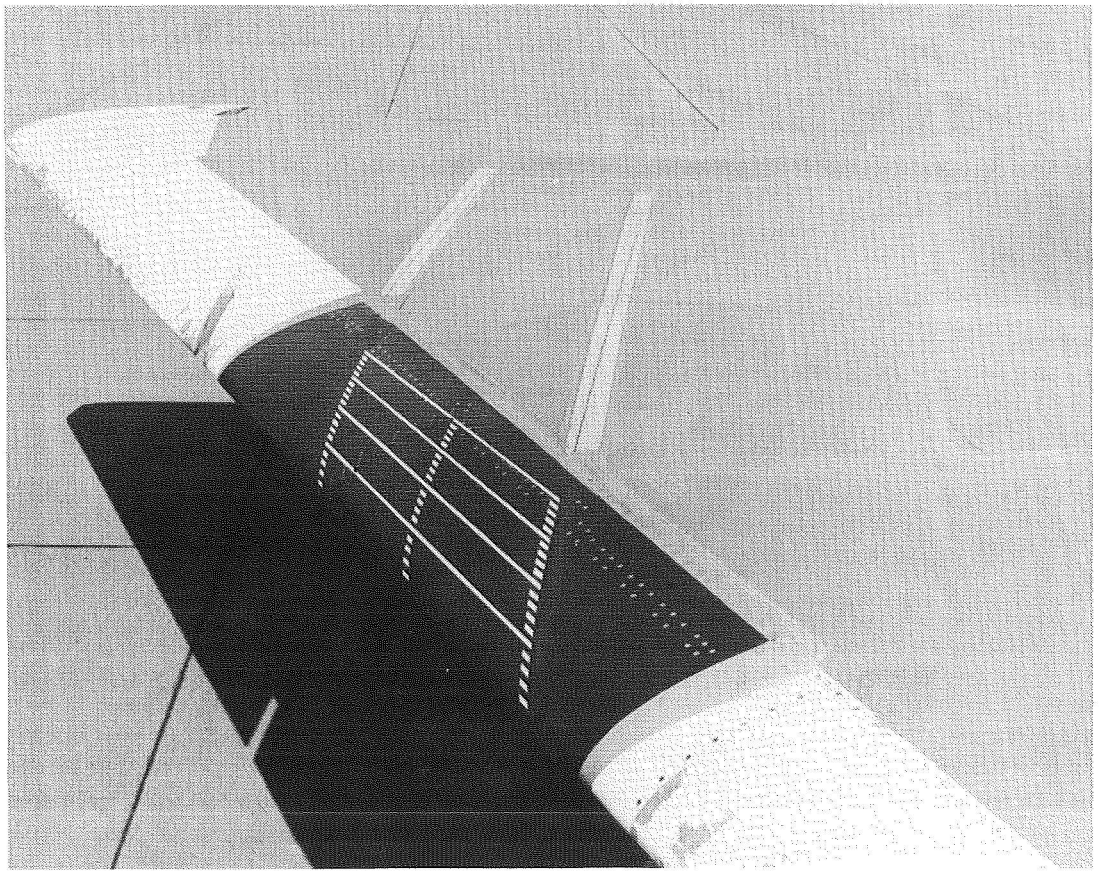

F-106 VERTICAL TAIL GLOVE

The surface clean-up glove for the vertical tail is shown in the figure below. There are two sets of pressure orifices as on the wing. The inboard row consists of 20 flush surface taps, and the outboard row has 16 flush surface taps. Each row is oriented in the streamwise direction. The inboard and outboard rows of pressure orifices are located approximately 15 and 31 inches from the fuselage, respectively. In addition, a set of eight hot-films were mounted on the glove for transition detection. The spacing of the hot films on the vertical tail glove was the same as that of the hot films on the wing glove. A Gaster bump was built on the leading edge near the inboard location of the glove to control attachment line contamination. On the vertical tail, the bump could be expected to be more effective than on the wing because the attachment line location (and hence the best position for the bump) was known.

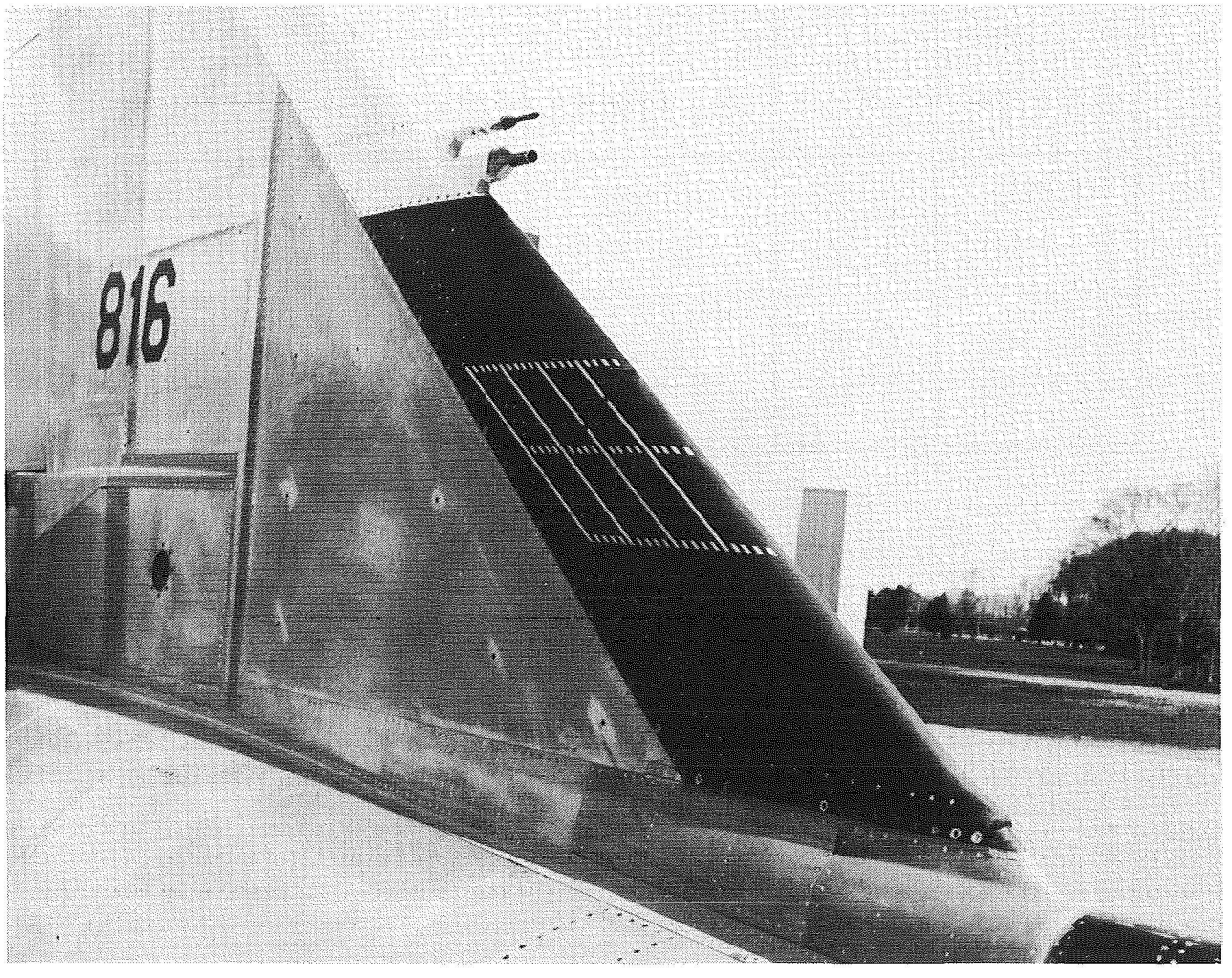

F-106 SUPERSONIC TRANSITION FLIGHT TEST RESULTS

The table below shows four test conditions where transition was observed downstream of the attachment line. For all other test points, turbulent flow existed at the first hot-film gage (0.5% chord). Transition was dominated by attachment line contamination and rapid cross-flow disturbance growth because of the high sweep angles. For many of the flight conditions, it seems that the Gaster bump, utilized to control attachment line contamination, may not have worked; but, it has been effective in other flight tests for controlling attachment line problems and may have just needed to be "fine tuned". It has been shown in previous studies that leading-edge suction is very effective in controlling cross-flow disturbance growth which is present in highly swept applications such as those considered here.

Surface	M_∞	Hp (feet)	α (degrees)	Transition location
Wing $\Lambda = 60°$	0.86 1.50	44000 52000	7.5 5.8	1.5% c 0.5% c
Vertical $\Lambda = 55°$	0.91 1.10	48500 51000	10.5 7.7	5.0% c 1.5% c

F-106 SUPERSONIC BOUNDARY-LAYER FLIGHT TEST RESULTS

Presented in the figure below is the effect of suction on the cross-flow N-factor as predicted by compressible, linear stability theory. The C_p distribution on the vertical tail is shown for M=1.72, altitude of 40,000 feet, and angle of attack of about 2 degrees. For the present flights with no suction on the glove, the results show that the cross-flow N-factor increases very rapidly in the region of the attachment line. As shown below, N_{cf} has a value of 10 at 2% chord. With the suction distribution shown on the right, the cross-flow N-factor is reduced significantly. The N_{cf} has a maximum of about 6 at 5 percent chord. The disturbances are stable or damped out to about 20 percent chord. This level of growth is considered to be below the critical value for transition.

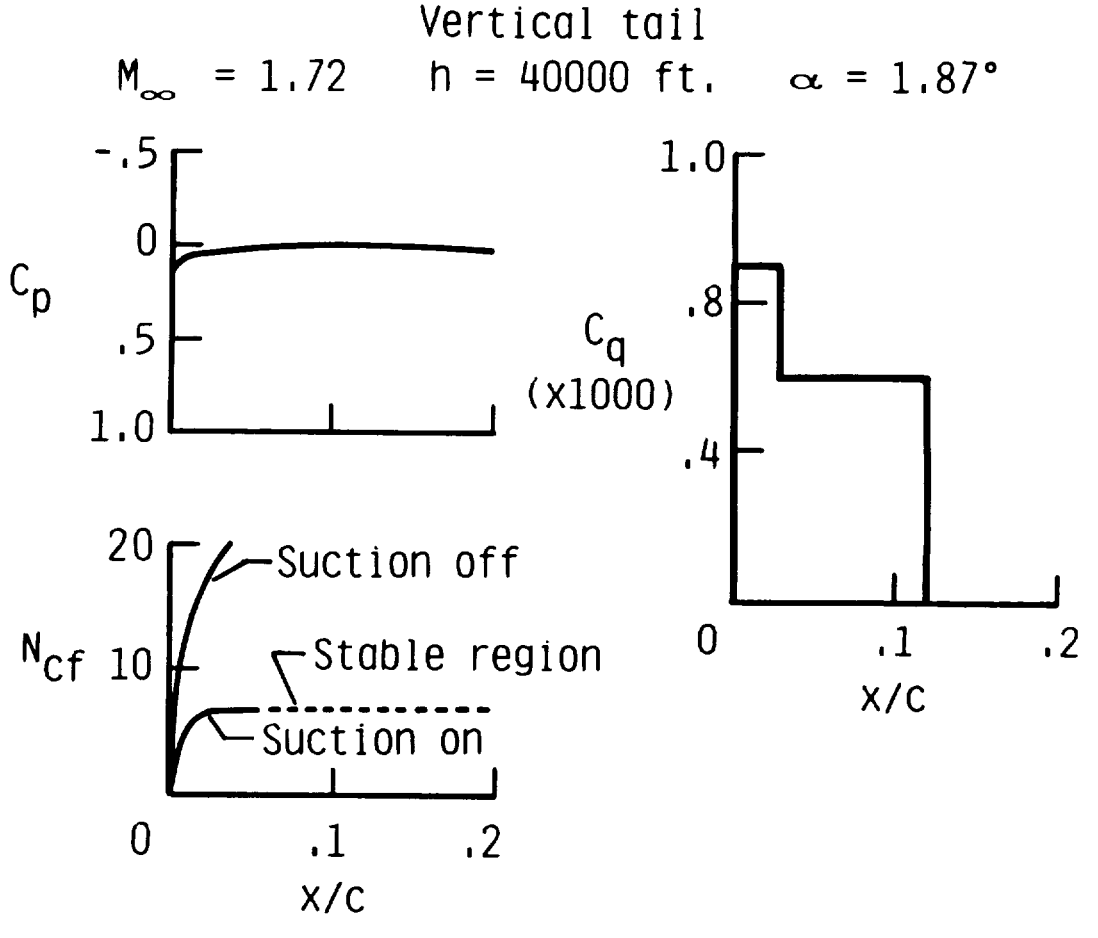

F-106 SUPERSONIC LAMINAR-FLOW FLIGHT EXPERIMENT

The results of these two exploratory supersonic flight tests seem to indicate that to achieve laminar flow past the leading-edge wing box consistently, suction must be utilized in the leading-edge region to control cross-flow disturbance growth. Also, the problem of attachment line contamination must be addressed. By properly designing the leading edge, contamination can be eliminated. Presently, there is growing interest in conducting a supersonic flight test with suction in the leading-edge region. Shown in the figure below, is an artist's rendition of how a test article including leading-edge box suction followed by a natural laminar-flow glove would appear on the LaRC F-106. The feasibility of such a flight test is currently being studied at the LaRC.

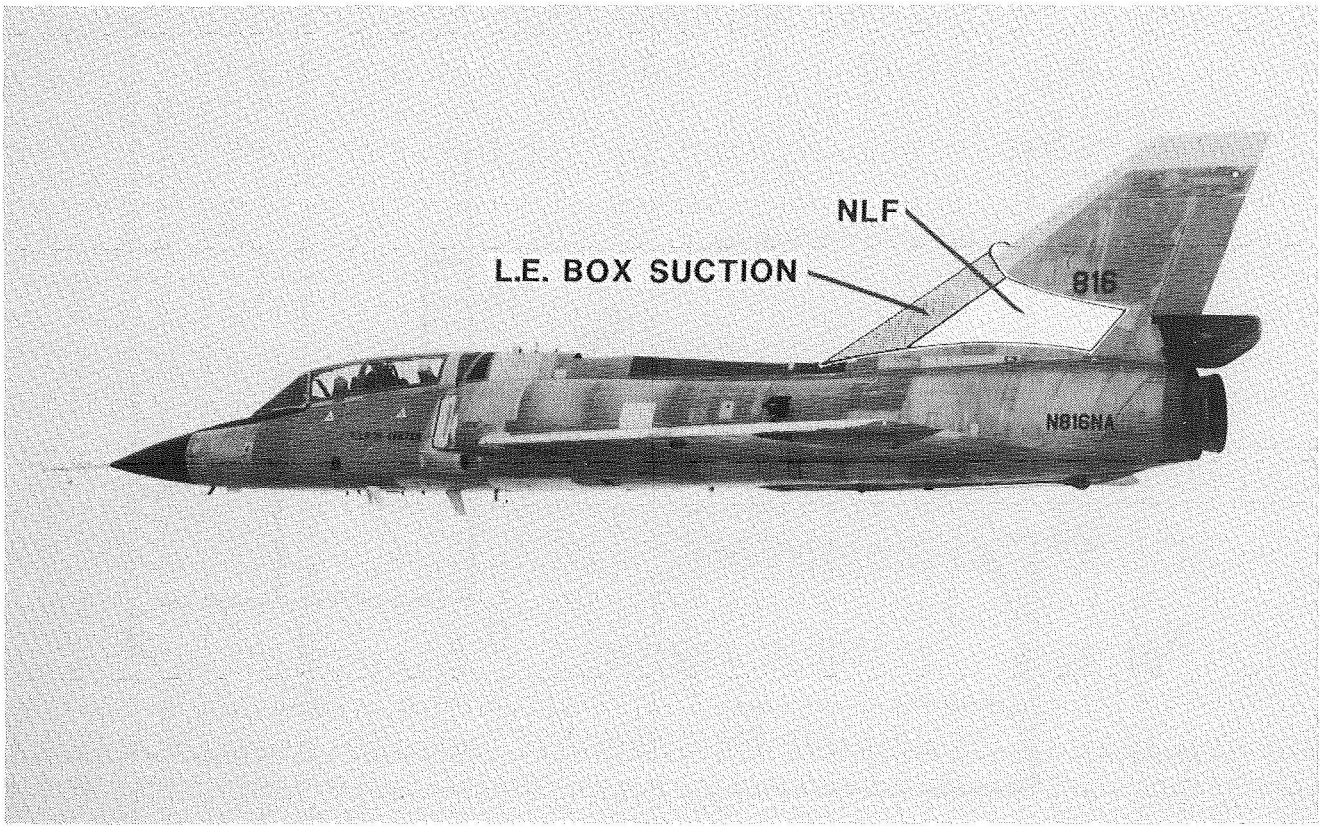

SUMMARY

For the case of the F-15 flight tests, boundary-layer transition was observed up to Mach numbers of 1.2. For very limited and specific flight conditions, laminar flow existed back to about 20% chord on the surface clean-up glove. The hot-film instrumentation was effective for locating the region of transition.

For the F-106 flight tests, transition on the wing or vertical tail generally occurred very near the attachment line. Transition was believed to be caused by either attachment line contamination or strong cross-flow development due to the high sweep angles of the test articles.

The compressible stability analysis showed that cross-flow N-factors were in the range of 5-12 at transition. Future plans are to analyze the results including the effects of surface curvature and non-stationary cross-flow disturbances. It was shown that cross-flow Reynolds numbers at transition correlated well with previous incompressible results.

F-15 Flight Tests

- Boundary layer transition was observed up to Mach numbers of 1.2
- Hot film instrumentation worked well for locating the region of transition

F-106 Flight Tests

- Transition on the wing or vertical tail generally occurred very near the attachment line
- Transition was believed to be due to either attachment line contamination or strong crossflow development due to the high sweep

Stability analysis

- N-factors at transition were in the range of 5-12
- Crossflow Reynolds numbers at transition correlated well with previous incompressible results

REFERENCES

1. Chiles, Harry R.; and Johnson, J. Blair: Development of a Temperature-Compensated Hot-Film Anemometer System for Boundary-Layer Transition Detection on High Performance Aircraft. NASA TM 86732, 1985.

2. Poll, D. I. A.: Some Aspects of the Flow Near a Swept Attachment Line with Particular Reference to Boundary Layer Transition. Cranfield Institute of Technology, CoA Report No. 7805, 1978.

PART II: AERODYNAMIC PREDICTIONS

O. J. Rose
PRC Kentron, Inc.
Hampton, Virginia

D. S. Miller
NASA Langley Research Center
Hampton, Virginia

[redacted]

INTRODUCTION

Current boundary-layer transition analysis methods require boundary-layer profiles generated from a code which requires as input the surface pressures and velocities taken from an inviscid flow code or from experimental data (ref. 1). The purpose of this study was to examine a specific nonlinear flow code (NCOREL) as a candidate for supplying the necessary inviscid flow information (refs. 2, 3).

The approach was to compare calculated pressures with the surface pressures measured in flight on the wing of an F-106 aircraft. Special attention was given to the location of the attachment line and the pressure distribution in the immediate vicinity of the wing leading edge. Comparisons were made at three different supersonic flight conditions.

AERODYNAMIC PREDICTIONS: INTRODUCTION

- Objective: Validate usefulness of non-linear full potential method for application to laminar flow research at supersonic speeds
- Approach: Compare full potential solutions and surface pressures measured in flight on F-106 A/C
  - NCOREL code (wing alone and wing body)
  - Comparisons at three flight conditions

FLIGHT PROFILE AND SENSOR LOCATION

The flight profile is shown in the upper portion of the figure in terms of angle of attack and Mach number. The angle of attack ranged from approximately 2 to 4 degrees and the Mach number ranged from approximately 0.80 to 1.75. The three specific flight conditions selected for making the pressure data comparison are indicated by the open symbols. Specifically, the three cases of respective angles of attack and Mach number are: 2.69° and 1.40; 5.92° and 1.43; 2.37° and 1.72.

As shown in the lower portion of the figure, the pressure sensors were arranged streamwise at two locations corresponding to semi-span fractions of 0.509 and 0.592. The pressure sensors were located from less than 1/2 percent chord on the lower surface around the leading edge to approximately 40 percent chord on the upper surface. This arrangement was selected to provide detailed coverage around the leading edge of the wing and on the wing's upper surface.

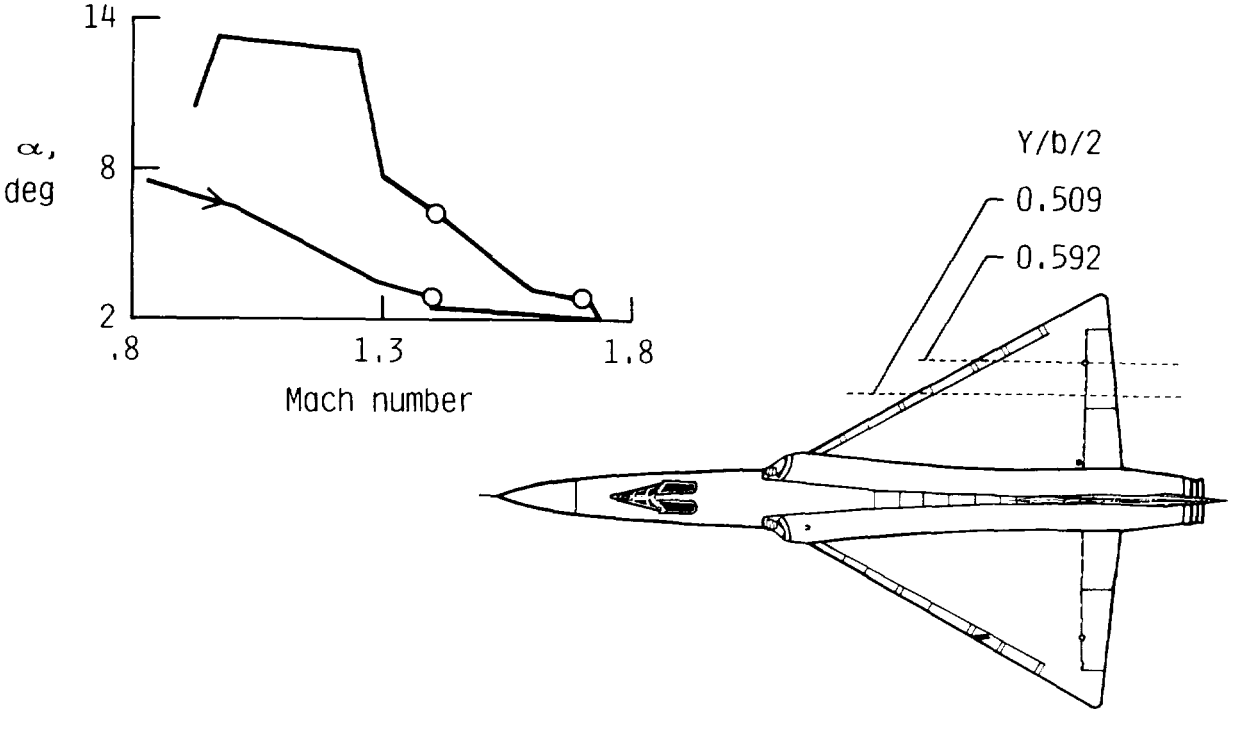

FEATURES OF NONLINEAR FLOW ANLAYSIS CODE (NCOREL)

The essential details of the full-potential flow code (NCOREL) are listed in the figure. This code solves the nonlinear full-potential equation for configurations having supersonic free-stream Mach number and attached bow shocks. The solution procedure uses an implicit marching scheme and is thus limited to flows supersonic in the marching direction. The grid generation is accomplished using conformal mapping techniques and is presently able to treat wing-body-inlet configurations. This grid generation is ideal for studying flow transition because it naturally clusters grid points around the leading edge. The inlet modeling assumes 100 percent captured mass flow, i.e., no spillage. The configuration geometry can be described as discrete points or analytic equations or a combination; the F-106 is described entirely by discrete points. In this study, only surface pressures are examined; however, all flow quantities are available. It will be necessary to have both surface pressures and velocities for application to fully three-dimensional boundary layers.

- Solves non-linear full potential equation
- Supersonic implicit marching scheme
- Configurations may have fuselage, wing, inlet
- Geometry representation can be
  - Pointwise
  - Analytic
  - Mixed
- Internally generated computational grid
- All flow field and surface quantities available

F-106 COMPUTATIONAL GEOMETRY

One of the objectives of the study was to examine the necessary configuration modeling requirements. Thus computational results were obtained for both a complex wing-body-inlet and a simple wing-alone representation. It was estimated that a factor of four in computational time and time required to prepare input could be saved if the wing-alone representation was found to be adequate.

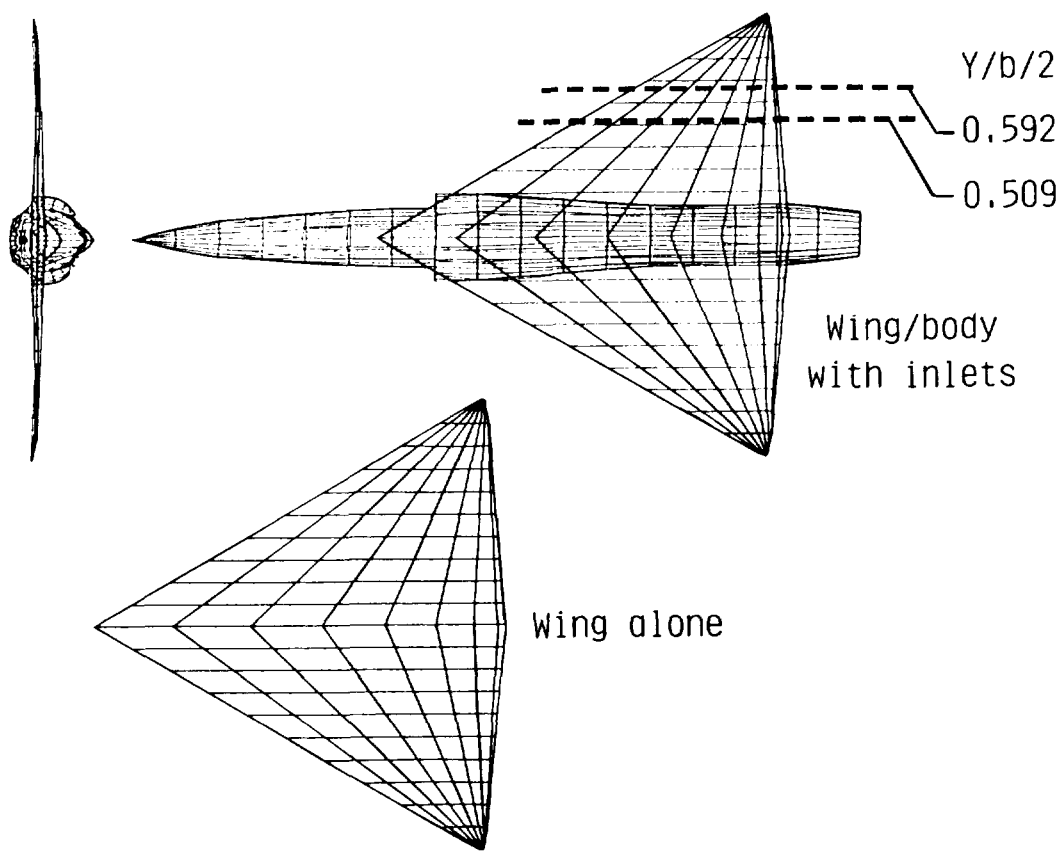

MEASUREMENT/THEORY COMPARISON

(M = 1.4, Alpha = 2.69)

Experimental and theoretical pressures are presented in the next three figures. In each figure, the results are displayed by plotting C_p as a function of Φ, where Φ is an angular representation of the chord fraction. As indicated in the sketch in the figure, the value of $\Phi = 0^0$ corresponds to the wing leading edge, and positive and negative values correspond to the upper and lower surface respectively.

The F-106 wing has leading-edge camber, and for the Mach number and angle of attack considered here the pressure measurements exhibit extreme variations. In particular, there are two strong suction peaks, one on the lower surface and one on the upper surface in addition to the high pressure value at the attachment line.

In the region of the leading edge, the character of the highly varying pressure distribution is faithfully predicted by both the wing alone and the wing-body-inlet configurations. The location of the flow attachment line, characterized by the maximum pressure coefficient, and the location of both suction peaks are well predicted. At this condition of Mach number and angle of attack, the pressure magnitude at the attachment line is accurately predicted at the outboard span station but is substantially underpredicted at the inboard station. The magnitudes of the suction peaks are underestimated. In the region of the upper surface suction peak and just downstream the wing-body-inlet pressures are in closer agreement with the experimental data than are the wing-alone pressures.

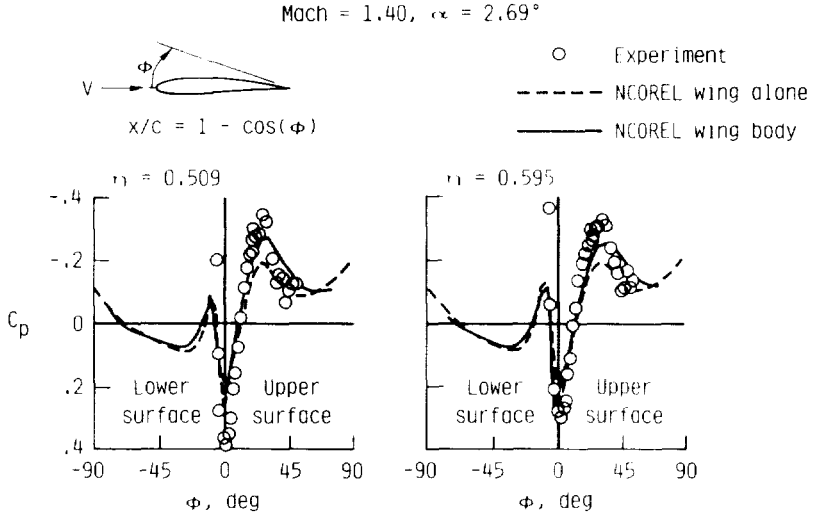

MEASUREMENT/THEORY COMPARISON

(M = 1.43, Alpha = 5.92)

The results shown in this figure are for a Mach number essentially the same as the previous case, but at a higher angle of attack. At this higher angle of attack, the measured pressures no longer exhibit a suction peak on the lower surface and the upper surface suction peak is significantly larger. The character of the pressure distribution is quite different from the previous case and is well predicted, with good agreement except near the upper surface suction peak where the theory underestimates the suction by about 15 percent. The wing-body-inlet and wing-alone results agree up to the upper surface suction peak which is near d = 40° or 23 percent of the local chord. For the region downstream of the suction peak, the wing-body-inlet results are in good agreement, and the wing alone significantly overpredicts pressure.

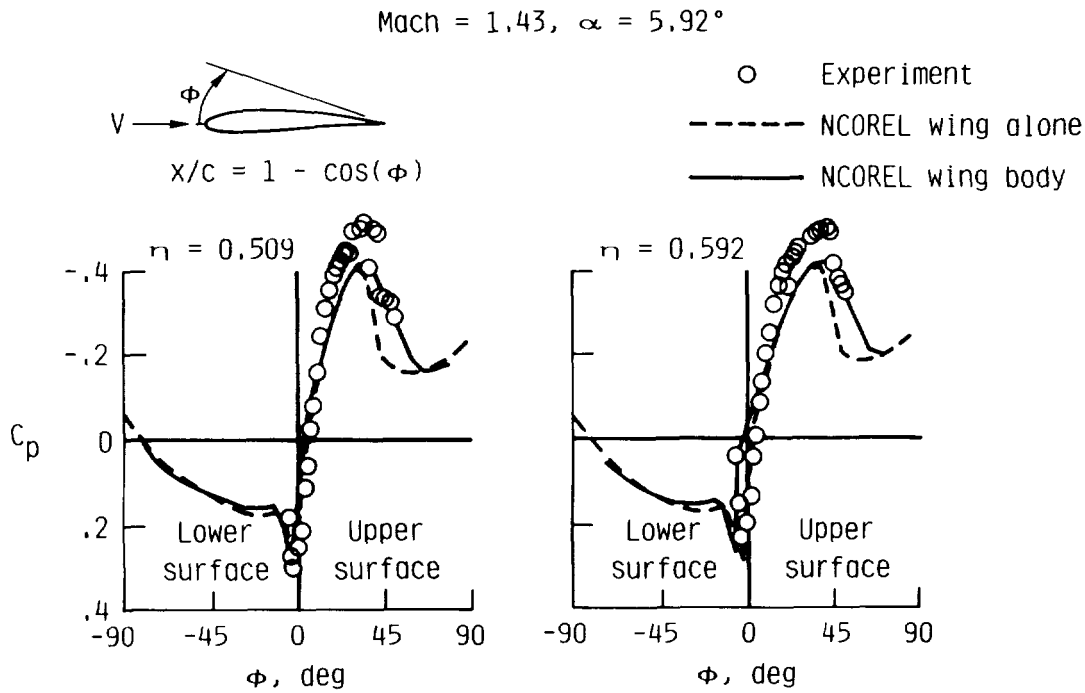

MEASUREMENT/THEORY COMPARISON

(M = 1.72, Alpha = 2.37)

The data shown in this figure are for a Mach number of 1.72 and an angle of attack of 2.37°. At this low angle-of-attack condition, the measured pressures again exhibit two suction peaks as there were for the M = 1.4 and alpha = 2.69 case. For the present case, the two suction peaks are of nearly equal strength.

As in the previous two figures, the character of the pressure distribution, the location of the attachment line, the location of attachment line, the location of the suction peaks, and the stagnation pressure magnitudes are well predicted.

Overall, the agreement between data and theory is closer for this higher Mach number case. Again, the wing alone and wing-body-inlet results agree except for the region downstream of the upper suction peak, which occurs at about $\Phi = 40°$ or 23 percent of chord.

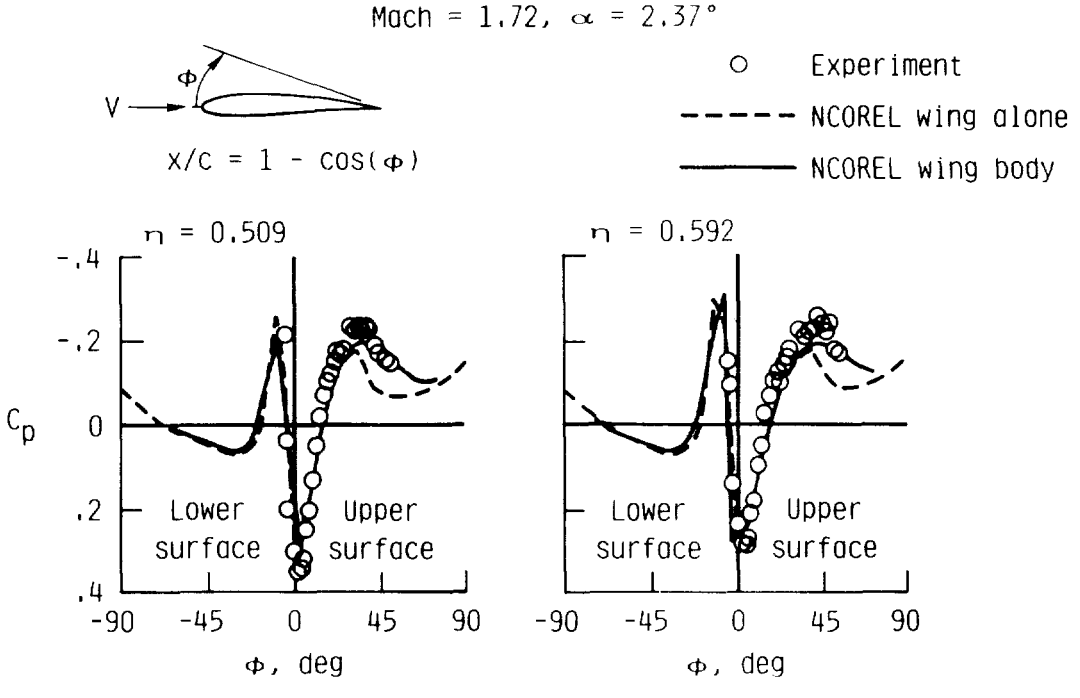

AERODYNAMIC PREDICTIONS: SUMMARY

In the leading-edge region, the measured pressure distributions exhibit extreme variations from strong suction peaks to a pressure maximum at the attachment line. These variations occur over short distances on the wing surface, and their character changes with changes in Mach number and angle of attack.

The data/theory comparisons show that the character of the measured pressure distributions is well predicted for every Mach number/angle-of-attack condition considered. There is good agreement between theory and experiment for the location of the attachment line and suction peaks. The pressure magnitudes are well represented in the critical leading-edge region, including the pressure maximum on the attachment line. The wing/body/inlet results agree well with the wing alone back to about 20 percent of chord where the upper surface suction peak typically occurs.

The largest differences between theory and measurement always occur in the vicinity of suction peaks, with the difference being approximately 15 percent or less. In the regions of largest error, the predicted pressures underestimate the suction peak strength for each case considered.

The results show the ability of the NCOREL code to reproduce all the essential characteristics of the wing pressure. Moreover, the wing-alone results agree well enough with the wing-body-inlet to justify use of this simplification at least for preliminary design. Although these results are encouraging, the suction peak magnitudes are underestimated, and the effect of this on the boundary-layer stability analysis must be determined.

REFERENCES

1. Malik, Mujeeb R.: COSAL--A Black Box Compressible Stability Analysis Code for Transition Prediction in Three-Dimensional Boundary Layers. NASA CR-165925, May 1982.

2. Siclari, Michael J.: The NCOREL Computer Program for 3D Nonlinear Supersonic Potential Flow Computations. NASA CR-3694, August 1983.

3. Siclari, Michael J.: Supersonic Nonlinear Potential Flow Analysis--Interim Report. NASA CR-172456, August 1984.

NASA National Aeronautics and Space Administration

Report Documentation Page

1. Report No.	2. Government Accession No.	3. Recipient's Catalog No.
NASA CP-2487, Part 3		

4. Title and Subtitle	5. Report Date
Research in Natural Laminar Flow and Laminar-Flow Control	December 1987
	6. Performing Organization Code

7. Author(s)	8. Performing Organization Report No.
Jerry N. Hefner and Frances E. Sabo, Compilers	L-16350
	10. Work Unit No. 505-60-31-06

9. Performing Organization Name and Address	11. Contract or Grant No.
NASA Langley Research Center Hampton, VA 23665-5225	
	13. Type of Report and Period Covered
12. Sponsoring Agency Name and Address	Conference Publication
National Aeronautics and Space Administration Washington, DC 20546-0001	14. Sponsoring Agency Code

15. Supplementary Notes

16. Abstract

Since the mid 1970's, NASA, industry, and universities have worked together to conduct important research focused at developing laminar-flow technology that could reduce fuel consumption for general aviation, commuter, and transport aircraft by as much as 40 to 50 percent. This research, which was initiated under the NASA Aircraft Energy Efficiency Program and continued through the Research and Technology Base Program, has proved very successful with many very significant and impressive results having been obtained.

This symposium was planned in view of the recent accomplishments within the areas of laminar-flow control and natural laminar flow, and the potential benefits of laminar-flow technology to the civil and military aircraft communities in the United States. The symposium included technical sessions on advanced theory and design tool development, wind tunnel and flight research, transition measurement and detection techniques, low and high Reynolds number research, and subsonic and supersonic research.

17. Key Words (Suggested by Author(s))	18. Distribution Statement
Laminar flow Natural laminar flow Aerodynamics	[redacted] Subject Category 02

19. Security Classif. (of this report)	20. Security Classif. (of this page)	21. No. of pages	22. Price
Unclassified	Unclassified	402	

[redacted]